

AD-A034 282

MCDONNELL AIRCRAFT CO ST LOUIS MO
TURBINE ENGINE MULTI-MISSION PROPULSION SIMULATOR WIND TUNNEL D--ETC(U)
NOV 76 M F EIGENMANN, R L BEAR, T C CHANDLER F33615-73-C-2051

F/6 21/5

UNCLASSIFIED

AFAPL-TR-76-73

NL

4
OF
AD
A034282

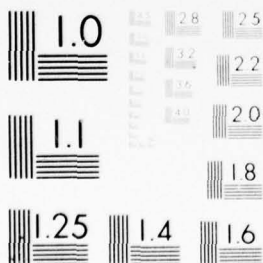


1 OF 4

AD

A034282

ADA034282



MICROCOPY RESOLUTION TEST CHART
NATIONAL BUREAU OF STANDARDS-1963-A

ADA 034282

AFAPL-TR-76-73

(12)

J

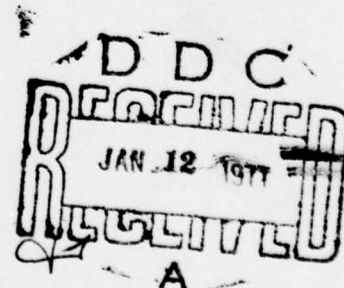
TURBINE ENGINE MULTI-MISSION PROPULSION SIMULATOR WIND TUNNEL DEMONSTRATION

**MCDONNELL DOUGLAS CORPORATION
MCDONNELL AIRCRAFT COMPANY
P.O. BOX 516
ST. LOUIS, MISSOURI 63166**

NOVEMBER 1976

**TECHNICAL REPORT AFAPL-TR-76-73
FINAL REPORT FOR PERIOD 29 JUNE 1973 - 30 OCTOBER 1976**

Approved for public release; distribution unlimited



**AIR FORCE AERO PROPULSION LABORATORY
AIR FORCE WRIGHT AERONAUTICAL LABORATORIES
AIR FORCE SYSTEMS COMMAND
WRIGHT-PATTERSON AIR FORCE BASE, OHIO 45433**

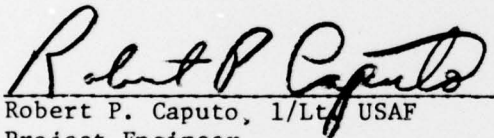
NOTICE

When Government drawings, specifications, or other data are used for any purpose other than in connection with a definitely related Government procurement operation, the United States Government thereby incurs no responsibility nor any obligation whatsoever; and the fact that the government may have formulated, furnished, or in any way supplied the said drawing, specifications, or other data, is not to be regarded by implication or otherwise as in any manner licensing the holder or any other person or corporation, or conveying any rights or permission to manufacture, use, or sell any patented invention that may in any way be related thereto.

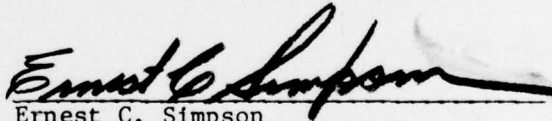
This report has been reviewed by the Information Office, (ASD/OIP) and is releasable to the National Technical Information Service (NTIS). At NTIS, it will be available to the general public, including foreign nations.

This technical report has been reviewed and is approved for publication.

For the Commander



Robert P. Caputo, 1/Lt, USAF
Project Engineer,
Turbine Engine Division
Air Force Aero Propulsion Laboratory



Ernest C. Simpson
Director,
Turbine Engine Division
Air Force Aero Propulsion Laboratory

Copies of this report should not be returned unless return is required by security considerations, contractual obligations, or notice on a specific document.

SECURITY CLASSIFICATION OF THIS PAGE (When Data Entered)

REPORT DOCUMENTATION PAGE		READ INSTRUCTIONS BEFORE COMPLETING FORM
1. REPORT NUMBER AFAPL-TR-76-73	2. GOVT ACCESSION NO.	3. RECIPIENT'S CATALOG NUMBER
4. TITLE (and Subtitle) Turbine Engine Multi-Mission Propulsion Simulator Wind Tunnel Demonstration		5. TYPE OF REPORT & PERIOD COVERED Final Report • July 1973 through October 1976
6. PERFORMING ORG. REPORT NUMBER		
7. AUTHOR(s) M.F. Eigenmann R.L. Bear T.C. Chandler		8. CONTRACT OR GRANT NUMBER(s) F33615-73-C-2051
9. PERFORMING ORGANIZATION NAME AND ADDRESS McDonnell Aircraft Co. McDonnell Douglas Corporation P.O. Box 516, St. Louis, Mo. 63166		10. PROGRAM ELEMENT, PROJECT, TASK AREA & WORK UNIT NUMBERS Project No. 668A
11. CONTROLLING OFFICE NAME AND ADDRESS Air Force Aero Propulsion Laboratory (TBP) Air Force Wright Aeronautical Laboratories Air Force Systems Command-WPAFB, Ohio 45433		12. REPORT DATE November 1976
14. MONITORING AGENCY NAME & ADDRESS (if different from Controlling Office)		13. NUMBER OF PAGES 328
		15. SECURITY CLASS. (of this report) Unclassified
		15a. DECLASSIFICATION/DOWNGRADING SCHEDULE
16. DISTRIBUTION STATEMENT (of this Report) Approved for public release; distribution unlimited.		
17. DISTRIBUTION STATEMENT (of the abstract entered in Block 20, if different from Report)		
18. SUPPLEMENTARY NOTES		
19. KEY WORDS (Continue on reverse side if necessary and identify by block number) Propulsion Simulator Inlet/Airframe/Nozzle Interactions Simulator Test Technique Conventional Test Technique Aerodynamic Performance Comparison		
20. ABSTRACT (Continue on reverse side if necessary and identify by block number) → A turbine engine multi-mission propulsion simulator, developed by the Air Force Aero Propulsion Laboratory (AFAPL) to permit improved aircraft performance prediction capability through the simultaneous simulation of inlet/airframe/nozzle flowfields, was successfully demonstrated in a wind tunnel model tested in the Arnold Engineering Development Center 16 ft. Transonic Tunnel. The model tested is simple, featuring the forebody, inlet and nozzle of an advanced fighter aircraft, but no wings or tail surfaces.		

403 111

log

It is adaptable to three different test modes - simulator - equipped, conventional aero flow-through and conventional jet effects, and provides for the simultaneous measurement of the total airframe, aft-end and simulator forces and moments. Extensive pressure instrumentation is also provided on the fuselage for flowfield interaction studies. Wind tunnel test data was obtained from Mach 0.6 to 1.45, and at angles of attack from -1.6° to 16.0 degrees.

The results of the test indicate that the propulsion simulator is a viable wind tunnel test tool that can be effectively operated under realistic test conditions. Comparison of the aerodynamic performance of this configuration, as obtained from both simulator and conventional test techniques, showed relatively small differences, thereby indicating small inlet/aft-end flowfield interactions for this inlet/nozzle spacing. Data repeatability obtained with the simulator model was comparable to that obtained on the conventional models.

Additional studies indicated that a compact simulator, capable of being installed within properly scaled aircraft moldlines, is feasible. Also, simulator-equipped models offer small potential cost savings over conventional models in the prediction of aircraft aerodynamic performance.

It is expected that the simulator will ultimately find extensive usage on aircraft with potentially significant inlet/airframe/nozzle flowfield interactions.

FOREWORD

This report was prepared by the McDonnell Aircraft Company (MCAIR), a division of the McDonnell Douglas Corporation, St. Louis, Missouri, for the Air Force Aero Propulsion Laboratory, Air Force Systems Command, United States Air Force, Wright-Patterson Air Force Base, Ohio. The study was performed under Air Force Contract F33615-73-C-2051, "Turbine Engine Multi-Mission Propulsion Simulator Wind Tunnel Demonstration," Project 668A. The work was performed from July 1973 through October 1976, with 1/Lt. R. P. Caputo (AFAPL/TBP) of the Air Force Aero Propulsion Laboratory as Project Engineer. The MCAIR efforts in this program were accomplished under the direction of R. E. Martens and M. F. Eigenmann with the assistance of R. L. Bear, T. C. Chandler, A. H. Knouff, E. L. Pilkington and T. L. Southerland.

The authors of this report, Mr. Eigenmann, Mr. Bear, and Mr. Chandler, are particularly indebted to J. H. Clark, D. A. Kopp, and E. R. Popham of MCAIR for their effort throughout the wind tunnel model preparation, calibration, and test phases. The authors also commend the AEDC ETF project engineer, J. O. Brooks, and PWT project engineer, J. F. Riddell, for their efforts. Additionally, the authors are indebted to B. R. Delaney, H. West, B. R. Romine, and R. G. Ruegg of the General Electric Company, Aircraft Engine Group, Cincinnati, Ohio, and D. J. Balster, Tech Development, Inc., Dayton, Ohio, for their efforts during this program. Special acknowledgements are due R. E. Martens, C. W. Miller, H. Sams, W. C. Trent, and W. B. Weber for their contributions.

This report was submitted by the authors in November 1976.

013		DATE	11/1/76
000		TIME	10:00
UNCLASSIFIED			
REPRODUCTION			
BY			
FOR			
DATE			
BY			
DATE			
BY			
DATE			

SUMMARY

The turbine engine multi-mission propulsion simulator was developed by the Air Force Aero Propulsion Laboratory (AFAPL) to permit improved aircraft performance prediction capability through the simultaneous simulation of inlet/airframe/nozzle flowfields on wind tunnel models. The simulator was successfully demonstrated installed in a model in a wind tunnel test program by the McDonnell Aircraft Company with major support by General Electric Company, under contract to AFAPL. The basic objectives of this program were to:

- o Determine if the simulator is a viable test tool
- o Evaluate the relative accuracy of the simulator test technique when compared to a conventional test technique.
- o Identify relative costs between test techniques for the performance prediction of advanced aircraft.

The model used in the test program is simple, incorporating an 8.5 percent scale F-15 forebody, a single inlet, and nozzle system, but no wings or tail surfaces. It was necessary to enlarge the mid-fuselage of the model from that of the scaled aircraft to accommodate the current simulator hardware. A compact simulator design was developed during this program to eliminate this problem for future aircraft model installations. The model is adaptable to three different test modes - simulator-equipped, conventional aero flow-thru, and conventional jet effects. The model also provides for the simultaneous measurement of the total airframe, aft-end, and simulator forces and moments, as well as extensive surface pressure instrumentation.

The test program was conducted in the Arnold Engineering Development Center (AEDC) 16-Foot Transonic (16T) Wind Tunnel. The testing was conducted primarily in the Mach 0.6 to 1.2 range and at angles of attack from -1.6° to 16° . Limited data was obtained at Mach 1.45. The conclusions from this test program, subsequent data analyses, and additional program studies are that:

- o The propulsion simulator is a viable test tool that can be effectively operated in a wind tunnel model behind a realistic aircraft inlet.
- o Relatively small differences ($\Delta C_D \leq .0004$ at Mach 0.9, $\alpha \leq 10^\circ$) exist in the aerodynamic performance of this far-coupled inlet/ nozzle configuration, as obtained from both the simulator and conventional test techniques.
- o Data repeatability ($2 \sigma_{C_D} \sim \pm .0003$) is comparable between the simulator and conventional test techniques.

- o The simulator test technique offers small potential savings of 4% in direct costs, and 13% in wind tunnel occupancy hours, in the performance prediction of a typical advanced fighter aircraft.

It is recommended that for installation in representative advanced aircraft configurations, the compact simulator be developed. It is expected that the simulator will ultimately find extensive usage on aircraft with potentially significant inlet/airframe/nozzle flowfield interactions.

TABLE OF CONTENTS

<u>Section</u>	<u>Page</u>
1. Introduction.	1
2. Simulator and Support Equipment	4
2.1 Simulator Components.	4
2.2 Simulator Control System.	7
2.3 Lubrication System.	7
3. Wind Tunnel Demonstration Model	12
3.1 Design Features	12
3.2 Instrumentation	24
4. Wind Tunnel Test Program.	29
4.1 Test Facility	29
4.2 Test Conditions and Procedures.	29
4.3 Data Reduction.	32
4.4 Data Accuracy	32
5. Wind Tunnel Test Results	39
5.1 Aerodynamic Performance Evaluation.	41
5.1.1 Thrust/Drag Accounting System	46
5.1.2 Test Technique Comparison	55
5.1.3 Inlet/Aft-End Interactions	67
5.2 Nozzle Performance Evaluation	90
5.2.1 Flow Characteristics.	90
5.2.2 Thrust Characteristics.	92
6. Simulator Mechanical Operation.	95
6.1 General Simulator Operation	95
6.2 Operational Flexibility	99
6.3 Diagnostic Data	101
6.4 Disassembly/Inspection Results.	102
7. Compact Simulator Design Study.	108
7.1 Conceptual Design Effort.	108
7.2 Design Envelope Verification.	109
7.3 Structural Life and Cost Reduction Analyses	112
8. Assessment of Potential Cost Savings for Simulator Models	114
8.1 Wind Tunnel Model Conceptual Designs.	115
8.2 Pre-Test Check-Out/Calibration Activities	116
8.3 Wind Tunnel Test Plans.	122
8.4 Cost Estimates.	125
9. Conclusions and Recommendations	127
 <u>APPENDICES</u>	
A. Proposed Future Simulator Utilization	130
B. Model Calibration	136
C. Simulator Static Test Programs.	146
D. Total Airframe and Aft-End Force and Moment Data	163
REFERENCES.	328

LIST OF FIGURES

<u>Figure No.</u>	<u>Title</u>	<u>Page</u>
1-1	Turbine Engine Multimission Propulsion Simulator	2
1-2	Simulator Wind Tunnel Demonstration Model	3
2-1	Simulator Schematic	4
2-2	Simulator Compressor/Turbine Characteristics	5
2-3	Simulator Control Console	8
2-4	Simulator Lubricating Oil Supply Pump	9
2-5	Simulator Lubricating Oil Scavenge System	11
3-1	General Features of the Wind Tunnel Model	13
3-2	Wind Tunnel Model Area Distribution	14
3-3	Model Test Modes	15
3-4	Inlet Geometry for Various Test Modes	16
3-5	Inlet Auxiliary Bypass Door for Simulator Protection During Supersonic Operation	17
3-6	Nozzle Geometry	18
3-7	Exit Chokes and Pressure Rakes	19
3-8	Force Balance Arrangement and Bridging Mechanisms	20
3-9	Reduction of Bias Error Due to Total Airframe Balance Thermal Stresses	22
3-10	Thermal Control System for the Total Airframe Balance	23
3-11	Thermal Control System for the Simulator Balance	23
3-12	Model/Simulator Pressure Instrumentation	25
3-13	Major Internal Model Pressure Instrumentation	26
3-14	External Surface Pressure Instrumentation	27
4-1	Model Installation in the AEDC 16 Foot Transonic Tunnel	30
4-2	Wind Tunnel Test Summary	31
4-3	Total Airframe Drag and Lift Data Reduction Summary for Simulator Test Mode	33
4-4	Total Airframe Drag and Lift Data Reduction Summary for Aero Flow-Thru Test Mode	34
4-5	Aft-End Drag and Lift Data Reduction Summary for Simulator and Jet Effects Test Modes	35
4-6	Simulator Thrust Data Reduction Summary	35
4-7	ESIP Error Analysis Procedure	36
4-8	Predicted Error in Important Vehicle Performance Parameters	37
4-9	Primary Contributors to Drag Coefficient Random Error	37

LIST OF FIGURES (Continued)

<u>Figure No.</u>	<u>Title</u>	<u>Page</u>
4-10	Experimental Data Repeatability	38
5-1	Typical Wind Tunnel Model Requirements for Aircraft Performance Prediction	39
5-2	Types of Error	40
5-3	Potential Bias Error Sources in Conventional Wind Tunnel Models	40
5-4	Actual Engine Operating Conditions for Aerodynamic Performance Definition	42
5-5	Typical Lift, Drag, and Pitching Moment Characteristics	43
5-6	Typical External Surface Pressure Distribution at Mach 0.9, $\alpha = 0^\circ$	44
5-7	Typical External Surface Pressure Distribution at Mach 0.9, $\alpha = 10^\circ$	45
5-8	Comparison of Analytical and Experimental Surface Pressure Distribution	46
5-9	A Typical Thrust/Drag Accounting System for Evaluation of Aircraft Performance	47
5-10	Procedure for Aerodynamic Performance Build-Up	48
5-11	Determination of Mass Flow Ratio Correction Increment	49
5-12	Determination of Nozzle Pressure Ratio and Geometry Correction Increments	50
5-13	Typical Buildup of Correction Increments to Basic Aero Flow-Thru Model Data	51
5-14	Drag Corrections to Basic Aero Flow-Thru Model Data	52
5-15	Lift Corrections to Basic Aero Flow-Thru Model Data	53
5-16	Pitching Moment Corrections to Basic Aero Flow-Thru Model Data	54
5-17	Total Airframe Lift, Drag, and Pitching Moment Comparison Between Simulator and Conventional Test Techniques at Mach 0.6 (Dry Power Nozzle, Operating Condition No. 2)	56
5-18	Total Airframe Lift, Drag, and Pitching Moment Comparison Between Simulator and Conventional Test Techniques at Mach 0.6 (Dry Power Nozzle, Operating Condition No. 4)	57
5-19	Total Airframe Lift, Drag, and Pitching Moment Comparison Between Simulator and Conventional Test Techniques at Mach 0.9 (Dry Power Nozzle, Operating Condition No. 2)	58
5-20	Total Airframe Lift, Drag, and Pitching Moment Comparison Between Simulator and Conventional Test Techniques at Mach 0.9 (Dry Power Nozzle, Operating Condition No. 4)	59
5-21	Total Airframe Lift, Drag, and Pitching Moment Comparison Between Simulator and Conventional Test Techniques at Mach 1.2 (Dry Power Nozzle, Operating Condition No. 2)	60

LIST OF FIGURES (Continued)

<u>Figure No.</u>	<u>Title</u>	<u>Page</u>
5-22	Total Airframe Lift, Drag, and Pitching Moment Comparison Between Simulator and Conventional Test Techniques at Mach 0.6 (A/B Power Nozzle, Operating Condition No. 5)	61
5-23	Total Airframe Lift, Drag, and Pitching Moment Comparison Between Simulator and Conventional Test Techniques at Mach 0.9 (A/B Power Nozzle, Operating Condition No. 5)	62
5-24	Incremental Drag Difference Between Simulator and Conventional Test Techniques	63
5-25	Incremental Lift Difference Between Simulator and Conventional Test Techniques	64
5-26	Incremental Pitching Moment Difference Between Simulator and Conventional Test Techniques	65
5-27	Comparison of Throttle-Dependent Effects Between Simulator and Conventional Test Techniques	66
5-28	Throttle Dependent Effect on Total Airframe Drag from the Simulator and Jet Effects Models	68
5-29	Throttle Dependent Effect on Aft-End Drag From the Simulator and Jet Effects Models	68
5-30	Effect of Nozzle Geometry on External Surface Pressures at Mach 0.9 (Simulator Model, $\alpha = 0^\circ$)	69
5-31	Effect of Nozzle Geometry on External Surface Pressures at Mach 0.9 (Jet Effects Model, $\alpha = 0^\circ$)	70
5-32	Variation of Total Airframe Performance Parameters with Inlet Mass Flow Ratio at Mach 0.6	72
5-33	Variation of Total Airframe Performance Parameters with Inlet Mass Flow Ratio at Mach 0.9	73
5-34	Variation of Total Airframe Performance Parameters with Inlet Mass Flow Ratio at Mach 1.2	74
5-35	Effect of Inlet Mass Flow Ratio on Aft-End Performance Parameters at Mach 0.6 (Simulator Model, Dry Power Nozzle)	75
5-36	Effect of Inlet Mass Flow Ratio on Aft-End Performance Parameters at Mach 0.9 (Simulator Model, Dry Power Nozzle)	76

LIST OF FIGURES (Continued)

<u>Figure No.</u>	<u>Title</u>	<u>Page</u>
5-37	Effect of Inlet Mass Flow Ratio on Aft-End Performance Parameters at Mach 1.2 (Simulator Model, Dry Power Nozzle)	77
5-38	Incremental Mass Flow Ratio Effects on Aft-End Performance Parameters at Mach 0.9 (Simulator Model, Dry Power Nozzle)	78
5-39	Effect of Inlet Mass Flow Ratio on External Surface Pressures at Mach 0.9 (Aero Flow-Thru Model, $\alpha = 0^\circ$)	79
5-40	Effect of Inlet Mass Flow Ratio on External Surface Pressures at Mach 0.9 (Aero-Flow-Thru Model, $\alpha = 10^\circ$)	80
5-41	Variation of Aft-End Performance Parameters with Nozzle Pressure Ratio at Mach 0.6 - $\alpha = 0^\circ$	82
5-42	Variation of Aft-End Performance Parameters with Nozzle Pressure Ratio at Mach 0.9 - $\alpha = 0^\circ$	83
5-43	Variation of Aft-End Performance Parameters with Nozzle Pressure Ratio at Mach 1.2	84
5-44	Effect of Nozzle Pressure Ratio on Forebody Performance Parameters at Mach 0.6 (Simulator Model, Dry Power Nozzle)	85
5-45	Effect of Nozzle Pressure Ratio on Forebody Performance Parameters at Mach 0.9 (Simulator Model, Dry Power Nozzle)	86
5-46	Effect of Nozzle Pressure Ratio on Forebody Performance Parameters at Mach 1.2 (Simulator Model, Dry Power Nozzle)	87
5-47	Incremental Nozzle Pressure Ratio Effects on Forebody Performance Parameters at Mach 0.9 (Simulator Model, Dry Power Nozzle)	88
5-48	Effect of Nozzle Pressure Ratio on External Surface Pressures at Mach 0.9 (Jet Effects Model, $\alpha = 0^\circ$)	89
5-49	Dry Power Nozzle Flow Characteristics from Wind Tunnel Test	91
5-50	Afterburning Nozzle Flow Characteristics from Wind Tunnel Test	91
5-51	Dry Power Nozzle Thrust Characteristics from Wind Tunnel Test	93
5-52	Afterburning Power Nozzle Thrust Characteristics from Wind Tunnel Test	93

LIST OF FIGURES (Continued)

<u>Figure No.</u>	<u>Title</u>	<u>Page</u>
6-1	Simulator Operating Procedures for Wind Tunnel Test Program	96
6-2	Inlet with Bellmouth Adapter	97
6-3	Pressure Distortion and Recovery Improvement with Inlet Bellmouth Adapter	98
6-4	Simulator Flexibility Demonstrated During Wind Tunnel Test - Dry Power Nozzle	100
6-5	Simulator Flexibility Demonstrated During Wind Tunnel Test - A/B Power Nozzle	100
6-6	Time History of Simulator Operation During AEDC 16T Tunnel Test	101
6-7	Forward Bearing Temperature History During Wind Tunnel Test	102
6-8	Rear Bearing Temperature History During Wind Tunnel Test	103
6-9	Rotor Thrust History During Wind Tunnel Test	103
6-10	Rotor Position History During Wind Tunnel Test	104
6-11	Simulator Vibration History During Wind Tunnel Test	104
6-12	Simulator Details Showing Rotor Lockup Cause	105
7-1	Current Simulator Geometric Details	108
7-2	XM2R Compact Simulator Geometric Details	109
7-3	Comparison of XM2R Compact Simulator Envelope with Scaled Engine Envelopes	110
7-4	Aircraft Configurations Used in Model Design Studies	111
7-5	Cost Reduction Associated with Multiple Simulator Buys	113
8-1	Advanced Fighter Aircraft Selected for Cost Study	114
8-2	Wind Tunnel Models Used for Aerodynamic Performance Cost Evaluations	115
8-3	Schematic of 10.5% Scale Simulator-Equipped Model	117
8-4	Estimate of Advanced Fighter Model and Simulator Instrumentation Requirements	118

LIST OF FIGURES (Continued)

<u>Figure No.</u>	<u>Title</u>	<u>Page</u>
8-5	Schematic of 10.5% Scale Aero Flow-Thru Model	119
8-6	Schematic of 10.5% Scale Jet Effects Model	120
8-7	Major Pre-Test/Test Related Activities for the Simulator-Equipped Model	121
8-8	Major Pre-Test/Test Related Activities for the Conventional Models	122
8-9	Wind Tunnel Test Plan for Simulator-Equipped Aircraft Models	123
8-10	Wind Tunnel Test Plan for Conventional Aircraft Models	124
8-11	Comparison of Simulator and Conventional Test Technique Costs for Aerodynamic Performance Definition	125
A-1	Airframe/Engine Development Program	131
A-2	Airframe Technology Data Sources	132
A-3	Typical Aircraft Thrust/Drag Accounting System Utilizing Conventional Models	134
A-4	Typical Aircraft Thrust/Drag Accounting System Utilizing Simulator-Equipped Models	135
B-1	Installed Balance Calibration Set-Up	137
B-2	Inlet Bleed/Leakage Airflow Calibration	138
B-3	Typical Inlet Bleed Airflow Calibration Results	139
B-4	Typical SN002 Simulator Compressor Map	140
B-5	Correlation of Map and Pressure-Computed Compressor Airflow	141
B-6	Inlet Duct Seal Tare Force Calibration Set-Up	142
B-7	Zero Thrust Nozzle Used Initially to Calibrate Bellows Tare Force	143
B-8	Dry Power Nozzle Thrust and Flow Characteristics from MCAIR Static Test Stand	144
B-9	Afterburning Power Nozzle Thrust and Flow Characteristics from MCAIR Static Test Stand	144
B-10	Bellows Post-Test Tare Force Evaluation	145

LIST OF FIGURES (Continued)

<u>Figure No.</u>	<u>Title</u>	<u>Page</u>
C-1	SN002 Simulator Installation in the AEDC Engine Test Facility R2C4 Test Cell	147
C-2	Typical 5000 RPM/SEC Simulator Acceleration Run Using the Control Console	148
C-3	Typical Control Console Automatic Shutdown Sequence	148
C-4	Effect on Forward Bearing Temperature of Eliminating the Bearing Dampener Oil	150
C-5	Nozzle Entrance Pressure and Temperature Profiles without Duct Screens	150
C-6	Simulator Drive Venturi Airflow Correction Factor	152
C-7	SN002 Simulator Compressor Characteristics, $P_{T2} = 7$ psia	153
C-8	SN002 Simulator Compressor Characteristics, $P_{T2} = 12$ psia	154
C-9	SN002 Simulator Compressor Characteristics, $P_{T2} = 16$ psia	155
C-10	Simulator Flexibility Demonstrated During ETF Static Tests; Dry Power Nozzle	156
C-11	Simulator Flexibility Demonstrated During ETF Static Tests; A/B Power Nozzle	157
C-12	Typical Forward Bearing Temperature Map-Dry Power Nozzle	158
C-13	Typical Forward Bearing Temperature Map - A/B Power Nozzle	159
C-14	Rotor Thrust Variation with Rotor Speed-Dry Power Nozzle	160
C-15	Rotor Thrust Variation with Rotor Speed-A/B Power Nozzle	160
C-16	Nozzle Entrance Pressure and Temperature Profiles with Duct Screens Installed	161
D-1 thru D-165	Basic Data Plots	163 thru 327

LIST OF ABBREVIATIONS AND SYMBOLS

<u>Symbol</u>	<u>Definition</u>
A/B	Afterburning condition
A_c	Inlet capture area (8.892 in^2)
A_{EXIT}	Nozzle exit area (in^2)
AF	Axial force (lb)
A_o	Total inlet captured stream tube area (in^2)
A_t	Nozzle throat area (in^2)
B.L.	Butt line (in)
\bar{c}	Reference moment length (17.860 in)
C_D	Total airframe drag coefficient ($D/Q_o S_{\text{REF}}$)
C_{DA}	Aft-end drag coefficient ($D_A/Q_o S_{\text{REF}}$)
C_{DF}	Forebody drag coefficient ($C_D - C_{DA}$)
C_{F_g}	Nozzle thrust coefficient ($F_g/F_{g_{\text{ID}}}$)
C_L	Total airframe lift coefficient ($L/Q_o S_{\text{REF}}$)
C_{LA}	Aft-end lift coefficient ($L_A/Q_o S_{\text{REF}}$)
C_{LF}	Forebody lift coefficient ($C_L - C_{LA}$)
C_m	Total airframe pitching moment coefficient ($PM/Q_o S_{\text{REF}} \bar{c}$)
C_{mA}	Aft-end pitching moment coefficient ($PM_A/Q_o S_{\text{REF}} \bar{c}$)
C_{mF}	Forebody pitching moment coefficient ($C_m - C_{mA}$)
C_P	Pressure coefficient ($P_L - P_o/Q_o$)
C_w	Nozzle flow coefficient ($W_g/W_{g_{\text{ID}}}$)
D	Total airframe drag (lb)
D_A	Aft-end drag (lb)
F_g	Nozzle gross thrust (lb)
$F_{g_{\text{ID}}}$	Nozzle ideal thrust (lb)
F.S.	Fuselage station (in)
L	Total airframe lift (lb)
L_A	Aft-end lift (lb)

LIST OF ABBREVIATIONS AND SYMBOLS (Continued)

<u>Symbol</u>	<u>Definition</u>
M, M_o	Freestream Mach number
MFR	Inlet mass flow ratio (A_o/A_c)
N	Simulator rotor speed (RPM)
NF	Normal force (lb)
NFF	Nozzle flow function ($W_8 \sqrt{T_{T8}}/P_{T8}$)
NPR	Nozzle pressure ratio (P_{T8}/P_o)
P	Static pressure (psia)
P_L	Local static pressure (psia)
PM	Total airframe pitching moment (in-lb)
PM_A	Aft-end pitching moment (in-lb)
P_o	Freestream static pressure (psia)
PRP	Compressor pressure ratio parameter - $(P_{13Q2} - P_{13Q2L}) / (P_{13Q2S} - P_{13Q2L})$
P_T	Total pressure (psia)
P_{T2}	Simulator compressor inlet total pressure (psia)
P_{T8}	Nozzle total pressure (psia)
P_{T13}	Simulator compressor exit total pressure (psia)
P_{13Q2}	Compressor pressure ratio (P_{T13}/P_{T2})
P_{13Q2L}	Compressor pressure ratio near minimum operating line
P_{13Q2S}	Compressor pressure ratio at stall
Q_o	Freestream dynamic pressure (psia)
R_N	Reynolds number
S_{REF}	Reference area (763.3 in ²)
TB1	Forward bearing temperature (°F)
TB1N	Corrected forward bearing temperature - $TB1 + (120 - T_{T2})$ - °F
TB2	Rear bearing temperature (°F)
TB2N	Corrected rear bearing temperature - $TB2 + (200 - T_{T4})$ - °F

LIST OF ABBREVIATIONS AND SYMBOLS (Continued)

<u>Symbol</u>	<u>Definition</u>
T_T	Total temperature (°F or °R)
T_{T0}	Freestream total temperature (°F)
T_{T2}	Simulator compressor inlet total temperature (°F or °R)
T_{T4}	Simulator turbine inlet total temperature (°F)
T_{T8}	Nozzle total temperature (°F or °R)
W_2	Simulator compressor airflow (lb/sec)
W_8	Nozzle airflow (lb/sec)
W_{8ID}	Nozzle ideal airflow (lb/sec)
WA_{2R}	Simulator compressor corrected airflow - $W_2 \sqrt{\theta_2 / \delta_2}$ (lb/sec)
W_{BM}	Simulator turbine bleed airflow (lb/sec)
W_{DM}	Simulator turbine drive airflow (lb/sec)
$W.L.$	Waterline (in)
α	Angle of attack (deg)
δ_C	Canard deflection angle (deg)
δ_H	Horizontal stabilator deflection angle (deg)
δ_2	Sea level static standard day pressure correction ($P_{T2}/14.696$)
Δ_1'	Inlet first ramp angle (deg)
Δ_2'	Inlet second ramp angle (deg)
Δ_3'	Inlet third ramp angle (deg)
η_a	Simulator compressor adiabatic efficiency
θ_2	Sea level static standard day temperature correction ($T_{T2} + 460/518.67$)

1. INTRODUCTION

As the performance requirements for advanced turbojet/turbofan powered aircraft have become more demanding, it has become increasingly important to accurately evaluate and understand the interactions of the propulsion system with the airframe. Many aircraft designs under development have potentially large propulsion-induced interaction effects on the basic performance and flying qualities. Without proper evaluation of these interaction effects, significant errors could be introduced into the aircraft overall performance predictions. Conventional wind tunnel model test techniques cannot totally assess these effects, since the interactions between the inlet/airframe/nozzle flowfields cannot be accurately simulated on one model. Improved test techniques which will properly assess all such effects are therefore highly desired.

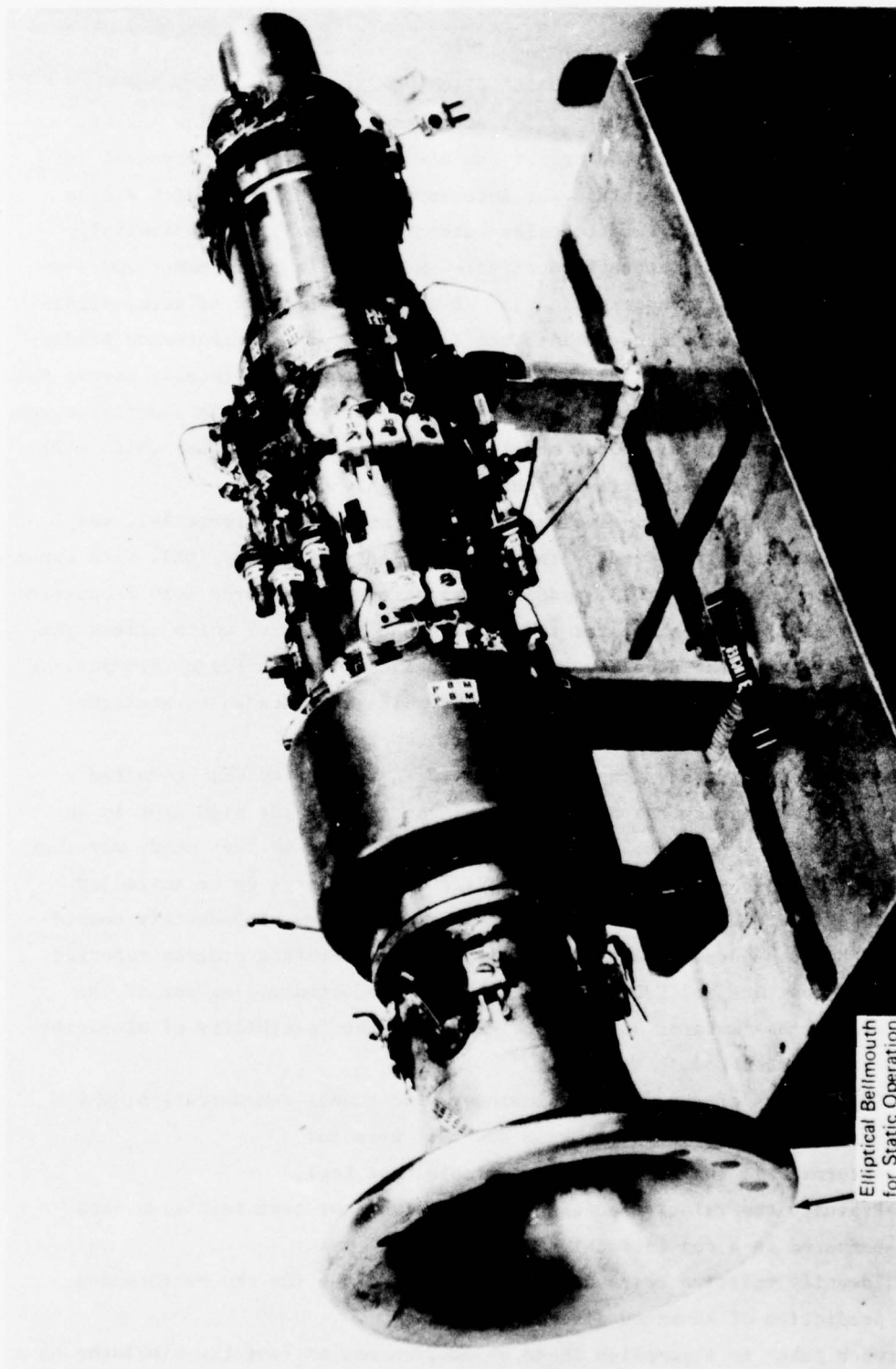
The turbine engine multi-mission propulsion simulator, Figure 1-1, was developed and statically tested by the General Electric Company (GE), with support by Tech Development, Inc. (TDI), under contract to the Air Force Aero Propulsion Laboratory (AFAPL). The simulator is a wind tunnel test tool which offers the potential to improve the accuracy and reduce the cost of pre-flight predictions of aircraft general performance, because it permits accurate inlet/airframe/nozzle flowfield simulation on a single wind tunnel model.

The McDonnell Aircraft Company (MCAIR), with support by GE, conducted a study in 1972 to identify the potential applications for the simulator in an aircraft development program. One of the major findings in that study was that the previously-developed simulator was physically too large to be installed within properly scaled aircraft model moldlines. Because of budgetary considerations, the subsequent simulator wind tunnel demonstration program reported herein (USAF Contract No. F33615-73-C-2051) was conducted making use of the current oversized simulator hardware to establish the feasibility of simulator-equipped wind tunnel models.

The objectives of the current simulator wind tunnel demonstration, which was conducted with major support by GE and TDI, were to:

- o Determine if the simulator is a viable test tool.
- o Evaluate the relative accuracy of the simulator test technique when compared to a conventional test technique.
- o Identify relative costs between test techniques for the performance prediction of advanced aircraft.

The approach taken to accomplish these objectives was to test the simulator in a partial aircraft wind tunnel model, Figure 1-2, and subsequently analyze the data.

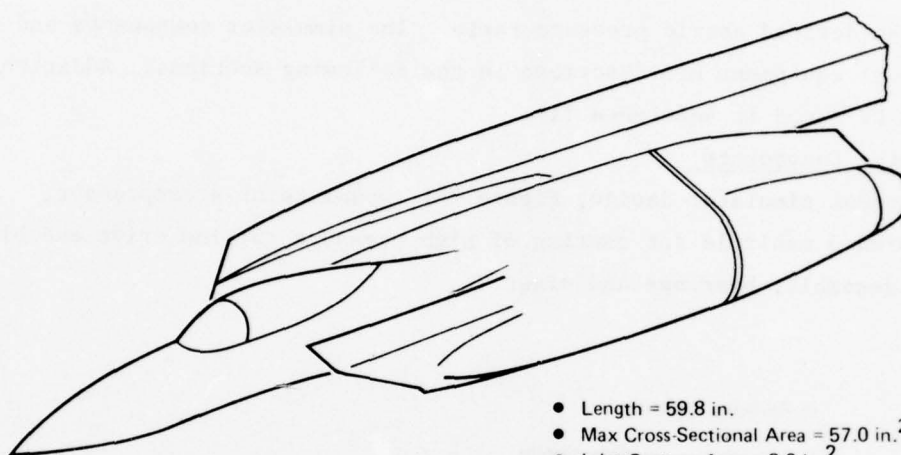


Elliptical Bellmouth
for Static Operation

FIGURE 1-1
TURBINE ENGINE MULTIMITATION PROPULSION SIMULATOR

GP76-0701-118

In addition, conceptual design studies of conventional and simulator-equipped models of an advanced fighter were conducted to provide the foundation for the cost comparison analysis.



GP76-0701-13

FIGURE 1-2
SIMULATOR WIND TUNNEL DEMONSTRATION MODEL

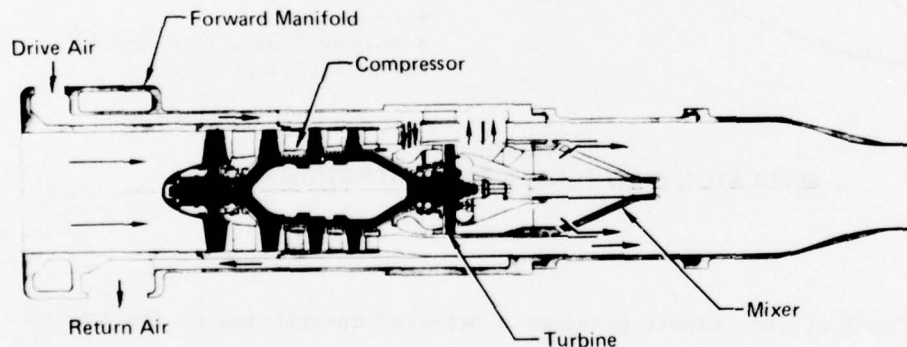
Section 2 of this report provides a detailed description of the current simulator design and support equipment. Sections 3 thru 6 discuss the wind tunnel model utilized in the test program, and an evaluation of the wind tunnel test results and operational aspects of the simulator during the test. In Section 7, the development of a reduced size (compact) simulator to permit testing in realistic aircraft models is described. Section 8 provides an estimate of the potential cost savings of a simulator-equipped model in the aerodynamic performance prediction of an advanced fighter aircraft. Section 9 presents the conclusions and recommendations from this program.

2. SIMULATOR AND SUPPORT EQUIPMENT

The simulator has a compressor and turbine similar to a miniature turbo-jet engine, and permits the simultaneous simulation of the scaled inlet/nozzle flows of many full scale engines. Energy for driving the compressor is supplied from an external source of high pressure air which is expanded through the turbine. Some of the turbine discharge air is then mixed with the compressor air to obtain the desired nozzle pressure ratio. The simulator components and required support equipment are described in the following sections. Additional details can be found in Reference (1).

2.1 Simulator Components

The current simulator design, Figure 2-1, consists of a compressor, turbine, forward manifold for routing of high pressure turbine drive and bleed air, frame assembly, bearings and mixer.



GP76 0701 12

FIGURE 2-1
SIMULATOR SCHEMATIC

Compressor/Turbine - A four stage axial flow compressor is utilized with a single stage, high pressure turbine. The single stage turbine permits a lighter weight turbine with a shorter span between bearings and minimum overhang of rotating hardware. Thus, rotor dynamic instability is minimized. The design features and operating conditions of the compressor and turbine are presented in Figure 2-2.

Compressor	
<ul style="list-style-type: none"> Design Features <ul style="list-style-type: none"> Design Pressure Ratio, $P_{T13}/P_{T2} = 2.82$ Design Rotor 1 Corrected Tip Speed, $U_T/\sqrt{\theta_2} = 984$ ft/sec Design Corrected Weight Flow, $W_2\sqrt{\theta_2}/\delta_2 = 1.554$ lb/sec Design Corrected Speed, $N/\sqrt{\theta_2} = 75,185$ RPM Compressor Inlet Specific Flow, $W_2\sqrt{\theta_2}/\delta_2 A_2$ Annulus = 39.8 lb/sec-ft² Compressor Inlet Hub to Tip Radius Ratio = 0.45 Design Point Efficiency, $\eta_c = 0.72$ Maximum Operating Conditions <ul style="list-style-type: none"> Compressor Inlet Total Pressure = 16 psia Compressor Inlet Total Temperature = 180°F Compressor Discharge Total Pressure = 55 psia Compressor Discharge Total Temperature = 500°F Compressor Steady-State Overspeed = 87,800 RPM 	
Turbine	
<ul style="list-style-type: none"> Design Features <ul style="list-style-type: none"> Turbine Pressure Ratio, $P_{4Q5} = 3.3$ Turbine Corrected Speed, $XNLR4 = 3050$ RPM/$\sqrt{\theta_R}$ Turbine Flow Function, $TFF = 0.106$ lb$\sqrt{\theta_R}$/sec · psia Turbine Efficiency, $\eta_t = 0.72$ Maximum Operating Conditions <ul style="list-style-type: none"> Turbine Inlet Pressure = 1500 psia Turbine Inlet Temperature = 250°F Turbine Exit Pressure = 650 psia 	

GP76 0701 93

FIGURE 2-2
SIMULATOR COMPRESSOR/TURBINE CHARACTERISTICS

Forward Manifold and Turbine Drive/Bleed Air Systems - The turbine drive air enters an annular manifold through a 0.960 inch diameter port perpendicular to the simulator centerline. The air is then routed axially through five 0.25 inch diameter holes along the periphery of the simulator manifold and frame assembly to five pairs of radial holes (0.25 inch and 0.16 inch diameter) in each of the five struts leading to the turbine drive plenum.

Downstream of the turbine and depending on the simulator operating condition, the air either exits through the mixer or turns 90° and travels out five pairs of holes .32 inches long and .25 inches wide (.125 inch radius at either end) through the struts to a manifold in the frame assembly. Five pairs of similar holes, located around the periphery then carry the air to a forward

manifold which bleeds the air perpendicular to the simulator centerline through a 1.5 inch diameter port.

Both the turbine drive and bleed air systems are capable of passing 6.5 lb/sec of air with normal turbine energy extractions and the turbine drive air temperature at 200°F. A summary of the limits of each system is presented below:

	Pressure (psia) Limit or Maximum
Turbine Drive Manifold	2000
Turbine Bleed Manifold	650
Turbine Drive Plenum	1500
Mixer Entrance Pressure or Turbine Exit Pressure	650

Bearings - A 12-millimeter-bore ball bearing manufactured by Marlin Rockwell Company supports the rotor at two points, just aft of the first stage of the compressor and just forward of the turbine. The bearings are of the split inner race design and capable of supporting bi-directional rotor axial forces. The cage is made of steel alloy and is silverplated for low friction, and the balls and races are made of M50 tool steel. The bearing DN is 1.06 million.

To aid in seating the bearings, a pre-load on the rotor of approximately 40 pounds aft is applied by using a thrust washer. To maintain this aft load during testing, the cavity downstream of the turbine is partially vented through a center vent tube in the turbine discharge frame. The amount of venting is controlled by removable thrust trim orifices which are 0.185 inches (nominal) in diameter.

Mixer - A mixer, located downstream of the turbine, permits residual turbine drive air to mix with the compressor air to obtain the desired simulation of full scale nozzle flow function ($\dot{w}\sqrt{T_T/P_T}$) which in full scale engines is accomplished by heat addition. This mass addition also permits simulation of nozzle pressure ratio. The amount of mixer flow can be varied by a bleed valve located in the turbine bleed air line outside the simulator. This permits nozzle pressure ratio to be varied from minimum (bleed valve full open) to maximum (bleed valve closed) while maintaining a constant corrected compressor airflow.

The mixer uses radial injection of the air through choked orifices from a conical afterbody, with staging of injection holes to avoid excess blockage. Early simulator test results showed that significant distortion (up to 20% in nozzle entrance total pressure and temperature profiles) was caused by this mixer design. To improve the mixing process and reduce the nozzle total pressure distortion for the wind tunnel demonstration program, a screen assembly was located just downstream of the mixer. Static testing with the screens showed that total pressure distortion was generally less than 5%. Individual mixers were used with the dry and afterburning power nozzles for the wind tunnel test program. The geometries of the nozzles and screens are discussed in Section 3.

2.2 Simulator Control System

A simulator control console was designed and fabricated by General Electric Company under USAF contract F33615-72-C-1849. This system, described in detail in Reference (2), is a portable unit complete with electronic controls, cables, hydraulic power package, hoses, and valves. It can be used for controlling either one simulator or two simulators simultaneously. The console requires 24 volts DC and 117 volts AC for operation.

To set simulator speed, the turbine drive air valve can be either manually controlled or operated in an automatic feedback mode where an adjustable pre-set speed is controlled automatically to within .125%. The turbine bleed valve used for varying the bleed flow is manually controlled.

A number of simulator operating parameters are automatically monitored, and if pre-set limits are exceeded, shut down occurs automatically. These parameters include the bearings temperature level and rate of increase, turbine inlet air temperature and pressure, maximum speed, speed rate of change, and vibration level. A photograph of the control console is shown in Figure 2-3.

2.3 Lubrication System

The lubrication system for the simulator consists of an adjustable constant volume supply pump and a scavenge system which supplies an electronic signal for monitoring the oil scavenge level. The pump has two channels which can each be adjusted to supply up to 160 cc/hr of oil. It has a maximum output pressure of 1000 psia, and uses a nominal 25 psia output back pressure for proper operation. MIL-L-23699 oil is supplied to each bearing at a normal flow rate of 20 cc/hr. A photograph of the oil pump is shown in Figure 2-4.

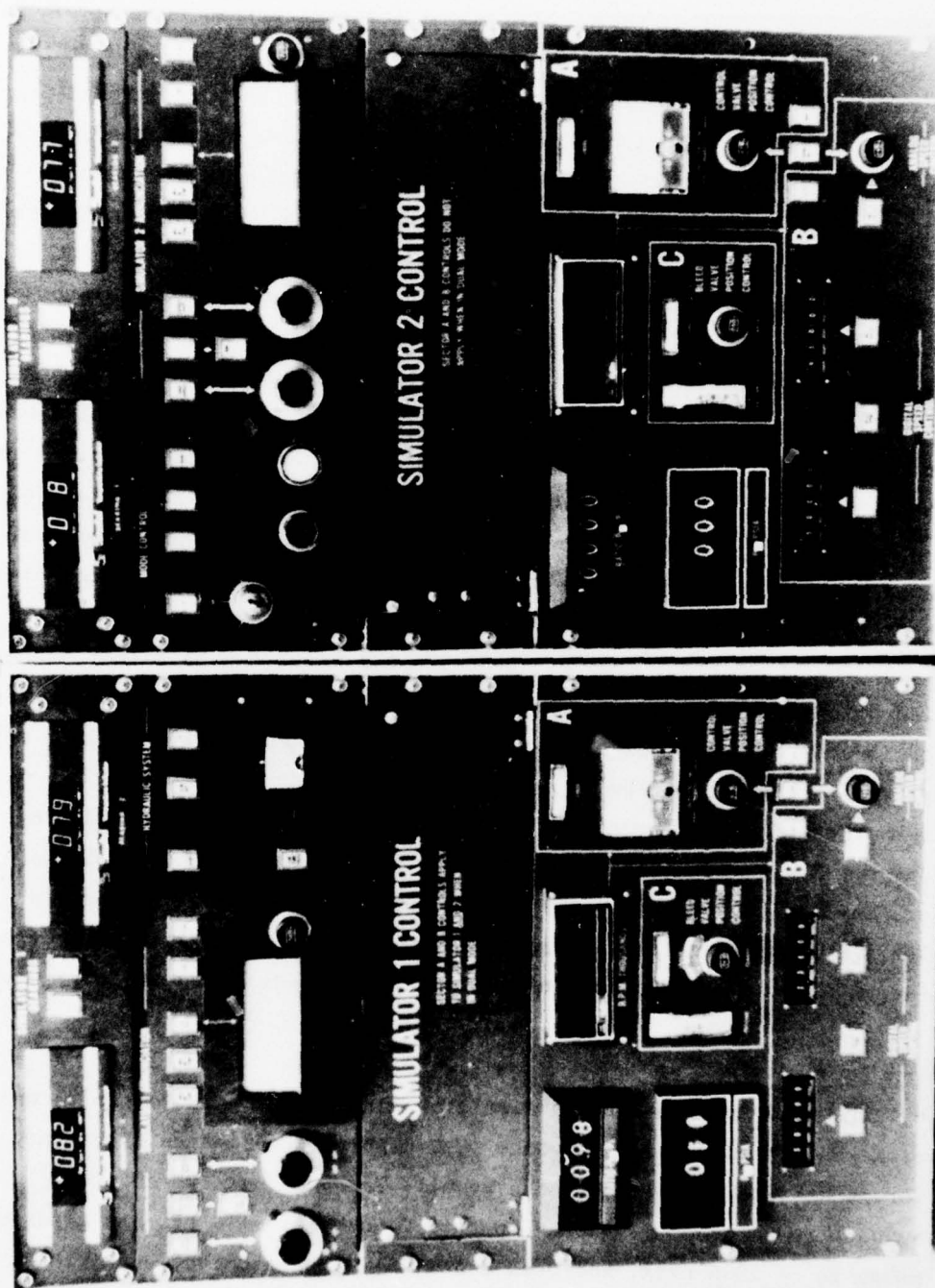


FIGURE 2-3
SIMULATOR CONTROL CONSOLE

GP76 0701 46

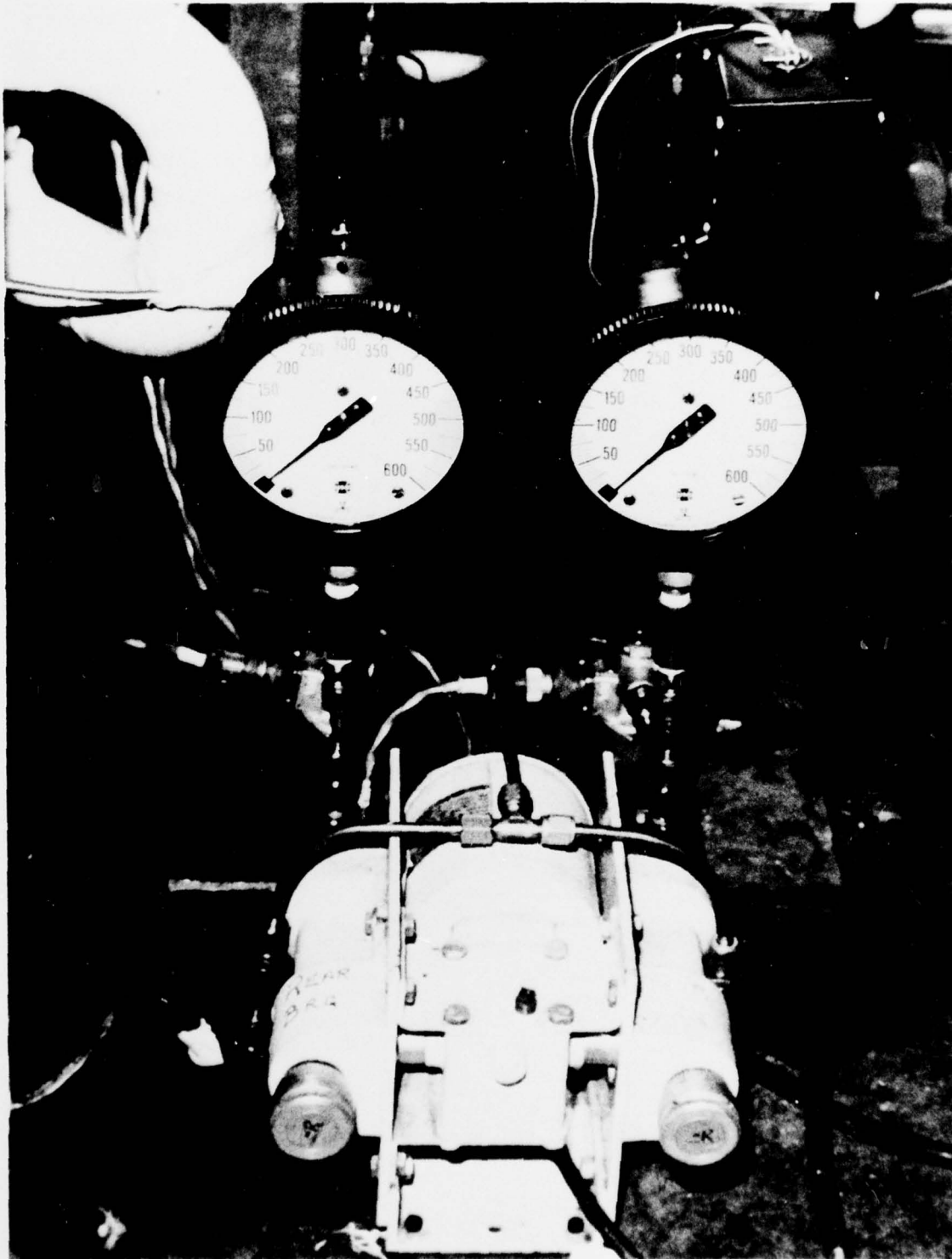


FIGURE 2-4
SIMULATOR LUBRICATING OIL SUPPLY PUMP

GP76 0701 47

The oil scavenge system has a capacitance rod with a transmitter which outputs a 1 to 5 volt DC signal for data processing. Each of the two channels (No. 1 forward bearing and No.2 aft bearing) has a 75 cc capacity. The oil can be dumped from the chamber while running without affecting the oil scavenge capability. The system, which operates on 117 volts AC, requires a vacuum of 3 to 5 psi below the compressor inlet pressure. A photograph of the oil scavenge system is shown in Figure 2-5.



FIGURE 2-5
SIMULATOR LUBRICATING OIL SCAVENGE SYSTEM

GP76-0701-10

3. WIND TUNNEL DEMONSTRATION MODEL

The wind tunnel model was designed with the goal of achieving the best overall configuration to thoroughly check-out and establish the simulator operational capabilities/limitations, and to assess the potential simulator benefits over conventional test techniques. As such, the major considerations in the model design were the: (1) realistic simulation of as many aircraft features as possible, (2) the availability of adequate internal model volume to house the simulator and force balances, (3) the use of an adequate number of force balances to provide the data necessary to meet the overall program objectives, and (4) the use of sufficient pressure instrumentation to substantiate the force balance data. The major model design features and model/simulator instrumentation are discussed briefly below. Additional details can be found in Reference (3).

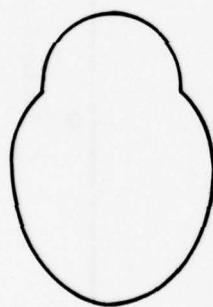
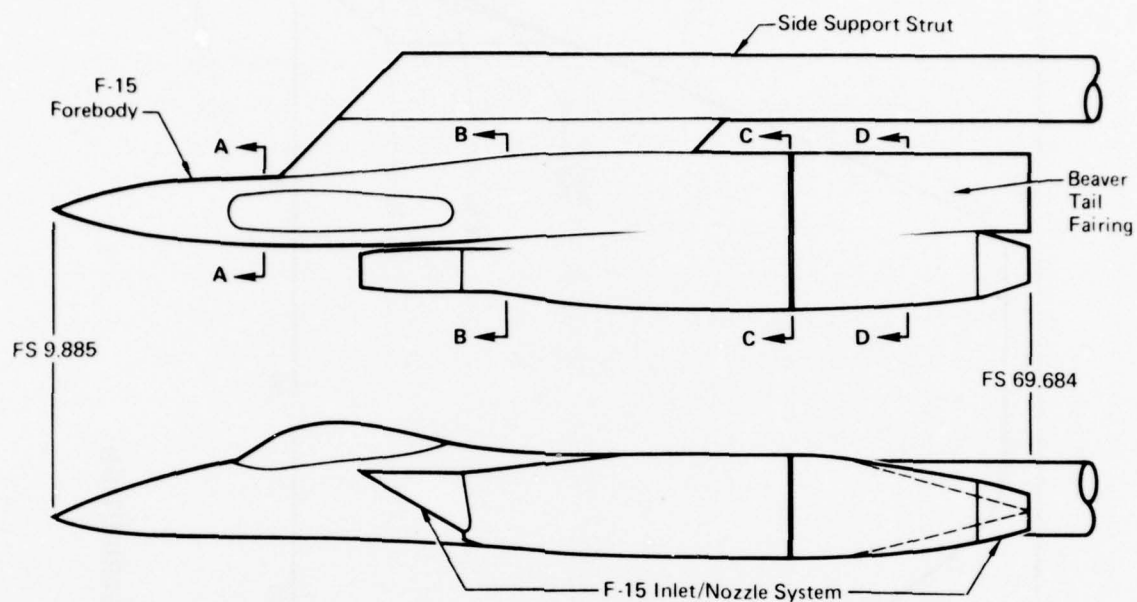
3.1 Design Features

The basic wind tunnel model, Figure 3-1, is a simple body configuration. The inlet, forward fuselage, nozzle, and inlet/nozzle axial spacing represent half of an 8.5% scale F-15 aircraft fuselage. The scale factor was established by ratioing the maximum corrected airflow of the F100 engine, used in the F-15, to that of the maximum simulator capability, as shown below:

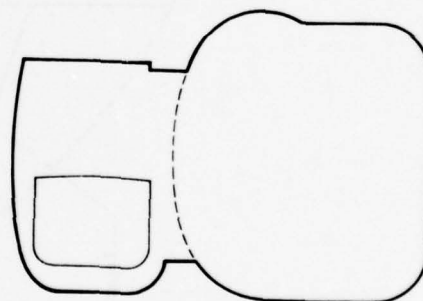
$$\text{Scale Factor} = \sqrt{\frac{\text{Max Simulator Compressor Corrected Airflow}}{\text{Max Engine Corrected Airflow}}}$$

To accommodate the simulator, force balances, and other required internal hardware, the body deviates from the scaled F-15 fuselage moldlines starting just aft of the inlet. This deviation results in a larger cross-section at midbody, as compared to the F-15 nacelle, and a wide beaver tail fairing next to the nozzle. An area distribution of the model is shown in Figure 3-2.

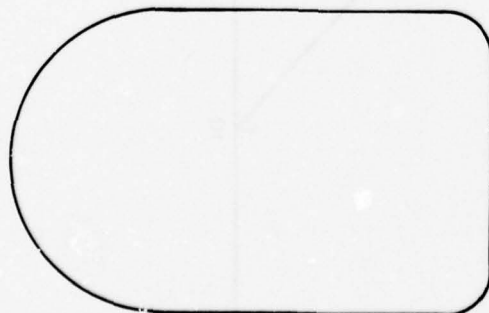
Test Modes - In order to obtain the test data required for a comparison between simulator and conventional test techniques, the model can be adapted to the three test modes illustrated in Figure 3-3. In the simulator-equipped mode, both total airframe (i.e., complete model without wings or tail surfaces) and aft-end aerodynamic forces and moments are measured as is the simulator thrust. These measurements are obtained while duplicating the inlet/nozzle flow characteristics using the actual aircraft nozzle geometry.



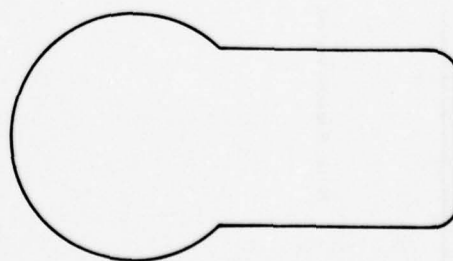
Section A-A



Section B-B



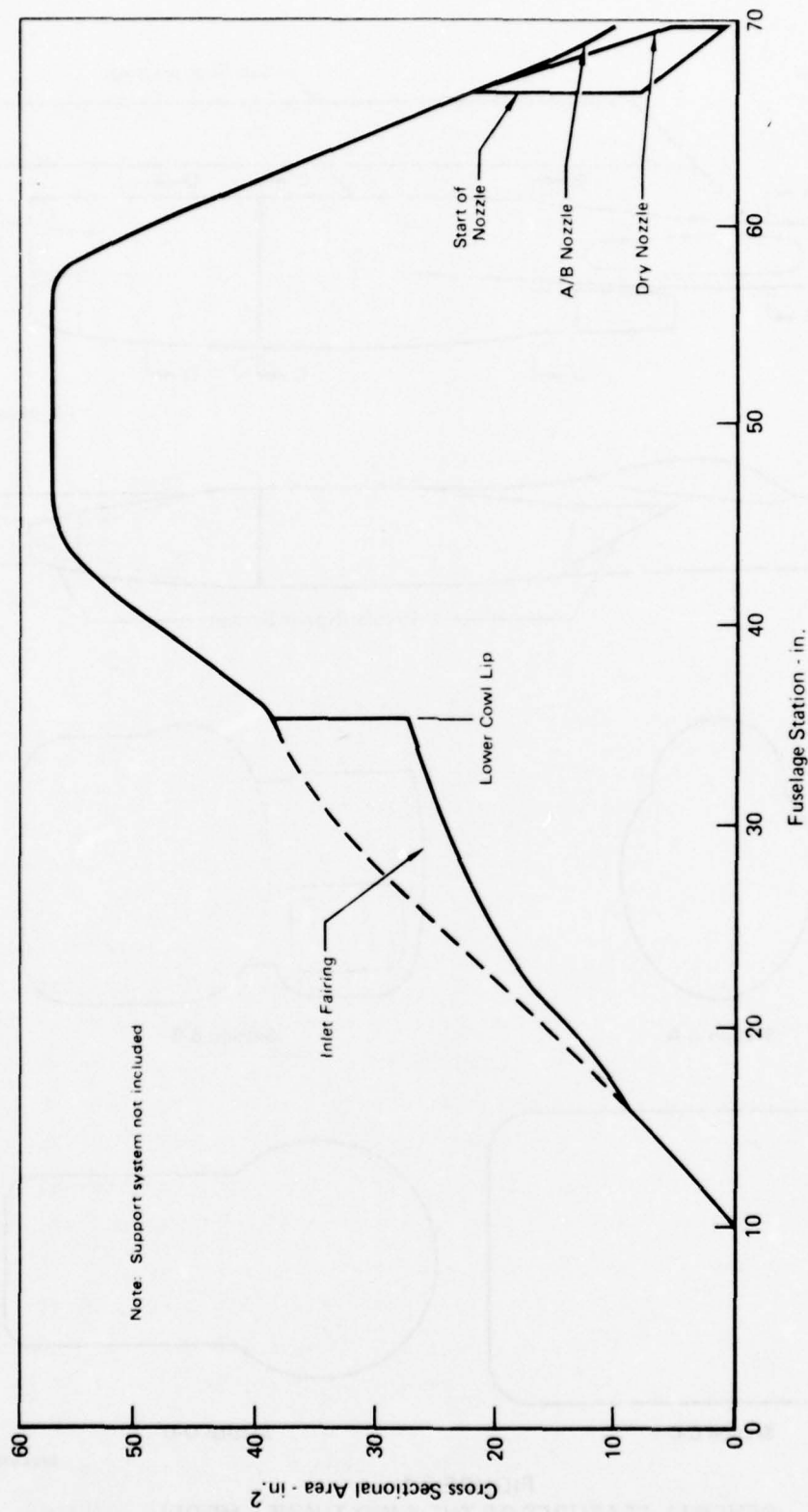
Section C-C



Section D-D

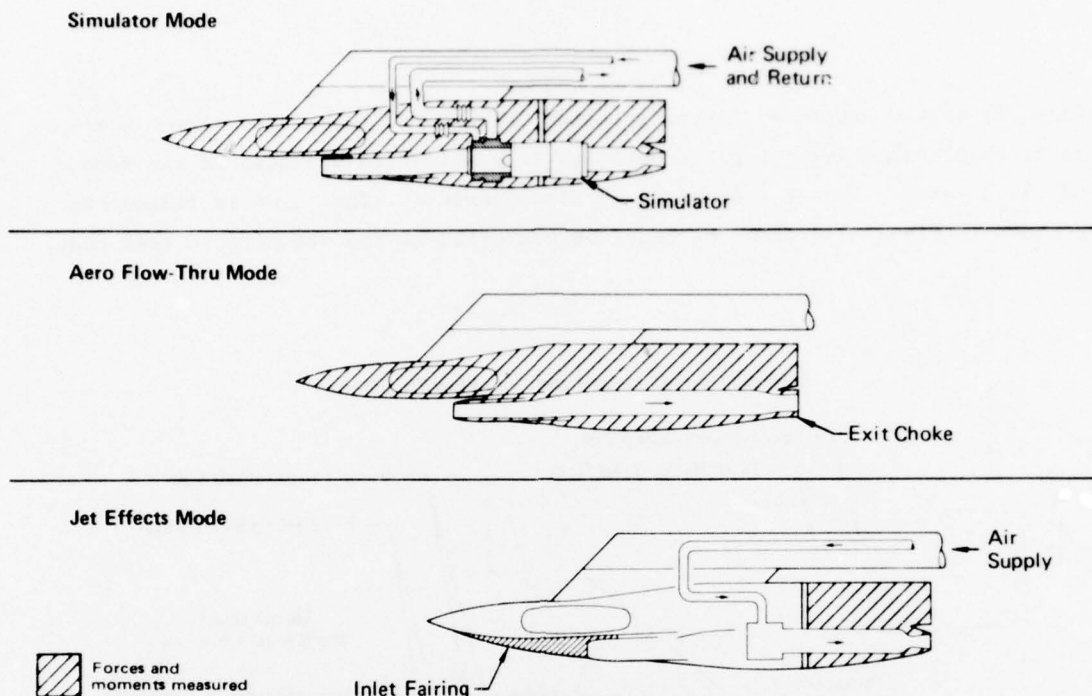
FIGURE 3-1
GENERAL FEATURES OF THE WIND TUNNEL MODEL

GP76.0701.17



GP76 0701 162

FIGURE 3-2
WIND TUNNEL MODEL AREA DISTRIBUTION



**FIGURE 3-3
MODEL TEST MODES**

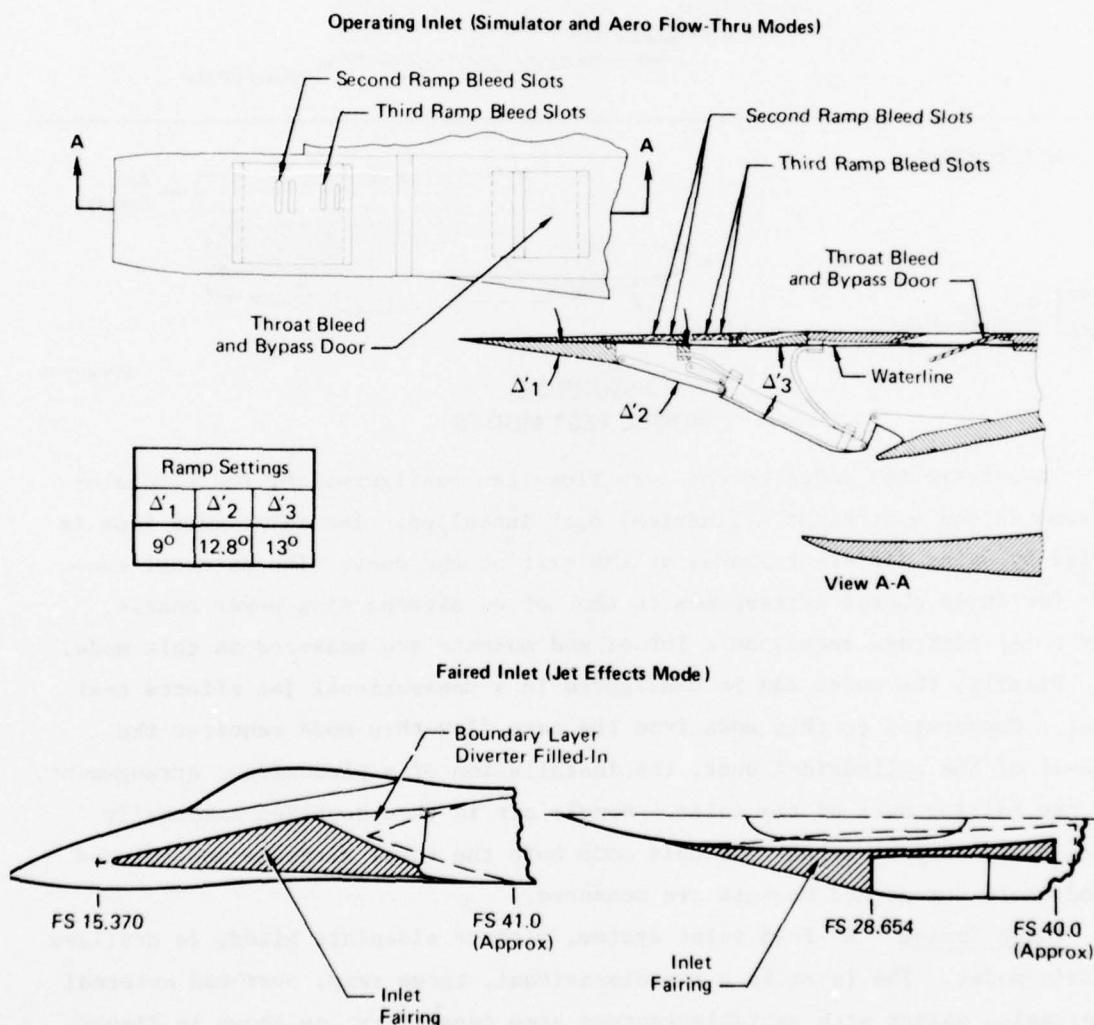
GP76 0701-18

To convert the model to the aero flow-thru configuration, the simulator is removed and a straight cylindrical duct installed. The inlet mass flow is varied by using different chokes at the exit of the duct. The external contour for these chokes corresponds to that of an afterburning power nozzle. Only total airframe aerodynamic forces and moments are measured in this mode.

Finally, the model can be configured in a conventional jet effects test model. Conversion to this mode from the aero flow-thru mode requires the removal of the cylindrical duct, the installation of a plenum/duct arrangement, and the fairing over of the inlet. Nozzle air is then supplied externally through the support strut. In this mode both the total airframe and aft-end aerodynamic forces and moments are measured.

Inlet System - An F-15 inlet system, without sideplate bleed, is utilized on this model. The inlet is a two-dimensional, three ramp, overhead external compression design with variable capture area capability, as shown in Figure 3-4. The first ramp angle, and hence the capture area, can be manually adjusted by rotating the entire upper cowl/ramp system about a pivot point near the lower cowl lip. The second and third ramp angles can also be manually adjusted inde-

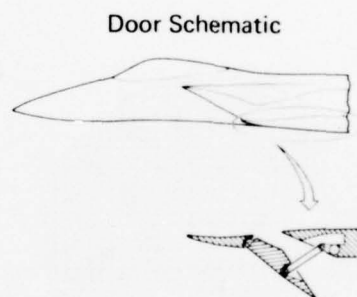
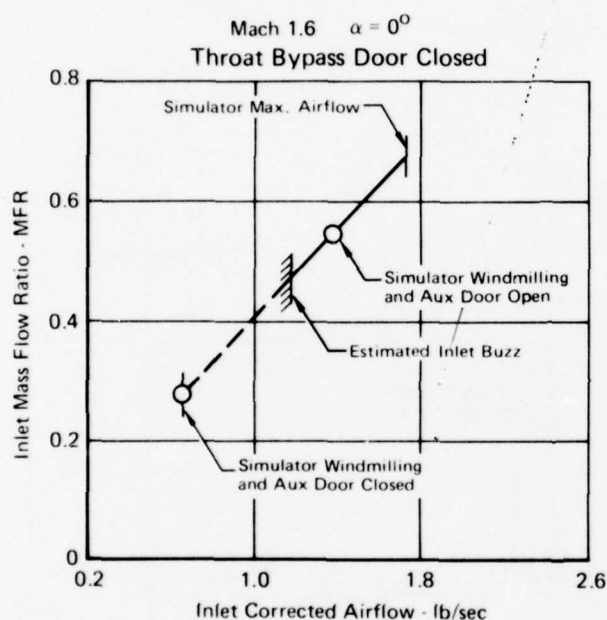
pendently of the cowl/ramp system rotation. These ramps are also slaved with the diffuser ramp. Porous plate boundary layer bleed is provided on the second and third ramps. Throat slot bleed is also provided. The inlet is faired over as shown in Figure 3-4 when the model is converted to the jet effects test mode.



GP76 0701 21

**FIGURE 3-4
INLET GEOMETRY FOR VARIOUS TEST MODES**

An inlet auxiliary bypass door, Figure 3-5, is located in the diffuser duct to safeguard the simulator during windmilling operation at supersonic Mach numbers. As indicated in Figure 3-5, the inlet without an auxiliary door is in a buzz condition supersonically (in this case Mach 1.6) at the simulator windmilling airflow. The resulting pressure fluctuations in the inlet could damage the simulator, but the increased airflow obtained with the auxiliary door open puts the inlet into its stable operating range.

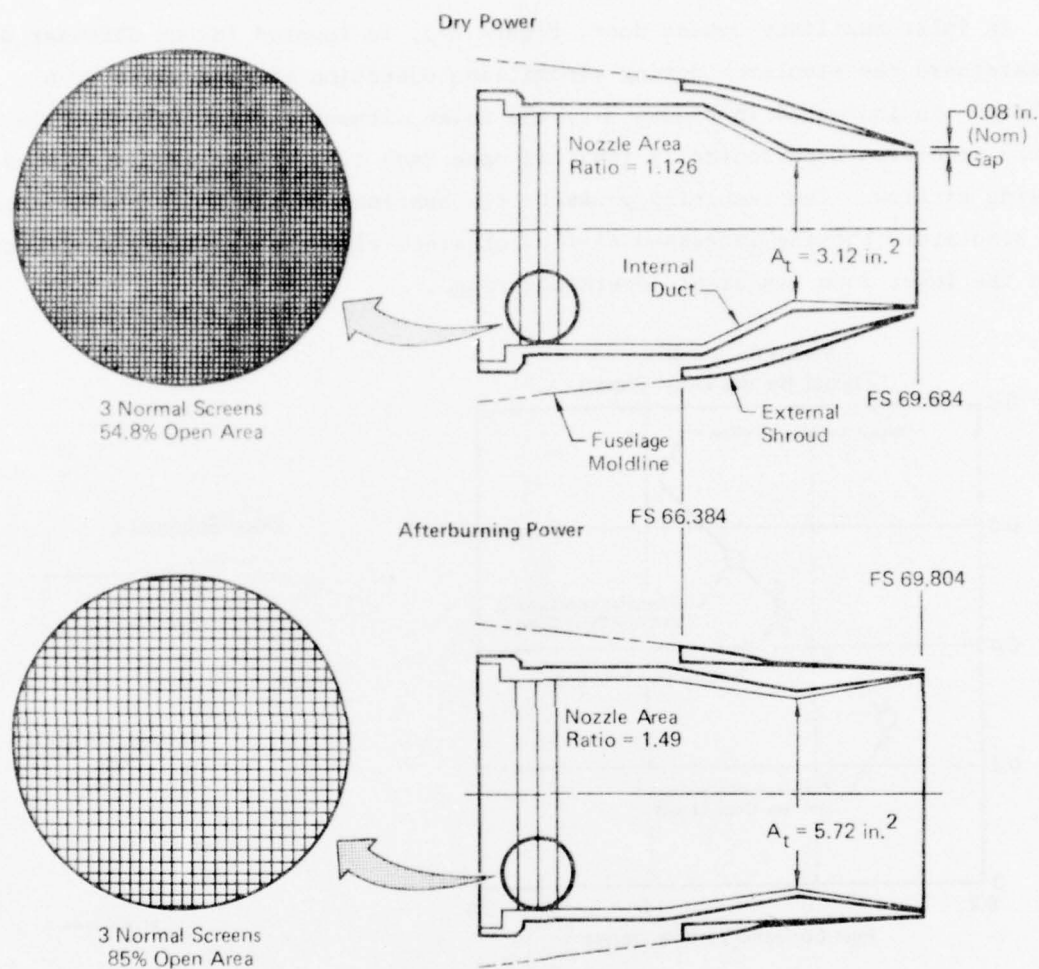


GP76 0701 95

FIGURE 3-5
INLET AUXILIARY BYPASS DOOR FOR SIMULATOR PROTECTION
DURING SUPERSONIC OPERATION

Nozzles - The geometries of the dry and afterburning power nozzles are illustrated in Figure 3-6. These nozzles are representative of those on the F-15 aircraft. The external shrouds and internal ducts are used in both the simulator and jet effects test modes. In the aero flow-thru mode, only the afterburning power shroud is used, while the internal nozzle ducts are replaced by exit chokes.

The nozzle ducts are equipped with three normal screens. These are used only in the simulator mode to improve the mixing between the simulator compressor and mixer flows.

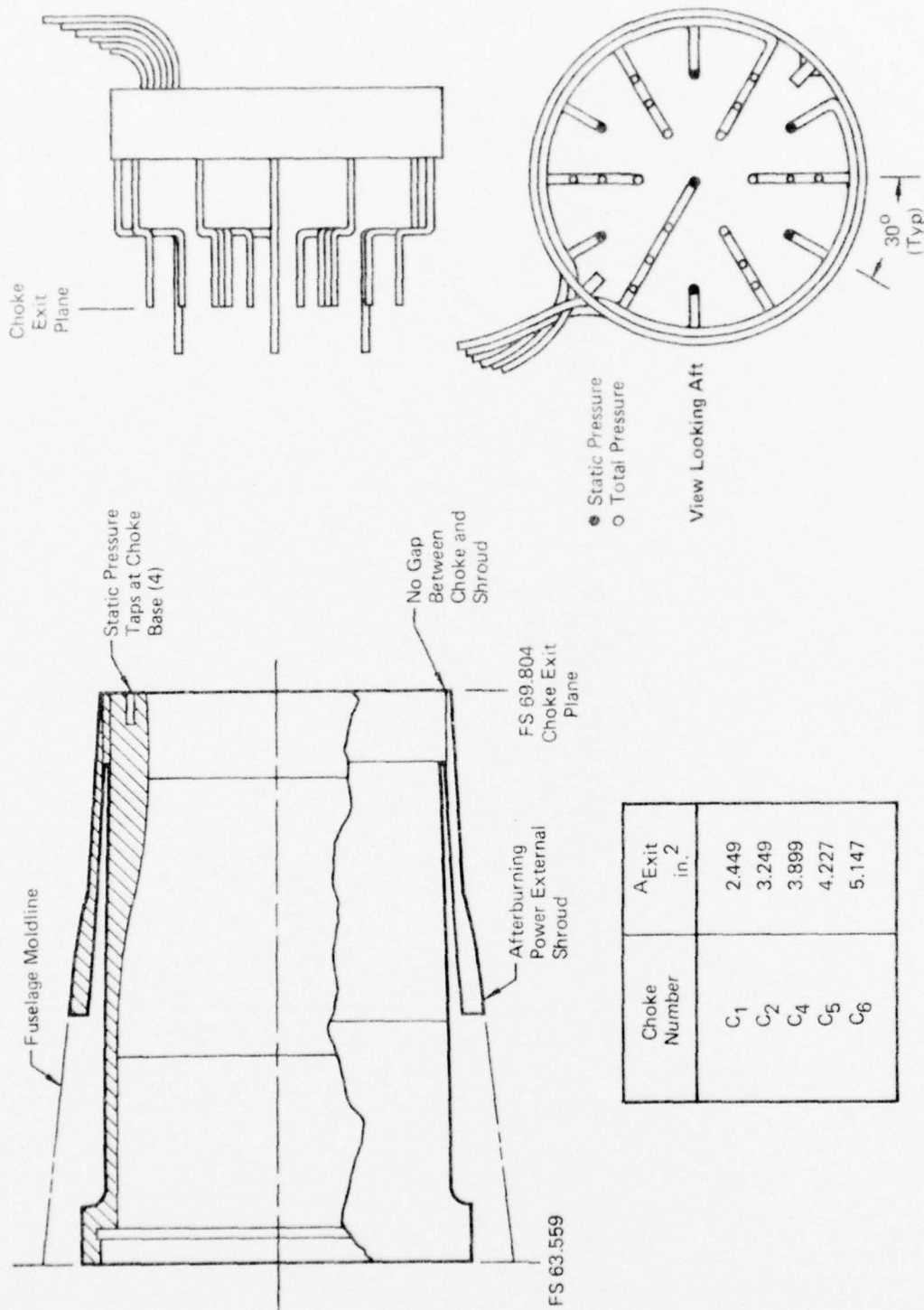


GP76 0701-22

FIGURE 3-6
NOZZLE GEOMETRY

Exit Chokes/Rakes - In the aero flow-thru mode, the inlet airflow is controlled by chokes at the nozzle exit. A series of five different chokes, Figure 3-7, provides the same range of inlet airflow that is obtainable with the simulator. A static/total pressure exit rake is used with each choke to determine its exact airflow characteristics. This airflow determination is accomplished during the wind tunnel test, but separate from the force measurement testing.

Force Balances - Figure 3-8 illustrates the location of the three conventional Task Corp balances used to measure forces and moments on the model. A 2.5 inch diameter Task MK XXIV balance is located in the forward fuselage to measure the total airframe aerodynamic forces and moments. This balance, which



GP76-0701-23

FIGURE 3-7
EXIT CHOKES AND PRESSURE RAKES
Aero Flow-Thru Mode

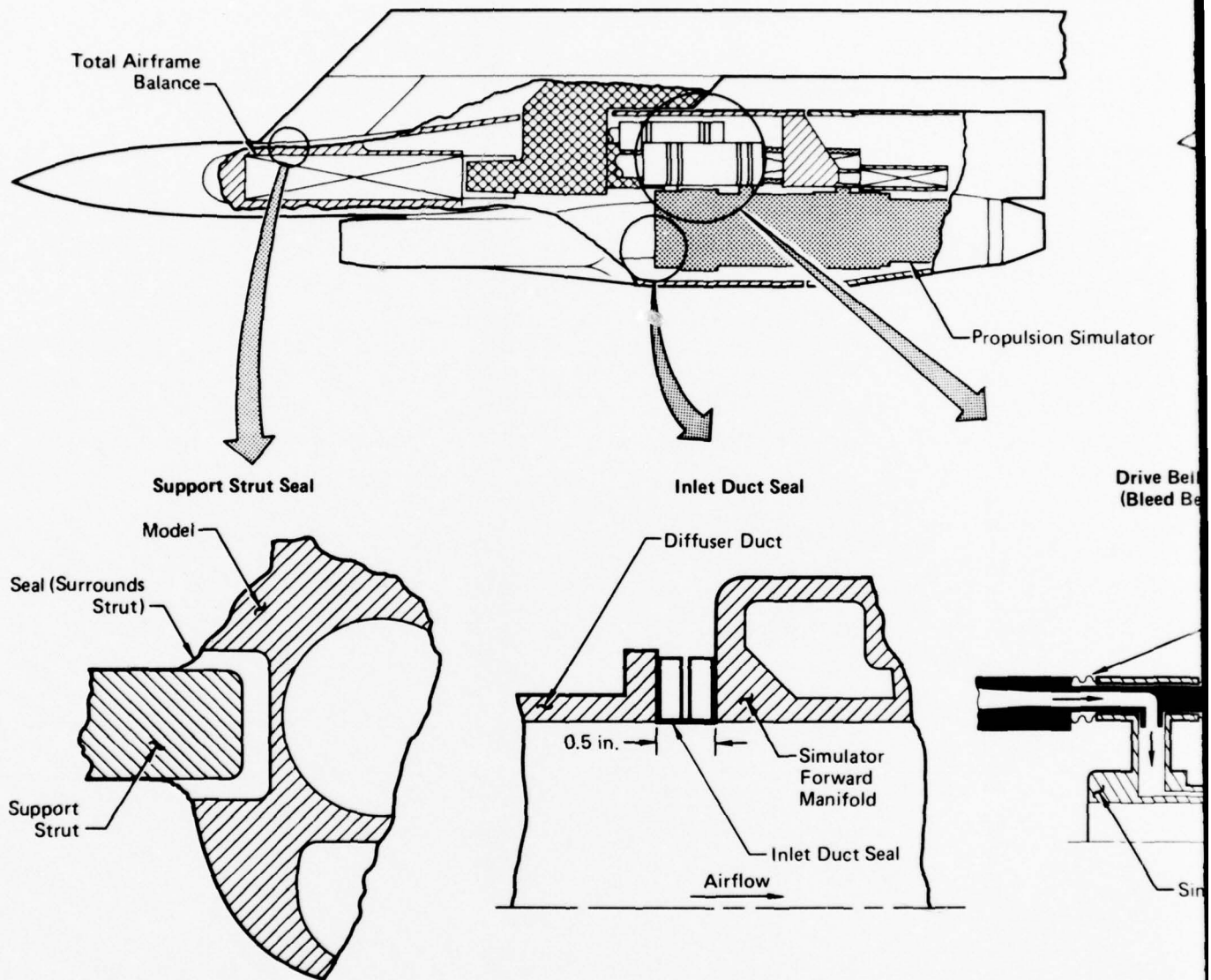
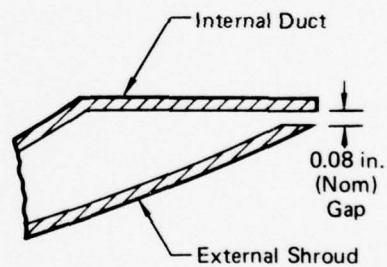
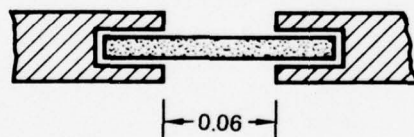
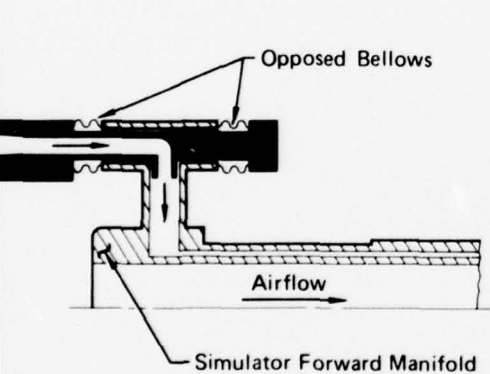
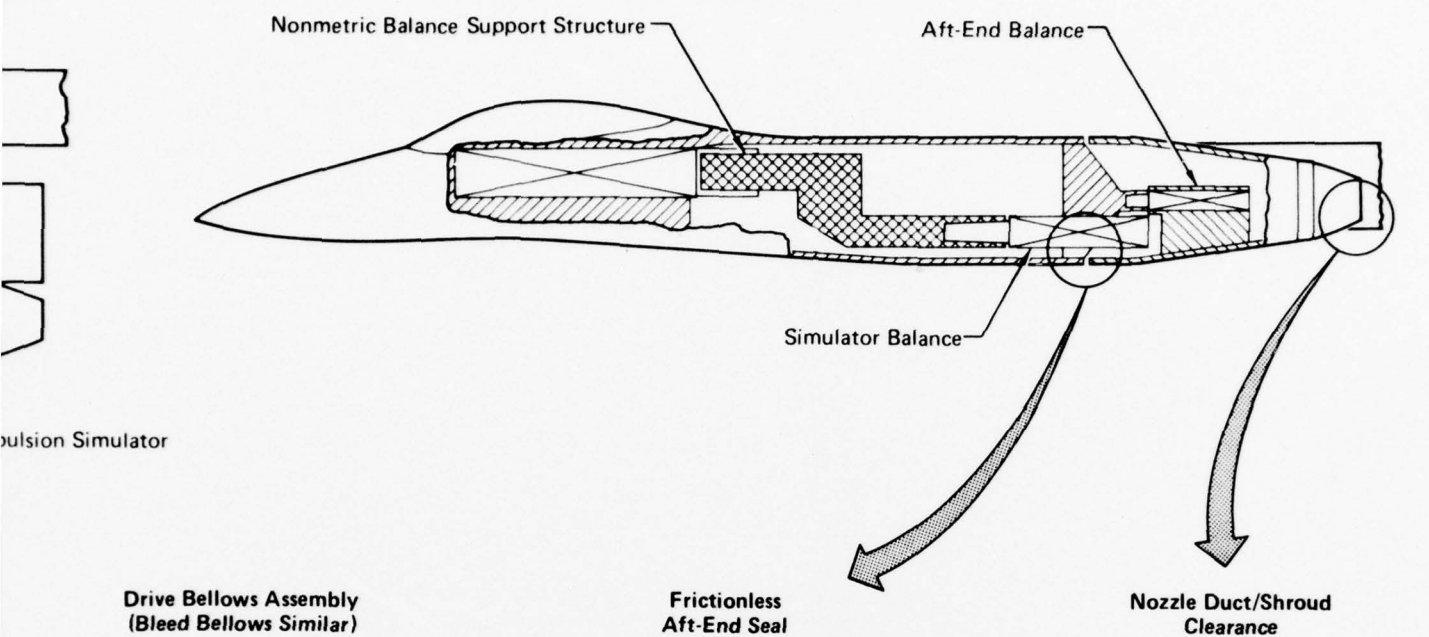


FIGURE 3-8
FORCE BALANCE ARRANGEMENT AND BRIDGING MECHANISMS

GP76-0701-4



is attached directly to the support system, is utilized in all three test configurations.

Aft-end forces and moments are measured by a 1.0 inch diameter Task MK XII balance in the aft portion of the model. This balance is attached directly to the center fuselage so that the aft-end forces and moments are also transmitted to and measured by the total airframe balance. A 0.060 inch gap separates the metric aft-end hardware from the rest of the model. A floating Teflon seal is inserted into this gap to prevent in-flow. The aft-end balance is used only in the simulator and jet effects modes. For the aero flow-thru mode, the floating seal is replaced by a rigid piece, and the "live" aft-end balance is replaced by a dummy.

In the simulator mode, a 1.5 inch diameter Task MK XXI balance is used to measure only the simulator thrust. This balance is connected directly to the support strut. Bridging between the inlet diffuser, which is metric to the total airframe balance, and the simulator is accomplished with a rubber seal, as shown in Figure 3-8. The tare force associated with this seal was calibrated prior to the test program, and is discussed in Appendix B. At the nozzle trailing edge, a 0.080 inch annular gap separates the internal nozzle duct from the external nozzle shroud, which is metric to the aft-end balance. Metal bellows bridge the simulator drive and bleed air lines between the metric simulator and the non-metric support strut. The tare force associated with these bellows was calibrated prior to the wind tunnel test.

Balance Thermal Control Systems - A thermal control system on the total airframe and simulator balances minimizes errors due to axial temperature gradients. These systems were incorporated after an extensive thermal analysis of the model/simulator combination indicated that bias errors could be introduced into the force balance output as a result of axial temperature gradients. The simulator, with its relatively hot turbine drive air and usually cool bleed air, was found to contribute significantly to these temperature gradients. Some results of the analysis on the total airframe balance are presented in Figure 3-9.

Without thermal control, it is seen that an axial force bias error of up to 5.5% of the measured value exists during the early portion of the testing. This error reduces with time as the balance and model approach steady-state conditions. However, if the balance is thermally controlled to a set temperature before the start of testing, and that temperature is then maintained during the testing, the bias error is reduced and remains nearly constant.

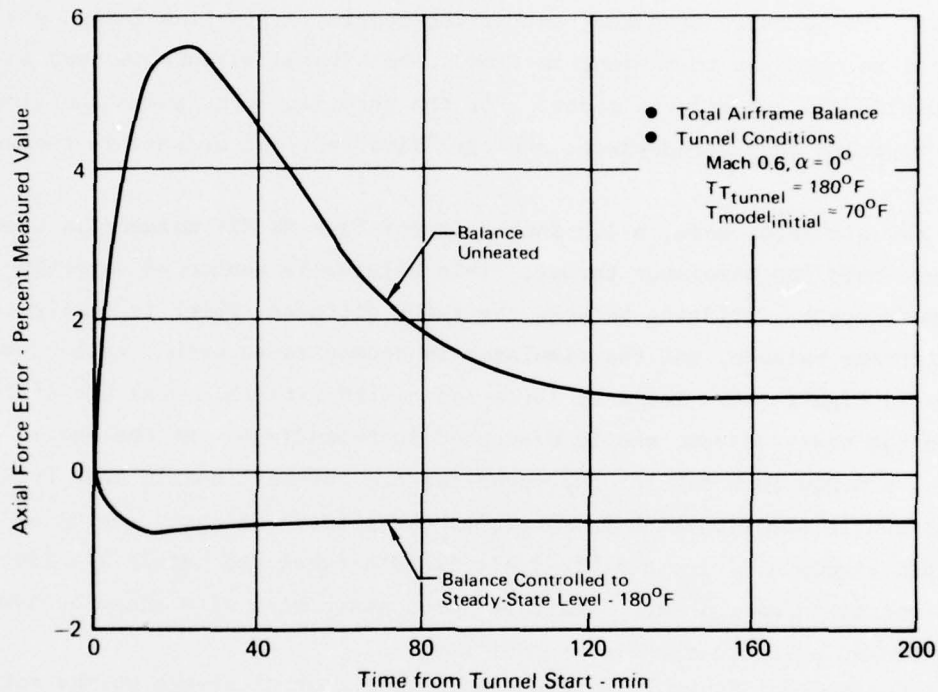
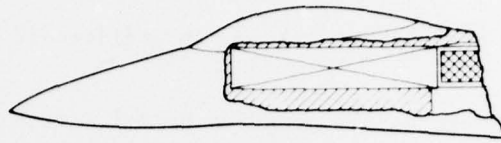


FIGURE 3-9
REDUCTION OF BIAS ERROR DUE TO TOTAL AIRFRAME
BALANCE THERMAL STRESSES

GP76 0701-94

The thermal control systems for the total airframe and simulator balances are shown in Figures 3-10 and 3-11, respectively. The system for the total airframe balance consists of two separate heating zones. One zone uses four thermal rods, each with a heating capacity of 12.3 watts/inch of length, inserted into the structure around the balance and running the entire length of the balance. The other zone consists of a thermal blanket, with a heating capacity of 2.2 watts/in², wrapped around the balance tang. The thermal control system for the simulator balance utilizes three separate heating zones. Each zone consists of a thermal blanket wrapped around the balance, with a heating capacity ranging from 2.6 to 5.4 watts/in².

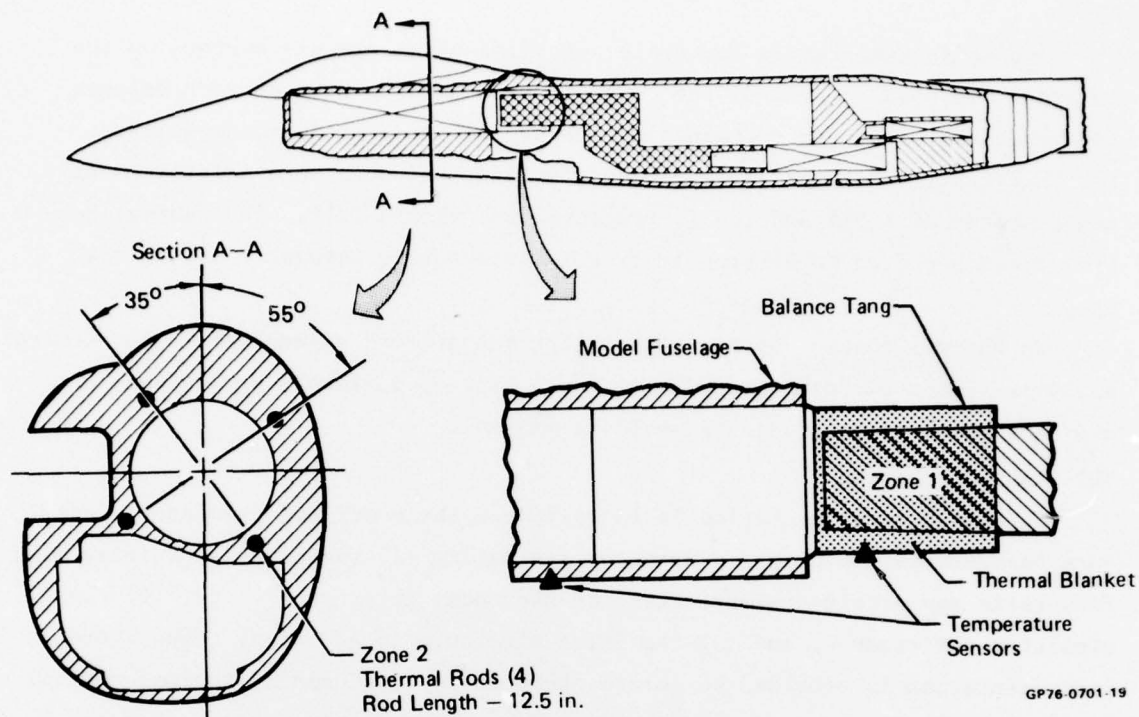


FIGURE 3-10
THERMAL CONTROL SYSTEM FOR THE TOTAL AIRFRAME BALANCE

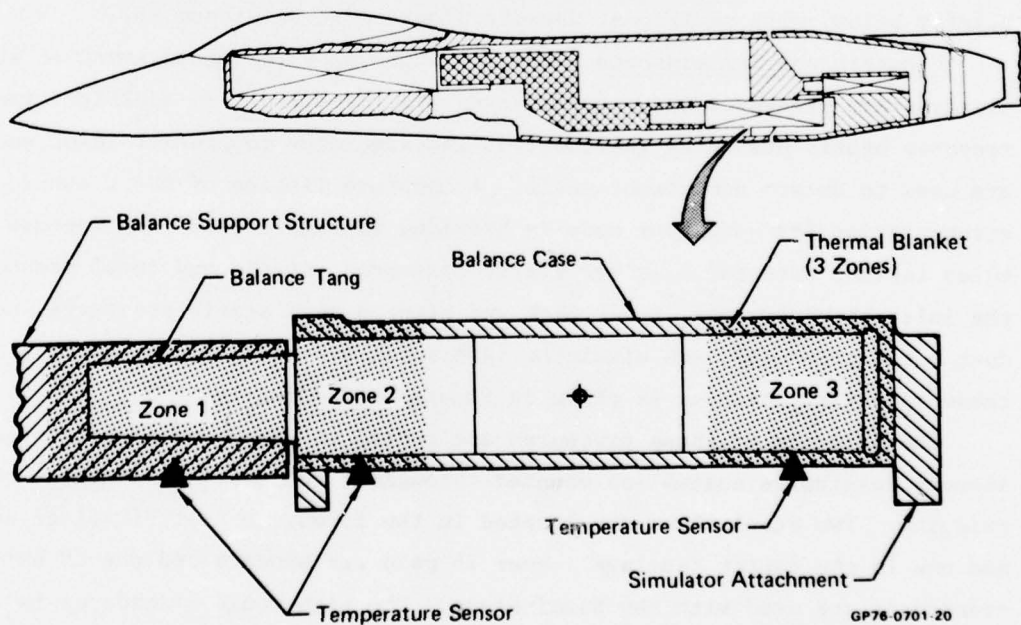


FIGURE 3-11
THERMAL CONTROL SYSTEM FOR THE SIMULATOR BALANCE

Automatic temperature controllers utilizing temperature sensors on the balances are used to control the power to each heating zone on each balance independently, in order to maintain each balance at a uniform temperature. For this test, the total airframe and simulator balances were maintained at temperatures of 135°F and 160°F, respectively, within $\pm 2^\circ\text{F}$. The thermal control systems proved to be trouble-free and completely automatic during the test.

No thermal control system is used for the aft-end balance since the thermal analysis indicated that this balance would heat up uniformly during the test and that temperature gradients would be minimal.

3.2 Instrumentation

Extensive instrumentation is installed on the model and simulator. Pressure instrumentation provides data for evaluating (1) the effects of inlet mass flow ratio and nozzle pressure ratio on the model external surface, (2) the simulator performance, and (3) the inlet airflow. In addition, temperature instrumentation is provided to obtain the data for the balance thermal control systems and simulator performance evaluation. A pendulous angle transducer in the forward fuselage measures model attitude, and electrical circuits are provided to indicate model hardware fouling. The instrumentation is discussed briefly below, with additional details provided in Reference (3).

Pressure and Temperatures - The model provides for measurement of 167 steady-state pressures when the simulator is installed. In addition, two high response static pressures (Kulites) at the simulator compressor inlet and exit are used to detect compressor stall. A complete listing of the pressure instrumentation for each test mode is provided in Figure 3-12. Parameters measured include external fuselage static pressures, static and total pressures for the inlet bleed systems, inlet duct and aft-end seal static pressures, nozzle duct total pressures, and simulator face total pressures. The location of these specific pressures is shown in Figure 3-13 and 3-14.

The majority of these pressures are routed to five single unit (type S2) 48-port Scanivalve assemblies mounted throughout the model to minimize balance bridging. Two Scanivalves are located in the forward and aft-fuselage sections and one in the center fuselage. Four 15 psid transducers and one 25 psid transducer are used with the Scanivalves. The high range transducer is used to measure the compressor inlet and exit total pressure, and nozzle total pressures. Eleven high pressure lines are routed out of the model and, consequently, bridge the simulator balance.

Model

Type of Instrumentation	Number of Measurements	Applicable Test Mode			Application
		Simulator	Aero Flow-Thru	Jet Effects	
Static Pressures	12	X	X		Inlet ramp/throat bleed airflow determination
	5	X			Inlet duct seal pressure tare correction
	8	X		X	Aft-end seal pressure tare correction
	12	X	X	X	Internal cavity pressure tare correction
	4		X		Nozzle choke base tare correction
	4	X			Bellows pressure tare correction
	7		X		Exit choke airflow determination
	83	X	X	X	External surface pressure distribution evaluation
Total Pressures	1	X	X		Inlet throat bleed airflow determination
	24		X		Exit choke airflow determination

Simulator

Static Pressures (Low Response)	1	X			Monitoring of bleed air pressure
	3	X			Rotor thrust determination for simulator health monitoring
Static Pressures (High Response)	2	X			Compressor stall detection
Total Pressures	25	X			Compressor entrance pressure for airflow and pressure recovery determination
	5	X			Nozzle pressure ratio and thrust coefficient determination
	1	X			Monitoring of drive air pressure
	6	X			Compressor exit pressure for airflow determination

GP76 0701 24

**FIGURE 3-12
MODEL/SIMULATOR PRESSURE INSTRUMENTATION**

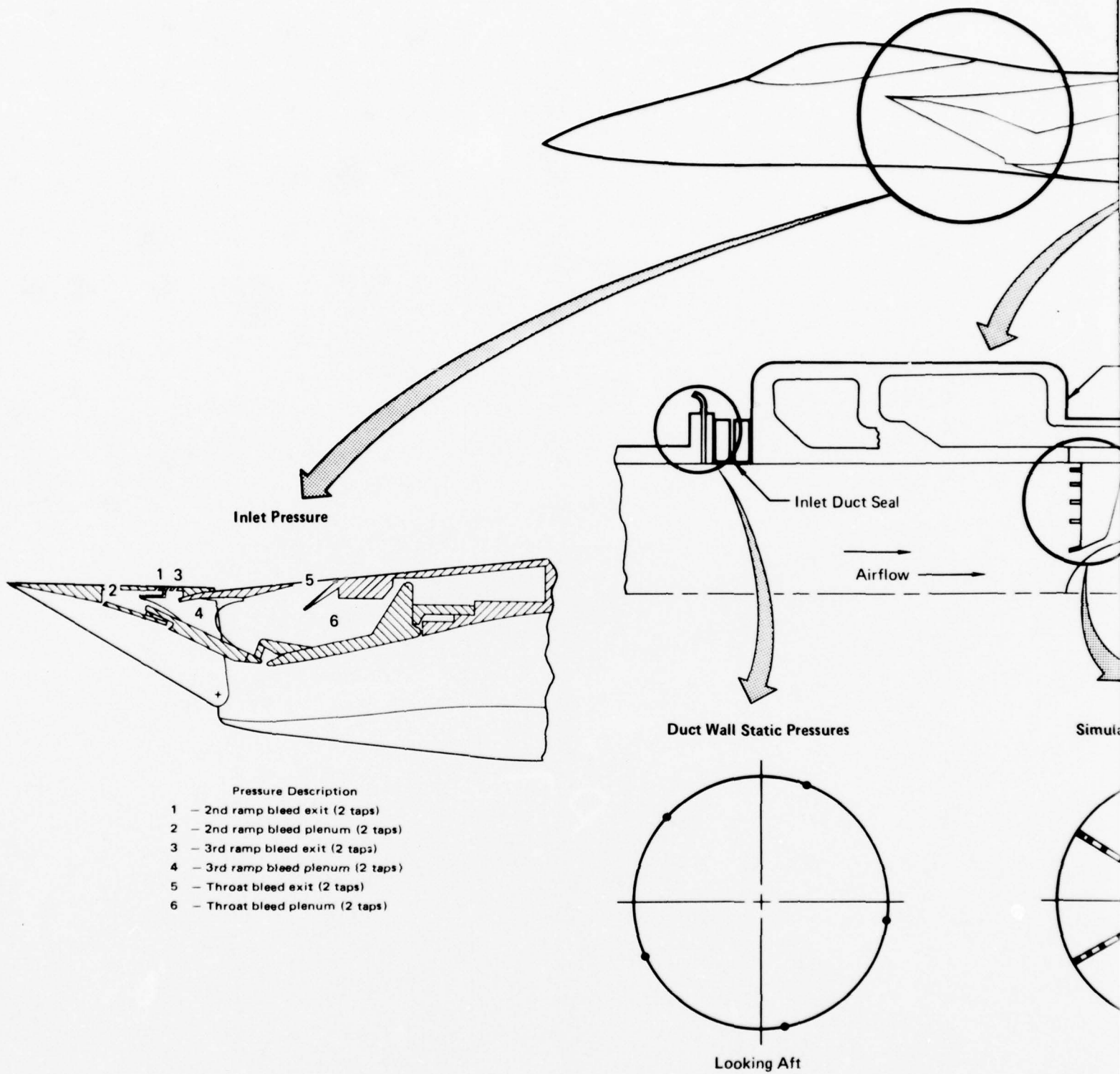
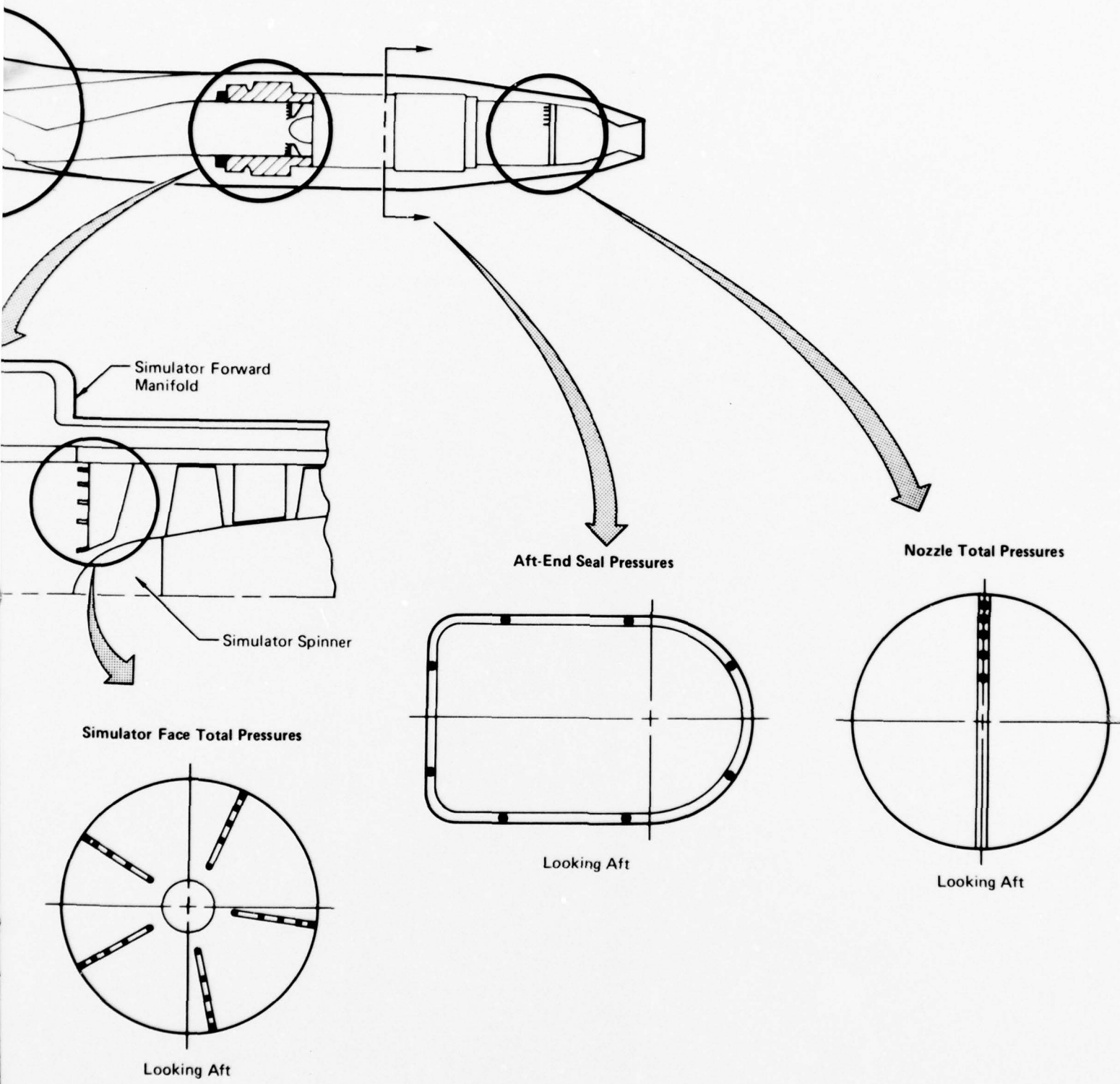
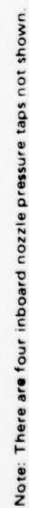


FIGURE 3-13
MAJOR INTERNAL MODEL PRESSURE INSTRUMENTATION

GP76 0701 5





FS 35.80

GP76-0701-48

Thirteen temperature measurements are also provided. These include force balance temperatures, simulator bearing and drive airflow temperatures, and nozzle airflow temperatures.

Miscellaneous - The axial position of the simulator rotor is measured using a Bently probe measuring system. This system uses a Proximity Detector located in the simulator and a Proximeter located outside the model. A 110 volt AC power supply is used with the system. The rotational speed of the simulator is measured using a magnetic speed pick-up. Two accelerometers are used to monitor the vibration of the simulator rotating machinery. Accelerometer signal conditioning is provided by pre-amps mounted on the simulator.

Two electrical circuits are provided in the model to indicate fouling between the trailing edge of the internal nozzle duct and external nozzle shroud. The other circuit monitors fouling inside the model between the fuselage shell and simulator.

4. WIND TUNNEL TEST PROGRAM

The test program was conducted in the Arnold Engineering Development Center (AEDC) 16-foot Transonic and Supersonic tunnels during October and November 1975. Details of test facilities, general test procedures, data reduction and accuracy are discussed in this section.

4.1 Test Facility

The AEDC 16-foot Transonic and Supersonic Wind Tunnels are continuous-flow, closed-circuit tunnels with normal Mach number ranges of 0.20 to 1.60 and 1.50 to 4.75, respectively. Each test section measures 16 feet square and 40 feet long. The contours of the flexible sidewall nozzle system is changed by electric (16T) or hydraulic (16S) actuators. The transonic tunnel test section, whose walls are perforated, is enclosed in a plenum chamber such that the boundary layer is reduced and wall effects are minimized. An air-to-water heat exchanger provides temperature control and is located in the stilling chambers for the 16T and at both ends of the compressor for the 16S.

4.2 Test Conditions and Procedures

The 16S tunnel was used to check out and verify the operation of the model/simulator subsystems prior to the performance testing in the 16T tunnel. The 16S tunnel was run at approximately Mach 0.5 with the tunnel operating in an abnormal, unstarted, subsonic run mode. During this running, the simulator was operated over its entire speed and pressure ratio range at varying model angles of attack.

The aerodynamic performance testing was conducted in the 16T tunnel at Mach numbers from 0.6 to 1.45. The installation of the model in the tunnel is shown in Figure 4-1. All control valves, venturis, and safety valves for the simulator drive and bleed air lines were located on the tunnel sector under a protective cover, approximately 8 feet from the tail end of the model. A summary of the testing conducted in each model test mode is presented in Figure 4-2.

Simulator Mode Test Procedures - For each test period, prior to start of the simulator mode testing, the simulator was operated statically at idle and 70% speed to verify its health. Several data points were taken during this operation, and key health-related measurands were then compared on a day-to-day basis to aid in detecting potential problems and performance deterioration. These measurands included the bearing temperatures, vibration levels, rotor axial

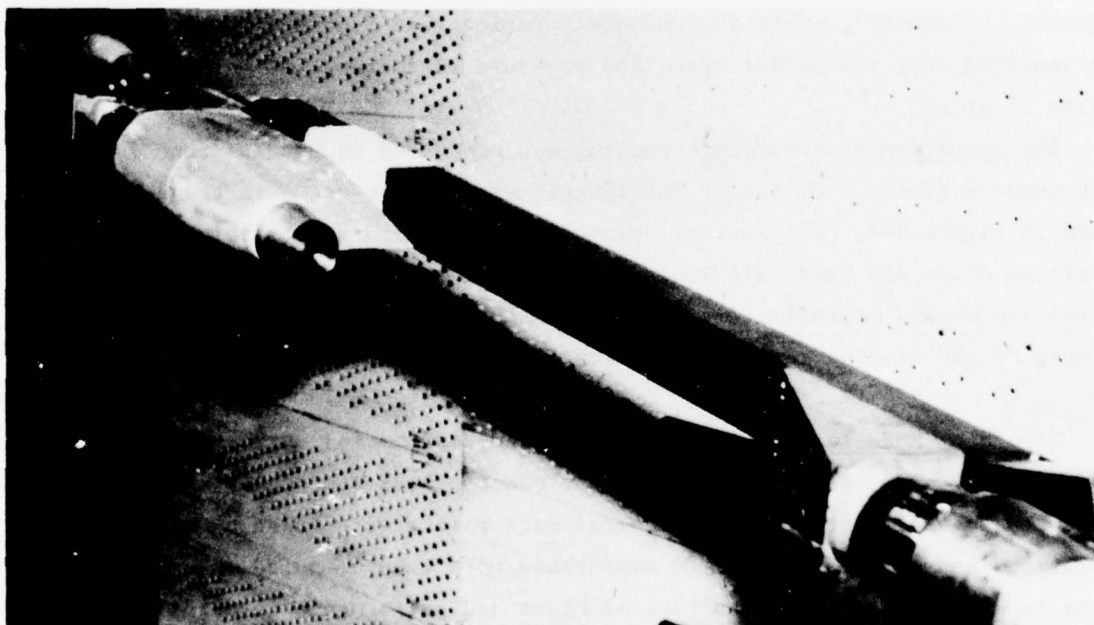
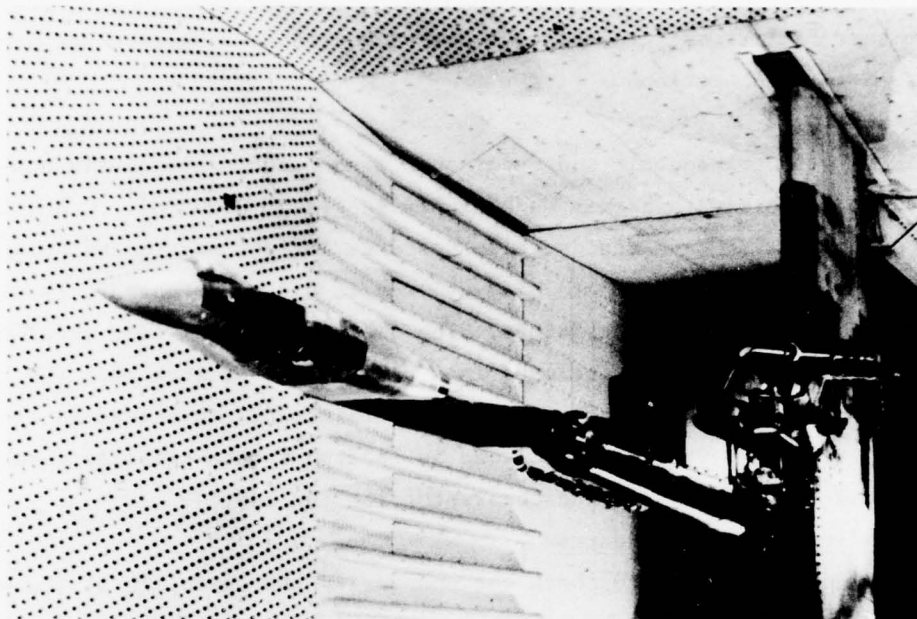


FIGURE 4-1
MODEL INSTALLATION IN THE AEDC 16 FOOT TRANSONIC TUNNEL

GP76-0701-33

Test Mode	Nozzle or Choke	$R_N/\text{ft} \times 10^{-6}$	$T_{T_0} - ^\circ\text{F}$	M_0	Nominal NPR	Nominal MFR	α ($^\circ$)			
Aero Flow-Thru ↓	C ₁ Choke ↓	2.50 ↓	120 ↓	0.60 0.90 1.20 0.60 0.90 1.20 1.45	Flow-Thru ↓	0.30 0.30 0.32 0.38 0.38 0.41 0.45 0.53 0.48 0.48 0.51 0.56 0.56 0.59 0.66	0 → 16 ↓ 0 → 10 ↓ -1.6 → 16 ↓ -1.6 → 10 ↓ 0 → 10			
	C ₂ Choke ↓	1.55 ↓	1.55 ↓	1.45 1.45 0.60 0.90 1.20 1.45 0.60 0.90 1.20 1.45		0.48 0.48 0.51 0.56 0.56 0.56 0.59 0.66	0 → 10 ↓ -1.6 → 16 ↓ -1.6 → 10 ↓ 0 → 10			
	C ₄ Choke ↓	1.55 ↓	1.55 ↓	1.45 1.45 0.60 0.90 1.20 1.45 0.60 0.90 1.20 1.45		0.48 0.48 0.51 0.56 0.56 0.56 0.59 0.66	0 → 10 ↓ -1.6 → 16 ↓ -1.6 → 10 ↓ 0 → 10			
	C ₅ Choke ↓	2.50 ↓	2.50 ↓	1.45 1.45 0.60 0.90 1.20 1.45 0.60 0.90 1.20 1.45		0.48 0.48 0.51 0.56 0.56 0.56 0.59 0.66	0 → 10 ↓ -1.6 → 16 ↓ -1.6 → 10 ↓ 0 → 10			
	C ₆ Choke ↓	1.55 ↓	1.55 ↓	1.45 1.45 0.60 0.90 1.20 1.45 0.60 0.90 1.20 1.45		0.48 0.48 0.51 0.56 0.56 0.56 0.59 0.66	0 → 10 ↓ -1.6 → 16 ↓ -1.6 → 10 ↓ 0 → 10			
	Total Number of Data Points 190									
	Jet Effects ↓	A/B W/Choke ↓	2.50 ↓	120 ↓		0.60 0.90 1.20 1.45 0.60 0.90 1.20 0.60 0.90 1.20 1.45	1.2 → 2.4 ↓ 2.4 → 3.6 1.4 → 5.4 1.8 → 6.6 ↓ 1.4 → 5.4 1.8 → 6.6 ↓ 5.4 → 9.0	N/A ↓	0 → 16 ↓ 0 → 10 0 → 16 ↓ 0 → 10	
		Dry Power ↓	1.55 ↓	1.55 ↓		1.45 0.60 0.90 1.20 0.60 0.90 1.20 1.45	2.4 → 3.6 1.4 → 5.4 1.8 → 6.6 ↓ 1.4 → 5.4 1.8 → 6.6 ↓ 5.4 → 9.0	N/A ↓	0 → 16 ↓ 0 → 10 0 → 16 ↓ 0 → 10	
		A/B Power ↓	1.55 ↓	1.55 ↓		1.45 0.60 0.90 1.20 1.45	5.4 → 9.0	N/A ↓	0 → 10	
		Total Number of Data Points 235								
		Simulator ↓	Dry Power ↓	2.50 ↓		120 ↓	0.60 ↓ 0.90 ↓ 1.20 ↓ 0.60 ↓ 0.90 ↓	1.9 1.5 → 2.5 2.0 → 2.5 2.5 → 3.2 3.1 → 3.4 2.6 2.1 → 3.1 3.3 2.7 → 3.3 4.1 3.5 → 4.1 4.2 → 4.6 2.9 → 3.7 4.0 → 4.7 5.8 5.0 5.8 5.8 2.1 2.1 3.2 1.8 → 3.7 2.8 2.4 → 5.1	0.31 0.41 0.49 0.57 0.62 0.29 0.35 0.38 0.43 0.46 0.50 0.54 0.37 0.44 0.48 0.51 0.54 0.47 0.54 0.57 0.61 0.48 0.53	0 → 10 ↓ -1.6 → 16 ↓ 0 → 10

FIGURE 4-2
WIND TUNNEL TEST SUMMARY

GP76 0701 101

position and rotor thrust.

The general procedure for taking data during the simulator testing was to (1) set freestream Mach number, (2) set simulator compressor airflow and overall pressure ratio conditions, and (3) perform a model angle of attack sweep. Setting the simulator operating conditions utilized a visual real-time update (~3 seconds) of the compressor airflow and pressure ratio values. As such, their calculation required a continuous on-line computer system. These conditions were set while the control console was in the automatic speed control mode. As the tunnel Mach number was changed, the simulator was maintained at the idle speed to minimize component wear. These procedures are discussed further in Section 6.

Conventional Mode Test Procedures - The procedures for testing in the conventional aero flow-thru and jet effects modes were the same as those used in past tests of models of this type.

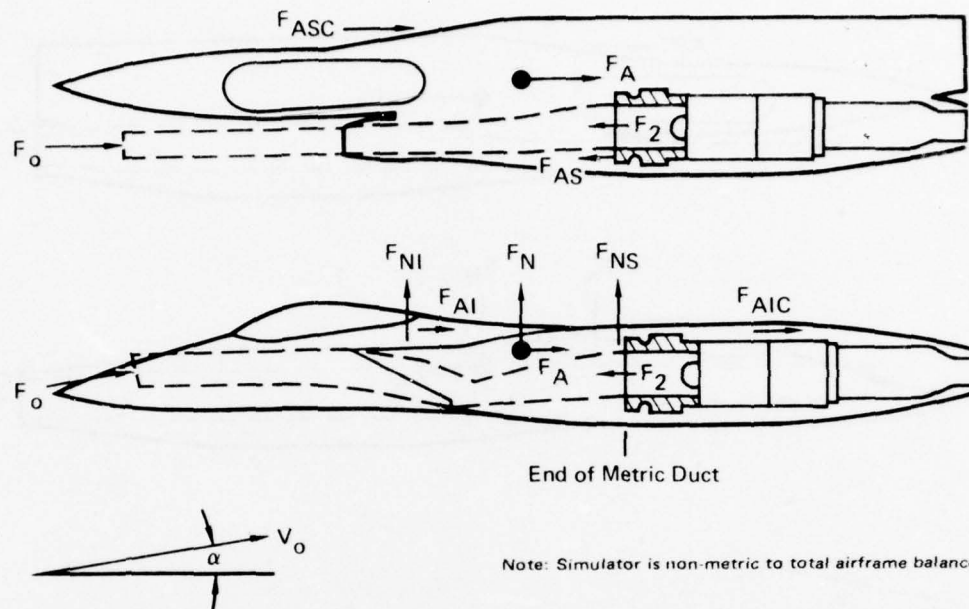
4.3 Data Reduction

Data reduction involved primarily the determination of the total airframe and aft-end forces and moments, and the simulator gross thrust. The forces acting on the total airframe and the applicable force and moment equations are shown in Figures 4-3 and 4-4 for the simulator and aero flow-thru modes, respectively. Those for the aft-end forces and moments and simulator thrust are shown in Figures 4-5 and 4-6, respectively. For the simulator mode, the compressor face stream thrust term (F_2) in the equations was calculated using the average compressor face total pressure and mass flow rates determined from the compressor face static and total pressure measurements. A complete listing of the data reduction equations can be found in Reference (3).

4.4 Data Accuracy

The data accuracy was assessed through a rigorous post-test error analysis and by reviewing the repeat data obtained at AEDC. An earlier pre-test error analysis was used to identify potentially large error sources and select the necessary instrumentation needed to minimize/eliminate them. The results of the post-test error analysis and analysis of the repeat data are discussed below.

Error Analysis - Estimates of the random error in the total airframe and aft-end drag, lift and pitching moment data were determined by considering the individual uncertainty of each term in the pertinent data reduction equations.



- Airframe Drag = $(F_A + F_2 + F_{AS} - F_{AI} - F_{ASC} - F_{AIC}) \cos \alpha + (F_N + F_{NI} - F_{NS}) \sin \alpha - F_O$
- Airframe Lift = $-(F_A + F_2 + F_{AS} - F_{AI} - F_{ASC} - F_{AIC}) \sin \alpha + (F_N + F_{NI} - F_{NS}) \cos \alpha$

where: F_A = Total airframe balance axial force

F_{AI} = Inlet bleed axial force

F_{AIC} = Internal cavity axial tare force

F_{AS} = Inlet duct seal axial tare force

F_{NS} = Inlet duct seal normal tare force

F_{ASC} = Strut cavity axial tare force

F_N = Total airframe balance normal force

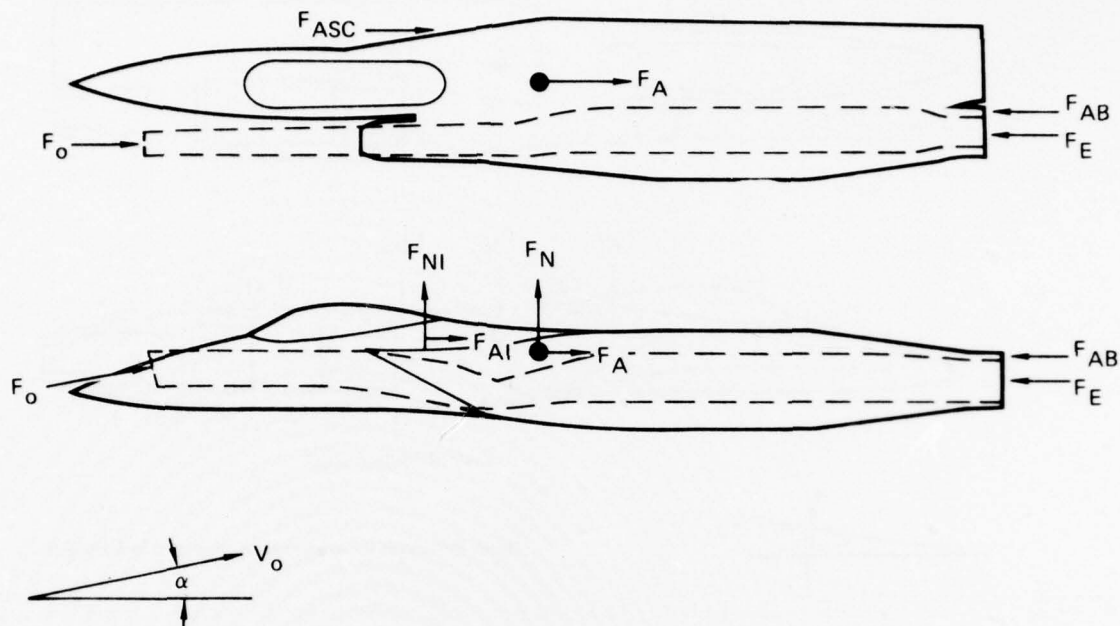
F_{NI} = Inlet bleed normal force

F_2 = Compressor face stream thrust

F_O = Freestream stream thrust

GP76 0701 49

FIGURE 4-3
TOTAL AIRFRAME DRAG AND LIFT DATA REDUCTION SUMMARY
FOR SIMULATOR TEST MODE



- Airframe Drag = $(F_A + F_{AB} + F_E - F_{ASC} - F_{AI}) \cos \alpha + (F_N + F_{NI}) \sin \alpha - F_O$

- Airframe Lift = $(F_A + F_{AB} + F_E - F_{ASC} - F_{AI}) \sin \alpha + (F_N + F_{NI}) \cos \alpha$

where: F_A = Total airframe balance axial force

F_{AB} = Exit choke base axial tare force

F_{AI} = Inlet bleed axial force

F_{ASC} = Strut cavity axial tare force

F_E = Internal duct exit stream thrust

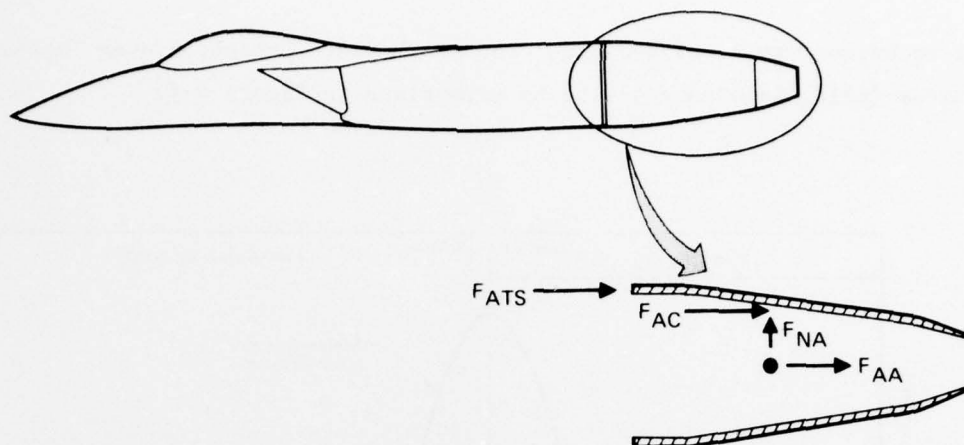
F_N = Total airframe balance normal force

F_{NI} = Inlet bleed normal force

F_O = Freestream stream thrust

GP76-0701-50

FIGURE 4-4
TOTAL AIRFRAME DRAG AND LIFT DATA REDUCTION SUMMARY FOR
AERO FLOW-THRU TEST MODE

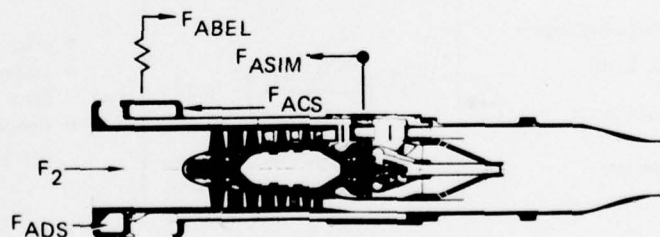


- Aft End Drag = $(F_{AA} - F_{AC} - F_{ATS}) \cos \alpha + (F_{NA}) \sin \alpha$
- Aft End Lift = $-(F_{AA} - F_{AC} - F_{ATS}) \sin \alpha + (F_{NA}) \cos \alpha$

where: F_{AA} = Aft end balance axial force
 F_{AC} = Internal cavity axial tare force
 F_{ATS} = Aft seal axial tare force
 F_{NA} = Aft end balance normal force

GP76 0701 51

FIGURE 4-5
AFT-END DRAG AND LIFT DATA REDUCTION SUMMARY
FOR SIMULATOR AND JET EFFECTS TEST MODES



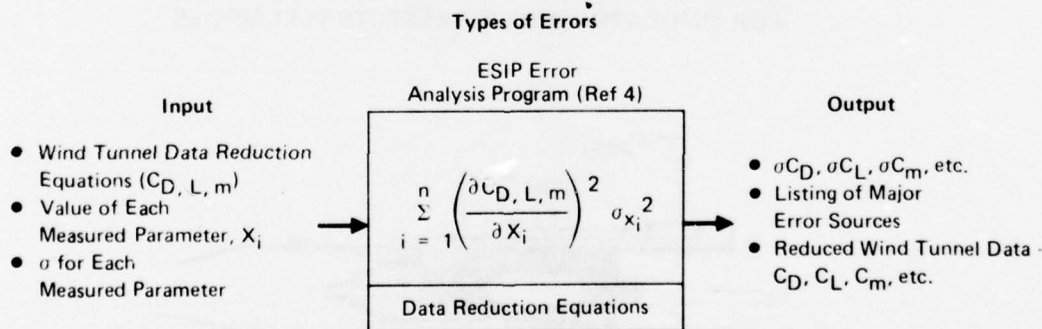
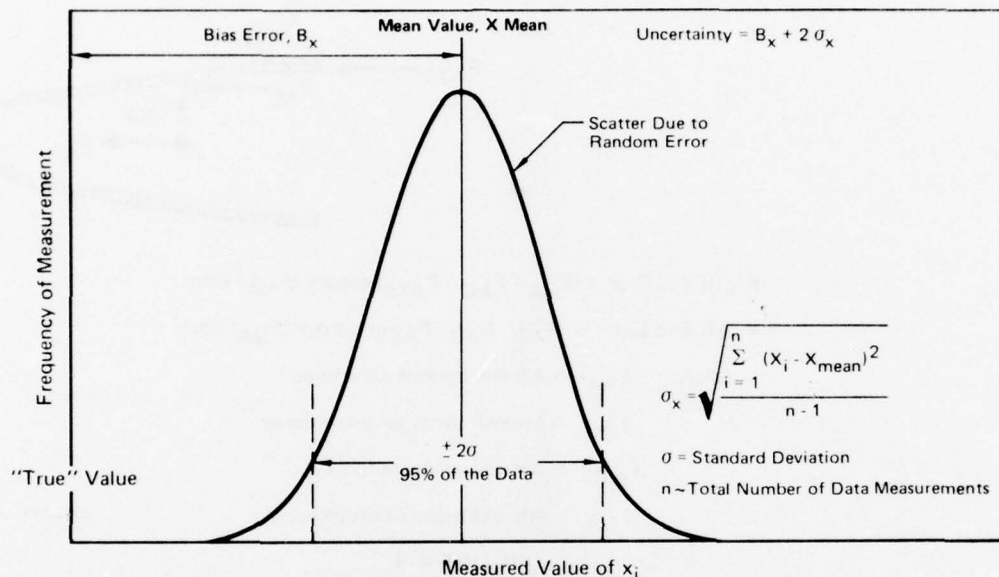
$$\text{Simulator Gross Thrust} = F_{ASIM} + F_{ADS} + F_2 + F_{ABEL} - F_{ACS}$$

where: F_{ASIM} = Simulator balance axial force
 F_2 = Compressor face stream thrust
 F_{ADS} = Inlet duct seal axial tare force
 F_{ABEL} = Bellows axial tare force
 F_{ACS} = Internal cavity axial tare force

GP76 0701 52

FIGURE 4-6
SIMULATOR THRUST DATA REDUCTION SUMMARY

The technique was developed under the AFAPL/MCAIR Exhaust System Interaction Program (ESIP, Reference 4) and is summarized in Figure 4-7.



GP76 0701 34

FIGURE 4-7
ESIP ERROR ANALYSIS PROCEDURE

The estimated random error in the important performance parameters ($C_L, C_D, C_m, C_{LA}, C_{DA}, C_{mA}, MFR, C_p$) for all three modes is summarized in Figure 4-8 at a typical Mach 0.9 condition. Figure 4-9 presents the major contributors to the random error in the total airframe drag for the simulator and aero flow-thru modes and the aft-end drag for the jet effects mode.

	Parameter	Predicted Random Error - $\pm 2\sigma$		
		Simulator Mode • Dry Nozzle • MFR = 0.53 • NPR = 4.6	Aero Flow-Thru Mode • A/B Choke • MFR = 0.48	Jet Effects Mode • Dry Nozzle • NPR = 4.2
Total Airframe	C_D	± 0.0002	± 0.0002	—
	C_L	± 0.0008	± 0.0008	—
	C_m	± 0.0002	± 0.0002	—
Aft-End	C_{DA}	± 0.0003	—	± 0.0003
	C_{LA}	± 0.0005	—	± 0.0005
	C_{mA}	± 0.0009	—	± 0.0009
	MFR	± 0.002	± 0.001	—
	C_p	± 0.005		

GP76 0701 53

FIGURE 4-8
PREDICTED ERROR IN IMPORTANT VEHICLE PERFORMANCE PARAMETERS
 Mach 0.9 $\alpha = 0^\circ$

Mean Value of C_D (or C_{DA})	Random Error - $2\sigma C_D$	Primary Contributors to Error	Percent Contribution to $\sigma^2 C_D$
Simulator Mode			
0.0105	0.0002	• Total Airframe Balance Axial Force Output • Freestream Static Pressure • Freestream Total Pressure • Miscellaneous	96.7 1.2 1.6 0.5
Aero Flow-Thru Mode			
0.0115	0.0002	• Total Airframe Balance Axial Force Output • Freestream Total Pressure • Miscellaneous	97.6 1.7 0.7
Jet Effects Mode			
0.0059	0.0003	• Cavity Pressure • Freestream Static Pressure • Miscellaneous	82.1 17.8 0.1

GP76 0701 54

FIGURE 4-9
PRIMARY CONTRIBUTORS TO DRAG COEFFICIENT RANDOM ERROR
 Mach 0.9 $\alpha = 0^\circ$

Data Repeatability - A realistic estimate of the random error can be derived by analyzing the repeatability of the data. Several test points at both subsonic and supersonic conditions were repeated in all three model test modes. Figure 4-10 summarizes the data repeatability at Mach 0.9. The repeatability at other Mach numbers is comparable.

The repeatability of the surface pressure coefficient data was also determined:

Mach Number	$2\sigma_{C_P}$
0.6	$\pm .006$
0.9	$\pm .005$
1.2	$\pm .005$
1.45	$\pm .004$

		Repeatability $\sim \pm 2\sigma$		
	Parameter	Simulator Mode	Aero Flow-Thru Mode	Jet Effects Mode
Total Airframe	C_D	± 0.0003	± 0.0002	± 0.0003
	C_L	± 0.0004	± 0.0006	± 0.0005
	C_m	± 0.0002	± 0.0003	± 0.0003
Aft-End	C_{DA}	± 0.0003	—	± 0.0002
	C_{LA}	± 0.0002	—	± 0.0002
	C_{mA}	± 0.0006	—	± 0.0002
	MFR	± 0.006	± 0.001	—

FIGURE 4-10
EXPERIMENTAL DATA REPEATABILITY
Mach 0.9

GP78 0701-103

5. WIND TUNNEL TEST RESULTS

Typically, aircraft performance predictions are made using the data obtained from an aero flow-thru model and a partially-metric jet effects model, as shown in Figure 5-1. The aero flow-thru model provides the basic aerodynamic force and moment data, as well as the data required to correct the basic results for mass flow ratio variations. The data from the jet effects model is used to obtain the corrections for nozzle pressure ratio and geometry variations. The testing of such models introduces both random and bias errors, as explained by Figure 5-2. Random errors represent the repeatability with which data are measured and recorded, whereas the bias errors represent a consistent shift in the average level of the data. The potential sources of bias errors in each of these models are illustrated in Figure 5-3. As noted in the figure, two of these potential error sources result directly from the inability to simultaneously duplicate, on one model, the complete aircraft geometry/flowfield and propulsion system flowfields. The magnitude of the bias errors from these two sources is dependent on the extent of interactions between the flowfields.

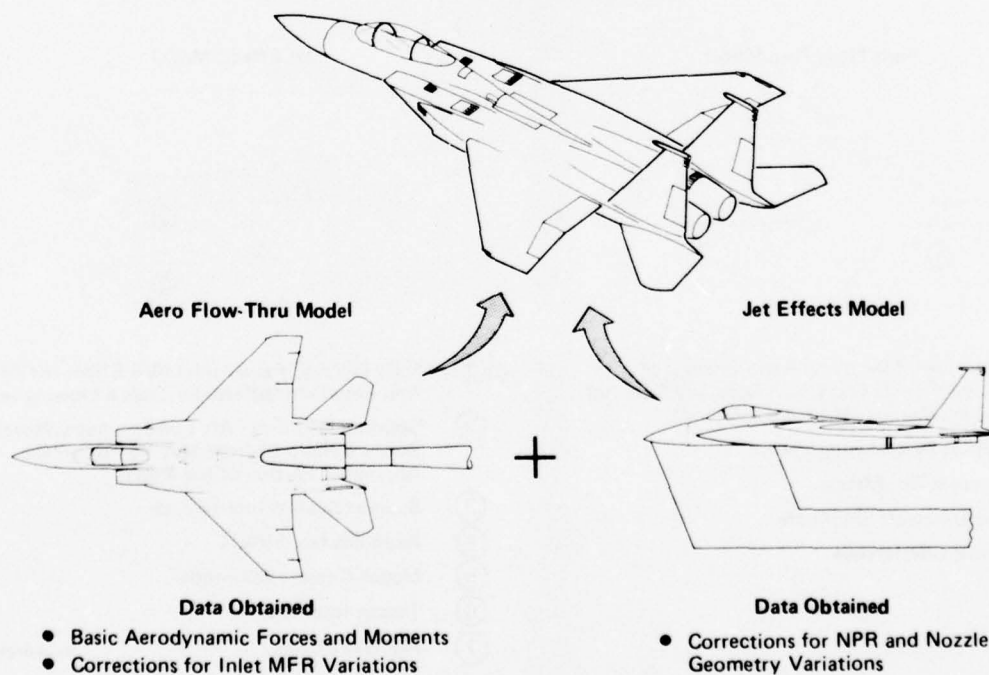
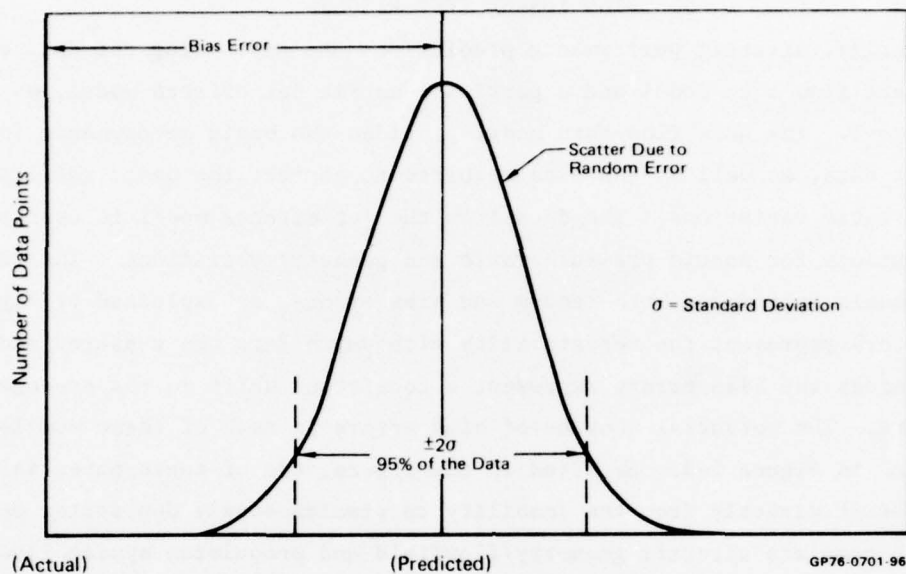


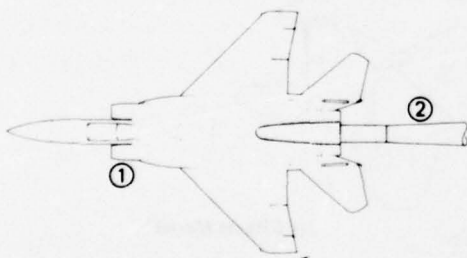
FIGURE 5-1
TYPICAL WIND TUNNEL MODEL REQUIREMENTS
FOR AIRCRAFT PERFORMANCE PREDICTION

GP76-0701-119



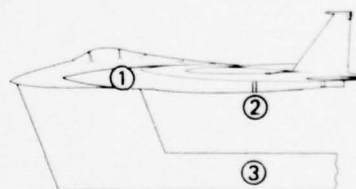
**FIGURE 5-2
TYPES OF ERROR**

Aero Flow-Thru Model



- ✓ ① Inlet Flow - Mass Flow Ratio Changes May be Felt on the Aft-End Which Normally Does not Entirely Simulate the Actual Aircraft
- ② Support System Interference
- ③ Reynolds No. Effects
- ④ Model/Aircraft Similitude
- ⑤ Tunnel Interference

Jet Effects Model



- ✓ ① Inlet Fairing - Faired Inlet May Effect the Aft-End Flowfield Differently Than a Flowing Inlet
- ② Splitline Location - Aft End Geometry/Nozzle Pressure Ratio Changes May be Felt on the Nonmetric Portion of the Model
- ③ Support System Interference
- ④ Reynolds No. Effects
- ⑤ Model/Aircraft Similitude
- ⑥ Tunnel Interference
- ⑦ Hot Gas Effects

GP76 0701 120

✓ Due to Lack of Simultaneous Aircraft Geometry/Flowfield Duplication

**FIGURE 5-3
POTENTIAL BIAS ERROR SOURCES IN CONVENTIONAL
WIND TUNNEL MODELS**

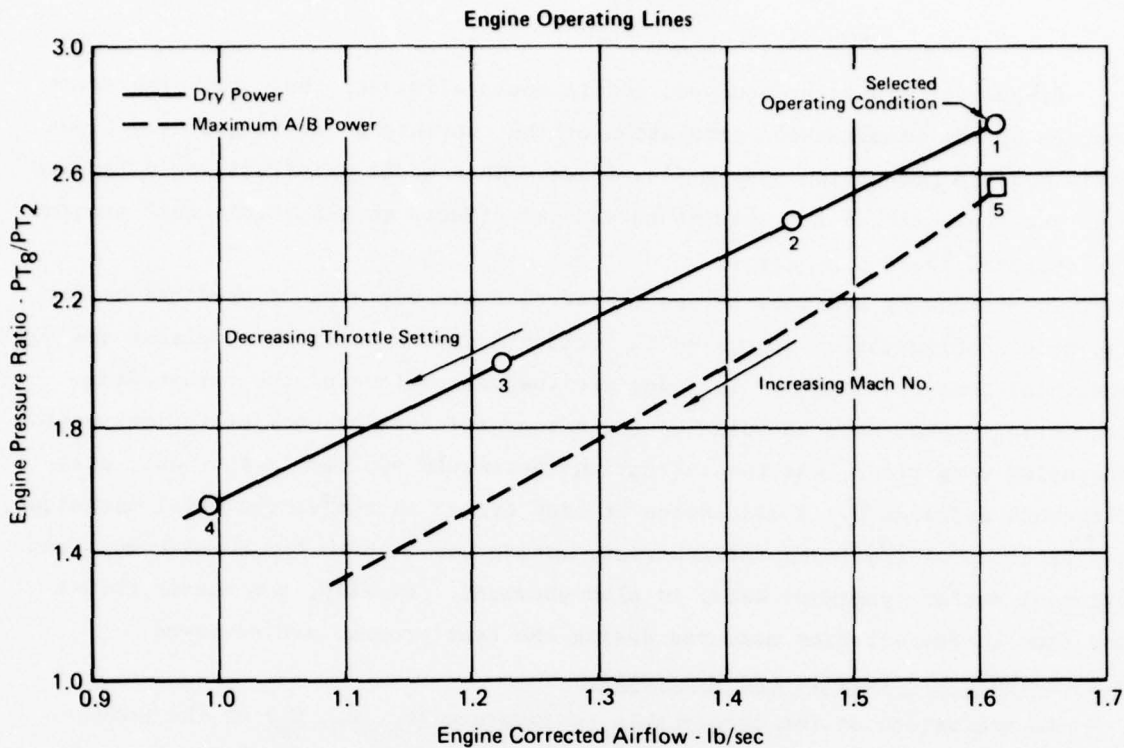
Propulsion simulator-equipped models could eliminate these two bias error sources by the simultaneous simulation of the complete aircraft geometry/flow-field and the propulsion system flowfields. This model in effect would replace both the conventional aero flow-thru and jet effects models. This test program investigated these bias errors.

The following sections review the aerodynamic performance predictions for the model configuration discussed in Section 3, using both the simulator and conventional test techniques. Included are the discussions of the thrust/drag accounting system used to build-up the aerodynamic performance at typical engine operating conditions, and the correction increments applied to the basic aero flow-thru model data. A discussion of bias errors in the conventional technique, and related inlet/aft-end interactions, making use of both the force/moment and external surface pressure data, is also provided. Finally, the nozzle thrust and flow characteristics measured during the test program are reviewed.

5.1 Aerodynamic Performance Evaluation

An evaluation of the aerodynamic performance (C_L , C_D , C_m) of the model configuration from both the conventional and simulator test techniques has been made at Mach 0.6, 0.9 and 1.2. This performance was defined at five typical engine operating conditions, representative of both dry and afterburning power operation. These conditions, Figure 5-4, are for an advanced afterburning turbo-fan engine and are expressed in terms of overall engine pressure ratio (P_{T8}/P_{T2}) and engine corrected airflow. As will be shown in Section 5.1.2, the performance difference between test techniques generally proved to be small.

An example of the typical total airframe lift, drag and pitching moment coefficients at Mach 0.9 is shown in Figure 5-5. These coefficients are based on a wing reference area and chord length which is typical of that of an advanced fighter aircraft. The absence of wings and tail surfaces on the model results in a maximum C_L of only 0.12. At the lower angles of attack the pitching moment trend is unstable, and then transitions to a stable condition above $\alpha = 10^\circ$. These characteristics indicate that the configuration neutral point, c.g. location for neutral static stability, at subsonic conditions varies between 20% and 50% of the body length, depending on the angle of attack. The pitching moment scale has been expanded for clarity.



Corresponding Inlet/Nozzle Conditions

Operating Condition	Mach = 0.6		Mach = 0.9		Mach = 1.2	
	MFR	NPR	MFR	NPR	MFR	NPR
1 (Int. Power)	0.62	3.4	0.53	4.6	—	—
2 (Cruise Cond.)	0.57	3.1	0.51	4.1	0.51	5.9
3 (Dash Cond.)	0.49	2.5	0.43	3.3	0.45	4.8
4	0.40	2.0	0.36	2.6	—	—
5 (Subsonic A/B)	0.62	3.2	0.53	4.2	—	—

**FIGURE 5-4
ACTUAL ENGINE OPERATING CONDITIONS FOR
AERODYNAMIC PERFORMANCE DEFINITION**

GP76-0701-121

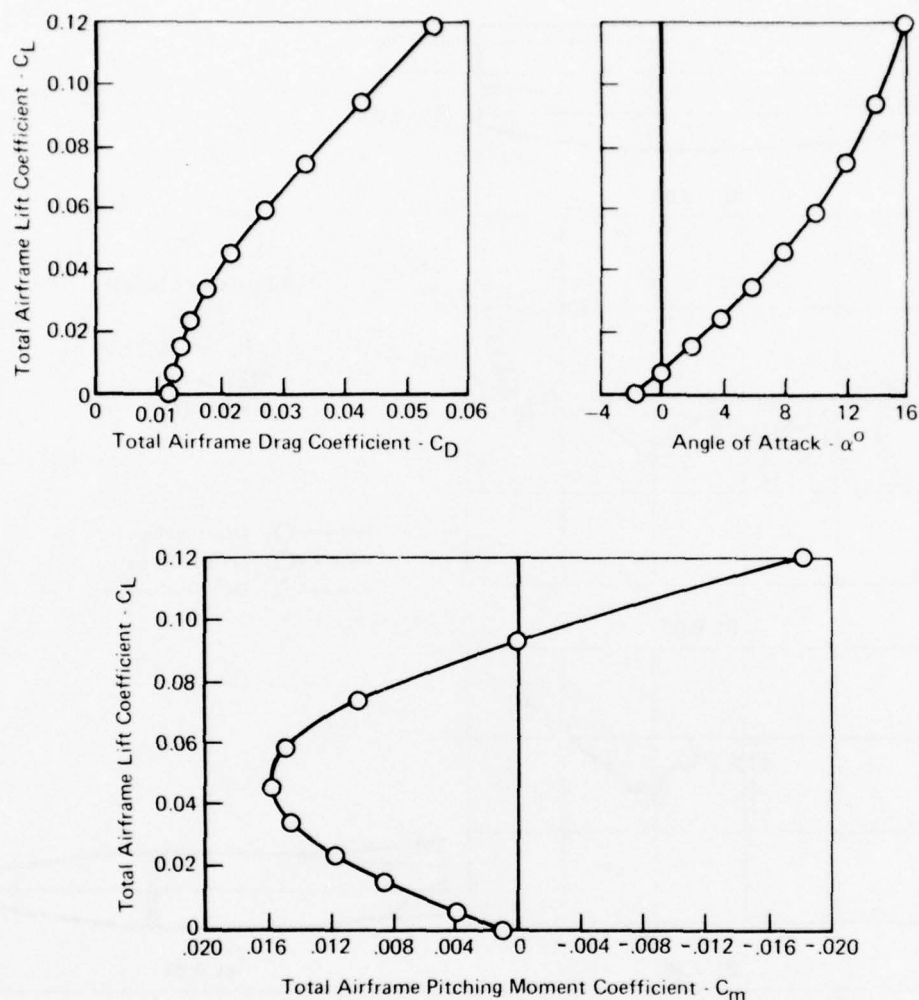


FIGURE 5-5
TYPICAL LIFT, DRAG AND PITCHING MOMENT CHARACTERISTICS

Simulator Model Dry Power Nozzle
Mach 0.9 NPR = 4.1 MFR = 0.51

GP76-0701-91

Typical external surface pressure distributions are shown in Figures 5-6 and 5-7 for the simulator model at Mach 0.9 and $\alpha = 0^\circ$ and 10° . An analytical prediction of the surface pressures has also been conducted to aid in explaining the variations in the measured pressures. This MCAIR prediction procedure, based on the representation of a particular body as an equivalent body of revolution, computes the turbulent, viscous flow over an isolated axisymmetric body with a supersonic exhaust jet.

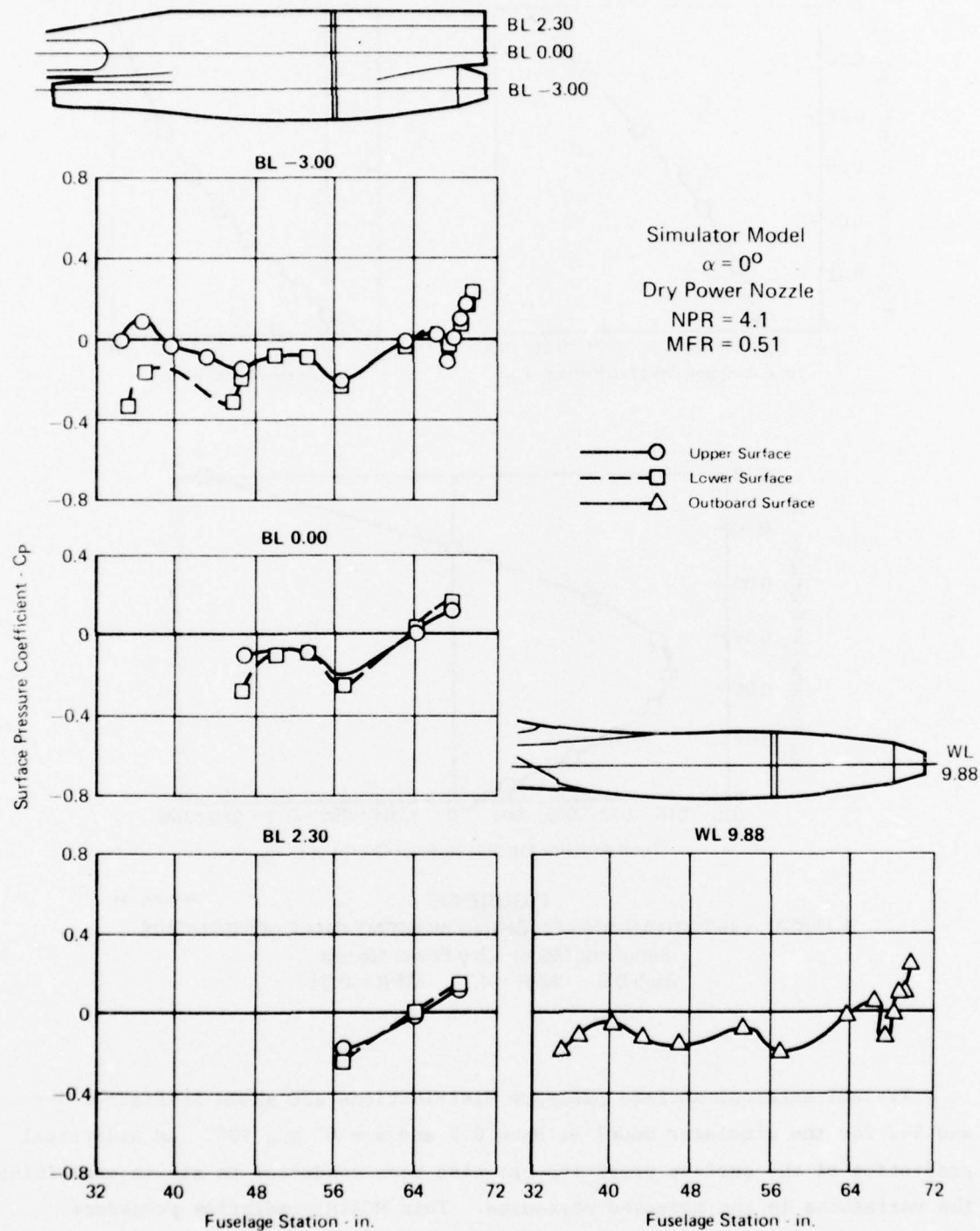


FIGURE 5-6
TYPICAL EXTERNAL SURFACE PRESSURE DISTRIBUTION
AT MACH 0.9

GP76 0701 164

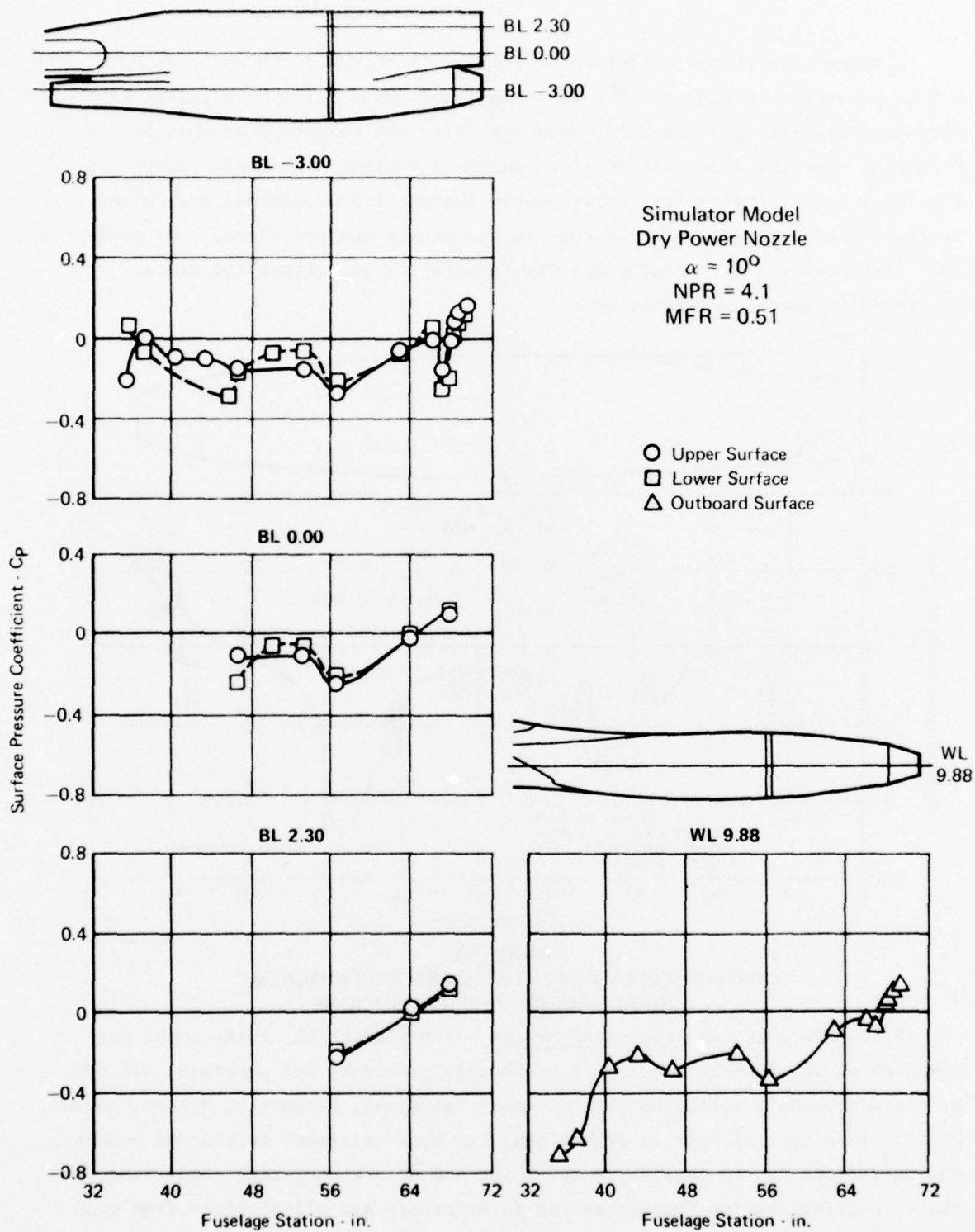


FIGURE 5-7
TYPICAL EXTERNAL SURFACE PRESSURE DISTRIBUTION
AT MACH 0.9

GP76 0701-165

A comparison of the analytical results with measured pressures at Mach 0.9 is presented in Figure 5-8. The comparison shows fairly consistent trends between analytical and measured pressures, with the largest discrepancies occurring near the inlet and nozzle. In these regions, the rapid changes in the local body geometry (and subsequently the surface pressures) are masked by the use of a two-dimensional body in the prediction procedure. The analytical procedure did not predict any flow separation for either the dry or afterburning power configuration.

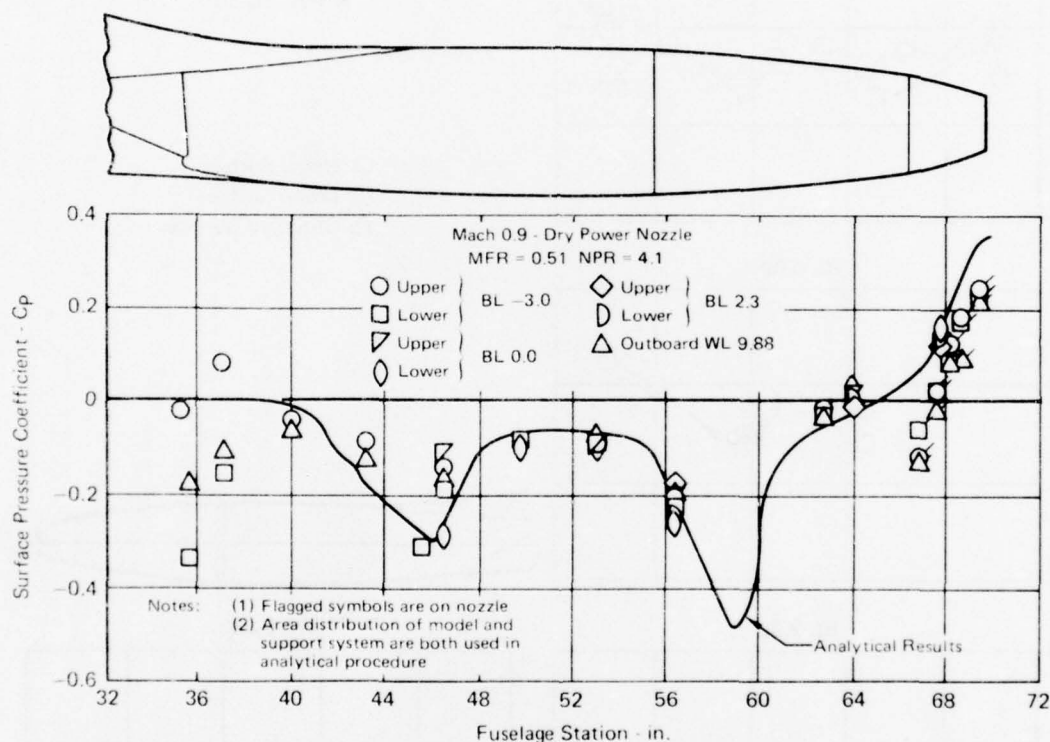


FIGURE 5-8
COMPARISON OF ANALYTICAL AND EXPERIMENTAL
SURFACE PRESSURE DISTRIBUTIONS

5.1.1 Thrust/Drag Accounting System - The prediction of the total performance of an aircraft requires a systematic procedure for combining all the forces and moments acting on that aircraft (airframe, propulsion system, engine, etc.). In a typical system, Figure 5-9, the basic airframe forces and moments, the variations due to changes in the inlet and nozzle operating conditions, and the corrections due to support system interference are all obtained from wind tunnel model tests. The engine performance data, thrust and fuel flow characteristics, are obtained from the manufacturer's test data. Additionally, corrections for Reynolds number, aircraft surface roughness and external stores

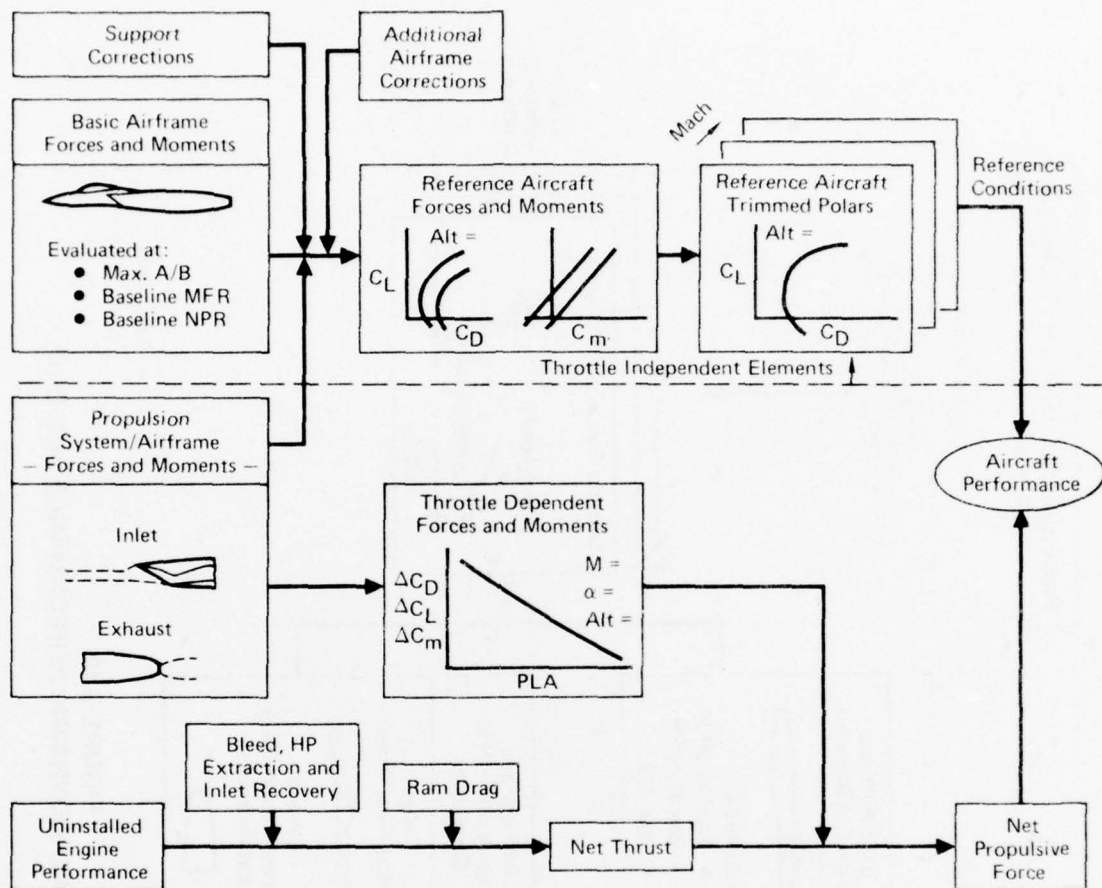
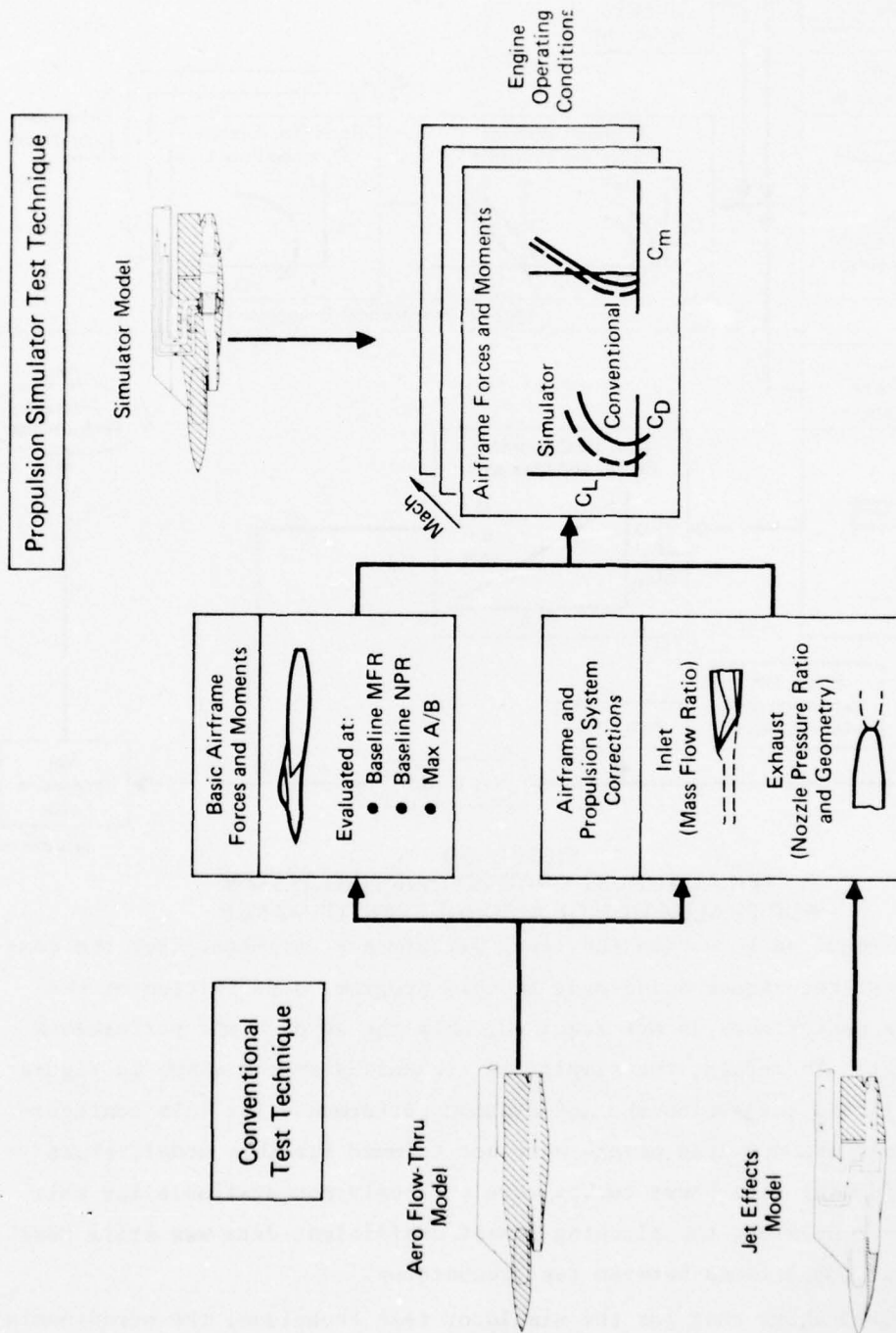


FIGURE 5-9
A TYPICAL THRUST/DRAG ACCOUNTING SYSTEM
FOR EVALUATION OF AIRCRAFT PERFORMANCE

are normally required to obtain the final performance estimate. For the comparison of test techniques being made in this program, a definition of the total vehicle performance is not required, only the aerodynamic performance is of interest. Therefore, the simplified accounting system shown in Figure 5-10, was utilized to develop the aerodynamic performance for this configuration. The performance drag polars were not trimmed for this model, since required horizontal tail power curves were obviously not available for this configuration. However, the pitching moment coefficient data was still used for additional comparisons between test techniques.

Figure 5-10 shows that for the simulator test technique, the aerodynamic performance is obtained directly at the actual inlet/nozzle operating conditions. This is possible because the propulsion simulator permits simultaneous matching of the inlet and nozzle flow/geometry conditions.



GP76 0701 85

FIGURE 5-10
PROCEDURE FOR AERODYNAMIC PERFORMANCE BUILD-UP

The data necessary to develop the aerodynamic performance for the conventional test technique are obtained from both the aero flow-thru model and the jet effects model. The basic airframe forces and moments are determined from the aero flow-thru model at a baseline mass flow ratio and nozzle pressure ratio conditions, differing from the actual inlet/nozzle operating conditions. In addition, the nozzle geometry is different from that of the actual operating nozzle. Therefore, to determine the aerodynamic performance at a simulated flight condition, the basic data must be corrected for differences in mass flow ratio, nozzle pressure ratio and nozzle geometry. The data necessary to correct for mass flow ratio differences are obtained on the aero flow-thru model, while the data necessary to make the other two corrections are obtained on the jet effects model. The data obtained on the jet effects model define the variation of aft-end drag, lift and pitching moment with nozzle pressure ratio for the actual operating nozzle geometries. In addition, the drag, lift and pitching moment variation is also determined for the nozzle geometry and pressure ratio used on the aero flow-thru model to provide a baseline from which to generate the necessary correction increments. Figures 5-11

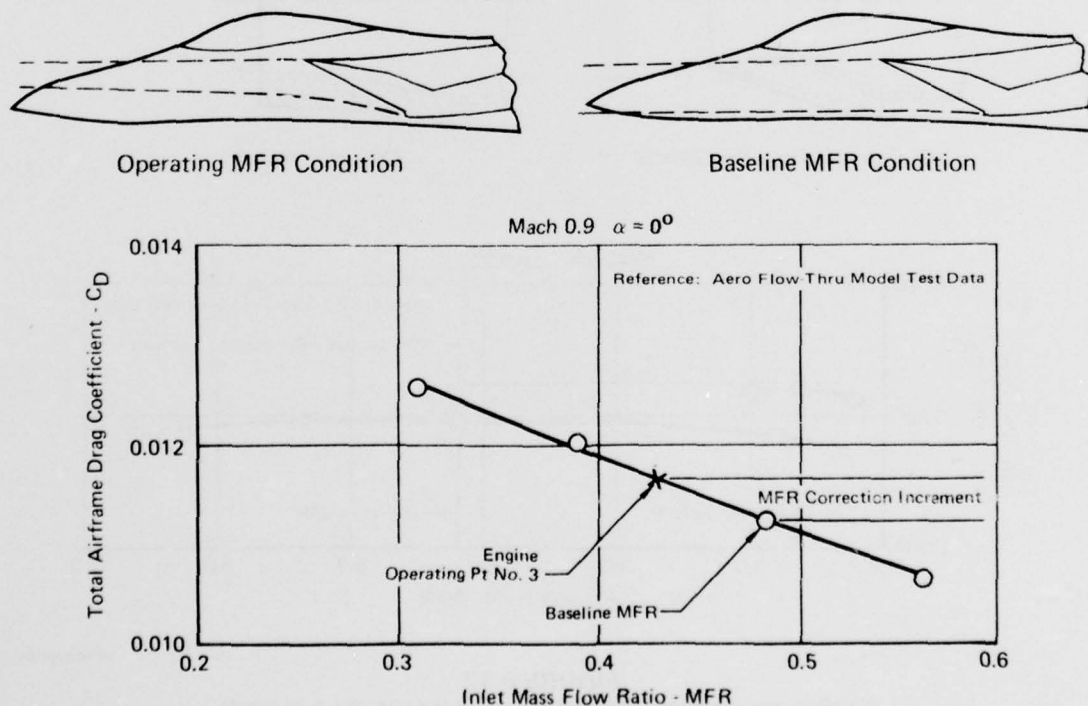


FIGURE 5-11
DETERMINATION OF MASS FLOW RATIO CORRECTION INCREMENT

and 5-12 illustrate the procedures used to determine the mass flow ratio and nozzle pressure ratio/geometry corrections to be applied to the basic airframe force and moment data.

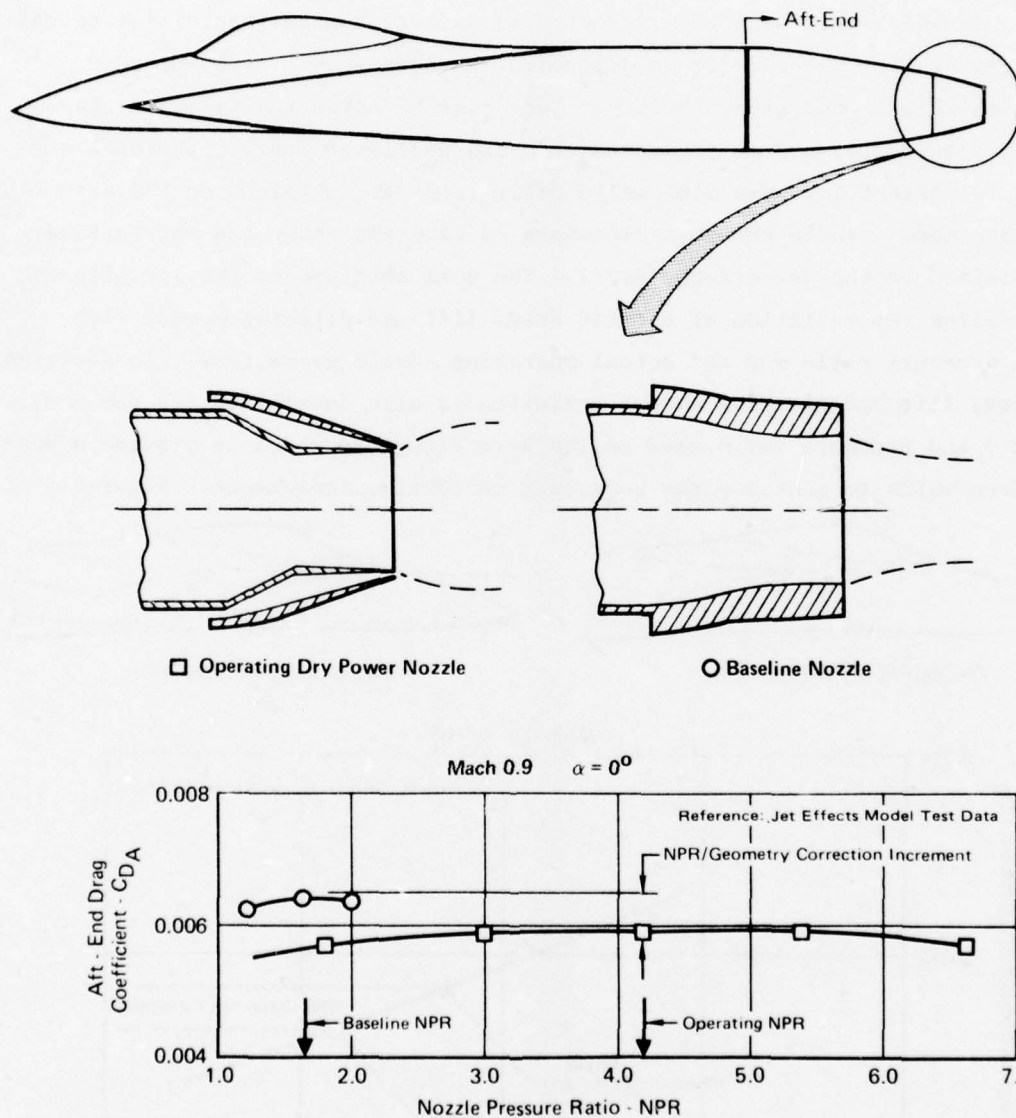


FIGURE 5-12
DETERMINATION OF NOZZLE PRESSURE RATIO AND
GEOMETRY CORRECTION INCREMENTS

GP76-0701 84

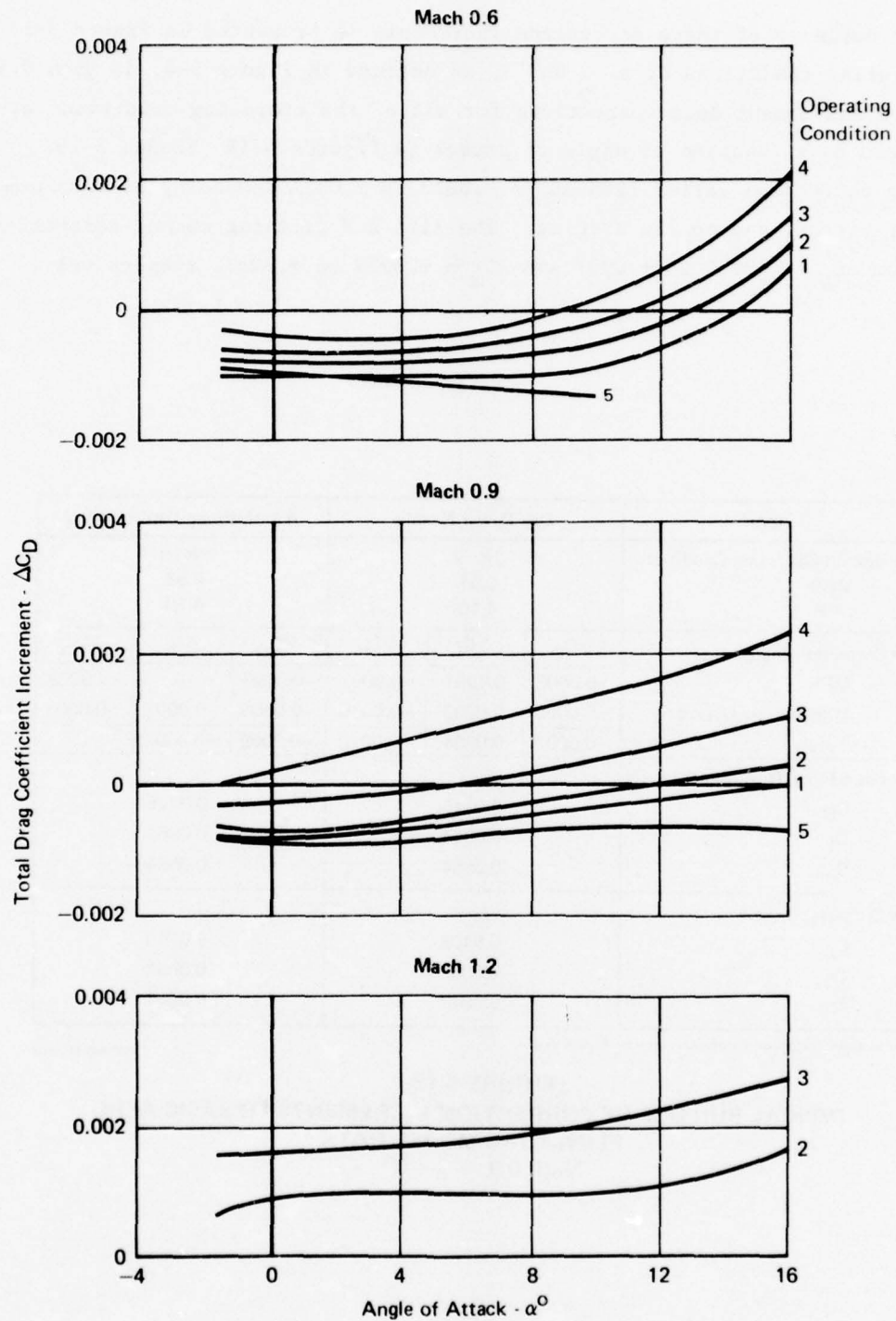
The build-up of these correction increments is presented in Figure 5-13 for operating conditions No's. 2 and 5, as defined in Figure 5-4, at Mach 0.9. The force and moment data corrections for all of the operating conditions are summarized as a function of angle of attack in Figures 5-14 through 5-16. The drag correction varies from $\Delta C_D = -.0013$ to $+.0027$ depending on Mach number, angle of attack, and nozzle setting. The lift and pitching moment corrections vary from $\Delta C_L = -.0050$ to $+.0007$ and $\Delta C_m = -.0027$ to $+.0084$, respectively.

Item	Dry Power Nozzle			Afterburning Power Nozzle		
• Desired Operating Condition	No. 2			No. 5		
– MFR	0.51			0.53		
– NPR	4.10			4.20		
• Correction Increments	ΔC_D	ΔC_L	ΔC_m	ΔC_D	ΔC_L	ΔC_m
– MFR	-0.0002	0.0001	-0.0002	-0.0003	0	-0.0003
– NPR/Nozzle Geometry	-0.0005	0.0003	-0.0010	-0.0006	-0.0007	0.0003
– Total	-0.0007	0.0004	-0.0012	-0.0009	-0.0007	0
• Basic Flow-Thru Model Levels						
– C_D	0.0115			0.0115		
– C_L	0.0064			0.0064		
– C_m	0.0054			0.0054		
• Corrected Levels						
– C_D	0.0108			0.0106		
– C_L	0.0068			0.0057		
– C_m	0.0042			0.0054		

Note: Operating Conditions Defined in Figure 5-4

GP76 0701 102

FIGURE 5-13
TYPICAL BUILDUP OF CORRECTION INCREMENTS TO BASIC AERO
FLOW-THRU MODEL DATA
Mach 0.9 $\alpha = 0^\circ$



GP76-0701-122

FIGURE 5-14
DRAG CORRECTIONS TO BASIC AERO FLOW-THRU MODEL DATA

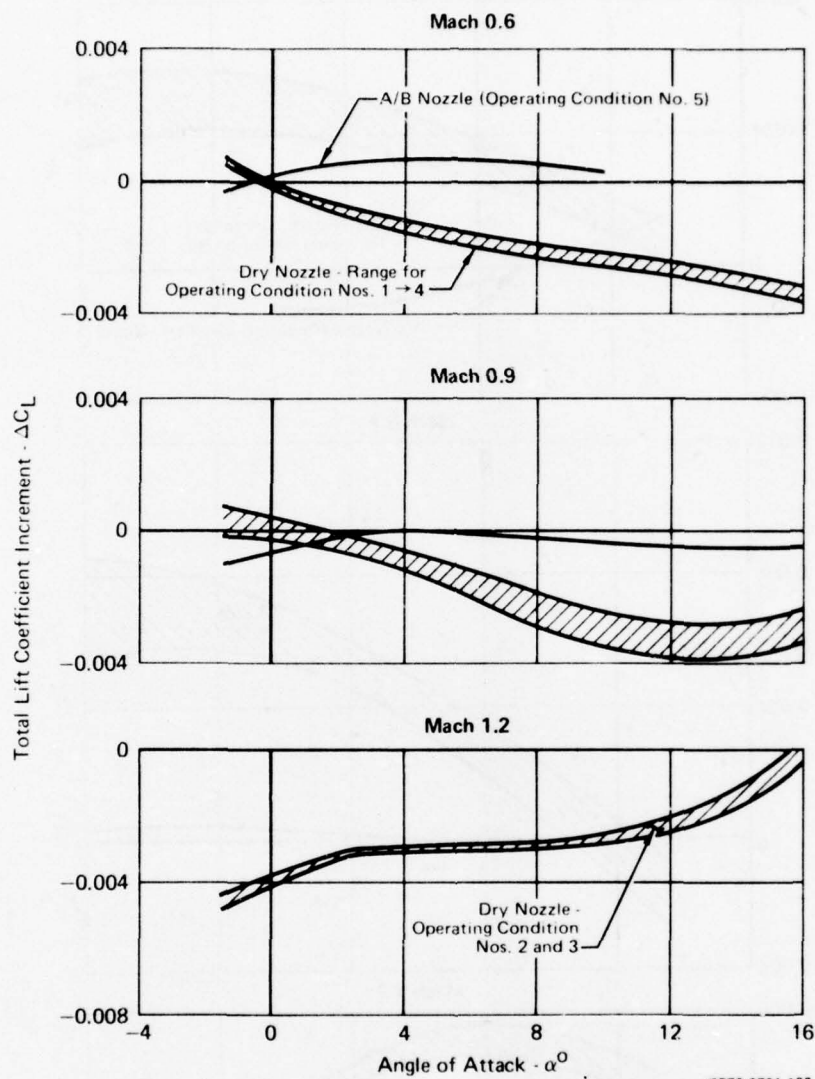
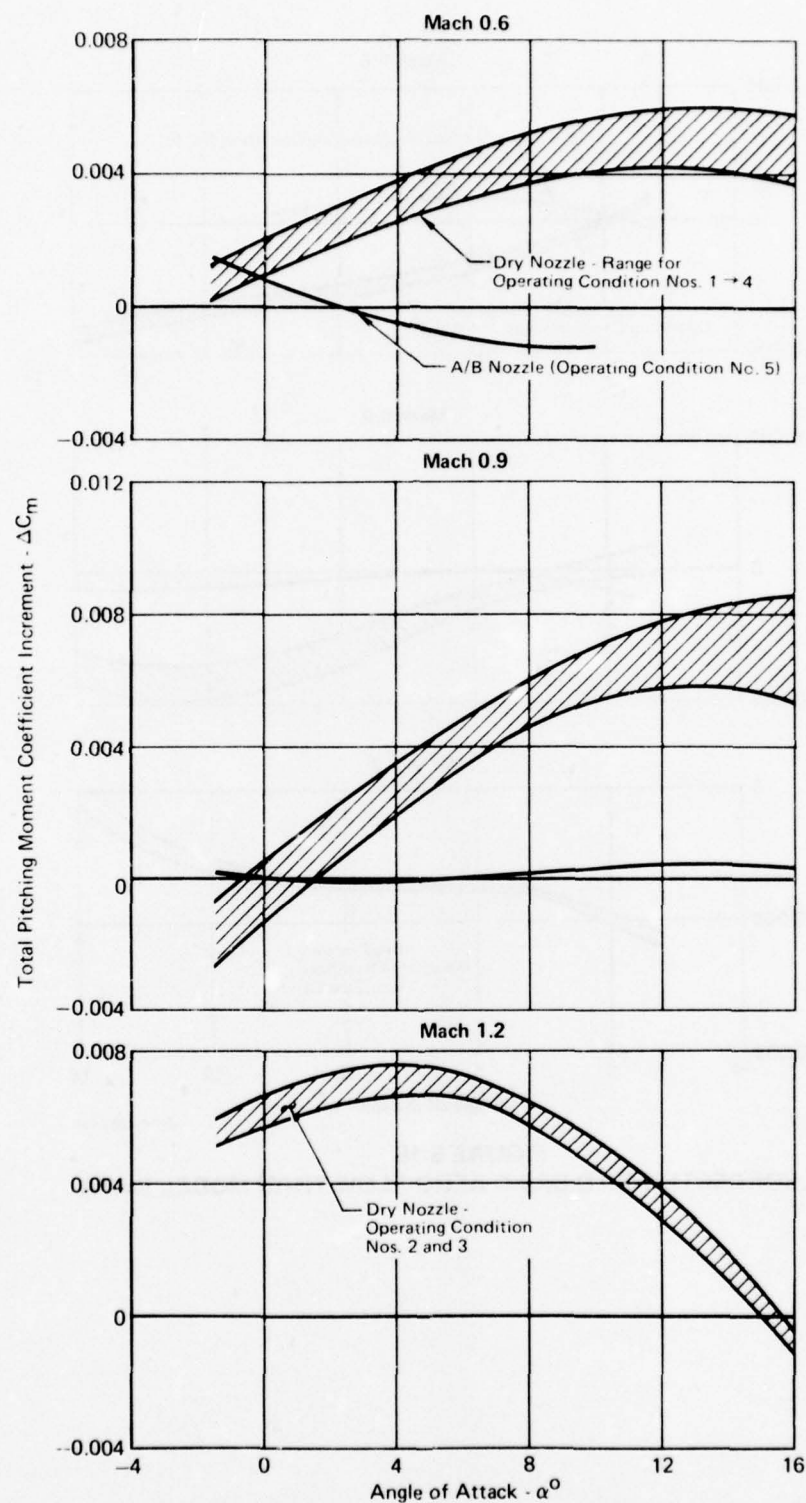


FIGURE 5-15
LIFT CORRECTIONS TO BASIC AERO FLOW-THRU MODEL DATA



GP76 0701 124

FIGURE 5-16
PITCHING MOMENT CORRECTIONS TO BASIC AERO
FLOW-THRU MODEL DATA

5.1.2 Test Technique Comparison - A comparison of the aerodynamic performance characteristics of this model, as determined from both the conventional and simulator test techniques, was made to assess the potential bias errors in the conventional technique. The comparisons were made at those operating conditions defined in Figure 5-4. The dry power nozzle comparisons for operating conditions No's. 2 and 4 are presented in Figures 5-17 through 5-21 at Mach 0.6, 0.9 and 1.2. The afterburning power nozzle comparisons for operating condition No. 5 are presented in Figures 5-22 and 5-23 for Mach 0.6 and 0.9. In general, these comparisons show small differences between the test techniques for the aerodynamic drag, lift and pitching moment coefficient data. Hence, the bias errors in the conventional technique due to the lack of simultaneous flowfield simulation are small. The comparisons at operating conditions No's. 1 and 3 showed similar results to those presented.

The magnitude of the differences between test techniques in all performance parameters are summarized in Figures 5-24 through 5-26. In these figures, the difference between techniques for all operating conditions is combined into an overall range of discrepancy. For the three Mach numbers tested, the drag differences between test techniques generally fall within the experimentally-determined data accuracy below $\alpha = 10^\circ$. Above $\alpha = 10^\circ$, the simulator technique consistently gives lower drag than the conventional, reaching a maximum discrepancy at $\alpha = 16^\circ$ of $\Delta C_D = -.0022$ and $-.0018$ at Mach 0.6 and 0.9, respectively.

The lift difference between test techniques varies from $\Delta C_L = -.0018$ to $+.0026$, while the pitching moment difference varies from $\Delta C_m = -.0020$ to $+.0038$. Although these differences are greater than the experimentally-determined data accuracy band, they are still considered negligible from a total aircraft system standpoint.

Further definition of the bias errors associated with the conventional technique is shown in Figure 5-27. Here the throttle-dependent effects (dry-minus-A/B power) are presented for both techniques. The data indicate a small but consistent bias error in the throttle-dependent drag for the conventional test technique. The noted differences in the throttle-dependent lift and pitching moment are negligible.

The throttle-dependent drag bias error discussed above could be due to the lack of inlet simulation during the jet effects model tests, or the lack of nozzle geometry/pressure ratio simulation during the aero flow-thru model

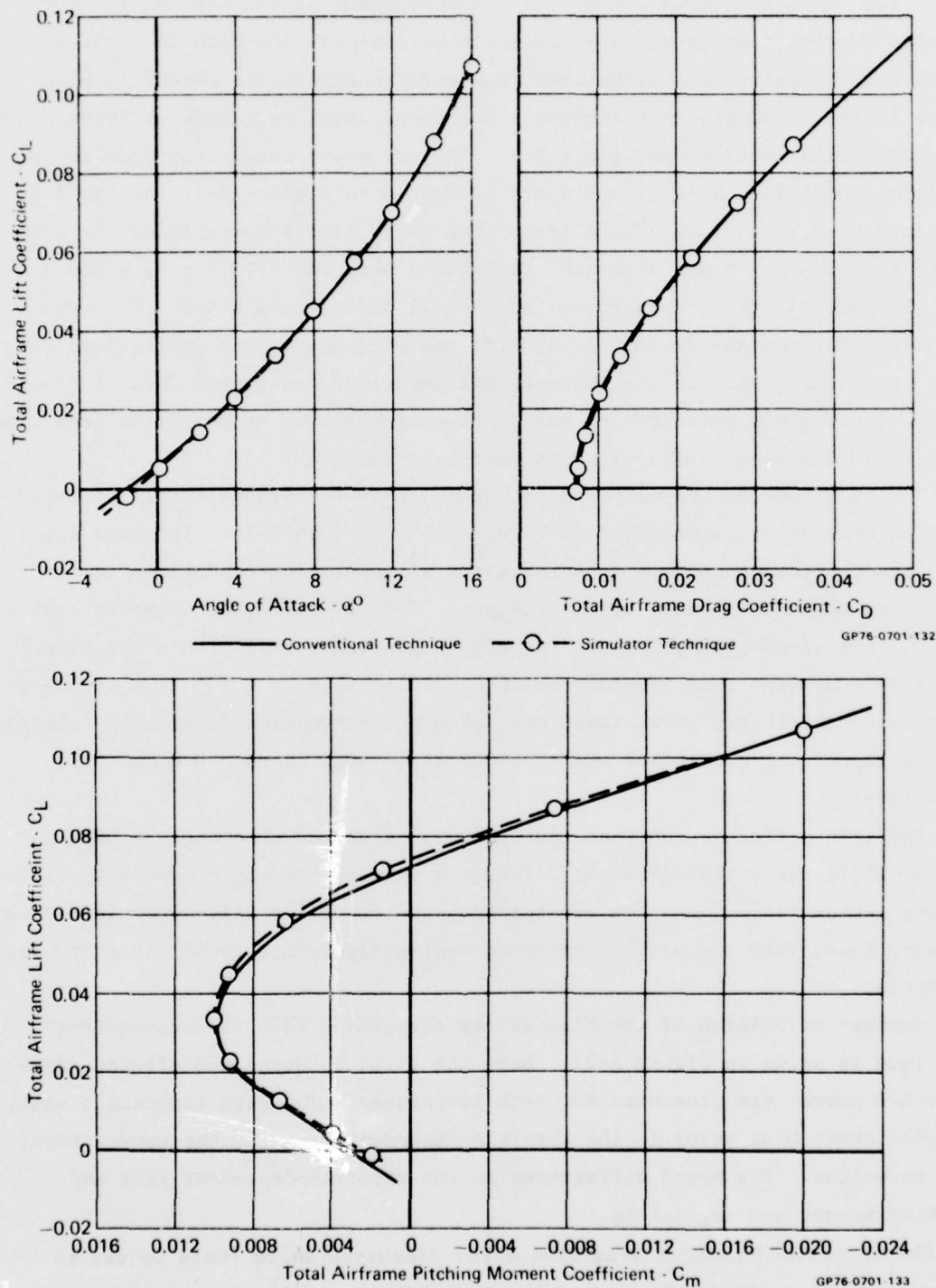
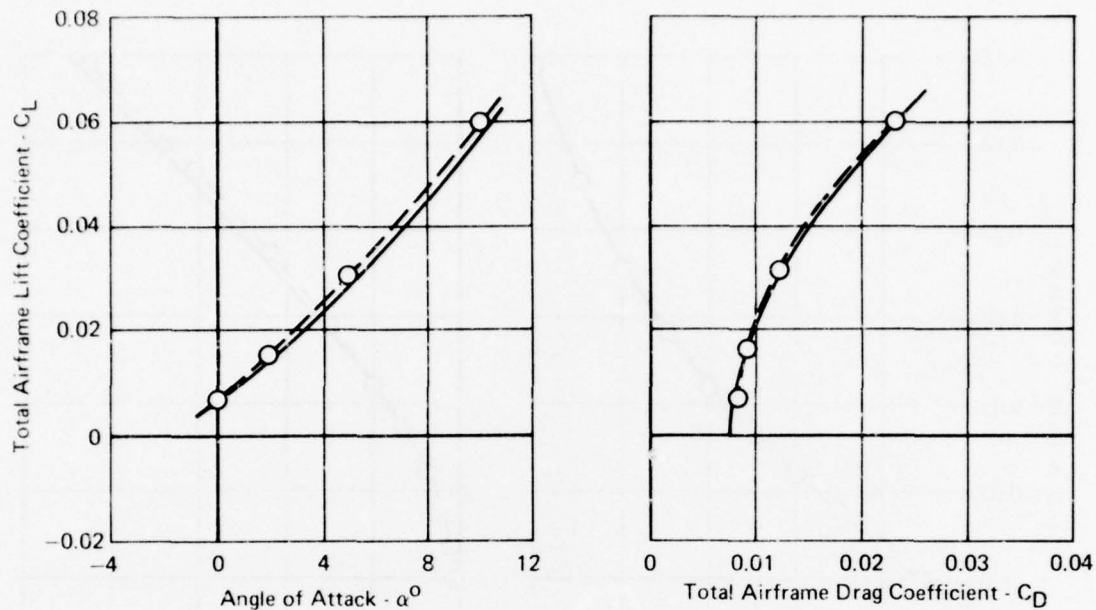
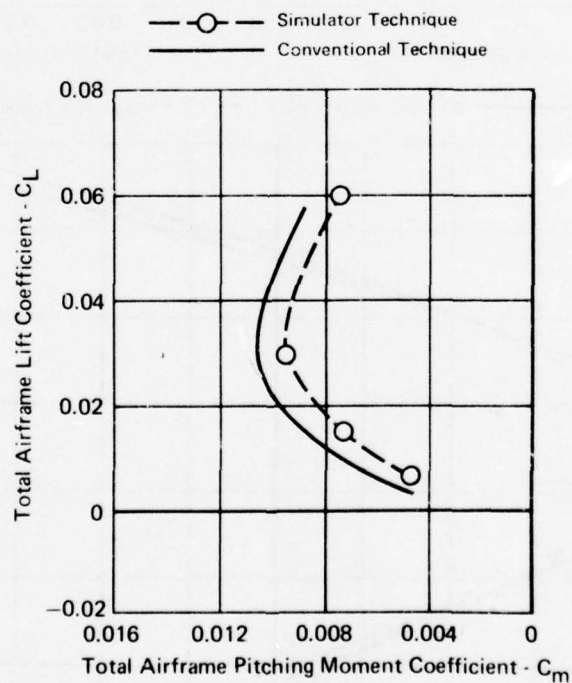


FIGURE 5-17
TOTAL AIRFRAME LIFT, DRAG AND PITCHING MOMENT COMPARISON BETWEEN
SIMULATOR AND CONVENTIONAL TEST TECHNIQUES AT MACH 0.6
 Dry Power Nozzle Operating Condition No. 2 MFR = 0.57 NPR = 3.1



GP76 0701-134



GP76 0701-135

FIGURE 5-18
TOTAL AIRFRAME LIFT, DRAG, AND PITCHING MOMENT COMPARISON
BETWEEN SIMULATOR AND CONVENTIONAL TEST TECHNIQUES AT
MACH 0.6

Dry Power Nozzle Operating Condition No. 4 MFR = 0.40 NPR = 2.0

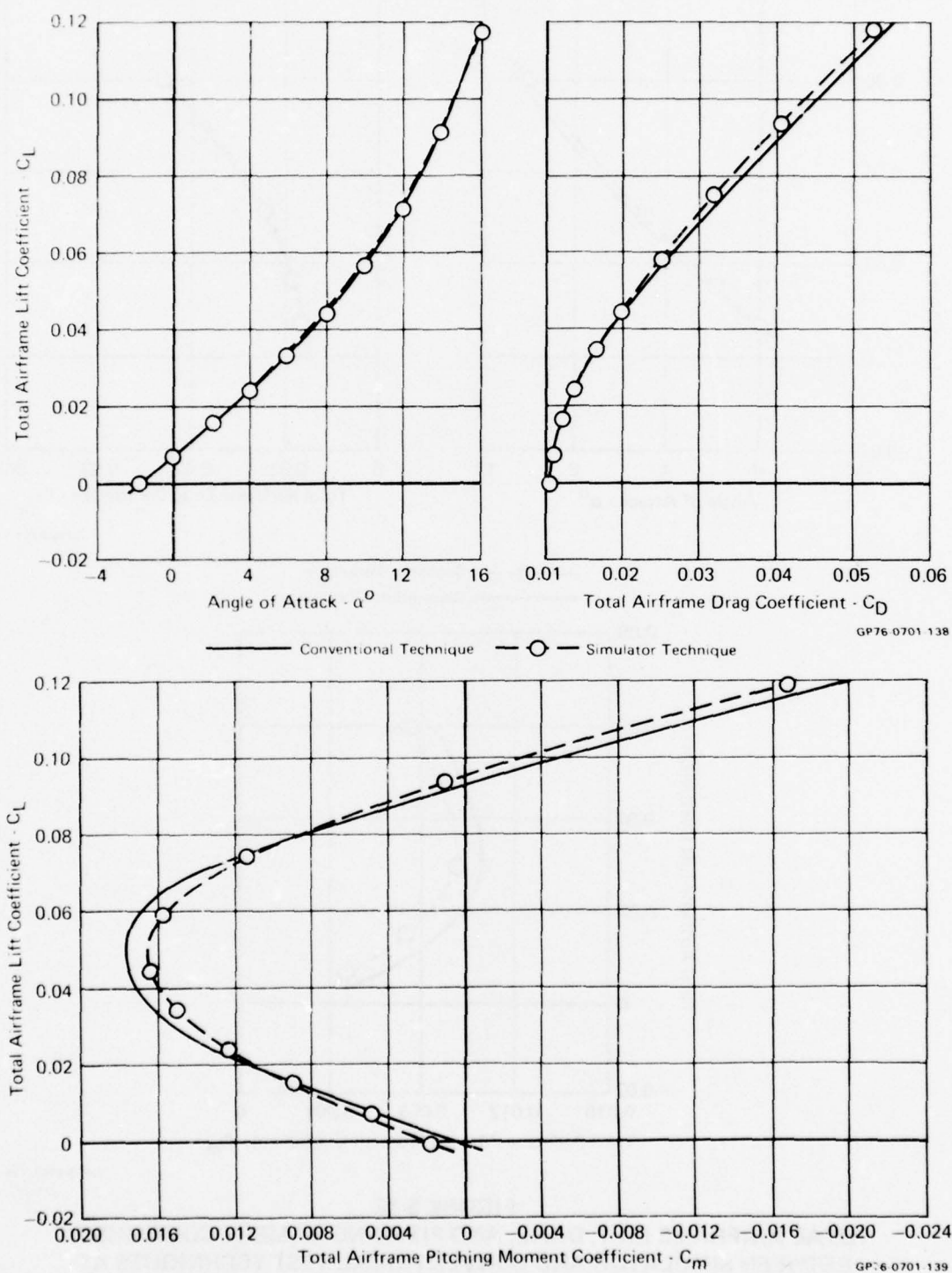


FIGURE 5-19
TOTAL AIRFRAME LIFT, DRAG AND PITCHING MOMENT COMPARISON BETWEEN
SIMULATOR AND CONVENTIONAL TEST TECHNIQUES AT MACH 0.9
 Dry Power Nozzle Operating Condition No. 2 MFR = 0.51, NPR = 4.1

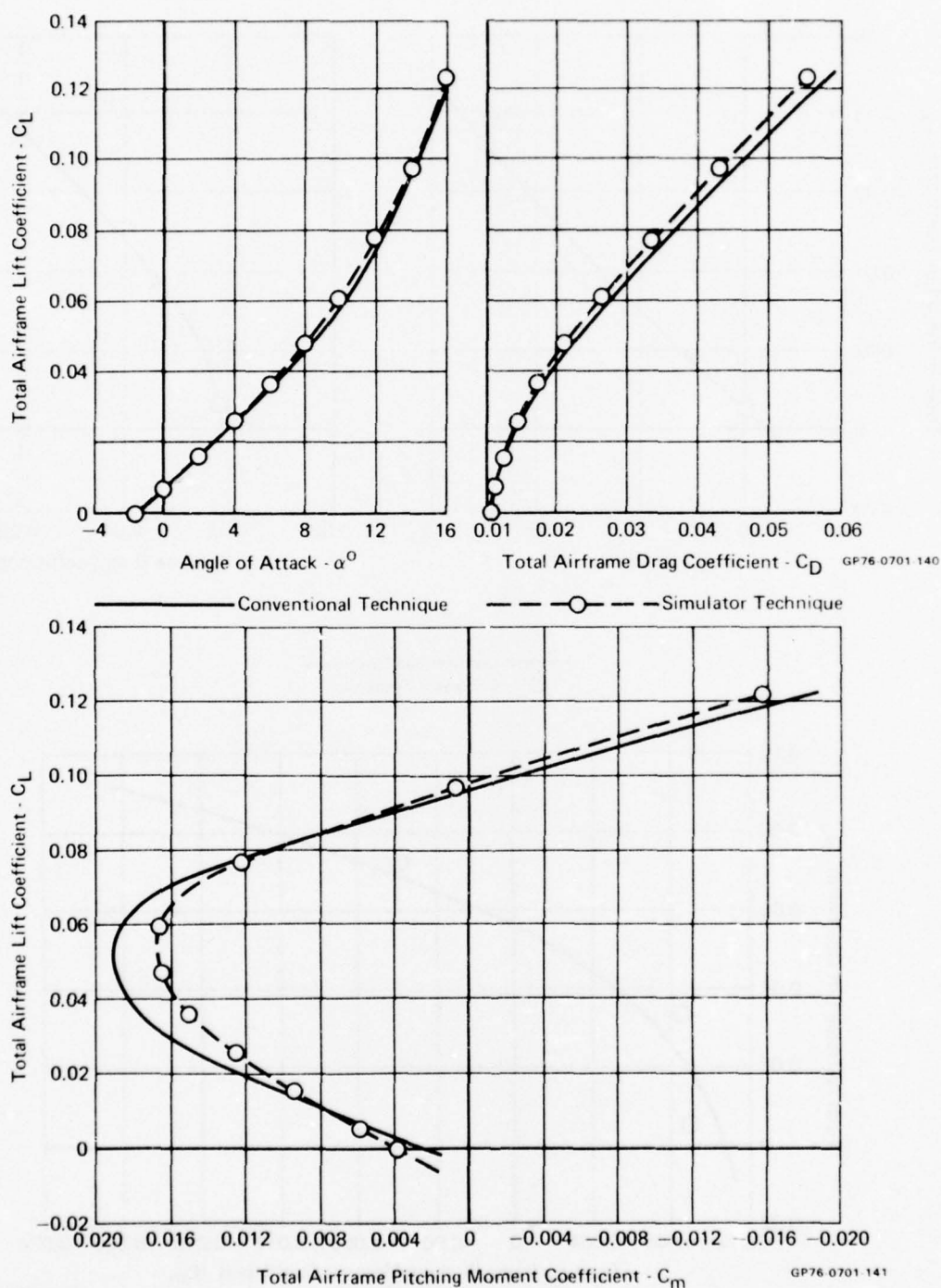
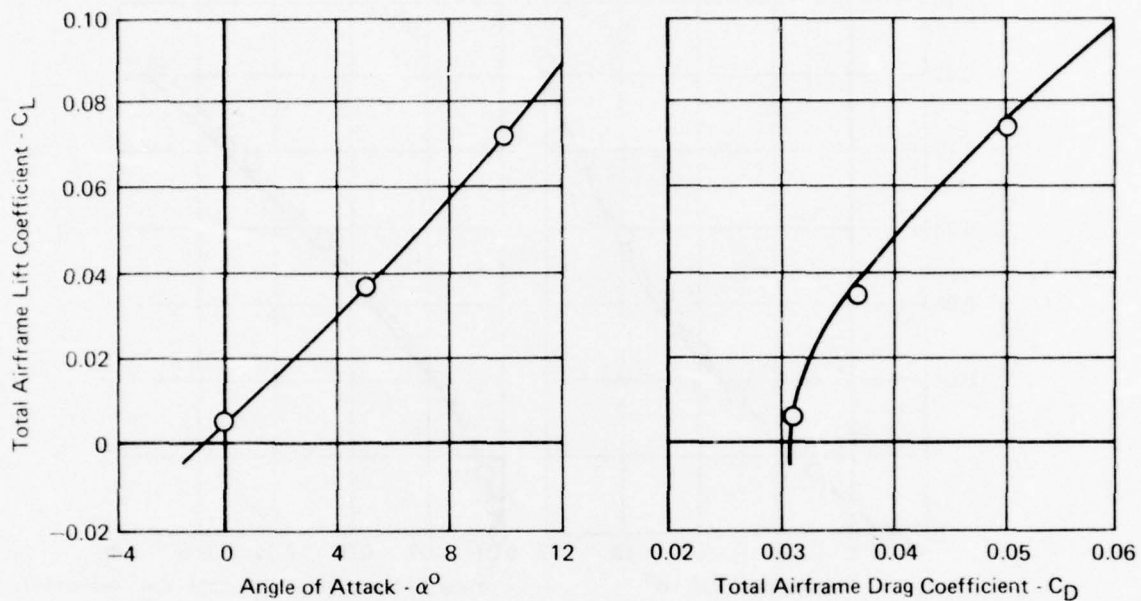
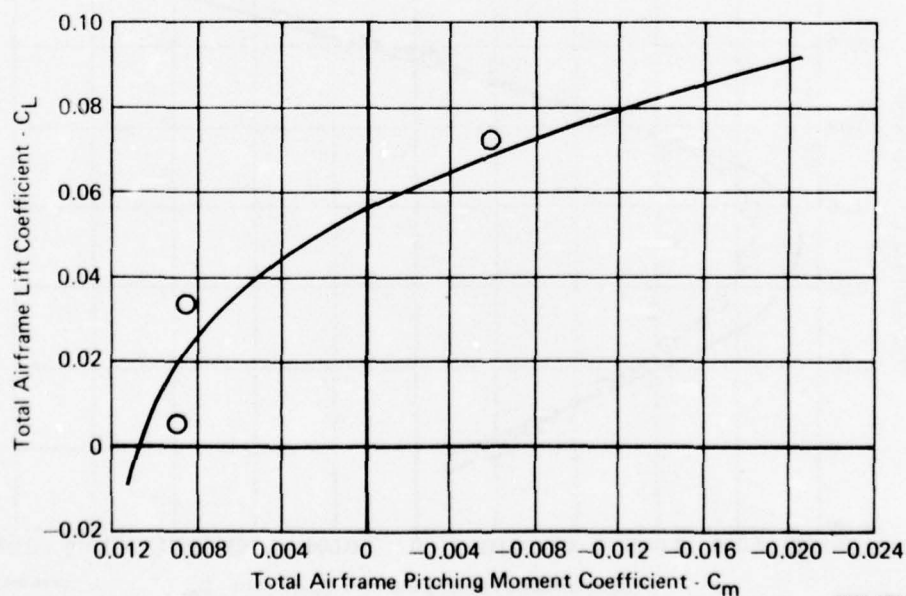


FIGURE 5-20
TOTAL AIRFRAME LIFT, DRAG, AND PITCHING MOMENT COMPARISON
BETWEEN SIMULATOR AND CONVENTIONAL TEST TECHNIQUES AT MACH 0.9
 Dry Power Nozzle Operating Condition No. 4 MFR = 0.36 NPR = 2.6



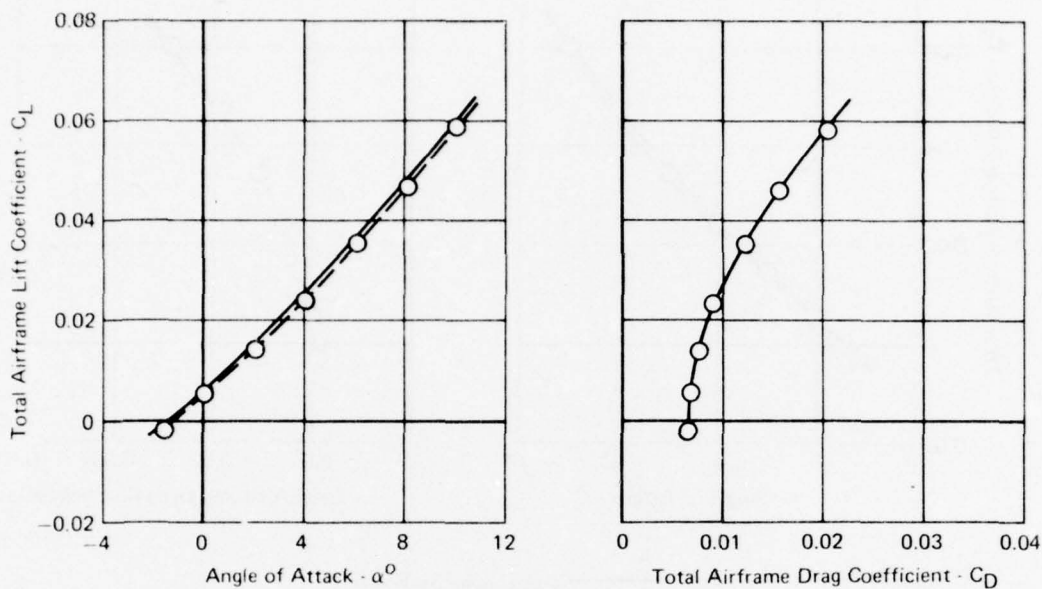
GP76 0701 144

— Conventional Technique
○ Simulator Technique



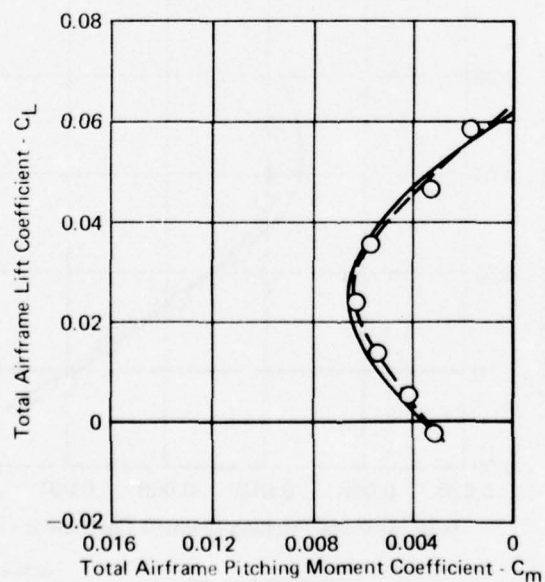
GP76 0701 145

FIGURE 5-21
TOTAL AIRFRAME LIFT DRAG AND PITCHING MOMENT COMPARISON
BETWEEN SIMULATOR AND CONVENTIONAL TEST TECHNIQUES AT MACH 1.2
 Dry Power Nozzle Operating Condition No. 2 MFR = 0.51, NPR = 5.9



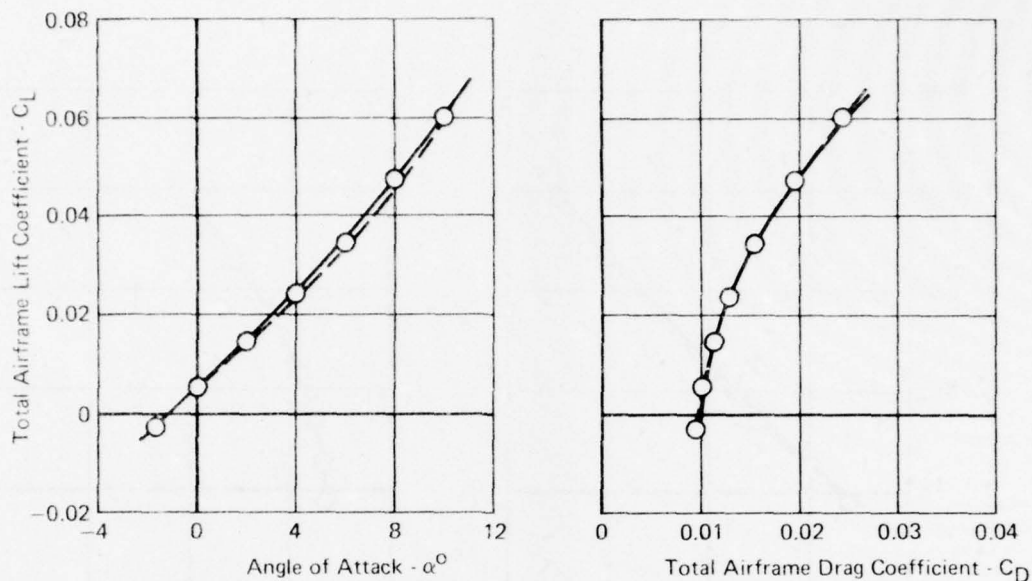
GP76 0701 136

—○— Simulator Technique
 — Conventional Technique



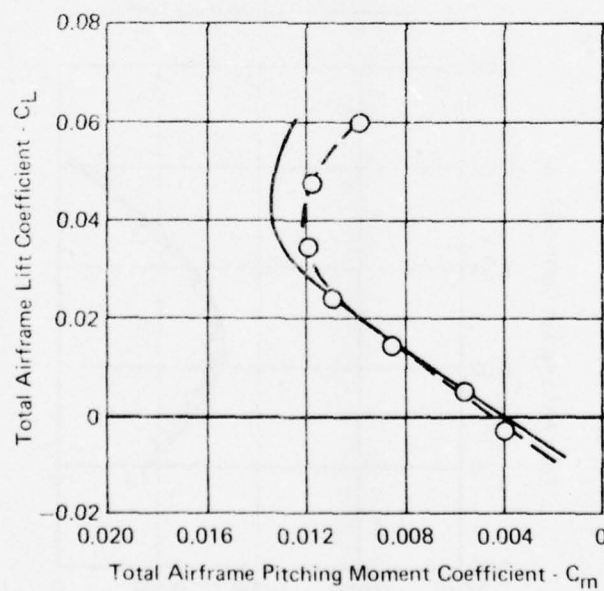
GP76 0701 137

FIGURE 5-22
TOTAL AIRFRAME LIFT DRAG AND PITCHING MOMENT COMPARISON BETWEEN
SIMULATOR AND CONVENTIONAL TEST TECHNIQUES AT MACH 0.6
 Afterburning Power Nozzle Operating Condition No. 5 MFR = 0.62 NPR = 3.2



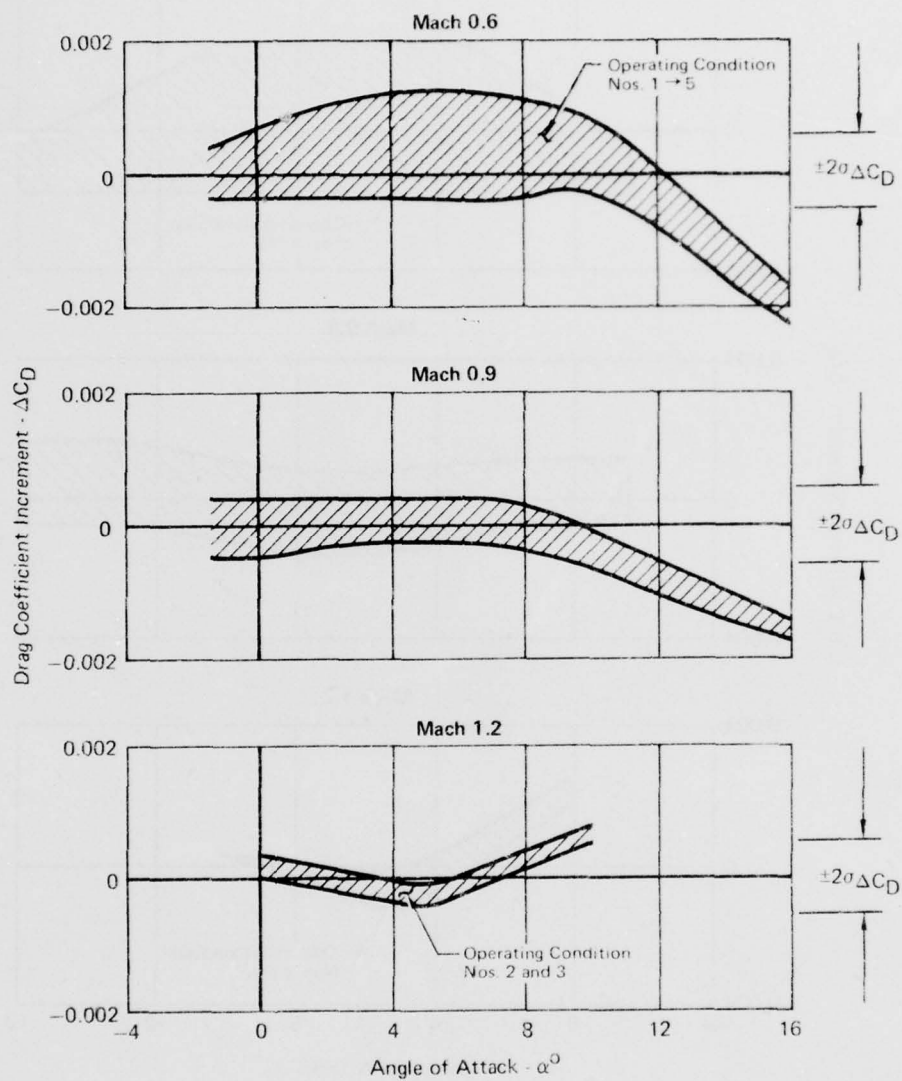
GP76 0701 142

— Conventional Technique
 -○- Simulator Technique



GP76 0701 142

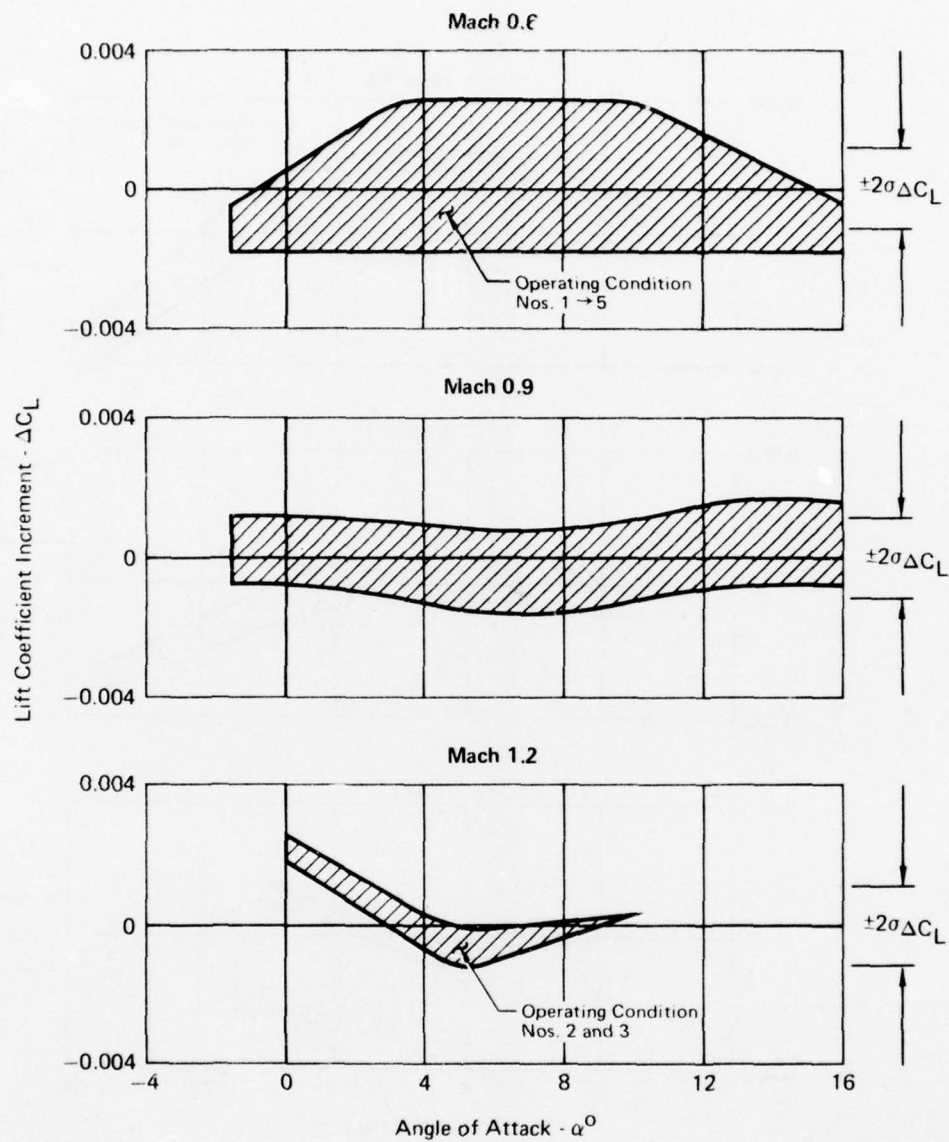
FIGURE 5-23
TOTAL AIRFRAME LIFT, DRAG AND PITCHING MOMENT COMPARISON BETWEEN
SIMULATOR AND CONVENTIONAL TEST TECHNIQUES AT MACH 0.9
 Afterburning Power Nozzle Operating Condition No. 5 MFR = 0.53 NPR = 4.2



$$\Delta C_D = (C_D)_{\text{simulator}} - (C_D)_{\text{conventional}}$$

GP76-0701-127

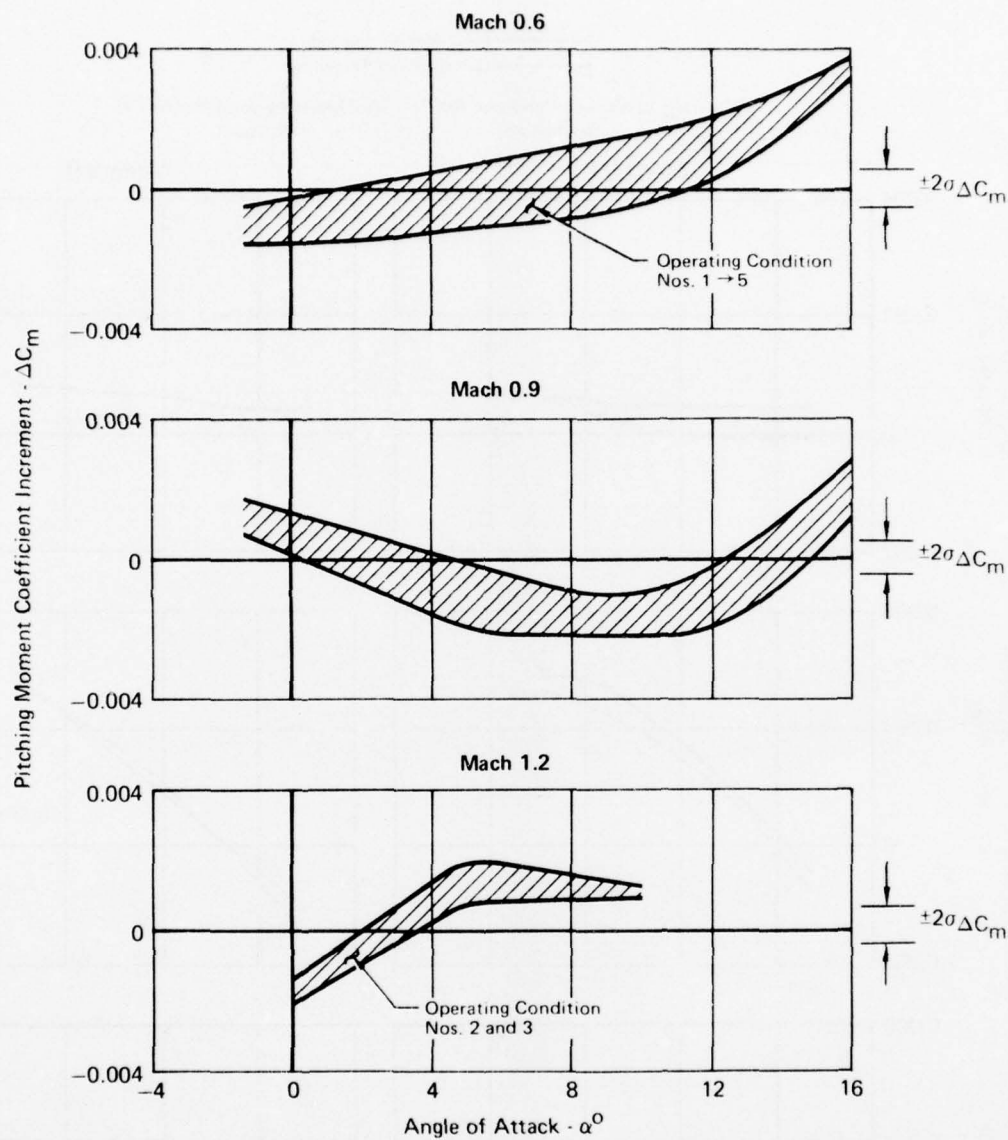
FIGURE 5-24
INCREMENTAL DRAG DIFFERENCE BETWEEN SIMULATOR
AND CONVENTIONAL TEST TECHNIQUES



$$\Delta C_L = (C_L)_{\text{simulator}} - (C_L)_{\text{conventional}}$$

GP76-0701-128

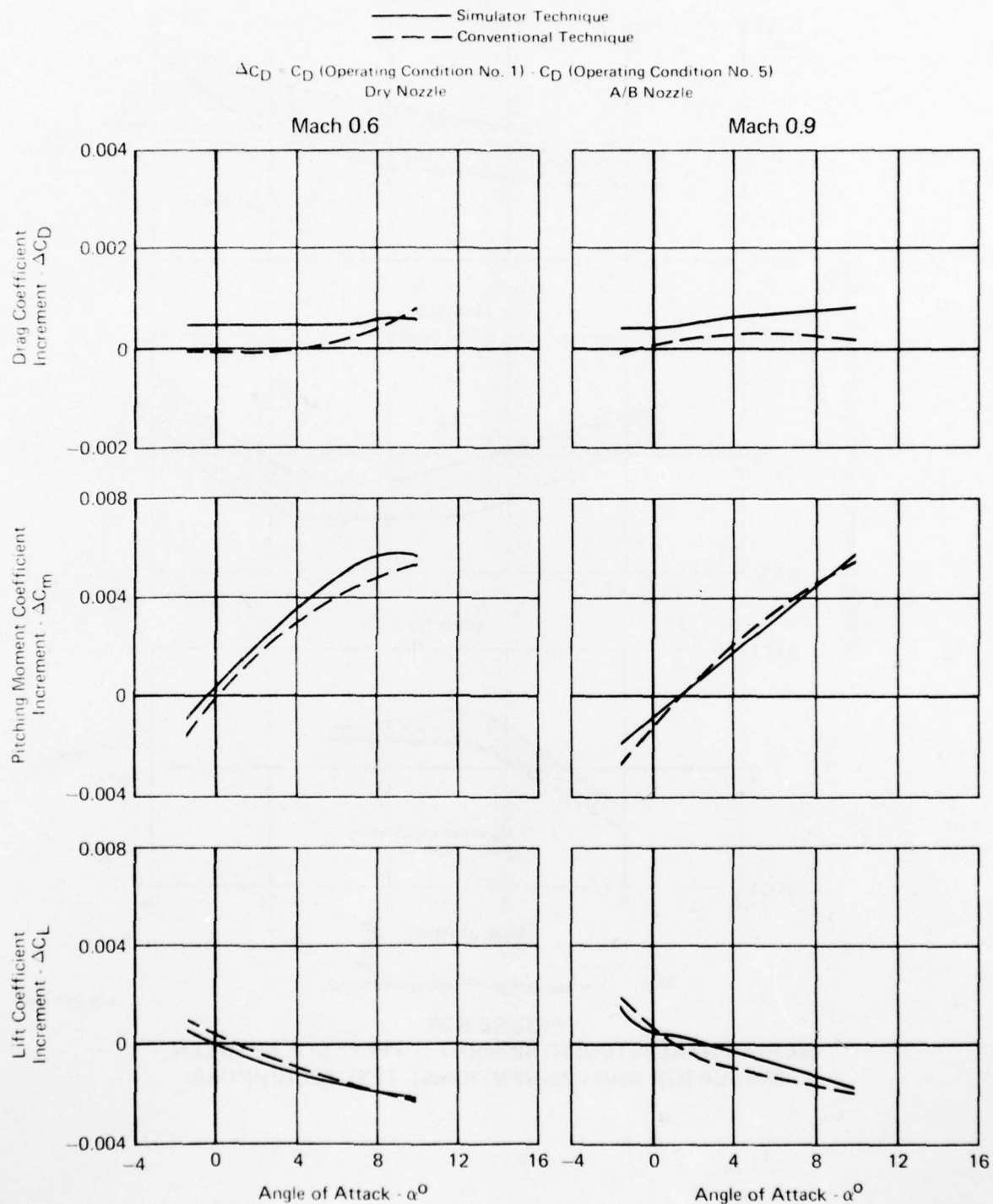
FIGURE 5-25
INCREMENTAL LIFT DIFFERENCE BETWEEN SIMULATOR
AND CONVENTIONAL TEST TECHNIQUES



$$\Delta C_m = (C_m)_{\text{simulator}} - (C_m)_{\text{conventional}}$$

GP76 0701 129

FIGURE 5-26
INCREMENTAL PITCHING MOMENT DIFFERENCE BETWEEN
SIMULATOR AND CONVENTIONAL TEST TECHNIQUES



GP76 0701-174

FIGURE 5-27
COMPARISON OF THROTTLE-DEPENDENT EFFECTS BETWEEN SIMULATOR
AND CONVENTIONAL TEST TECHNIQUES

tests. The source was identified by comparing the total airframe throttle-dependent drag increment obtained on the simulator model with that obtained on the jet effects model, as shown in Figure 5-28. Using the total airframe data permitted eliminating the aft-end splitline as an error source. The subject data comparison shows the same nominal level of throttle-dependent drag discrepancy as Figure 5-27. Since the only difference in the latter comparison is the inlet condition, then the bias error noted previously can be attributed to the lack of inlet flow simulation on the jet effects model, and consequently different inlet/aft-end flowfield interactions than the simulator model.

The throttle-dependent drag increment, as determined from aft-end drag measurements on the two models, has also been compared in Figure 5-29. Since the drag discrepancy is larger than shown previously with the total airframe balance data, it could be concluded that part of the interactions between the inlet/aft-end are felt on the forebody as well as the aft-end. However, this is only true for the simulator model with the flowing inlet, since the total airframe and aft-end throttle-dependent drag are the same for the jet effects model with the inlet faired.

The incremental surface pressure differences between the dry and after-burning power nozzles are shown in Figures 5-30 and 5-31 for both the simulator and jet effects models at Mach 0.9. The aft-end incremental pressures on the simulator model are generally lower than on the jet effects model, implying larger throttle-dependent drag increments for the simulator model, which supports the force data results. Forebody pressure data are limited, and the variation with nozzle geometry for each model is inconclusive.

The exact mechanism by which the inlet/aft-end flowfields interact to cause the type of throttle-dependent drag discrepancy noted above is not understood at this time.

5.1.3 Inlet/Aft-End Interactions - In the previous section, the flowing inlet interactions with the aft-end flowfield were shown to be small but measurable for the test configuration. There is additional data available to study these interactions as well as those due to nozzle pressure ratio. These interactions, and their impact on the test technique differences shown previously, are discussed below.

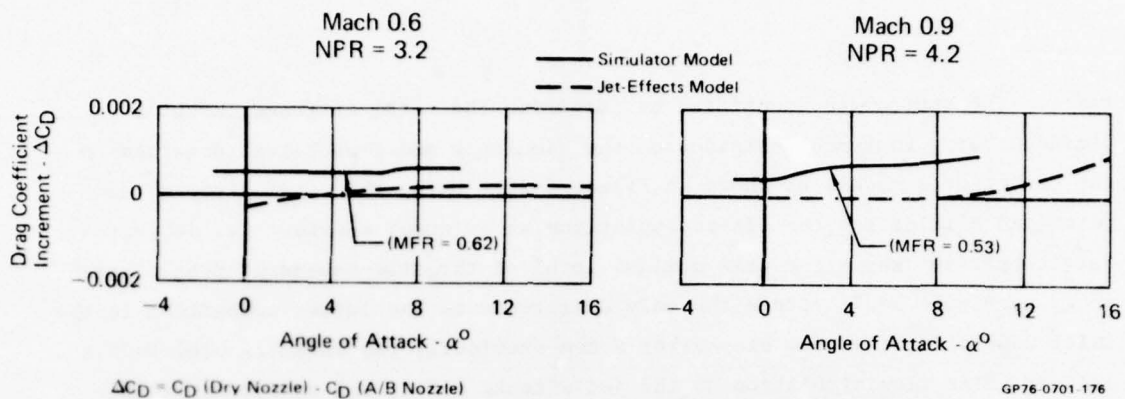


FIGURE 5-28
THROTTLE-DEPENDENT EFFECT ON TOTAL AIRFRAME DRAG FROM
THE SIMULATOR AND JET EFFECTS MODELS

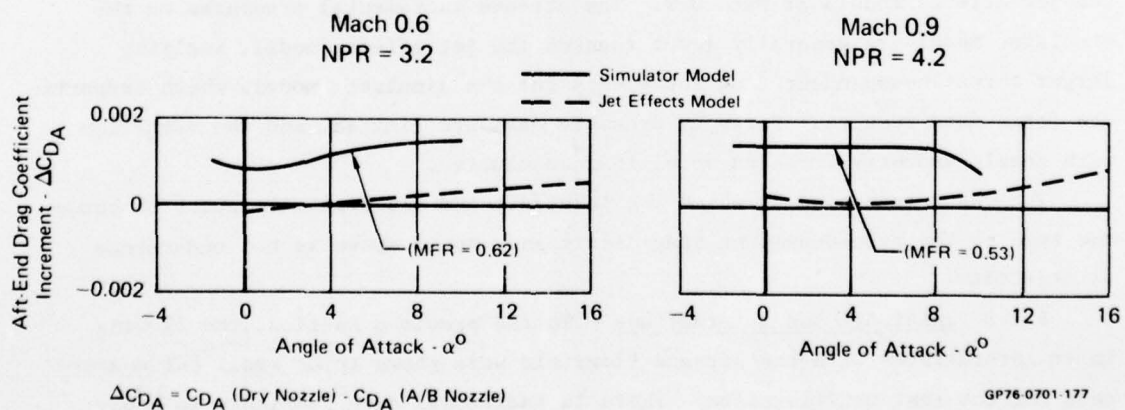


FIGURE 5-29
THROTTLE DEPENDENT EFFECT ON AFT-END DRAG FROM
THE SIMULATOR AND JET EFFECTS MODELS

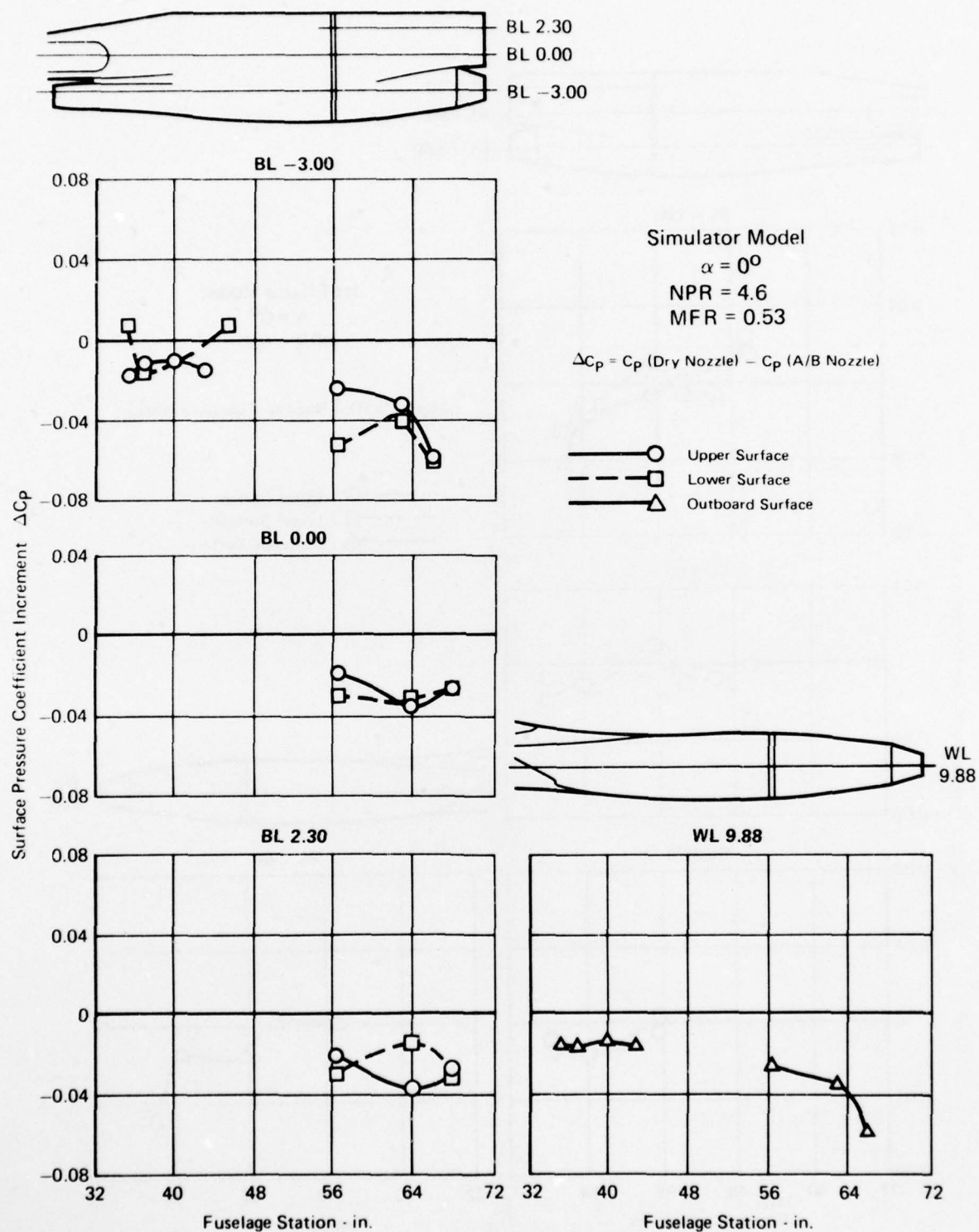


FIGURE 5-30
EFFECT OF NOZZLE GEOMETRY ON EXTERNAL
SURFACE PRESSURES AT MACH 0.9

GP76-0701-163

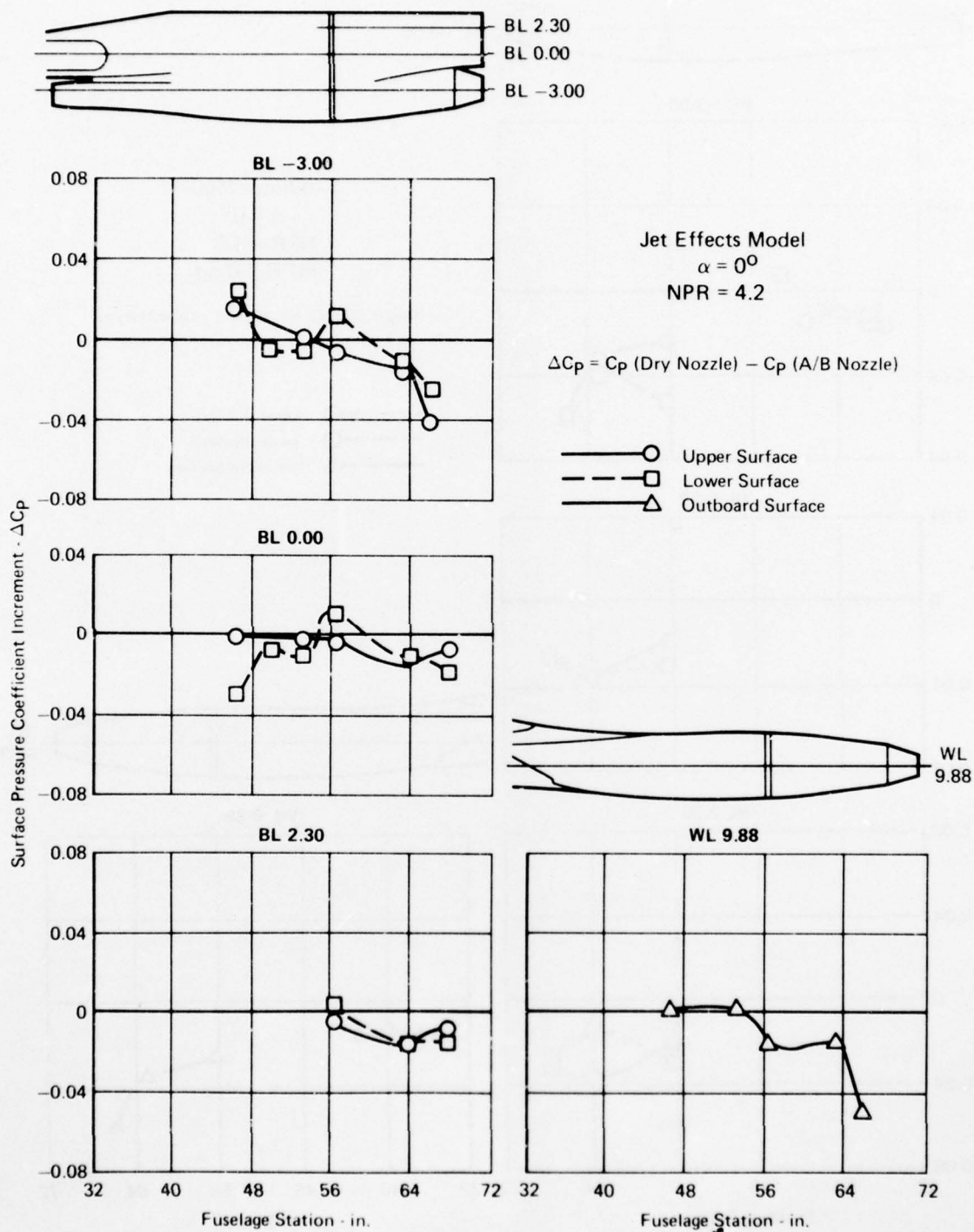


FIGURE 5-31
EFFECT OF NOZZLE GEOMETRY ON EXTERNAL
SURFACE PRESSURES AT MACH 0.9

GP76 0701 72

Inlet Mass Flow Ratio Effects - With the conventional wind tunnel test technique, the total airframe performance variation with inlet mass flow ratio is accomplished by changing the exit chokes on the aero flow-thru model. This precludes simulation of the operating nozzle geometry and pressure ratio. If the inlet flow would interact significantly with the nozzle and aft-end flowfields, then bias errors in the evaluation of the mass flow ratio correction increment could have resulted.

The total airframe force and moment variation with mass flow ratio, as obtained from both the aero flow-thru and simulator models, is shown in Figures 5-32 through 5-34. Since the simulator model data were found to be relatively insensitive to nozzle pressure ratio, these data are presented for a range of pressure ratio. From these figures, the aerodynamic drag, lift and pitching moment variation with mass flow ratio, over the range tested, is nearly the same for both models. Since the aft-end conditions are different for the two models, this would also indicate that the flowing inlet and aft-end flowfields did not appreciably interact to change the basic performance variation with mass flow ratio.

This can be investigated further by considering just the aft-end force and moment data from the simulator model. The effects of mass flow ratio on the aft-end are shown in Figures 5-35 through 5-37, for the dry power nozzle configuration. It is difficult to discern any consistent trend with mass flow ratio from these plots. For Mach 0.9, the data is shown incrementally in Figure 5-38. At a constant nozzle pressure ratio, the data at the maximum mass flow ratio tested are used as a reference level from which the other data is incremented. From the resulting incremental data, a definite trend with mass flow ratio can be seen for both the aft-end lift and pitching moment, even though the variation is small. A drag trend is not clear, although there appears to be some small effect. The limited data obtained with the afterburning power nozzle showed a negligible mass flow ratio effect on the aft-end.

The mass flow ratio effects on the external surface pressure distribution at Mach 0.9 and $\alpha = 0^\circ$ and 10° are shown in Figures 5-39 and 5-40 for the aero flow-thru model. As might be expected, the largest changes in surface pressures are seen in the area of the inlet. However, small mass flow ratio effects on the aft-end pressures are evident, but only at $\alpha = 0^\circ$.

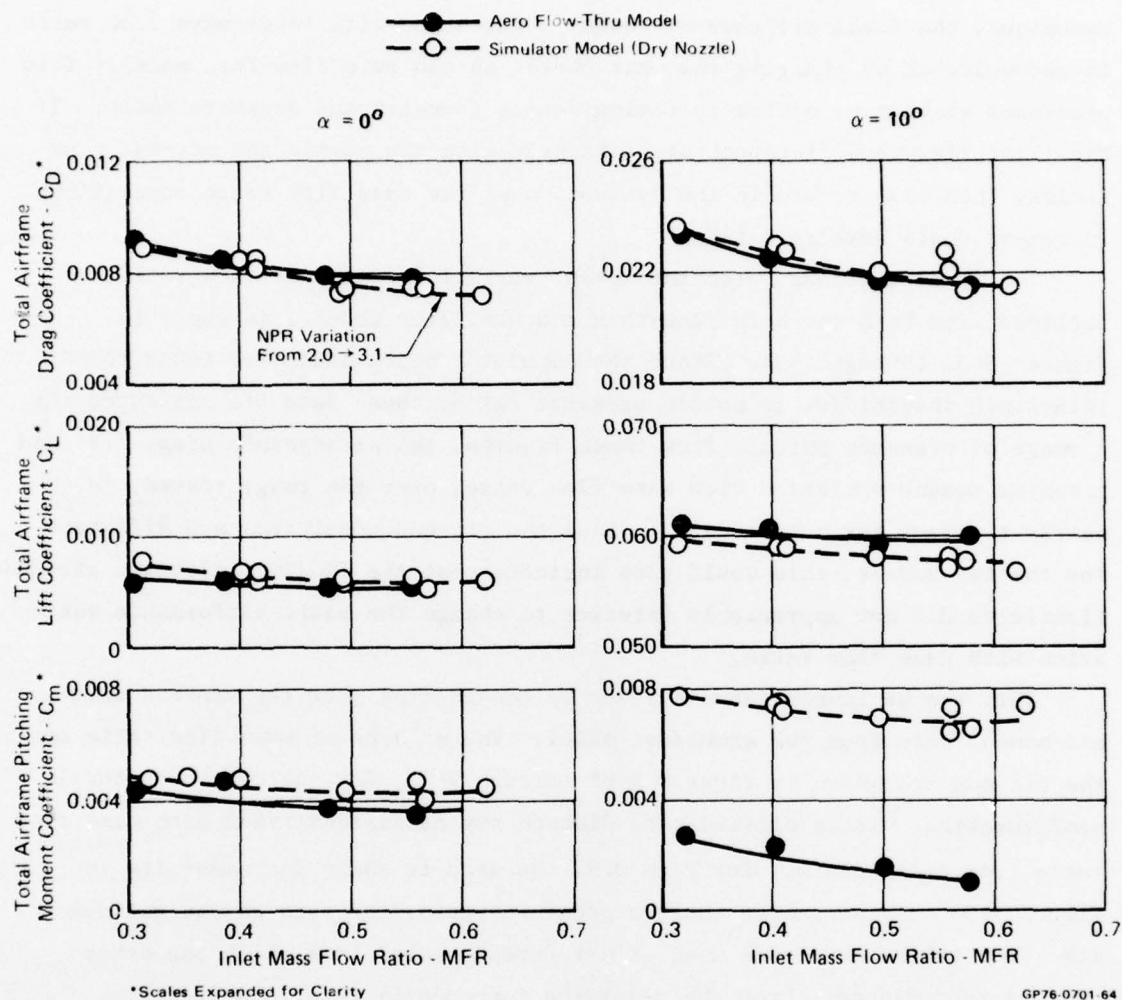


FIGURE 5-32
VARIATION OF TOTAL AIRFRAME PERFORMANCE PARAMETERS
WITH INLET MASS FLOW RATIO AT MACH 0.6

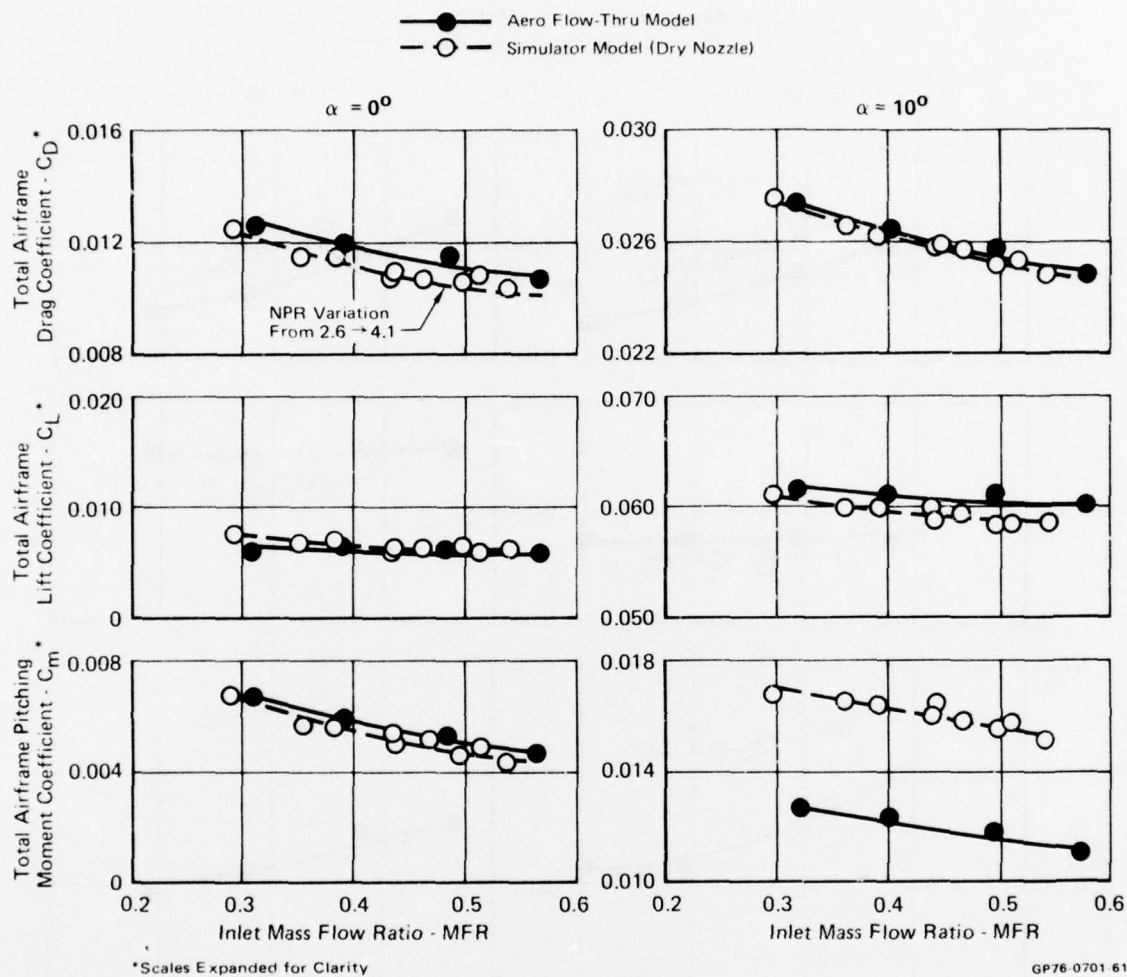


FIGURE 5-33
VARIATION OF TOTAL AIRFRAME PERFORMANCE PARAMETERS
WITH INLET MASS FLOW RATIO AT MACH 0.9

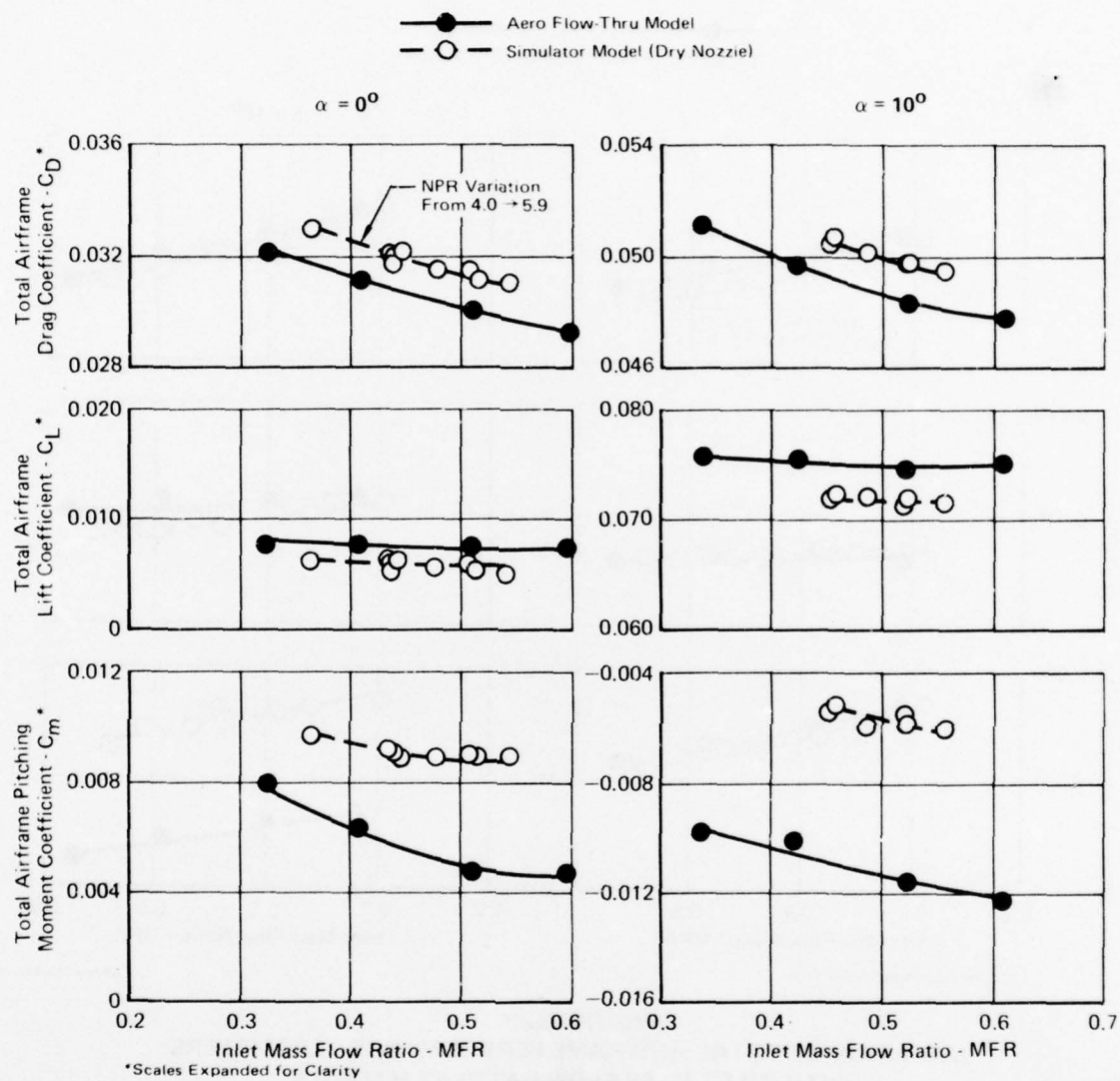
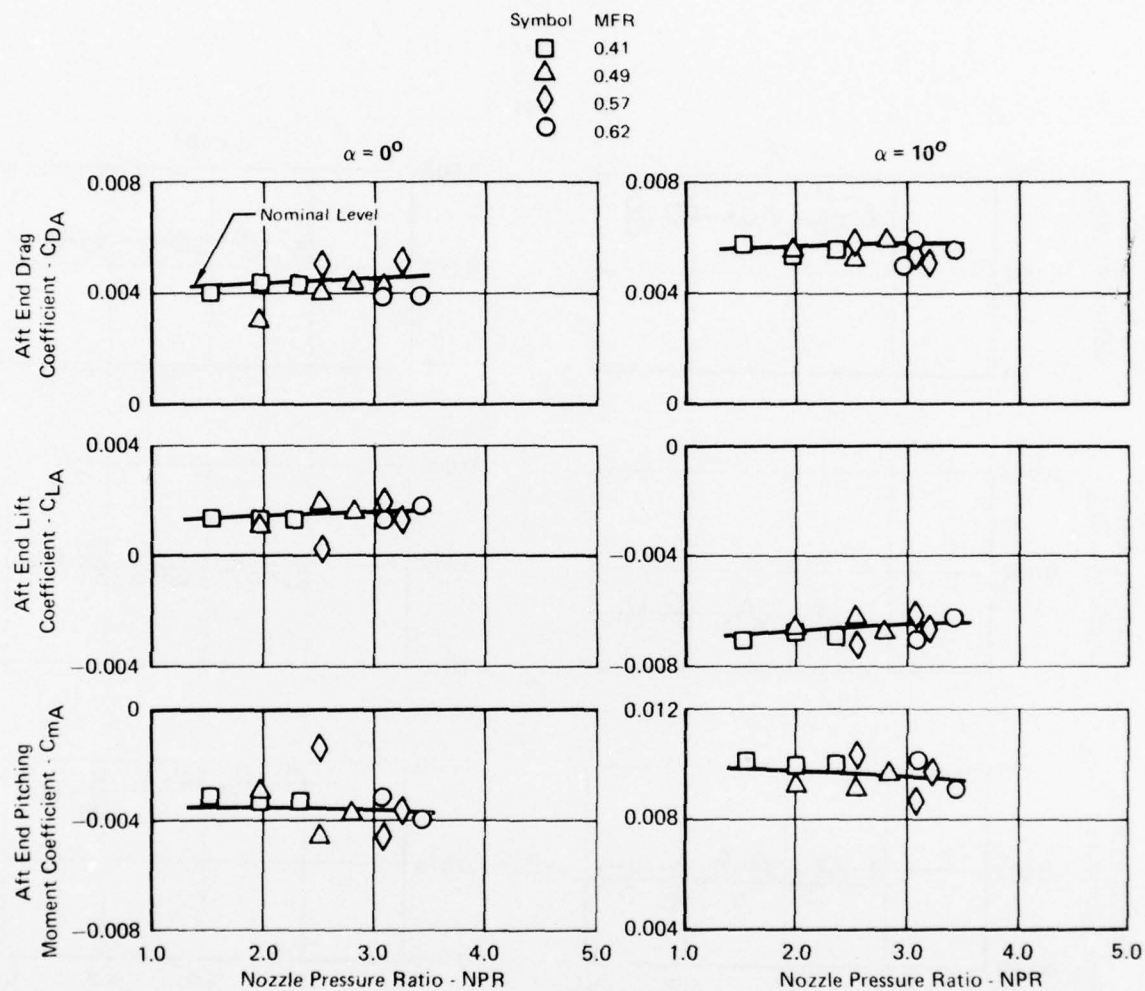


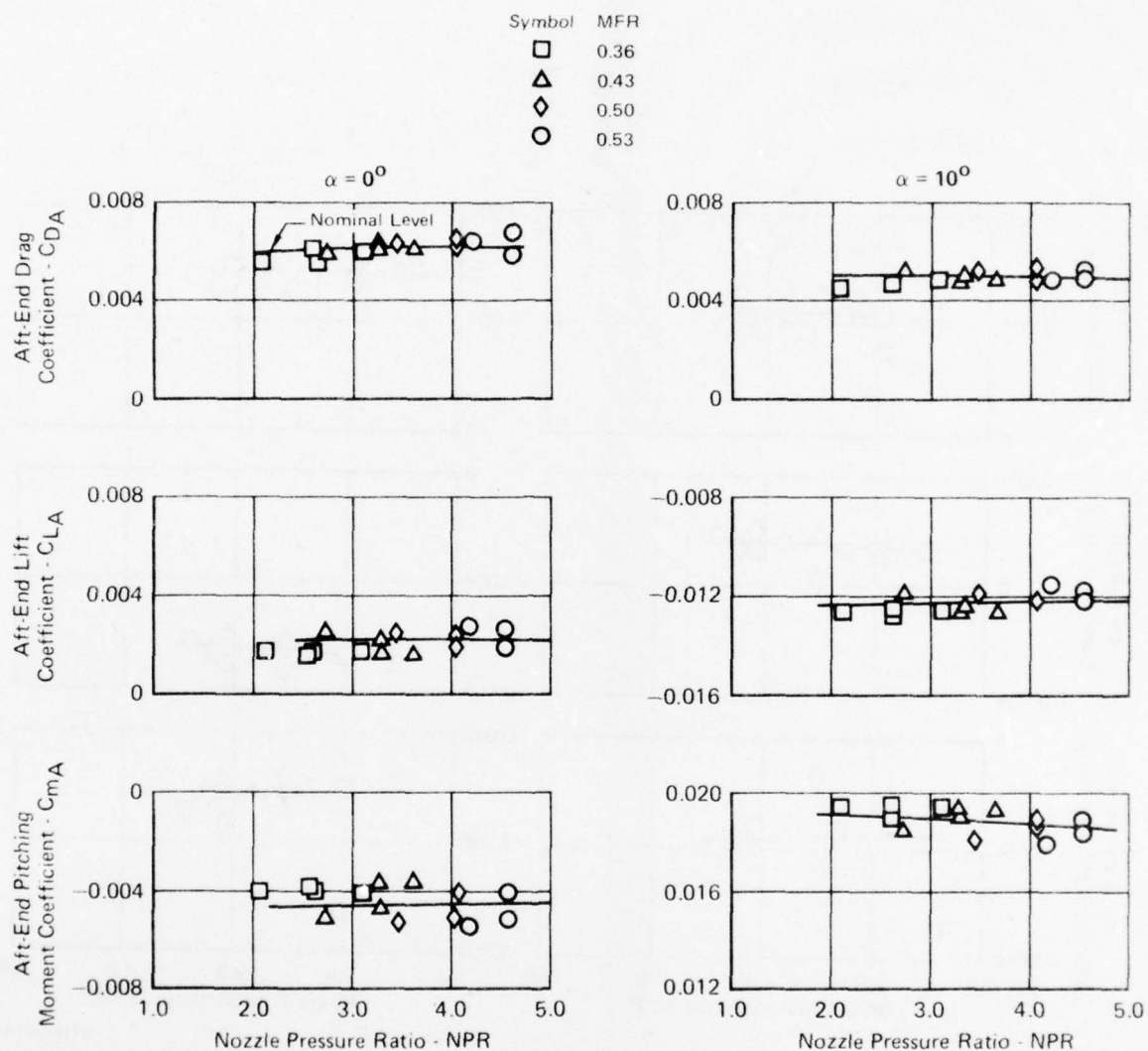
FIGURE 5-34
 VARIATION OF TOTAL AIRFRAME PERFORMANCE PARAMETERS
 WITH INLET MASS FLOW RATIO AT MACH 1.2

GP76 0701 62



GP76 0701 63

FIGURE 5-35
EFFECT OF INLET MASS FLOW RATIO ON AFT-END
PERFORMANCE PARAMETERS AT MACH 0.6
 Simulator Model Dry Power Nozzle



GP76-0701-59

FIGURE 5-36
EFFECT OF INLET MASS FLOW RATIO ON AFT-END PERFORMANCE
PARAMETERS AT MACH 0.9
 Simulator Model Dry Power Nozzle

AD-A034 282

MCDONNELL AIRCRAFT CO ST LOUIS MO

F/6 21/5

TURBINE ENGINE MULTI-MISSION PROPULSION SIMULATOR WIND TUNNEL D--ETC(U)

NOV 76 M F EIGENMANN, R L BEAR, T C CHANDLER F33615-73-C-2051

AFAPL-TR-76-73

NL

UNCLASSIFIED

2 OF 4
AD
A034282



2 OF 4
AD
A034282



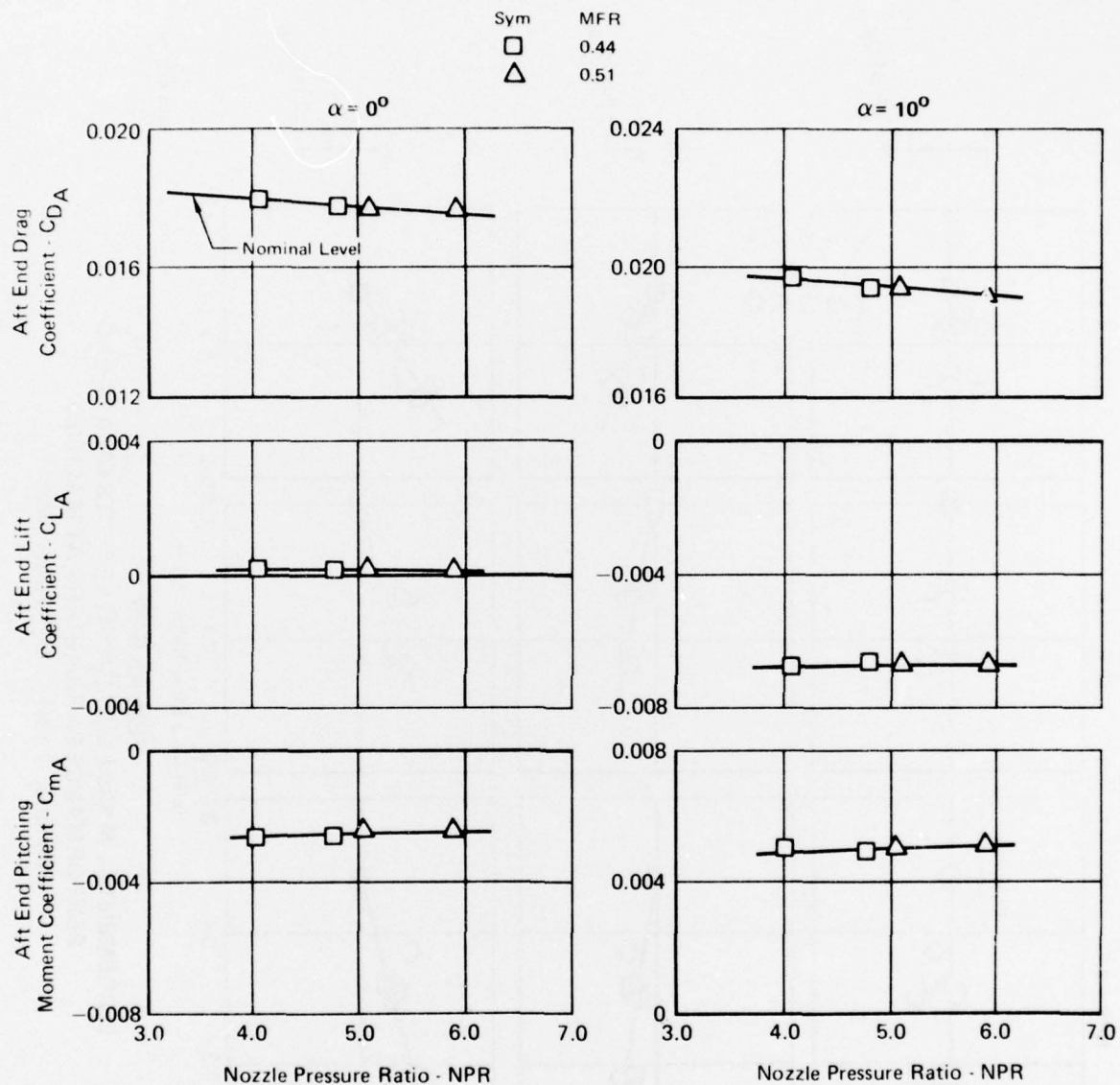
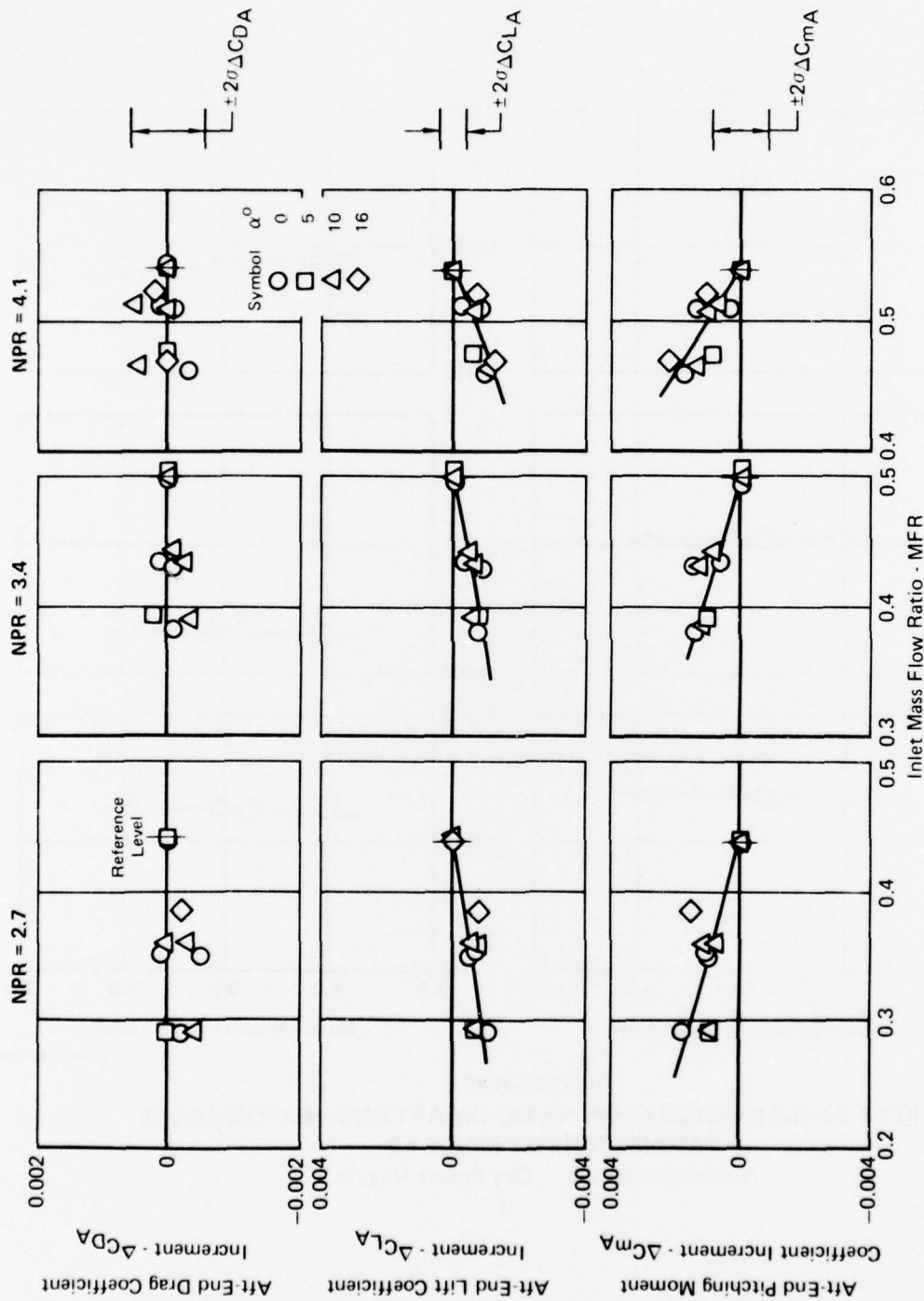


FIGURE 5-37
EFFECT OF INLET MASS FLOW RATIO ON AFT END PERFORMANCE
PARAMETERS AT MACH 1.2
 Simulator Model Dry Power Nozzle

GP76 0701-151



GP76 0701 60

FIGURE 5-38
INCREMENTAL MASS FLOW RATIO EFFECTS ON AFT-END
PERFORMANCE PARAMETERS AT MACH 0.9
 Simulator Model Dry Power Nozzle

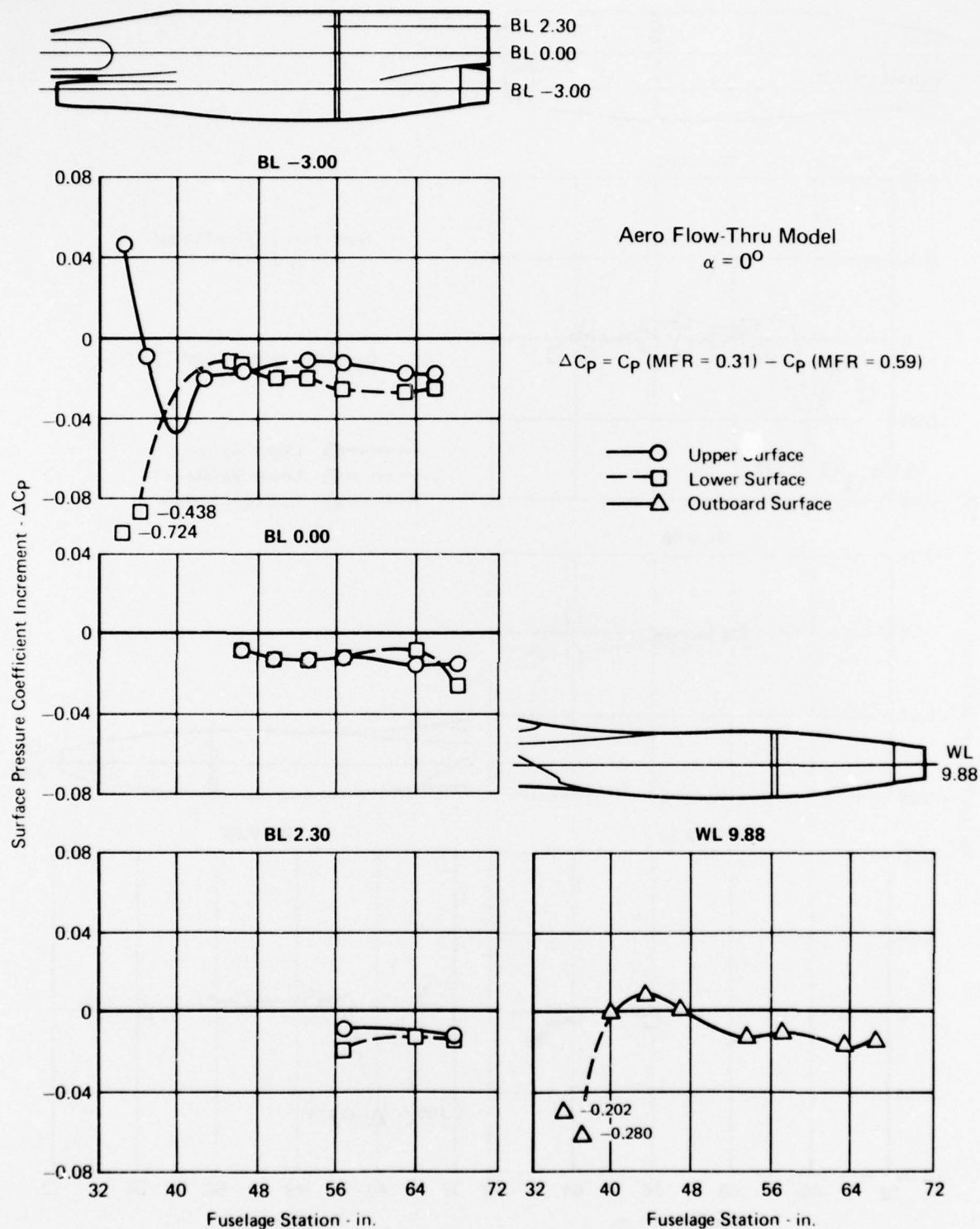


FIGURE 5-39
EFFECT OF INLET MASS FLOW RATIO ON EXTERNAL
SURFACE PRESSURES AT MACH 0.9

GP76 0701-65

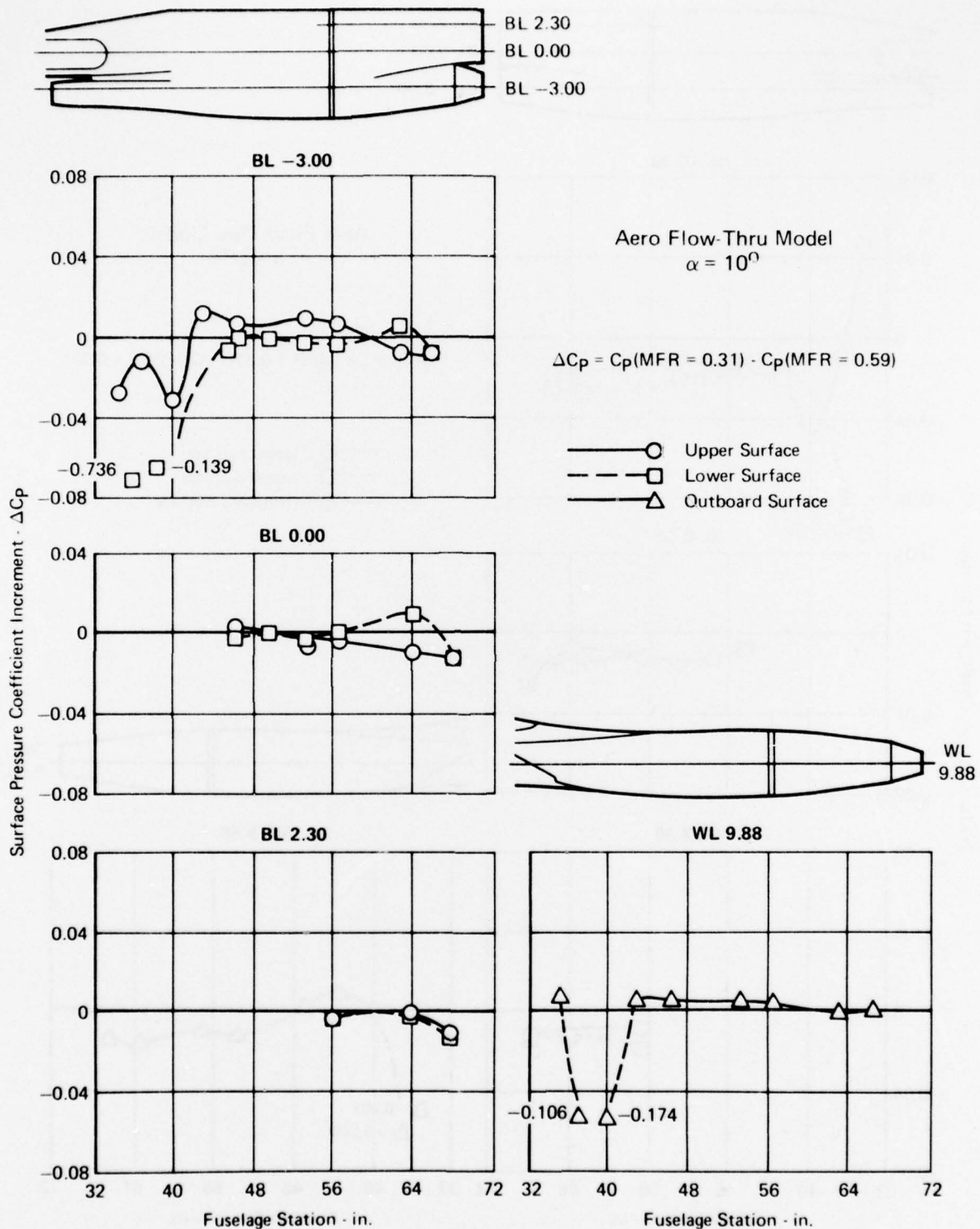


FIGURE 5-40
EFFECT OF INLET MASS FLOW RATIO ON
EXTERNAL SURFACE PRESSURES AT MACH 0.9

GP76 0701-149

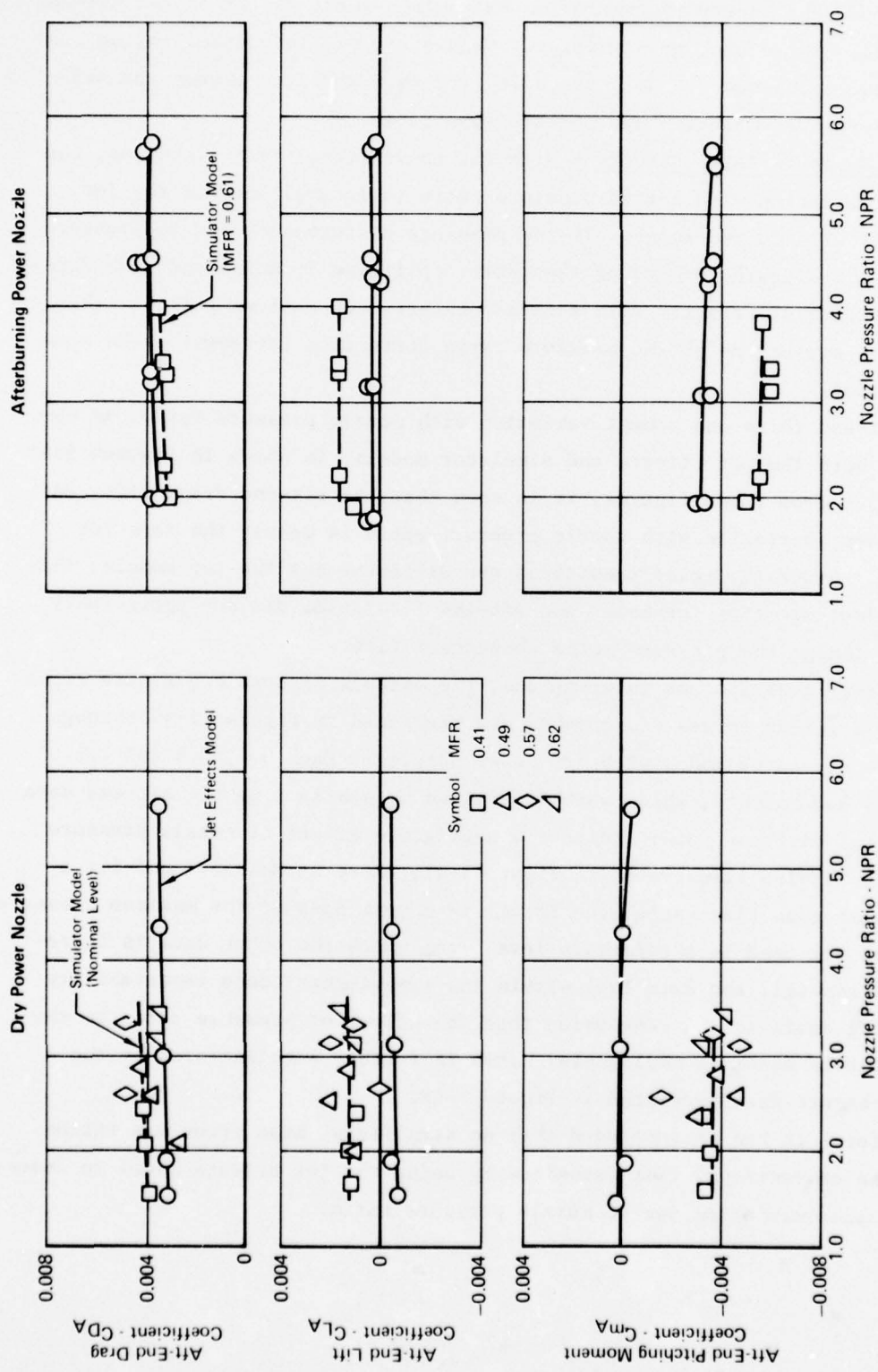
Based on all the data presented, it can be concluded that inlet flowfield changes due to mass flow ratio variation had only a small effect on the aft-end of this model. Therefore, no significant bias error was introduced in the conventional test technique by using the aero flow-thru model to assess the aerodynamic performance variation due to mass flow ratio.

Nozzle Pressure Ratio Effects - With the conventional test technique, the performance variation with nozzle pressure ratio is accomplished on the jet effects model with faired inlet. If the pressure disturbances due to pressure ratio changes propagate forward of the metric splitline location onto the forebody, or interact differently with a faired rather than a flowing inlet, then errors in the evaluation of the pressure ratio correction increment could have been introduced.

The aft-end force and moment variation with nozzle pressure ratio, as obtained from both the jet effects and simulator models, is shown in Figures 5-41 through 5-43. From these figures, it is seen that the aft-end drag, lift, and pitching moment variation with nozzle pressure ratio is nearly the same for both models. Since the inlet conditions are different for the two models, this would also indicate that the inlet and aft-end flowfields did not appreciably interact to change the pressure ratio characteristics.

To further evaluate any interactions, the effects of nozzle pressure ratio on just the forebody forces and moments are presented in Figures 5-44 through 5-46 for the simulator model with dry power nozzle at Mach 0.6, 0.9 and 1.2. These forces and moments, which were determined by subtracting the aft-end data from the total airframe data, indicate a negligible effect of nozzle pressure ratio. This is also illustrated in Figure 5-47, where at Mach 0.9 and for a constant inlet mass flow ratio, the force and moment data at the maximum pressure ratio tested are used as a reference level from which the other data is incremented. In general, the data fall within the experimental data repeatability band, leading again to the conclusion that the effect of pressure ratio on the forebody of this model is negligible. This is further substantiated by the external pressure data presented in Figure 5-48.

Therefore, it can be concluded that no significant bias error was introduced in the conventional test technique by using the jet effects model to assess the performance variation due to nozzle pressure ratio.



GP76 0701 66

FIGURE 5-41
VARIATION OF AFT-END PERFORMANCE PARAMETERS WITH
NOZZLE PRESSURE RATIO AT MACH 0.6
 $\alpha = 0^\circ$

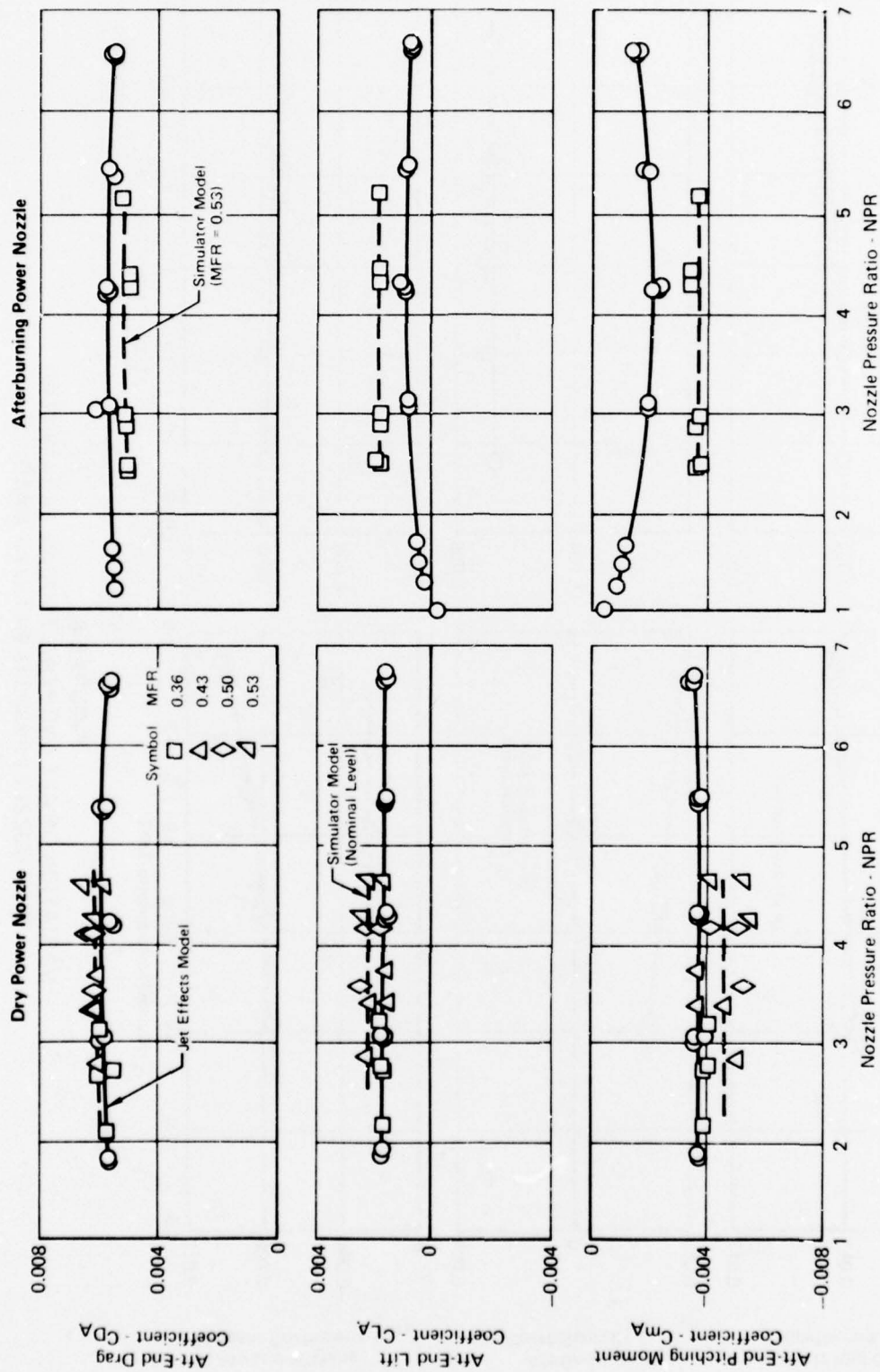


FIGURE 5-42
 VARIATION OF AFT-END PERFORMANCE PARAMETERS WITH
 NOZZLE PRESSURE RATIO AT MACH 0.9
 $\alpha = 0^\circ$

GP76 0701 67

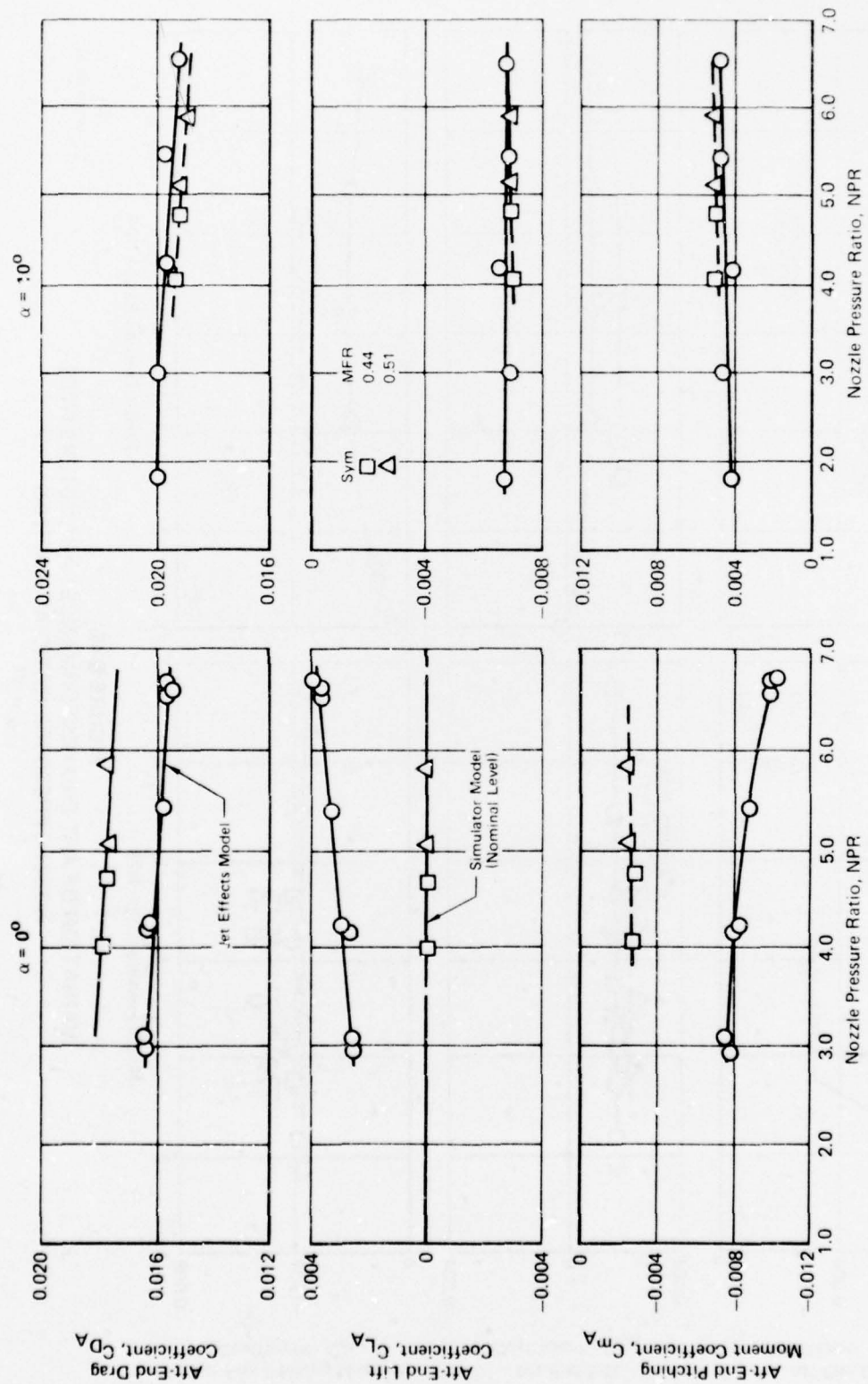


FIGURE 5.43
VARIATION OF AFT END PERFORMANCE PARAMETERS
WITH NOZZLE PRESSURE RATIO AT MACH 1.2

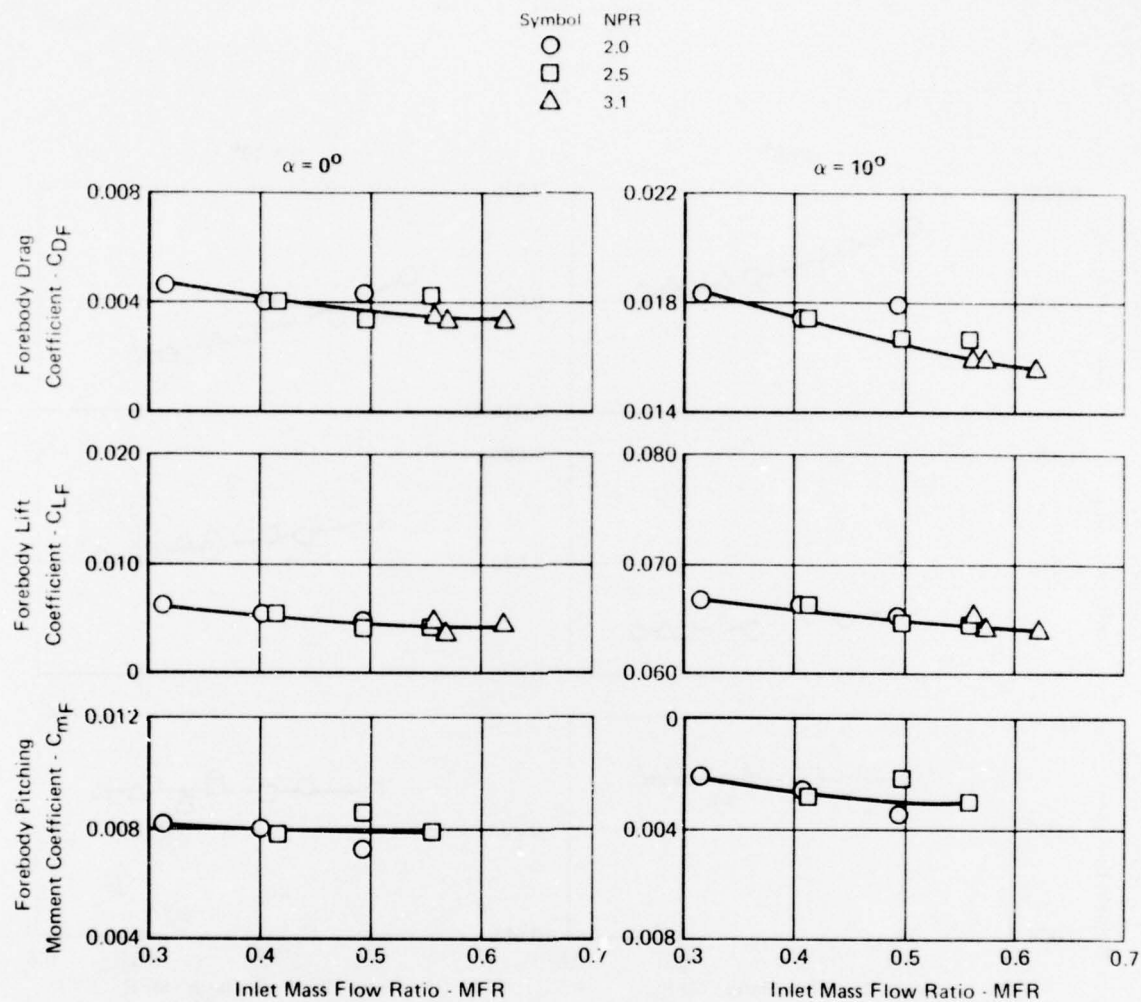
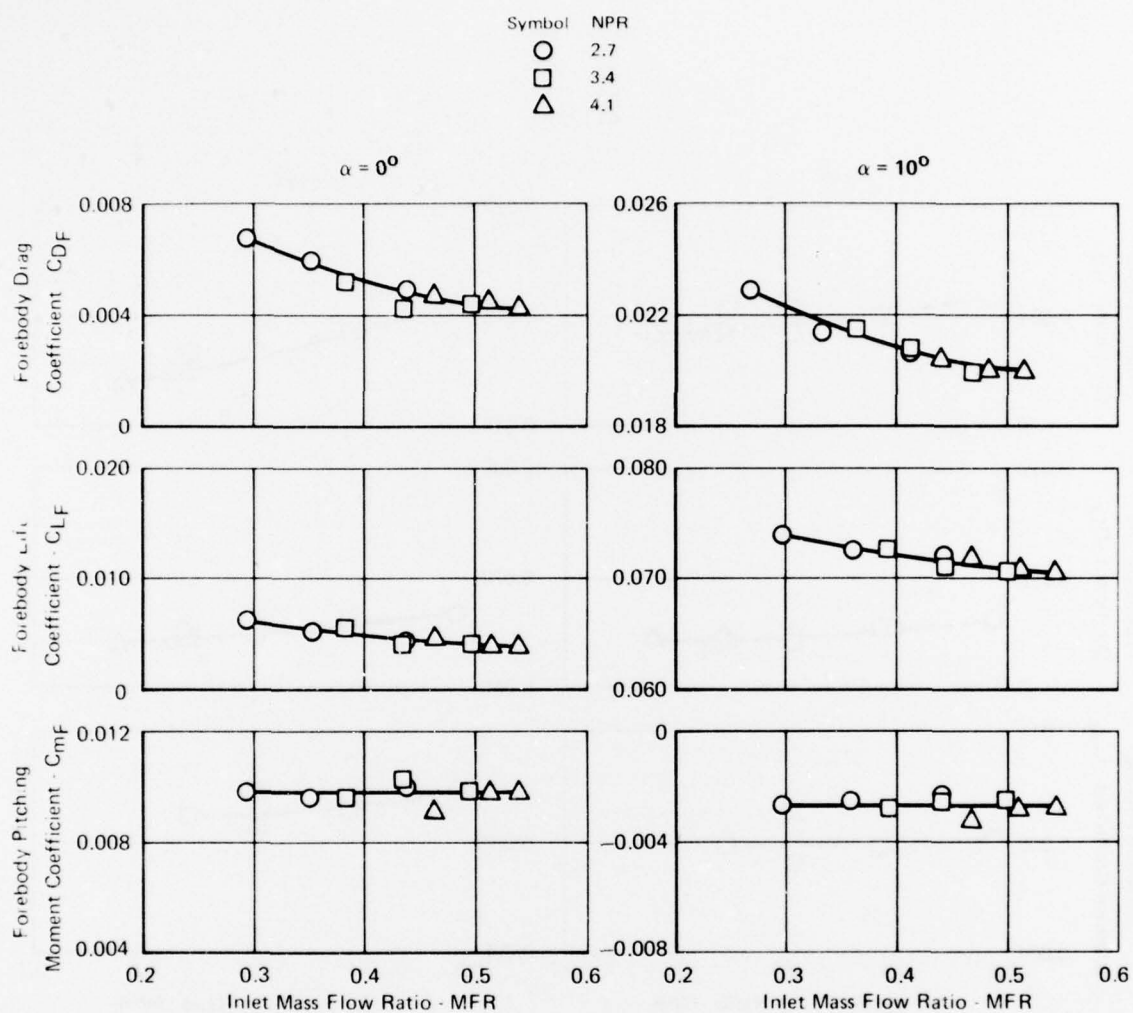
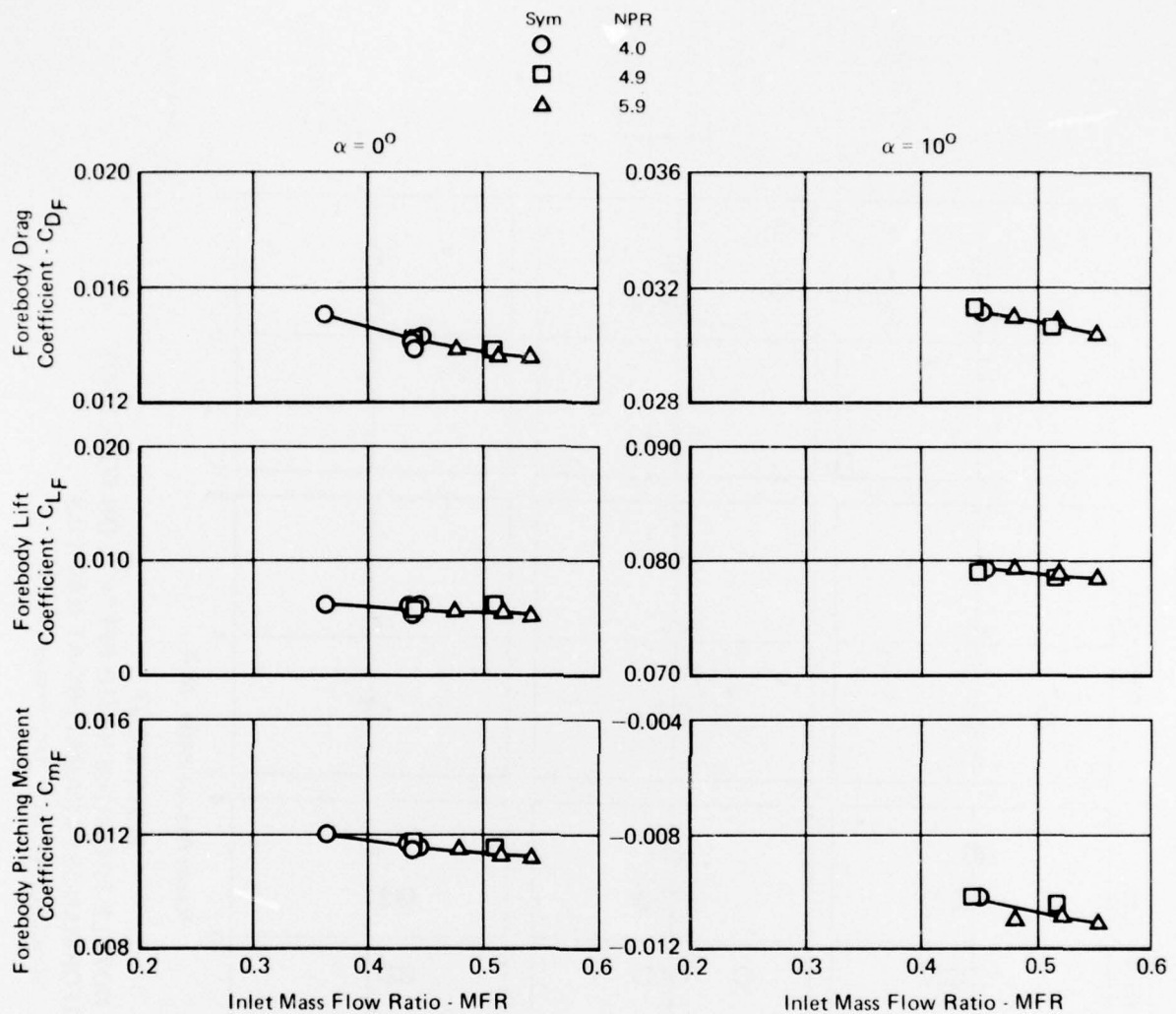


FIGURE 5-44
EFFECTS OF NOZZLE PRESSURE RATIO ON FOREBODY
PERFORMANCE PARAMETERS AT MACH 0.6
 Simulator Model Dry Power Nozzle



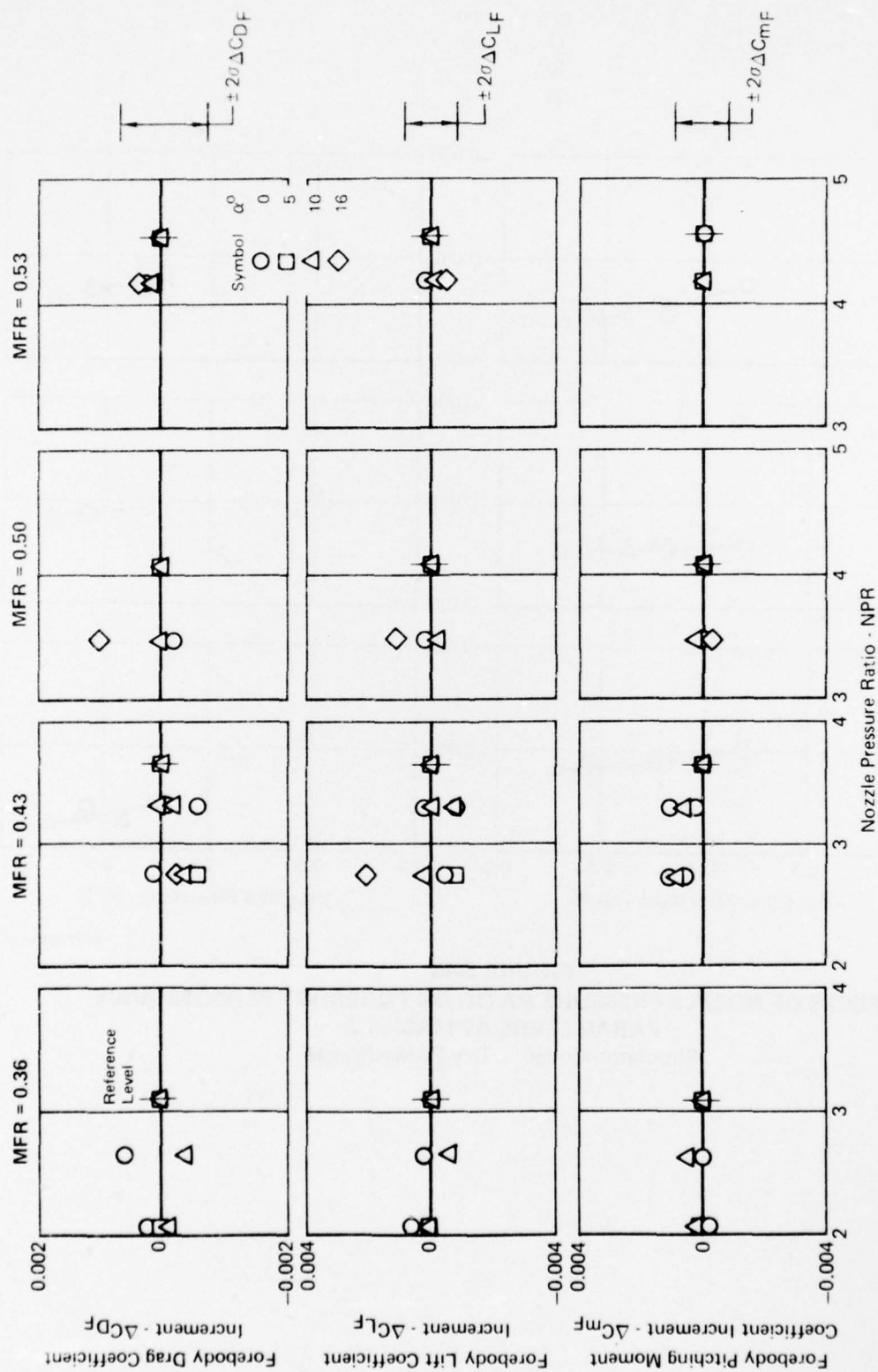
GP76 0701 74

FIGURE 5-45
EFFECTS OF NOZZLE PRESSURE RATIO ON FOREBODY
PERFORMANCE PARAMETERS AT MACH 0.9
 Simulator Model Dry Power Nozzle



GP76-0701-126

FIGURE 5-46
EFFECTS OF NOZZLE PRESSURE RATIO ON FOREBODY PERFORMANCE
PARAMETERS AT MACH 1.2
 Simulator Model Dry Power Nozzle



GP76 0701 75

FIGURE 5-47
INCREMENTAL NOZZLE PRESSURE RATIO EFFECTS ON FOREBODY
PERFORMANCE PARAMETERS AT MACH 0.9
 Simulator Model Dry Power Nozzle

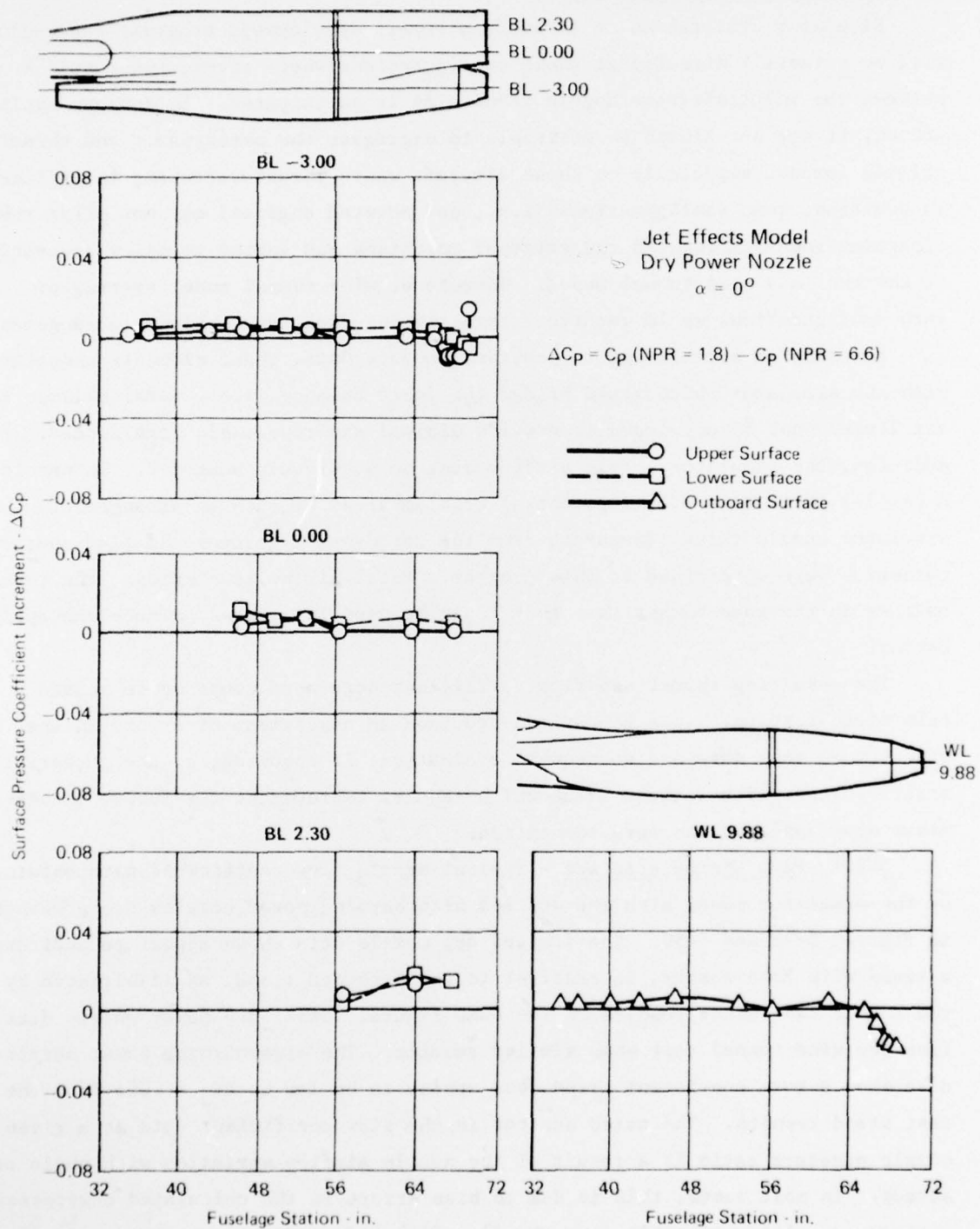


FIGURE 5-48
EFFECT OF NOZZLE PRESSURE RATIO ON EXTERNAL
SURFACE PRESSURES AT MACH 0.9

GP76 0701 68

5.2 Nozzle Performance Evaluation

Simulator utilization in advanced aircraft development programs (Appendix A) will be primarily directed at those configurations where strong interactions between the inlet/airframe/nozzle flowfields is anticipated. In such an application, it may not always be desirable to segregate the aerodynamic and thrust-related forces, especially on those aircraft where thrust-vectoring is utilized. In addition, some configurations (i.e., pod mounted engines) may not offer the clearance required between the external moldlines and engine to allow separation of the two in a wind tunnel model. Therefore, wind tunnel model testing of such configurations would require a thrust-minus-drag force balance arrangement.

For such an arrangement to provide accurate data, those elements associated with the simulator which would bridge the force balance (i.e., metal bellows for air lines) must be developed to provide minimal and repeatable tare forces. In addition, the simulator nozzle airflow must be accurately measured. To provide a partial indication of the potential problem areas of such an arrangement, the simulator nozzle thrust (separate from the aerodynamic forces) and flow characteristics were determined in this program. Metal air bellows bridge the thrust balance in the same manner that they could be used in a thrust-minus-drag application.

The resulting thrust and flow coefficient data were compared to static test stand results. This comparison provided an assessment of errors in the wind tunnel test data and subsequent evaluation, if required, of the potential error sources. Thus, those areas which require improvement for future thrust-minus-drag applications were identified.

5.2.1 Flow Characteristics - Typical nozzle flow coefficient data obtained on the simulator model with the dry and afterburning power nozzles are presented in Figures 5-49 and 5-50. The limited dry nozzle data shown appear to indicate a trend with Mach number, in contrast to the expected trend, as illustrated by the static test stand results on the same figure. Other dry power nozzle data from the wind tunnel test show similar results. The afterburning power nozzle data show a more consistent trend, but appear to be low by $\Delta C_w = .006$ from the test stand results. The noted scatter in the flow coefficient data at a given nozzle pressure ratio is a result of the nozzle airflow variation with angle of attack. In most cases, this is due to bias errors in the calculated compressor airflow, resulting possibly from the flow distortion effects on the duct wall static pressure measurements near the compressor face. However, this does not

fully explain the flow coefficient discrepancy problem as shown by the $\alpha = 0^\circ$ data in Figures 5-49 and 5-50.

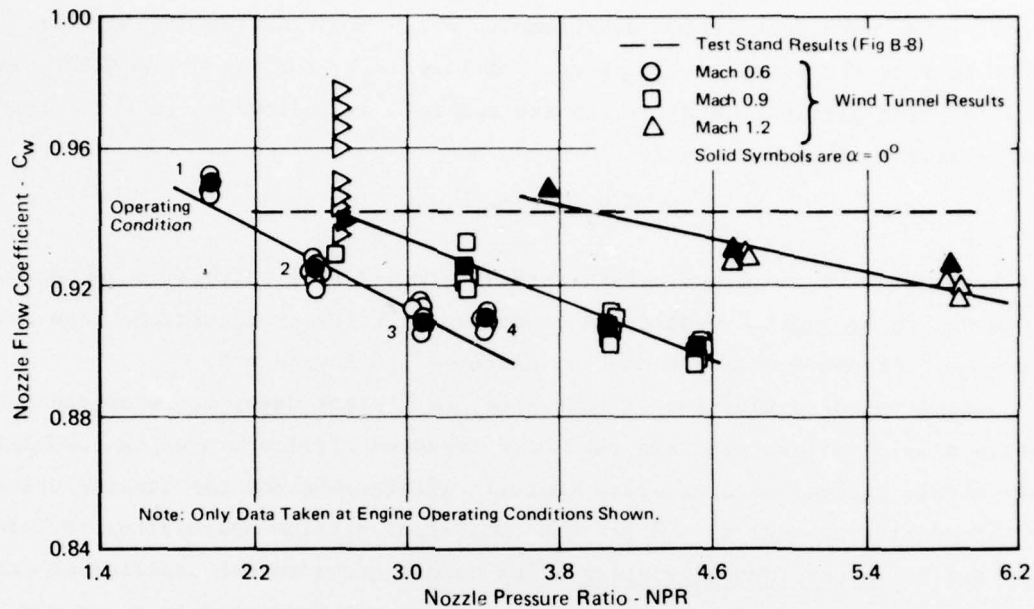


FIGURE 5-49
DRY POWER NOZZLE FLOW CHARACTERISTICS FROM
WIND TUNNEL TEST

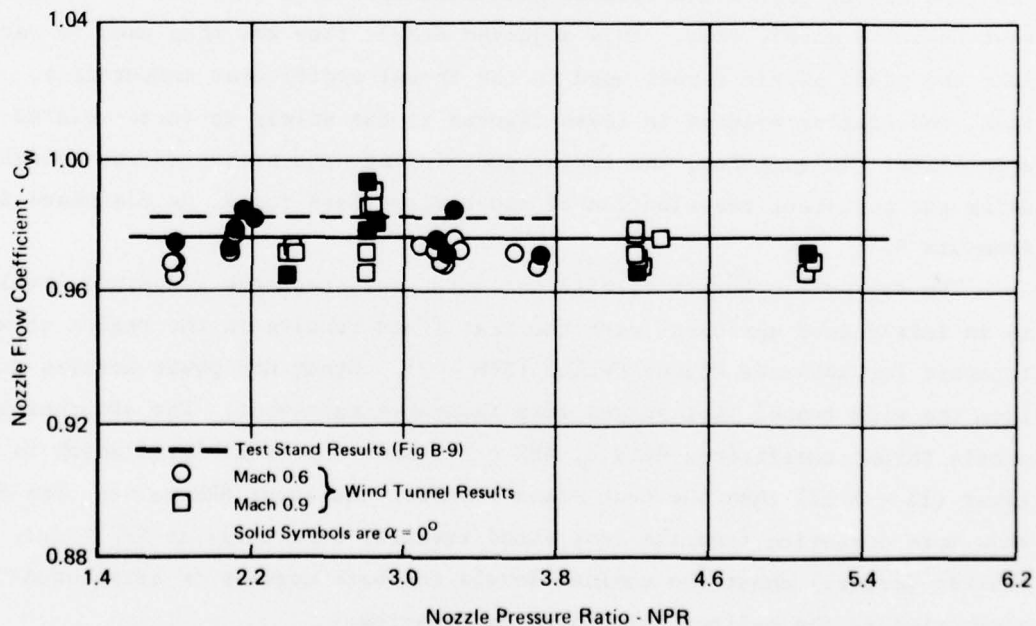


FIGURE 5-50
AFTERBURNING POWER NOZZLE FLOW CHARACTERISTICS
FROM WIND TUNNEL TEST

In general, these flow coefficient errors are attributed to errors in all three of the separate airflow measurements which comprise the nozzle flow. These include the simulator compressor airflow (W_2), turbine drive (WDM), and turbine bleed airflows (WBM), which are combined as follows to give the total nozzle airflow (W_8).

$$W_8 = W_2 + (WDM - WBM)$$

The turbine drive and bleed airflow are determined from calibrated venturis, as discussed in Appendix C, while the compressor airflow is determined from total and static pressure measurements, as discussed in Appendix B.

Based on the evaluation of this flow coefficient data, it is apparent that future simulator test programs must have improved airflow measuring capability. This should include more accurate venturi calibrations for the turbine drive and bleed air, as well as a different compressor airflow calculation technique.

5.2.2 Thrust Characteristics - The nozzle gross thrust coefficient data for both the dry and afterburning power nozzles are presented in Figures 5-51 and 5-52, respectively. The data presented in these figures have been adjusted for the correct nozzle flow. That is, the known nozzle flow characteristics from the static test stand results have been used to adjust the wind tunnel test-computed nozzle flow. This adjusted nozzle flow was then used to recalculate the ideal nozzle thrust used in the thrust coefficient computation. Therefore, the scatter evident in these figures is due solely to force-related inaccuracies. In addition, the thrust coefficient data presented was calculated using the post-test reevaluation of the bellows tare force, as discussed in Appendix B.

The dry nozzle thrust coefficient data presented show a nominal level which is in fairly good agreement with the test stand results in the region of most interest for advanced engine cycles ($NPR > 3$). Other dry power nozzles data from the wind tunnel test showed less favorable agreement. The afterburning nozzle thrust coefficient data at $NPR \geq 2.6$ show a nominal level which is slightly lower (1% - 1.5%) than the test stand results. At lower NPR values, the data show more deviation from the test stand results, especially at $NPR \sim 2.1$. The scatter (errors) about the nominal levels for both nozzles is attributed to inaccuracies in the bellows tare force calibration.

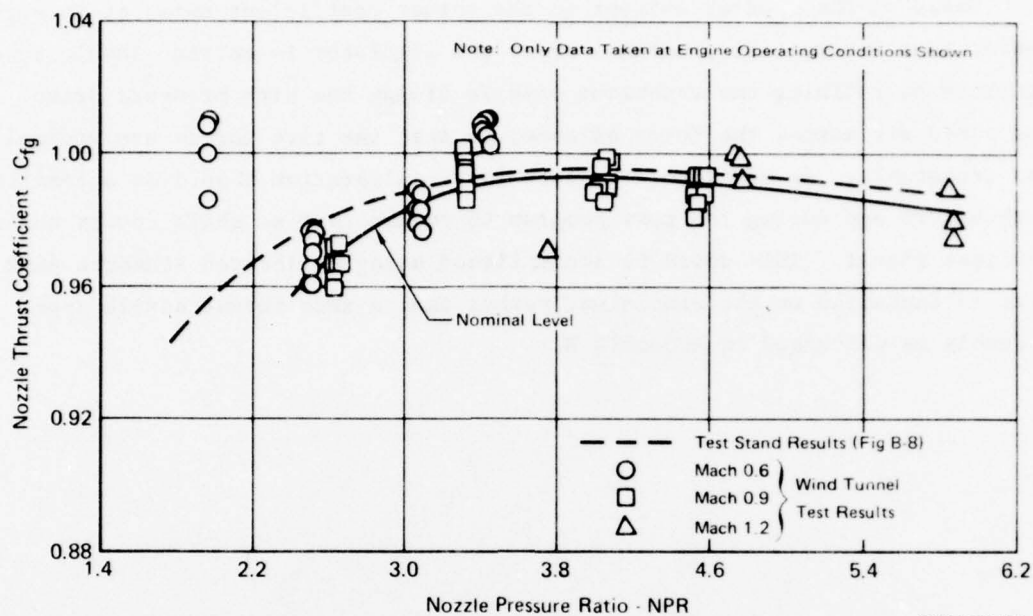


FIGURE 5-51
DRY POWER NOZZLE THRUST CHARACTERISTICS
FROM WIND TUNNEL TEST

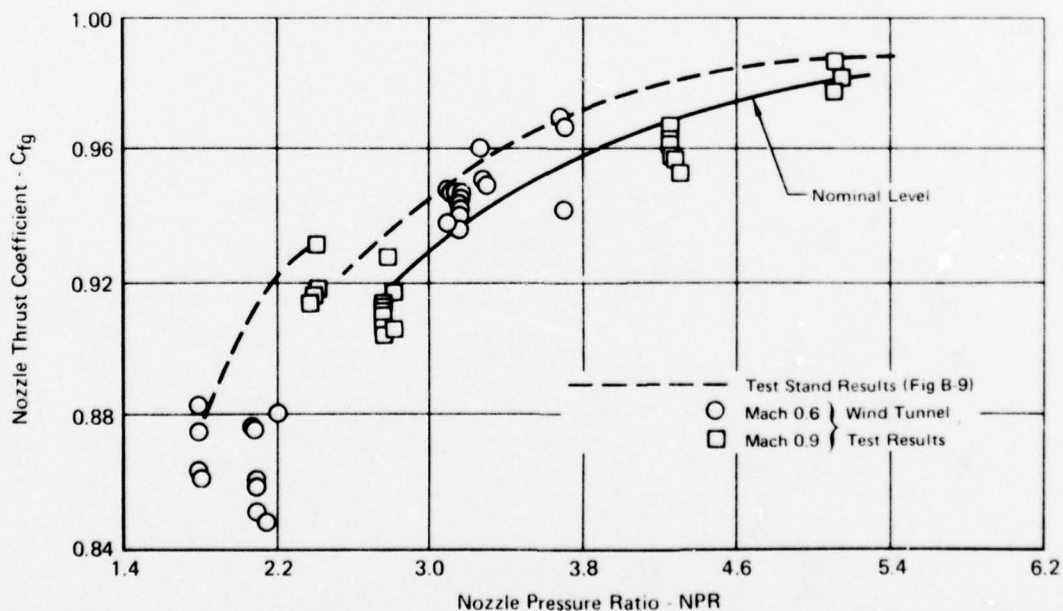


FIGURE 5-52
AFTERBURNING POWER NOZZLE THRUST CHARACTERISTICS
FROM WIND TUNNEL TEST

Based on the scatter evident in the thrust coefficient data, it is suggested that future test programs, where the simulator is metric, should concentrate on refining the technique used to bridge the high pressure drive and bleed air across the force balance, so that the tare forces are minimal and repeatable. In addition, the tare force calibration should be accomplished both before and during the test program to ensure that no shift occurs during the test itself. This could be accomplished using calibrated standard ASME nozzles installed on the simulator, rather than a zero thrust nozzle type assembly as discussed in Appendix B.

6. SIMULATOR MECHANICAL OPERATION

Although three static test programs have been conducted (Appendix C), this wind tunnel test was the first time that this type of simulator had been demonstrated in a wind tunnel model test program. As such, an evaluation of the simulator operational capabilities/limitations is of special interest. The SN002 simulator used in this test accumulated 29.4 powered hours with the wind tunnel operating, a rotor lock-up terminated the test.

The following paragraphs review the general simulator operation during the test, the demonstrated operational flexibility, health-monitoring data, and simulator post-test disassembly/inspection.

6.1 General Simulator Operation

Prior to the wind tunnel test, a systematic set of operating procedures was defined for the simulator and all facility-related operational items. These procedures, Figure 6-1, ensured safe and efficient operation of the model/simulator system, and covered simulator operation in the pre-test, test and post-test phases.

During this test program, three people were required to control and monitor the simulator operation: a control console operator/monitor, a mechanical health monitor and a dynamic pressure/run log monitor. As more experience is gained with the simulator operation, however, only two people should be required.

Simulator control console operation in the wind tunnel test was essentially the same as experienced during the static test in the AEDC Engine Test Facility (ETF). The simulator and controls were easily maintained and operated with minimal problems for the experienced operators. The only major problem was the inability to efficiently set the desired inlet mass flow and nozzle pressure ratio conditions. This was due to the limited instrumentation devoted to real-time updating of these parameters. For future test programs, those modifications required to the control console to improve the simulator operating efficiency include:

- o Addition of a self-contained computer system which calculates critical run parameters such as compressor airflow and simulator pressure ratio, and provides real-time update capability.

Pre-Ops
<ul style="list-style-type: none"> ● Check and fill bearing oil supply tank ● Start oil supply and vacuum pumps 2 hours before test starts ● Turn power on the console 2 hours before test starts ● Hook up electronic simulator to console ● Start hydraulic system for air valves ● Verify all aspects of console operation <ul style="list-style-type: none"> — Drive and bleed air valves (open/close sequence) — Manual and automatic run modes — Automatic shutdown circuitry — Automatic shutdown limits (i.e. speed, accel rate, etc.) — Digital displays of speed, bearing temps, etc ● Disconnect electronic simulator and hook-up simulator to console ● Check oil scavenge rates from both bearings ● Supply high pressure heated air to simulator drive air valve ● Open drive air valve and bring simulator to idle speed (~35,000 RPM) ● Maintain speed until all monitored simulator parameters are stable (i.e. bearing temps, etc) ● Accelerate simulator to 70% speed (~52,000 RPM) ● Take steady-state data point ● Push emergency shutdown button on console to verify closing of drive air valve and opening of dump valve ● Acknowledgement that simulator operation is satisfactory and tunnel can be turned on
Test-Ops
<ul style="list-style-type: none"> ● Start tunnel and bring to Mach No. condition with simulator windmilling ● Open drive air valve and bring simulator to idle speed ● Transfer control console from manual to automatic operational mode ● Set simulator to desired airflow and pressure ratio conditions ● Take steady-state data point at $\alpha = 0^\circ$ and continue through α sweep. Check simulator settings at each α. ● Reset simulator to next desired airflow and pressure ratio condition and take data again ● Maintain simulator at idle speed when changing Mach No. condition ● Shut simulator down and let windmill when ready to bring tunnel off line ● In case of simulator auto shutdown, return model to $\alpha = 0^\circ$. Diagnose problem and either shutdown tunnel for further evaluation or bring simulator back to desired conditions and continue taking data.
Post-Ops
<ul style="list-style-type: none"> ● Turn off power to control console, oil pump, hydraulic system ● Wait 2 hours and then turn off power to vacuum pumps ● Conduct visual inspection of simulator after tunnel is open

**FIGURE 6-1
SIMULATOR OPERATING PROCEDURES FOR WIND TUNNEL
TEST PROGRAM**

- Incorporation of an improved visual display which continually displays
 - Rotor Speed - Bearing Oil Supply/Scavenge Rates
 - Rotor Thrust - Bearing Temperatures
 - Rotor Position - Compressor Airflow
 - Vibration Levels - Simulator Pressure Ratio (PT8/PT2)
- Incorporation of an improved automatic shutdown capability to decrease sensitivity to electronic noise spikes, and allow easy identification of shutdown cause.

- o Redesign of the dual simulator mode to provide separate control of each simulator.

The use of an oscilloscope to monitor the compressor inlet/exit dynamic static pressures proved to be an excellent operational aid in the detection of compressor stall onset. Such monitoring can prevent excessive strain on the compressor blades, rotor, and bearings of the simulator due to stalls which can significantly reduce the life of the simulator. A few stalls or stall onsets are desirable during the static calibration of the simulator to determine the stall line of the compressor.

A considerable amount of static simulator operation, approximately 11 hours, was logged during the AEDC 16S wind tunnel check-out runs and the bellows tare force calibration. During these runs, there were numerous compressor stalls and front-end dynamic shock loading, which were attributed to the flow distortion levels into the simulator. For static testing conducted in the 16T following the 16S check-out runs, the inlet was fitted with a rectangular bellmouth adapter with large radius lips, as shown in Figure 6-2. Operation with the bellmouth significantly improved the static operation of the simulator, and essentially eliminated the stall problem. The improvement in steady-state pressure distortion and inlet recovery with the bellmouth at static operation is shown in Figure 6-3.

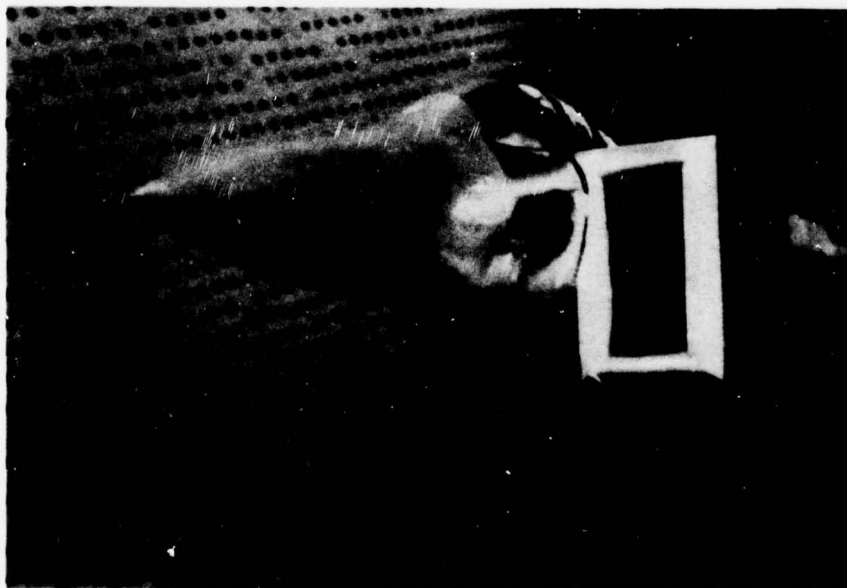
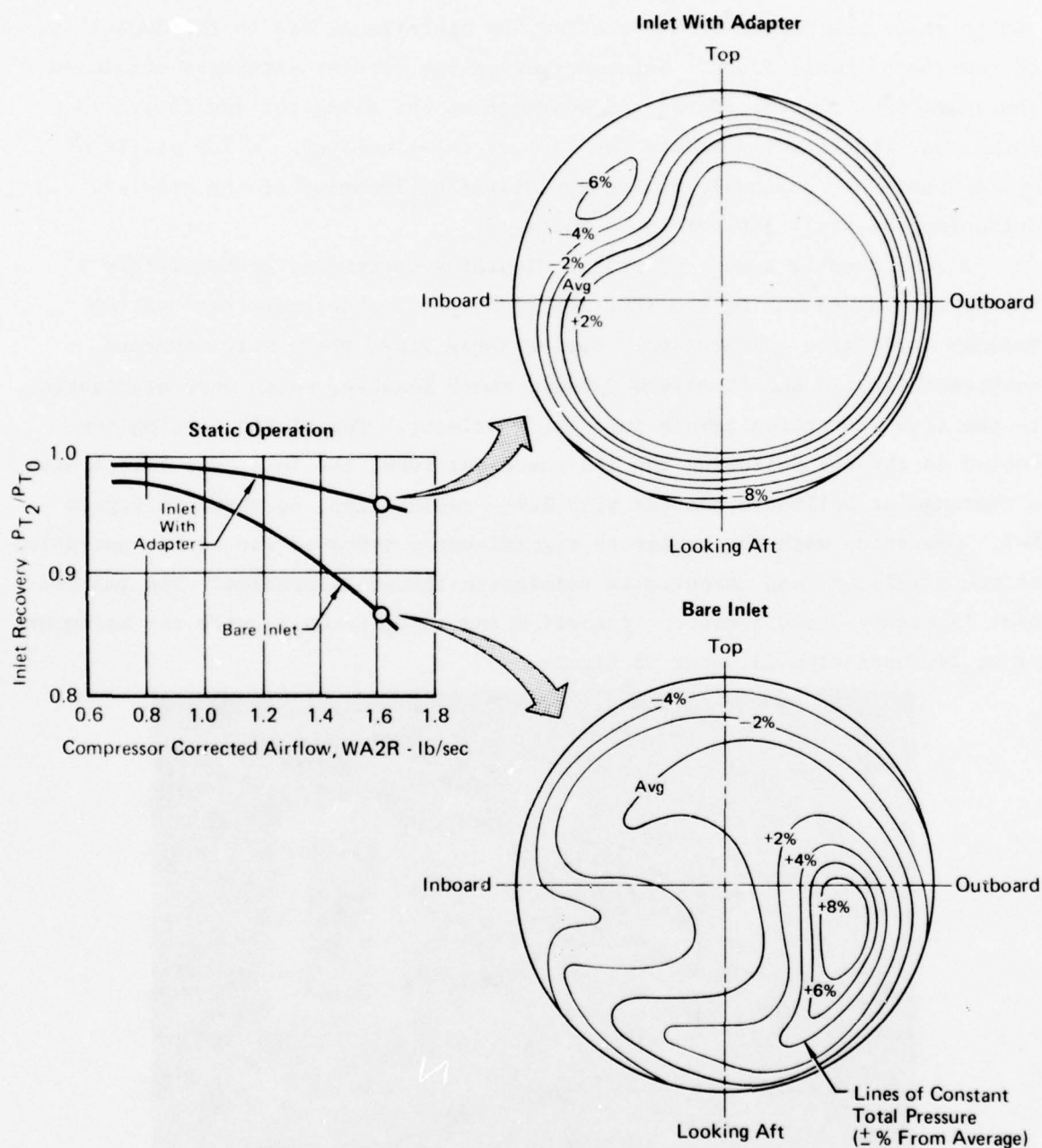


FIGURE 6-2
INLET WITH BELLMOUTH ADAPTER



GP76 0701 36

FIGURE 6-3
PRESSURE DISTORTION AND RECOVERY IMPROVEMENT WITH
INLET BELLMOUTH ADAPTER

In the area of simulator mechanical service systems, the most significant problem in the wind tunnel test was the lubrication oil scavenge system. This system was designed to provide a positive oil scavenge of both bearings and keep oil out of the tunnel airflow, and permit measurement of the scavenge oil for analysis of scavenge efficiency. In the ETF testing, this system performed as planned primarily because of the short distance, ~6 feet, between the simulator and the scavenged oil reservoirs. However, in the wind tunnel test, a much longer distance, ~200 feet, between the simulator and reservoirs was required. The result was a two-hour time delay between the time the oil left the simulator and the time it entered the reservoirs. This proved to be impractical for diagnosing oil system problems. Therefore, for future wind tunnel test programs, a simulator-mounted transducer should be developed to measure both the lubrication oil supply and scavenge rates.

Overall, the general operation of the simulator during this first wind tunnel demonstration test was good. The minor problems that arose can be easily remedied for future test programs. With the experience gained from this test and incorporation of the control console modifications identified earlier, simulator model testing can become a very efficient way to obtain test data. Although the simulator was not tested above Mach 1.2, there are no indications that testing at higher Mach numbers will cause problems.

6.2 Operational Flexibility

A key feature of the simulator is its ability to independently vary compressor airflow at a fixed overall pressure ratio (P_{T8}/P_{T2}), or to vary pressure ratio at a fixed airflow. This allows it to match the operating characteristics of many engine cycles without major hardware changes. This had been demonstrated during static testing, and was investigated further during the wind tunnel tests.

Figures 6-4 and 6-5 present the simulator flexibility maps demonstrated during the test for the dry and afterburning power nozzles, respectively. The dry nozzle map is essentially identical to that obtained from the ETF testing with uniform inlet pressure profiles. It shows that the inlet pressure profiles experienced during the wind tunnel test did not degrade the flexibility. Although only limited data are available for the afterburning nozzle, the test data tend to agree with the predictions.

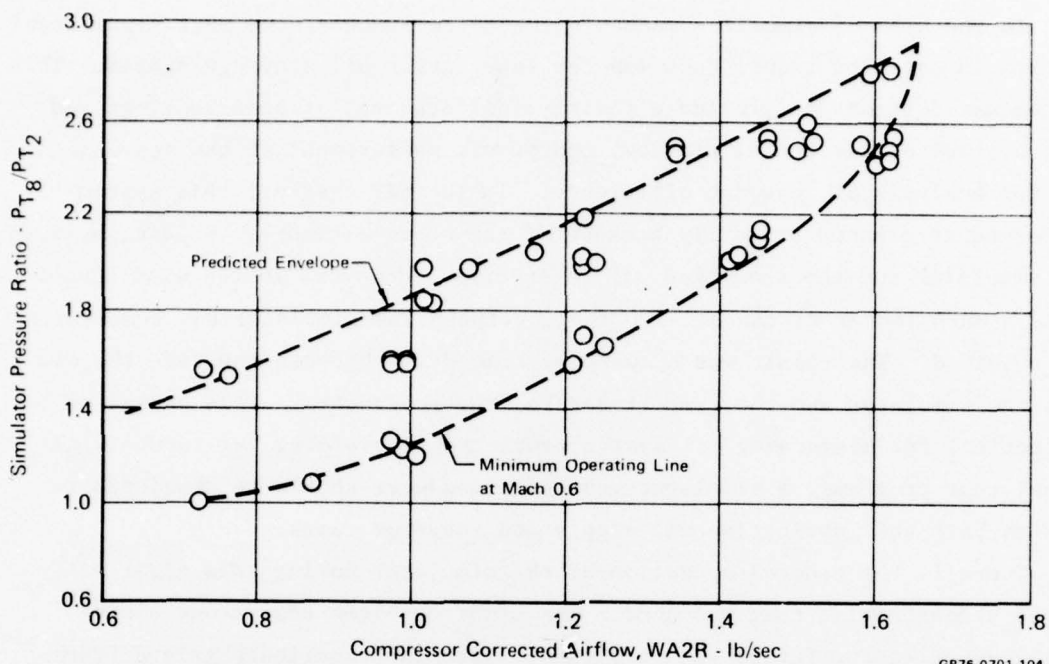


FIGURE 6-4
SIMULATOR FLEXIBILITY DEMONSTRATED DURING WIND TUNNEL TEST
 Dry Power Nozzle

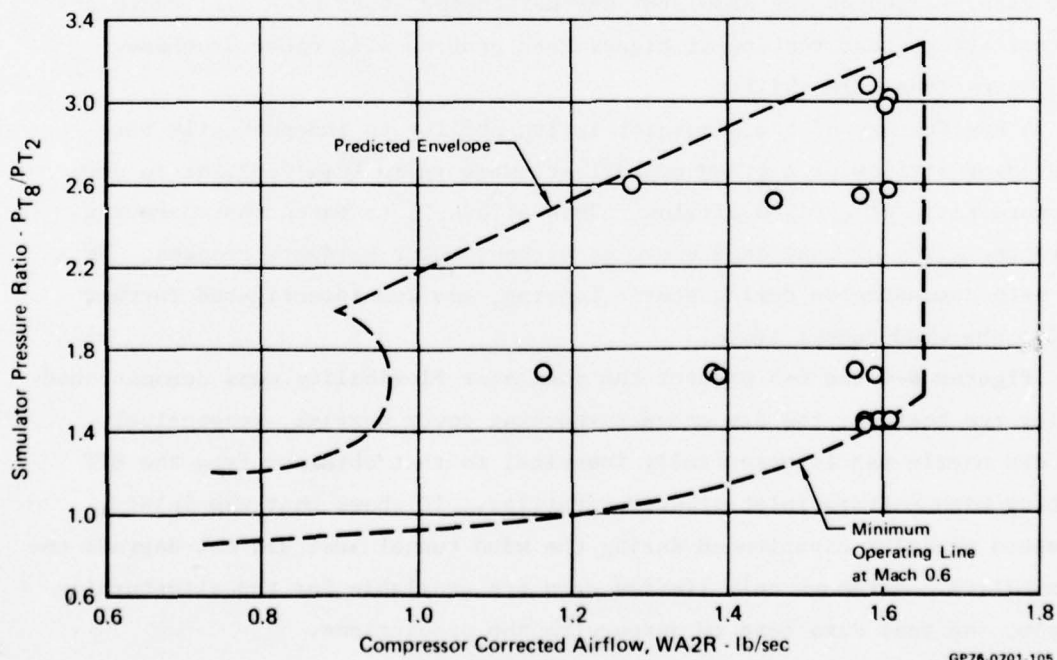


FIGURE 6-5
SIMULATOR FLEXIBILITY DEMONSTRATED DURING WIND TUNNEL TEST
 A/B Power Nozzle

6.3 Diagnostic Data

Five key parameters were used to monitor the mechanical health of the simulator during both the static and wind tunnel test programs. These are the (1) forward bearing temperature, (2) rear bearing temperature, (3) vibration levels, (4) rotor thrust, and (5) rotor axial position. All but rotor thrust were measured directly. A brief analysis of these parameters from the wind tunnel test is presented in the following paragraphs.

The focus of the analysis is the forward bearing temperature, since it proved to be the parameter which indicated potential bearing problems. To simplify the discussion, the wind tunnel test time history is divided into four phases, as identified in Figure 6-6.

Phase	Nozzle Config.	Tunnel Temperature	Test Mach No.	Data Part/Point	Remarks
1	Dry Power	120°F	0.6 → 0.9	1013 → 1054/8	Major Bearing Damage at Shutdown A
2	Dry Power	↓	0.6 → 1.2	1054/9 → 1104	
3	A/B Power		0.6 → 0.9	1109 → 1132	
4	Dry Power		0.6	1148 → 1150	Larger Thrust Trim Orifice; Shutdown R Occurs; Rotor Locks Up

FIGURE 6-6
TIME HISTORY OF SIMULATOR OPERATION DURING
AEDC 16T TUNNEL TEST

GP76 0701 108

The condition of the forward bearing during the wind tunnel test is shown qualitatively in Figure 6-7, in terms of bearing temperature change from a "normal health" standard. For this analysis, the normal health standard, i.e., bearing temperature vs corrected rotor speed, was defined as the bearing temperature characteristics during the static testing in the AEDC Engine Test Facility. A slight deterioration of simulator health during the wind tunnel test is evidenced by the increase in forward bearing temperature level. The automatic shutdown "A" shown in Figure 6-7 was the first major indication of this deterioration. Eventually, shutdown "R" brought the simulator to a windmilling state, followed closely by a rotor lock-up. This terminated the simulator model testing.

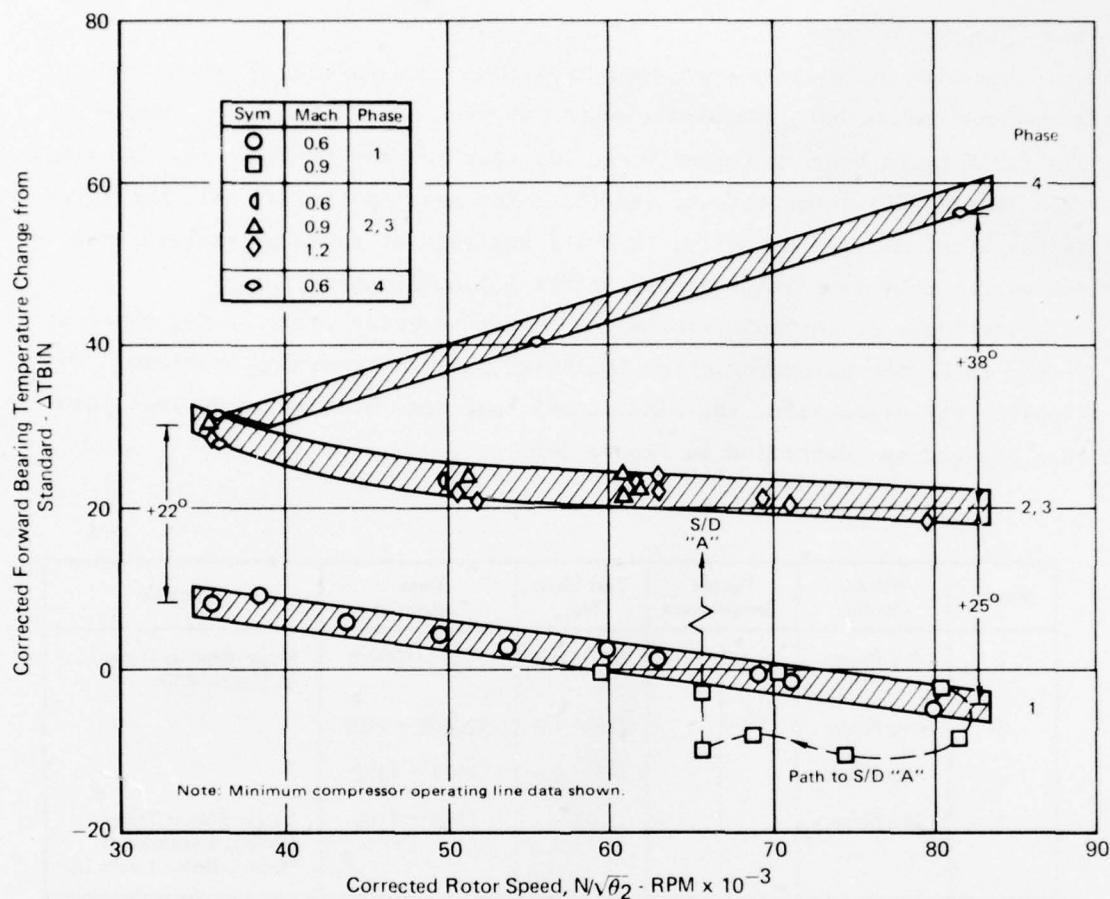


FIGURE 6-7
FORWARD BEARING TEMPERATURE HISTORY
DURING WIND TUNNEL TEST

Figures 6-8 through 6-11 trace the same time history (Phases 1 through 4) for the rear bearing temperature, rotor thrust, rotor position, and vibration levels. The rotor position data also provided an indication of the possible degradation of simulator health starting with shutdown "A". The other parameters provided little indication of the deterioration.

6.4 Disassembly/Inspection Results

Following the wind tunnel test, the SN002 simulator was disassembled and inspected to determine the general condition of the components and cause of the rotor lock-up. The major results of this effort are discussed briefly below, with details presented in Reference (5).

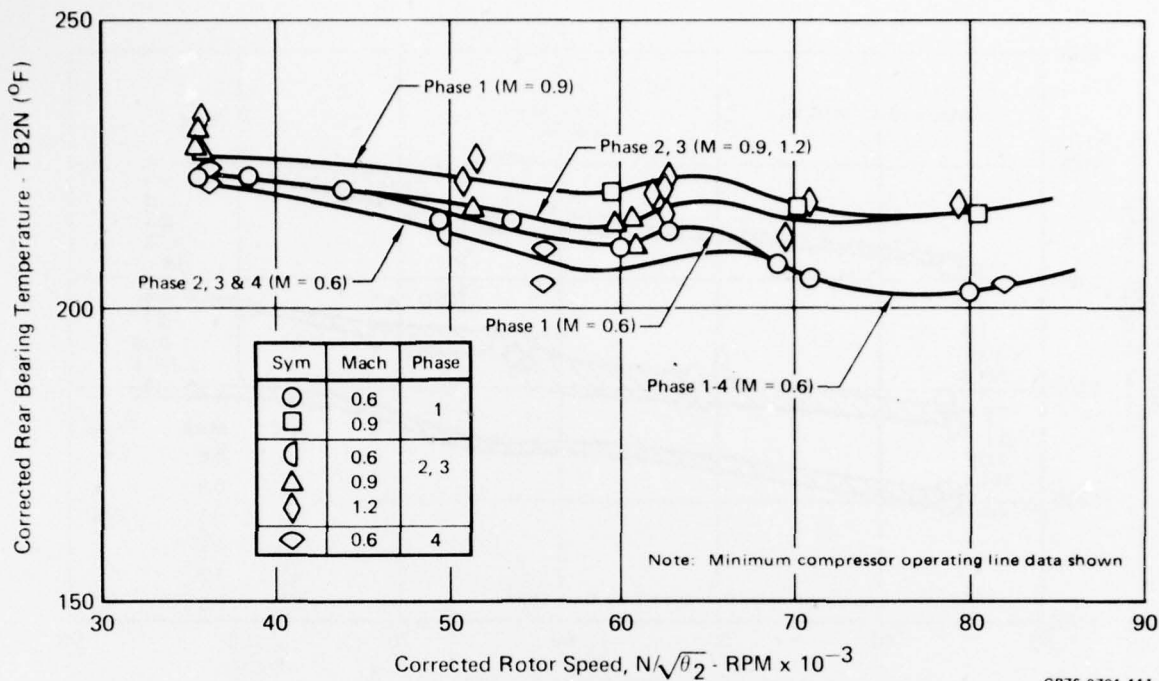


FIGURE 6-8
REAR BEARING TEMPERATURE HISTORY DURING WIND TUNNEL TEST

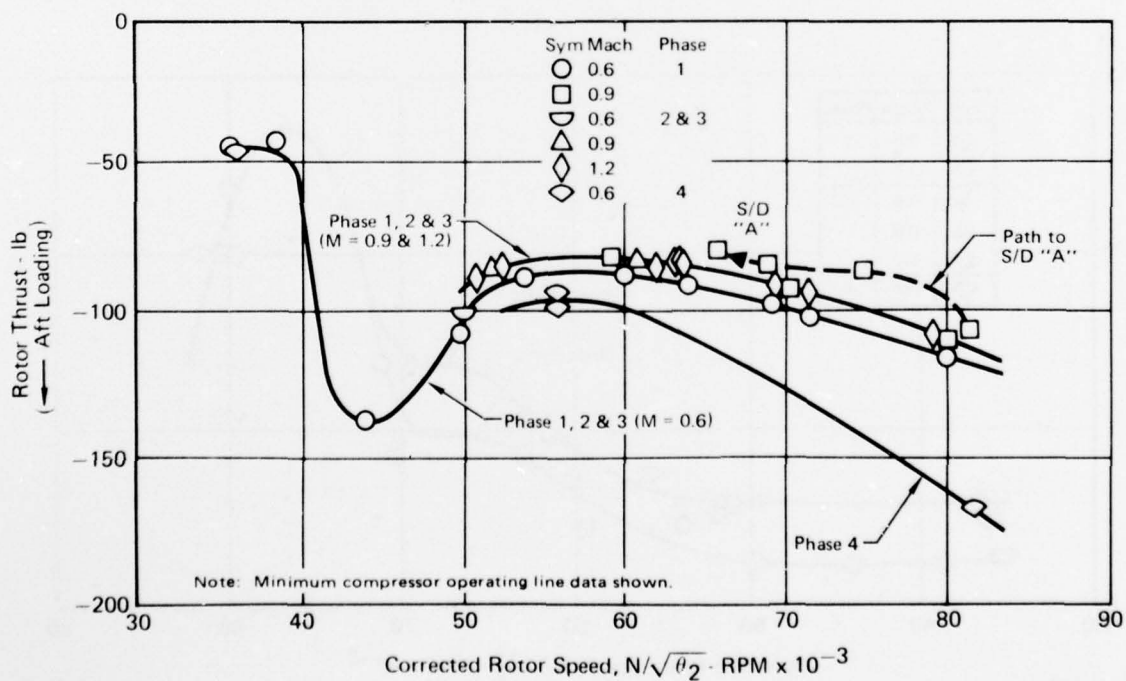
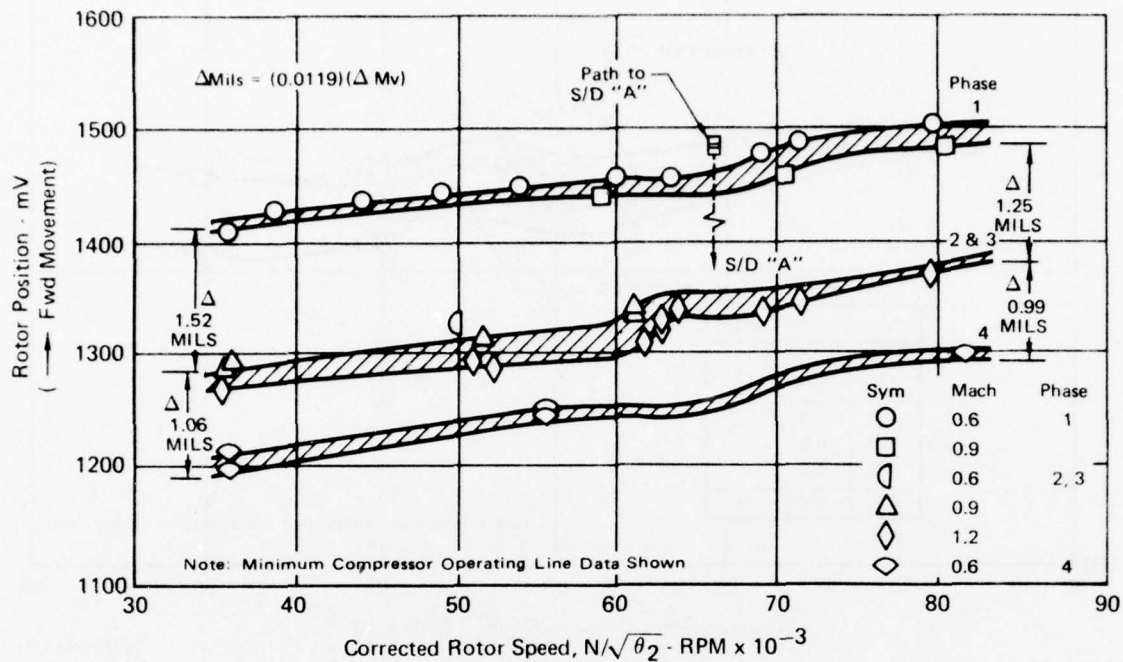
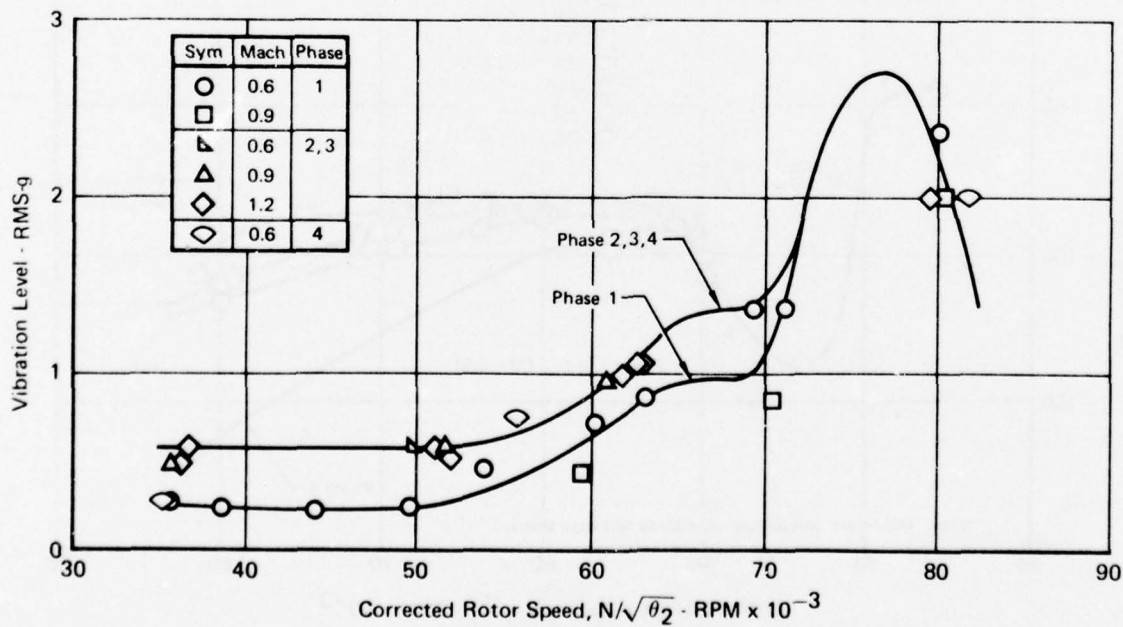


FIGURE 6-9
ROTOR THRUST HISTORY DURING WIND TUNNEL TEST



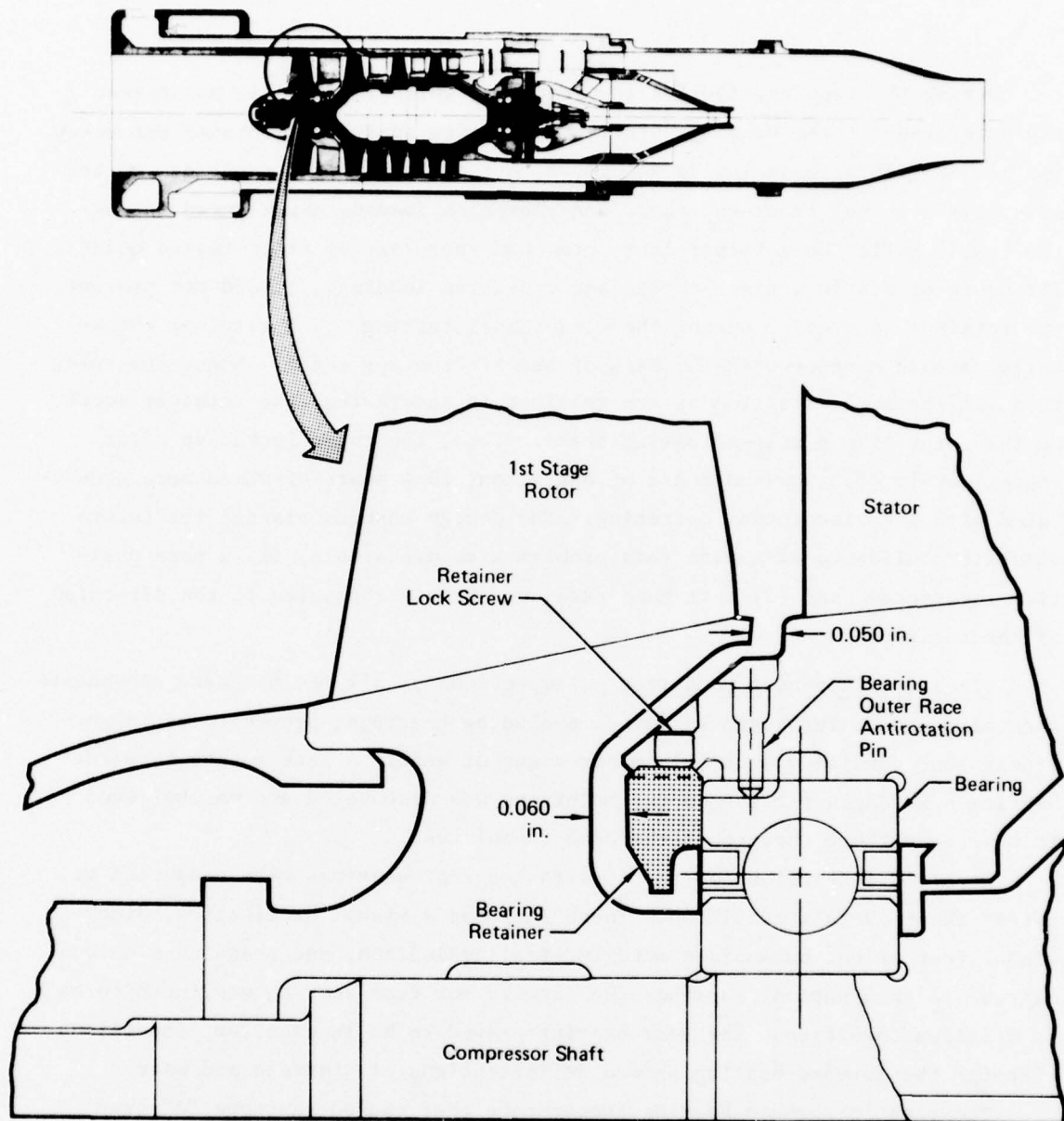
GP76 0701-112

FIGURE 6-10
ROTOR POSITION HISTORY DURING WIND TUNNEL TEST



GP76 0701-113

FIGURE 6-11
SIMULATOR VIBRATION HISTORY DURING WIND TUNNEL TEST



GP76-0701-150

FIGURE 6-12
SIMULATOR DETAILS SHOWING ROTOR LOCK-UP CAUSE

Rotor Lock-Up - The disassembly of the simulator revealed that the forward bearing retainer lock screw was the cause of the lock-up. Figure 6-12 is a blow-up of the section of the simulator where the problem originated. A portion of the first stage rotor and shaft assembly, the first stage stator, the forward bearing, bearing retainer and lock screw are shown.

During the testing, the bearing retainer, which is normally up against the outer race of the bearing, started to unscrew against a loosened set screw. The cause of this loosening is not known, but it is believed to be due to the simulator abnormal front-end shock and vibration loading experienced during the test. While the retainer lock screw had successfully proof-tested under 112 hours of static windage torque and vibration loadings, it did not prevent the retainer unscrewing during the wind tunnel testing. The retainer eventually came in contact with the back of the first stage rotor. Since the rotor turns in the same direction as the retainer is unscrewing, the retainer acted on the rotor like a self-actuating brake. Thus, the rotor locked up after approximately 90.5 powered hours of operation, 29.4 hours of which were accumulated with the wind tunnel operating. The design changes planned for future simulator builds to eliminate this problem area are simple, (1) a more positive lock screw, and (2) left hand retainer threads (opposite to the direction of the rotation).

Simulator Component Condition - Inspections of all the hardware components were also made. The basic hardware, excluding bearings, proved to be in generally good condition with only minor signs of wear. A leak in the forward bearing oil supply fitting on the mainframe was discovered and was believed to have been there throughout the wind tunnel test.

Detailed inspections of the forward and rear bearings were conducted to assess their overall condition. These included a visual examination, dimensional inspection, subsurface metallurgical evaluation, and scanning electron microscope examination. Neither the forward nor rear bearing was found to be in a failed condition. The rear bearing proved to be in excellent condition, although the forward bearing showed definite signs of distress and wear.

The rise in forward bearing temperature that caused shutdown "A" (see Figure 6-7) is believed to have been primarily due to increased bearing friction caused by roughening of the bearing surfaces. This roughness was probably caused either by unintentional extended operation in the rotor thrust cross-over (+ to -) regime or by a marginal lubrication oil supply. It is not felt that this and subsequent overtemperature problems were significantly affected by the unscrewing of the bearing retainer which eventually locked-up the rotor.

No deficiencies in the basic bearing design have been identified, but to minimize the chances of this type of problem from recurring in future tests,

some simulator design changes are planned. First, the oil supply fittings on the outer case will be improved to eliminate any leakage at this point. Second, a method of directly measuring the rotor thrust will be developed, rather than continuing to use a value calculated from internal pressure measurements. Accurate knowledge of the rotor thrust at all times can be used to eliminate operation in the undesirable thrust cross-over regime and minimize the bearing deterioration. Also, selected improvements in the bearing sump and seal area will be incorporated.

7. COMPACT SIMULATOR DESIGN STUDY

During the Simulator Application Study (Reference 6), it became apparent that the current propulsion simulator was too large for installation within the moldlines of advanced fighter aircraft models. Therefore, before the simulator can become an operational wind tunnel test tool, a more compact unit must be developed. The results of a conceptual design of a compact simulator, conducted as part of this program, are presented in the following sections.

7.1 Conceptual Design Effort

The current simulator design, Figure 7-1, utilizes a forward manifold to route the required high pressure drive and bleed air. This manifold adds approximately 28% in length and 25% in diameter to the basic simulator, excluding instrumentation fittings. Therefore, a key part of the compact simulator design effort was to eliminate the forward manifold. In addition, the mixer was redesigned to reduce the overall simulator length and provide improved mixing between the compressor and mixer flows. The other major constraint in the design was that the internal rotating hardware would not be changed from that of the current simulator to minimize development cost and time.

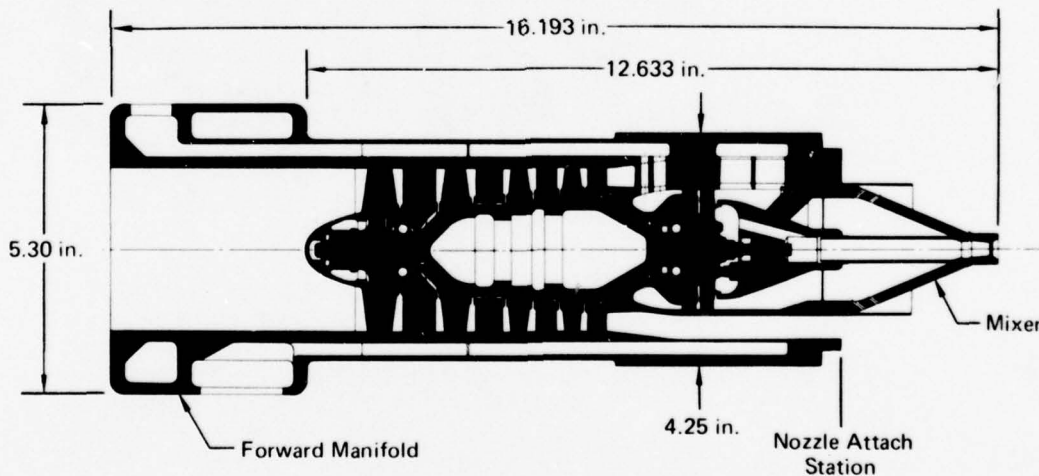


FIGURE 7-1
CURRENT SIMULATOR GEOMETRIC DETAILS

GP76 0701 37

Several candidate compact simulator designs were developed during this effort. The primary differences in these designs were in the drive/bleed air manifold and mixer areas. Trade studies led to the selection of one of these configurations for additional design development. This configuration, designated XM2R and shown in Figure 7-2, includes several innovative ideas: (1)

a fully modular mainframe, bleed frame, manifold and exhaust system, (2) precision mini-castings as the foundation of the manufacturing process, (3) high efficiency flow paths for directing the turbine drive air in and the bleed air out, (4) an axially short mixer and (5) compact instrumentation. This compact simulator design provides ~34% reduction in length and ~26% reduction in diameter as compared to the current simulator design with the forward manifold.

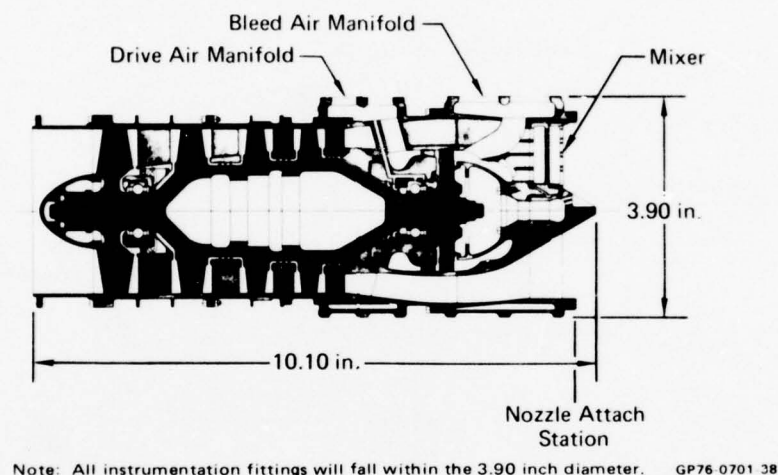


FIGURE 7-2
XM2R COMPACT SIMULATOR GEOMETRIC DETAILS

7.2 Design Envelope Verification

Two separate studies were conducted to ensure that the geometric envelope of the XM2R design would be compatible with advanced fighter aircraft models. The first study involved a comparison of the simulator envelope with the scaled envelope of several advanced turbofan engines for fighter application: The geometric envelope of the simulator, excluding nozzles, compares favorably with the scaled envelopes of five GE advanced engines, Figure 7-3. The engine scale factors were established as follows:

$$\text{Scale Factor} = \sqrt{\frac{\text{Max Simulator Compressor Corrected Airflow}}{\text{Max Engine Corrected Airflow}}}$$

These factors were used to linearly scale each dimension of the engine.

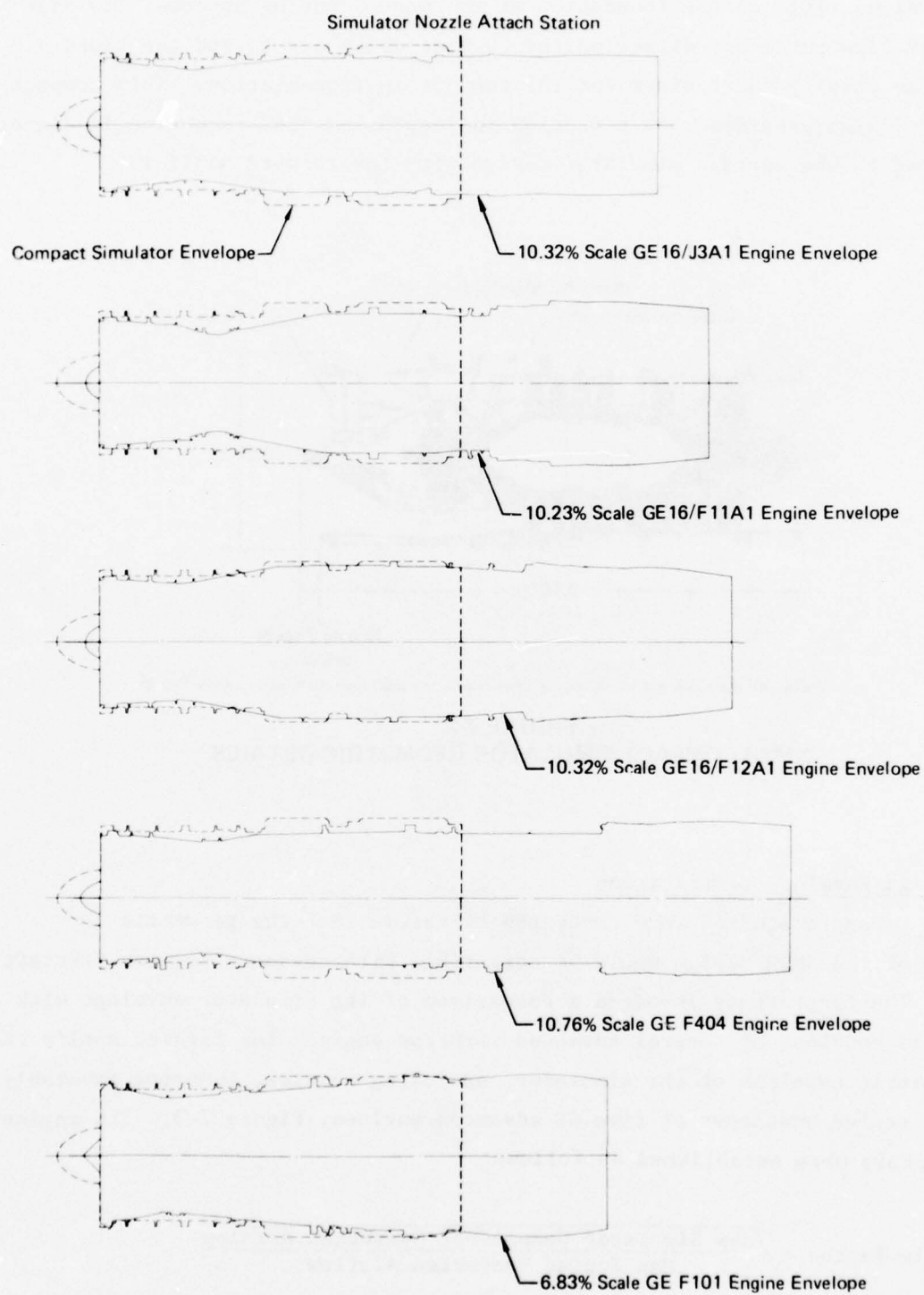
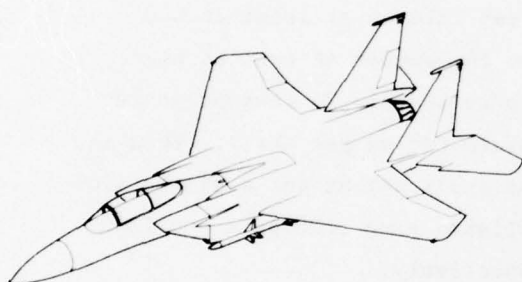


FIGURE 7-3
COMPARISON OF XM2R COMPACT SIMULATOR ENVELOPE
WITH SCALED ENGINE ENVELOPES

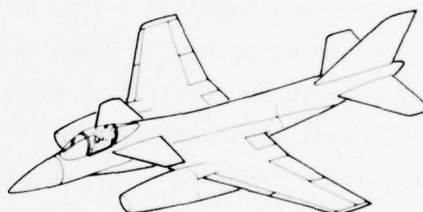
GP76 0701-11

The second study involved conceptual designs of wind tunnel models of several advanced fighter aircraft. This effort was necessary since it was realized that installing the simulator in a wind tunnel model is complicated by the requirement for routing high pressure air to and from the simulator.

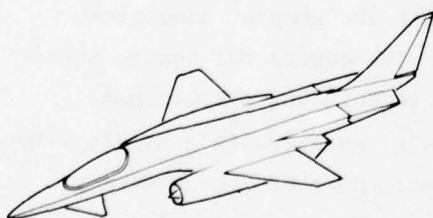
The four MCAIR aircraft configurations used in this study are shown in Figure 7-4. The F-15 was used since it represented conventional installations with twin engines buried in the fuselage. The other three MCAIR advanced aircraft had pod-mounted engines. As might be expected, these installations placed the most demanding constraints on the simulator envelope.



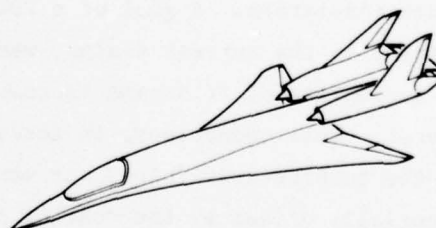
- F-15 Fighter
- Twin Engine Buried in Fuselage
- Model Scale - 8.5%



- MCAIR Advanced Aircraft
- Wing Podded Engines
- Model Scale - 10.5%



- MCAIR Advanced Fighter
- Wing Podded Engines
- Model Scale - 10.6%



- MCAIR Advanced Fighter
- Fuselage Podded Engines
- Model Scale - 10.1%

GP76-0701-39

FIGURE 7-4
AIRCRAFT CONFIGURATIONS USED IN MODEL DESIGN STUDIES

The purpose of the study was to determine whether; (1) the simulator would fit within the scaled aircraft moldlines, (2) the necessary drive/bleed air lines could be routed to/from the simulator, and (3) the simulator could be structurally supported. In all of the model designs investigated, it was found that these three criteria could be met.

7.3 Structural Life and Cost Reduction Analyses

A preliminary structural life analysis was conducted to obviate predictable deficiencies in the high pressure hardware of the compact simulator. This analysis, reported in detail in Reference (7), indicated that designing the high pressure hardware of the XM2R simulator to meet the hydrostatic test requirements resulted in a low cycle fatigue/creep life of at least 20,000 cycles for this hardware. This is equivalent to the number of typical high pressure operating cycles that would occur in approximately 25 test programs of 200 powered hours duration each (at 800 pressure cycles per test). This is probably well above the practical number of test applications for a single simulator. The hydrostatic test requirements established were 3000 psia and 1200 psia for the drive and bleed/mixer systems, respectively.

The compact simulator time between overhauls will be established primarily by the need to replace the bearings. The time between bearing replacement must be determined from test experience; however, the goal is for at least a 200 powered hour bearing life. This is consistent with the bearing life characteristics of subsonic powered simulators.

The compact simulator conceptual design effort emphasized cost reduction of future simulators. A goal of a 20% cost reduction for the compact simulator, relative to the current design, was established. As the conceptual design effort was accomplished, it became increasingly apparent that this was a tough goal to meet. Cost reductions, in terms of machining costs, were realized by simplifying the turbine drive/bleed air manifold and passages. However, these were essentially offset by the cost of other modifications made to the simulator to improve the installation characteristics, i.e., reduced length and diameter.

The potential fabrication cost reductions that may be realized are dependent on the techniques used. Using only machined parts in the fabrication, the estimated cost of a single compact simulator is actually 8% more than the current design. However, using cast parts and ignoring the initial investment required for casting tooling, the estimated unit cost is 7% lower than for the current design.

The initial investment for casting tooling would amount to about 25% to 40% of the cost of the first compact simulator fabricated. This investment would be paid for in the first 2 to 3 units fabricated, by the cost savings realized from using cast rather than machined parts. Once the tooling has been paid for, each subsequent compact simulator would be about 7% lower in cost than the current design. However, for multiple buys of compact simulators, the estimated unit cost is reduced as shown in Figure 7-5.

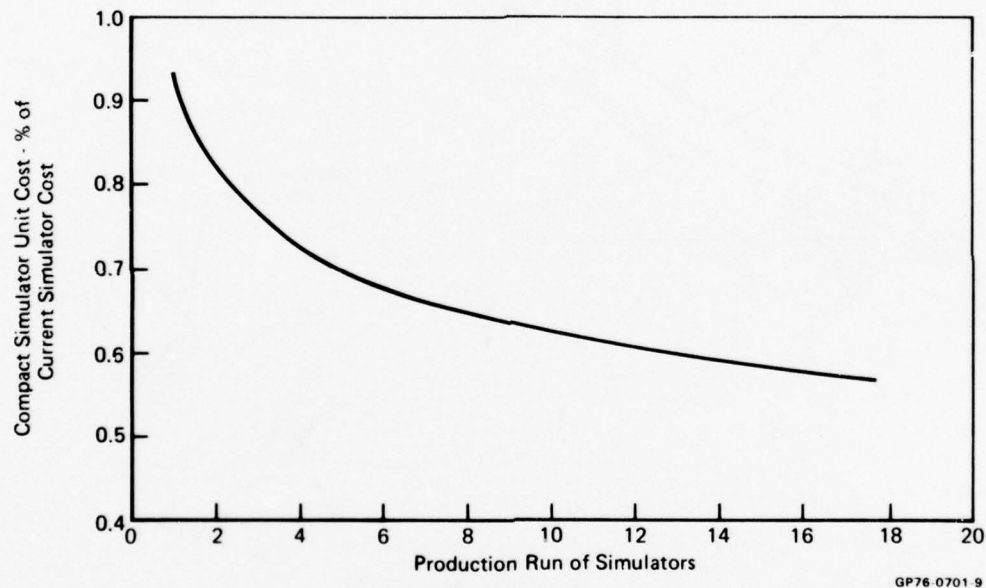
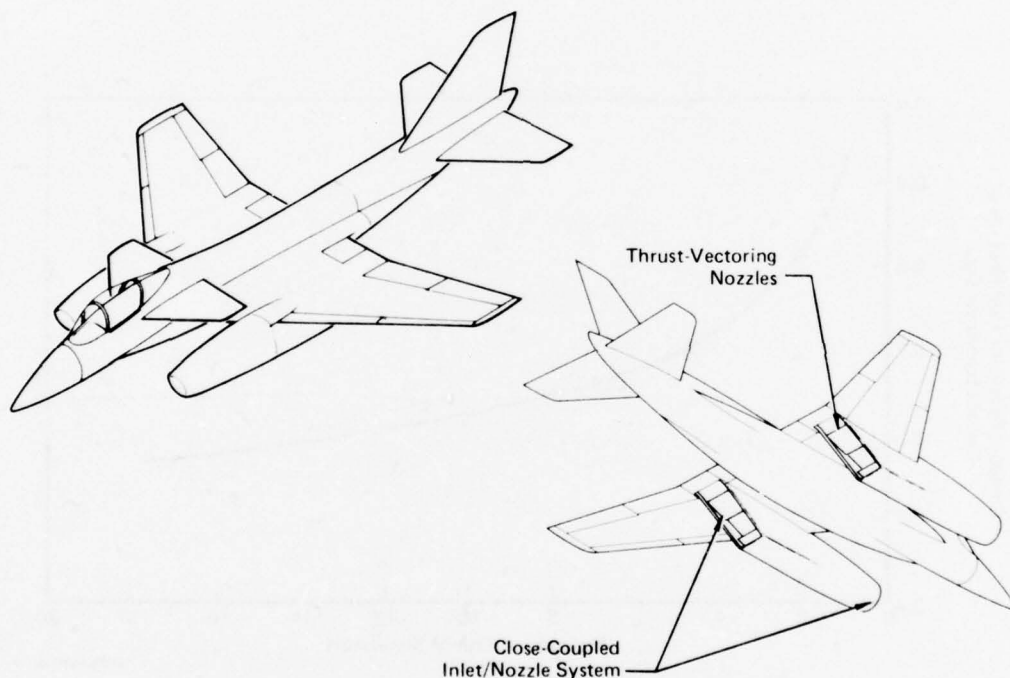


FIGURE 7-5
COST REDUCTION ASSOCIATED WITH MULTIPLE
SIMULATOR BUYS

8. ASSESSMENT OF POTENTIAL COST SAVINGS FOR SIMULATOR MODELS

The propulsion simulator offers the potential for cost savings in the determination of aircraft aerodynamic performance. This potential exists because a single simulator-equipped model (with GFE compact simulators) can provide the same aerodynamic performance data as conventional aero flow-through and jet effects models, with subsequent reductions in model costs and test time.


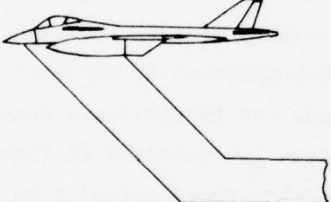
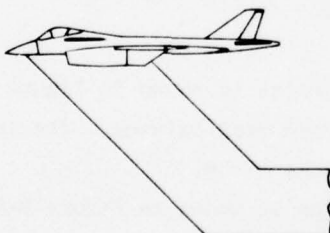


**FIGURE 8-1
ADVANCED FIGHTER AIRCRAFT
SELECTED FOR COST STUDY**

GP76 0701 40

To quantify these savings, the cost was estimated for obtaining the aerodynamic performance of the advanced fighter aircraft shown in Figure 8-1, using both simulator and conventional models. This aircraft configuration was selected because it is a representative next generation fighter which incorporates thrust vectoring nozzles, close coupled inlets/nozzles, and lifting surface augmentation. In addition, with wing podded engines, it places severe constraints on the geometric envelope of the simulator.

A two-model conventional technique was compared with the single simulator model technique. A summary of the models used in the cost evaluation and the data requirements are shown in Figure 8-2. The principal cost elements of any wind tunnel test program are (1) model design and fabrication, (2) pre-test check out and calibration activities, and (3) wind tunnel test activities. In the next sections, these elements and their impact on each specific model are discussed and estimated costs provided.

Conventional Models (10.5% Scale)	
 <p>Aero F&M Flow-Thru Model</p>	<p>Data Obtained</p> <ul style="list-style-type: none"> • Basic Drag Polars • Inlet Drag Variation
 <p>Jet Effects Model</p>	<ul style="list-style-type: none"> • Nozzle Drag Variation
Simulator Model (10.5% Scale)	
	<p>Data Obtained</p> <ul style="list-style-type: none"> • Basic Drag Polars • Inlet Drag Variation • Nozzle Drag Variation

GP76 0701 41

FIGURE 8-2
WIND TUNNEL MODELS USED FOR AERODYNAMIC PERFORMANCE
COST EVALUATIONS

8.1 Wind Tunnel Model Conceptual Designs

Conceptual designs of each of the wind tunnel models were developed in sufficient detail to allow realistic detailed design and fabrication costs to be estimated. All of the model designs were 10.5% scale. This scale factor was derived based on simulator model requirements as discussed in Section 7.2.

Simulator-Equipped Model

A schematic of the 10.5% simulator model design is shown in Figure 8-3. The design, which uses the compact simulator discussed in Section 7, is characterized by the following features.

- o Two Compact Simulators
- o Single Thrust-Minus-Drag Balance
- o Thermal Control of Balance
- o Underside Support Strut with Internal High Pressure Air Lines
- o Four Sets of Vertically-Arranged Bellows for the Simulator Drive and Bleed Air
- o Three Internally-Mounted Scanivalves

The use of a thrust-minus-drag balance was necessary since the simulator could not be isolated from the external pod geometry. This means that in the testing of such a model, the thrust characteristics of the installed nozzles must be known so that the aerodynamic drag can be determined. This can be accomplished by obtaining tunnel-off thrust data and subtracting it from the tunnel-on thrust-minus-drag data.

A summary of the model and simulator instrumentation is presented in Figure 8-4. The simulator instrumentation listed is an estimate of what would actually be required on a future simulator model test. It is based on the experience gained at AEDC during the test program conducted under this contract.

Conventional Models

A schematic of the aero flow-thru model design is shown in Figure 8-5. The design incorporates an aft sting support system and drag balance. The inlet mass flow ratio is varied by changing the nozzle exit choke areas.

A schematic of the jet effects model design is shown in Figure 8-6. The design incorporates an underside support strut through which the high pressure nozzle air is supplied. Consequently, the inlet is faired-over. A thrust-minus-drag balance arrangement is used to measure the forces and moments on this fully metric model. As a result, the nozzle thrust characteristics must be known so that the aerodynamic drag can be determined. Consequently, tunnel-off data must be obtained in the manner discussed for the simulator model.

8.2 Pre-Test Check-Out/Calibration Activities

A thorough pre-test check-out of the model/instrumentation systems and subsequent calibration of all subsystems (i.e., force balance, bellows, etc.) must be accomplished on any wind tunnel model to ensure accurate wind tunnel test data. Depending on the model and its complexity, these activities can be rather detailed and time-consuming. Each of the model designs in this study has been reviewed in detail and the required

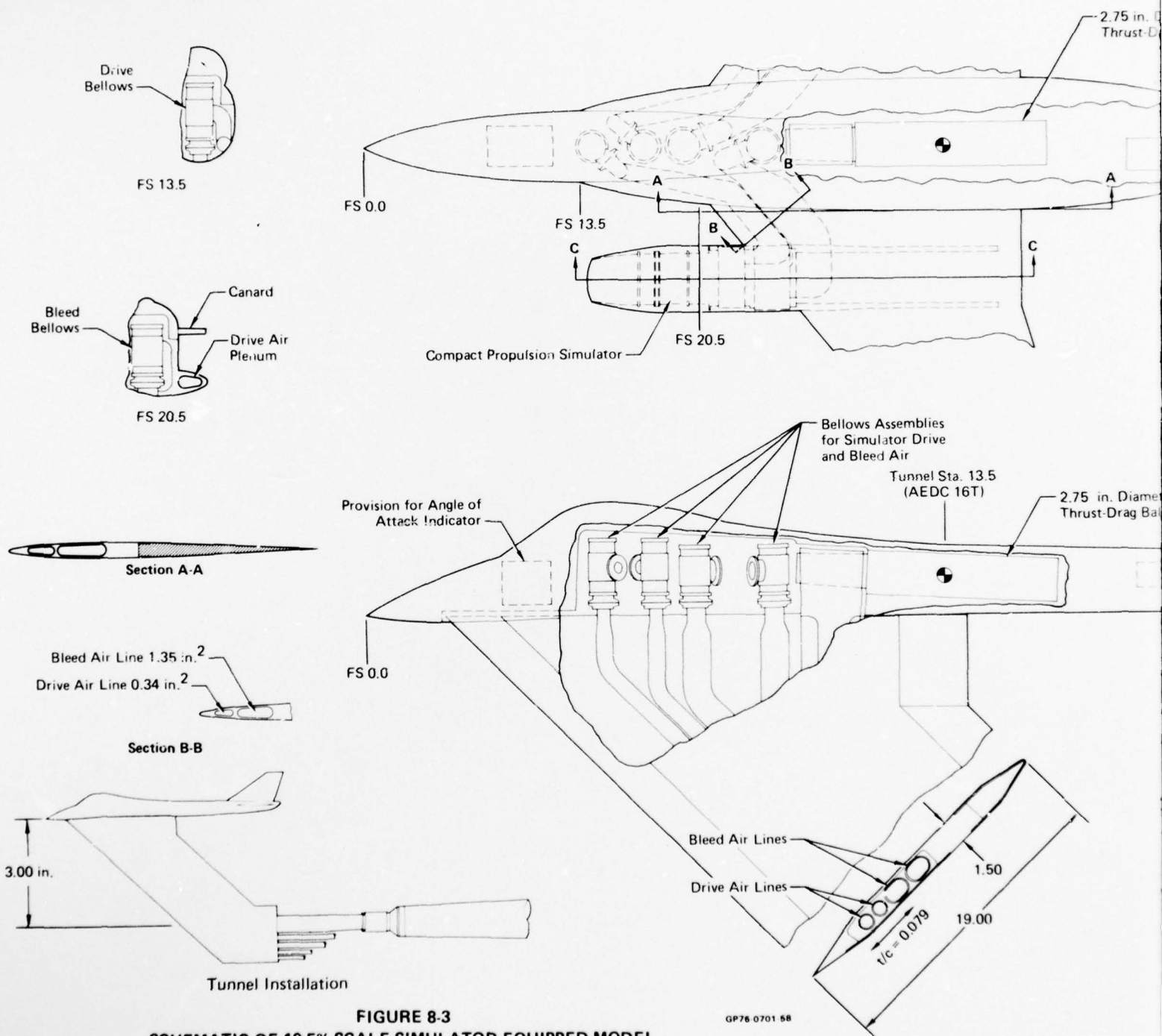
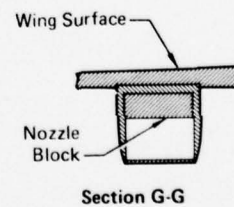
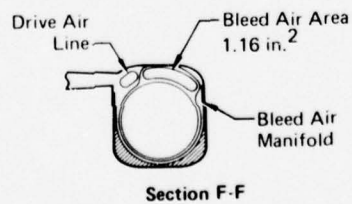
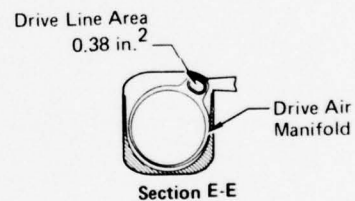
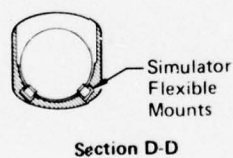
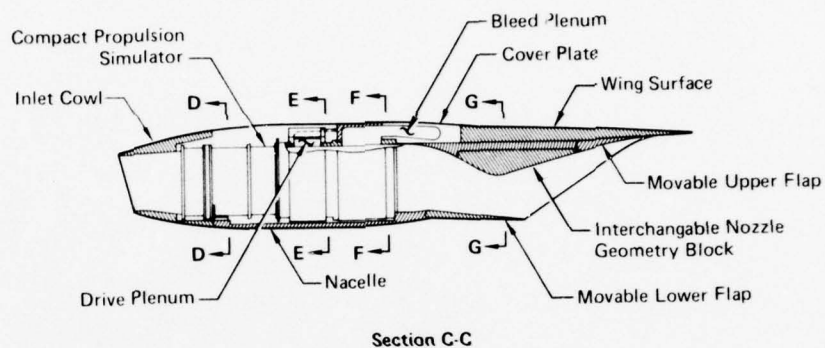
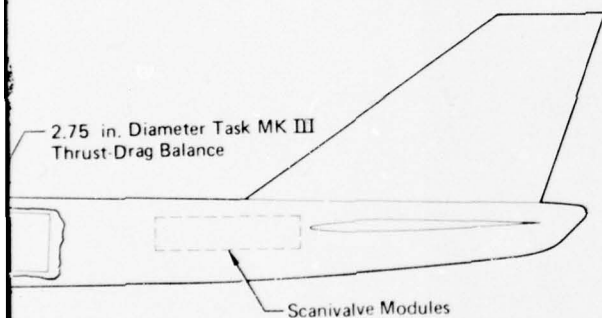
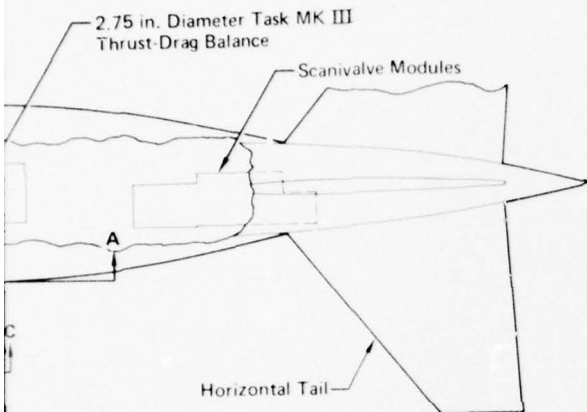


FIGURE 8-3
SCHEMATIC OF 10.5% SCALE SIMULATOR-EQUIPPED MODEL



2

	Type of Instrumentation	Symbol	No. of Measurements*	Location
Model	Static Pressures	P_C	5	Internal Model Cavity
		P_F	25	Fuselage/Nozzle Surfaces
	Thermocouples	T_{BAL}	2	Balance Case
	Dangleometer	α	1	Angle of Attack Measurement
Simulator	Static Pressures (Low Response)	P_{13}	6	Compressor Exit
		P_{57}	2	Mixer Plenum
		P_B	4	Internal Bellows
	Static Pressures (High Response)	P_{2K}	2	Compressor Inlet
		P_{13K}	2	Compressor Exit
	Total Pressures	P_{T2}	30	Compressor Inlet
		P_{T13}	18	Compressor Exit
		P_{T7}	10	Nozzle Throat
		P_{T4}	2	Turbine Inlet
	Total Temperatures	T_{T13}	6	Compressor Exit
		T_{T4}	2	Turbine Inlet
		T_{T7}	6	Nozzle Throat
		T_B	4	Forward/Rear Bearings
		T_{T57}	2	Mixer Plenum
	Speed Pick-Up	—	2	Rotor Speed
	Accelerometers	—	4	Simulator Case
	Position Indicator	—	2	Rotor Axial Position
	Internal Strain Gage	—	2	Rotor Thrust

* For two simulators.

GP76 0701 42

FIGURE 8-4
ESTIMATE OF ADVANCED FIGHTER MODEL AND SIMULATOR
INSTRUMENTATION REQUIREMENTS

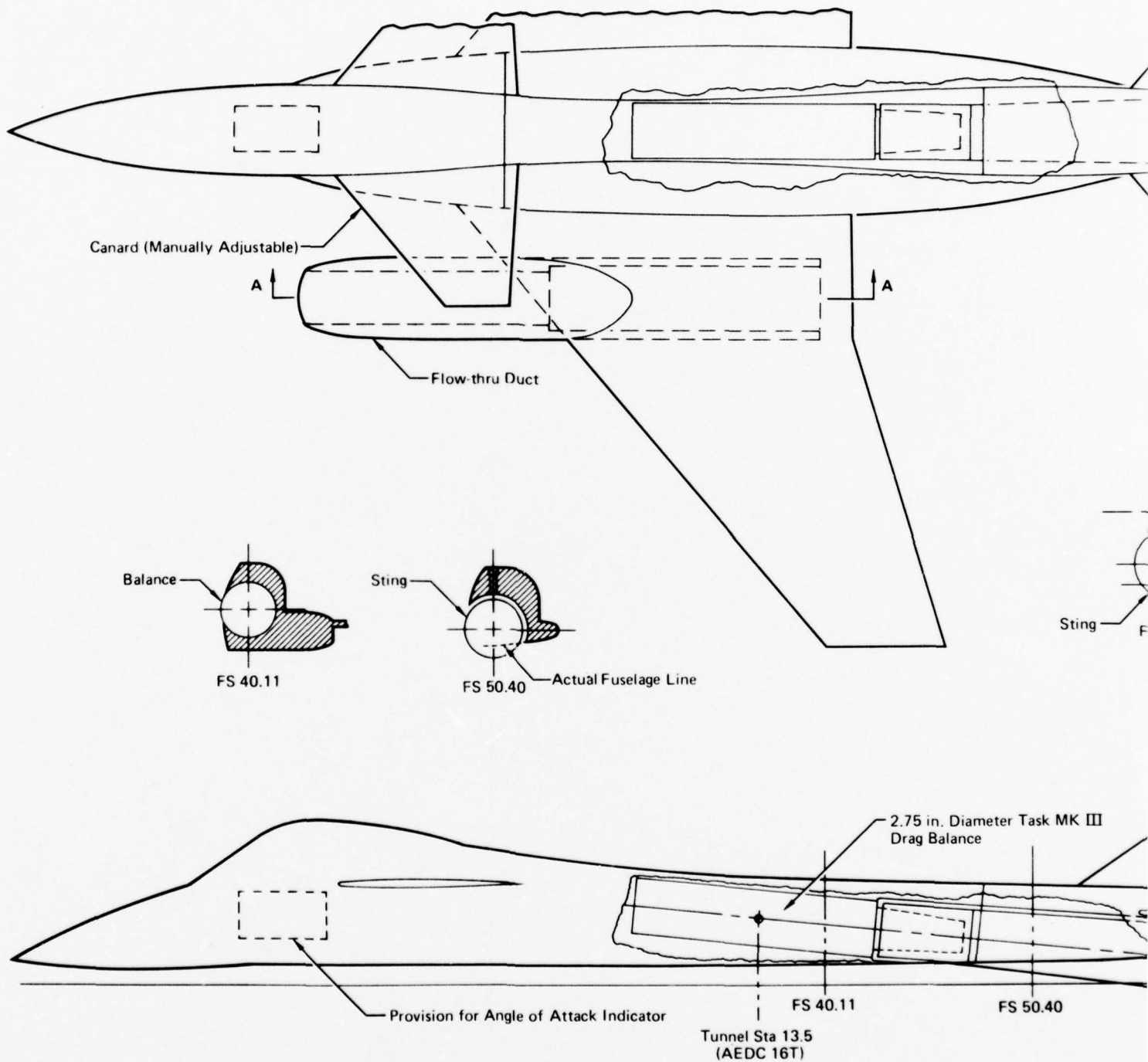
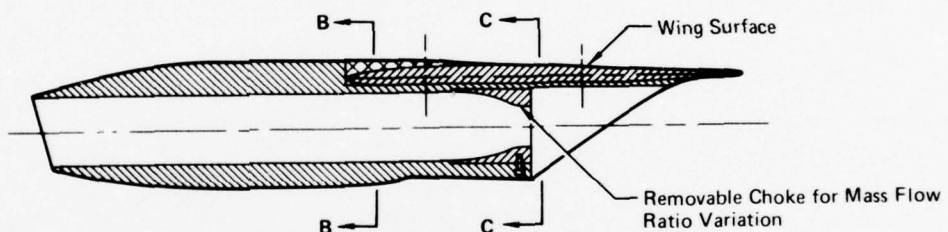
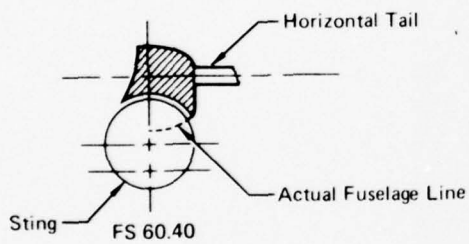
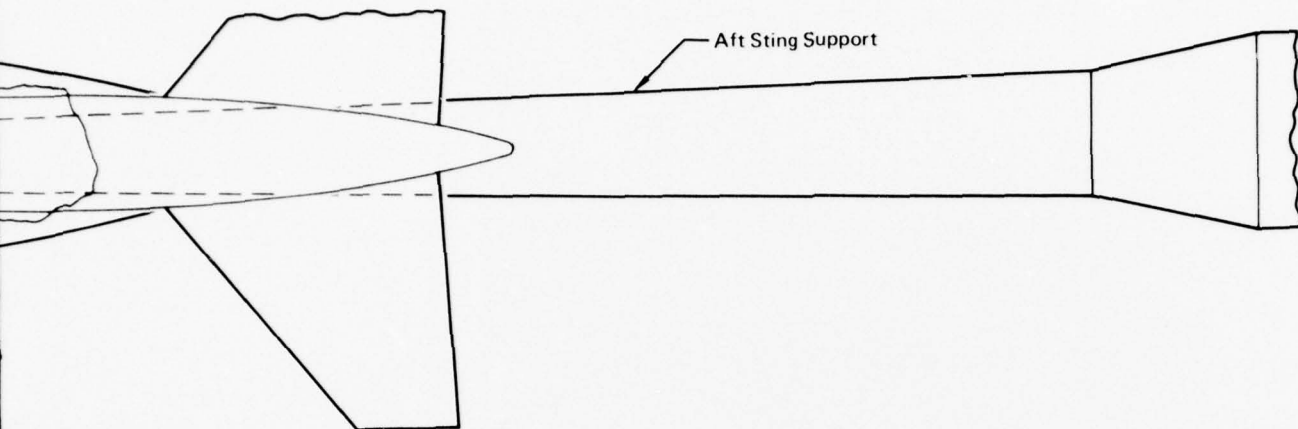
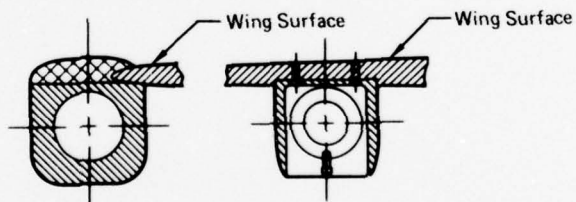


FIGURE 8-5
SCHEMATIC OF 10.5% SCALE AERO FLOW-THRU MODEL

GP76 0701 57

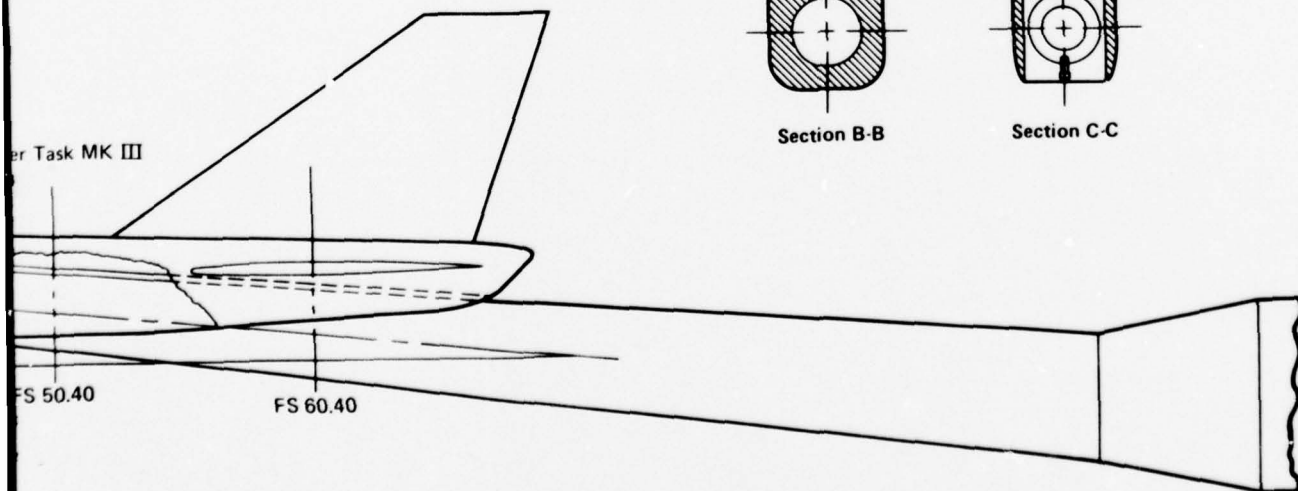


Section A-A



Section B-B

Section C-C



2

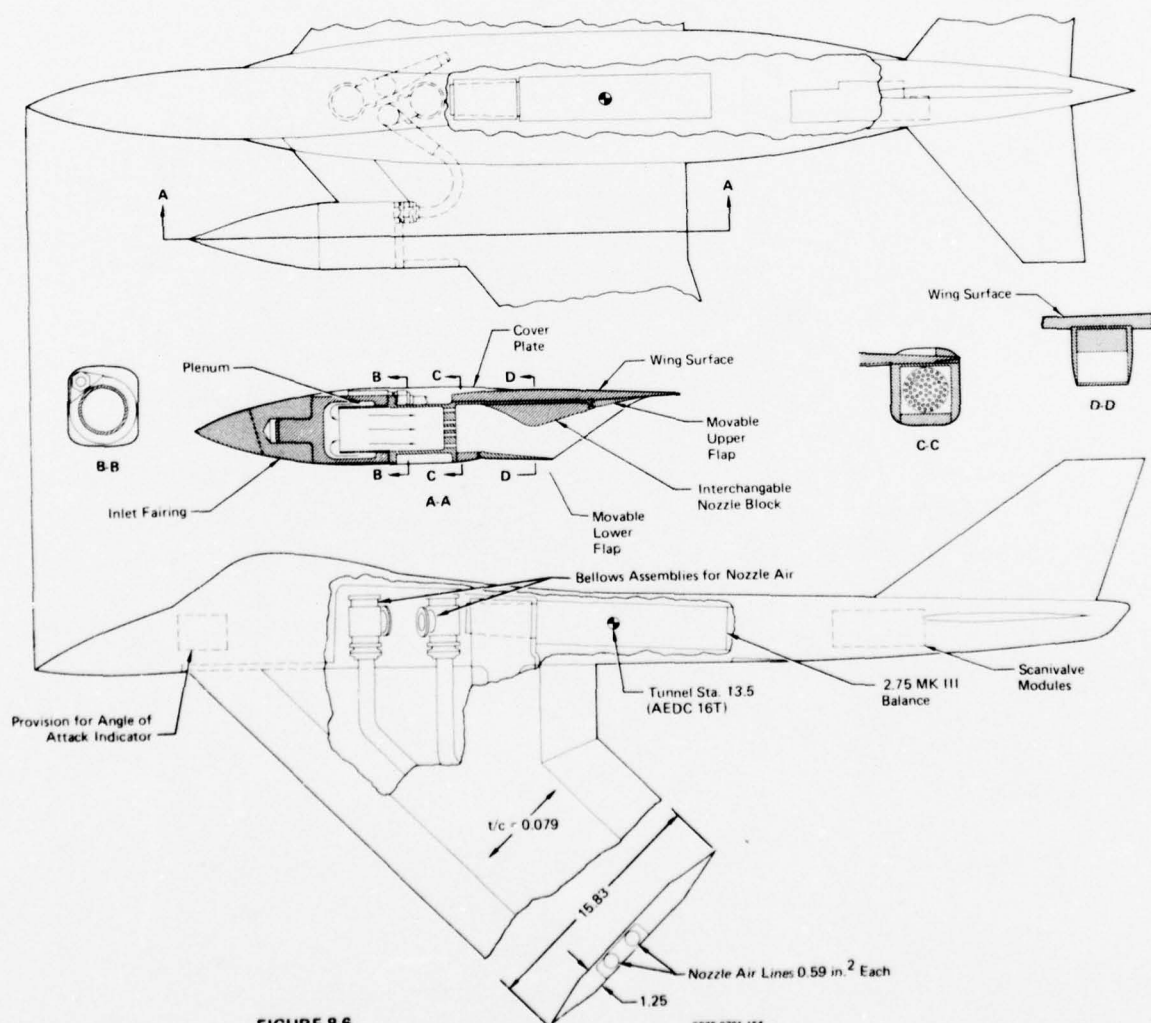


FIGURE 8-6
SCHEMATIC OF 10.5% SCALE JET EFFECTS MODEL

GP78 0701 154

check-out/calibration activities have been identified. These activities are summarized in Figures 8-7 and 8-8 for the simulator and conventional models respectively. Also shown are the direct activities associated with the wind tunnel tests. It was assumed in defining these activities that the wind tunnel testing would be accomplished in the AEDC 16-foot tunnels. The calibration activities for the simulator model would be conducted in the 16S tunnel. As a result, the supersonic portion of the wind tunnel testing would be accomplished prior to the transonic portion.

Activity Location	Activity
Airframe Company	Model build-up/check-out with simulators and instrumentation installed Installed balance check calibration and bellows tare force checkout
AEDC 16S Tunnel	Model installation in 16S cart/tunnel Installed balance calibration Bellows pressurization and tare force calibration Final model preparation for testing Model testing in 16S tunnel Model removal from 16S and build-up in 16T cart
AEDC 16T Tunnel	Model installation in 16T tunnel Balance and bellows tare force check calibrations Model testing in 16T tunnel Model removal from 16T and shipment

GP76 0701 55

**FIGURE 8-7
MAJOR PRE-TEST/TEST RELATED ACTIVITIES FOR THE SIMULATOR-EQUIPPED MODEL**

Test Model	External Nozzle Config.	Internal Nozzle Config.	R _g /L x 10 ⁶	Mach No./ α Schedule	δ H Schedule	δ C Schedule	Inlet MFR	Nozzle Pressure Ratio	Simulator Airflow	Simulator Pressure Ratio	Data Application	Remarks	Estimated Data Pts.			
Simulator	Low Mach A/B	Low Mach A/B	2.5	A	A	0 ⁰	N/A	N/A	Ref (1 Value)	Ref (1 Value)	Reference Aircraft Forces & Moments		483			
	Dry Power	Dry Power		B	0 ⁰	0 ⁰							3 Sets of Conditions	Aircraft Forces & Moments at Actual Engine Operating Conditions.	111	
				A	0 ⁰	A									414	
				A	B	B									276	
				D	C	0 ⁰									168	
	Low Mach A/B	Low Mach A/B		E	0 ⁰	0 ⁰							2 Sets of Conditions		30	
				D	0 ⁰	B										84
				F	C	0 ⁰										80
				E	0 ⁰	0 ⁰										20
	High Mach A/B	High Mach A/B		F	0 ⁰	B							3 Sets of Conditions		40	
				H	C	0 ⁰										108
	Low Mach A/B	Low Mach A/B		Low Mach A/B	G	0 ⁰							0 ⁰	Ref (1 Value)	Reynolds No. Investigation	12
					C	0 ⁰							0 ⁰			
	Low Mach A/B	Low Mach A/B	Higher Lower	C	0 ⁰	0 ⁰							36			

Subtotal: 1898
 Static Nozzle Perf: 40
 5% Repeats: 96
 Total: 2034

Mach No./Angle of Attack (α) Schedules		Horizontal Tail Setting (δ_H) Schedules		Canard Setting (δ_C) Schedules	
Mach	α°				
A. 0.6, 0.9 1.2	-20° → +24° ($\Delta\alpha = 10^\circ$) -20° → +12° ($\Delta\alpha = 10^\circ$)	A. -25°, -15°, -10°, -5° 0°, +5°, +15°		A. -20°, -10°, -5°, +5° +10°, +20°	
B. 0.7, 0.8, 0.95 1.1, 1.4	-20° → +24° ($\Delta\alpha = 10^\circ$) -20° → +12° ($\Delta\alpha = 10^\circ$)	B. -25°, -10°		B. -10°, +10°	
C. 0.6, 0.9 1.2	-20° → +24° ($\Delta\alpha = 20^\circ$)	C. -10°, -5°, 0°, +5°			
D. 0.6, 0.9 1.2	0, 5, 10, 15, 20 0, 4, 8, 12				
E. 0.8, 0.95	0, 5, 10, 15, 20				
F. 0.6, 0.9	0, 5, 10, 15, 20				
G. 1.6	0, 4, 8, 12				
H. 0.9 1.2	0, 5, 10, 15, 20 0, 4, 8, 12				

FIGURE 8-9
 WIND TUNNEL TEST PLAN FOR SIMULATOR-EQUIPPED
 AIRCRAFT MODELS
 Estimated AEDC Wind Tunnel Occupancy Hours: 160

8.4 Cost Estimates

The costs associated with the detailed design/fabrication, pre-test check-out/calibration, and wind tunnel tests of each of the models have been estimated. A summary of these costs and applicable assumptions is presented in Figure 8-11. The costs for both conventional models have been combined and compared directly against the simulator model. Also, all costs are ratioed to the total costs for the conventional models. The cost estimates indicate that for this particular fighter aircraft, use of a simulator model would provide approximately a 4% savings, exclusive of test facility costs. It is evident that the potential savings resulting from a reduction in number of models from two to one is partially offset by the increased complexity of the simulator model. A 13% savings in wind tunnel occupancy hours at AEDC would also be realized by using a simulator model.

Activity	Cost Ratio (Exclusive of Facility)		
	Conventional Models	Simulator Model	Δ
Model Design and Fabrication	0.47	0.46	0.01
Pre-Test Checkout and Calibration	0.33	0.31	0.02
Wind Tunnel Test	0.20	0.19	0.01
Total:	1.00	0.96	0.04
AEDC Wind Tunnel Occupancy Hour Ratio:	1.00	0.87	0.13

Assumptions:

1. Calibrated simulators and user's control console are GFE.
2. Comparison is for aircraft proposal or system development phases.
3. Models at 10.5% scale based on propulsion simulator size and inlet simulation.
4. Support system interference obtained using small scale concept development phase aerodynamic model.

GP76 0701 45

**FIGURE 8-11
COMPARISON OF SIMULATOR AND CONVENTIONAL TEST TECHNIQUE
COSTS FOR AERODYNAMIC PERFORMANCE DEFINITION**

These savings for the simulator model are based on groundrules which should be reassessed for subsequent usage. The presented test program is designed to provide aerodynamic parameters in sufficient detail to allow detailed analysis of the aerodynamic performance of a selected aircraft configuration. Testing at high angles of attack and at sideslip angles consistent with a more complete analysis of the stability and control characteristics was not included. Also, the configuration component optimization parametrics are assumed to be completed. The

support system interference effects are also assumed to be available from other wind tunnel tests.

The generally large scale simulator models would usually dictate the use of specific wind tunnels for simulator model testing. For testing of smaller conventional models, it may be possible to use a tunnel with lower costs and improved test time availability. It should be noted that the presented cost comparison assumes the use of the same tunnel for all models. It is also assumed that the test facilities and simulators are GFE.

9. CONCLUSIONS AND RECOMMENDATIONS

The turbine engine multi-mission propulsion simulator, developed to permit improved aircraft performance prediction capability through the simultaneous simulation of inlet/airframe/nozzle flowfields on wind tunnel models, has been successfully demonstrated in a partial aircraft wind tunnel model. Data were obtained during the test to:

- o Determine if the simulator is a viable test tool.
- o Evaluate the relative accuracy of the simulator test technique when compared to a conventional test technique.

In addition, separate studies were conducted to identify relative costs between test techniques for the performance prediction of advanced aircraft, and to develop a compact simulator design for improved model installation capability. The following significant conclusions and recommendations were drawn from the results of this program.

Simulator Operational Viability

- o The simulator is a workable test tool that can be effectively operated in a wind tunnel model behind a realistic fighter aircraft inlet.
- o The simulator has been successfully tested in a model up to Mach 1.2 and $\alpha = 10^\circ$. No problems are anticipated at higher Mach numbers.
- o Minor improvements are required to the simulator and control console to improve operational characteristics.
- o Improved simulator balance bridging techniques for the high pressure drive and bleed air are required.
- o Improved simulator drive and bleed airflow venturi calibrations are also required.
- o Standard nozzles should be used in wind tunnel test programs to calibrate the tare forces associated with the simulator balance bridging devices, and verify simulator airflow measurement capabilities.

Aerodynamic Performance Comparison

- o A comparison of the aerodynamic performance of this far-coupled inlet/nozzle configuration, as obtained from both the simulator and conventional test techniques, shows generally small differences ($\Delta C_D \sim \pm .0004$ at Mach 0.9, $\alpha \leq 10^\circ$).
- o Small but measurable throttle-dependent drag discrepancies ($\Delta C_D \sim .0005$) were found between the test techniques, and attributed to the lack of inlet flow simulation on the jet effects model.

- o Flowfield disturbances due to inlet mass flow ratio and nozzle pressure ratio variations exhibit similar characteristics between the simulator and conventional models for this configuration.
- o The random data errors associated with the simulator model and conventional models are comparable ($2\sigma_{C_D} \sim \pm .0003$). The added sophistication of simulator models did not compromise the test data.

Performance Cost Savings

- o A potential cost savings associated with using a simulator-equipped model to determine the aerodynamic performance of one advanced fighter aircraft configuration has been identified.
- o For the aircraft studied, the design, fabrication, calibration and testing of a simulator model is estimated to offer a 4% cost savings (exclusive of facility costs) over that of a conventional aero flow-thru model and jet effects model combined.
- o A simulator model test is also estimated to offer a 13% savings in AEDC 16-foot wind tunnel occupancy hours over that of the combined conventional models tests.
- o The savings identified were based on groundrules which should be reassessed for each potential application. These groundrules include:
 - Calibrated simulators and user's control console are GFE.
 - Model support system interference data are already available.
 - All models evaluated at same scale in same tunnel.

Compact Simulator

- o A compact simulator design that compares favorably with the scaled envelope of five current and advanced turbojet/turbofan engines has been developed. Limited design studies have also shown that this compact design can be installed in four representative advanced fighter aircraft wind tunnel models.
- o The compact simulator design provides approximately a 34% reduction in length and a 26% reduction in diameter over the current simulator design.
- o The compact simulator design potentially offers a 7% per unit cost savings over the current design.

The general conclusions and recommendations from this program concerning future simulator model usage are:

- o The compact simulator should be developed to provide a confident aircraft configuration development technique which will pinpoint problems and identify directions for improvement.
- o Aircraft with relatively far-coupled inlet/nozzle systems (i.e., F-15) will probably not require simultaneous simulation of the inlet/airframe/nozzle flowfields because of the expected small magnitude of the flowfield interactions. Therefore, conventional models should be adequate.
- o Aircraft with close-coupled inlets/nozzles/aerodynamic surfaces are expected to require simulator-equipped models for performance and stability and control evaluation, due to the likelihood of significant flowfield interactions. In addition, aircraft which feature in-flight thrust vectoring/reversing, high attitude flight capability, or V/STOL capability, may also require simulator usage for the same reason.

APPENDIX A

PROPOSED FUTURE SIMULATOR UTILIZATION

The use of the simulator for wind tunnel testing was initiated because it offered potential for improving aerodynamic prediction capabilities for advanced aircraft. However, for the simulator to be an effective wind tunnel test tool, it is necessary to know when and how to use it in an aircraft development cycle.

A.1 Simulator Testing Placement in an Aircraft Development Cycle

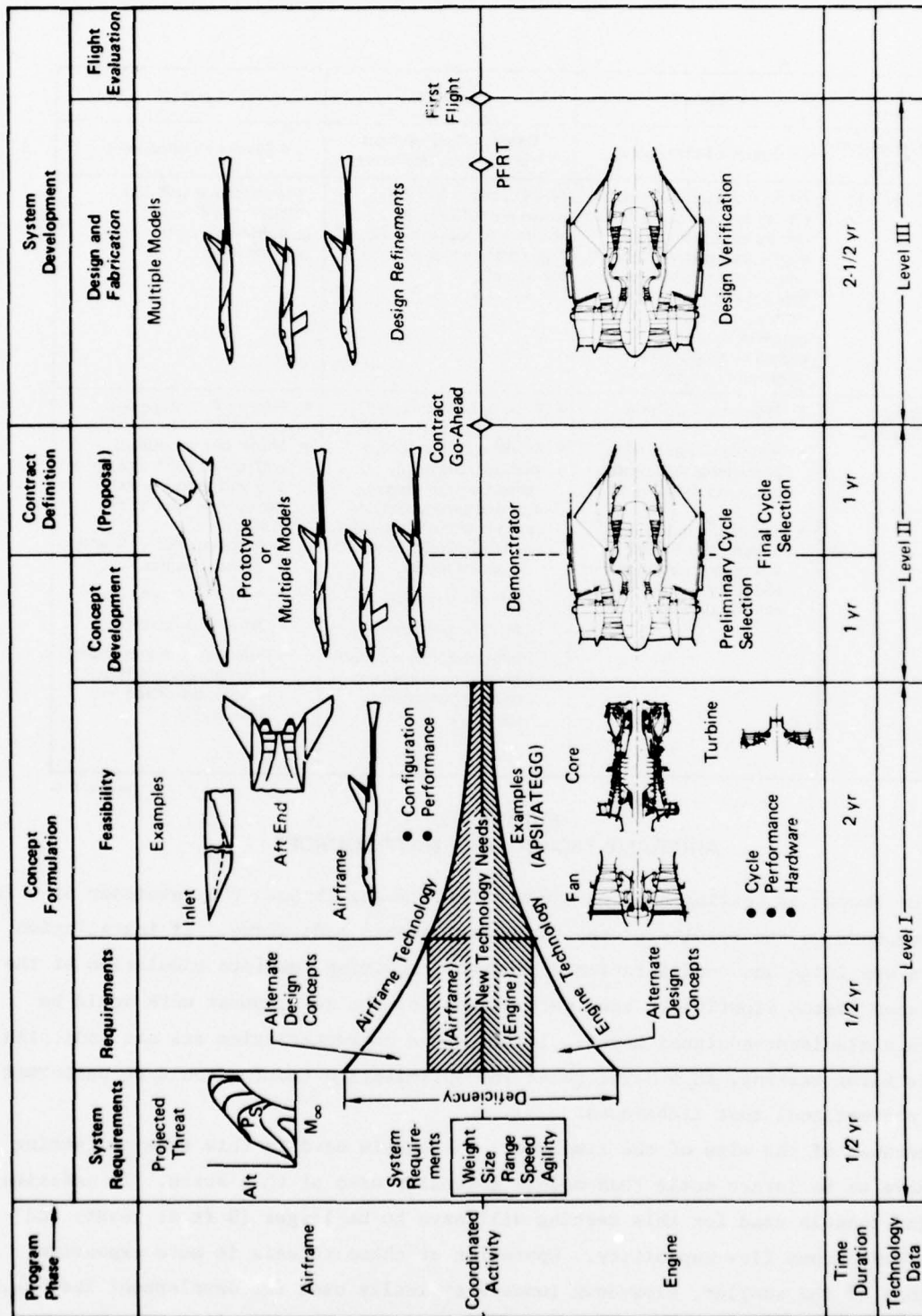
A systematic plan for development and optimization of an airframe/engine system was formulated under the AFAPL/MCAIR Exhaust System Interaction Program (Reference 4). This plan, summarized in Figure A-1, is based on parallel and integrated development of the airframe and engine. The simulator has the potential of being used during all three levels in the experimental development of the airframe configuration.

The sources of technical data used throughout the airframe development program are shown in Figure A-2. In the Concept Formulation phase, data is obtained from analytical estimates, from empirical correlations with previous test data, or from airframe and engine parametric test data. Usage of the simulator at this time could benefit basic aircraft technology applications and improve engine/airframe capability. The significance of the simulator application at this time will be dependent on the expected inlet/airframe/nozzle flowfield interactions.

During the Concept Development, Contract Definition, and System Development phases, the engine cycle is defined, airframe characteristics are selected and details of the inlet/engine/nozzle integration with the fuselage are finalized. It is during these phases that the simulator will be used most often as a testing tool with significant benefit. These are discussed below.

Concept Development Phase - Simulator testing in this phase would be conducted shortly after the basic aircraft configuration has been defined and the preliminary engine cycle selected. Use of simulator testing at this time would allow three important assessments to be made.

- o A realistic evaluation of the propulsion system installation effects on the aerodynamic performance.
- o A determination of how important airframe/engine integration is in the optimization procedure for that particular system.
- o An evaluation of the inlet/airframe/nozzle flowfield interactions to determine if these effects have to be simulated in future optimization testing.



GP76-0701-14

FIGURE A-1
AIRFRAME/ENGINE DEVELOPMENT PROGRAM

Technology Level	Level I	Level II	Level III
Development Stage	Concept Formulation	Concept Development and Contract Definition	System Development
Definition	General theoretical and empirical data which are sufficiently applicable to the engine and airframe design under consideration, to ensure a viable aircraft concept, even if maximum potential data errors caused by technology uncertainty are included.	Analytical and test data which are sufficiently accurate to guarantee the final performance of the aircraft.	Analytical and test data sufficient to ensure guaranteed aircraft performance.
Data Sources	<ul style="list-style-type: none"> • Theoretical analyses • Historical results from operational A/C prototypes and model tests • Parametric model tests directed at needed technology developments and preliminary aircraft concept definition. 	<ul style="list-style-type: none"> • Prior to Prototype A/C • Model tests conducted with approximately correct airframe geometry and aerodynamic flow simulation, typically: <ul style="list-style-type: none"> – Aerodynamic force and moment model – Inlet drag model – Jet effects model – Inlet performance model (Including pressure recovery, distortion and stability) 	<ul style="list-style-type: none"> • Prior to Prototype A/C • Model test conducted with correct airframe geometry and proper aerodynamic flow simulation, typically: <ul style="list-style-type: none"> – Aerodynamic force and moment model – Inlet drag model – Jet effects model – Inlet performance model (Including pressure recovery, distortion and stability)

GP76-0701-15

FIGURE A-2
AIRFRAME TECHNOLOGY DATA SOURCES

The amount of testing done on the simulator model through the remainder of this phase depends on the results of the three assessments made above. If installation effects are large and configuration dependent, requiring complete simulation of the propulsion system flowfield, then perhaps most of the development work would be done on a simulator-equipped model. If the above characteristics are not indicated by this first testing, then development and optimization testing could be performed using conventional test techniques.

Because of the size of the simulator, the models used in this type of testing will have to be larger scale than models generally used at this state. In addition, the wind tunnels used for this testing will have to be larger (8 ft at least) and have a continuous flow capability. Operation of these tunnels is more expensive than that of the smaller, blow-down tunnels typically used for development testing. Also, the availability of the larger tunnels for testing is not as favorable.

Therefore, the decision to initially test a simulator model in this phase must weigh heavily on the aircraft configuration itself. That is, if propulsion system installation effects are expected to have a significant impact on the aerodynamic performance, then such testing should certainly be conducted at this time.

Contract Definition Phase - In this phase the airframe configuration could change significantly from that tested in the previous phase as a result of configuration trade-off and optimization studies. At this time, the airframe manufacturer must establish performance guarantees for the aircraft. Simulator testing in this phase would be used as the basis for these guarantees for the particular airframe/engine system.

Final System Development Phase - After contract go-ahead, the detailed airframe design is accomplished. This involves additional testing to refine specific areas of the design. Because only localized areas are normally changed, small scale conventional models would be used for most of this testing. Although many small changes may be made in this time period, drastic configuration changes are not usually encountered. As a final evaluation of these changes on the aircraft performance and substantiation of the overall performance capability, the airframe manufacturer and the procuring agency normally require a final wind tunnel test before the go-ahead to start fabrication is given. The simulator can be effectively used at this point.

Each of the placements for simulator testing identified above achieves a separate objective in the overall airframe/engine development cycle. The first use in the Concept Formulation/Development phase is effective in achieving overall system optimization by early assessment of the potential propulsion system installation effects. Information is also obtained to determine if the simulator technique should be used throughout the development testing to enable simulation of the propulsion system flowfield.

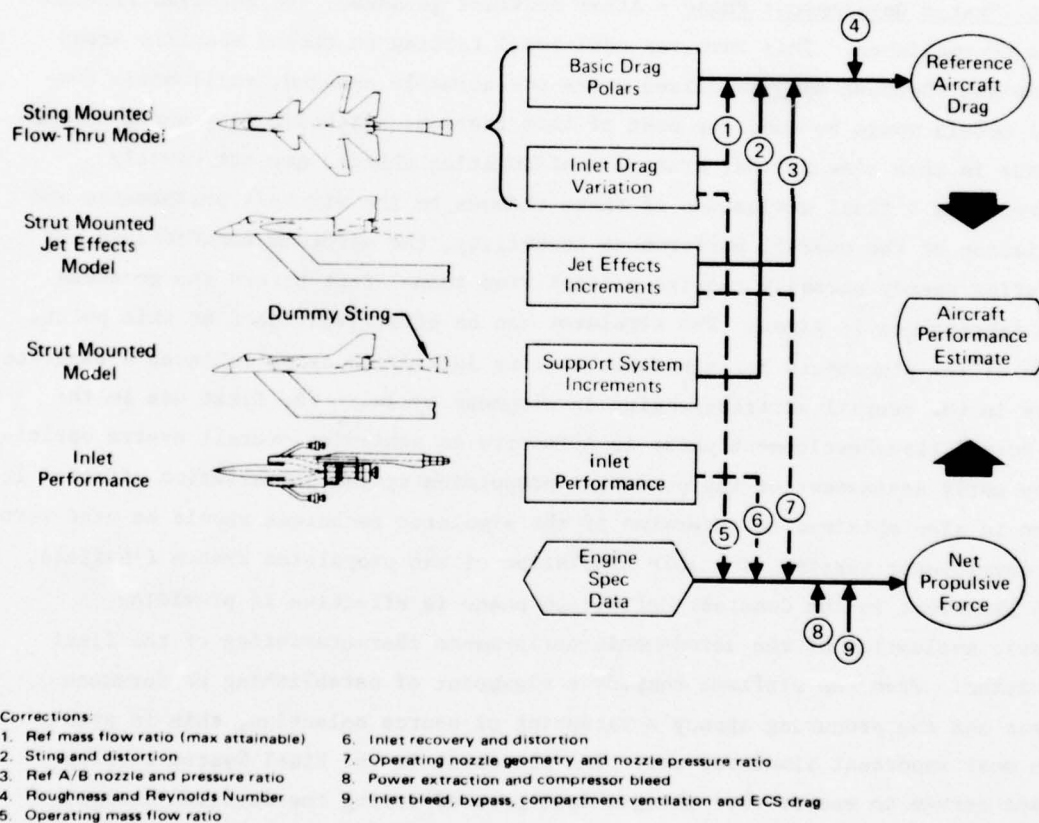
The placement in the Contract Definition phase is effective in providing a realistic evaluation of the aerodynamic performance characteristics of the final configuration. From the airframe company's viewpoint of establishing performance guarantees and the procuring agency's viewpoint of source selection, this is probably the most important simulator use. The placement in the Final System Development phase serves to ensure that changes incorporated during the detailed design, either to the airframe or the engine cycle, have not degraded the expected performance.

A.2 Aircraft Thrust/Drag Accounting Using Simulator Models

The purpose of a thrust/drag accounting system is to define a systematic procedure for combining all the forces acting on an aircraft (airframe, propulsion

system, engine, etc.) to obtain the total vehicle performance. As such, it requires the definition of what portion of the total system forces are to be obtained on a particular test model.

Most conventional thrust/drag accounting systems use thrust and drag as separate elements throughout the system. An example of an experimental data-based system is presented in Figure A-3. With this system, the aerodynamic drag is obtained from airframe wind tunnel tests and the engine thrust and fuel flow characteristics from the engine manufacturer's test data. The effects of airframe/engine integration are then added to these two elements to arrive at an estimate of the total vehicle performance.

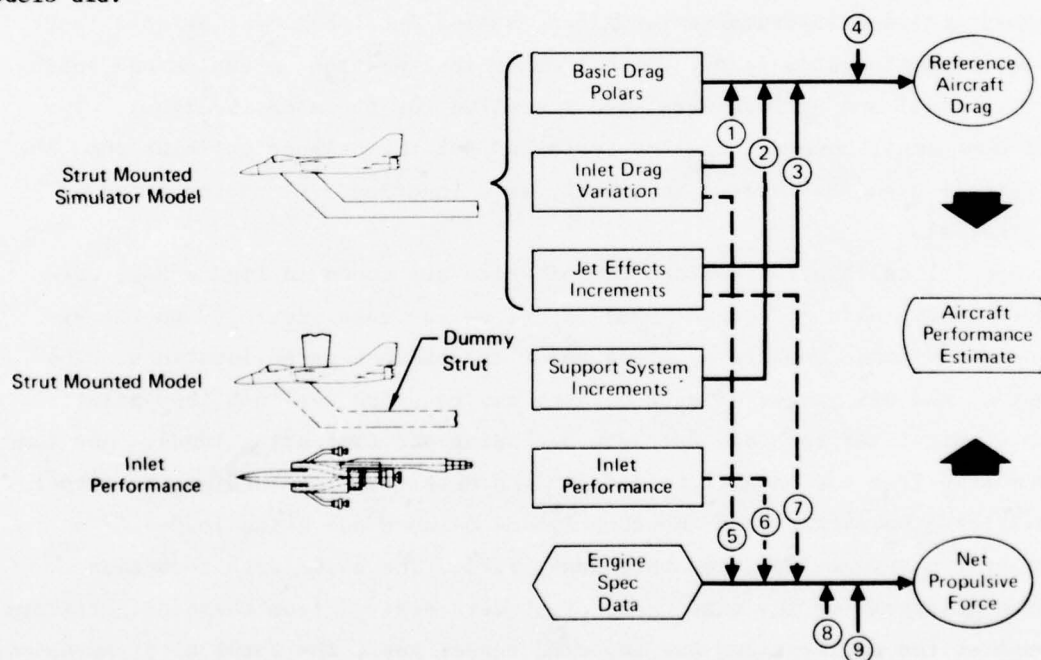


GP76-0701-2

FIGURE A-3
TYPICAL AIRCRAFT THRUST/DRAG ACCOUNTING SYSTEM UTILIZING
CONVENTIONAL MODELS

The conventional wind tunnel models from which the necessary aerodynamic data is normally obtained are also shown in Figure A-3. A sting-supported aero flow-thru model is used to generate the basic aerodynamic forces and moments, as well as the force and moment variation due to inlet flow changes. A strut-supported partially-metric jet effects model with faired inlets provides the aerodynamic force and moment variation due to nozzle geometry and flow changes. In addition, a strut-supported model provides support system corrections to the basic data.

The basic thrust/drag accounting system does not change when simulator models are used. As shown in Figure A-4, the only difference is that a single simulator model provides the same data that the conventional aero flow-thru and jet effects models did.



Corrections:

- | | |
|---|--|
| 1. Ref mass flow ratio (max attainable) | 6. Inlet recovery and distortion |
| 2. Support strut interference | 7. Operating nozzle geometry and nozzle pressure ratio |
| 3. Ref A/B nozzle and pressure ratio | 8. Power extraction and compressor bleed |
| 4. Roughness and Reynolds Number | 9. Inlet bleed, bypass, compartment ventilation and ECS drag |
| 5. Operating mass flow ratio | |

FIGURE A-4
TYPICAL AIRCRAFT THRUST/DRAG ACCOUNTING SYSTEM UTILIZING
SIMULATOR-EQUIPPED MODELS

GP76-0701-3

APPENDIX B

MODEL CALIBRATION

An extensive check-out and calibration of all necessary model subsystems was conducted prior to the wind tunnel test. Calibrations were conducted on the force balances, inlet bleed and leakage airflows, simulator compressor airflow, inlet duct seal, and metal bellows. The following sections briefly discuss the procedure and the results from each of these calibration activities. Further details on the calibrations can be found in Reference (8). Appendix C summarizes the SN002 simulator calibration test conducted in the AEDC Engine Test Facility.

B.1 Force Balance Calibrations

The three force balances were calibrated while installed in the model to account for the effects of the elements which bridged the balances. These elements included instrumentation lines, seals, metal bellows, balance leads, thermal control system leads, and all other instrumentation cables and tubing. The strut seal and bellows were also installed for these calibrations. The inlet duct seal, however, was not installed for the balance calibrations, but was installed and calibrated separately as a function of load and pressure differential.

Special calibration bodies, two of which are shown in Figure B-1, were used to apply loads at several model stations in close proximity to the expected aerodynamic centers of pressure or the balance gauge locations. The output of all six gauges of each balance was recorded for each load point. Balance output was recorded for both ascending and descending loads. Any load transmitted from one balance to another was detected by recording the output of all three balances, even though only one balance was being loaded. No interactions between balances were identified. The basic data reduction balance matrices for the wind tunnel test were derived from these calibrations. Throughout the calibrations and the wind tunnel test, the total airframe balance and simulator balance were maintained at uniform temperatures of 135°F and 160°F respectively with the thermal control system.

B.2 Inlet Bleed and Leakage Airflow Calibration

All bleed exits were calibrated in place on the inlet to simulate actual test conditions. The calibration setup and pressure instrumentation are illustrated in Figure B-2. The front of the inlet was sealed by a block between the upper and lower cowl leading edges. The inlet duct was also

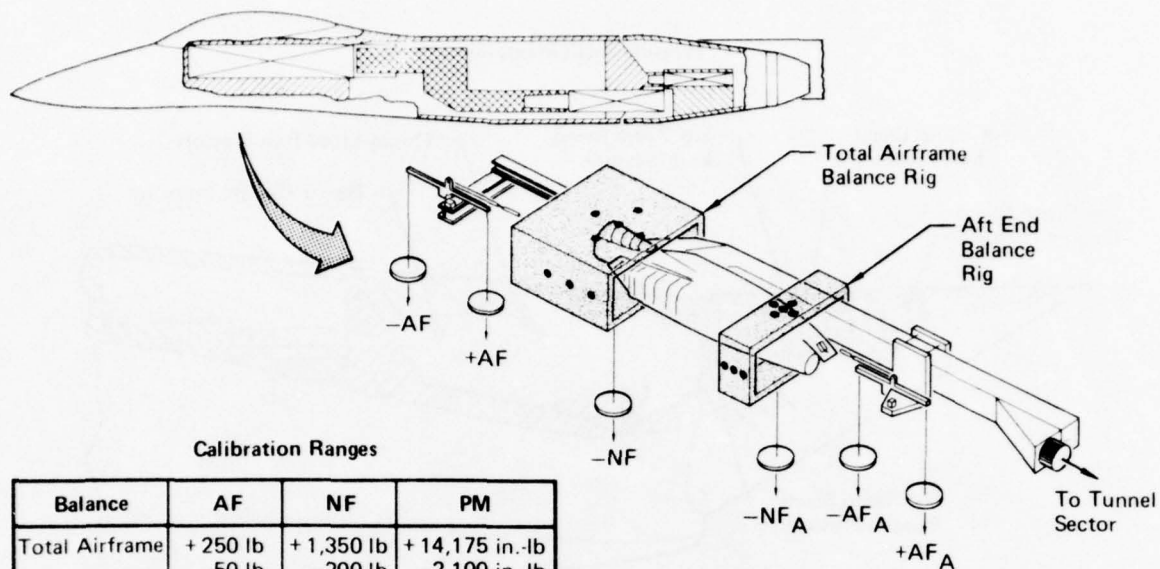
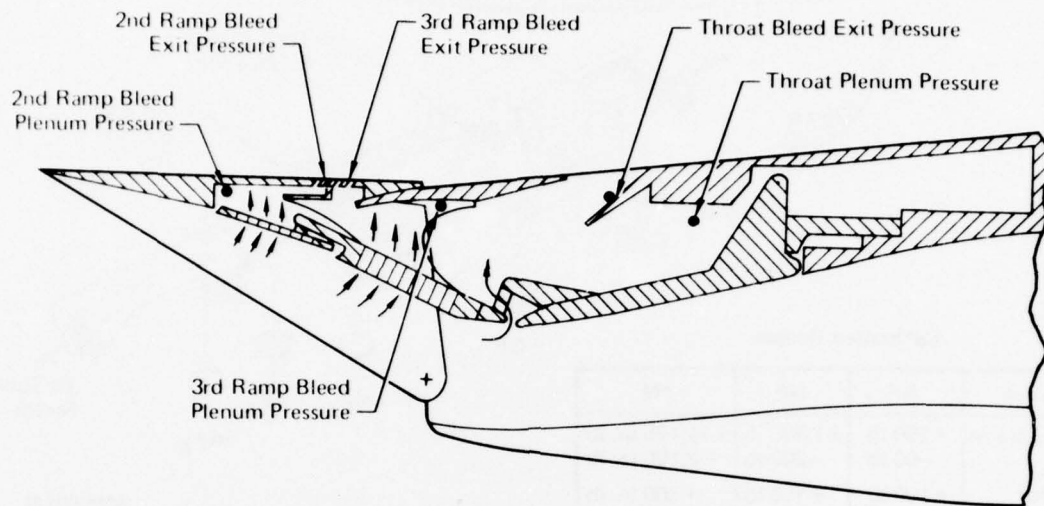


FIGURE B-1
INSTALLED BALANCE CALIBRATION SET-UP

Pressure Instrumentation



Typical mass flow function for each bleed system defined as:

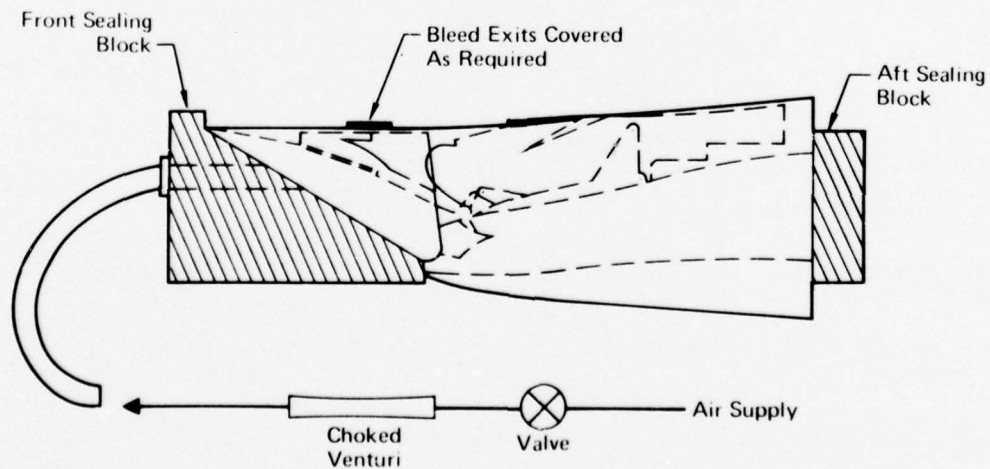
$$MFF = \omega \sqrt{T_T / P_p}$$

where ω = Bleed airflow

T_T = Bleed air total temperature

P_p = Bleed air plenum pressure

Hardware Set-Up



GP76 0701 26

FIGURE B-2
INLET BLEED/LEAKAGE AIRFLOW CALIBRATION

sealed at the end of the diffuser. The airflow for each bleed calibration was ducted through a choked venturi into the front of the inlet. Each bleed exit was calibrated separately by sealing all other bleed and leakage exits. Inlet leakage was determined by sealing all bleed exits.

The measured flow rates for each bleed system were correlated with the ratio of bleed slot static to exit total pressure. Typical results from the second ramp and third ramp bleed calibrations are shown in Figure B-3.

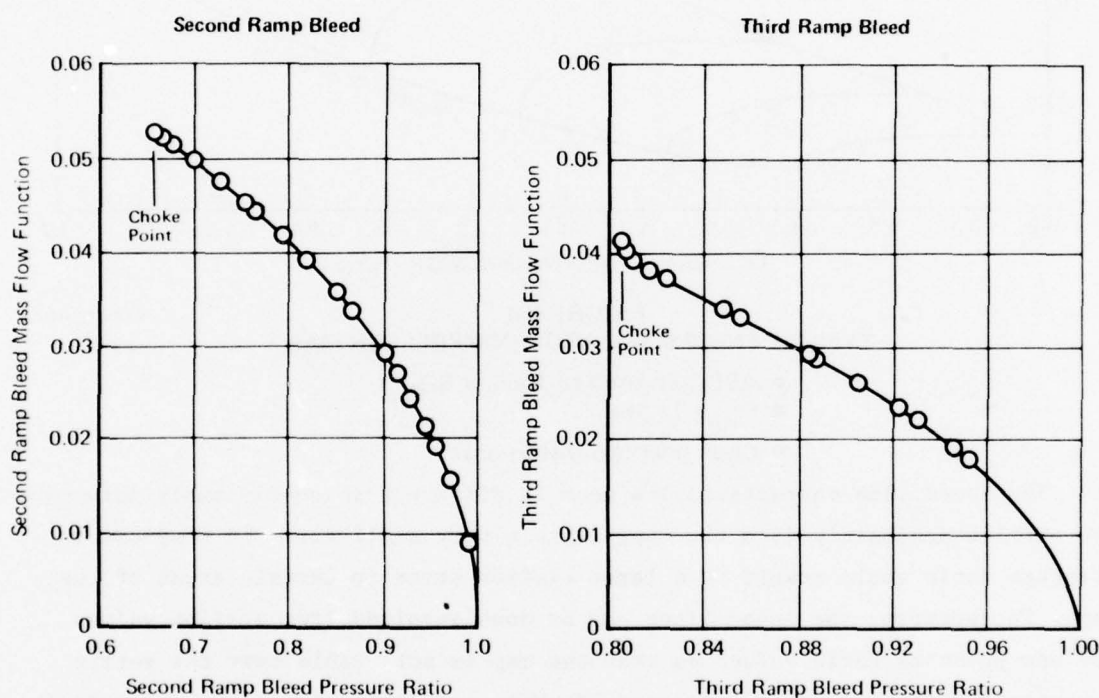


FIGURE B-3
TYPICAL INLET BLEED AIRFLOW CALIBRATION RESULTS

GP76 0701 27

B.3 Simulator Compressor Airflow Calibration

Initially it was planned to determine the simulator compressor corrected airflow during the wind tunnel test using the compressor maps generated during the simulator static calibration test program at the AEDC Engine Test Facility. A compressor map from that calibration, Figure B-4, demonstrates that as stall is approached, the speed lines become very flat. This trend occurs over most of the map and is thought to be peculiar to the SN002 simulator, since the SN001 simulator did not exhibit such flat speed lines. The flatter speed lines are attributed to increased clearances between the compressor blade tips and stator shrouds.

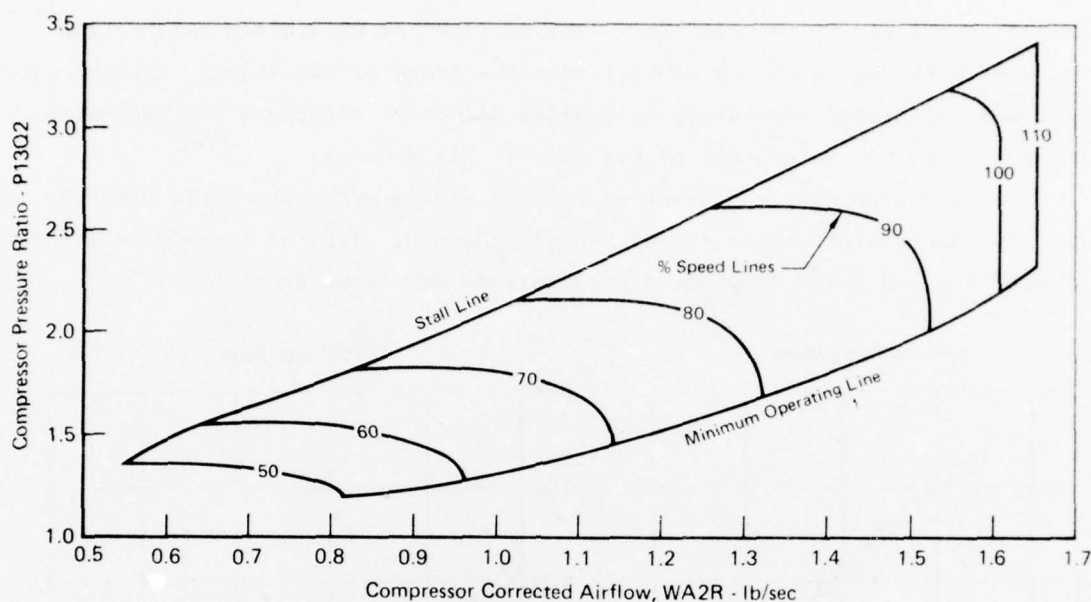


FIGURE B-4
TYPICAL SN002 SIMULATOR COMPRESSOR MAP

GP76 0701 28

- AEDC Engine Test Facility Results
- $P_{T2} = 12$ psia
- Clean Inlet (No Distortion)

The speed line characteristics made it difficult to consistently determine the airflow accurately from the map, since a very small error in compressor pressure ratio could result in a large airflow error in certain areas of the map. Furthermore, the speed lines can be double-valued (two airflow values for one pressure ratio value) so that the map is not usable over the entire compressor operating range. Because of these map limitations, it was decided to compute airflow from the static and total pressure measurements at the compressor face. The location of the compressor face pressure instrumentation used to compute the airflow is shown in Figure 3-13.

To improve the accuracy of the airflow measurement, the pressure-computed airflow was calibrated during the tunnel-on testing against that determined from the compressor map. Calibration with static test results was not used due to the adverse distortion effects on the airflow calculations. The calibration was done only at those operating conditions near the lower portion of the map where the map-determined airflow is the most accurate, i.e., nearly vertical speed lines. This final correlation, shown in Figure B-5, was determined using all of the available data. The correlation proved to be independent of free-stream Mach number and angle of attack.

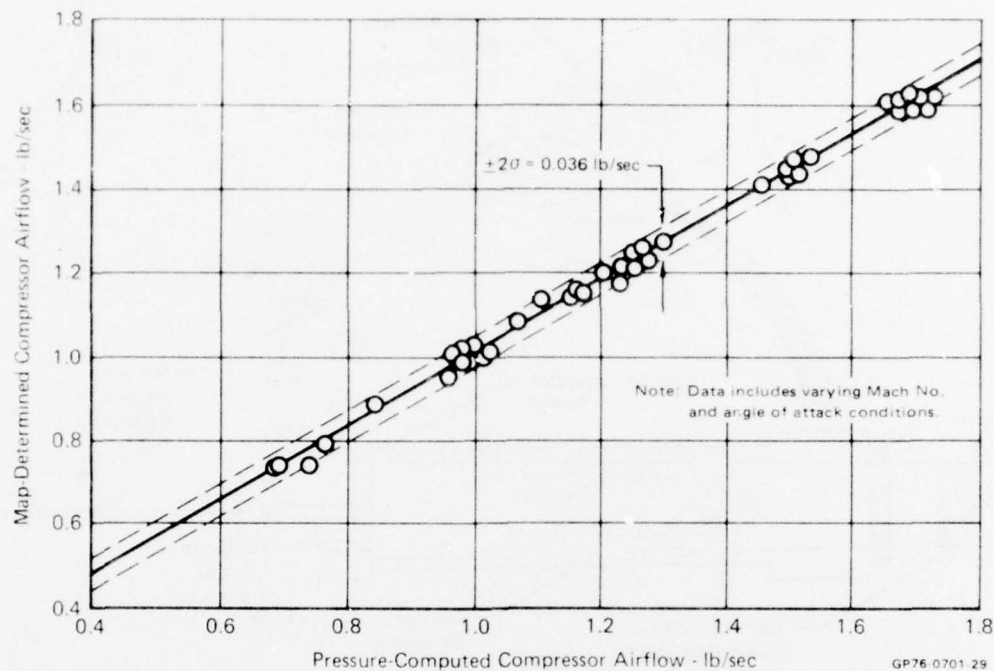
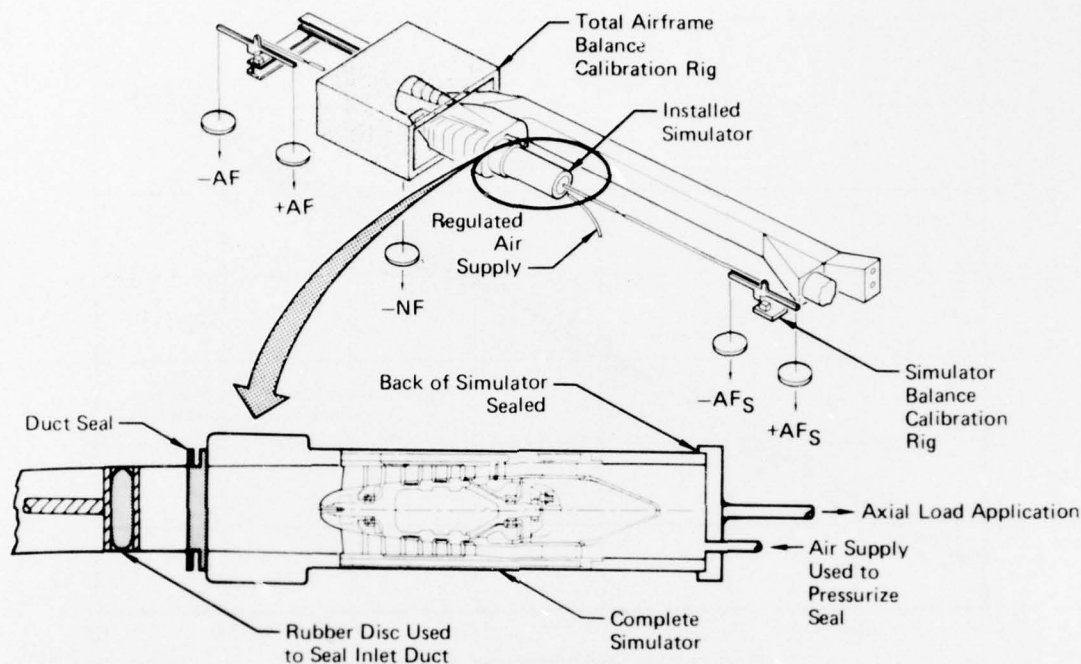


FIGURE B-5
CORRELATION OF MAP AND PRESSURE-COMPUTED COMPRESSOR AIRFLOW

B.4 Inlet Duct Seal Calibration

A rubber seal was used to bridge between the inlet duct, which was metric to the total airframe balance, and the simulator, which was metric to the thrust balance. This calibration was conducted to evaluate the effects of the seal on both the total airframe and simulator balance outputs. The overall effect includes both an installation effect, since the seal was not in place during the basic installed balance calibrations, and a pressurization effect.

The calibration of the seal, Figure B-6, included the application of various loads to both the total airframe and simulator balances with the seal in place. This loading was accomplished at five pressure differentials (-2, 0, 4, 8, 12 psid) across the seal. The output from each balance was recorded for each loading and compared against the results from the basic installed balance matrix generated previously with the seal uninstalled.



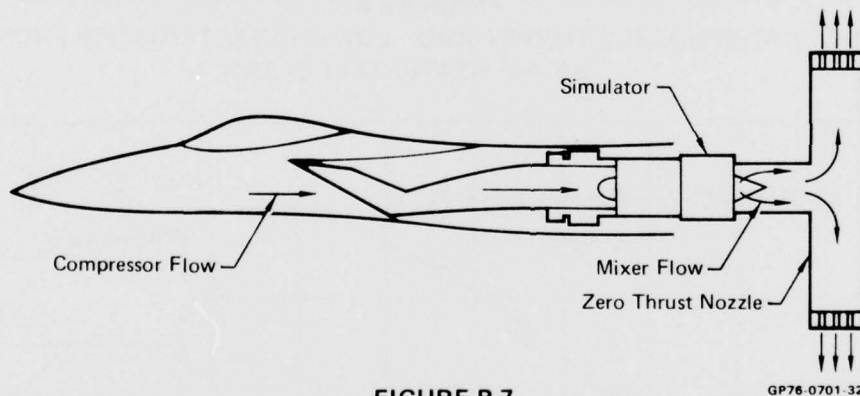
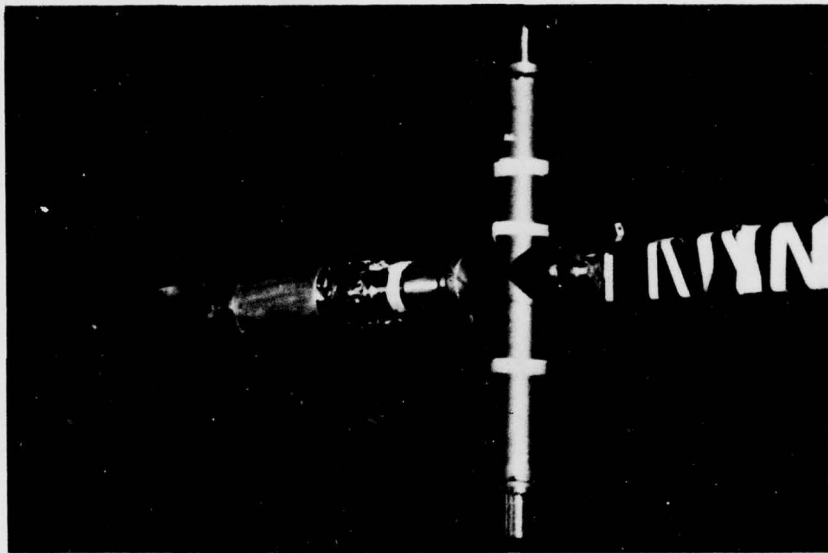
GP76 0701 30

FIGURE B-6
INLET DUCT SEAL TARE FORCE CALIBRATION SET-UP

This calibration indicated that there is seal installation effect on both the basic total airframe and simulator balance calibrations, as well as a seal pressurization effect. The installation effect was found to be linear with respect to the applied load, but the pressurization effect proved to be non-linear with respect to the seal pressure differential. Corrections to the basic calibrations of the total airframe and simulator balances were then generated as a function of the indicated balance loads and the seal pressure differential.

B.5 Metal Bellows Calibration

A full flow zero thrust nozzle assembly, Figure B-7, was initially used to calibrate the thrust balance for the tare force associated with the metal air bellows. The nozzle attached directly to the simulator and passed the total simulator flow out through two opposed exits of the same area. During the calibration, the nozzle was rotated top to bottom and fore and aft. Large scatter in the nozzle thrust coefficient data obtained early in the wind tunnel test disclosed an apparent error in the bellows tare force calibration.



GP76-0701-32

**FIGURE B-7
ZERO THRUST NOZZLE USED INITIALLY TO CALIBRATE BELLOWS
TARE FORCE**

This error could be due to:

- (1) Extensive flow interference in the tunnel during the calibration causing external loading on the nozzle.
- (2) Bellows repositioning following removal of the nozzle.

Consequently, a reevaluation of the bellows tare force calibration was conducted after the wind tunnel test. This reevaluation was centered around the known nozzle thrust characteristics. Since the dry and afterburning nozzles are convergent/divergent, the thrust characteristics are independent of external flow effects as long as the nozzles are choked and flowing full. The nozzle thrust and flow characteristics as determined from a separate static test program at MCAIR are presented in Figures B-8 and B-9. These known nozzle

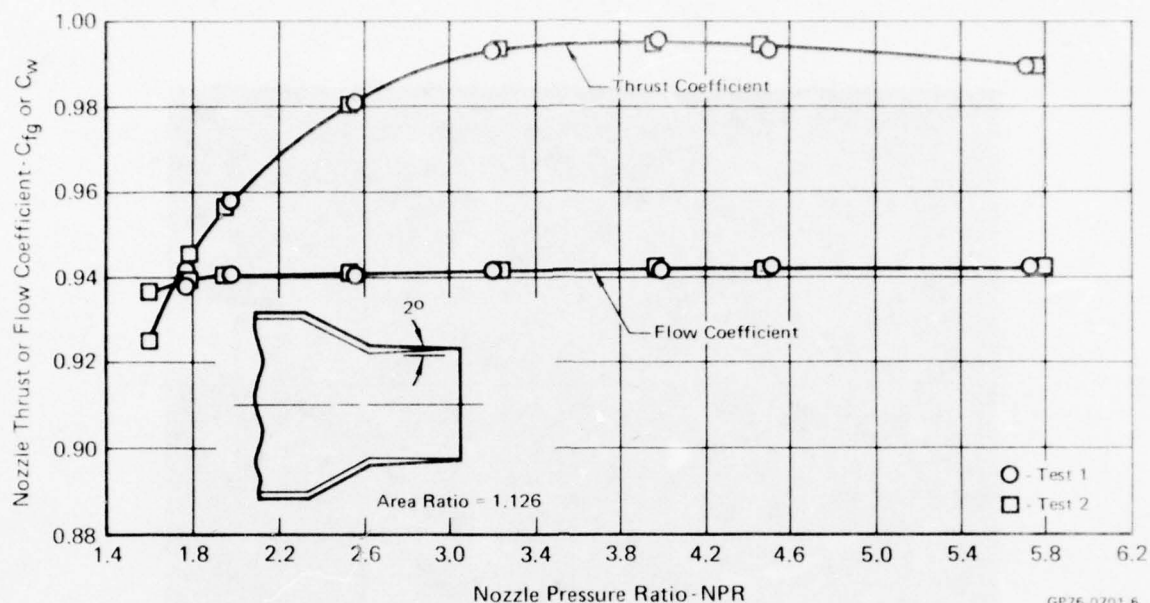


FIGURE B-8
DRY POWER NOZZLE THRUST AND FLOW CHARACTERISTICS FROM
MCAIR STATIC TEST STAND

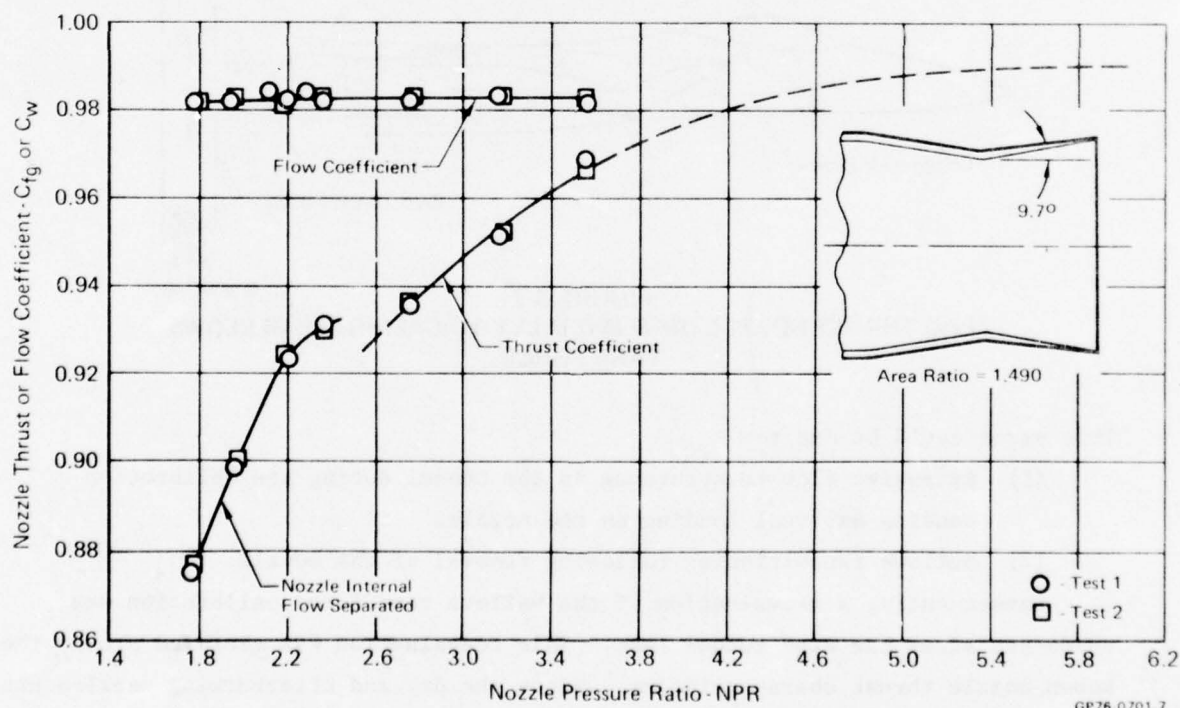


FIGURE B-9
AFTERBURNING POWER NOZZLE THRUST AND FLOW CHARACTERISTICS
FROM MCAIR STATIC TEST STAND

thrust characteristics were used with the wind tunnel test data to generate a new bellows tare force calibration. The result is shown in Figure B-10. This new calibration was considered applicable for the entire wind tunnel test.

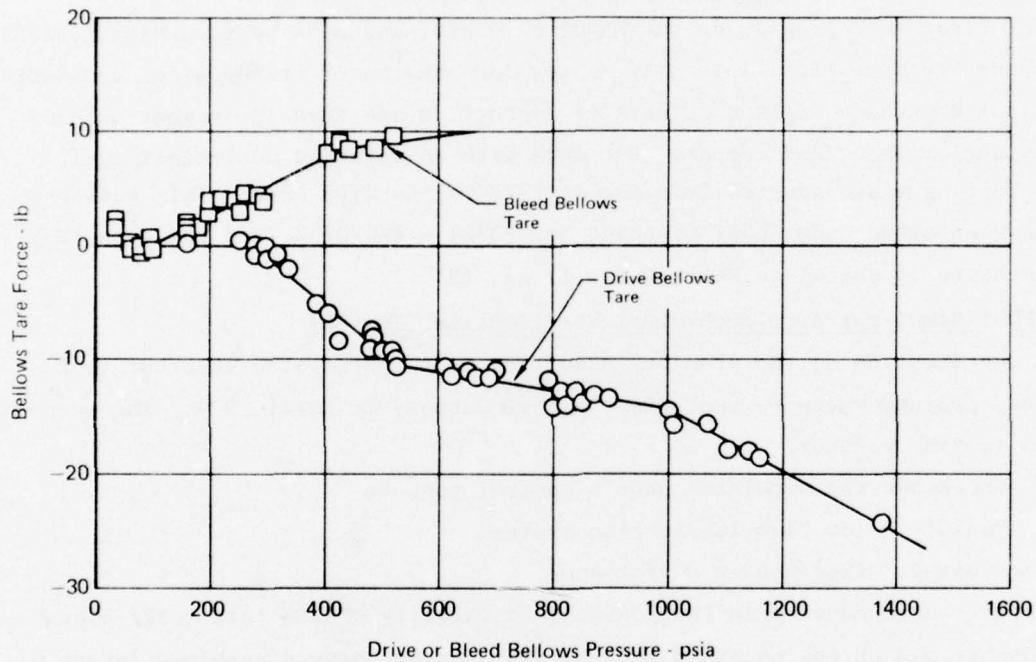


FIGURE B-10
BELLOWS POST - TEST TARE FORCE EVALUATION

GP76-0701 8

APPENDIX C

SIMULATOR STATIC TEST PROGRAMS

Three static test programs have been conducted to date in the AEDC Engine Test Facility (ETF) to develop the supersonic propulsion simulator as a potentially useful wind tunnel test tool for aircraft models. These programs are described below.

C.1 SN001 Simulator Aero/Mechanical Verification (Test 1)

The first test program on the SN001 simulator was a 38 hour aero/mechanical test to verify mechanical integrity, determine compressor performance, demonstrate mechanical endurance, define effects of distortion and Reynolds number on compressor performance, and compare test data with an existing analytical cycle deck. Testing was conducted from August 1972 to February 1973. This test program was conducted under USAF Contract No. F33615-71-C-0792, and the results are discussed in detail in References (1) and (9).

C.2 SN001 Simulator Aero/Mechanical Verification (Test 2)

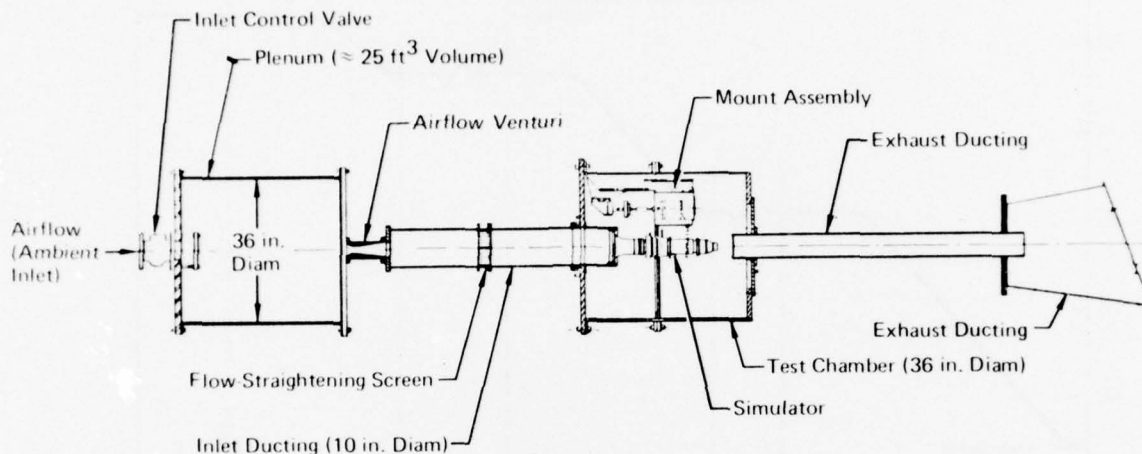
A continuation of the previous simulator component/system checkout test was conducted under the current program from January to April 1974. The purpose of this testing was to:

- o Check-out the simulator user's control console
- o Qualify a low flow lubrication system
- o Evaluate mixer/nozzle performance

All testing was conducted in the Engine Test Facility's R2C4 test cell. The test chamber and extension are 3 feet in diameter and have a combined length of approximately 3.5 feet. In addition to the basic test chamber, the R2C4 exhaust diffuser was installed prior to testing. An exhaust pipe carried the exhaust gases from the simulator into the diffuser. Downstream in the diffuser, a stream/air ejector was installed to reduce the test chamber pressure to the desired level. A schematic of the simulator installation in this test cell is shown in Figure C-1. Summaries of the results of each test phase are presented in the following paragraphs.

Control Console Check-Out - The purpose of this phase was to verify for the first time the operational capabilities of the control console, including the rotational speed control, acceleration rate control, and automatic shut down control when pre-set operating limits are exceeded.

The console was successfully used to control and monitor the operation of the simulator at steady-state speeds ranging from idle (~35,000 RPM) to 110%



GP76 0701 77

FIGURE C-1
SN002 SIMULATOR INSTALLATION IN THE AEDC ENGINE TEST
FACILITY R2C4 TEST CELL

design corrected speed ($\sim 84,000$ RPM), and acceleration rates from 500 to 10,000 RPM per second. A plot of simulator corrected speed versus time, during a typical acceleration run, is presented in Figure C-2. It is seen that the transition from peak acceleration to the desired steady-state speed occurs with no overshoot. Figure C-3 shows the rotor speed and forward bearing temperature variation during a typical automatic shutdown sequence. This particular shutdown was due to an excessive forward bearing temperature rate-of-rise.

As a result of the control console check-out, specific changes were made to the console before the wind tunnel test. These were as follows:

- o The acceleration rate controller was changed from a 50,000 RPM per second maximum value unit to a 10,000 RPM per second unit to permit more accurate control of the simulator acceleration rates.
- o The rear bearing temperature limit was changed from 225°F to 250°F to allow for transient conditions during initial simulator start-up.
- o The front bearing temperature limit was changed from 110°F at 0 RPM and 270°F at 84,000 RPM to 160°F and 260°F, respectively. This change was made to prevent automatic simulator shutdown during decelerations.

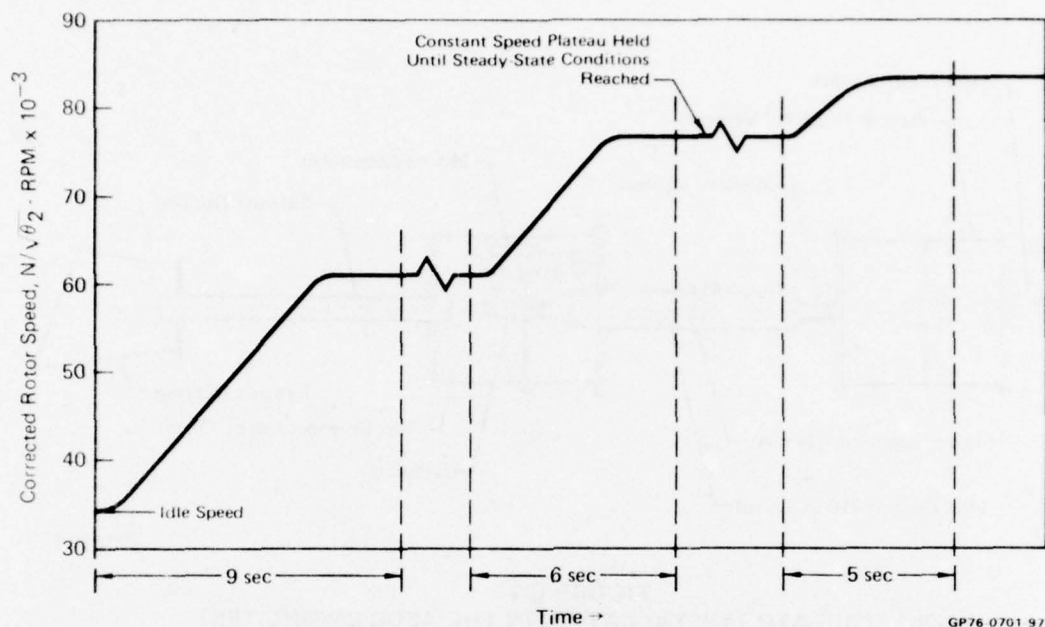


FIGURE C-2
TYPICAL 5000 RPM/SEC SIMULATOR ACCELERATION
RUN USING THE CONTROL CONSOLE

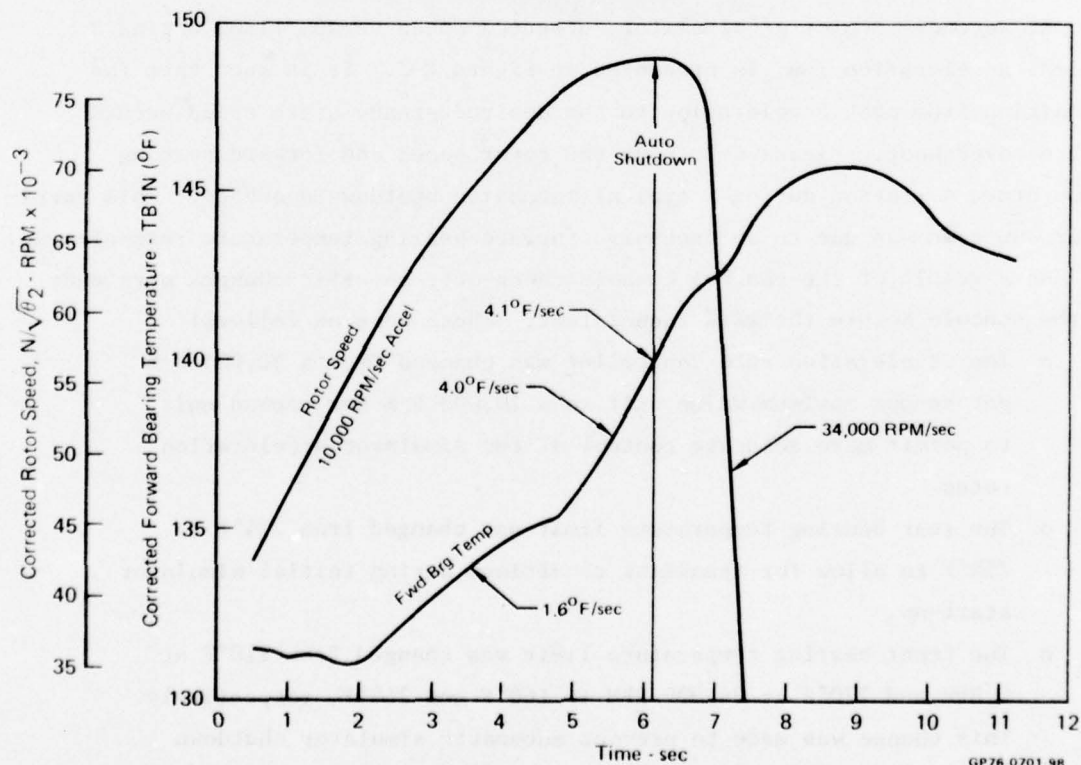


FIGURE C-3
TYPICAL CONTROL CONSOLE AUTOMATIC SHUTDOWN SEQUENCE

- o Digital bearing temperature meters, which monitor the front and rear bearing temperature levels, were added to the console. These meters filter the facility noise from the bearing temperature signals and feed the filtered signal into the control console automatic simulator shutdown circuit. The change was made because erroneous bearing temperature level and rate of rise signals to the control console were causing unnecessary automatic shutdowns of the simulator.

With the check-out and noted changes completed, the console was used to control the simulator operation in the other two phases of this testing.

Low Flow Lube System Qualification - The purpose of this phase was to (a) qualify the mini-pump oiler for supplying the simulator bearing lubrication oil, and (b) reduce the total bearing oil flow rate. During the initial check-out of the mini-pump, lubrication oil was supplied to the bearings at about 45 cc/hr, with an additional 12 cc/hr of dampening oil. The mini-pump performed well with no problems. Following this, elimination of the dampening oil resulted in a maximum increase of 13°F in the forward bearing temperature, as shown in Figure C-4. The temperature change shown in this figure is also considered representative for the rear bearing. A subsequent reduction in the lubrication oil flow rate from 45 cc/hr to the target value of 20 cc/hr caused no additional increase in the bearing temperature.

As a result of this testing, all further testing of the simulator was conducted with 20 cc/hr lubrication oil flow rate.

Mixer/Nozzle Performance - In this testing, the performance of the simulator with the porous mixers installed was evaluated for the first time. In all previous testing, the solid mixer had been used, with the turbine drive air bled entirely overboard. With the porous mixers, a portion of the drive air is mixed with the compressor airflow. The results of this testing demonstrated the ability of the simulator to independently vary compressor airflow and overall engine pressure ratio.

The total pressure and temperature profiles at the entrance to the nozzle were also evaluated during this testing, using a rake with 22 pressure probes and 7 temperature probes. The results show significant pressure and temperature distortion in the nozzle. An example of this distortion is shown in Figure C-5.

The SN001 simulator accumulated 68.7 power hours during these test programs, and was in stall either intentionally or unintentionally 22 times for approxi-

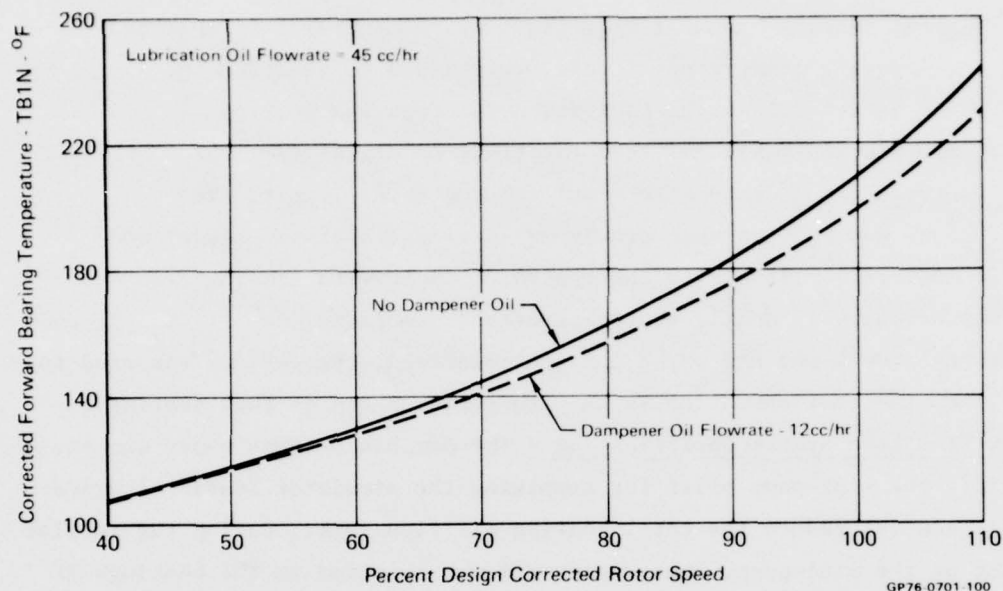


FIGURE C-4
EFFECT ON FORWARD BEARING TEMPERATURE OF ELIMINATING
THE BEARING DAMPENER OIL

Mach 0.0
Dry Power Nozzle
Nozzle Airflow = 1.53 LB/SEC
Average P_{T8} = 27.8 PSIA
Average T_{T8} = 185°F

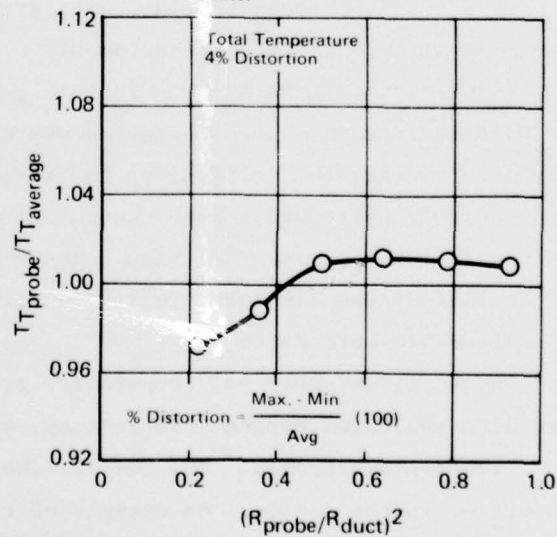
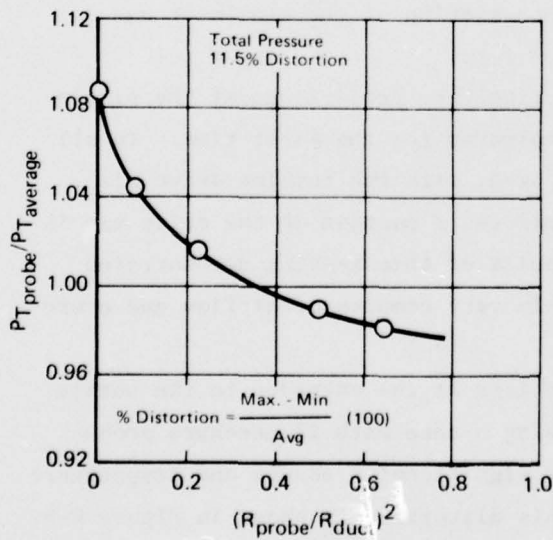
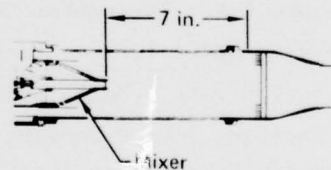


FIGURE C-5
NOZZLE ENTRANCE PRESSURE AND TEMPERATURE
PROFILES WITHOUT DUCT SCREENS

GP76 0701 130

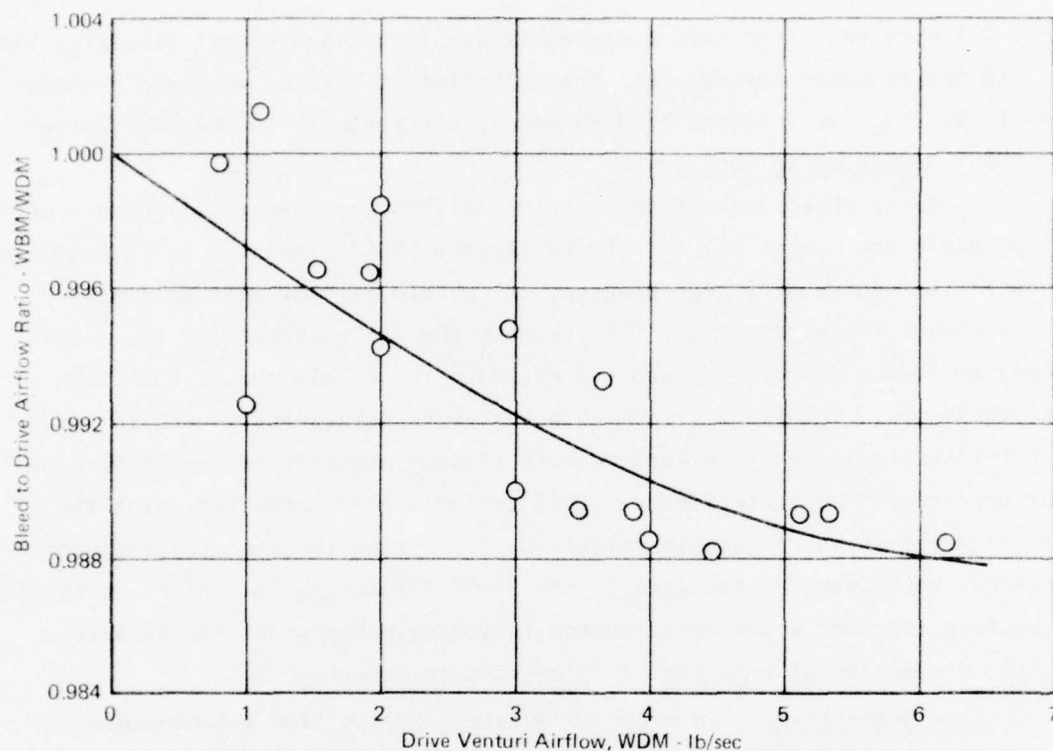
mately 2.1 minutes. Post-test disassembly and inspection of all simulator hardware did not indicate any damage. The only visible sign of wear was the erosion of the compressor stator leading edges, particularly in the first stage.

C.3 SN002 Simulator Calibration

The primary objectives of this static calibration were to (1) obtain aero/thermodynamic and mechanical data to verify the SN002 simulator operation prior to use in the wind tunnel test program, (2) obtain airflow data to evaluate the compressor characteristics, (3) evaluate the effectiveness of the nozzle screens to reduce distortion, and (4) evaluate the nozzle thrust and flow characteristics. The results from this test were subsequently used to update the existing simulator cycle deck to more closely approximate the SN002 simulator performance characteristics. This test was also conducted using the same set-up as shown previously (Figure C-1). During the test, approximately 42 powered hours were accumulated on the SN002 simulator. A limited discussion of the test results is presented in the following paragraphs. A complete detailed discussion of this test is presented in Reference 10.

Airflow Measurement - In order to obtain accurate flow measurements during this calibration test, critical flow venturis were used to measure compressor inlet, turbine drive, and turbine bleed airflows. Prior to conducting the test, these venturis were calibrated by Colorado Engineering Experiment Station, Inc. (CEESI) by connecting each of the three venturis in series with a previously-calibrated critical flow venturi. Each of the three venturis was instrumented such that inlet static pressure, throat static pressure and inlet total temperature could be measured. The discharge coefficient for each venturi was calculated based on these measurements and the actual airflow from the calibrated venturi. At each condition for which flow was determined, the throat Reynolds number was also calculated.

Following the CEESI calibrations, the turbine drive and bleed venturis were checked against each other at AEDC by connecting the two in series. The flow through each venturi was calculated, with the ratio of the two venturi airflows implying as much as a 1.5% discrepancy at high flow rates. This error is attributed to the drive venturi real gas corrections at the high pressure (>1500 psia). Subsequently, it was decided to adjust the turbine drive venturi flow to account for these differences. The correction factor for adjusting the drive airflow is presented in Figure C-6.



GP76 0701 99

FIGURE C-6
SIMULATOR DRIVE VENTURI AIRFLOW CORRECTION FACTOR

Compressor Maps - Compressor operating maps were obtained at inlet total pressures of 7, 12 and 16 psia. These levels were evaluated to encompass the pressure levels anticipated in the wind tunnel test program and to provide empirically-derived Reynolds number modifiers for the basic map. These mapping excursions ranged from the minimum operating line to stall at corrected rotor speeds of 45, 60, 70, 80, 90, 100 and 110%. These basic maps are presented in Figures C-7 through C-9. Curves on the extreme right are compressor efficiencies along each speed line. The dashed lines are predictions based on results from the first simulator static test program.

These comparisons show reasonably good agreement between the predictions and test data. The slight difference noted in airflow at a constant speed is attributed to a combination of 1) instrument inaccuracy, 2) manufacturing tolerances on the compressor blading and 3) the limited data for cycle deck fits to the SN001 simulator compressor maps. More importantly, it is noticed that as stall is approached, the SN002 simulator speed lines become flatter than those for SN001. This trend occurs at all speed lines and inlet pressure levels and appears to be real and peculiar to the SN002 simulator fabrication

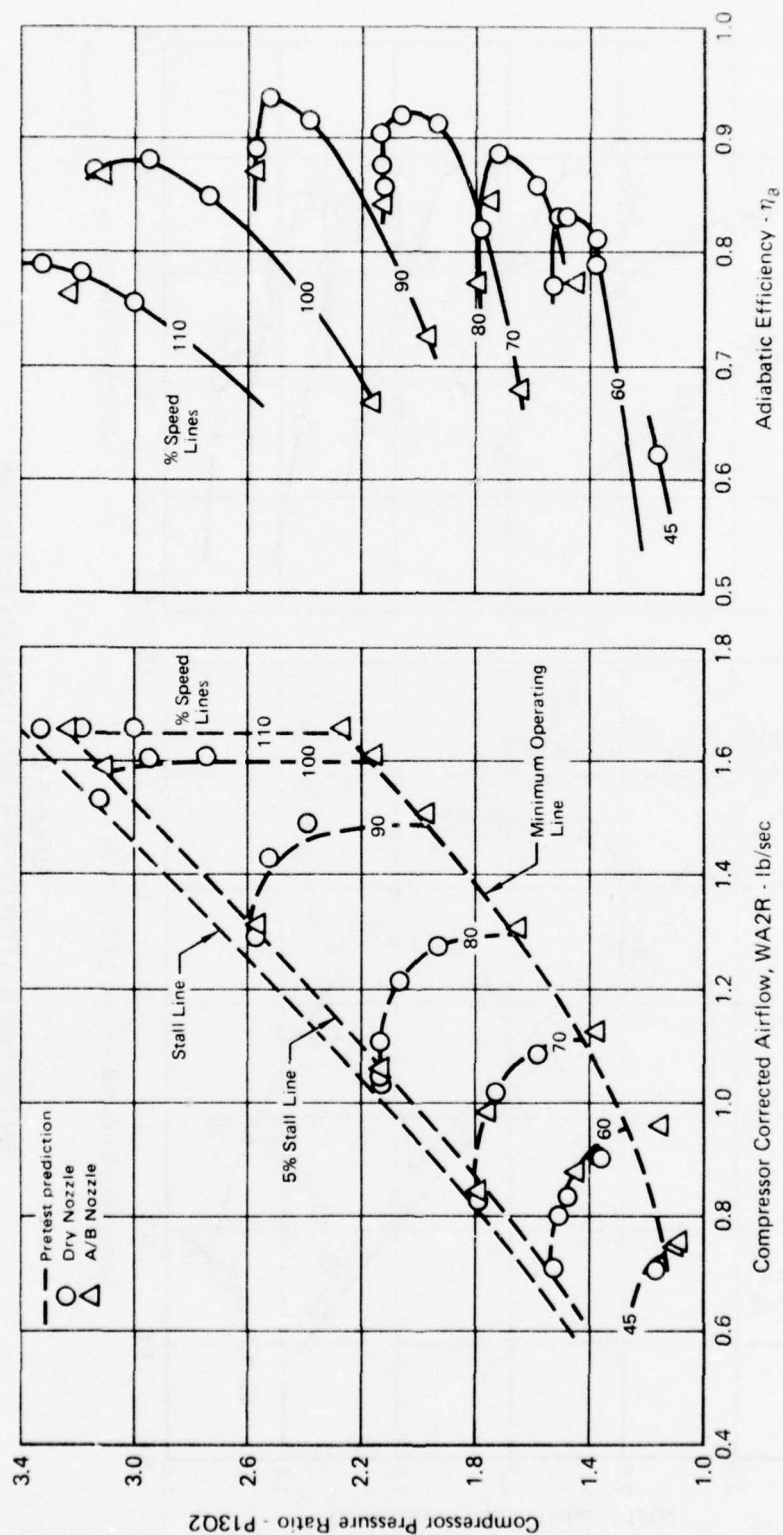
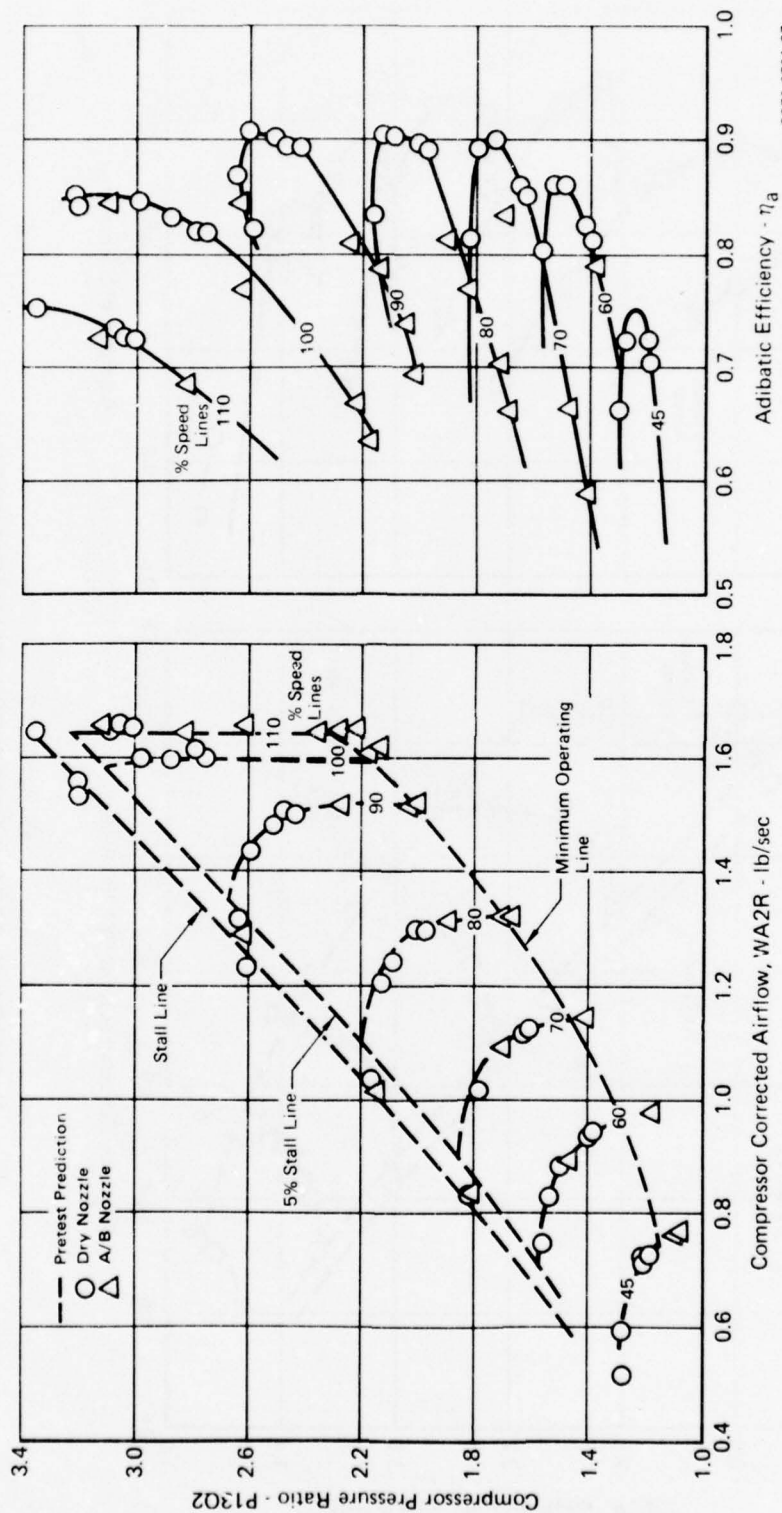
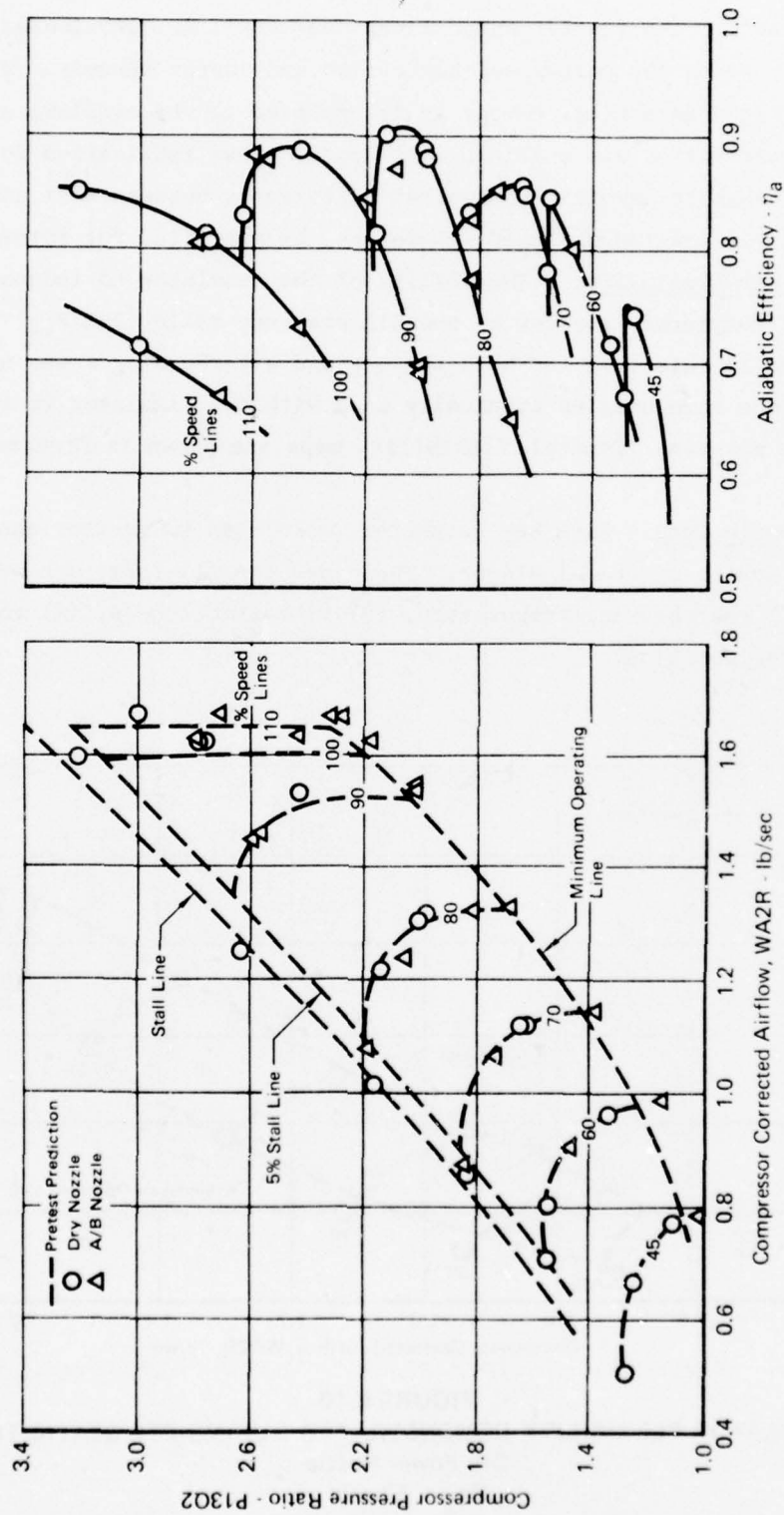


FIGURE C-7
SN 002 SIMULATOR COMPRESSOR CHARACTERISTICS
 $P_{T2} = 7 \text{ PSIA}$



GP76 0701 87

FIGURE C-8
SN 002 SIMULATOR COMPRESSOR CHARACTERISTICS
 $P_{T2} = 12 \text{ PSIA}$



GP76 0701 88

FIGURE C-9
SN 002 SIMULATOR COMPRESSOR CHARACTERISTICS
 $P_{T2} = 16 \text{ PSIA}$

and/or assembly. The flatter speed lines near stall are attributed to increased clearances between the compressor blade tips and stator shrouds. With larger clearances, less mechanical energy is transmitted to the airflow, and thus lower pressure ratios are obtained. It appears that fabrication tolerances are large enough to permit the observed differences between test and predictions. Tighter clearance should, therefore, be specified for future builds.

Simulator Flexibility - The ability of the simulator to independently vary either compressor airflow or overall pressure ratio (P_{T8}/P_{T2}) was also demonstrated in this test for both the dry and afterburning power nozzles. These were the same nozzles eventually used with the simulator in the wind tunnel test program. Typical flexibility maps are shown in Figures C-10 and C-11.

Diagnostic Data - Five key parameters were used to monitor and evaluate the mechanical health of the simulator. These are the (1) forward bearing temperature, (2) rear bearing temperature, (3) vibration levels, (4) rotor thrust and (5) rotor position.

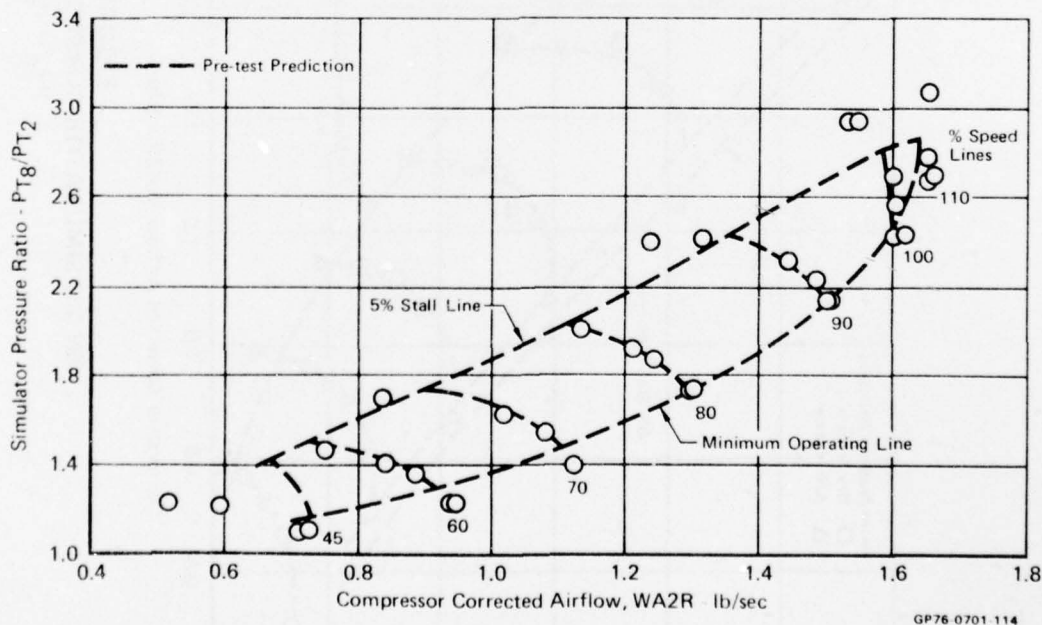
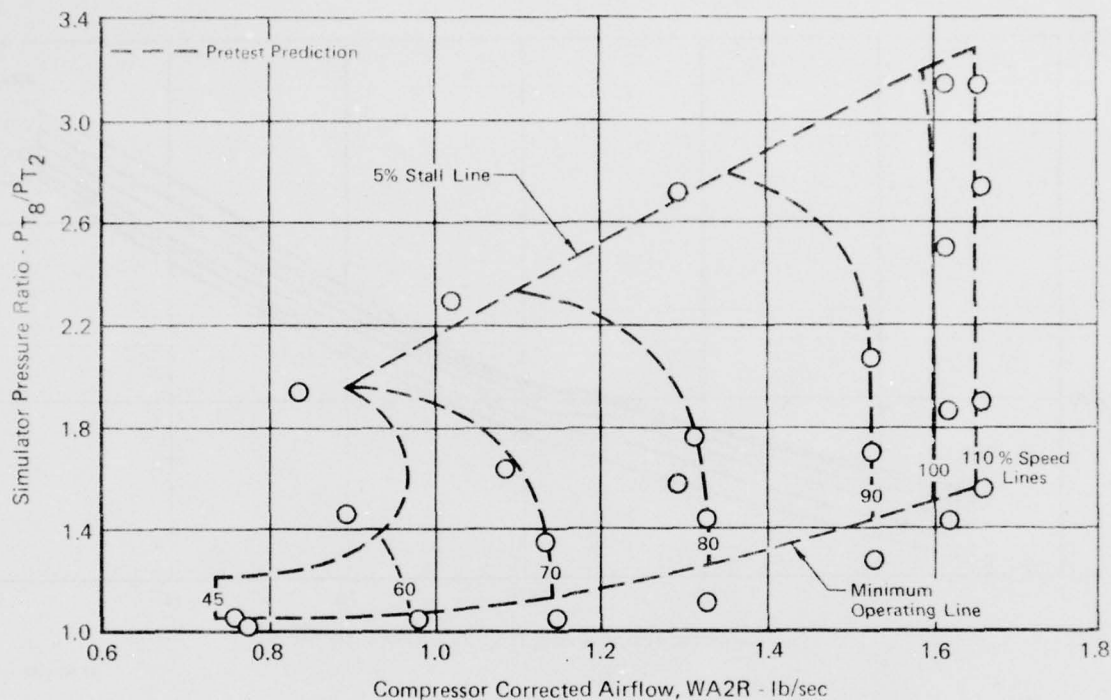


FIGURE C-10
SIMULATOR FLEXIBILITY DEMONSTRATED DURING ETF STATIC TESTS
 Dry Power Nozzle
 $P_{T2} = 12$ psia



GP76-0701-115

FIGURE C-11
SIMULATOR FLEXIBILITY DEMONSTRATED DURING ETF STATIC TESTS
 A/B Power Nozzle
 $P_{T2} = 12$ psia

Typical forward bearing temperature and rotor thrust maps determined from this testing are shown in Figures C-12 through C-15. The bearing temperatures were measured using thermocouples, but the rotor thrust was calculated from internal pressure measurements. Because it is a complex calculation, the accuracy of the rotor thrust values is in doubt. These data, and others of the same type, were used during the wind tunnel test program to continually monitor and assess the health of the simulator and any deterioration that was occurring.

The forward bearing temperature maps shown resulted after a mixer blow-out that occurred during the testing. The mixer used with the afterburning nozzle blew out the rear of the unit through the nozzle due to a failure of the threads that hold the mixer in place. After a careful analysis, it was concluded that the failure resulted from (1) a fine thread design that is intolerant of distortion, and (2) axial and circumferential thread distortion caused by welding conducted on the unit during its final assembly.

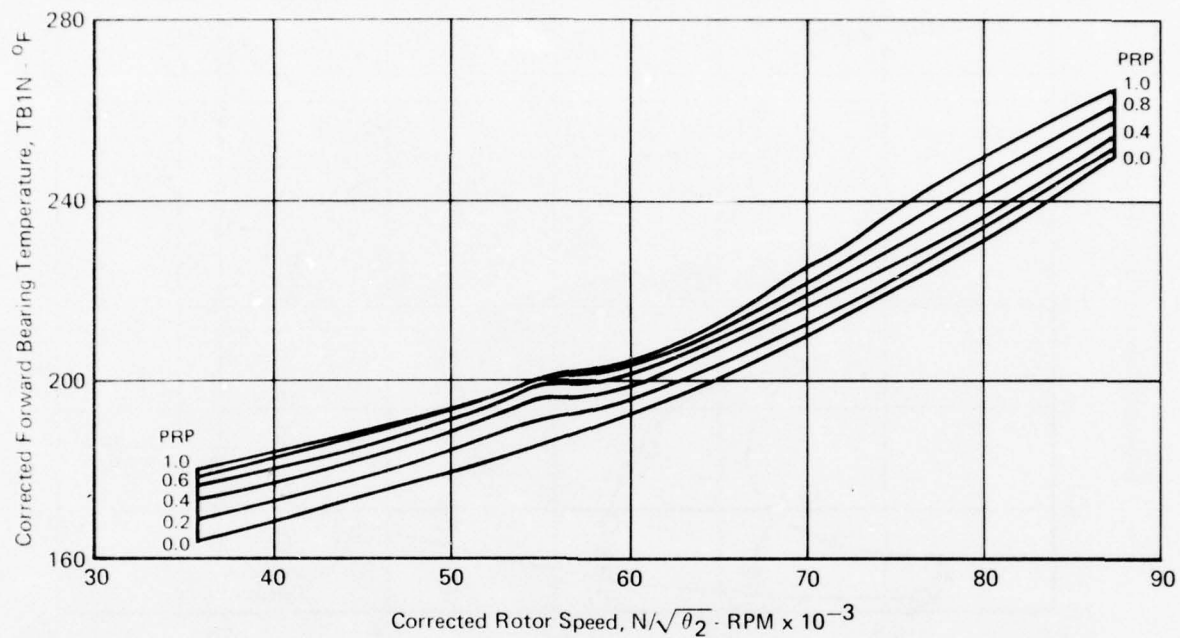


FIGURE C-12
TYPICAL FORWARD BEARING TEMPERATURE MAP
 Dry Power Nozzle
 $P_{T2} = 12 \text{ psia}$

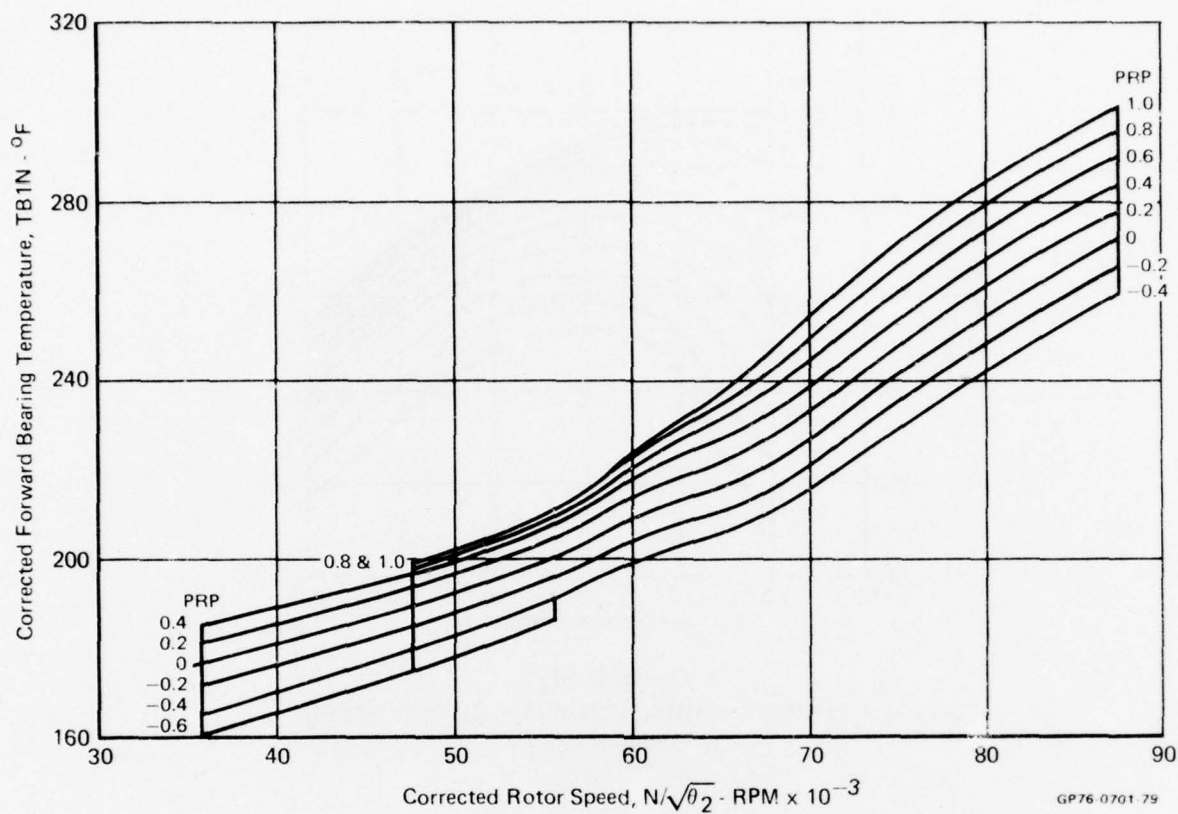


FIGURE C-13
TYPICAL FORWARD BEARING TEMPERATURE MAP
 A/B Power Nozzle
 $P_{T2} = 12 \text{ PSIA}$

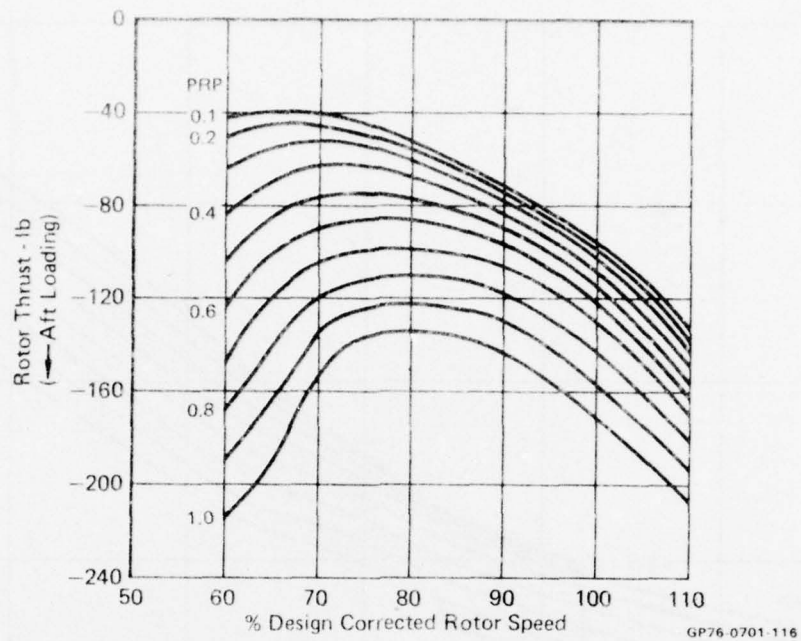


FIGURE C-14
ROTOR THRUST VARIATION WITH ROTOR SPEED
 Dry Power Nozzle
 $P_{T2} = 12$ psia

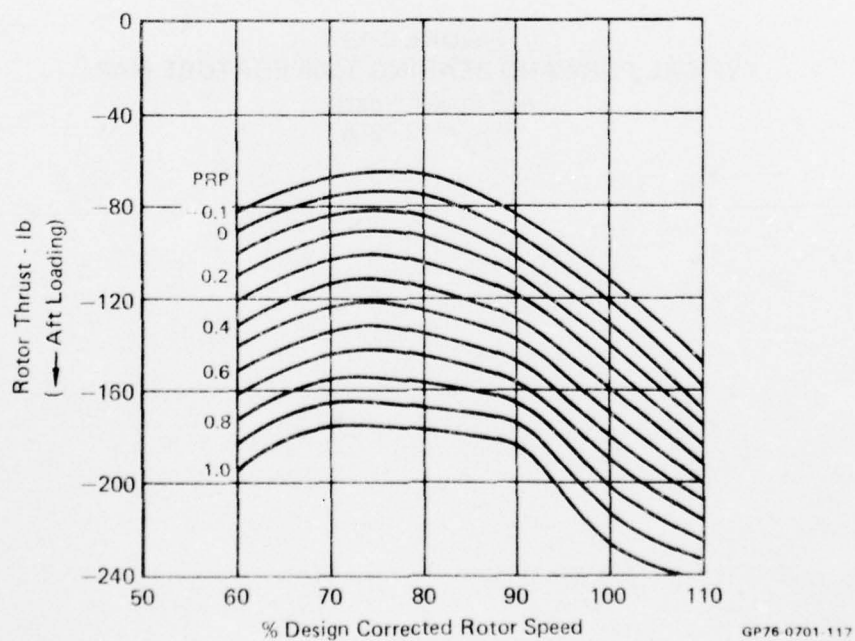


FIGURE C-15
ROTOR THRUST VARIATION WITH ROTOR SPEED
 A/B Power Nozzle
 $P_{T2} = 12$ psia

The mixer blow-out changed the relative positioning of the rotor, since after the blow-out, the level of the rotor thrust decreased by as much as 30 pounds (at max speed) from what it had been. In addition, the forward bearing temperature level was lowered by about 20°F. An inspection of the simulator following the blow-out indicated no apparent effect on the overall mechanical integrity of the simulator. After the mixer was repaired, the testing was resumed without further incident.

Nozzle Pressure/Temperature Distortion - The testing indicated that the three screens located in the nozzle duct to improve mixing of the compressor and mixer flows significantly lowered the total pressure distortion, as seen in Figure C-16.

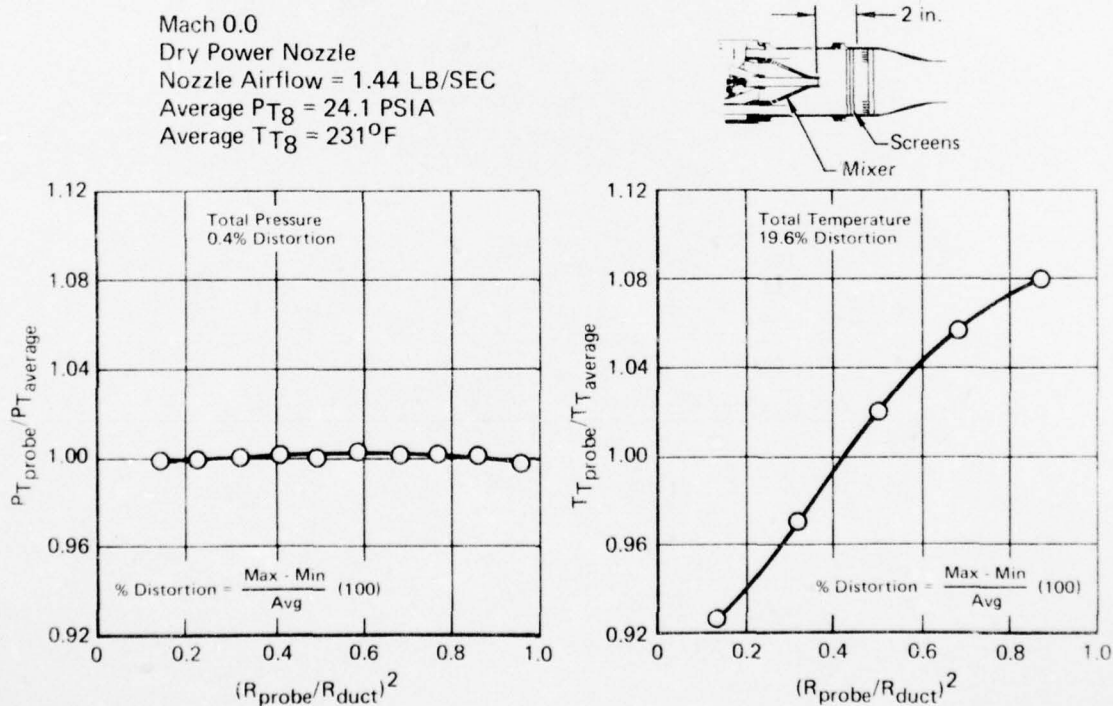


FIGURE C-16
NOZZLE ENTRANCE PRESSURE AND TEMPERATURE PROFILES
WITH DUCT SCREENS INSTALLED

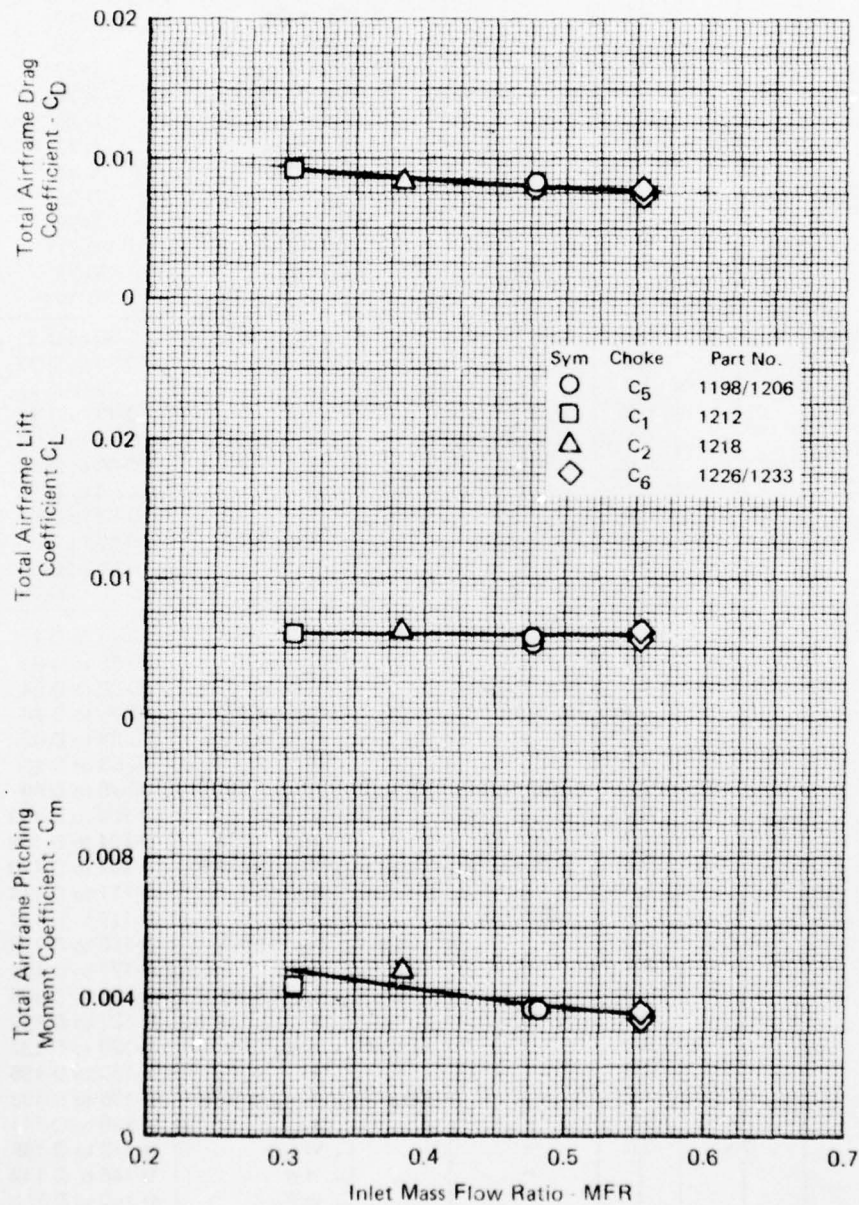
GP76-0701 131

APPENDIX D

TOTAL AIRFRAME AND AFT-END FORCE AND MOMENT DATA

The total airframe and aft-end drag, lift, and pitching moment coefficients obtained from the three model test modes are provided in this appendix. An index of the data presented is given in Figure D-1. The data from the aero flow-thru mode are presented first, followed by the data obtained from the jet effects mode and simulator mode respectively.

Test Mode - Aero Flow-Thru
 Nozzle Choke - As Noted
 Mach No. - 0.6
 Angle of Attack - 0°



GP76 0701 169

FIGURE D-2
 TOTAL AIRFRAME PERFORMANCE VARIATION WITH INLET MASS FLOW RATIO

Test Mode - Aero Flow Thru
 Nozzle Choke - As Noted
 Mach No. - 0.6
 Angle of Attack - 5°

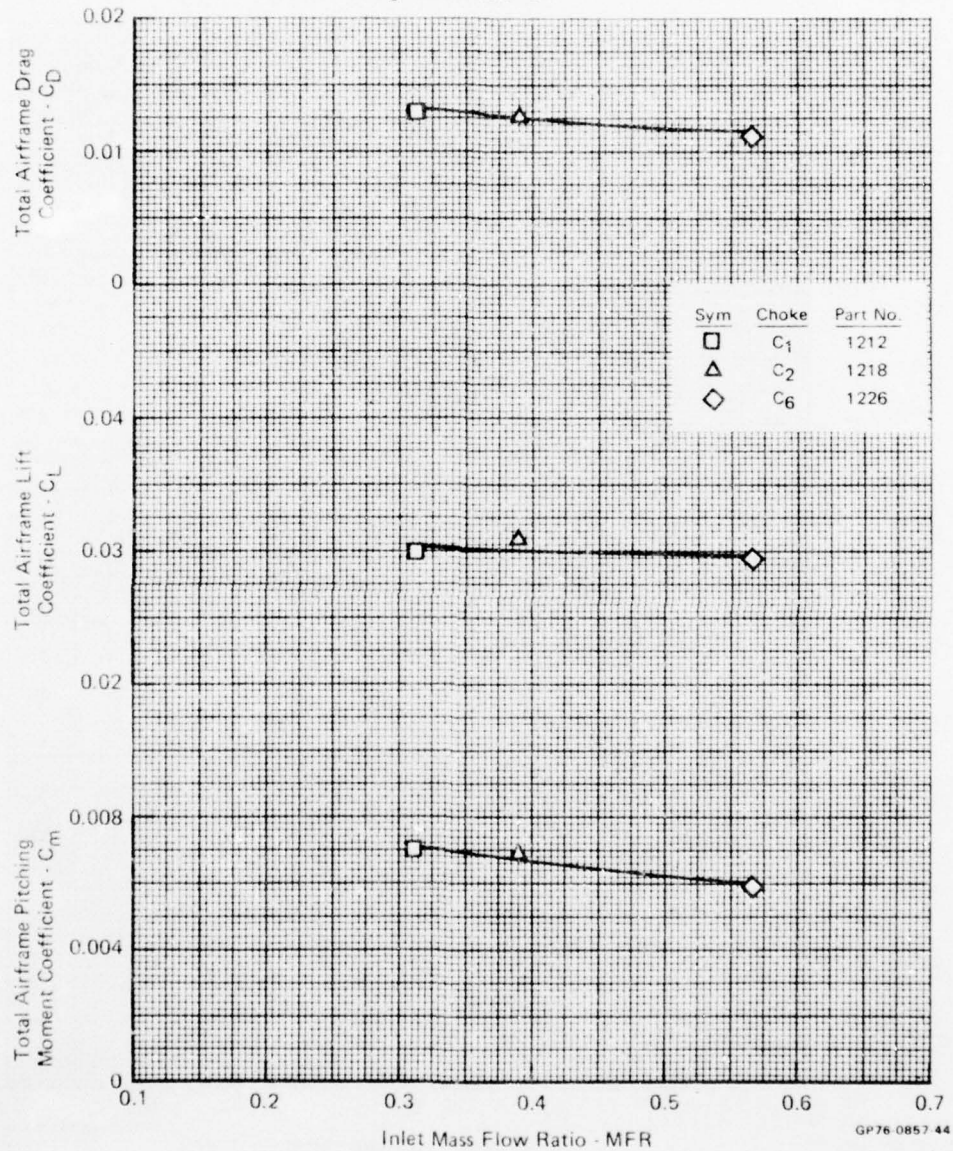


FIGURE D-3
 TOTAL AIRFRAME PERFORMANCE VARIATION WITH INLET MASS FLOW RATIO

Test Mode - Aero Flow-Thru
 Nozzle Choke - As Noted
 Mach No. - 0.6
 Angle of Attack - 10^0

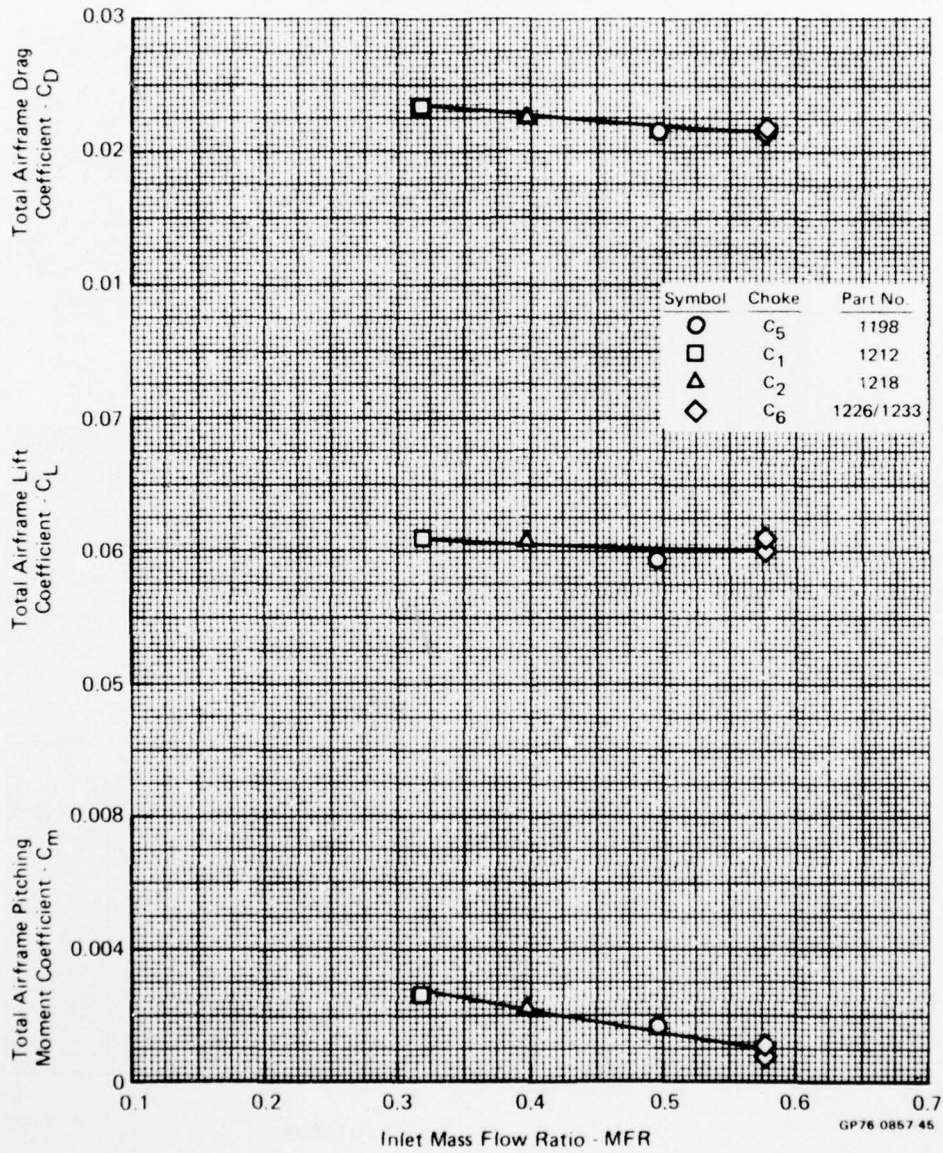


FIGURE D-4
 TOTAL AIRFRAME PERFORMANCE VARIATION WITH INLET MASS FLOW RATIO

Test Mode - Aero Flow Thru
 Nozzle Choke - As Noted
 Mach No. - 0.6
 Angle of Attack - 16°

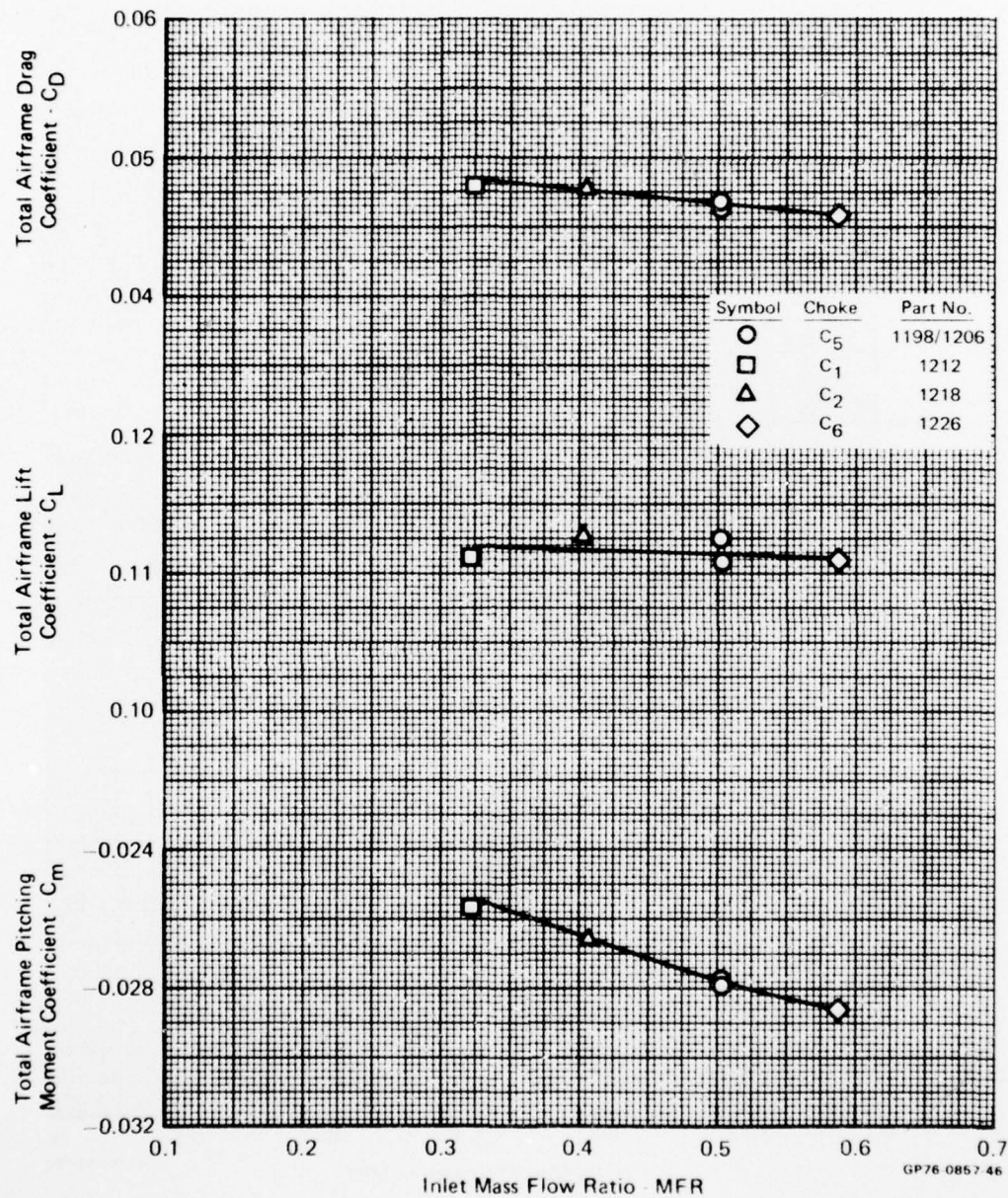


FIGURE D-5
 TOTAL AIRFRAME PERFORMANCE VARIATION WITH INLET MASS FLOW RATIO

Test Mode - Aero Flow-Thru

Nozzle Choke - As Noted

Mach No. - 0.9

Angle of Attack - 0°

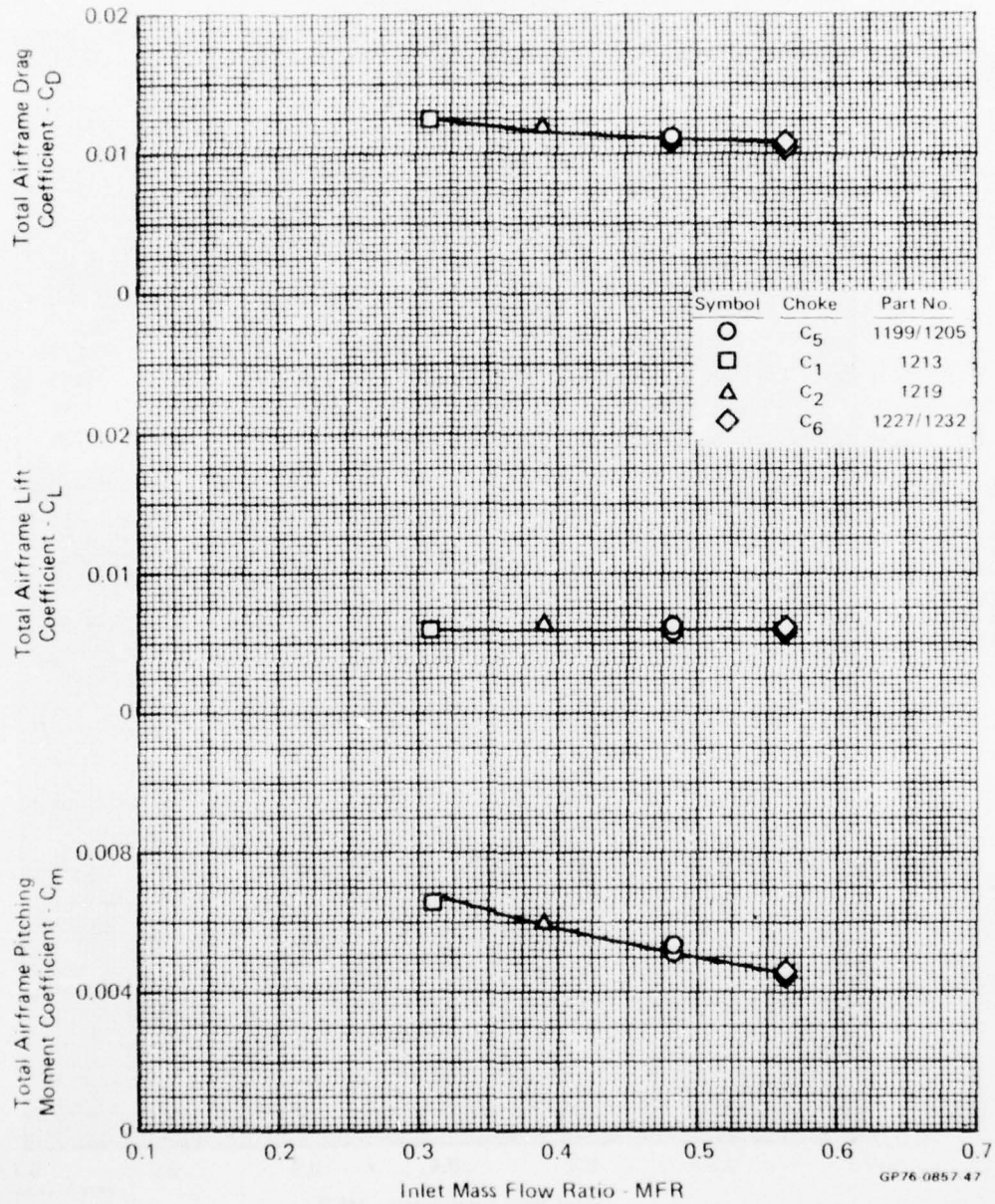


FIGURE D-6
TOTAL AIRFRAME PERFORMANCE VARIATION WITH INLET MASS FLOW RATIO

Test Mode - Aero Flow-Thru
 Nozzle Choke - As Noted
 Mach No. - 0.9
 Angle of Attack - 5°

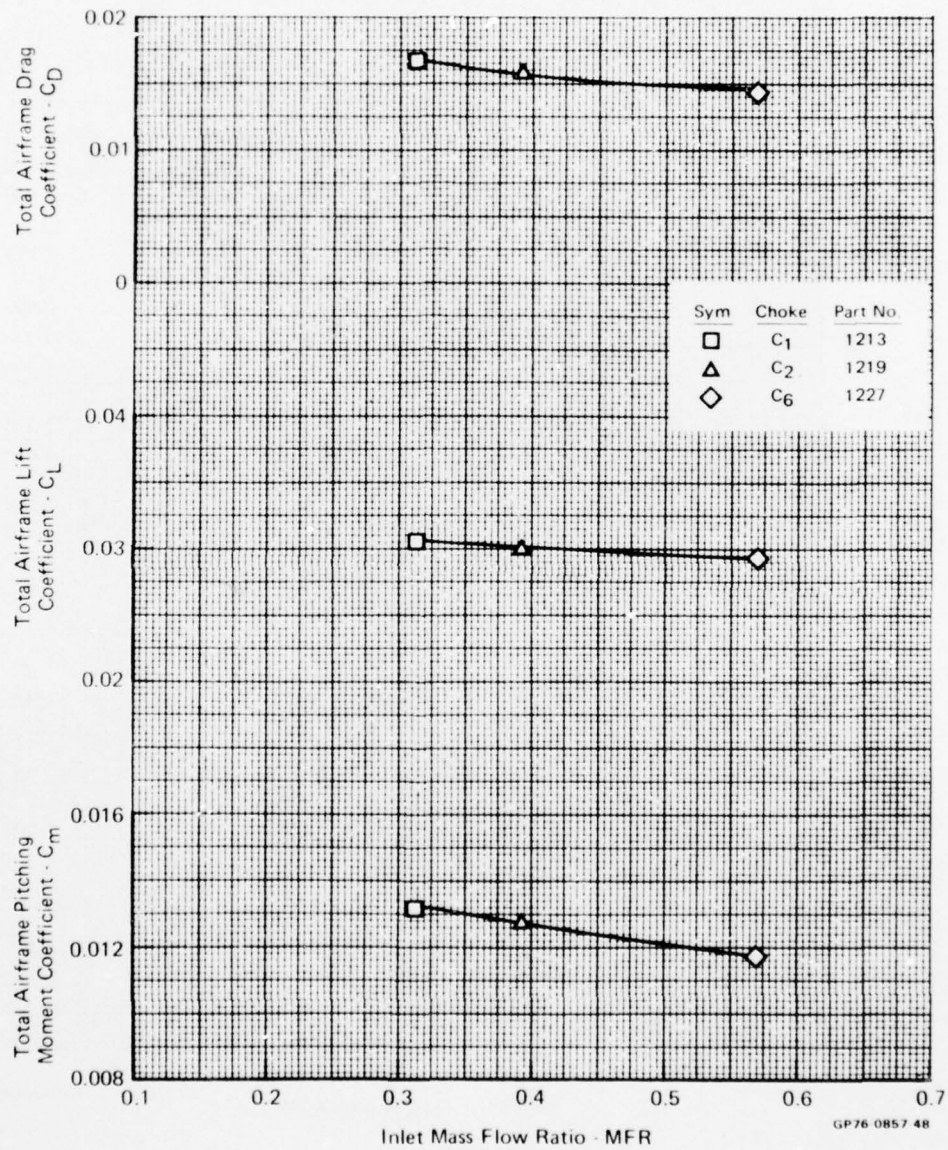


FIGURE D-7
 TOTAL AIRFRAME PERFORMANCE VARIATION WITH INLET MASS FLOW RATIO

Test Mode - Aero Flow-Thru
 Nozzle Choke - As Noted
 Mach No. - 0.9
 Angle of Attack - 10^0

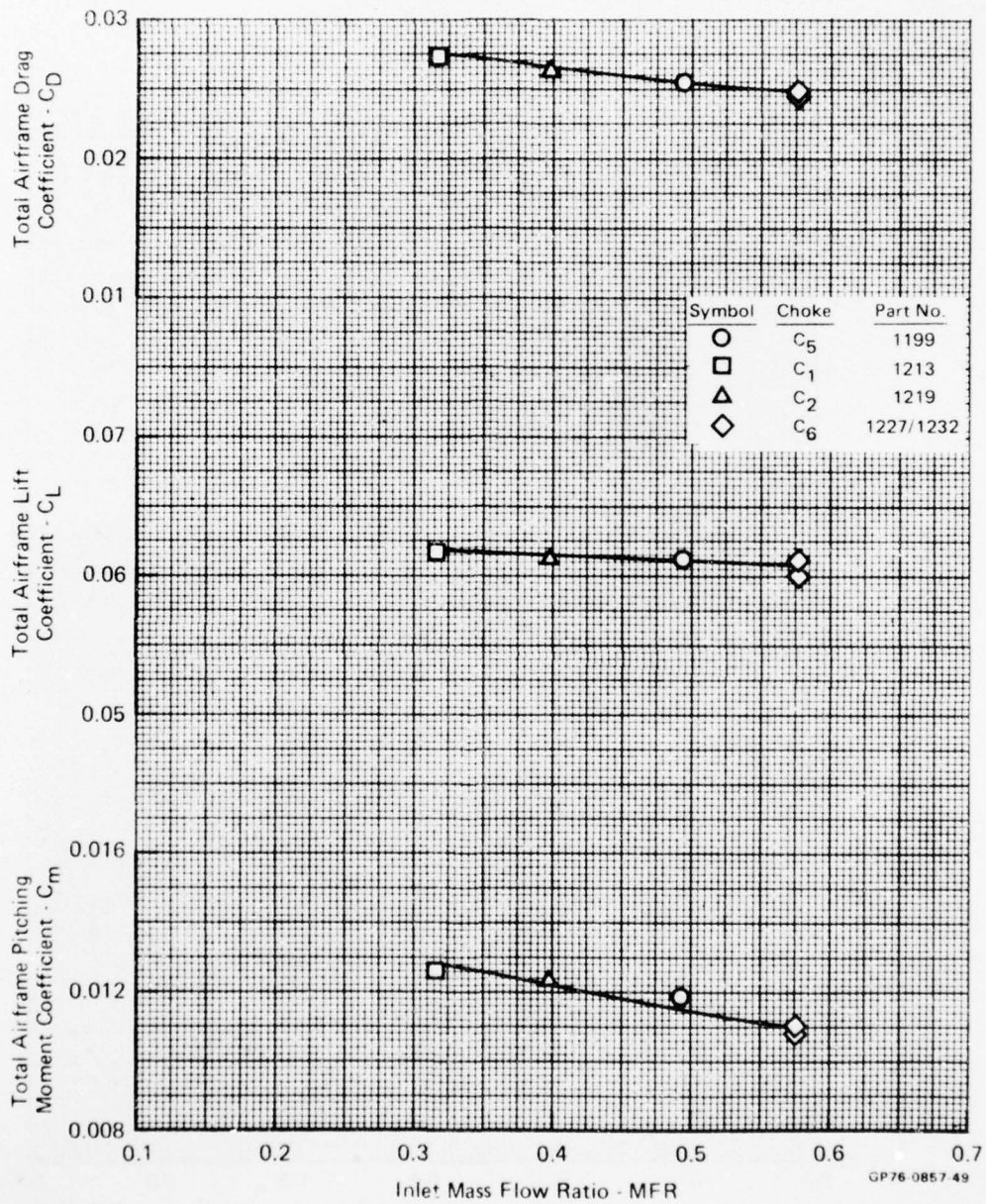


FIGURE D-8
 TOTAL AIRFRAME PERFORMANCE VARIATION WITH INLET MASS FLOW RATIO

AD-A034 282

MCDONNELL AIRCRAFT CO ST LOUIS MO
TURBINE ENGINE MULTI-MISSION PROPULSION SIMULATOR WIND TUNNEL D--ETC(U)
NOV 76 M F EIGENMANN, R L BEAR, T C CHANDLER F33615-73-C-2051

F/G 21/5

UNCLASSIFIED

AFAPL-TR-76-73

NL

3 OF 4
AD
A034282



OF 4
34282

Test Mode - Aero Flow Thru
 Nozzle Choke - As Noted
 Mach No. - 0.9
 Angle of Attack - 16°

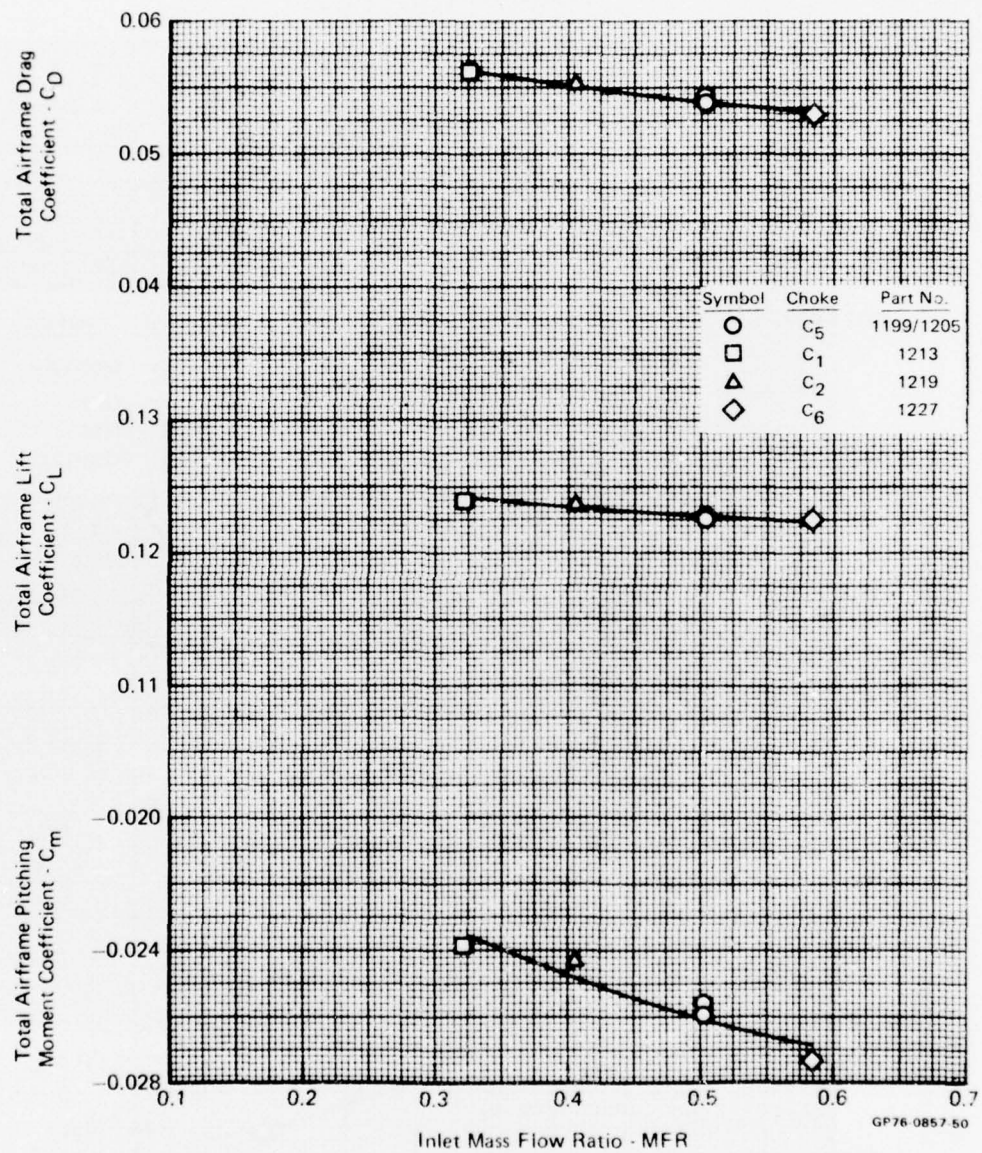


FIGURE D-9
 TOTAL AIRFRAME PERFORMANCE VARIATION WITH INLET MASS FLOW RATIO

Test Mode - Aero Flow-Thru
 Nozzle Choke - As Noted
 Mach No. - 1.2
 Angle of Attack - 0°

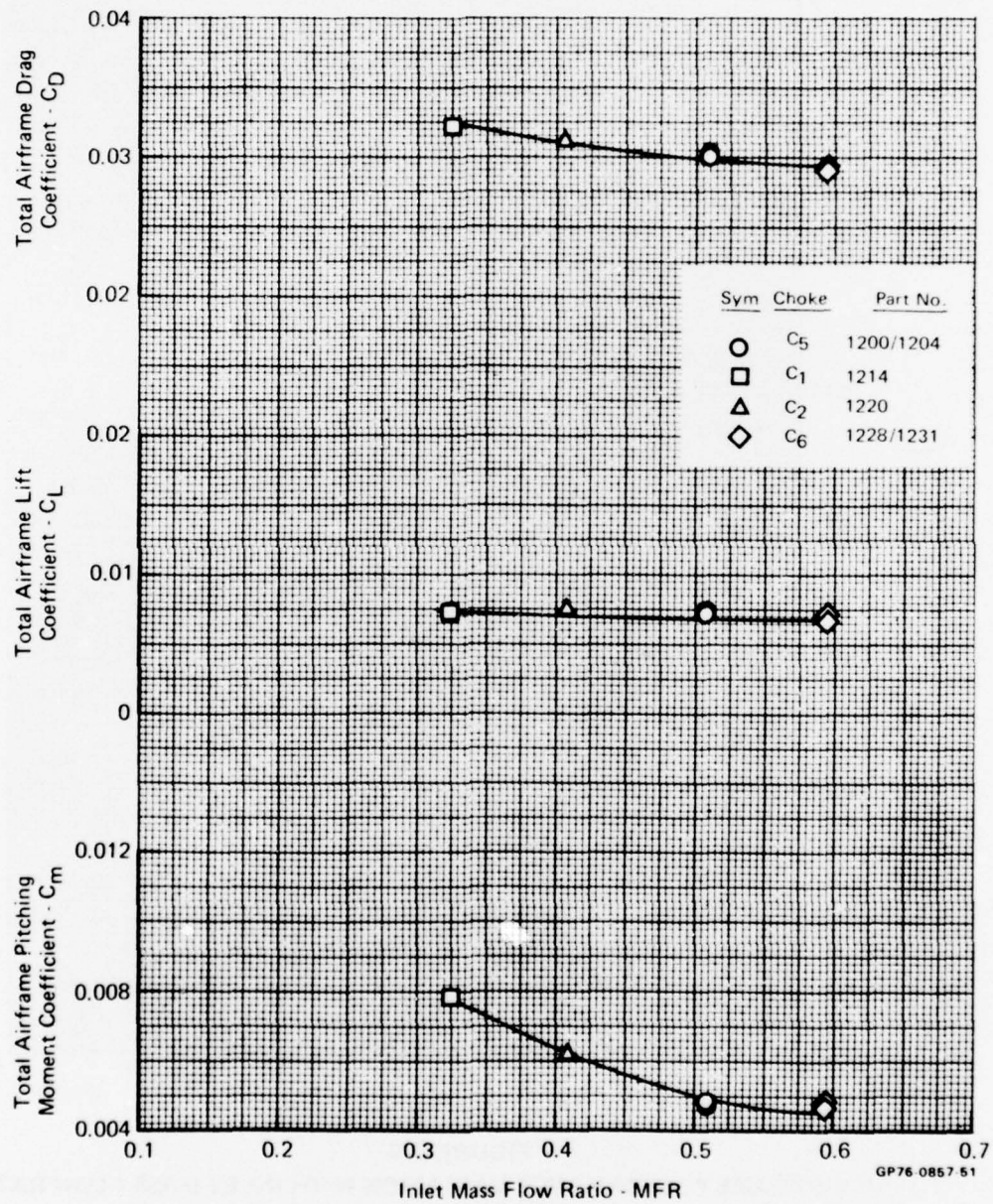


FIGURE D-10
 TOTAL AIRFRAME PERFORMANCE VARIATION WITH INLET MASS FLOW RATIO

Test Mode - Aero Flow Thru
 Nozzle Choke - As Noted
 Mach No. - 1.2
 Angle of Attack - 5°

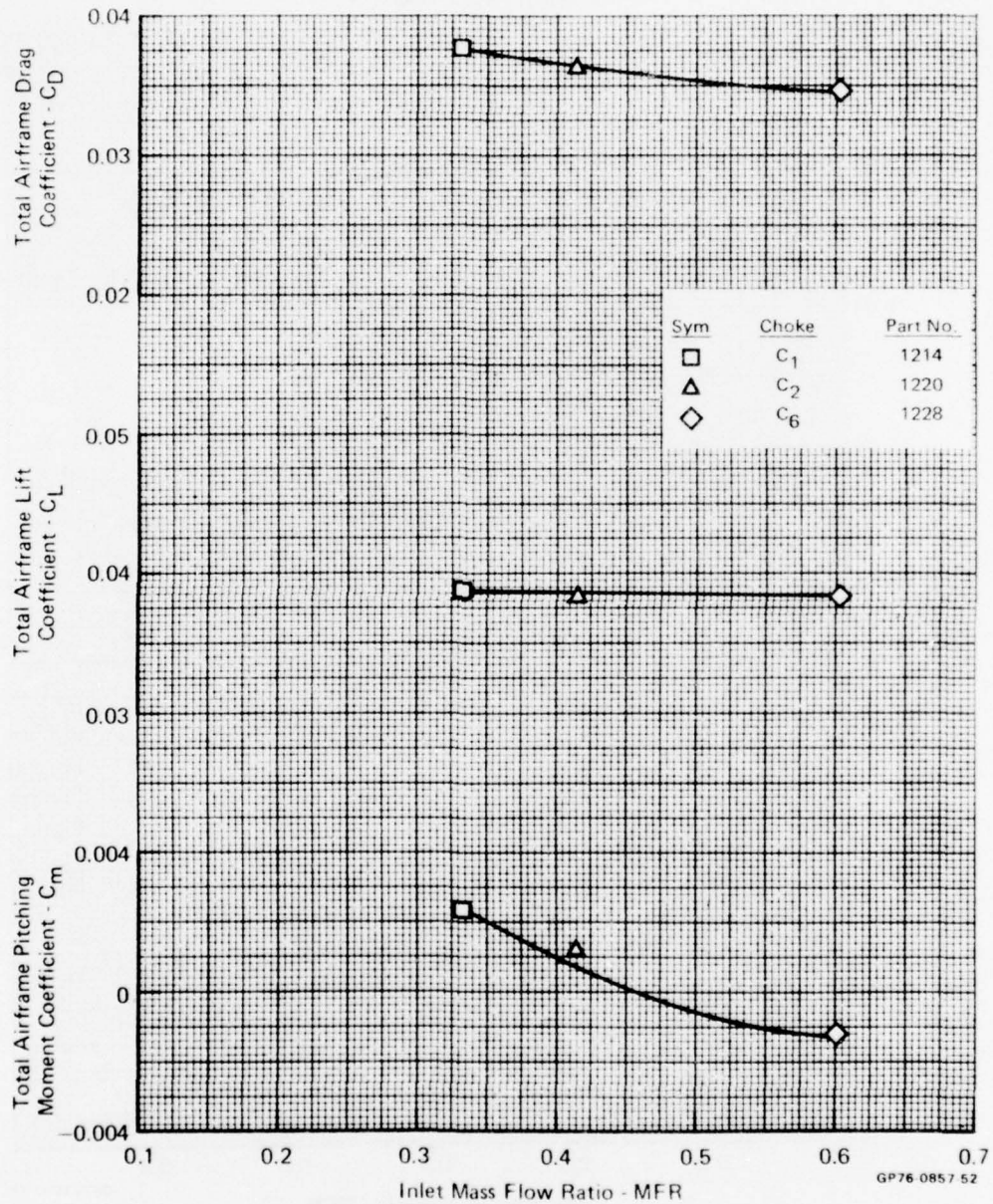


FIGURE D-11
 TOTAL AIRFRAME PERFORMANCE VARIATION WITH INLET MASS FLOW RATIO

Test Mode - Aero Flow-Thru
 Nozzle Choke - As Noted
 Mach No. - 1.2
 Angle of Attack - 10°

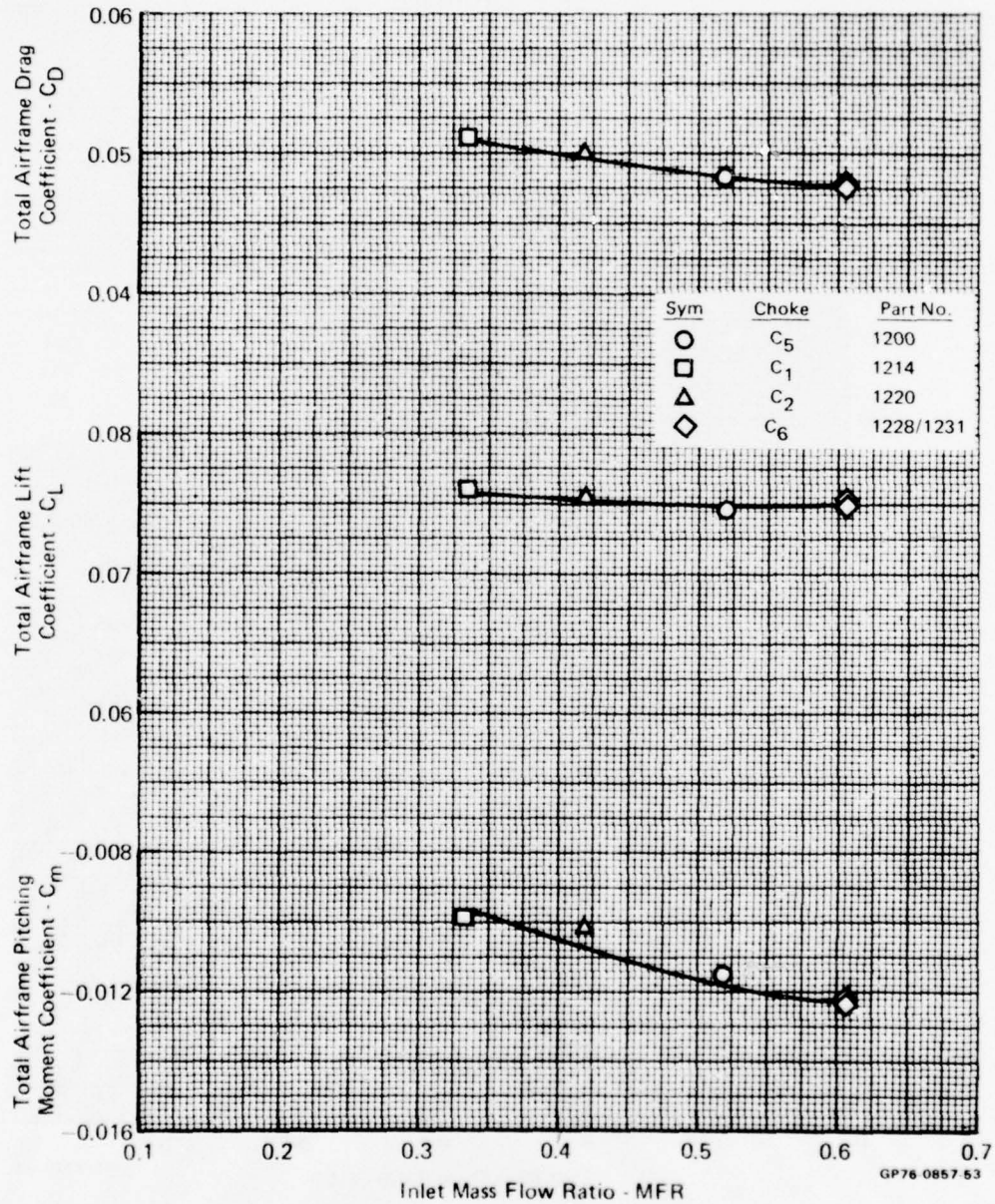


FIGURE D-12
 TOTAL AIRFRAME PERFORMANCE VARIATION WITH INLET MASS FLOW RATIO

Test Mode - Aero Flow-Thru
 Nozzle Choke - As Noted
 Mach No. - 1.2
 Angle of Attack - 16°

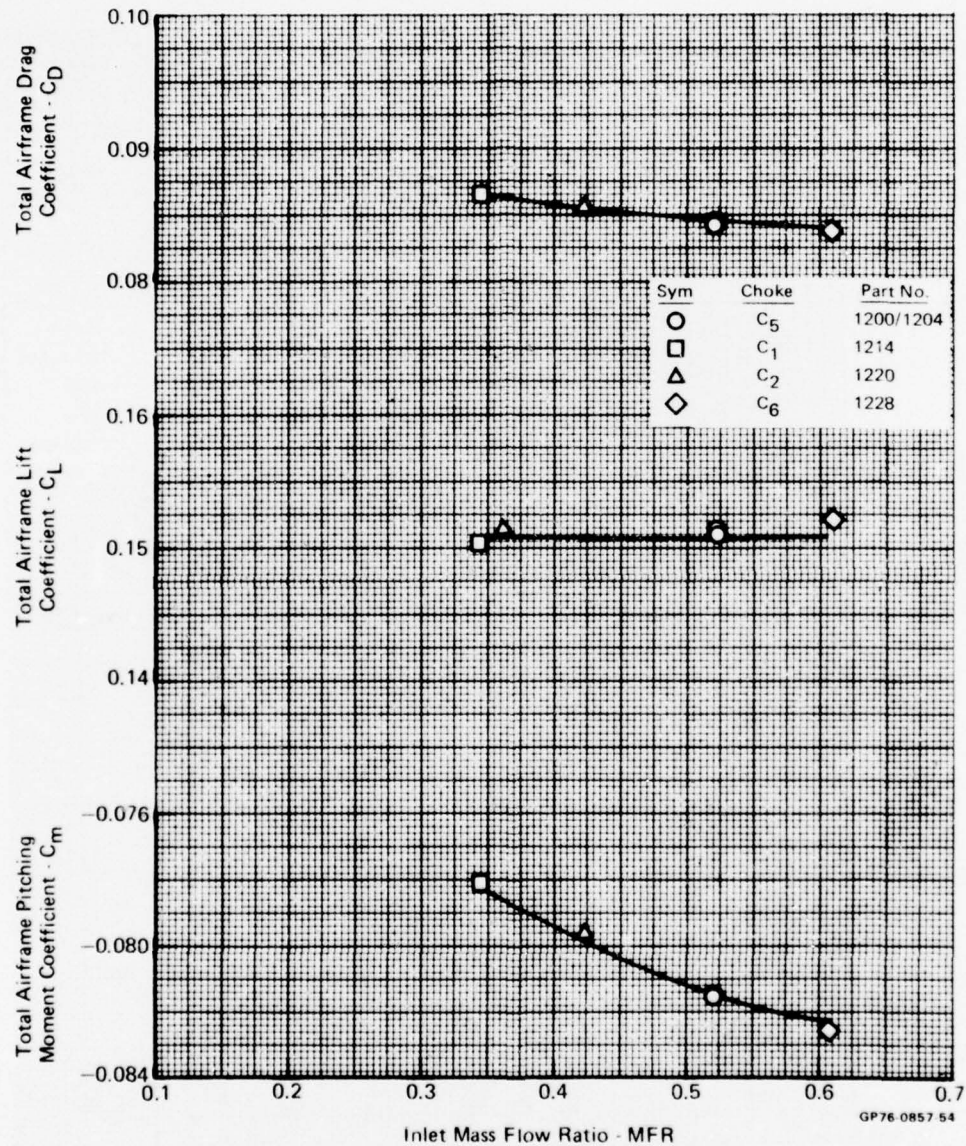


FIGURE D-13
 TOTAL AIRFRAME PERFORMANCE VARIATION WITH INLET MASS FLOW RATIO

Test Mode - Aero Flow Thru
 Nozzle Choke - As Noted
 Mach No. - 1.45
 Angle of Attack - 0°

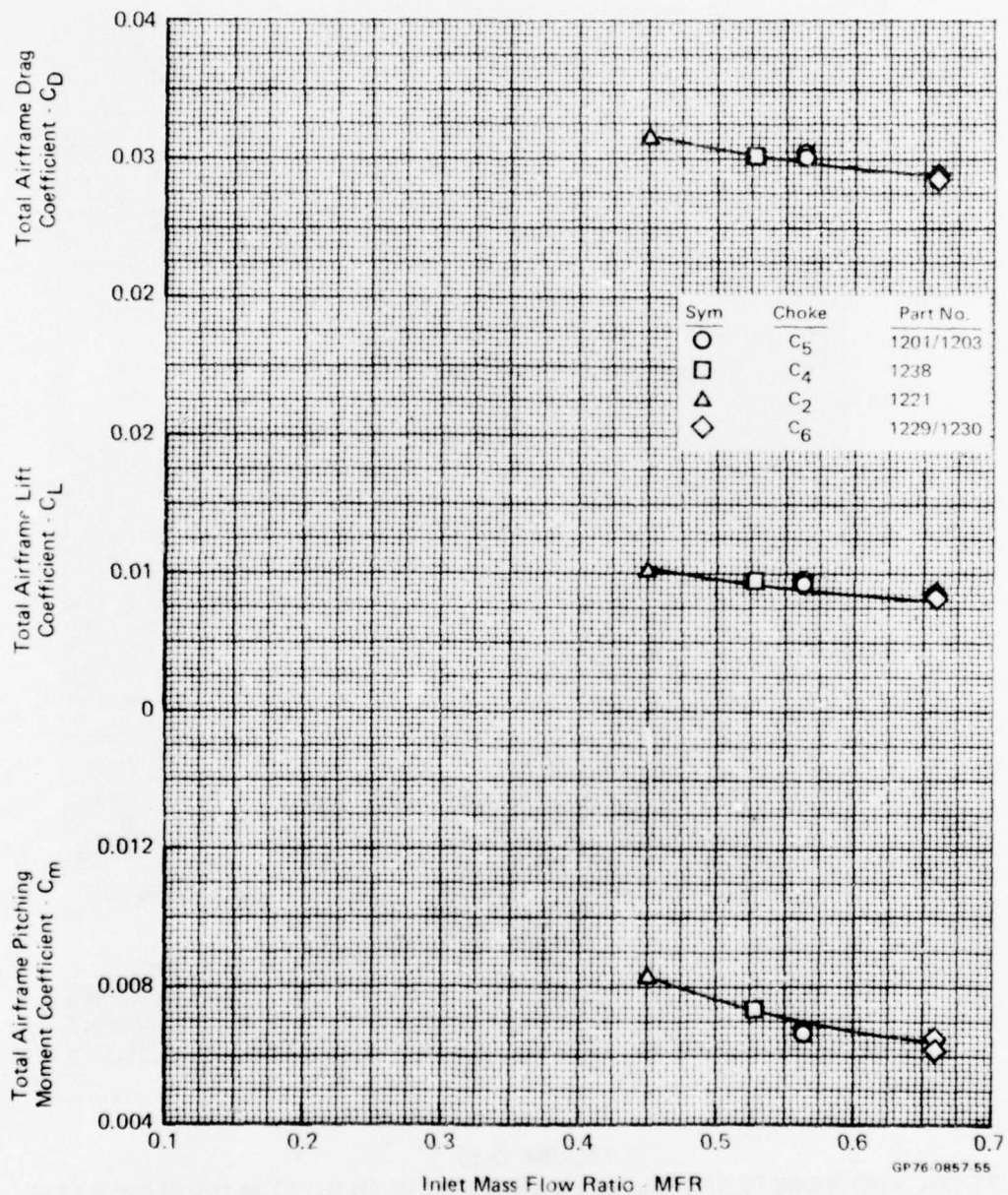


FIGURE D-14
 TOTAL AIRFRAME PERFORMANCE VARIATION WITH INLET MASS FLOW RATIO

Test Mode - Aero Flow-Thru
 Nozzle Choke - As Noted
 Mach No. - 1.45
 Angle of Attack - 3°

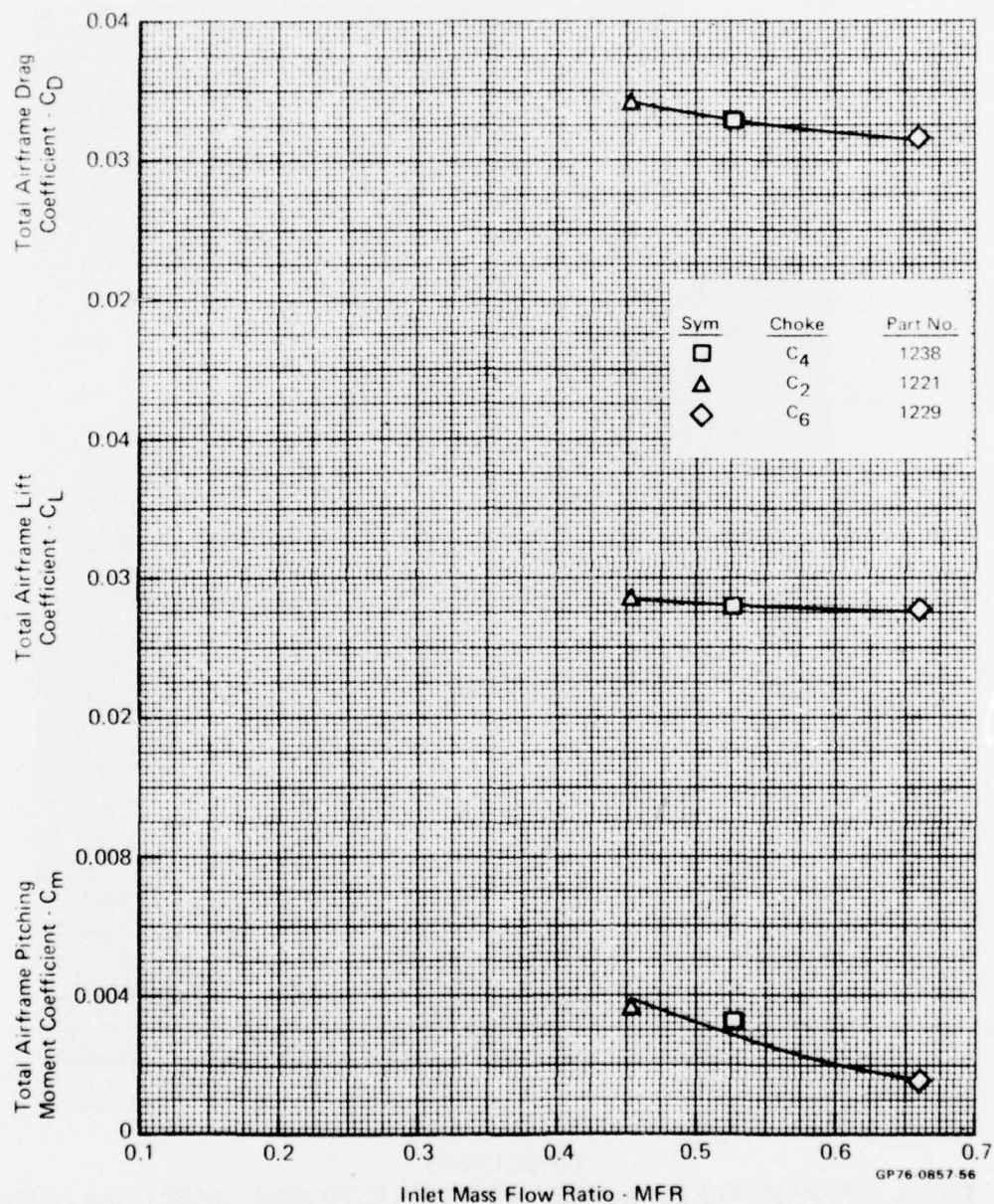


FIGURE D-15
TOTAL AIRFRAME PERFORMANCE VARIATION WITH INLET MASS FLOW RATIO

Test Mode - Aero Flow-Thru
 Nozzle Choke - As Noted
 Mach No. - 1.45
 Angle of Attack - 6°

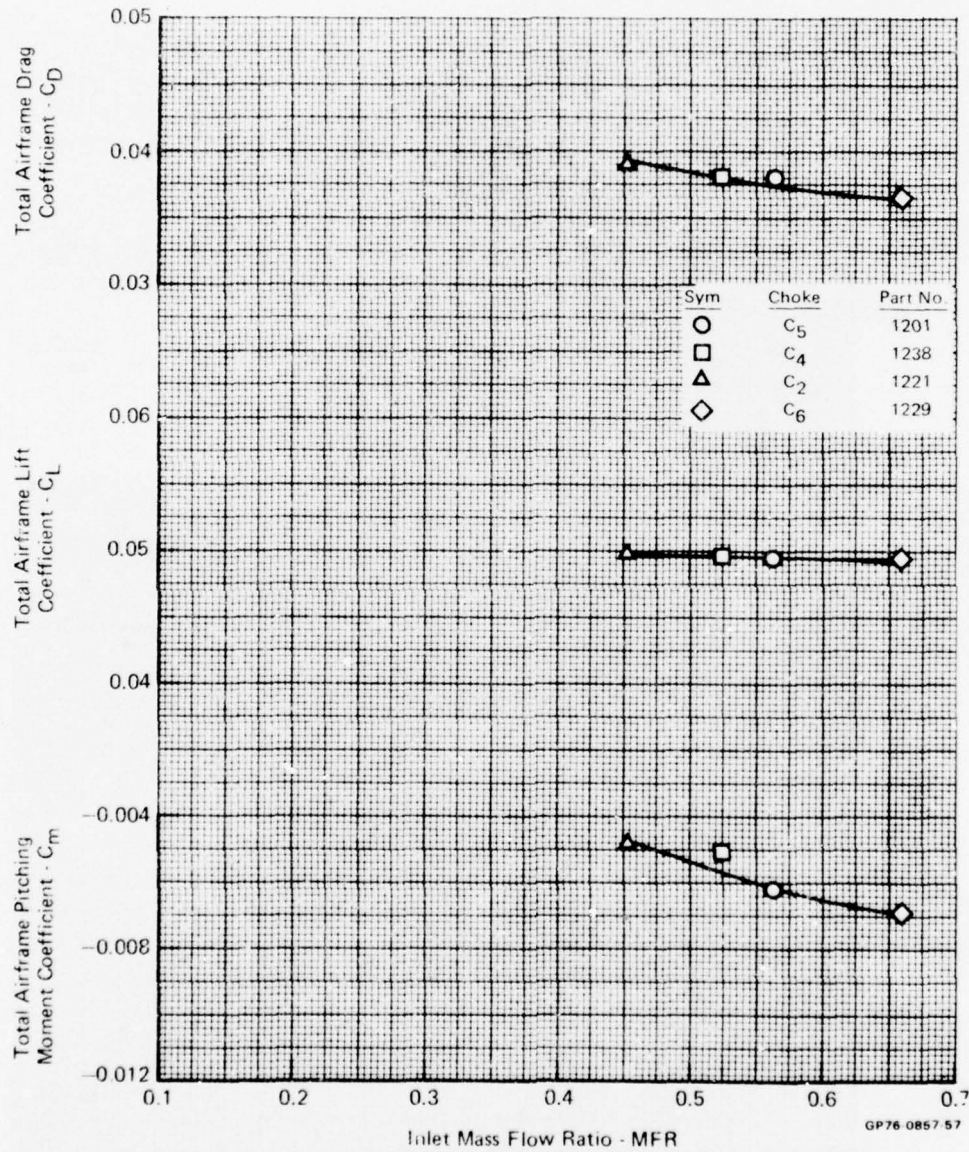


FIGURE D-16
 TOTAL AIRFRAME PERFORMANCE VARIATION WITH INLET MASS FLOW RATIO

Test Mode - Aero Flow-Thru
 Nozzle Choke - As Noted
 Mach No. - 1.45
 Angle of Attack - 10^0

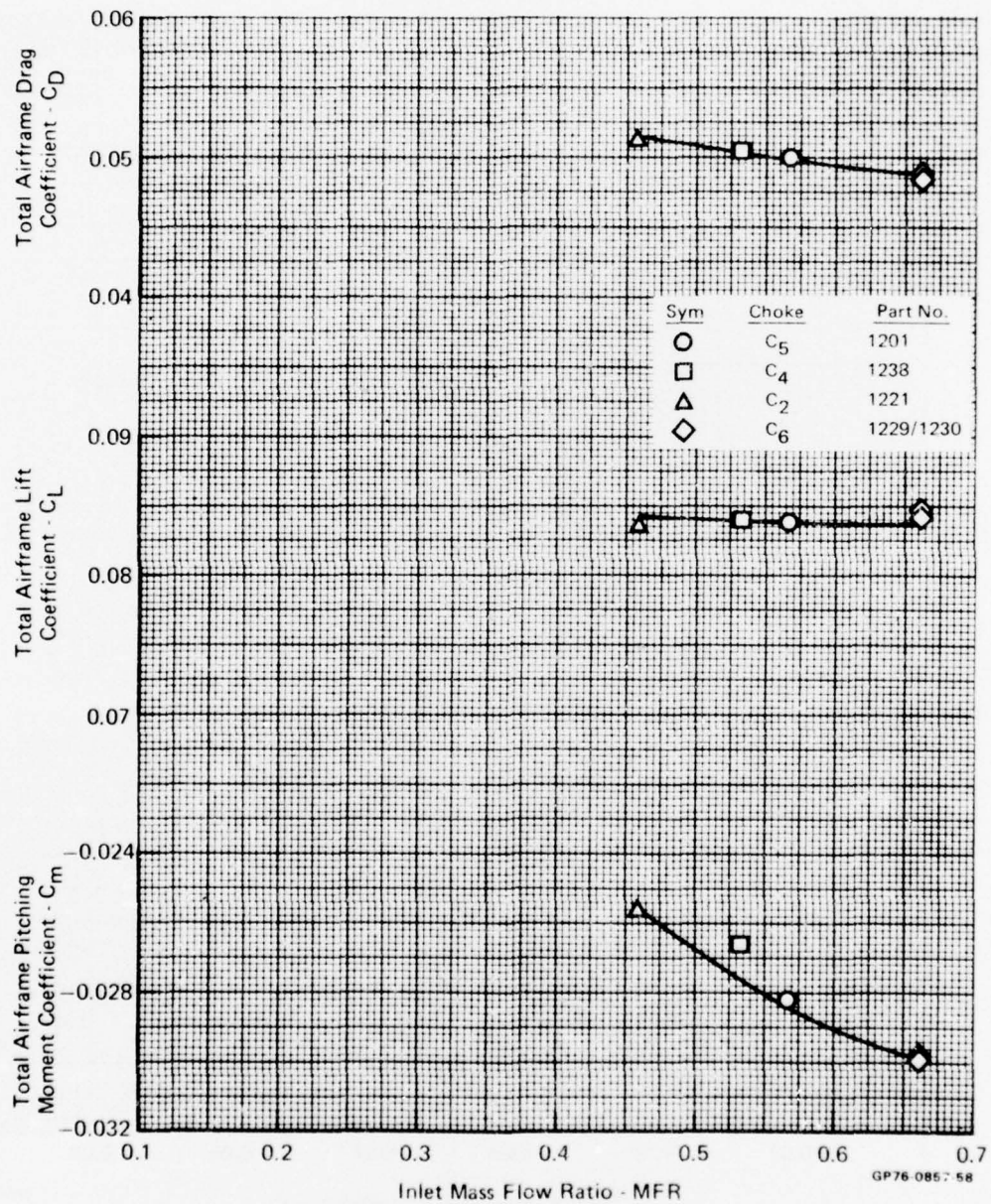


FIGURE D-17
 TOTAL AIRFRAME PERFORMANCE VARIATION WITH INLET MASS FLOW RATIO

Test Mode - Aero - Flow-Thru

Nozzle Choke - C_5

Mach No. - 0.6

MFR - 0.48

NPR - 1.26

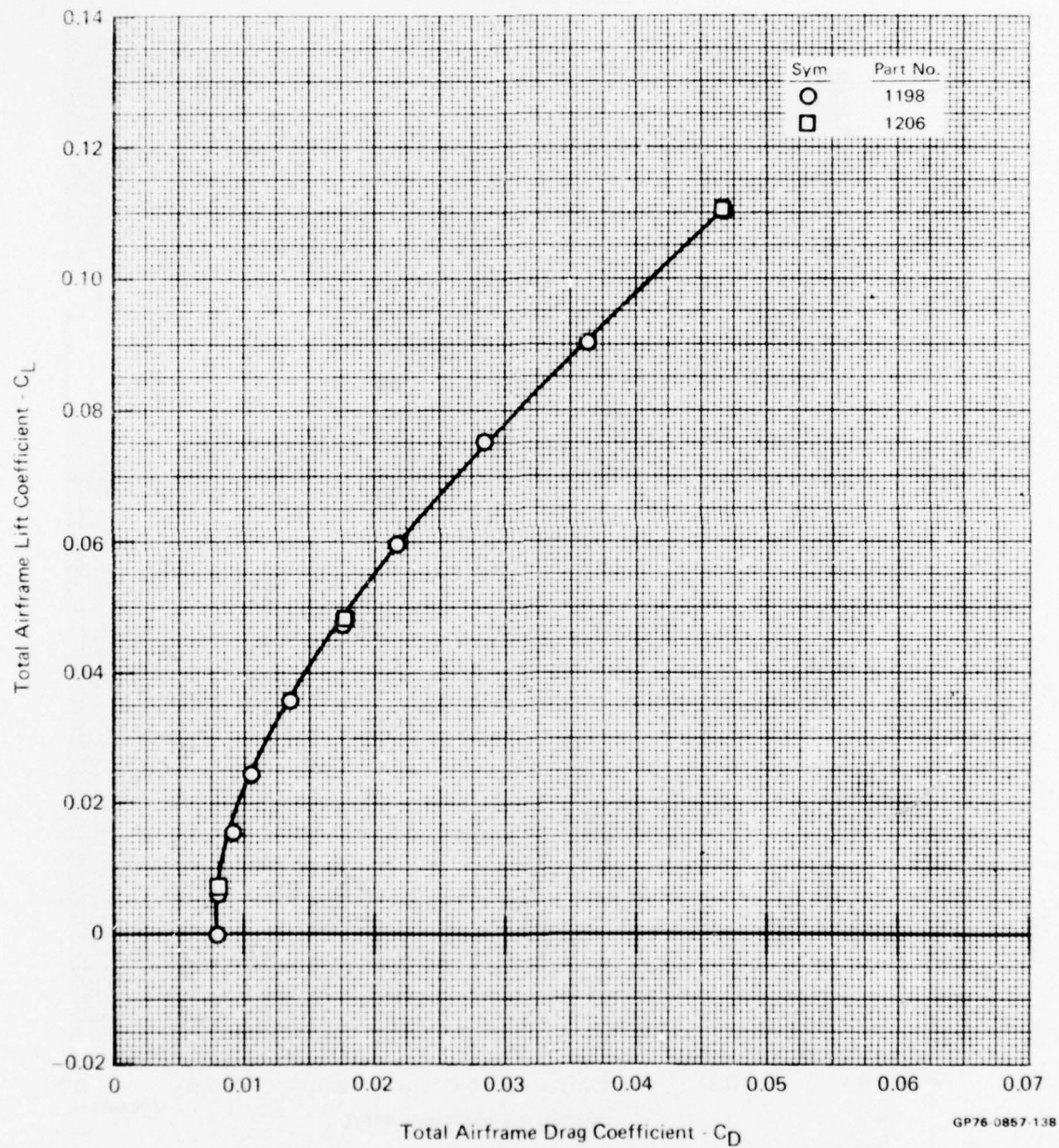


FIGURE D-18
TOTAL AIRFRAME LIFT/DRAG POLAR

Test Mode - Aero Flow-Thru
Nozzle Choke - C₅
Mach No. - 0.6
MFR - 0.48
NPR - 1.26

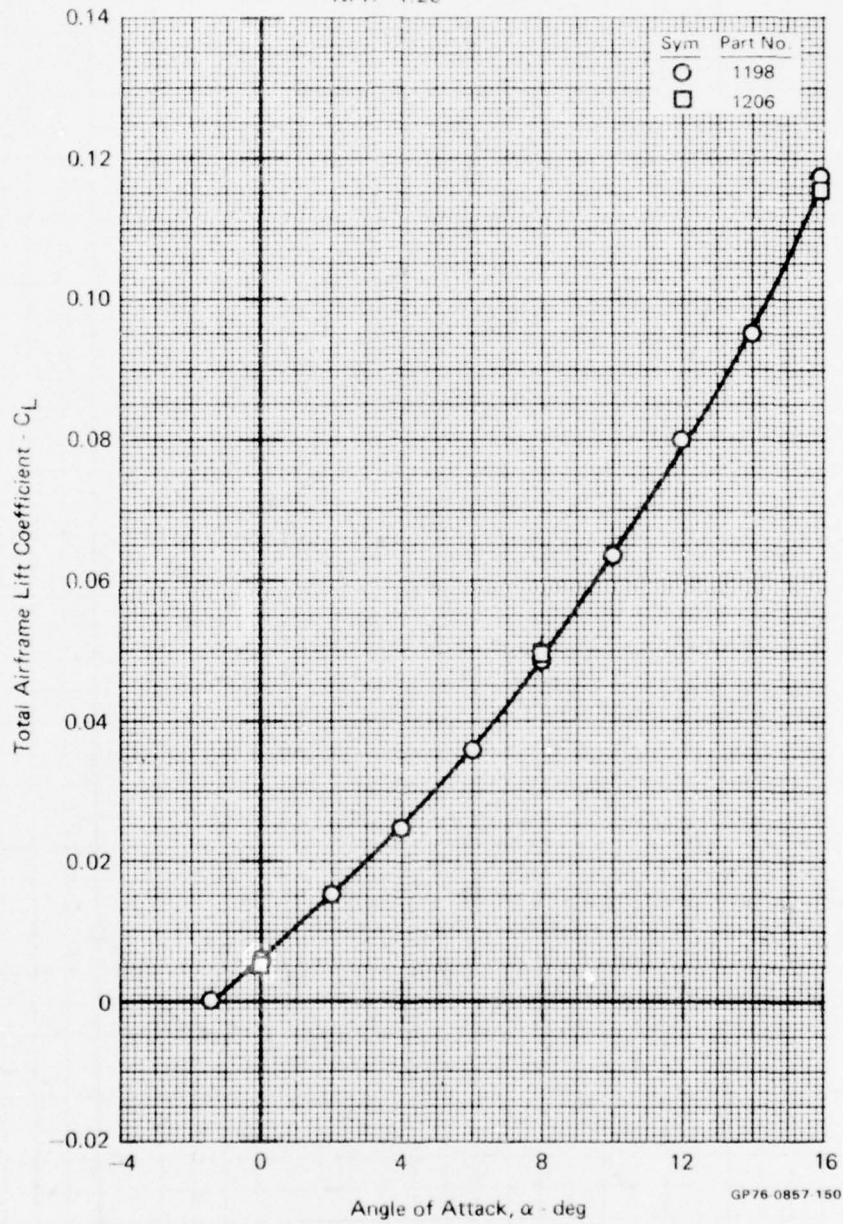


FIGURE D-19
TOTAL AIRFRAME LIFT VARIATION WITH ANGLE OF ATTACK

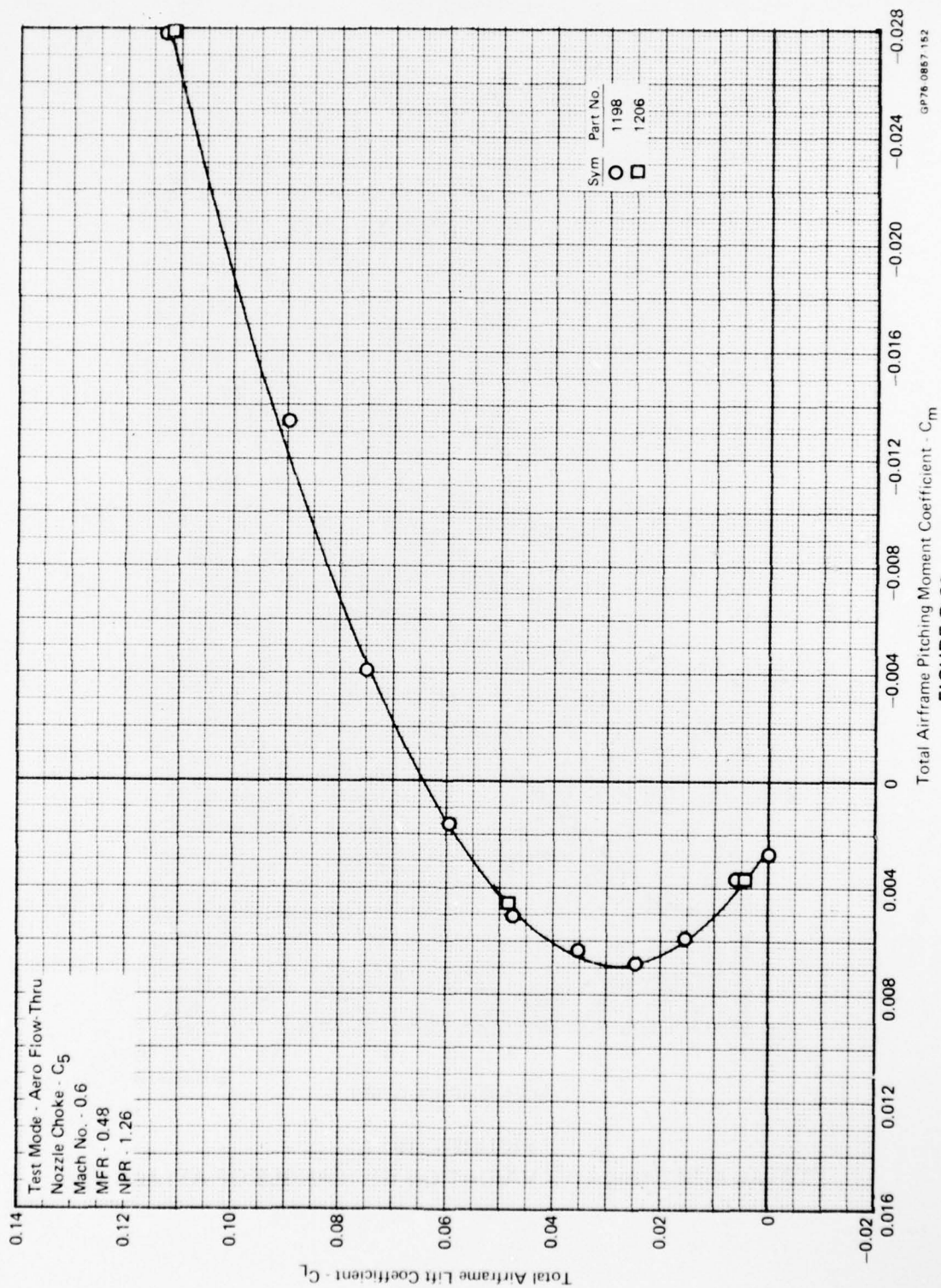


FIGURE D-20
 TOTAL AIRFRAME LIFT/PITCHING MOMENT VARIATION

Test Mode - Aero - Flow-Thru

Nozzle Choke - C_5

Mach No. - 0.9

MFR - 0.49

NPR - 1.66

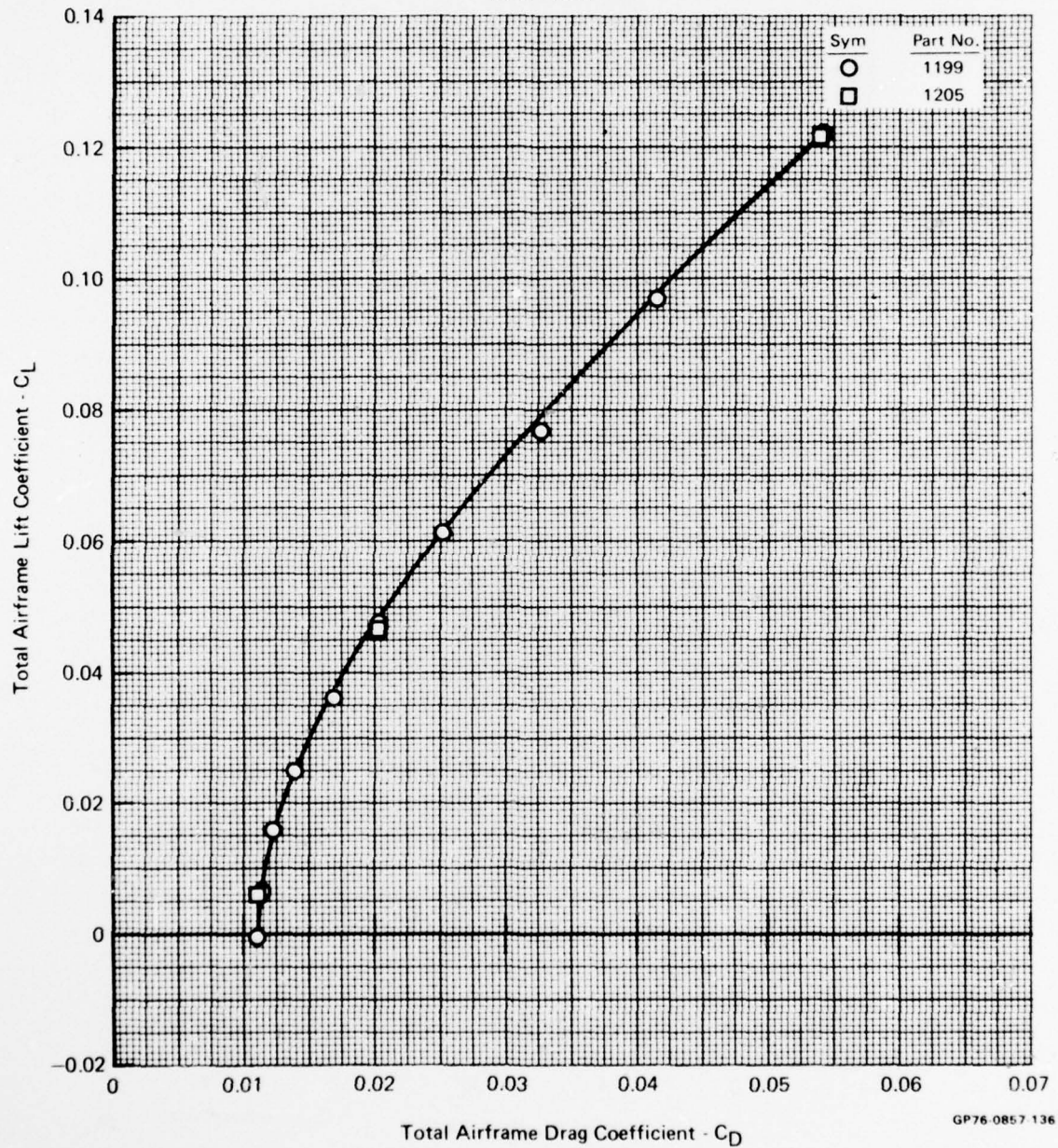


FIGURE D-21
TOTAL AIRFRAME LIFT/DRAG POLAR

Test Mode - Aero - Flow Thru

Nozzle Choke - C_5

Mach No. - 0.9

MFR - 0.49

NPR - 1.66

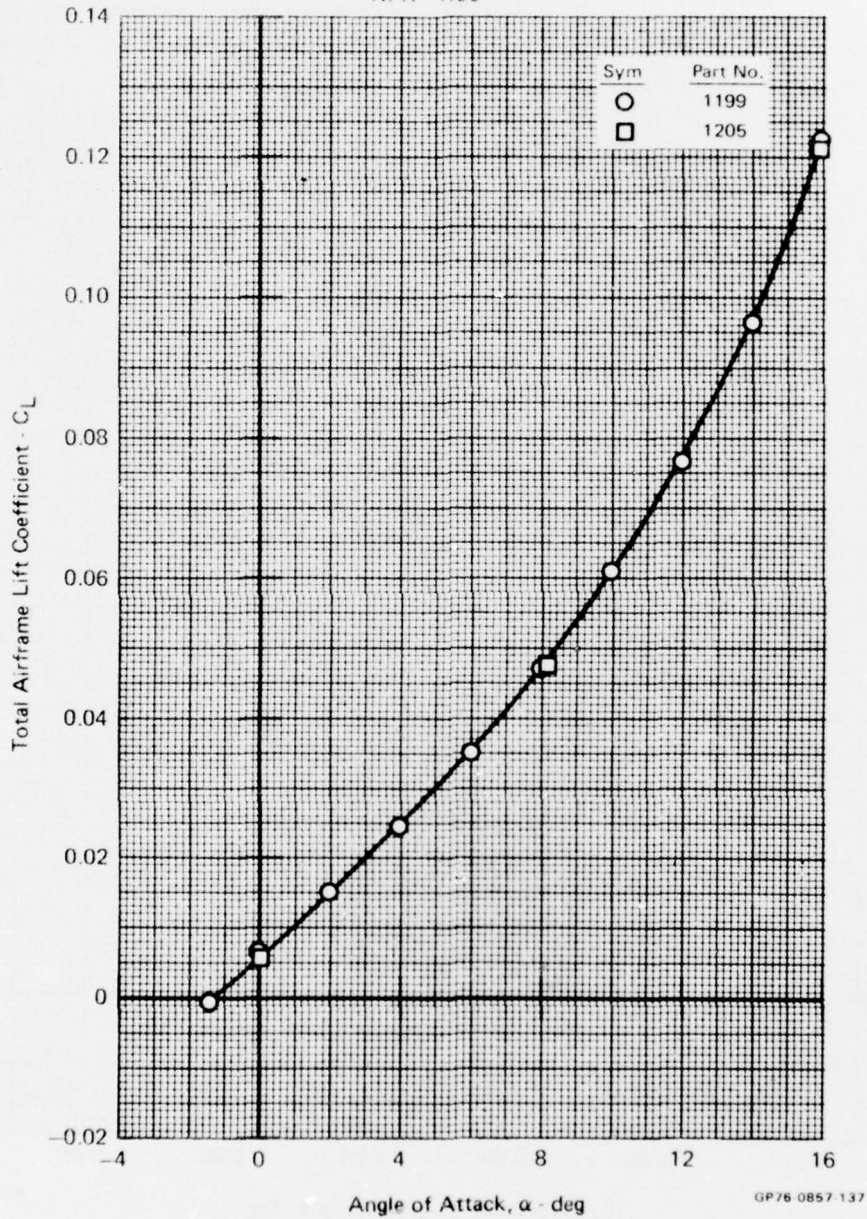


FIGURE D-22
TOTAL AIRFRAME LIFT VARIATION WITH ANGLE OF ATTACK

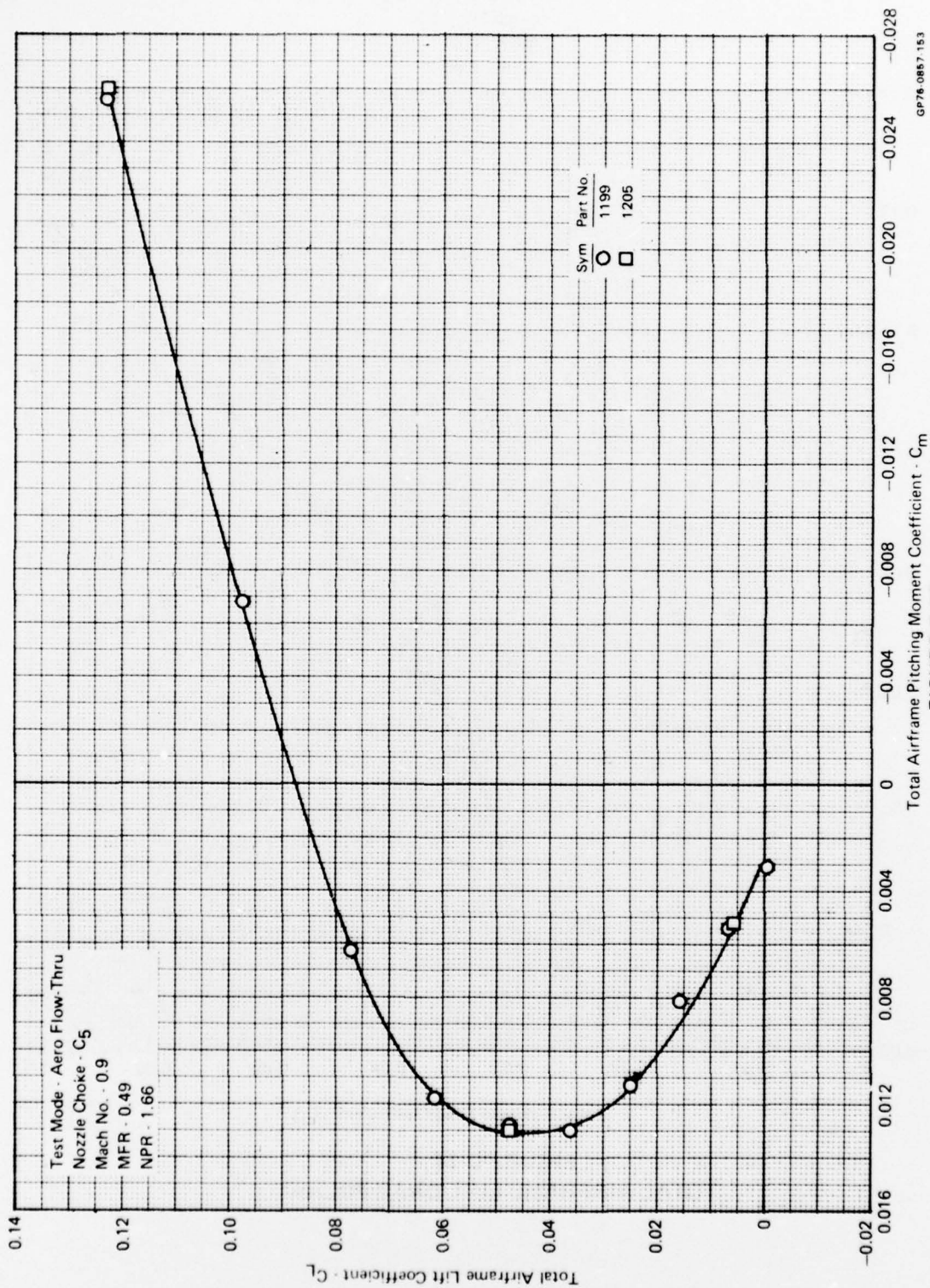


FIGURE D-23
 TOTAL AIRFRAME LIFT/PITCHING MOMENT VARIATION

Test Mode - Aero - Flow-Thru

Nozzle Choke - C_5

Mach No. - 1.2

MFR - 0.51

NPR - 2.36

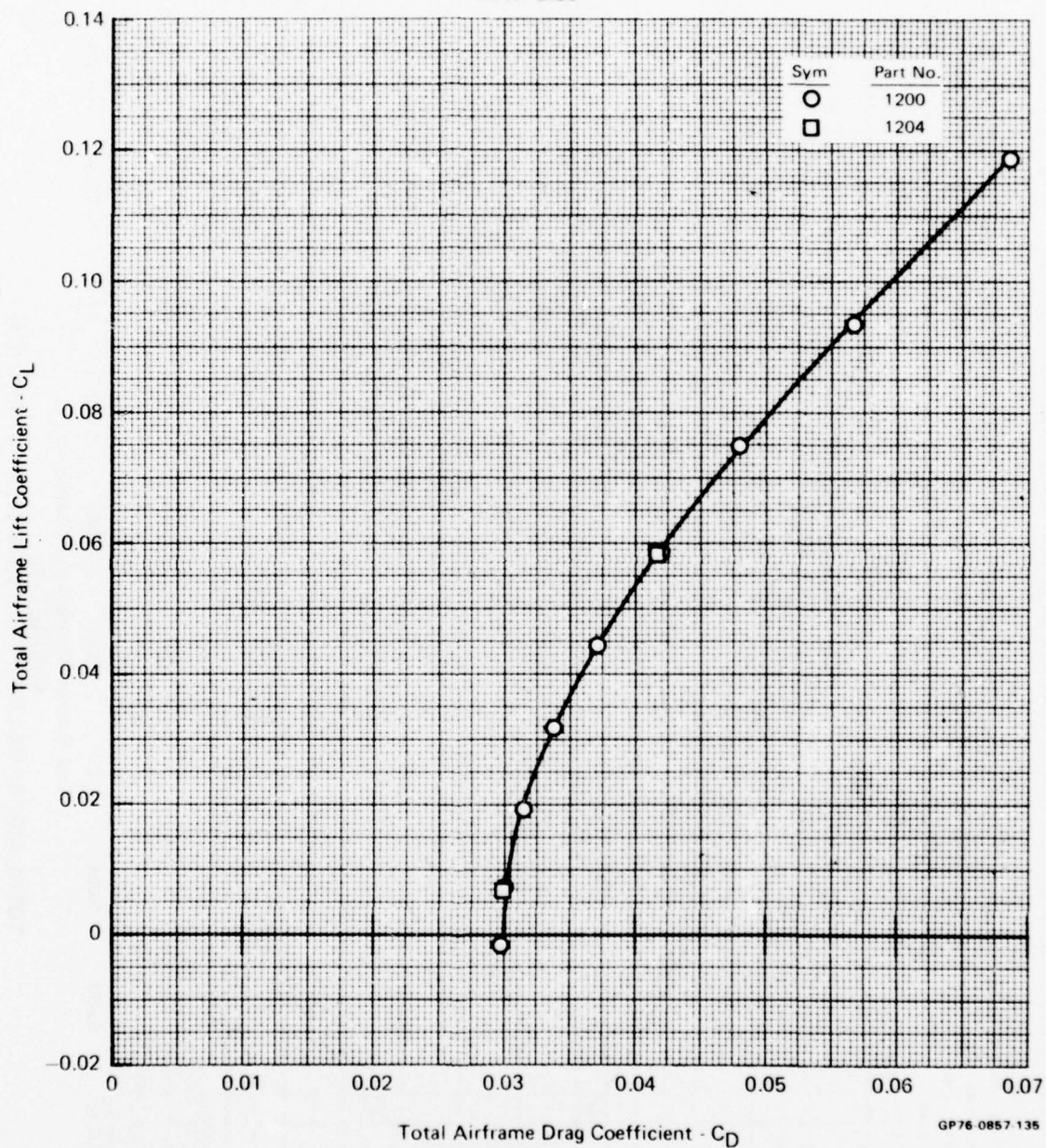


FIGURE D-24
TOTAL AIRFRAME LIFT/DRAGE POLAR

Test Mode - Aero Flow-Thru
 Nozzle Choke - C_5
 Mach No. - 1.2
 MFR - 0.51
 NPR - 2.36

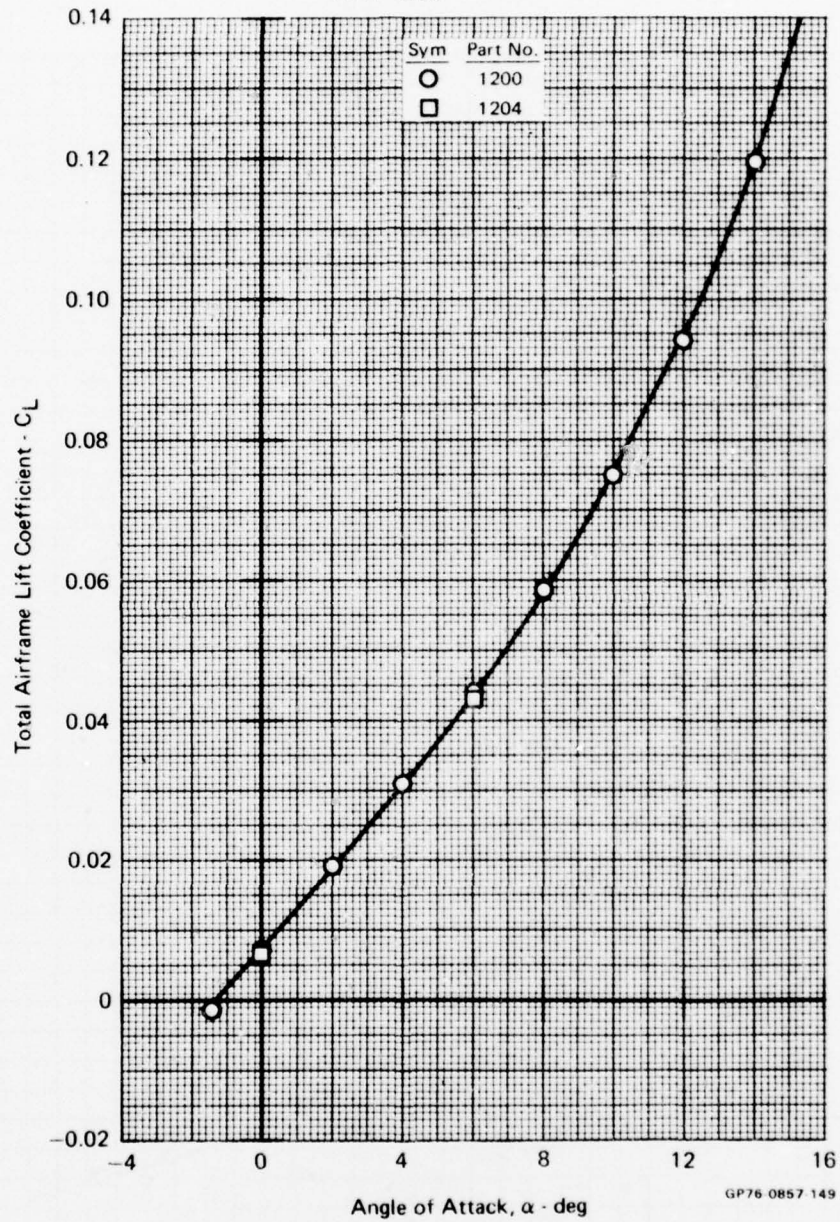


FIGURE D-25
 TOTAL AIRFRAME LIFT VARIATION WITH ANGLE OF ATTACK

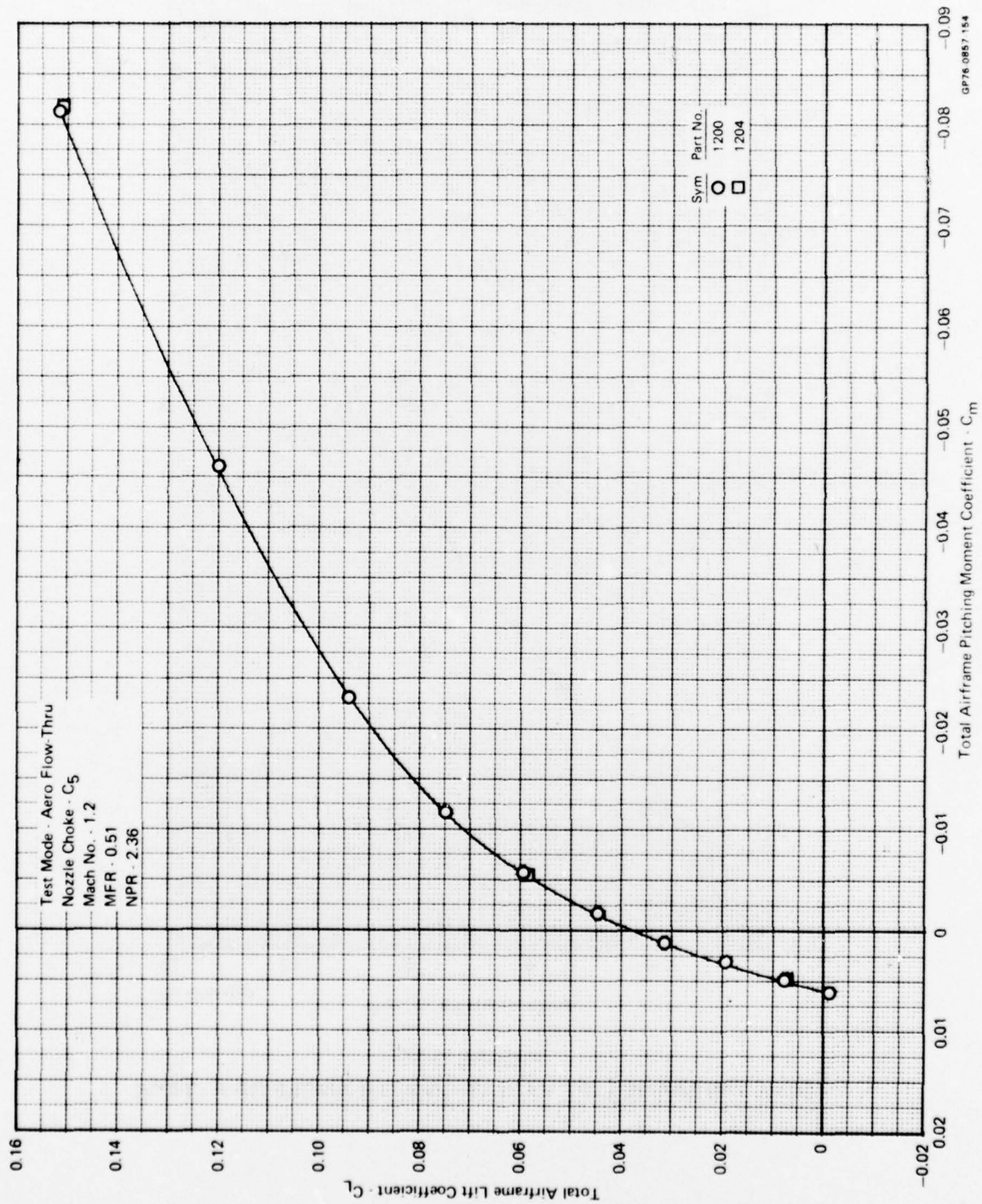


FIGURE D-26
 TOTAL AIRFRAME LIFT/PITCHING MOMENT VARIATION

Test Mode - Aero - Flow-Thru

Nozzle Choke - C_5

Mach No. - 1.45

MFR - 0.56

NPR - 3.29

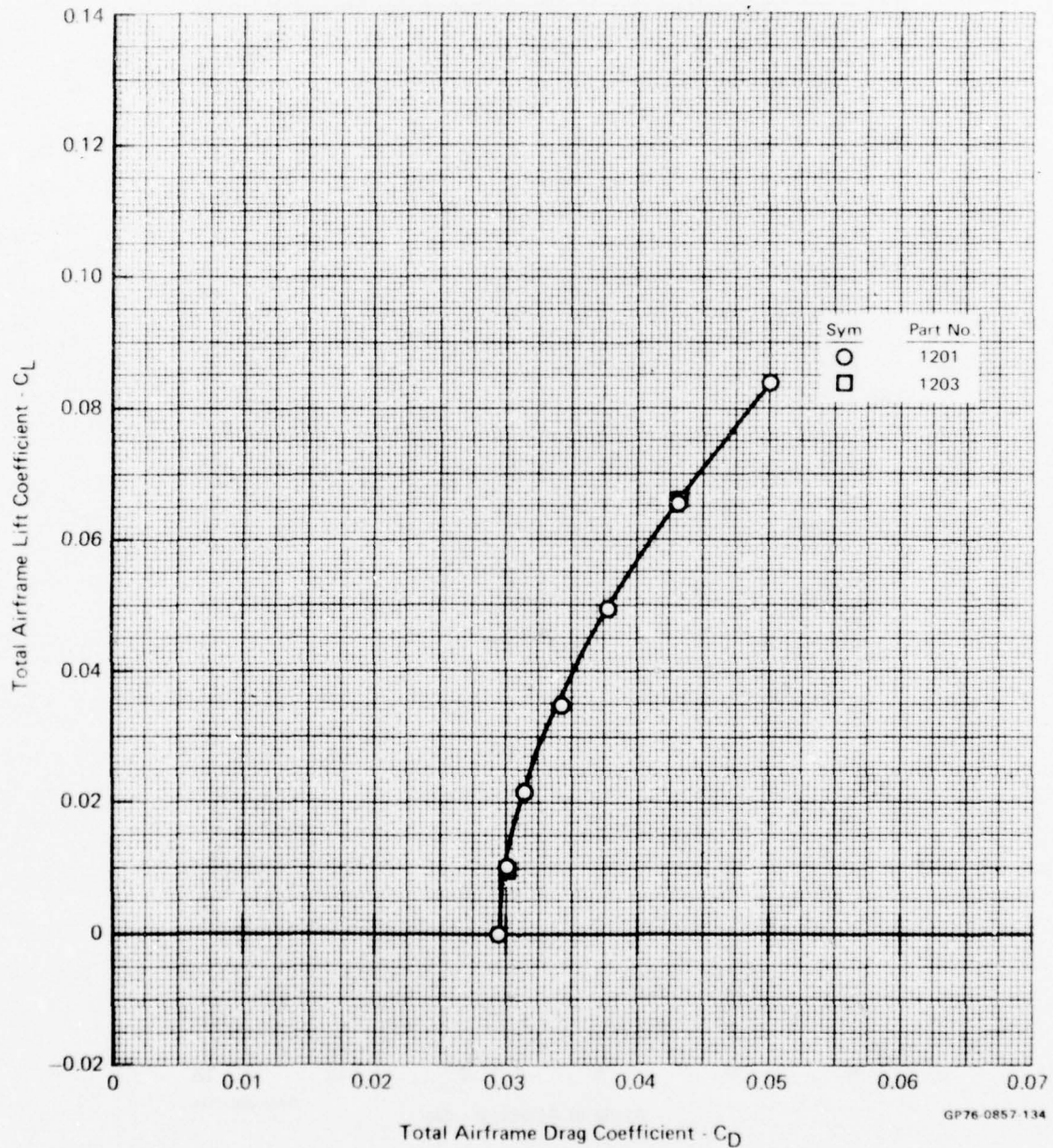


FIGURE D-27
TOTAL AIRFRAME LIFT/DRAG POLAR

Test Mode - Aero Flow-Thru
 Nozzle Choke - C_5
 Mach No. - 1.45
 MFR = 0.56
 NPR = 3.29

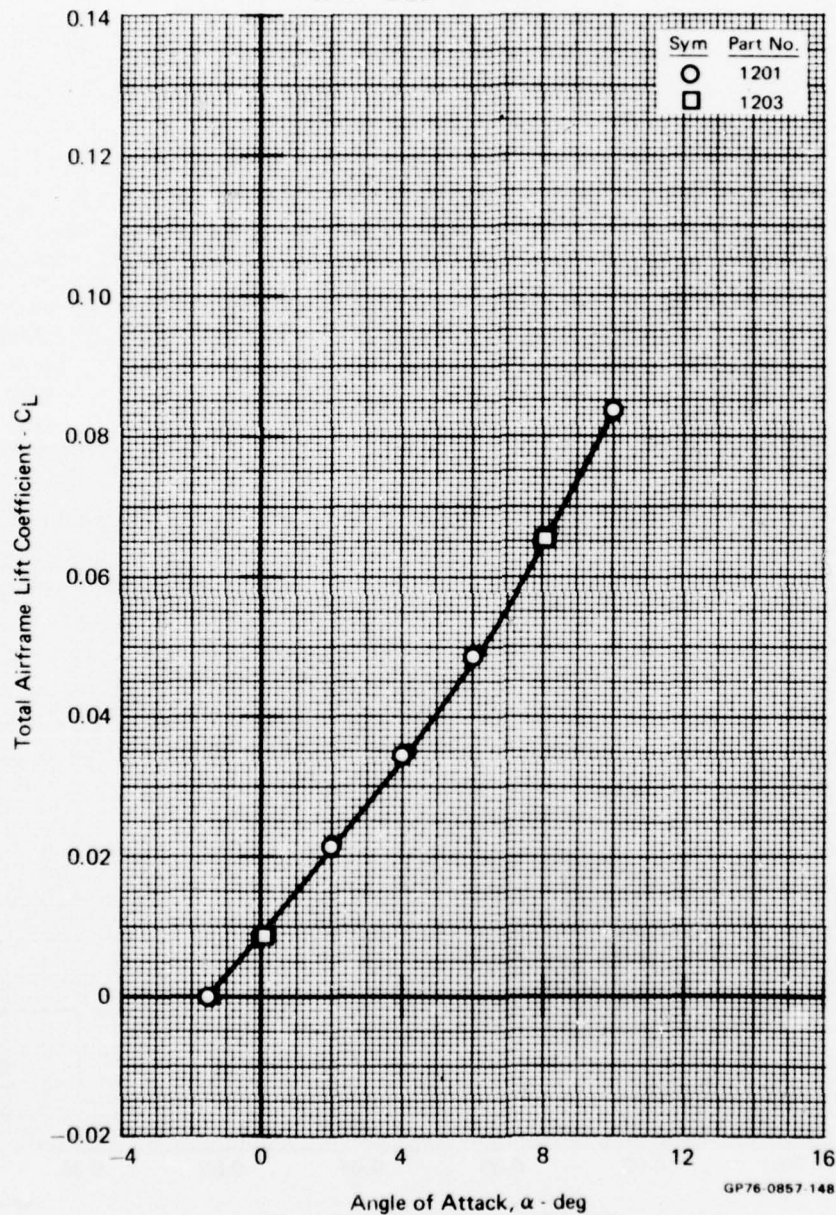


FIGURE D-28
TOTAL AIRFRAME LIFT VARIATION WITH ANGLE OF ATTACK

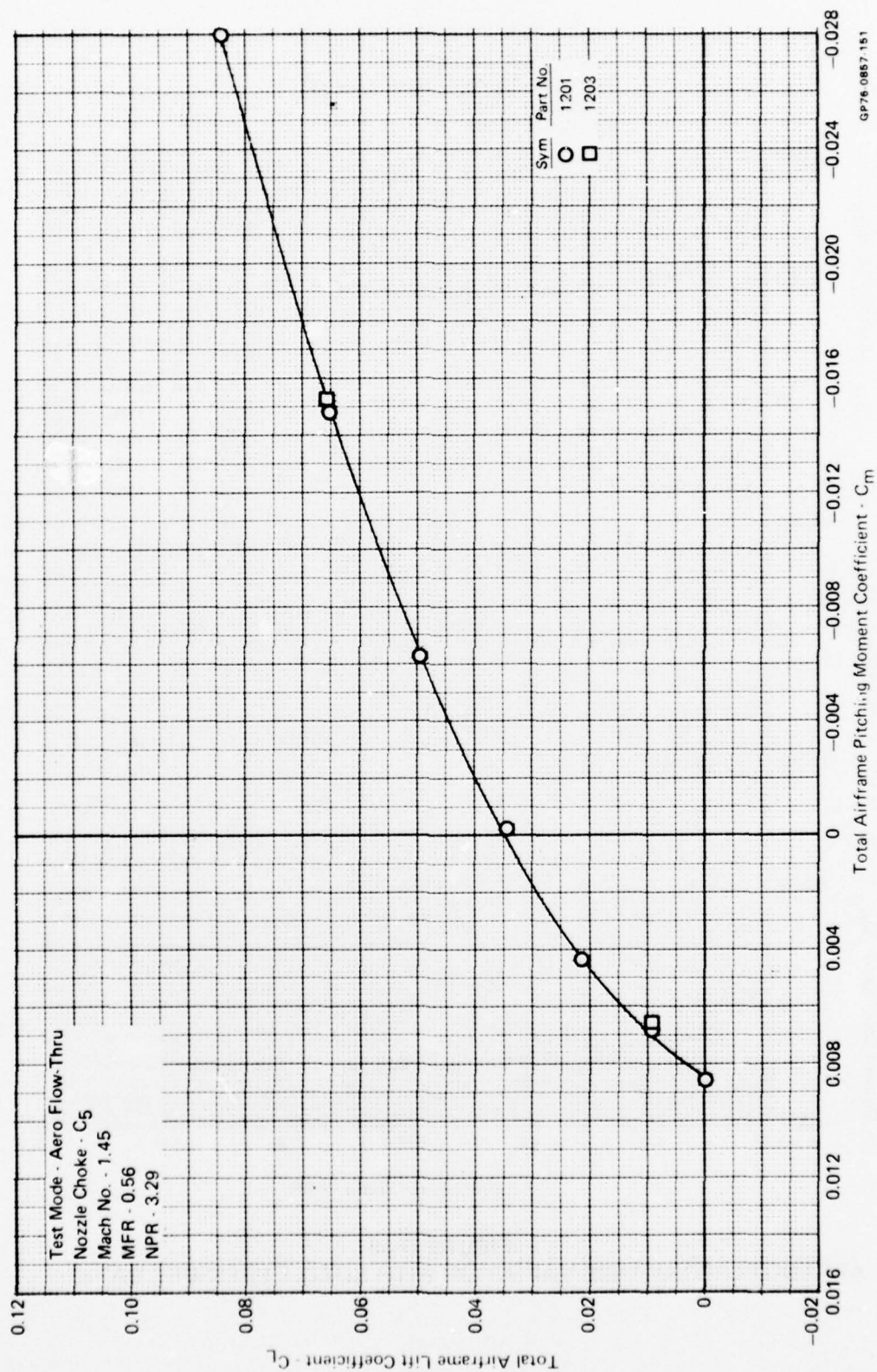


FIGURE D-29
 TOTAL AIRFRAME LIFT/PITCHING MOMENT VARIATION

Test Mode - Jet Effects
 Nozzle - Afterburning with Choke
 Mach No. - 0.6
 Angle of Attack - 0°

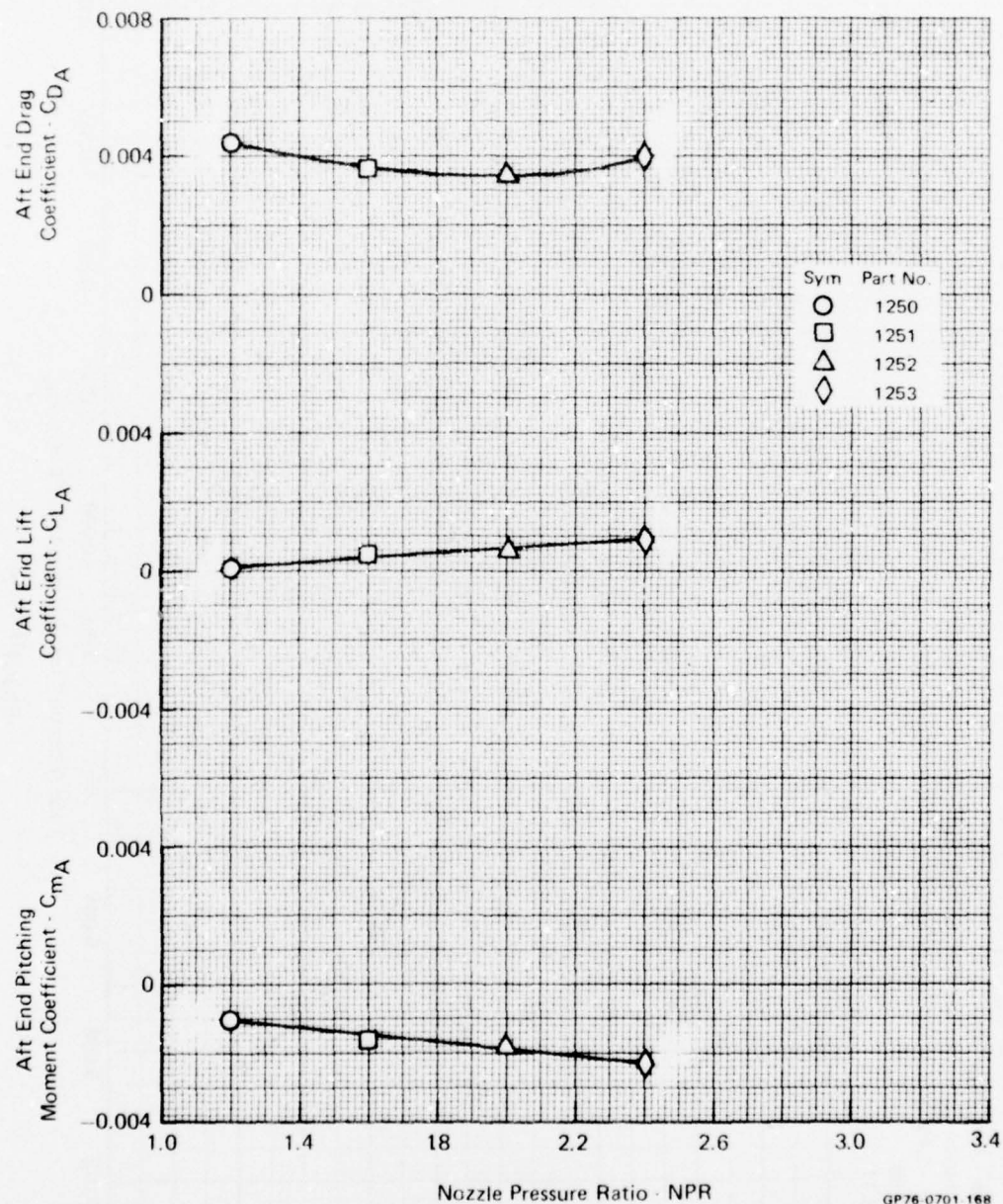


FIGURE D-30
AFT END PERFORMANCE VARIATION WITH NOZZLE PRESSURE RATIO

Test Mode - Jet Effects
 Nozzle - Afterburning with Choke
 Mach No. - 0.6
 Angle of Attack - 5°

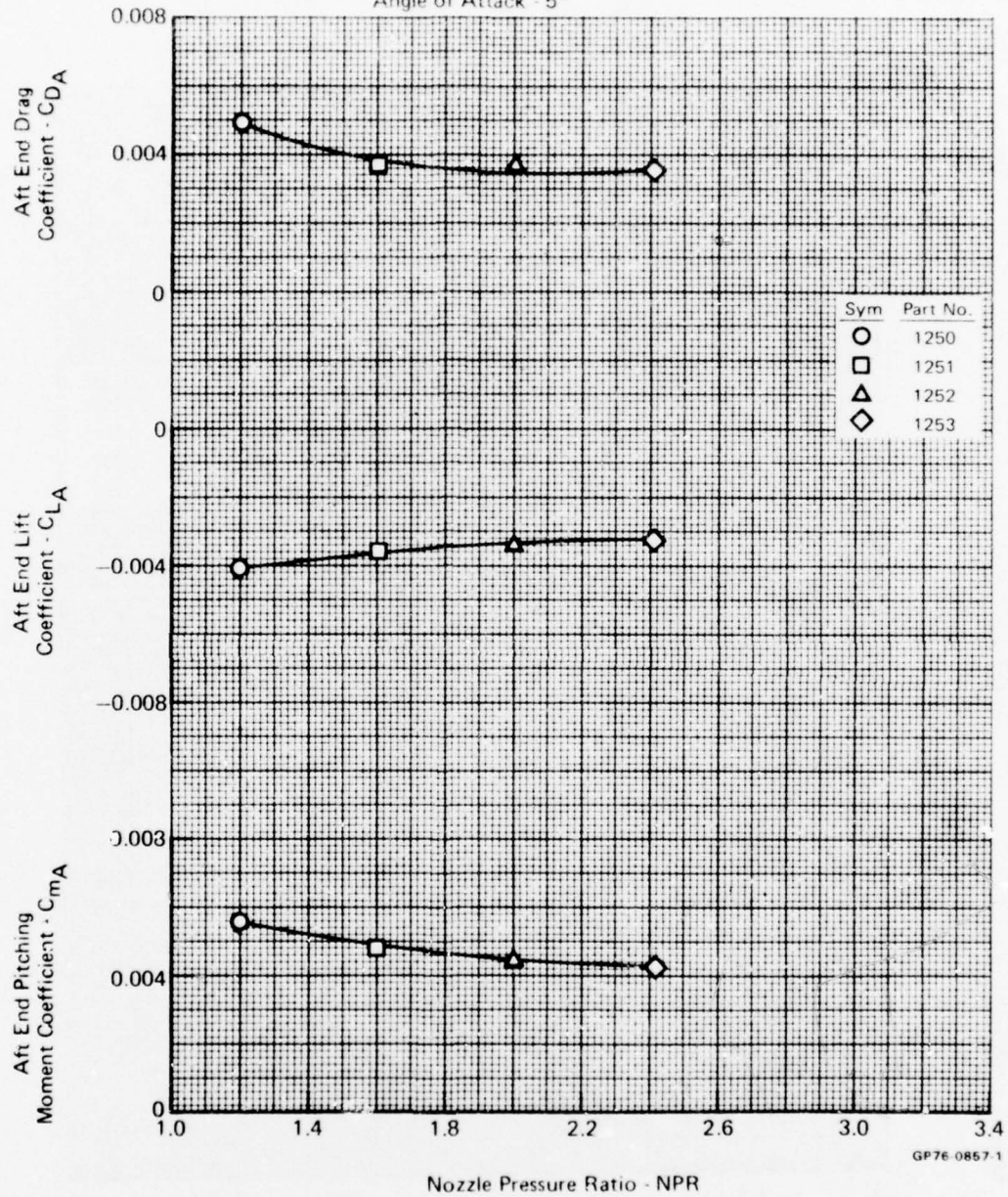


FIGURE D-31
AFT END PERFORMANCE VARIATION WITH NOZZLE PRESSURE RATIO

Test Mode - Jet Effects
 Nozzle - Afterburning with Choke
 Mach No. - 0.6
 Angle of Attack - 10°

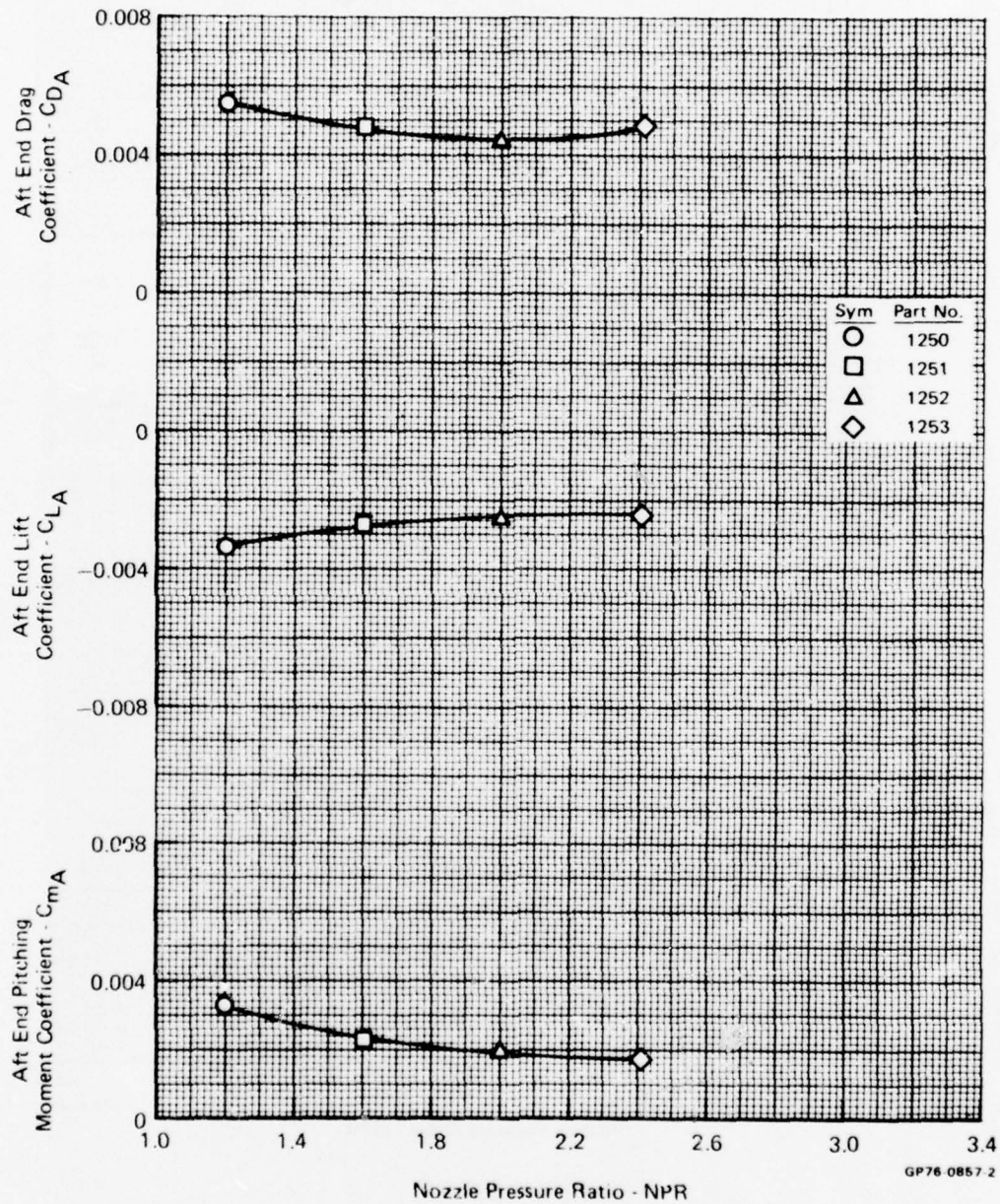


FIGURE D-32
 AFT END PERFORMANCE VARIATION WITH NOZZLE PRESSURE RATIO

Test Mode - Jet Effects
 Nozzle - Afterburning with Choke
 Mach No. - 0.6
 Angle of Attack - 16°

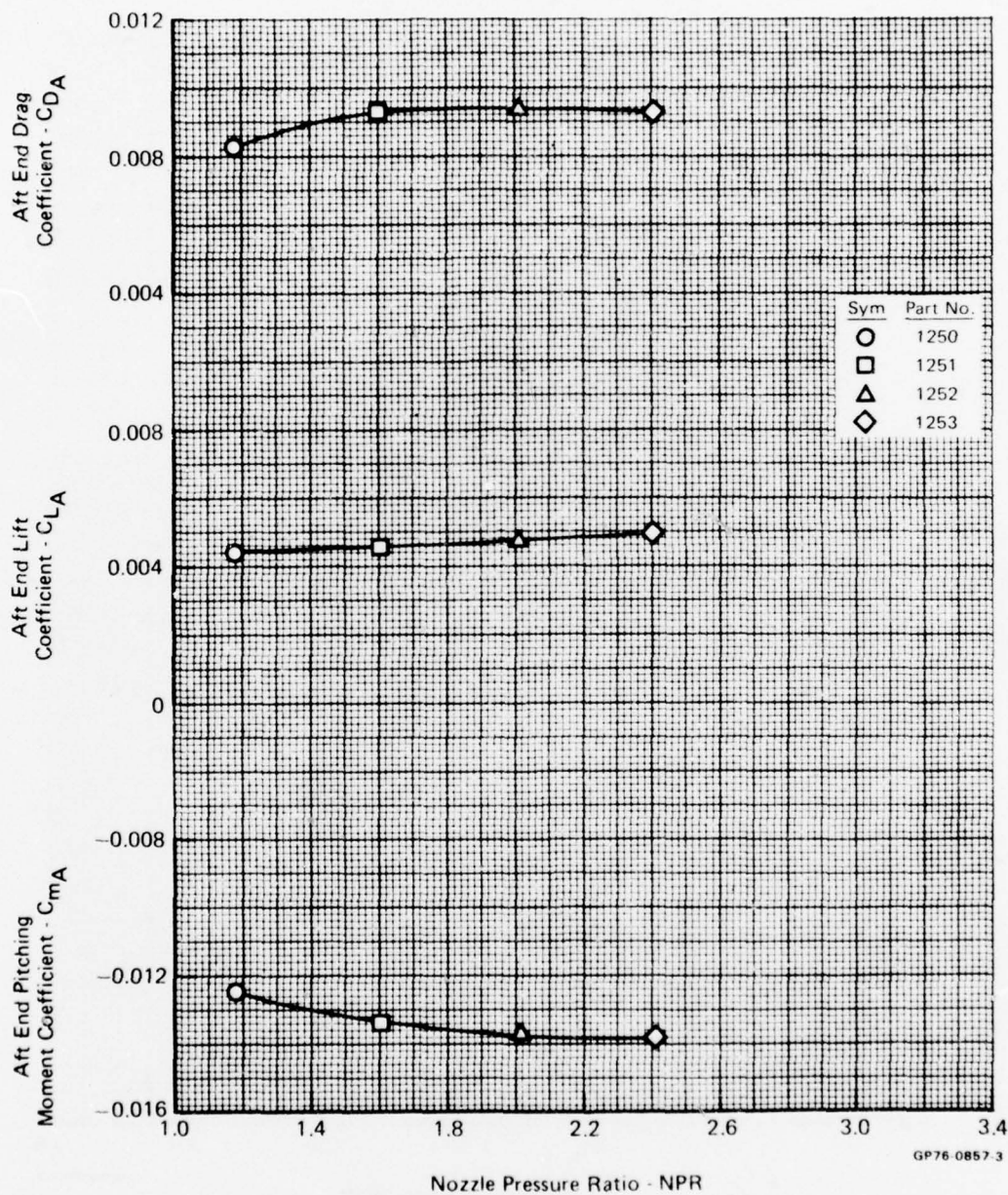


FIGURE D-33
 AFT END PERFORMANCE VARIATION WITH NOZZLE PRESSURE RATIO

Test Mode - Jet Effects
 Nozzle - Afterburning with Choke
 Mach No. - 0.9
 Angle of Attack - 0°

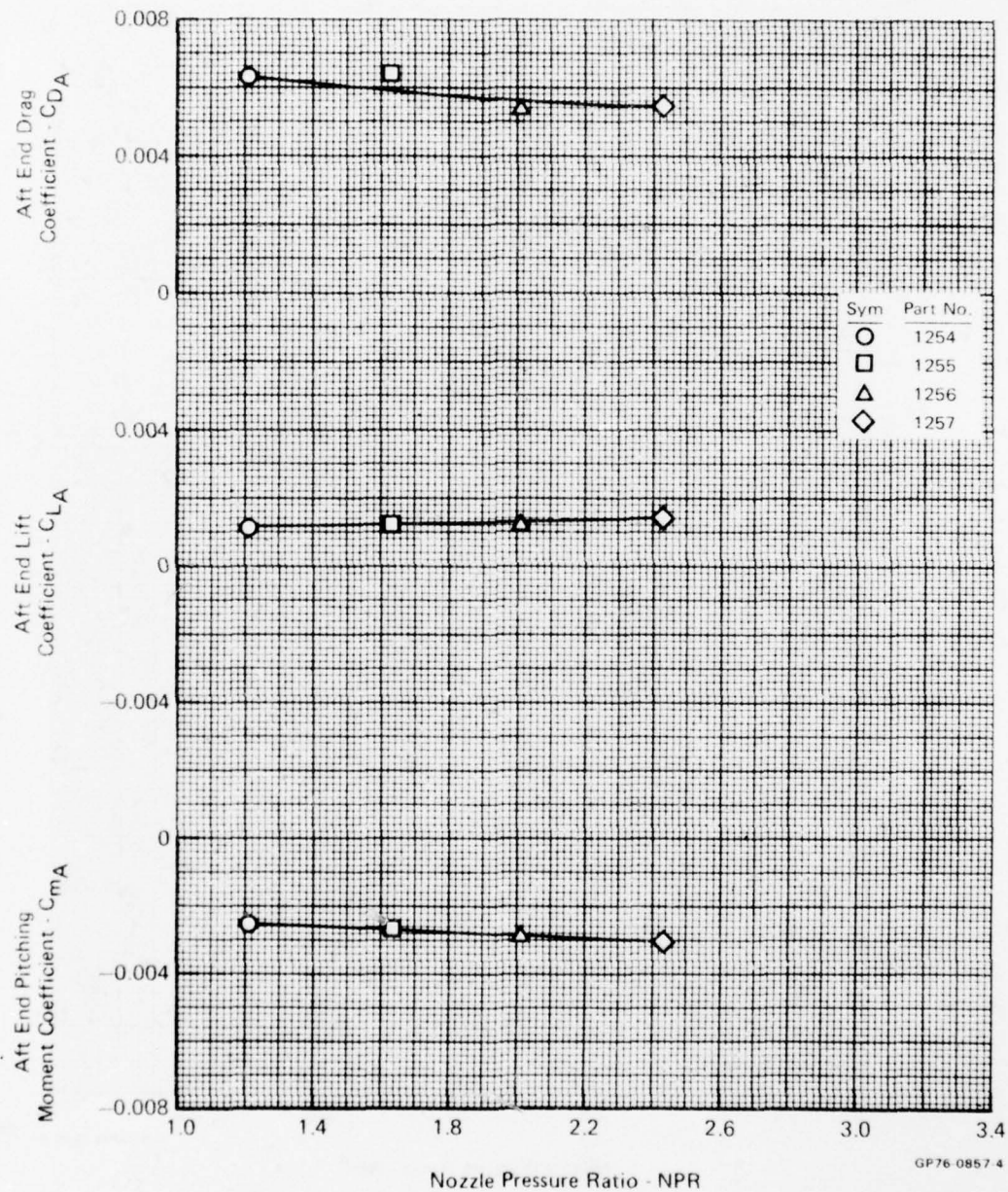


FIGURE D-34
 AFT END PERFORMANCE VARIATION WITH NOZZLE PRESSURE RATIO

Test Mode - Jet Effects
 Nozzle - Afterburning with Choke
 Mach No. - 0.9
 Angle of Attack - 5°

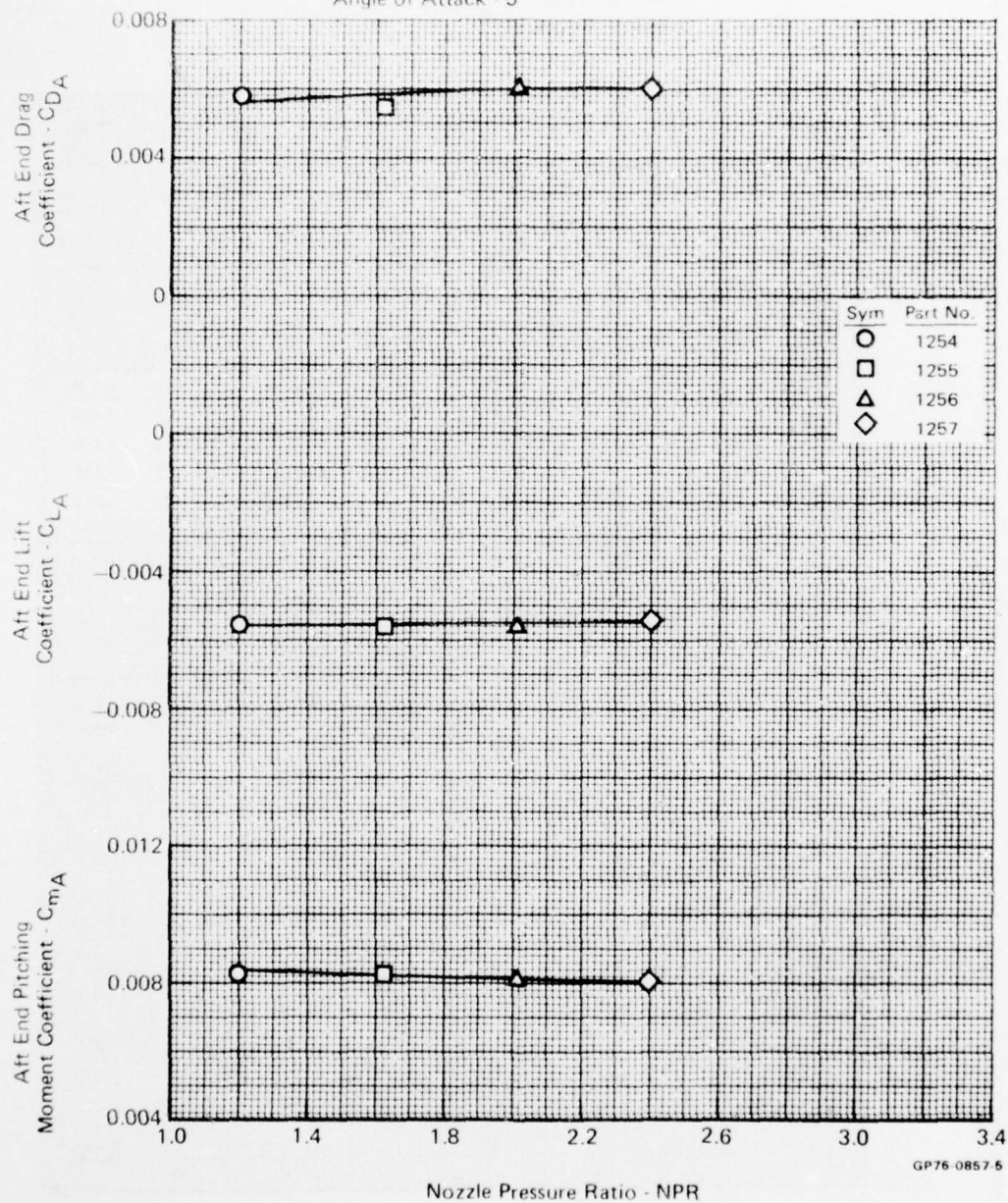


FIGURE D-35
 AFT END PERFORMANCE VARIATION WITH NOZZLE PRESSURE RATIO

Test Mode - Jet Effects
 Nozzle - Afterburning with Choke
 Mach No. - 0.9
 Angle of Attack - 10°

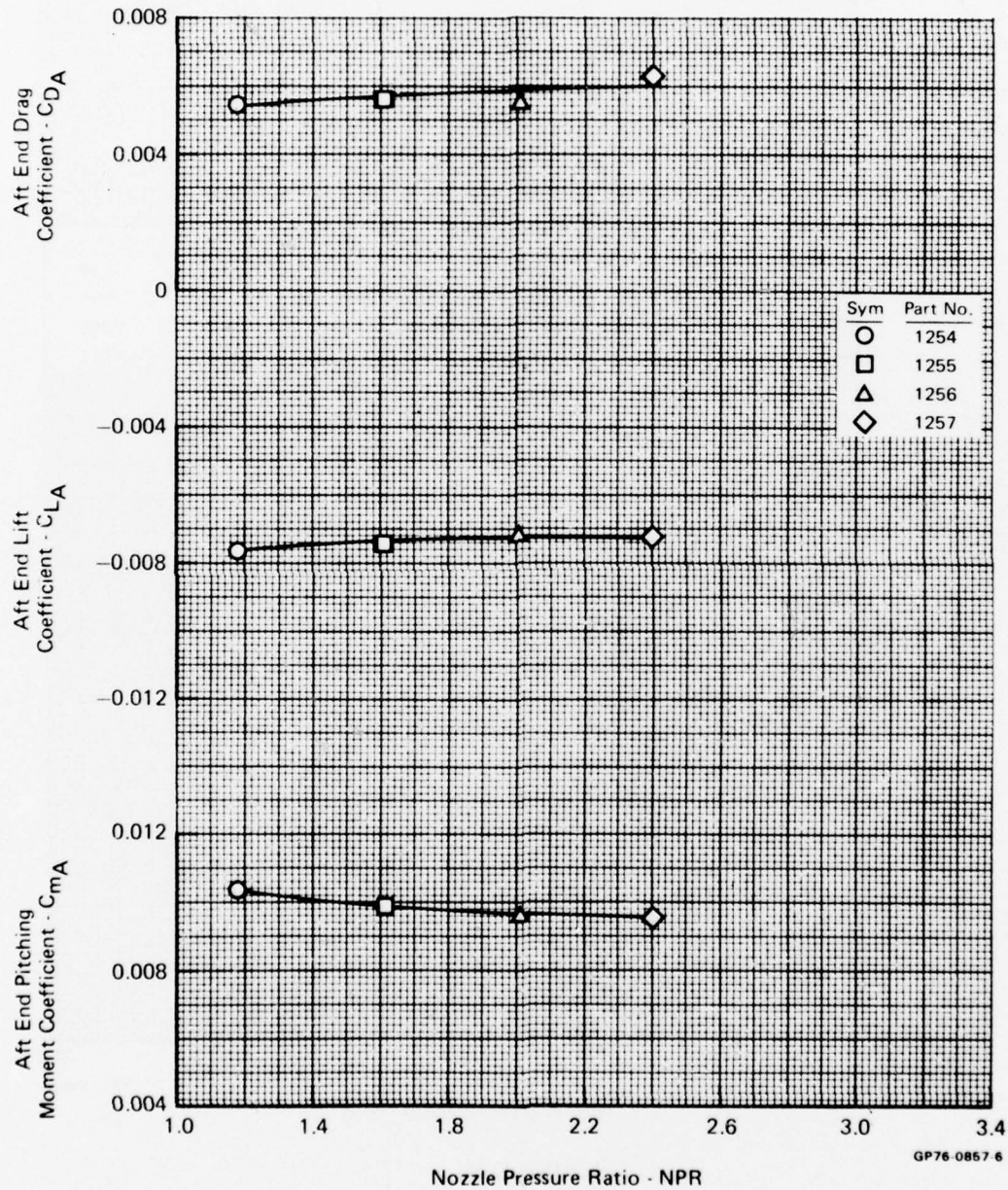


FIGURE D-36
 AFT END PERFORMANCE VARIATION WITH NOZZLE PRESSURE RATIO

Test Mode - Jet Effects
 Nozzle - Afterburning with Choke
 Mach No. - 0.9
 Angle of Attack 16°

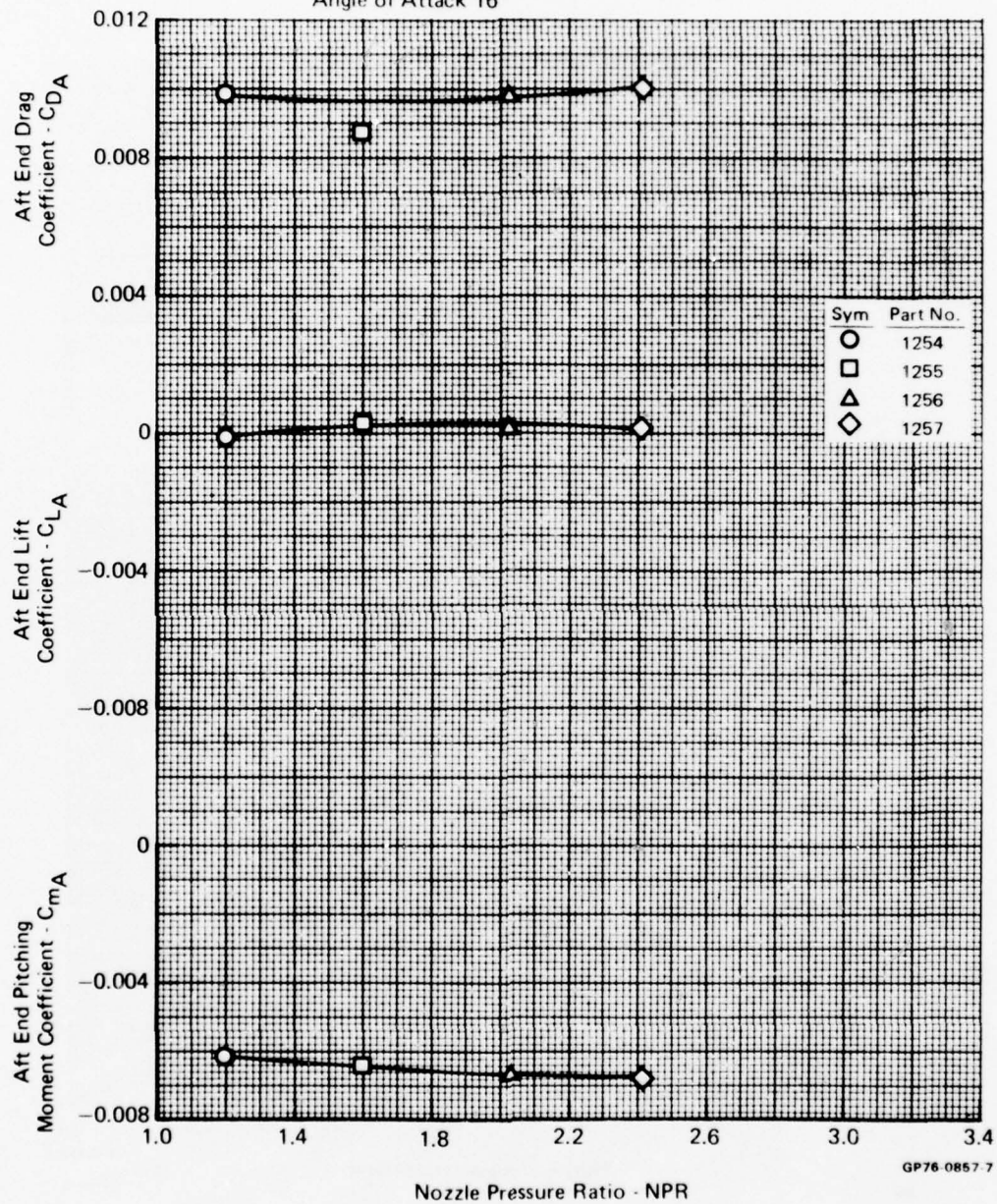


FIGURE D-37
 AFT END PERFORMANCE VARIATION WITH NOZZLE PRESSURE RATIO

Test Mode - Jet Effects
 Nozzle - Afterburning with Choke
 Mach No. - 1.20
 Angle of Attack 0°

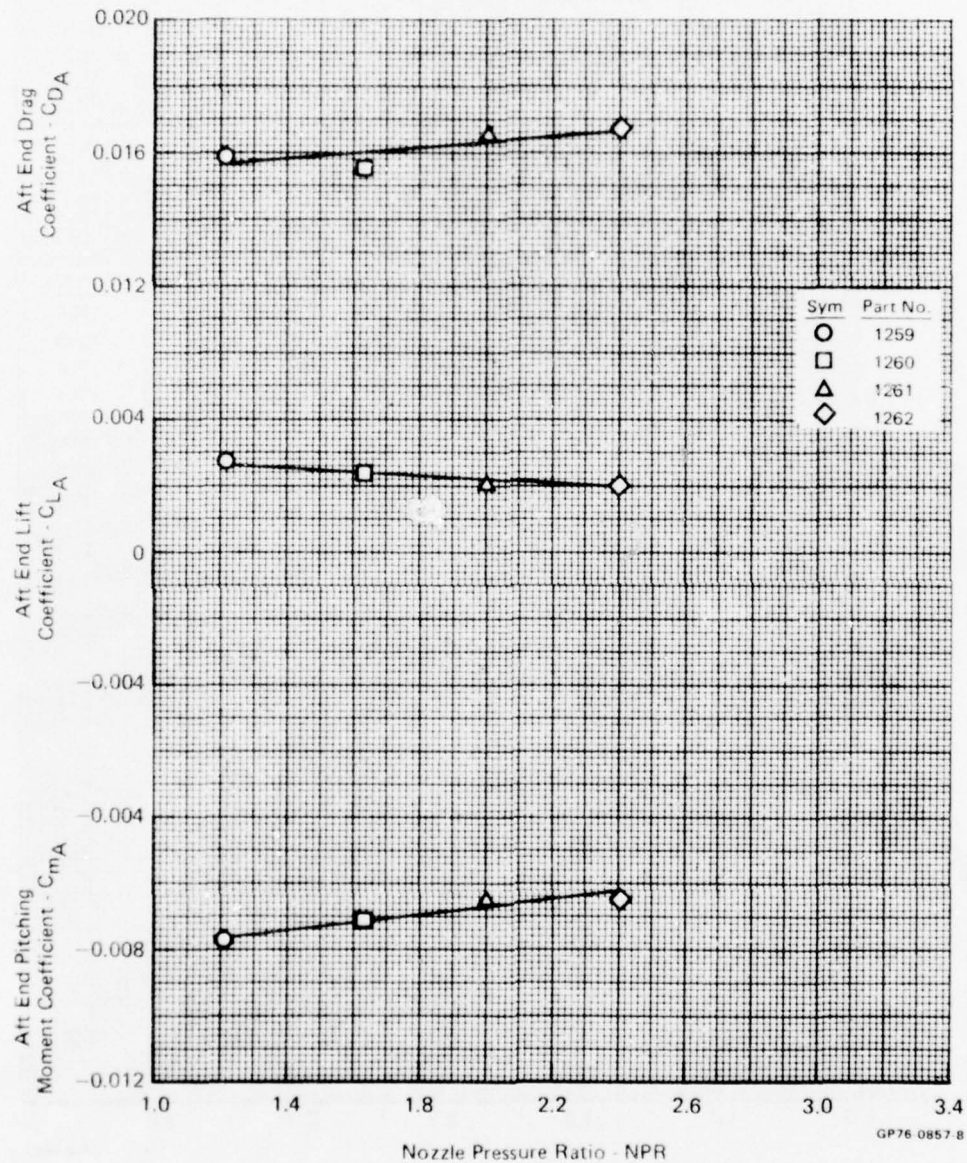


FIGURE D-38
 AFT END PERFORMANCE VARIATION WITH NOZZLE PRESSURE RATIO

Test Mode - Jet Effects
 Nozzle - Afterburning with Choke
 Mach No. - 1.20
 Angle of Attack - 5°

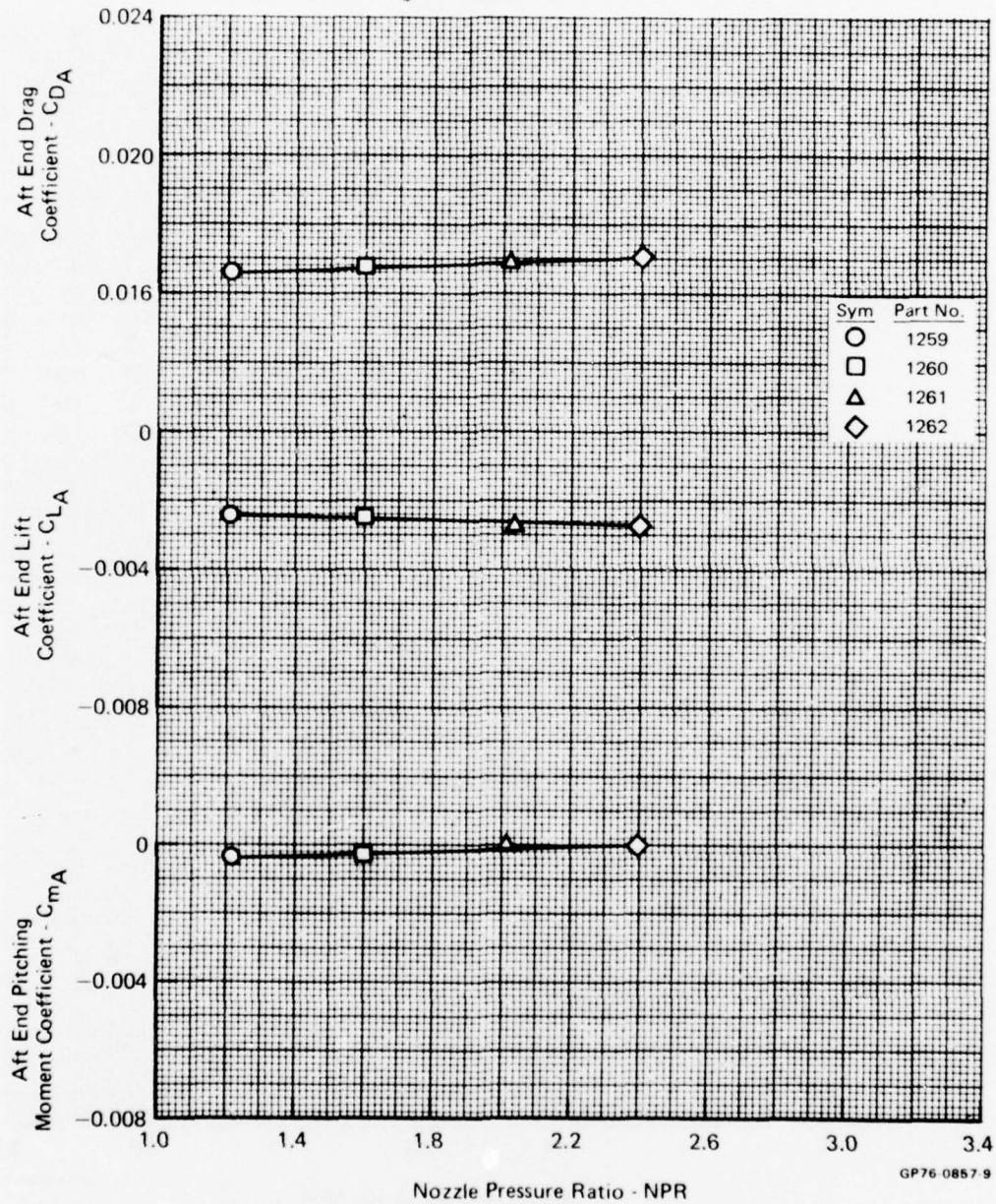


FIGURE D-39
 AFT END PERFORMANCE VARIATION WITH NOZZLE PRESSURE RATIO

Test Mode - Jet Effects
 Nozzle - Afterburning with Choke
 Mach No. - 1.20
 Angle of Attack - 10°

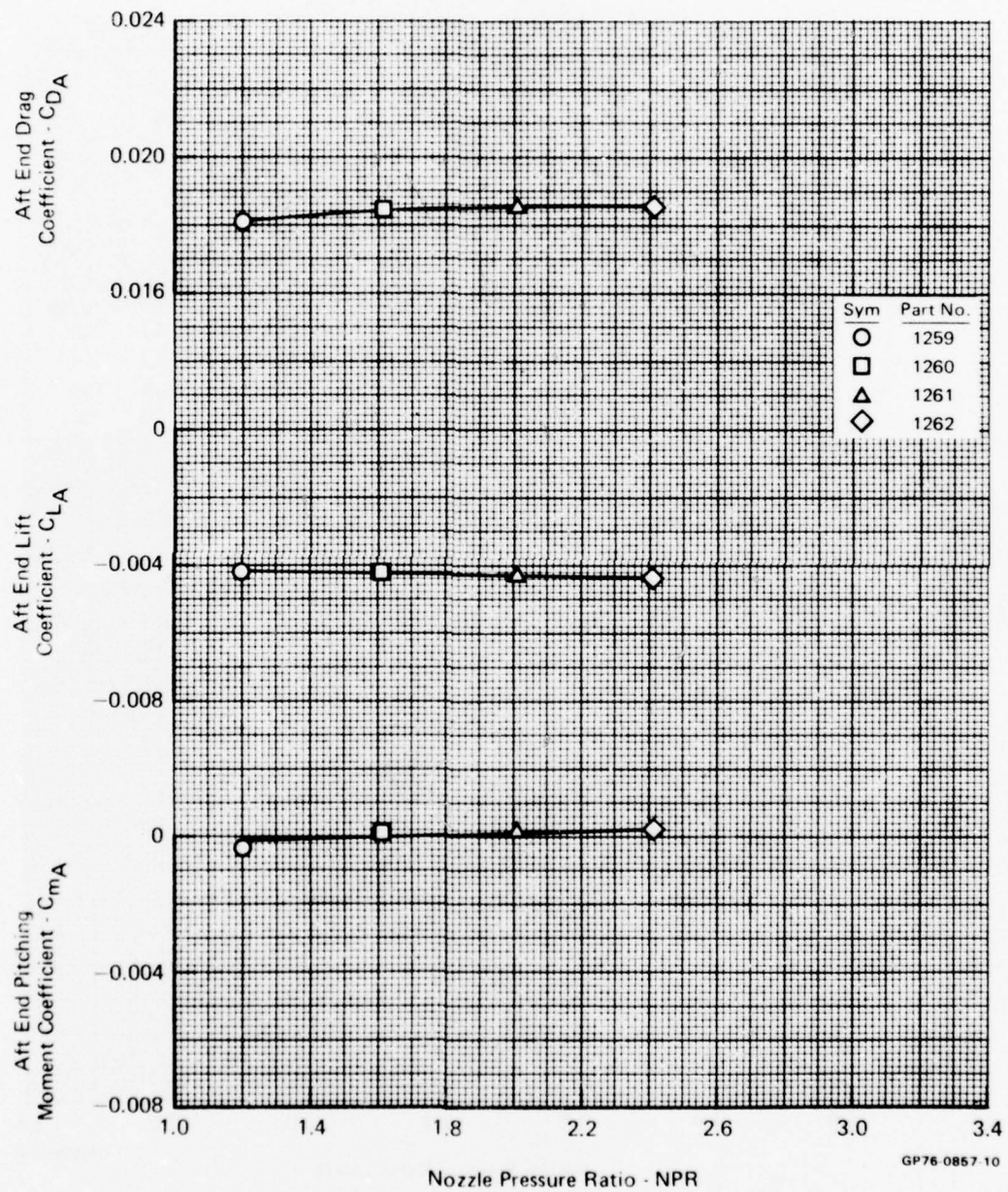


FIGURE D-40
 AFT END PERFORMANCE VARIATION WITH NOZZLE PRESSURE RATIO

Test Mode - Jet Effects
 Nozzle - Afterburning with Choke
 Mach No. - 1.20
 Angle of Attack - 14.4°

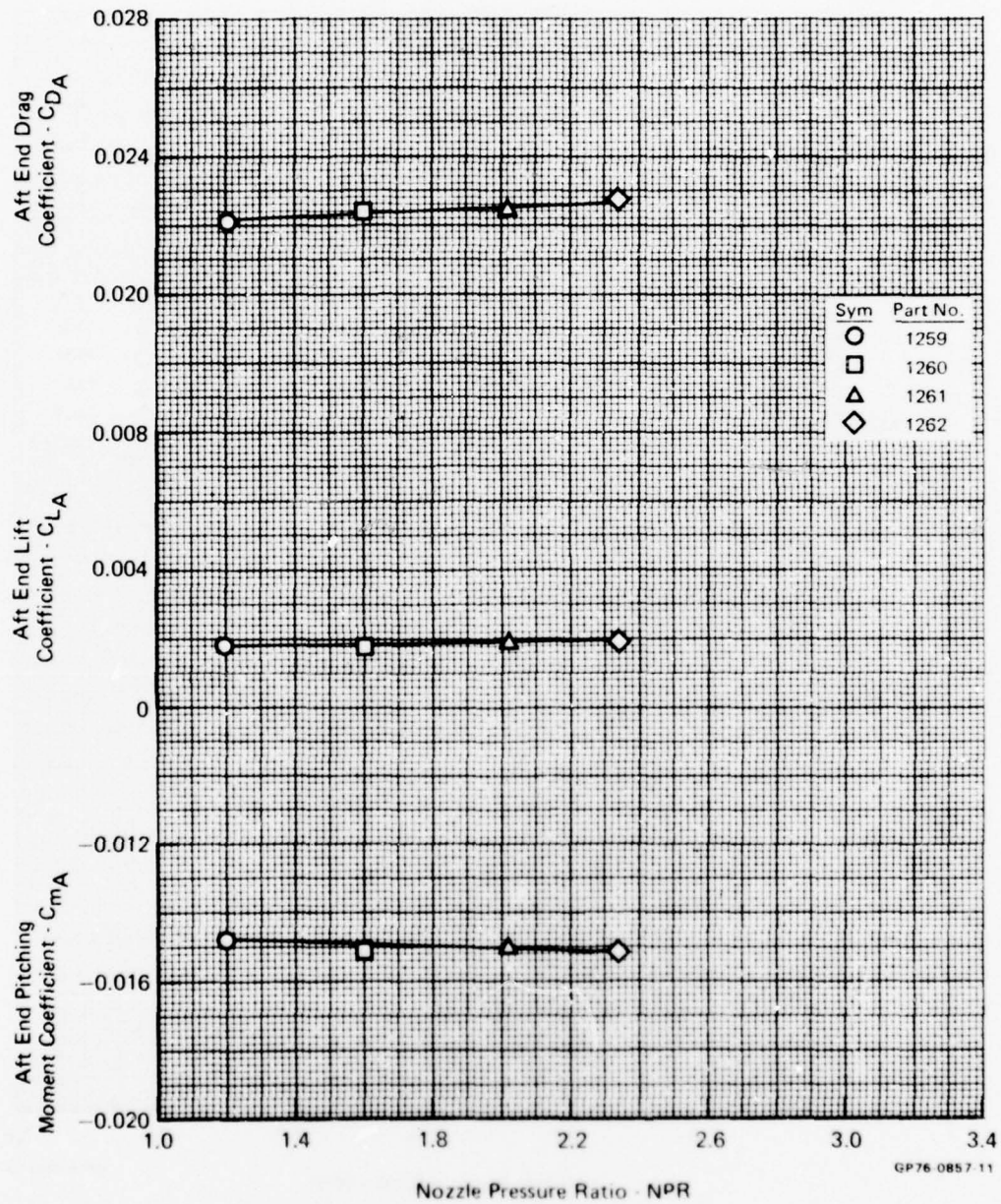


FIGURE D-41
 AFT END PERFORMANCE VARIATION WITH NOZZLE PRESSURE RATIO

Test Mode - Jet Effects
 Nozzle - Afterburning with Choke
 Mach No. - 1.45
 Angle of Attack - 0°

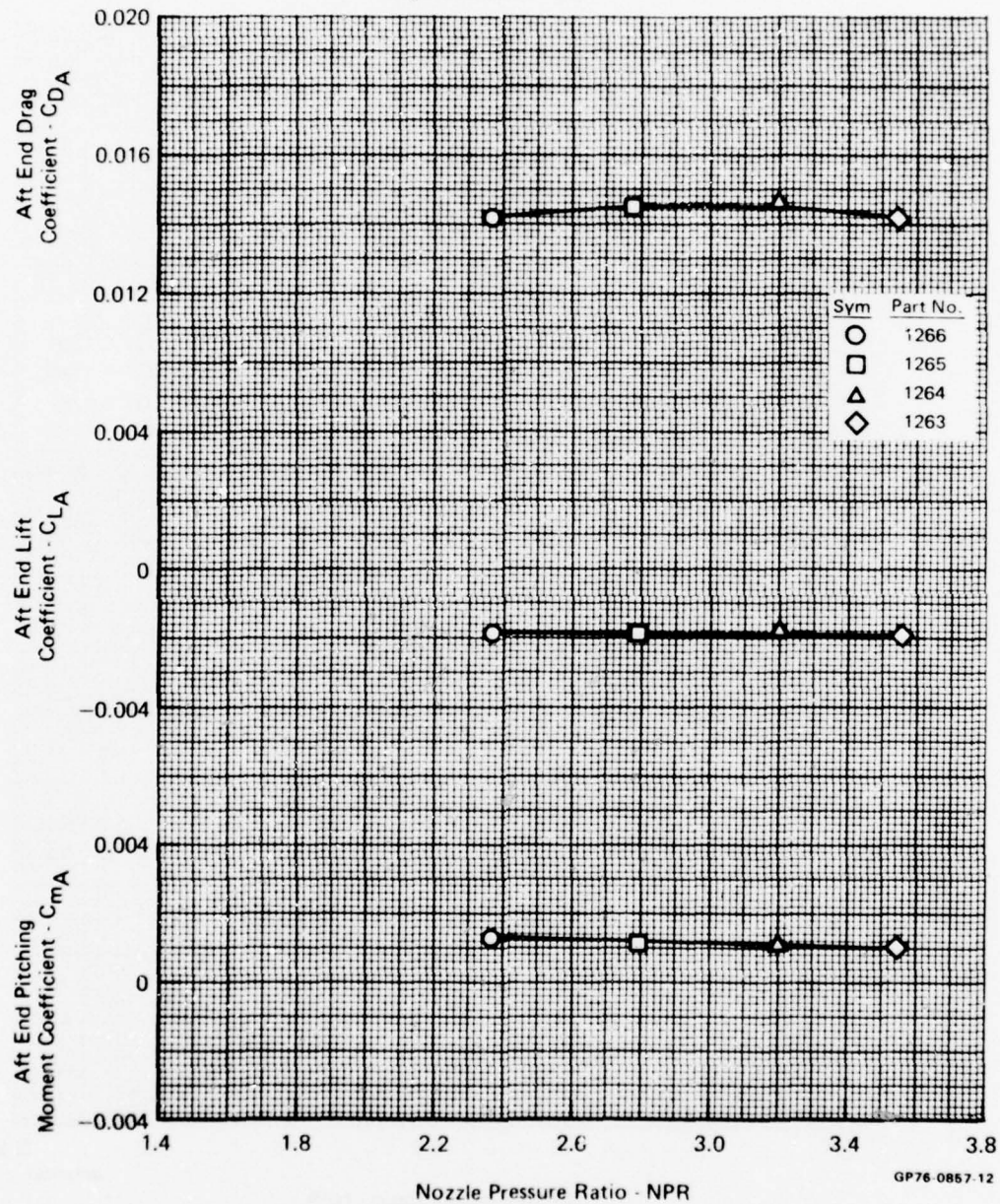


FIGURE D-42
AFT END PERFORMANCE VARIATION WITH NOZZLE PRESSURE RATIO

Test Mode - Jet Effects
 Nozzle - Afterburning with Choke
 Mach No. - 1.45
 Angle of Attack - 3°

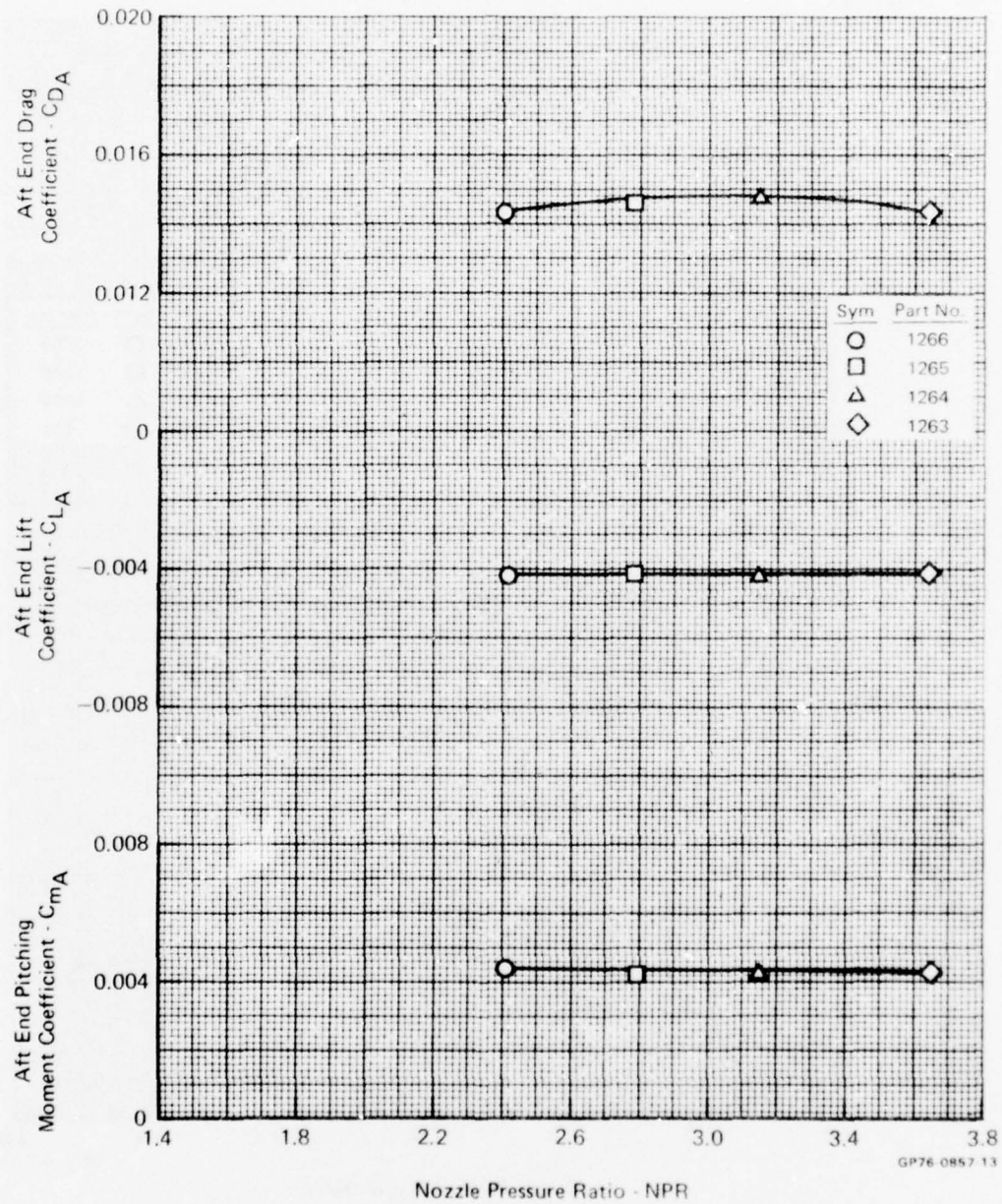


FIGURE D-43
 AFT END PERFORMANCE VARIATION WITH NOZZLE PRESSURE RATIO

Test Mode - Jet Effects
 Nozzle - Afterburning with Choke
 Mach No. - 1.45
 Angle of Attack - 6°

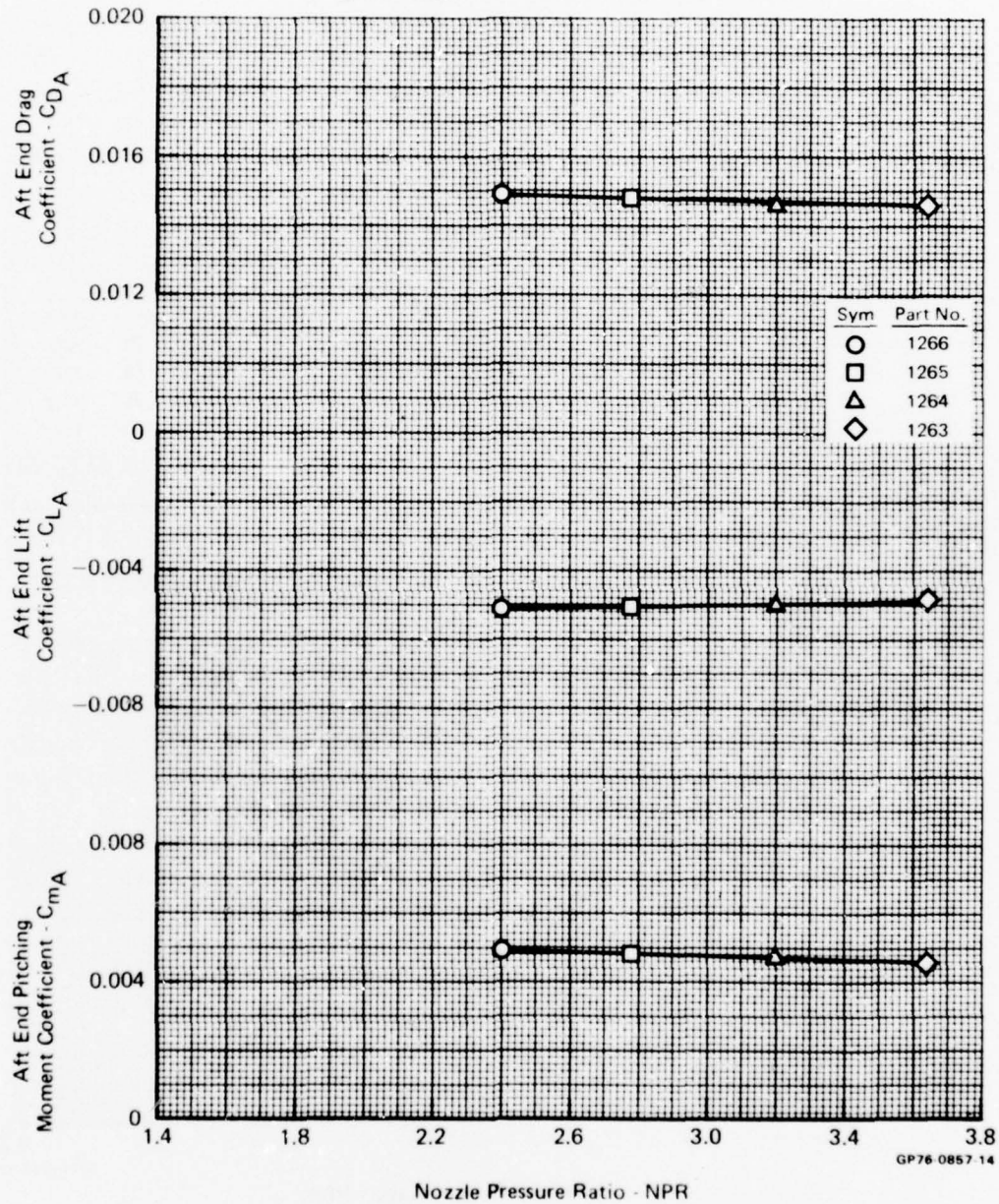


FIGURE D-44
 AFT END PERFORMANCE VARIATION WITH NOZZLE PRESSURE RATIO

Test Mode - Jet Effects
 Nozzle - Afterburning with Choke
 Mach No. - 1.45
 Angle of Attack 10°

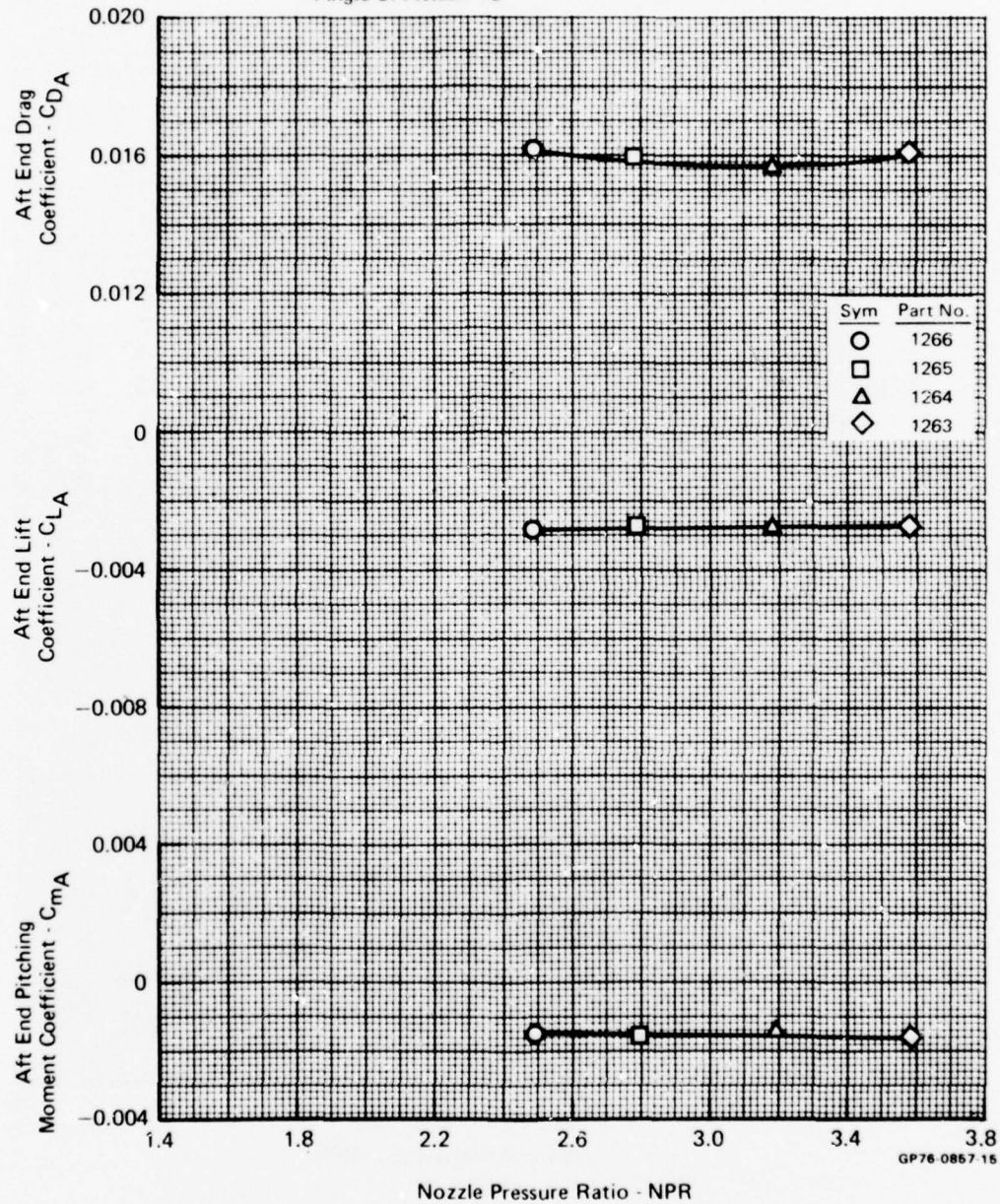


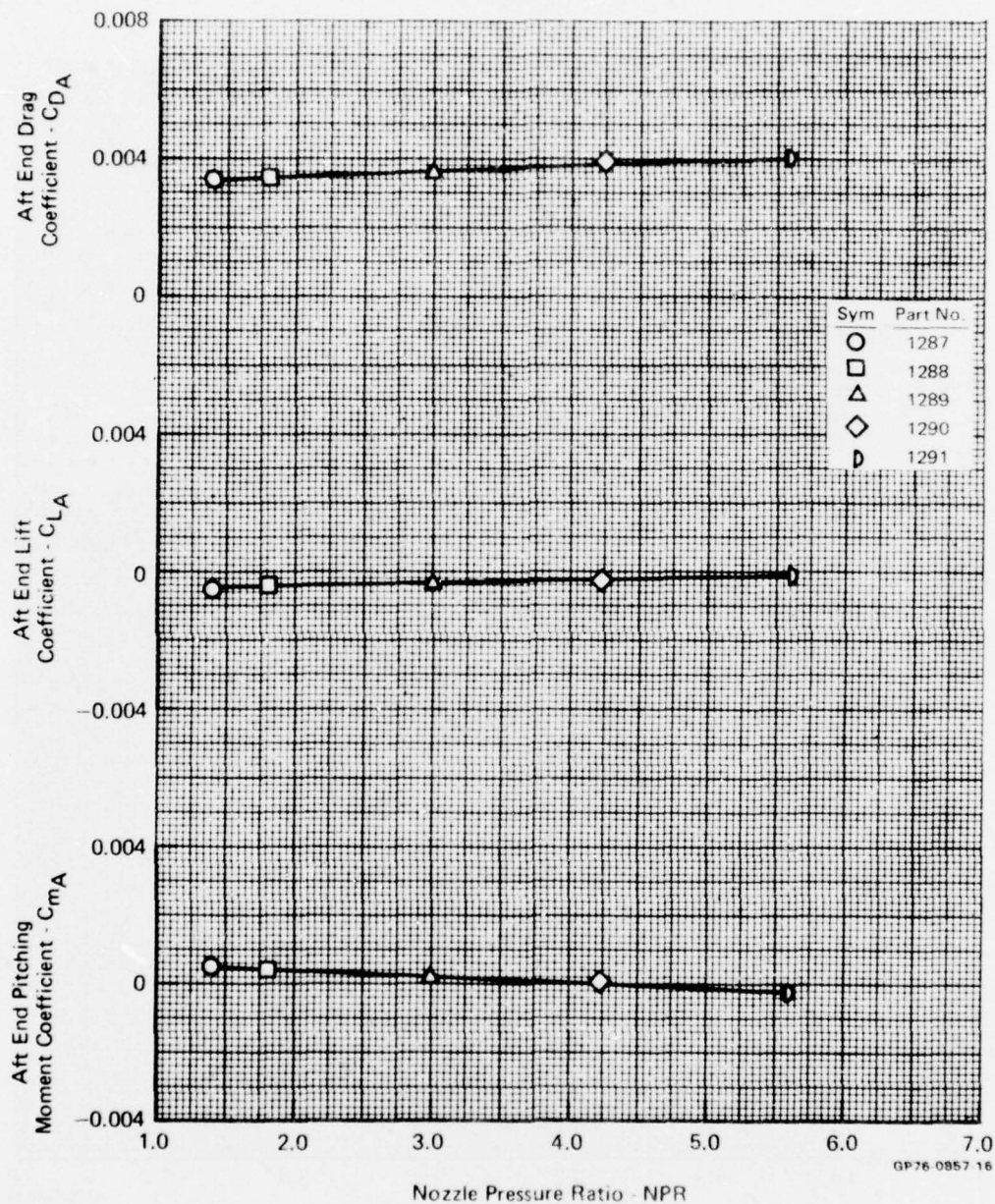
FIGURE D-45
 AFT END PERFORMANCE VARIATION WITH NOZZLE PRESSURE RATIO

Test Mode - Jet Effects

Nozzle - Dry

Mach No. - 0.6

Angle of Attack - 0°



GP76 0857 16

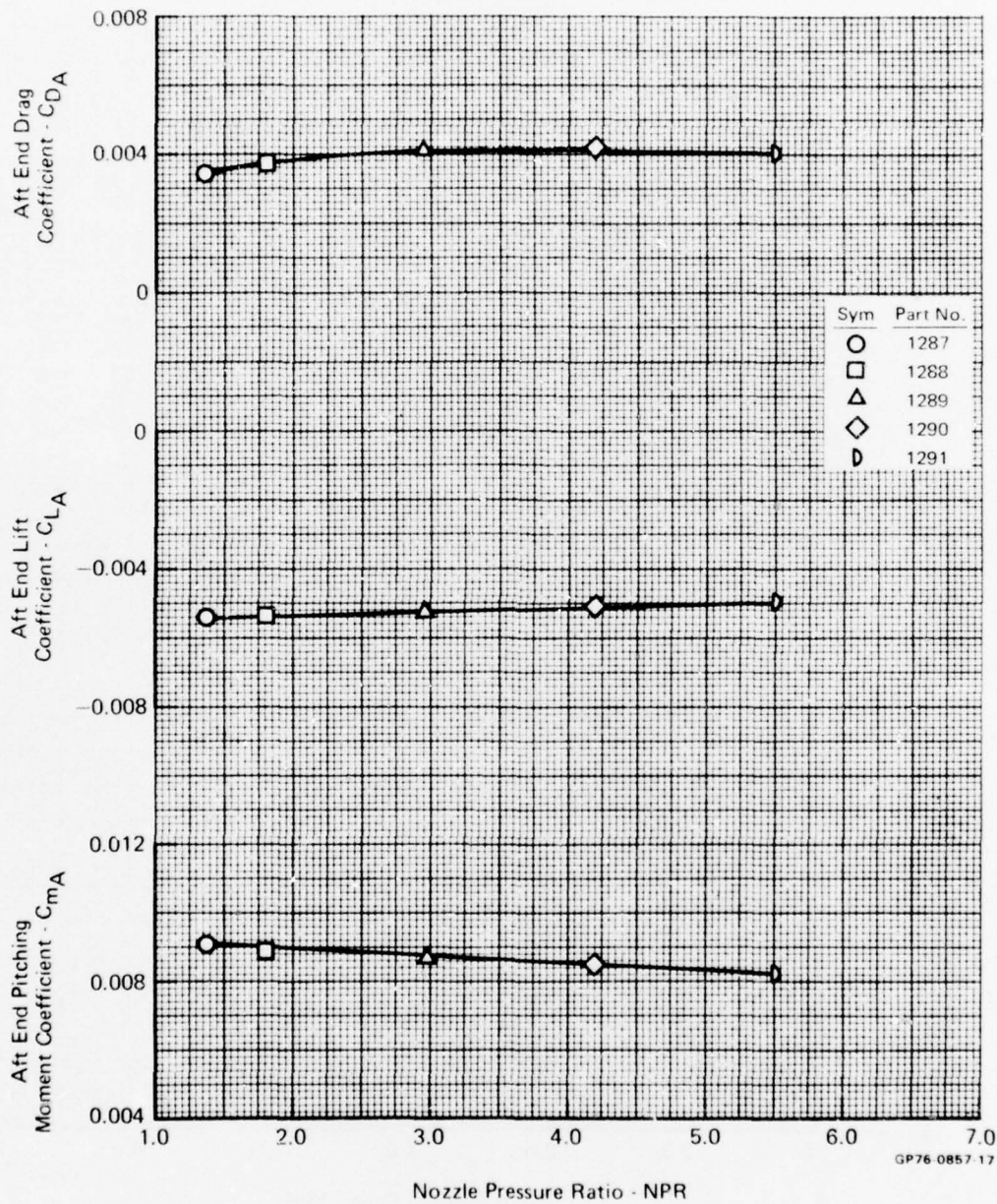
FIGURE D-46
AFT END PERFORMANCE VARIATION WITH NOZZLE PRESSURE RATIO

Test Mode - Jet Effects

Nozzle - Dry

Mach No. - 0.6

Angle of Attack - 5°



GP76 0857-17

FIGURE D-47
AFT END PERFORMANCE VARIATION WITH NOZZLE PRESSURE RATIO

Test Mode - Jet Effects

Nozzle - Dry

Mach No. - 0.6

Angle of Attack - 10^0

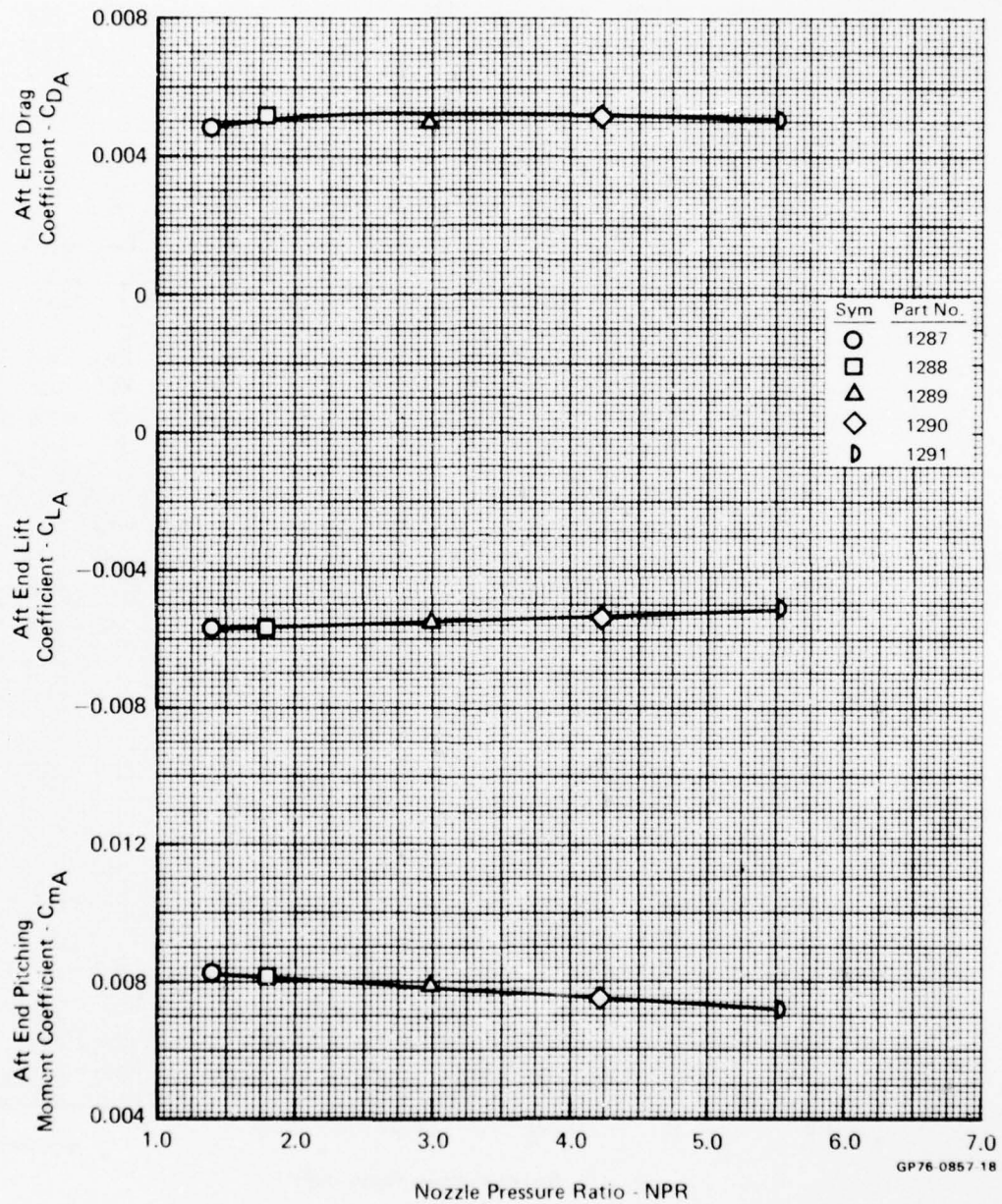


FIGURE D-48
AFT END PERFORMANCE VARIATION WITH NOZZLE PRESSURE RATIO

Test Mode - Jet Effects
 Nozzle - Dry
 Mach No. - 0.6
 Angle of Attack - 16°

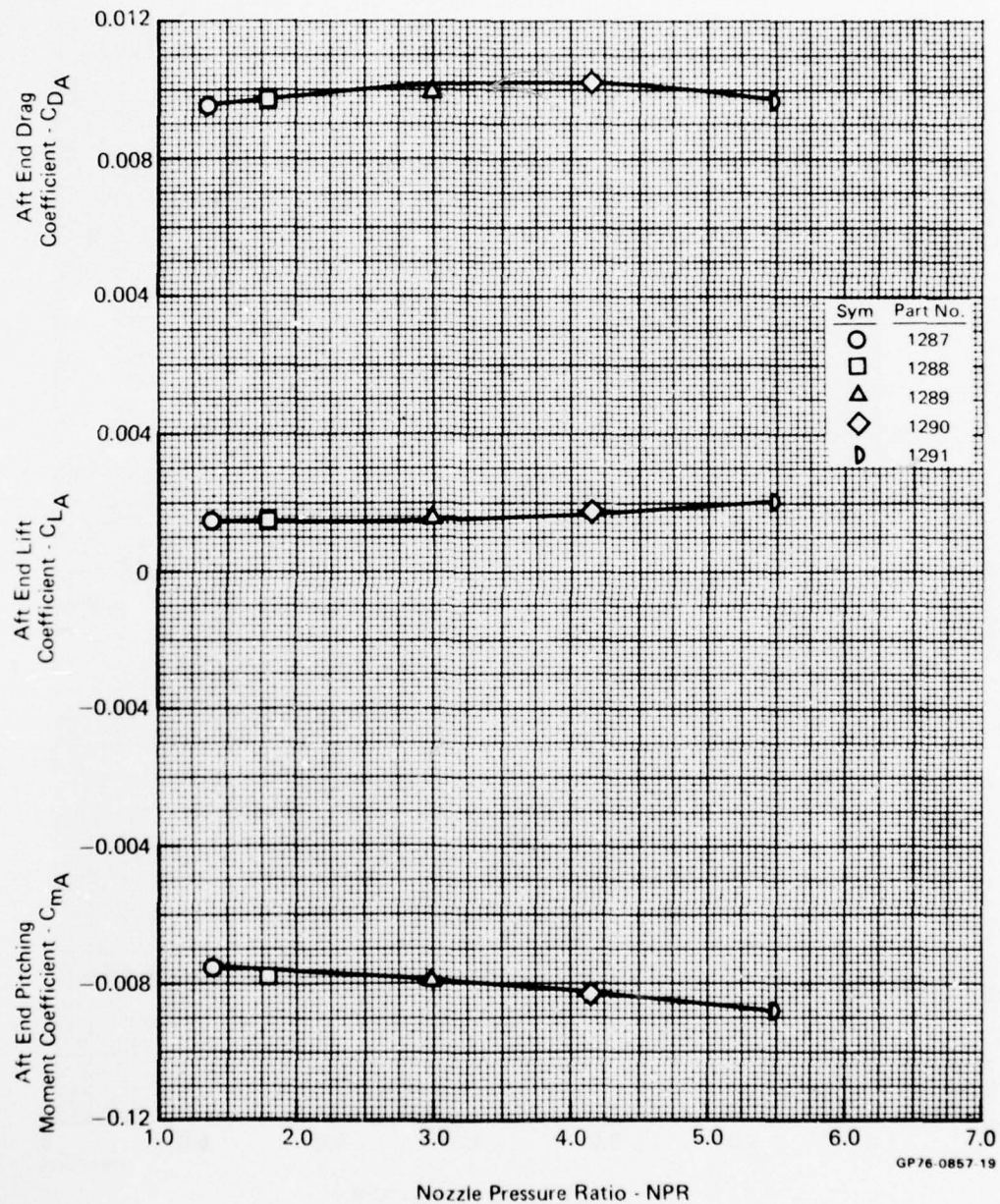


FIGURE D-49
 AFT END PERFORMANCE VARIATION WITH NOZZLE PRESSURE RATIO

Test Mode - Jet Effects
 Nozzle - Dry
 Mach No. - 0.9
 Angle of Attack - 0°

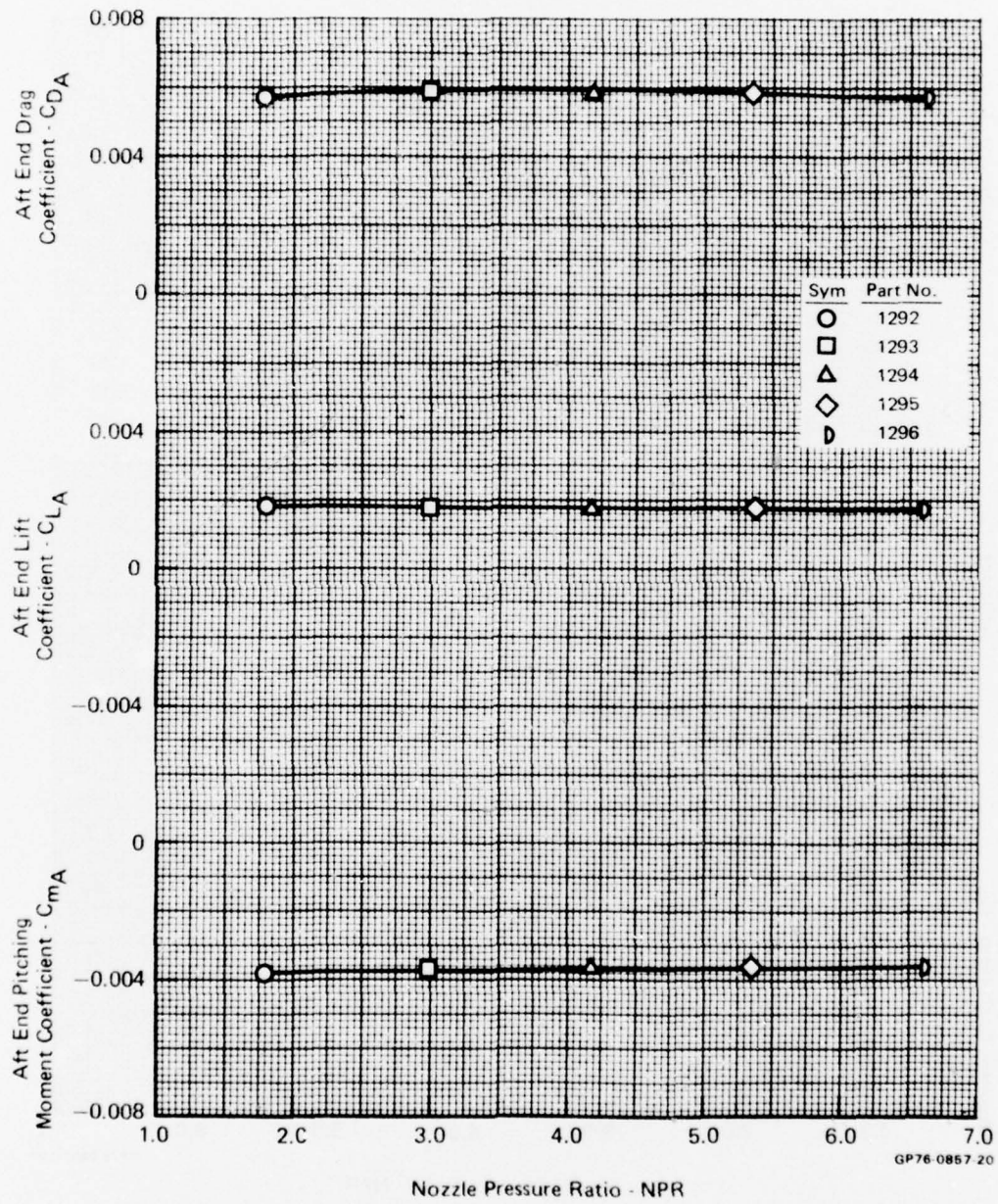


FIGURE D-50
 AFT END PERFORMANCE VARIATION WITH NOZZLE PRESSURE RATIO

Test Mode - Jet Effects
 Nozzle - Dry
 Mach No. - 0.9
 Angle of Attack - 5°

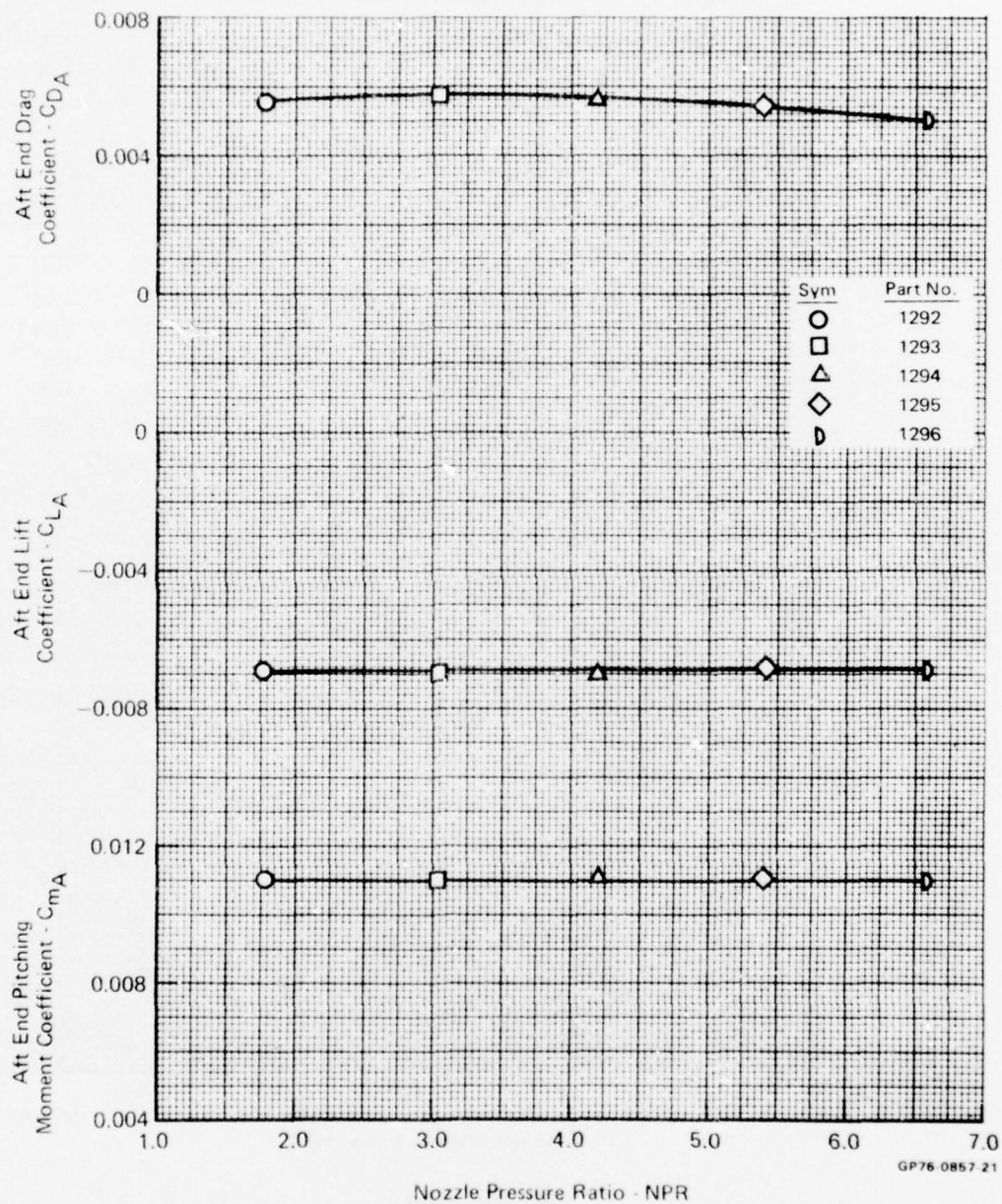


FIGURE D-51
 AFT END PERFORMANCE VARIATION WITH NOZZLE PRESSURE RATIO

Test Mode - Jet Effects

Nozzle - Dry

Mach No. - 0.9

Angle of Attack - 10°

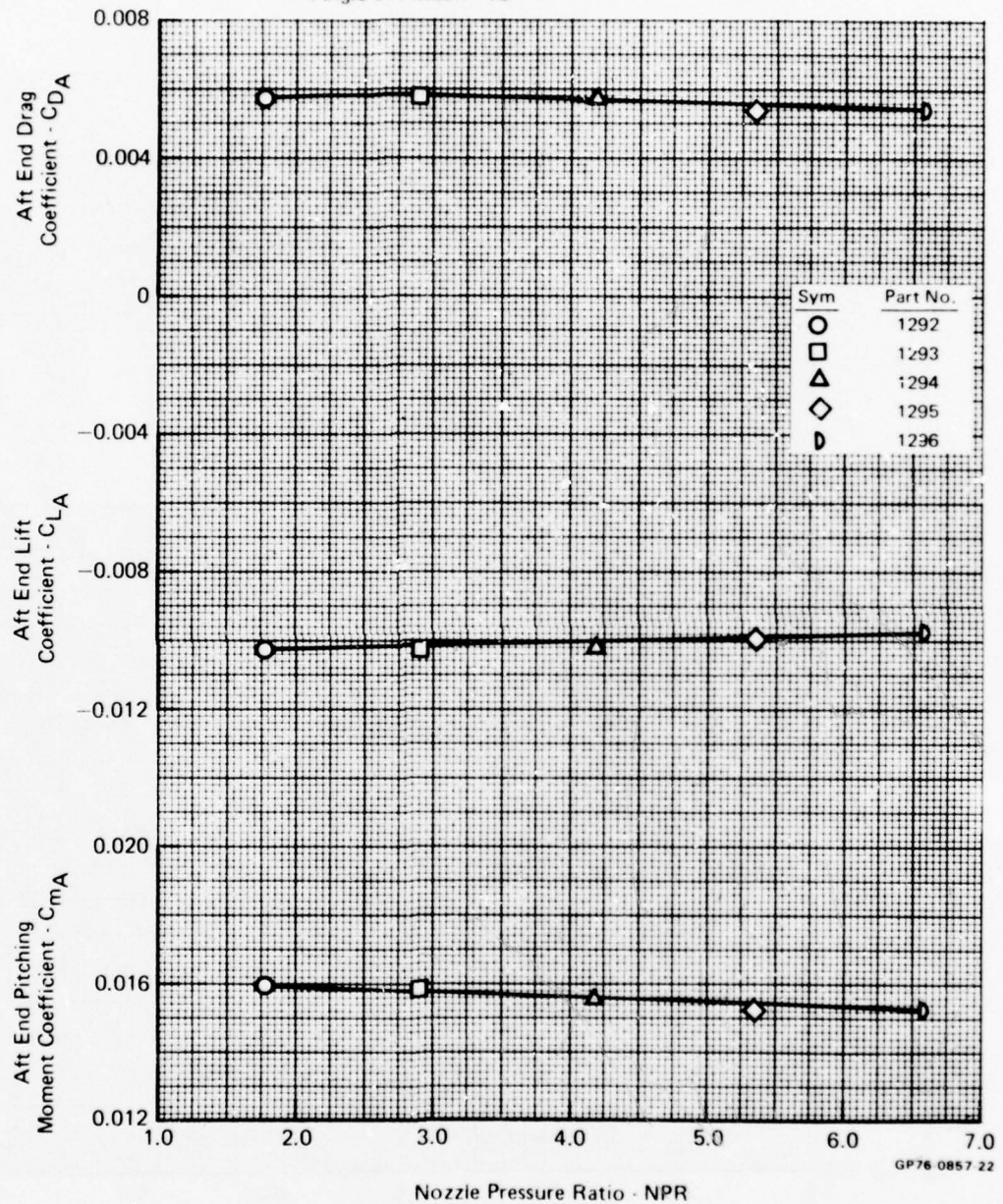


FIGURE D-52
AFT END PERFORMANCE VARIATION WITH NOZZLE PRESSURE RATIO

Test Mode - Jet Effects

Nozzle - Dry

Mach No. - 0.9

Angle of Attack - 16°

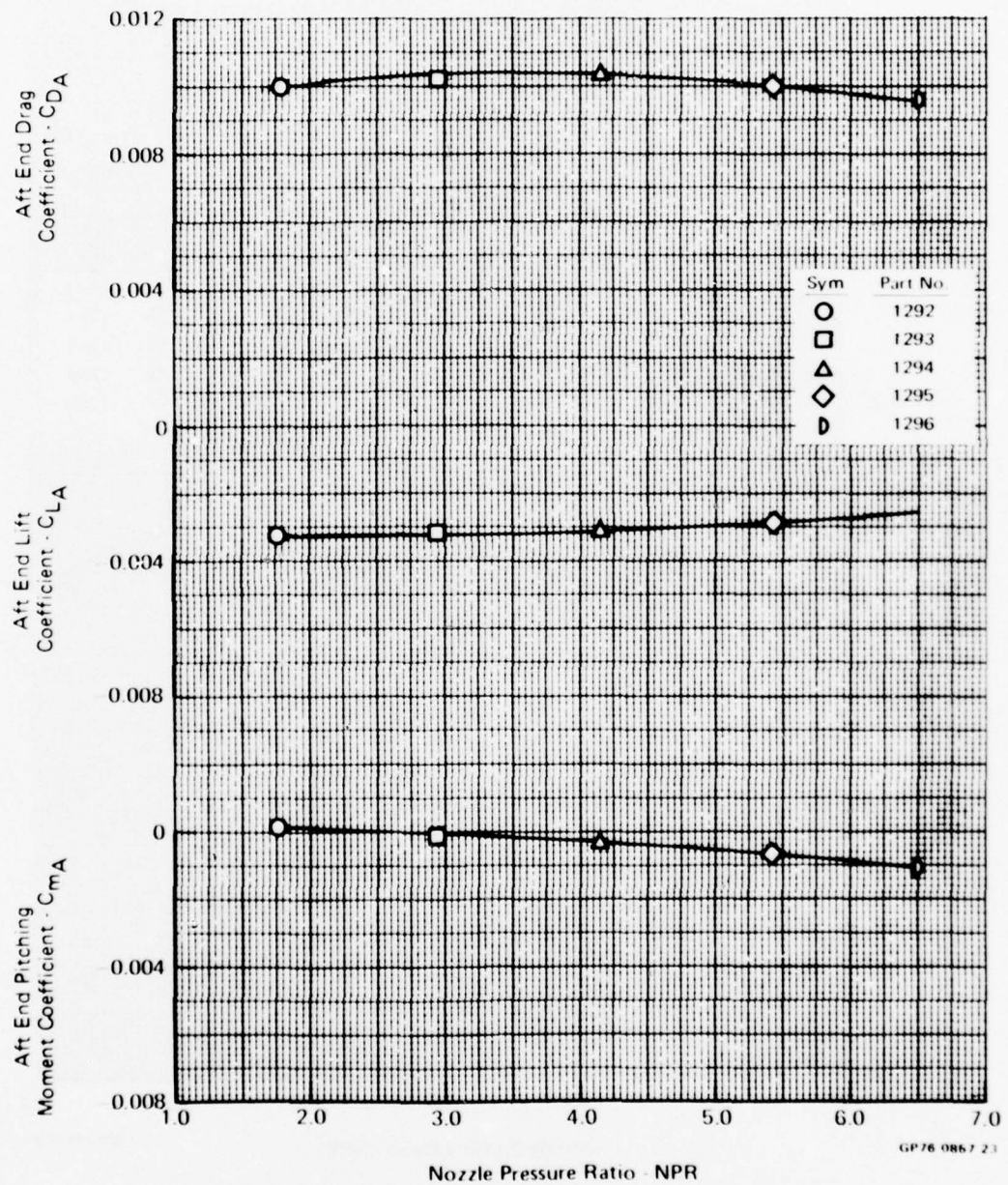


FIGURE D-53
AFT END PERFORMANCE VARIATION WITH NOZZLE PRESSURE RATIO

Test Mode - Jet Effects
 Nozzle - Dry
 Mach No. - 1.2
 Angle of Attack - 0°

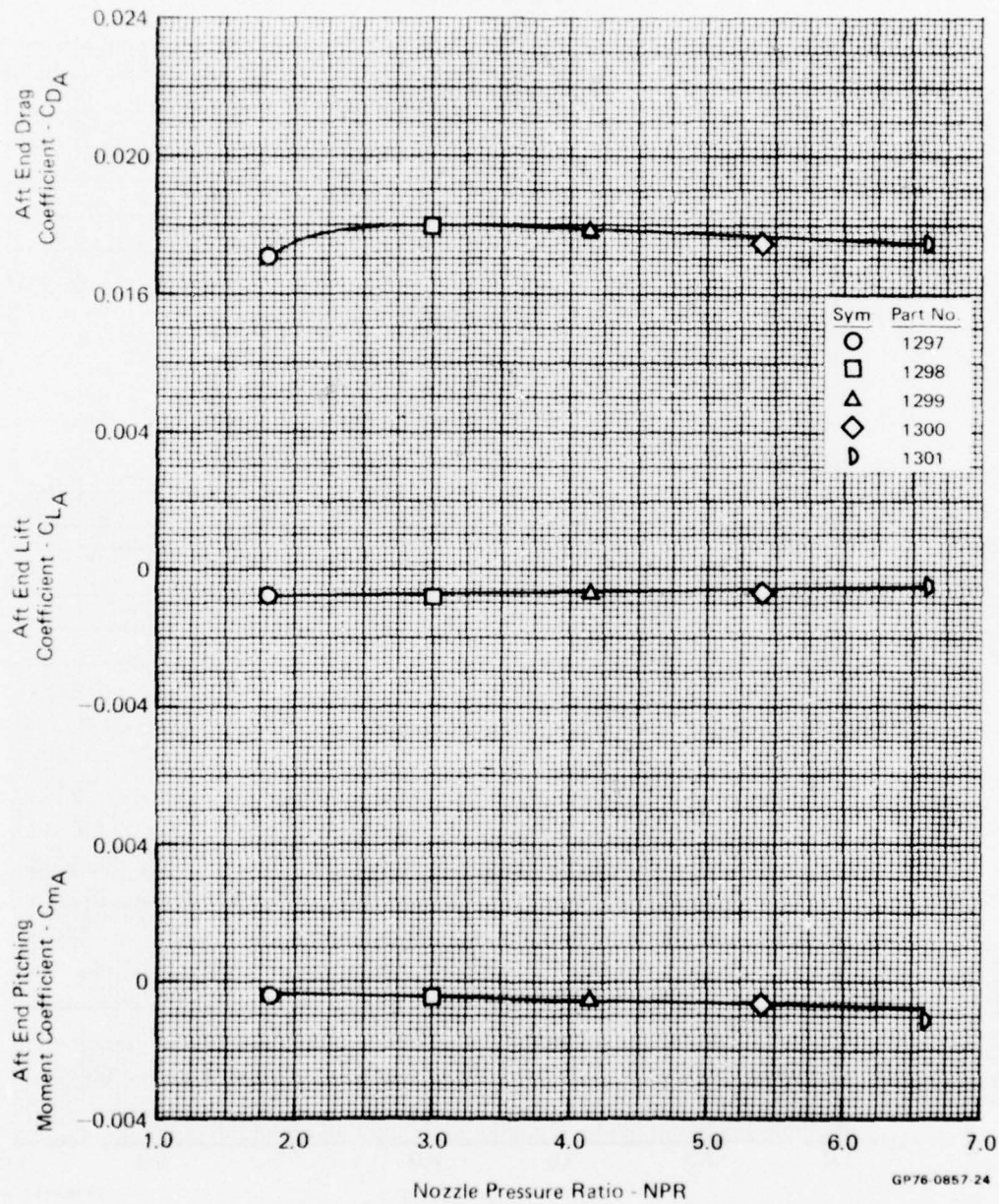


FIGURE D-54
 AFT END PERFORMANCE VARIATION WITH NOZZLE PRESSURE RATIO

Test Mode - Jet Effects
 Nozzle - Dry
 Mach No. - 1.2
 Angle of Attack - 5°

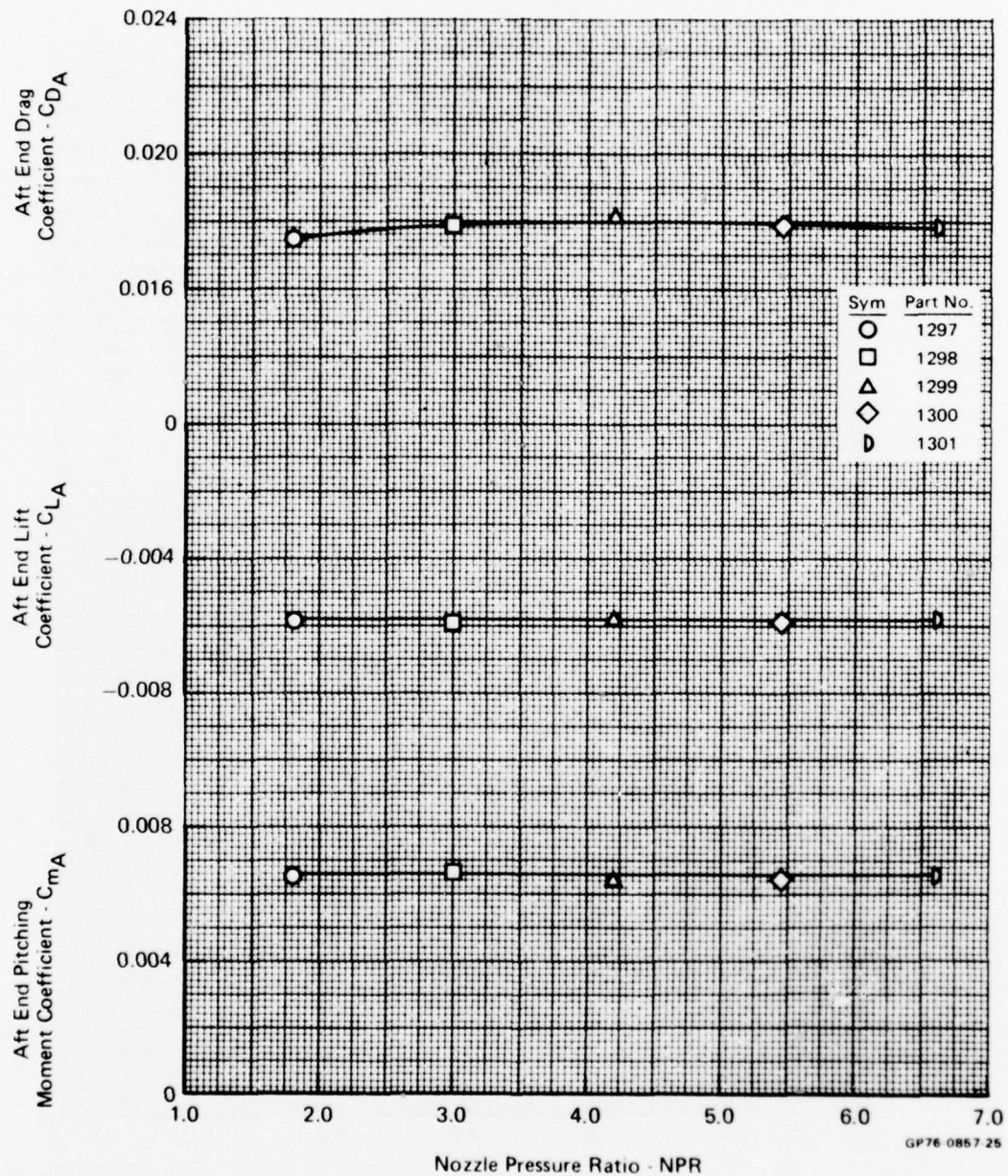


FIGURE D-55
 AFT END PERFORMANCE VARIATION WITH NOZZLE PRESSURE RATIO

Test Mode - Jet Effects
 Nozzle - Dry
 Mach No. - 1.2
 Angle of Attack - 10°

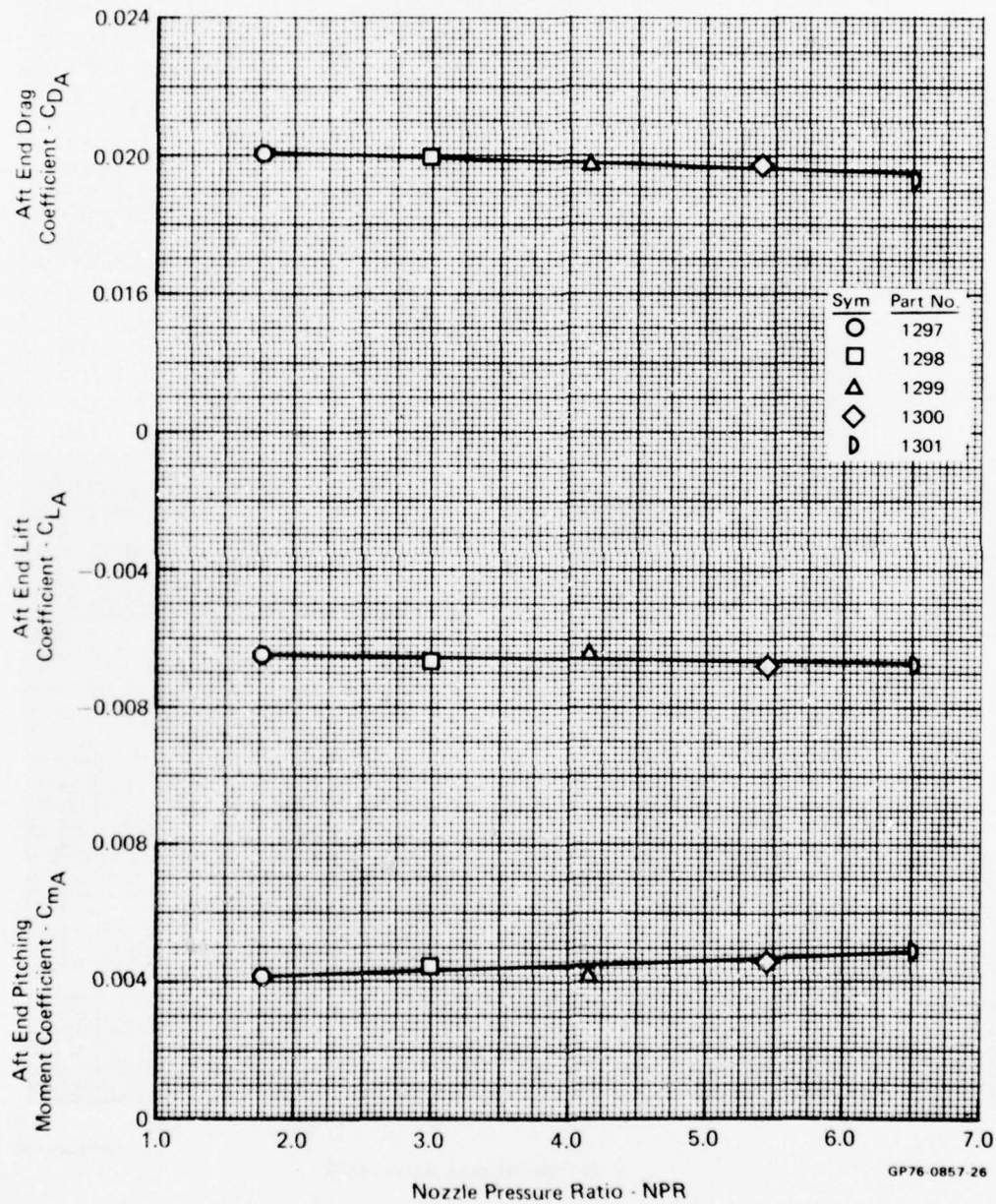


FIGURE D-56
 AFT END PERFORMANCE VARIATION WITH NOZZLE PRESSURE RATIO

Test Mode - Jet Effects
 Nozzle - Dry
 Mach No. - 1.2
 Angle of Attack - As Noted

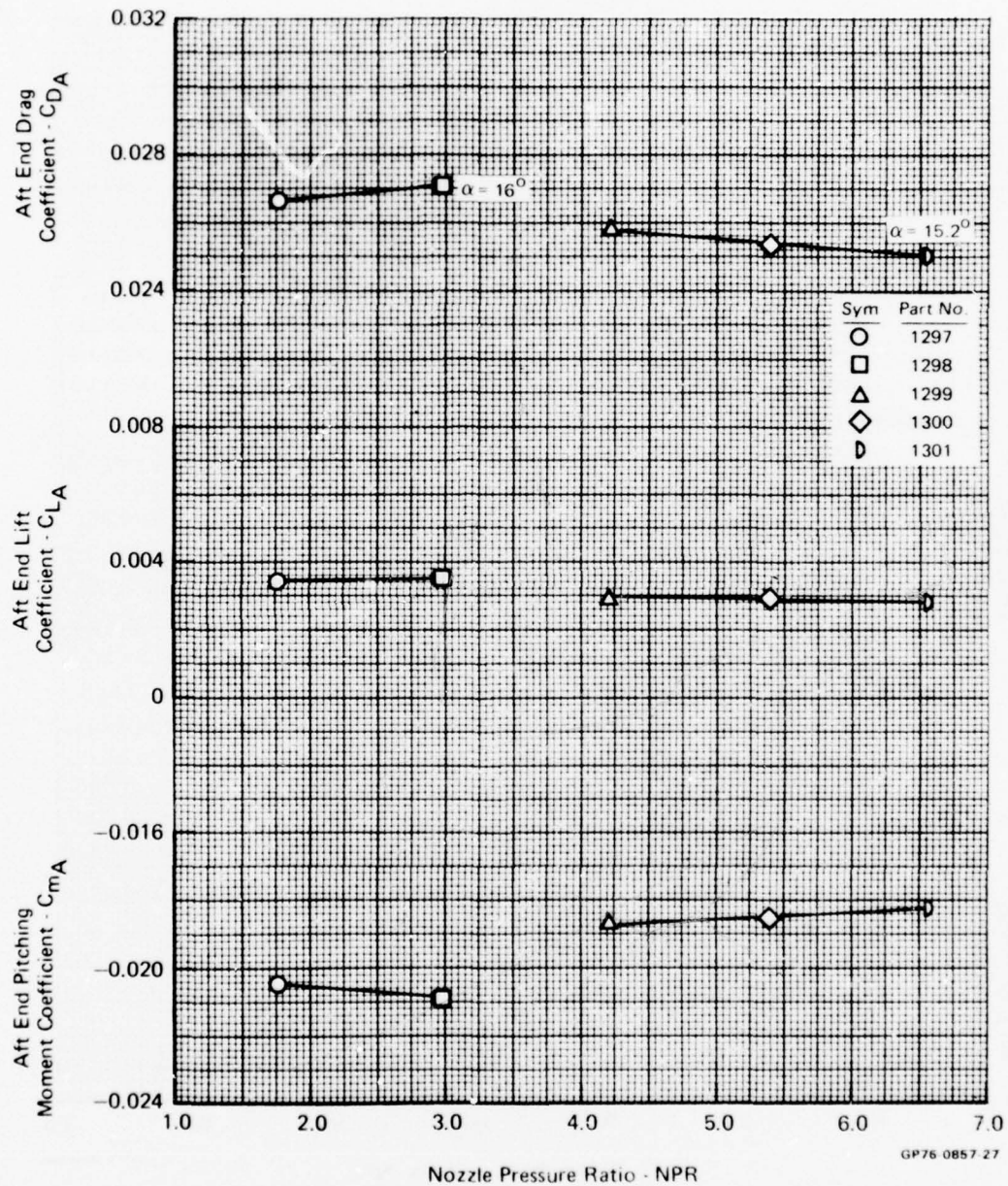


FIGURE D-57
 AFT END PERFORMANCE VARIATION WITH NOZZLE PRESSURE RATIO

Test Mode - Jet Effects
 Nozzle - Afterburning
 Mach No. - 0.6
 Angle of Attack - 0°

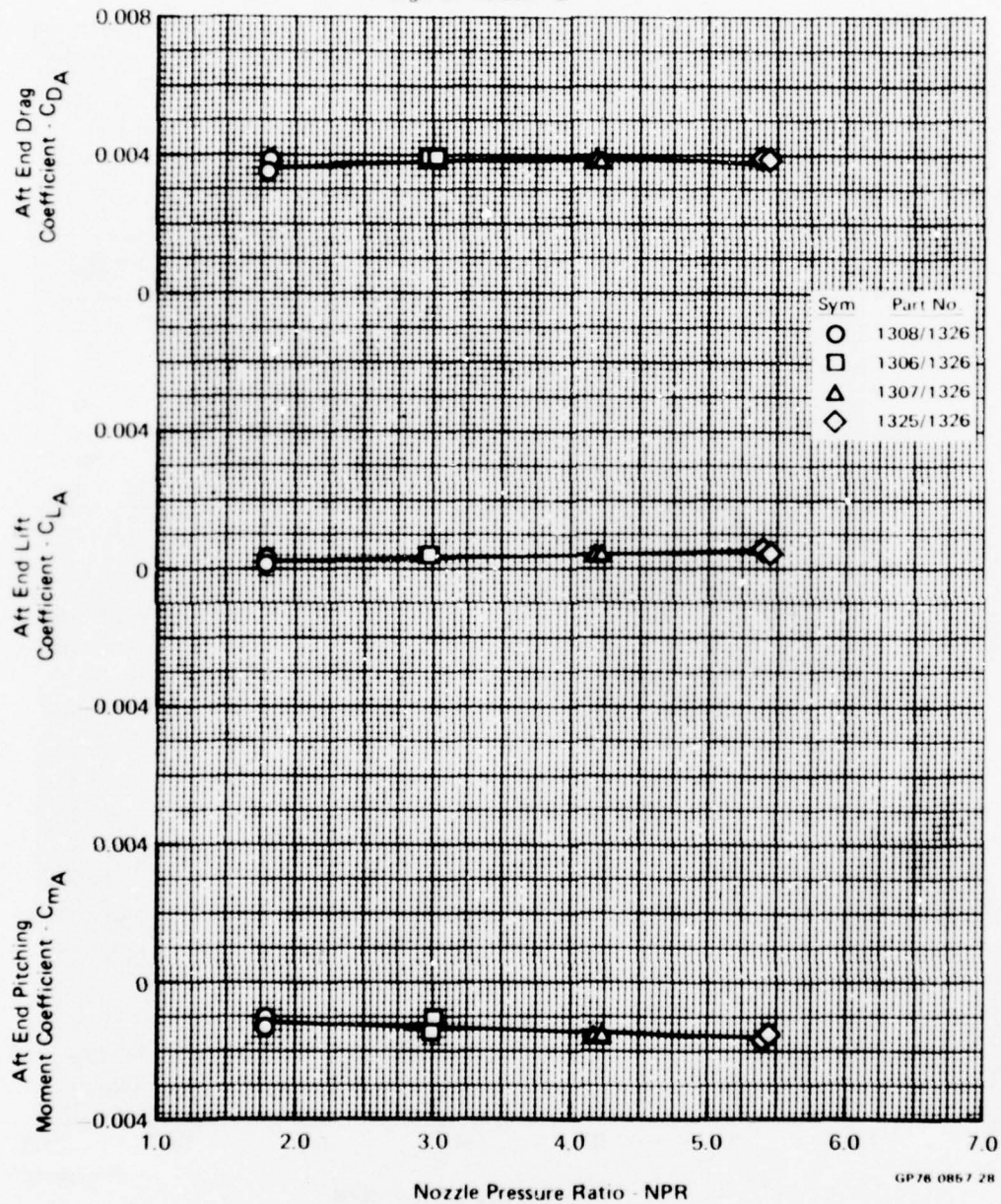


FIGURE D-58
 AFT END PERFORMANCE VARIATION WITH NOZZLE PRESSURE RATIO

Test Mode - Jet Effects
 Nozzle - Afterburning
 Mach No. - 6.6
 Angle of Attack - 5°

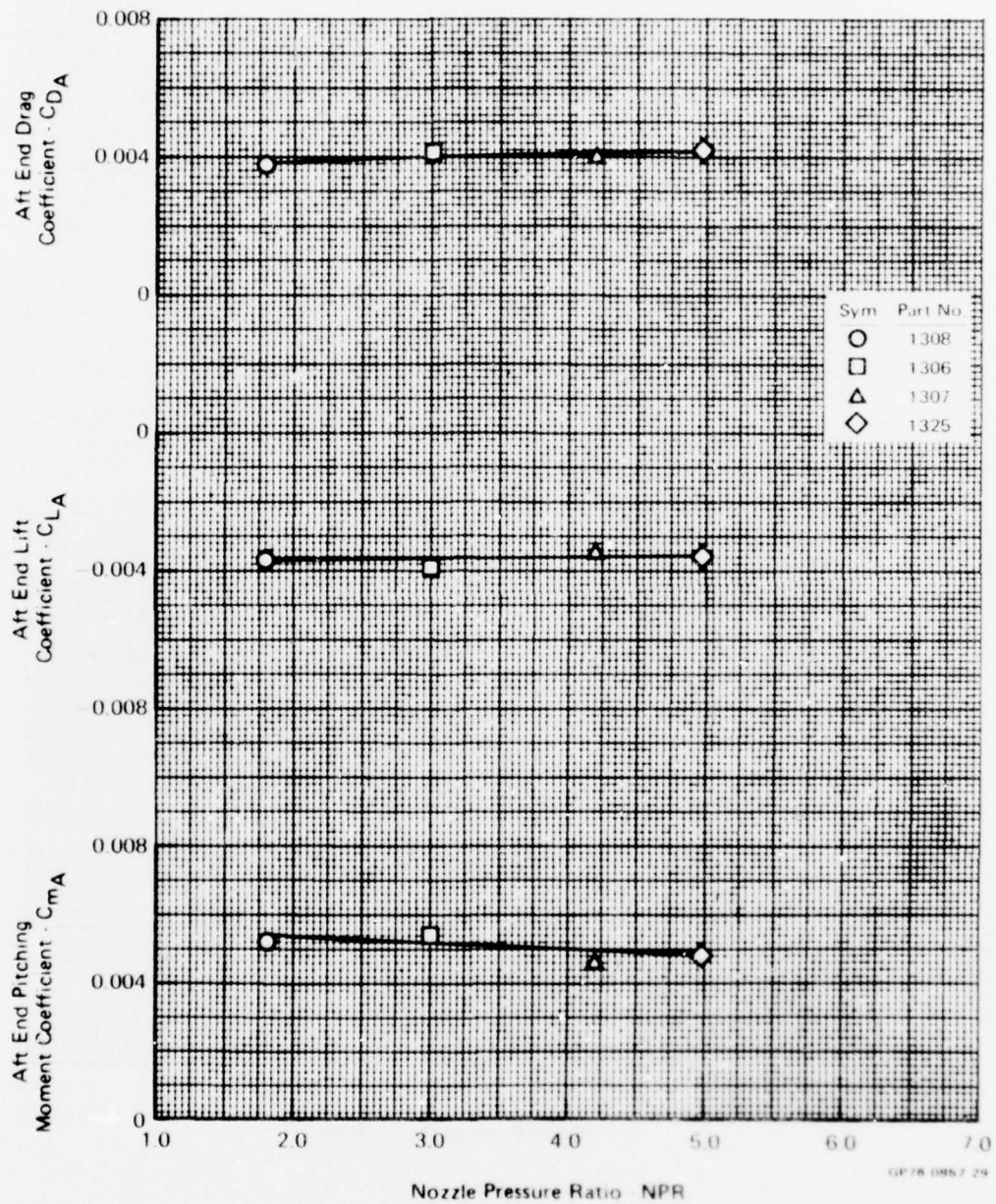


FIGURE D 59
 AFT END PERFORMANCE VARIATION WITH NOZZLE PRESSURE RATIO

Test Mode - Jet Effects
 Nozzle - Afterburning
 Mach No. - 0.6
 Angle of Attack - 10°

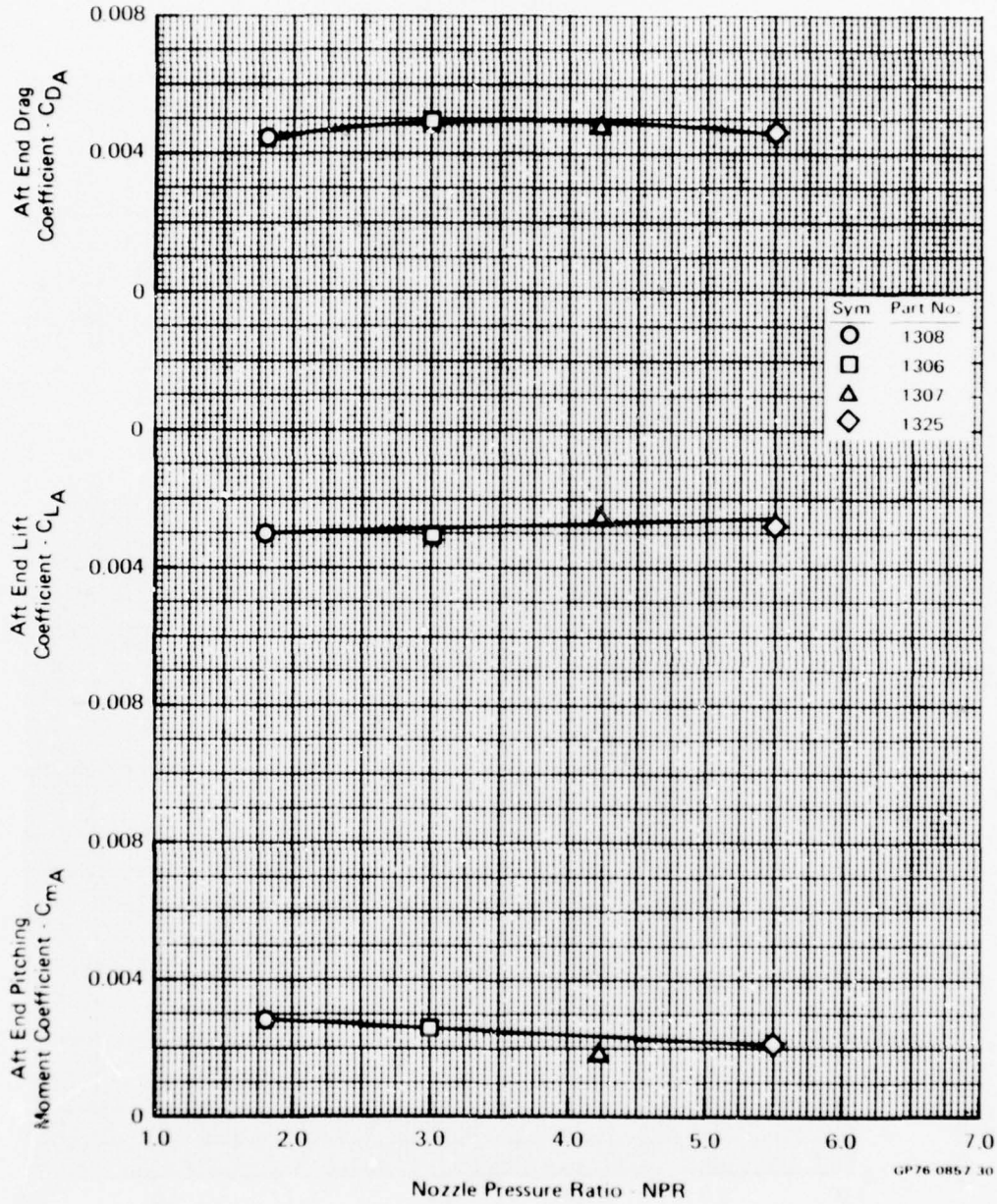


FIGURE D-60
 AFT END PERFORMANCE VARIATION WITH NOZZLE PRESSURE RATIO

Test Mode - Jet Effects
 Nozzle - Afterburning
 Mach No. - 0.6
 Angle of Attack - 16°

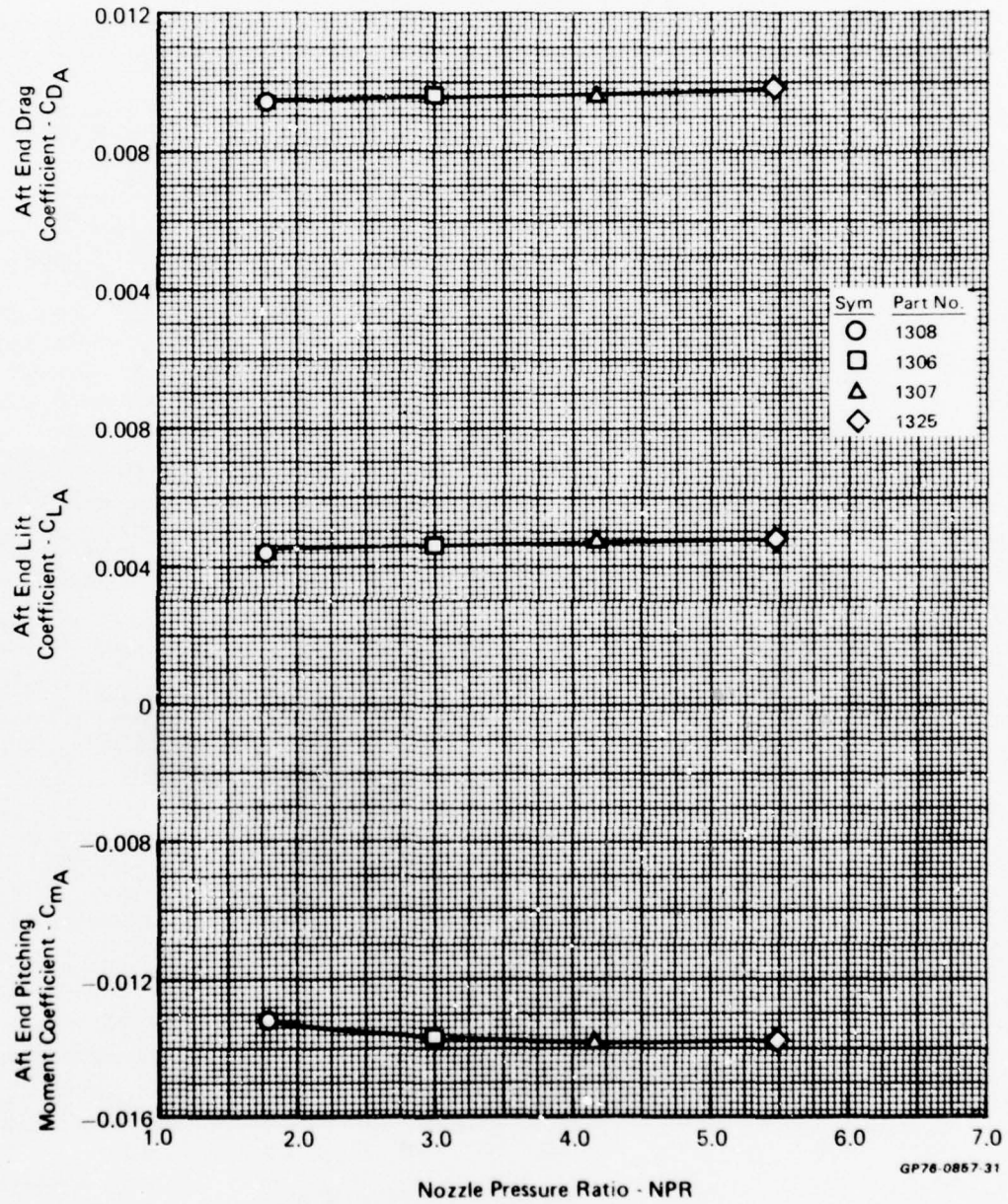


FIGURE D-61
 AFT END PERFORMANCE VARIATION WITH NOZZLE PRESSURE RATIO

Test Mode - Jet Effects
 Nozzle - Afterburning
 Mach No. - 0.9
 Angle of Attack - 0°

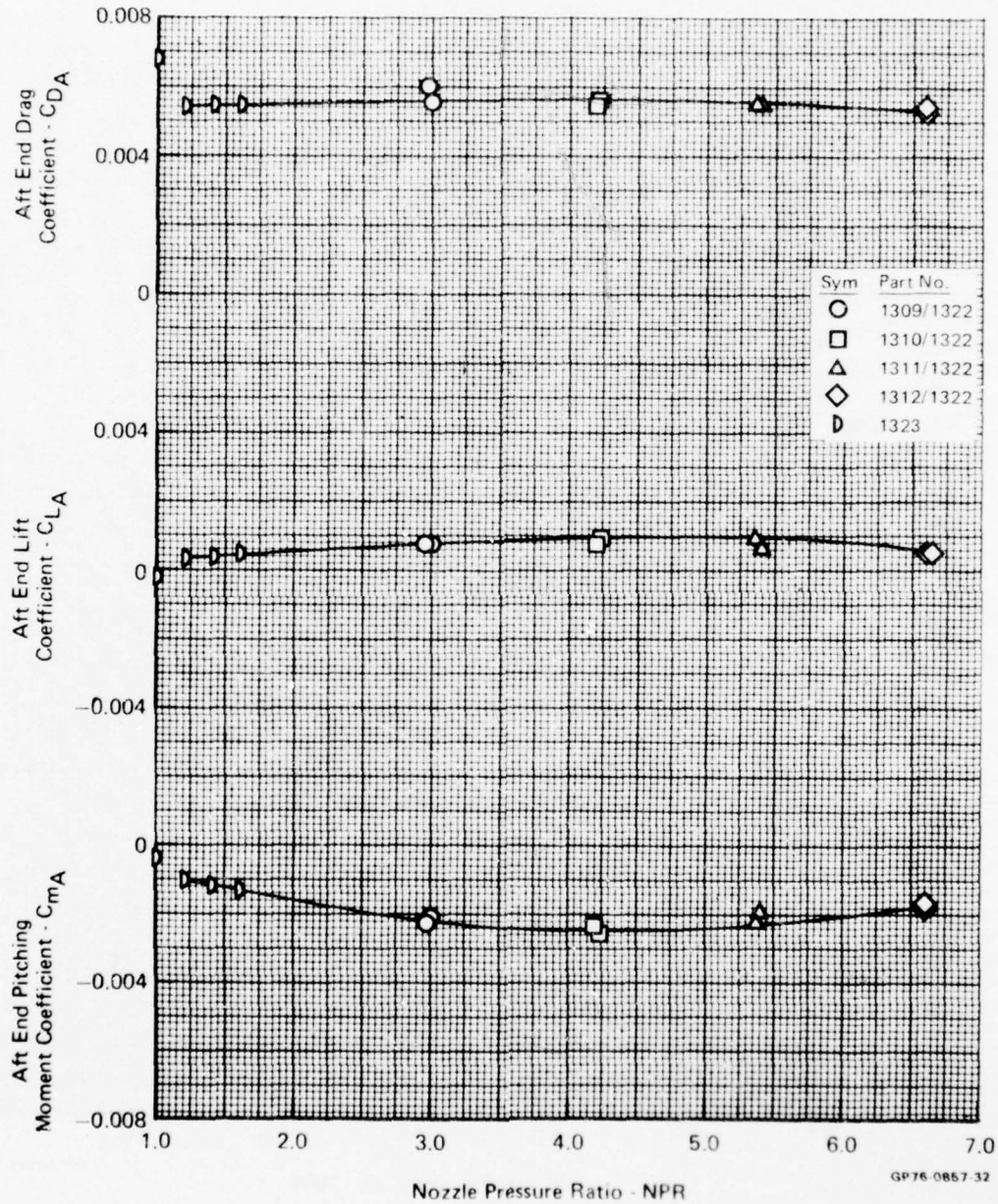


FIGURE D-62
 AFT END PERFORMANCE VARIATION WITH NOZZLE PRESSURE RATIO

Test Mode - Jet Effects
 Nozzle - Afterburning
 Mach No. - 0.9
 Angle of Attack - 5°

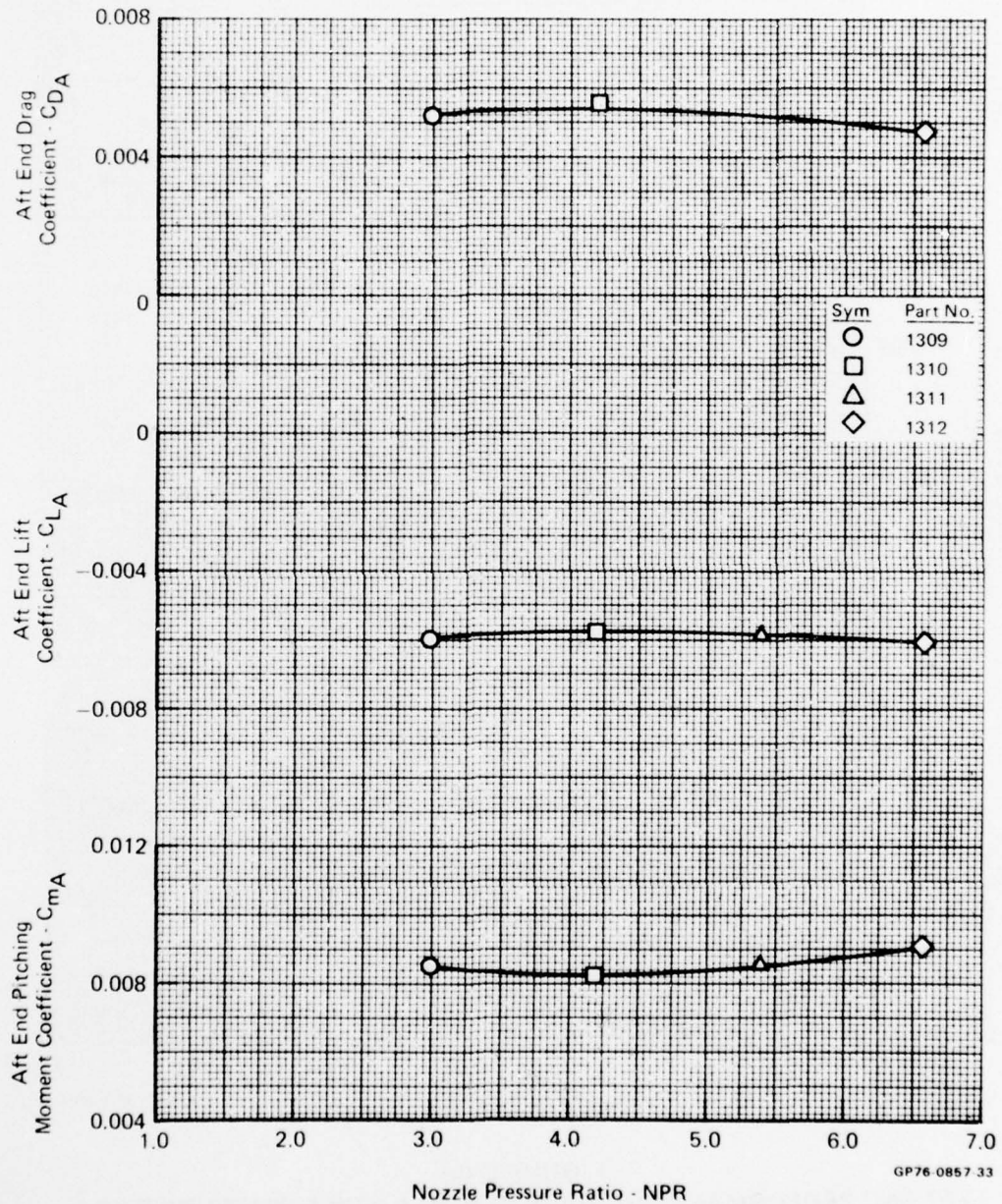


FIGURE D-63
 AFT END PERFORMANCE VARIATION WITH NOZZLE PRESSURE RATIO

Test Mode - Jet Effects
 Nozzle - Afterburning
 Mach No. - 0.9
 Angle of Attack - 10°

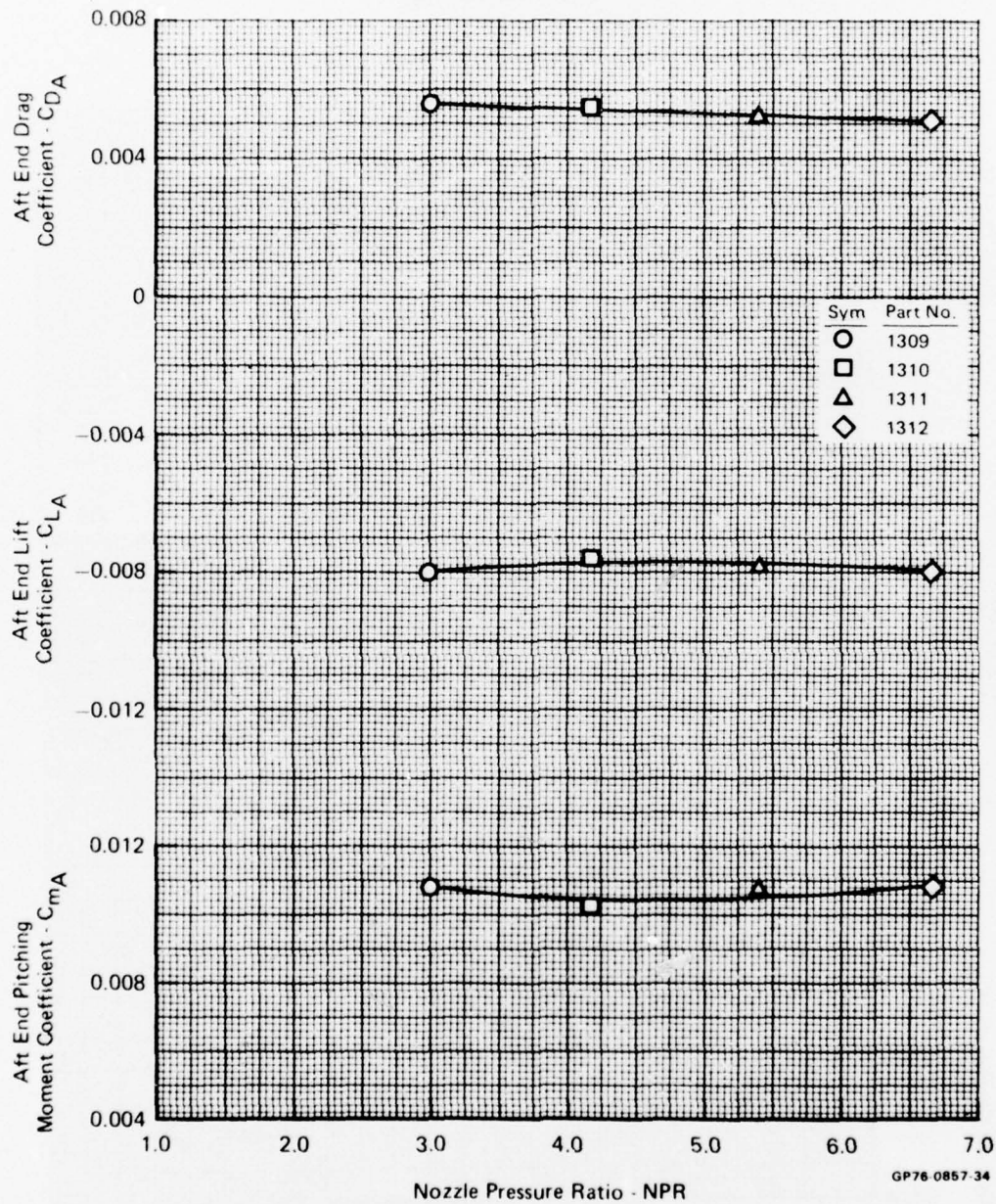


FIGURE D-64
 AFT END PERFORMANCE VARIATION WITH NOZZLE PRESSURE RATIO

Test Mode - Jet Effects
 Nozzle - Afterburning
 Mach No. - 0.9
 Angle of Attack - 16°

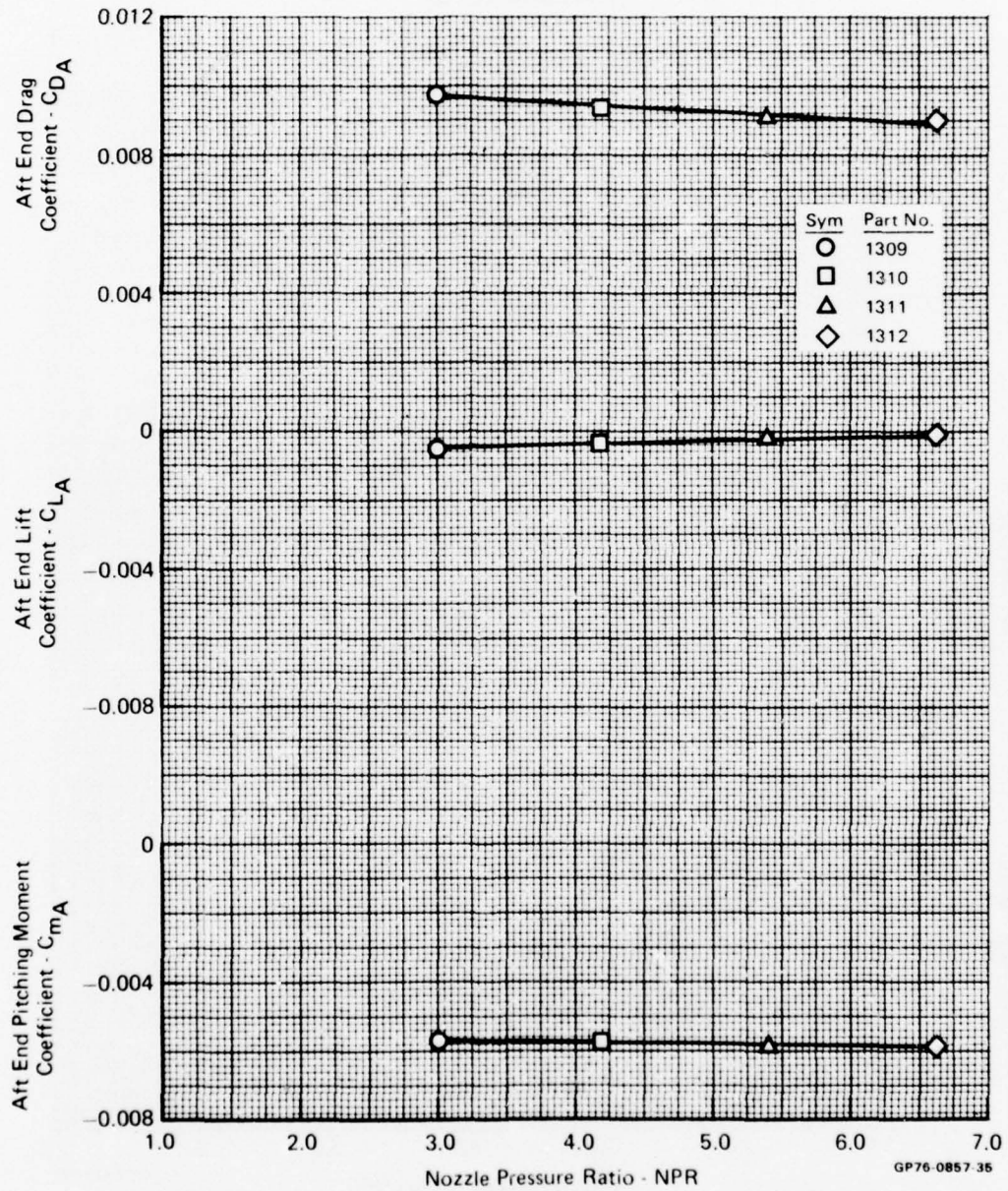


FIGURE D-65
AFT END PERFORMANCE VARIATION WITH NOZZLE PRESSURE RATIO

Test Mode - Jet Effects
 Nozzle - Afterburning
 Mach No. - 1.2
 Angle of Attack - 0°

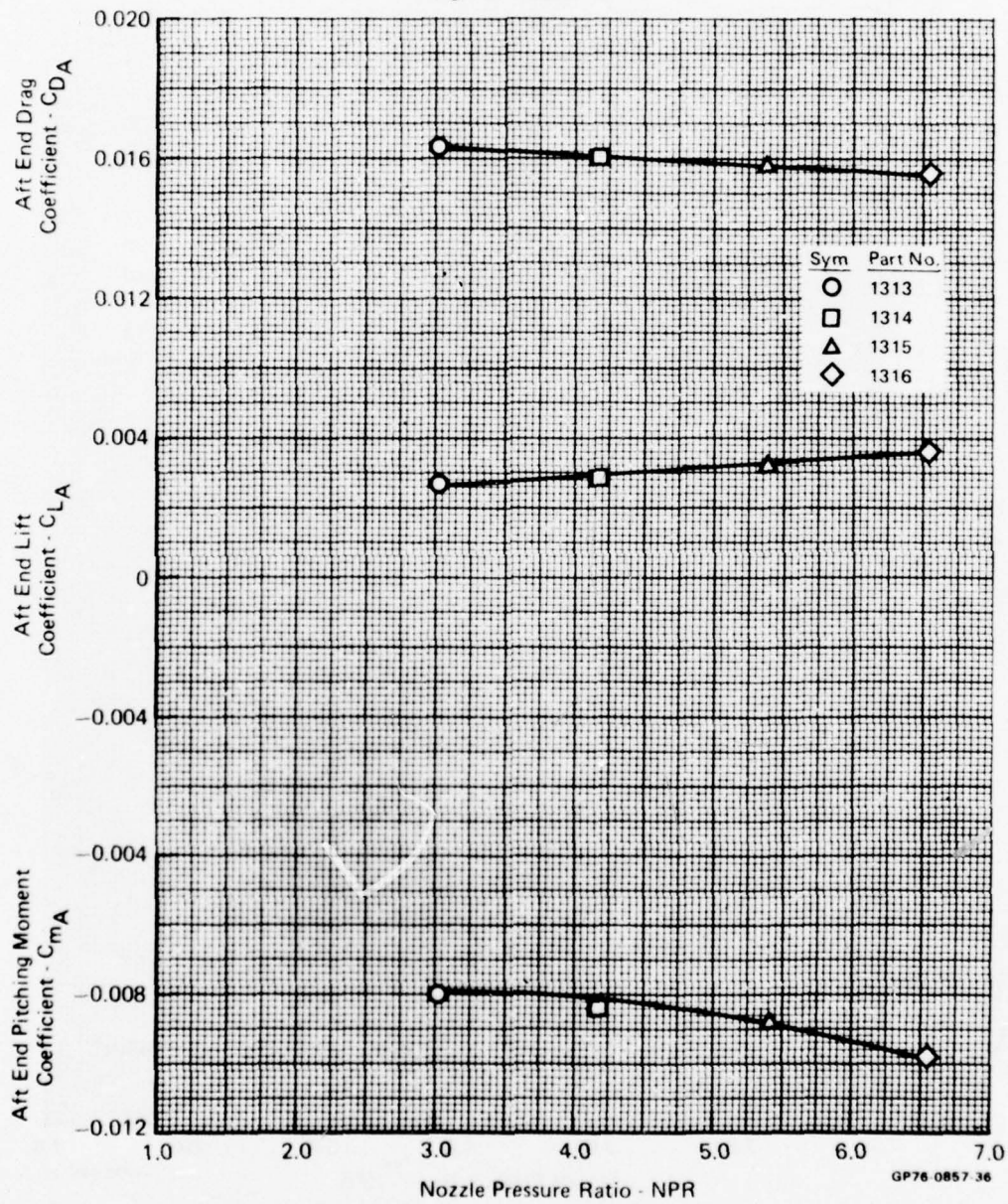


FIGURE D-66
AFT END PERFORMANCE VARIATION WITH NOZZLE PRESSURE RATIO

Test Mode - Jet Effects
 Nozzle - Afterburning
 Mach No. - 1.2
 Angle of Attack - 5°

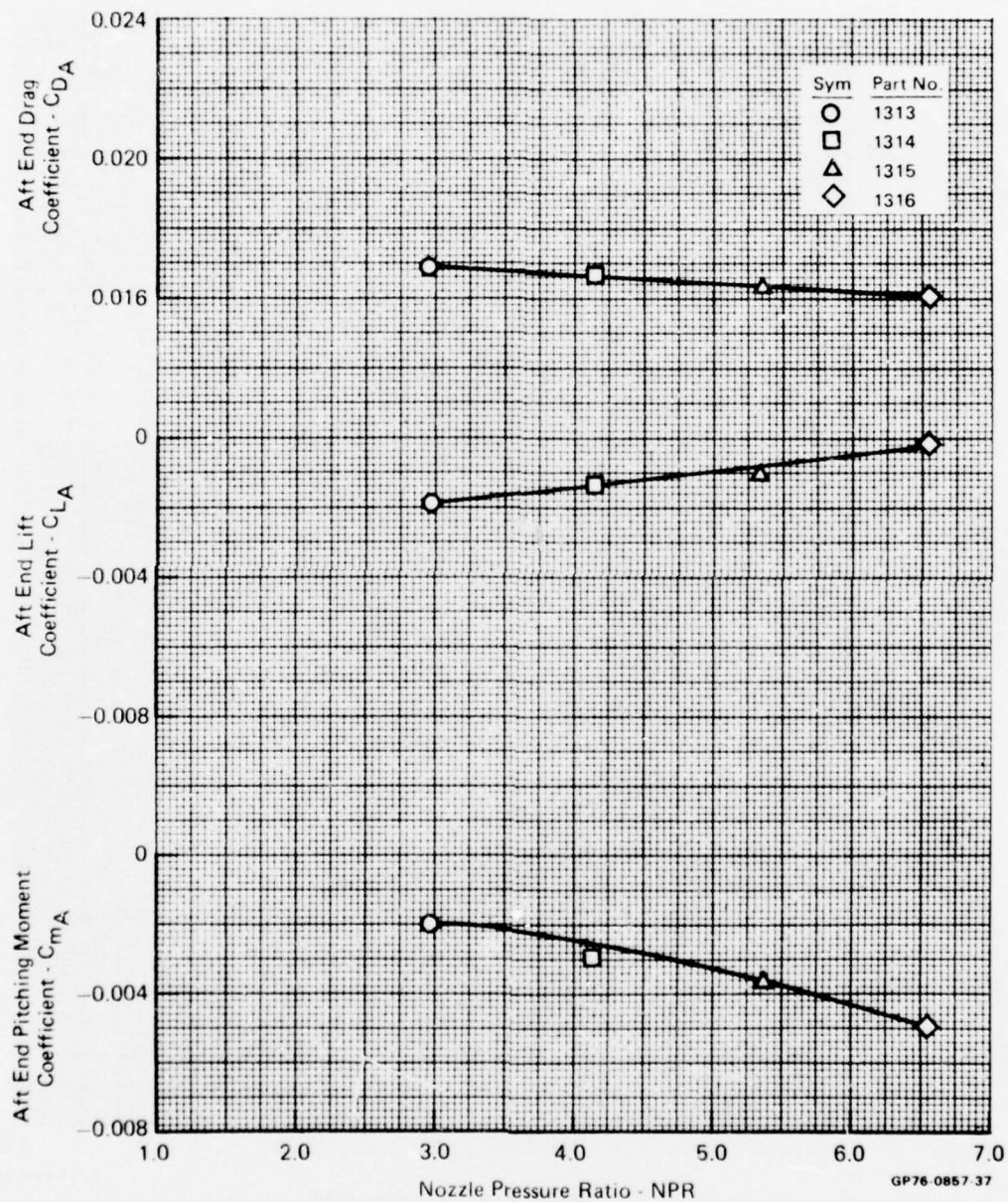


FIGURE D-67
 AFT END PERFORMANCE VARIATION WITH NOZZLE PRESSURE RATIO

Test Mode - Jet Effects
 Nozzle - Afterburning Power
 Mach No. - 1.2
 Angle of Attack - 10°

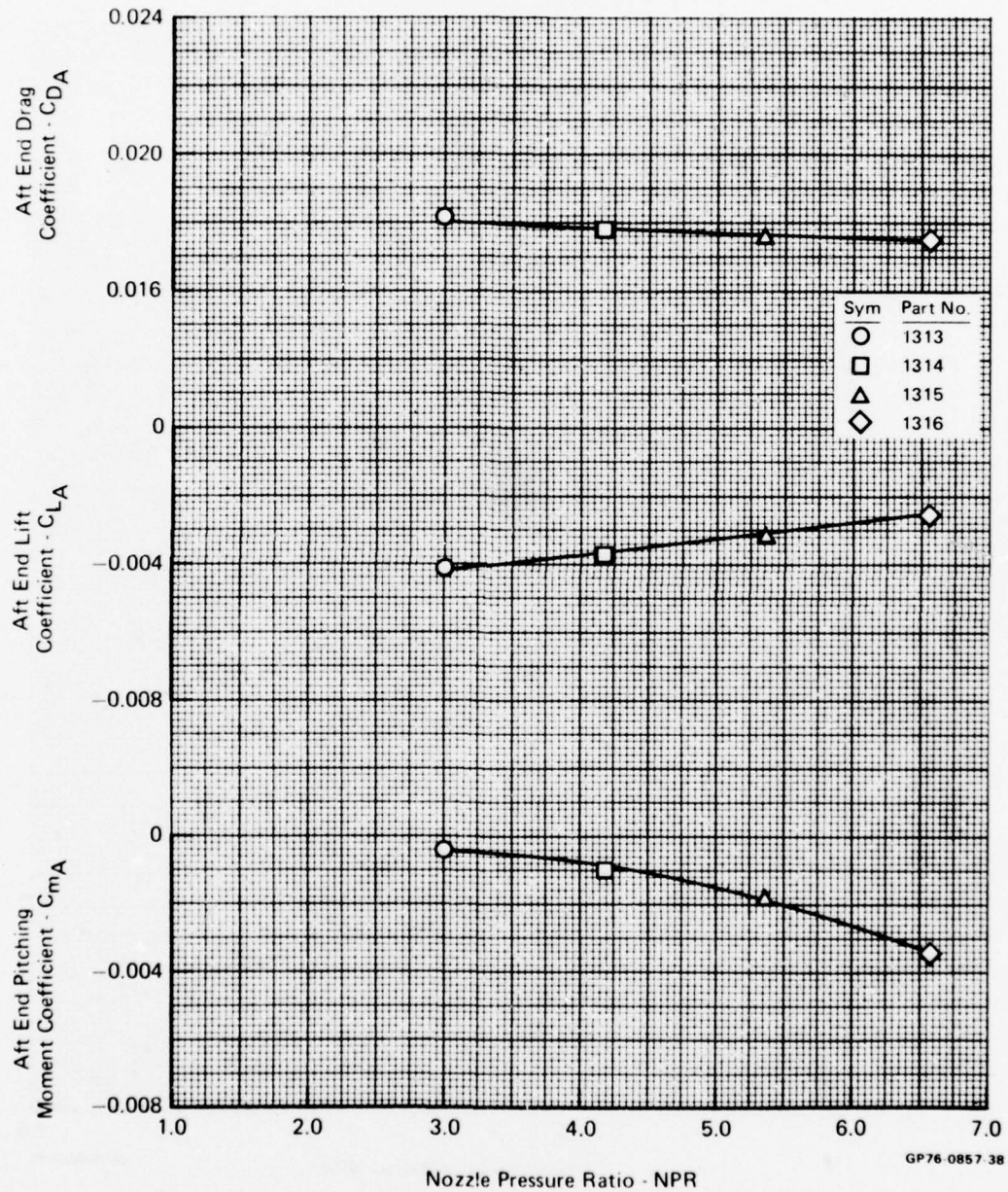


FIGURE D-68
AFT END PERFORMANCE VARIATION WITH NOZZLE PRESSURE RATIO

Test Mode - Jet Effects
 Nozzle - Afterburning
 Mach No. - 1.2
 Angle of Attack - 16°

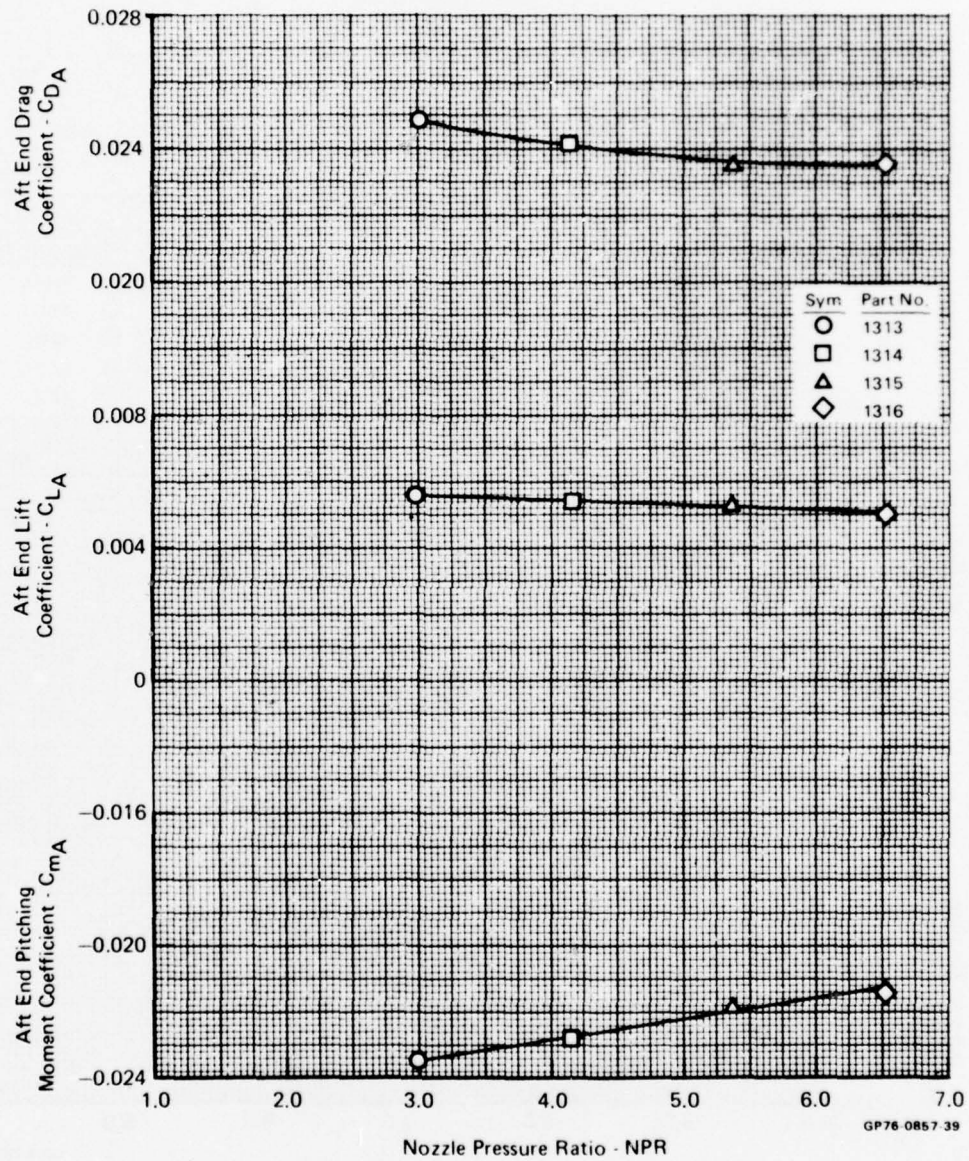


FIGURE D-69
 AFT END PERFORMANCE VARIATION WITH NOZZLE PRESSURE RATIO

Test Mode - Jet Effects
 Nozzle - Afterburning
 Mach No. - 1.45
 Angle of Attack - 0°

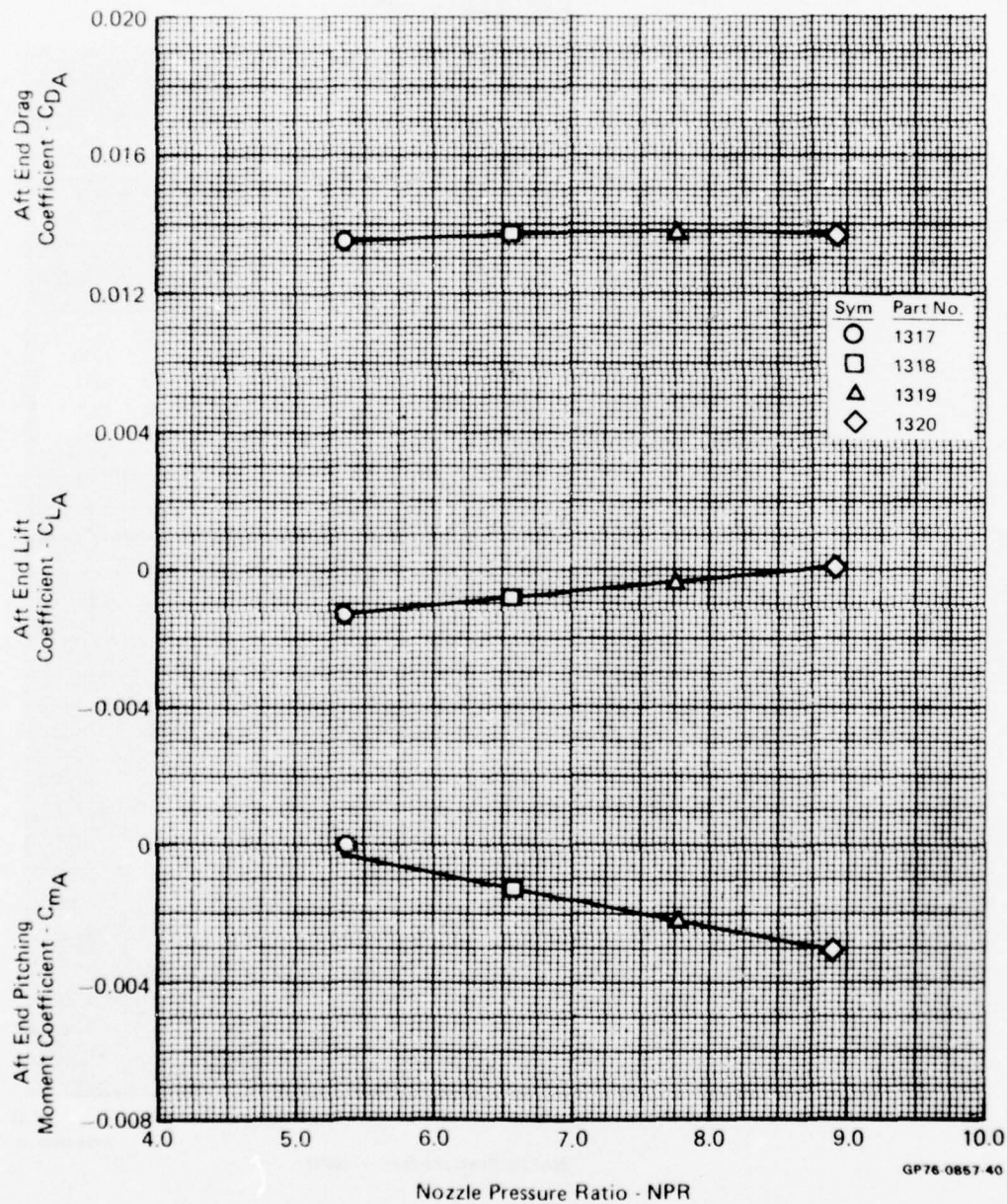


FIGURE D-70
AFT END PERFORMANCE VARIATION WITH NOZZLE PRESSURE RATIO

Test Mode - Jet Effects
 Nozzle - Afterburning
 Mach No. - 1.45
 Angle of Attack - 3°

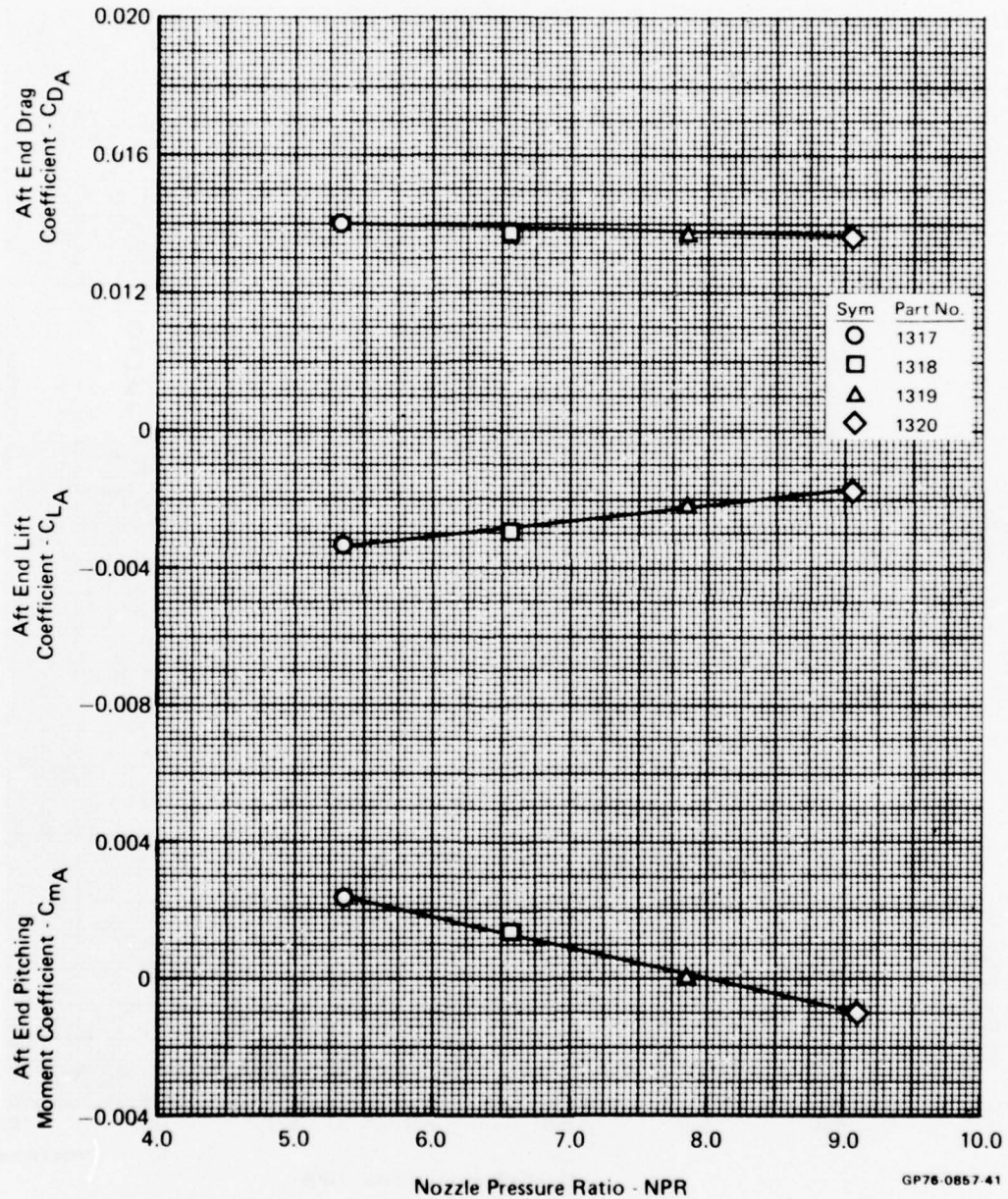


FIGURE D-71
 AFT END PERFORMANCE VARIATION WITH NOZZLE PRESSURE RATIO

Test Mode - Jet Effects
 Nozzle - Afterburning
 Mach No. - 1.45
 Angle of Attack - 6°

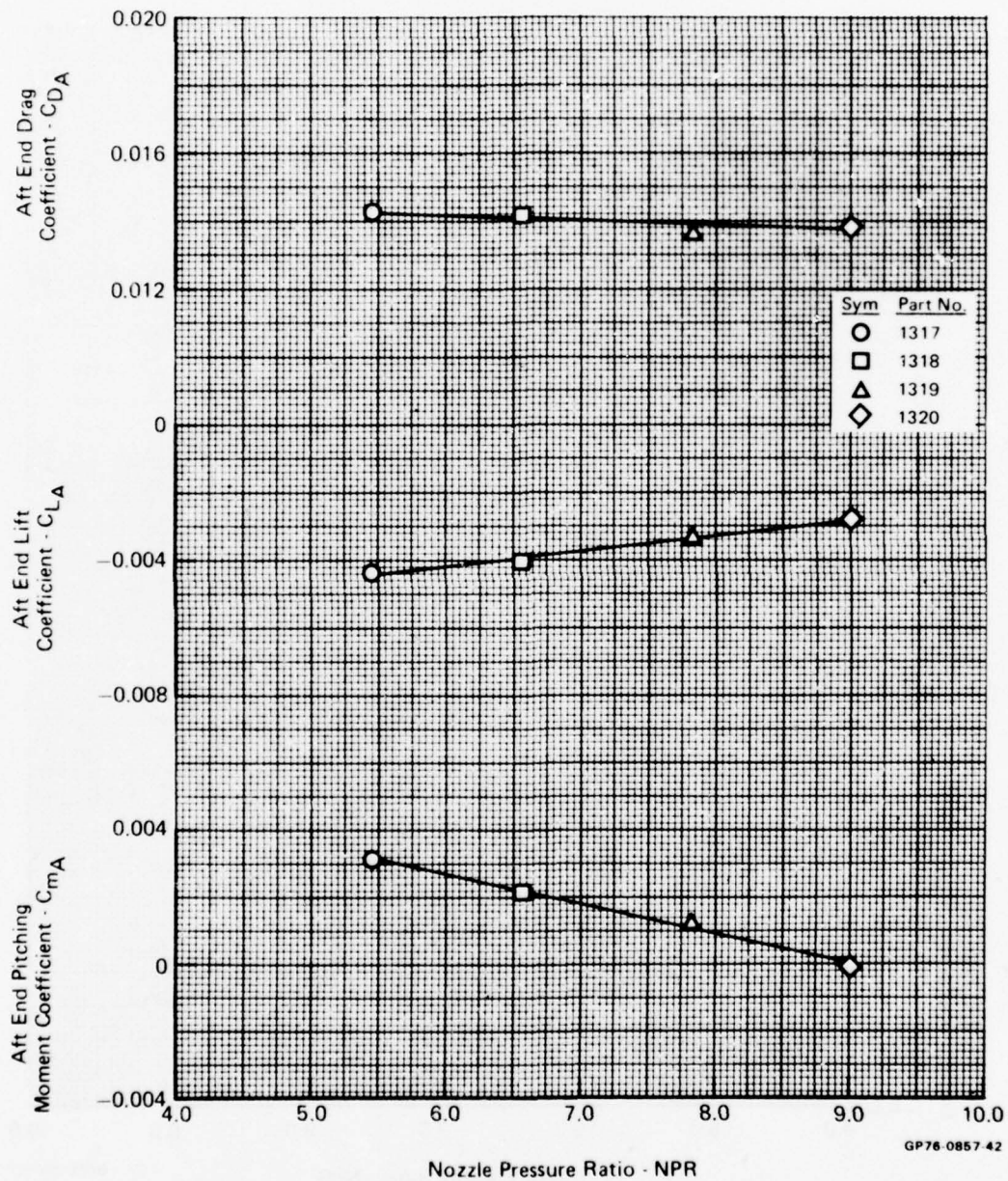


FIGURE D-72
 AFT END PERFORMANCE VARIATION WITH NOZZLE PRESSURE RATIO

Test Mode - Jet Effects
 Nozzle - Afterburning
 Mach No. - 1.45
 Angle of Attack - 10°

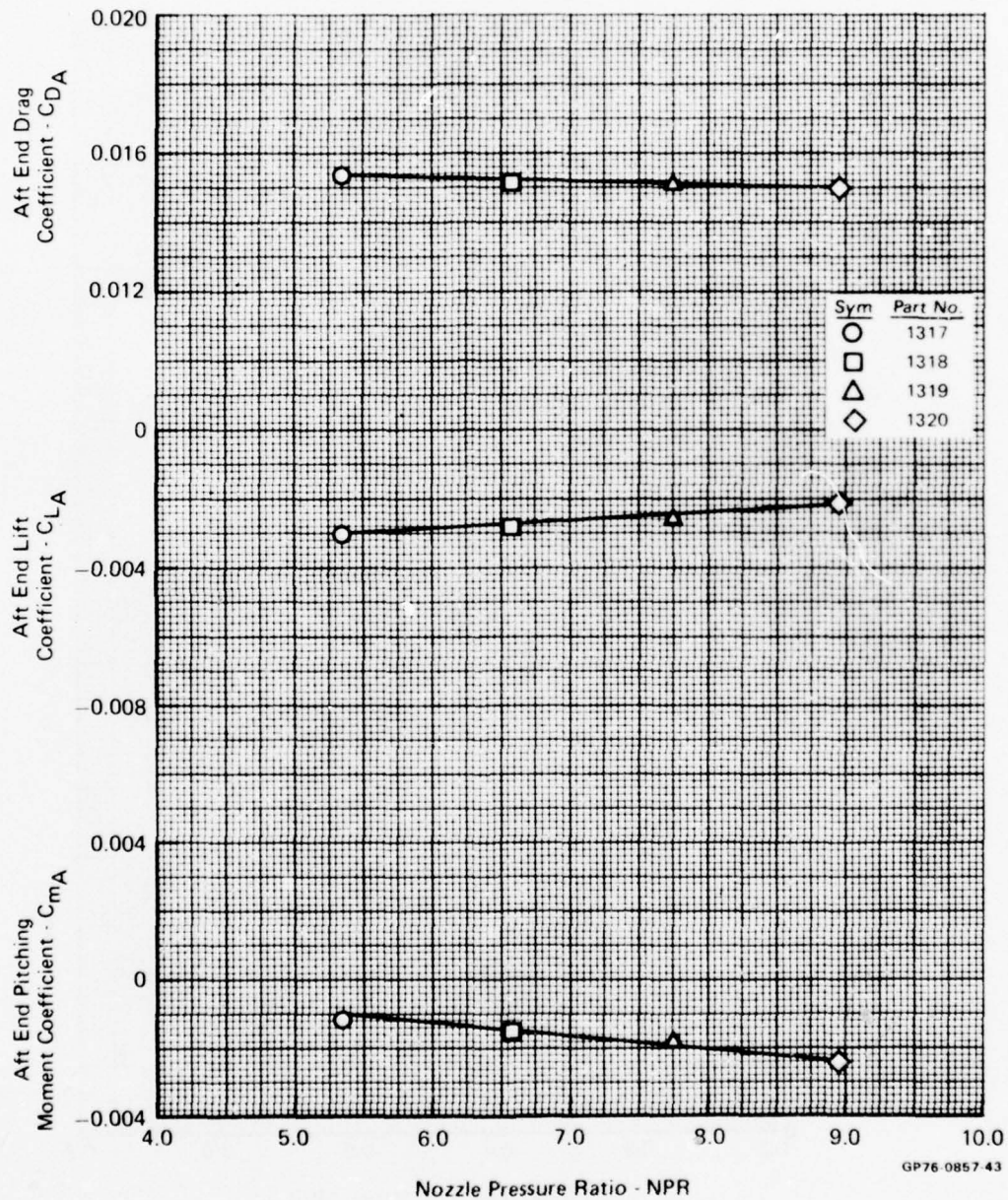


FIGURE D-73
 AFT END PERFORMANCE VARIATION WITH NOZZLE PRESSURE RATIO

Test Mode - Simulator
 Nozzle - Dry
 Mach No. - 0.6
 Angle of Attack - 0°

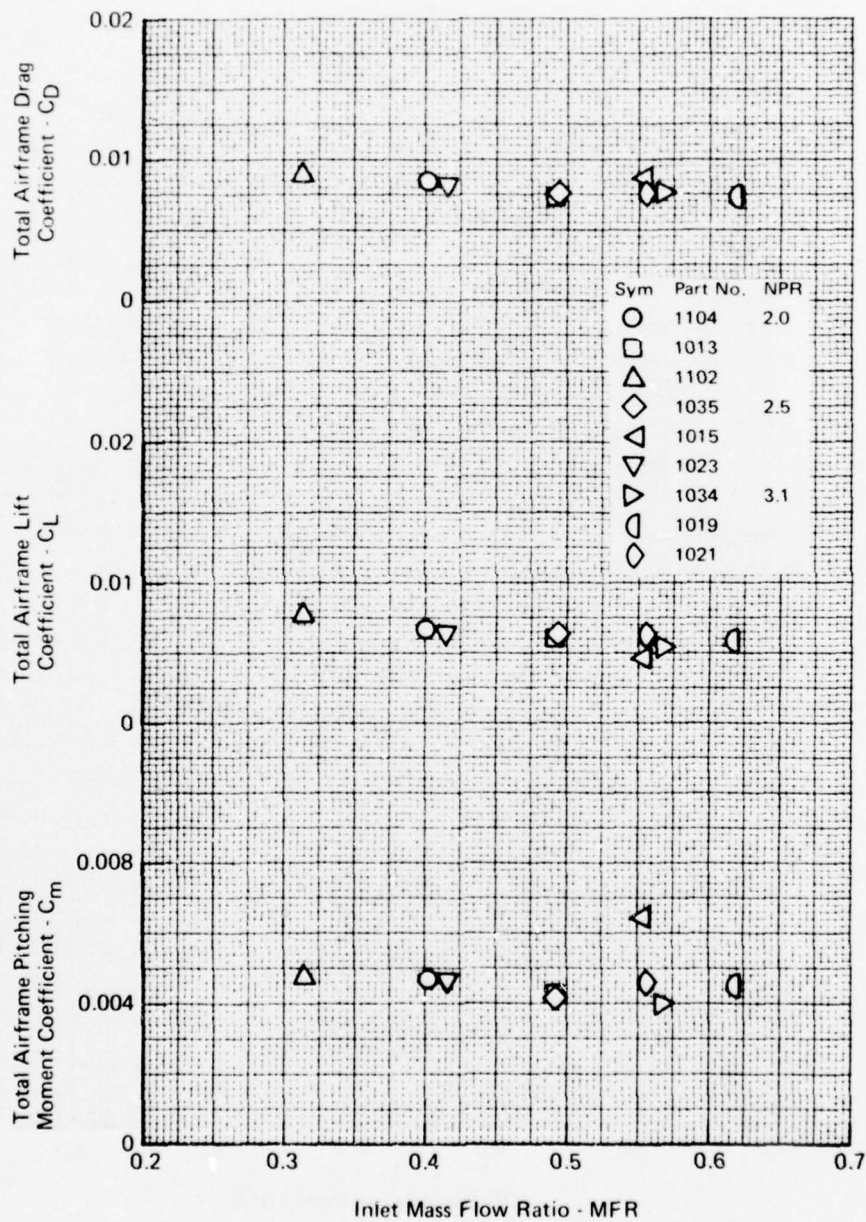


FIGURE D-74
TOTAL AIRFRAME PERFORMANCE VARIATION WITH INLET MASS FLOW RATIO

GP76 0701 171

Test Mode - Simulator
 Nozzle - Dry
 Mach No. - 0.6
 Angle of Attack - 5°

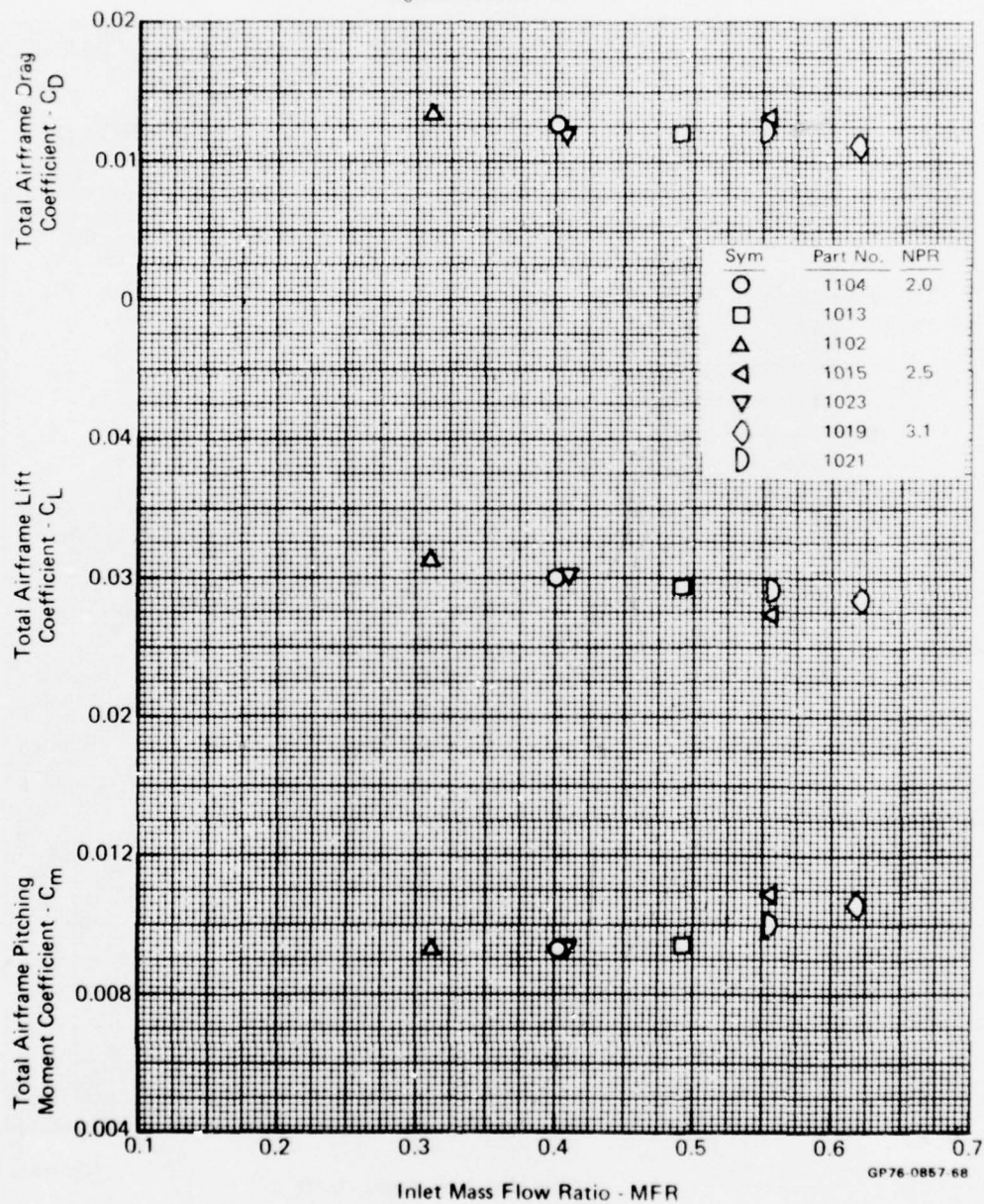


FIGURE D-75

TOTAL AIRFRAME PERFORMANCE VARIATION WITH INLET MASS FLOW RATIO

Test Mode - Simulator
 Nozzle - Dry
 Mach No. - 0.6
 Angle of Attack - 10°

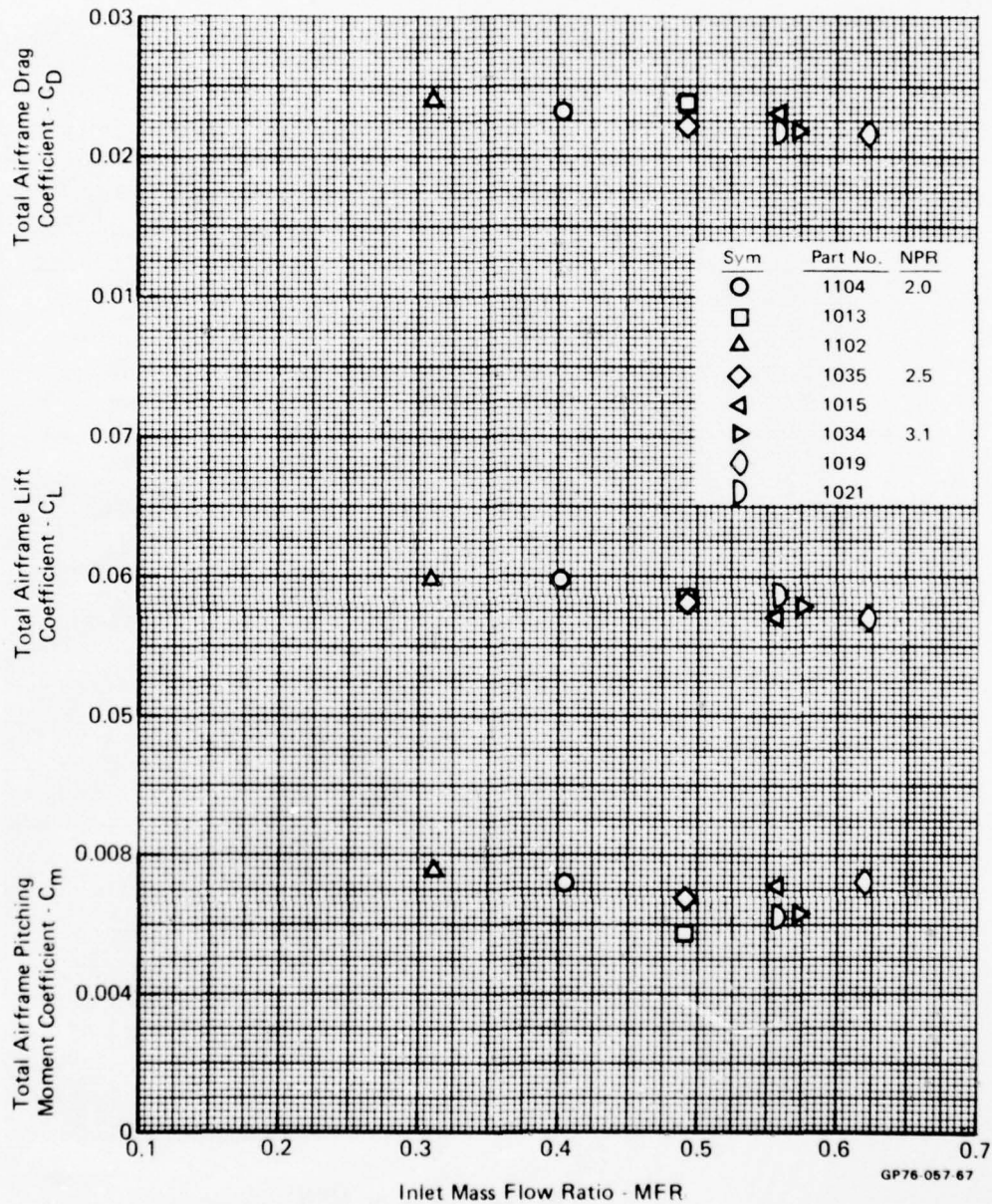


FIGURE D-76
 TOTAL AIRFRAME PERFORMANCE VARIATION WITH INLET MASS FLOW RATIO

Test Mode - Simulator

Nozzle - Dry

Mach No. - 0.6

Angle of Attack - 16°

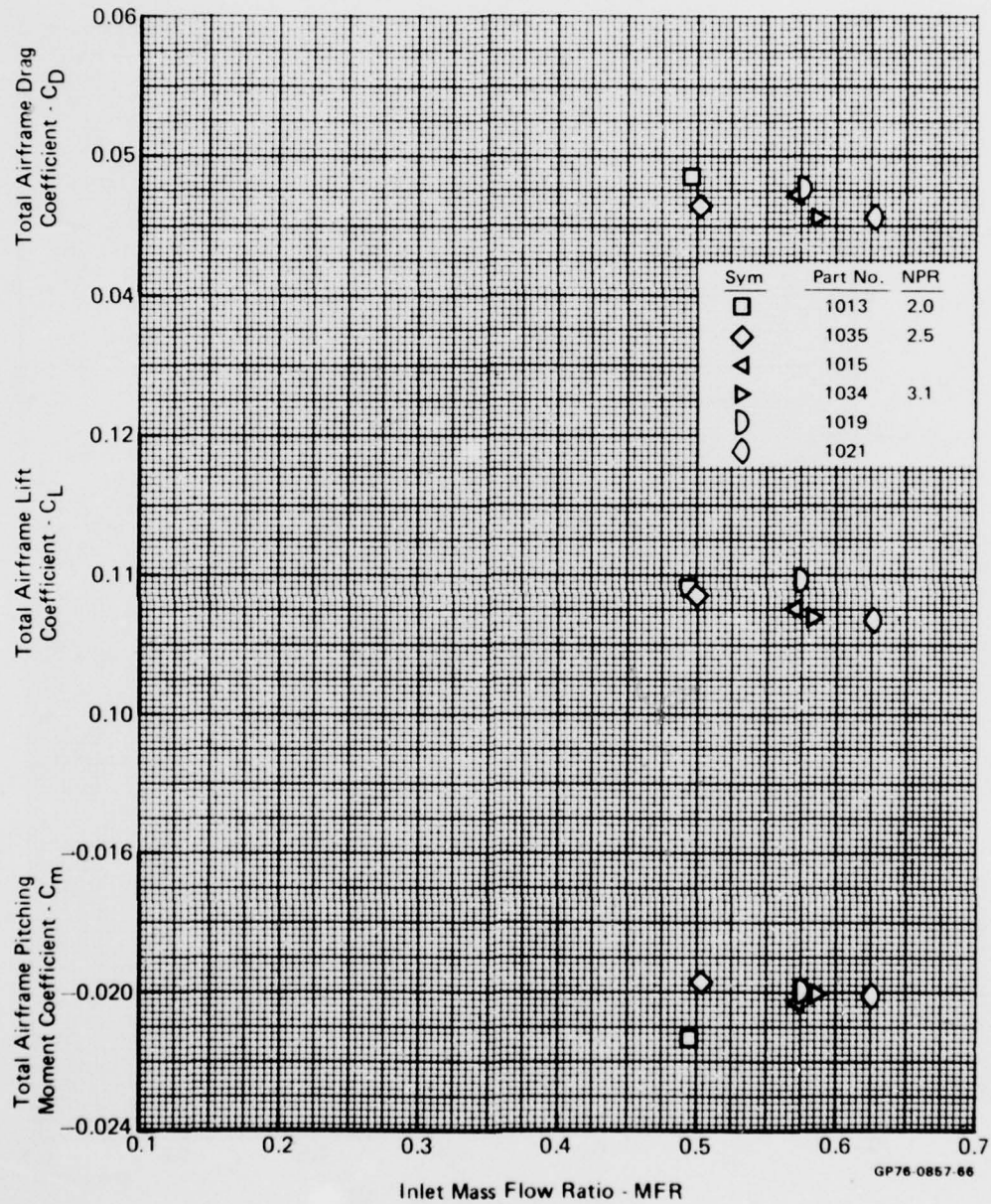


FIGURE D-77

TOTAL AIRFRAME PERFORMANCE VARIATION WITH INLET MASS FLOW RATIO

Test Mode - Simulator
 Nozzle - Dry
 Mach No. - 0.9
 Angle of Attack - 0°

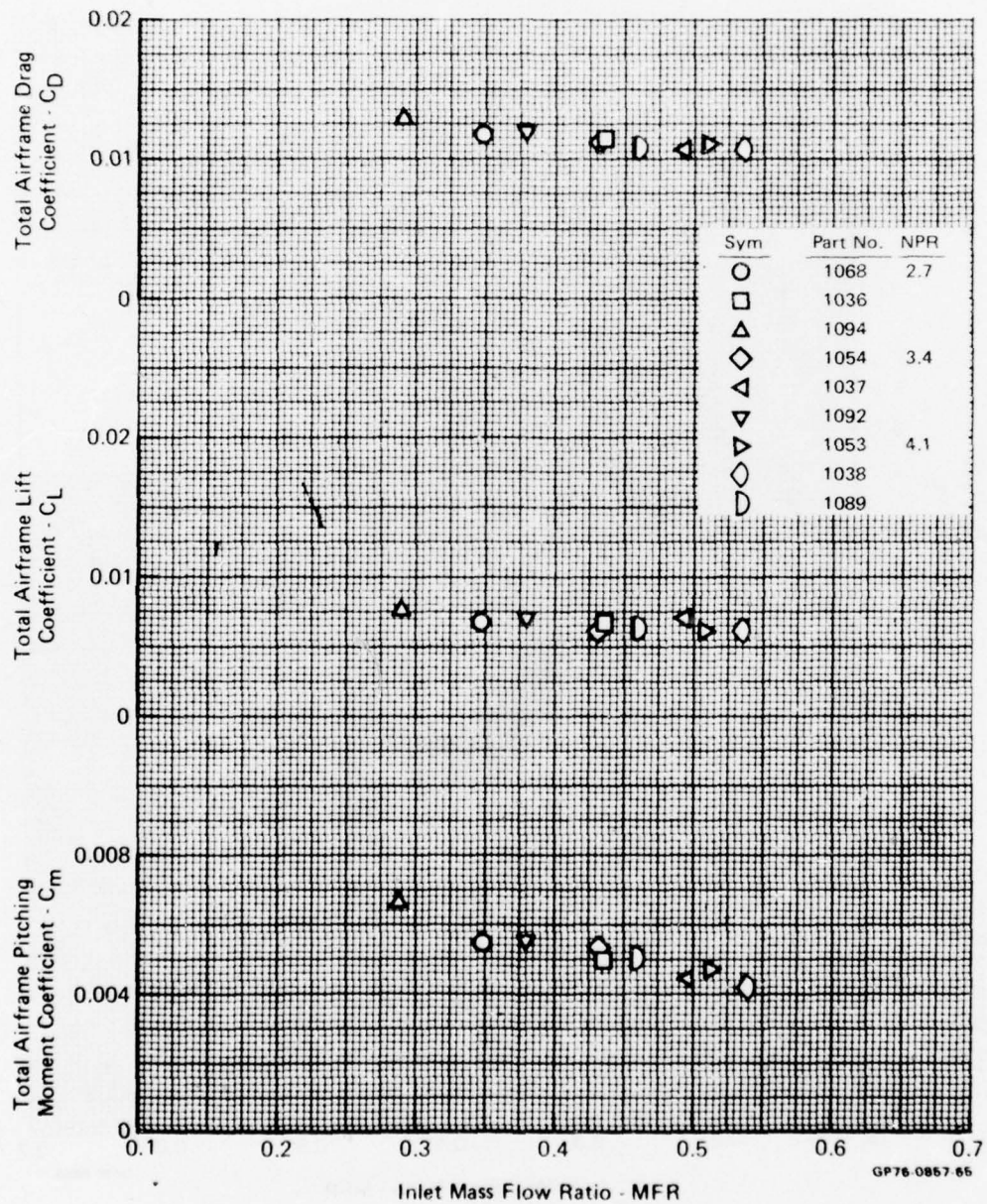


FIGURE D-78
 TOTAL AIRFRAME PERFORMANCE VARIATION WITH INLET MASS FLOW RATIO

Test Mode - Simulator

Nozzle - Dry

Mach No. - 0.9

Angle of Attack - 5°

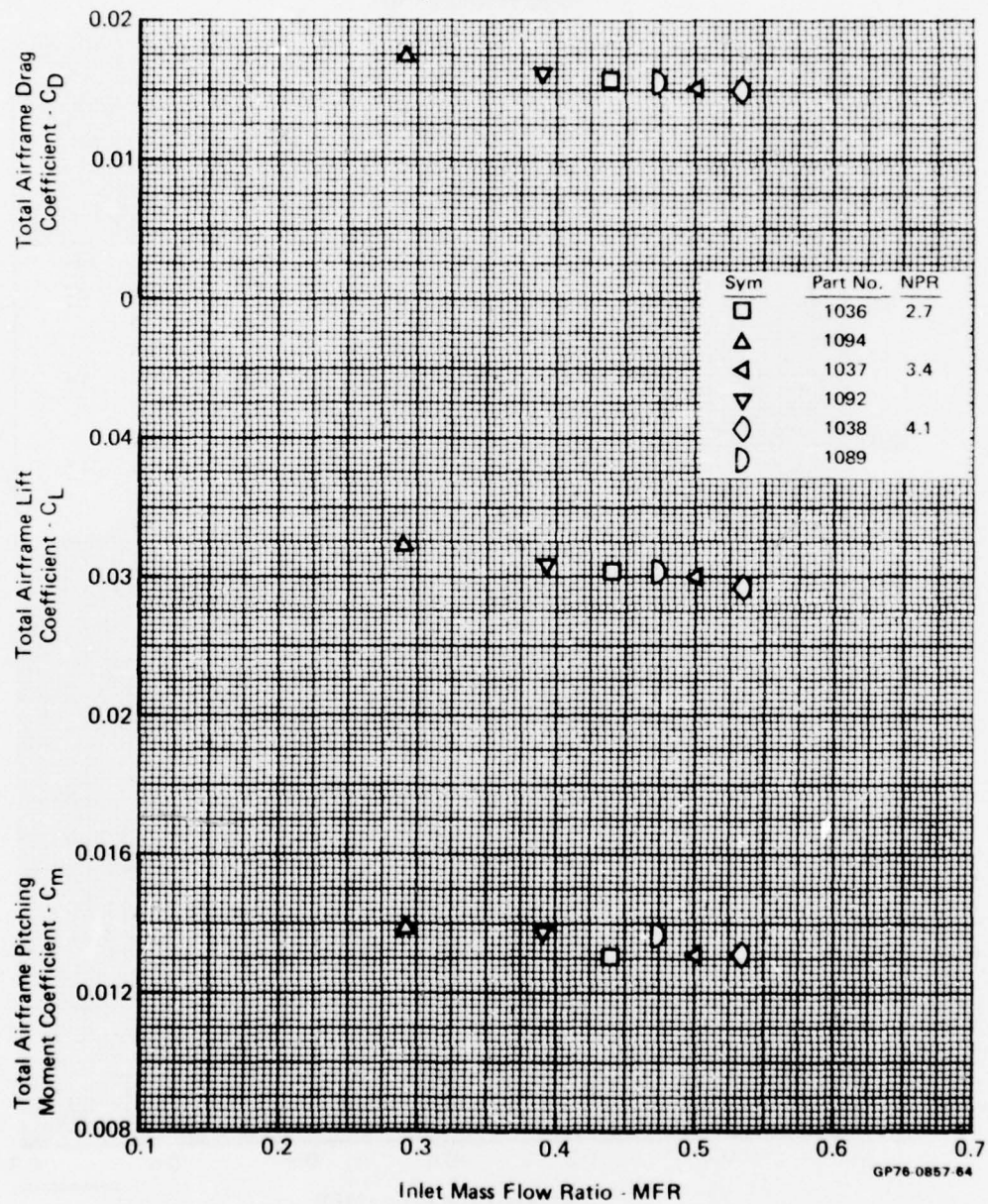


FIGURE D-79

TOTAL AIRFRAME PERFORMANCE VARIATION WITH INLET MASS FLOW RATIO

Test Mode - Simulator
 Nozzle - Dry
 Mach No. - 0.9
 Angle of Attack - 10°

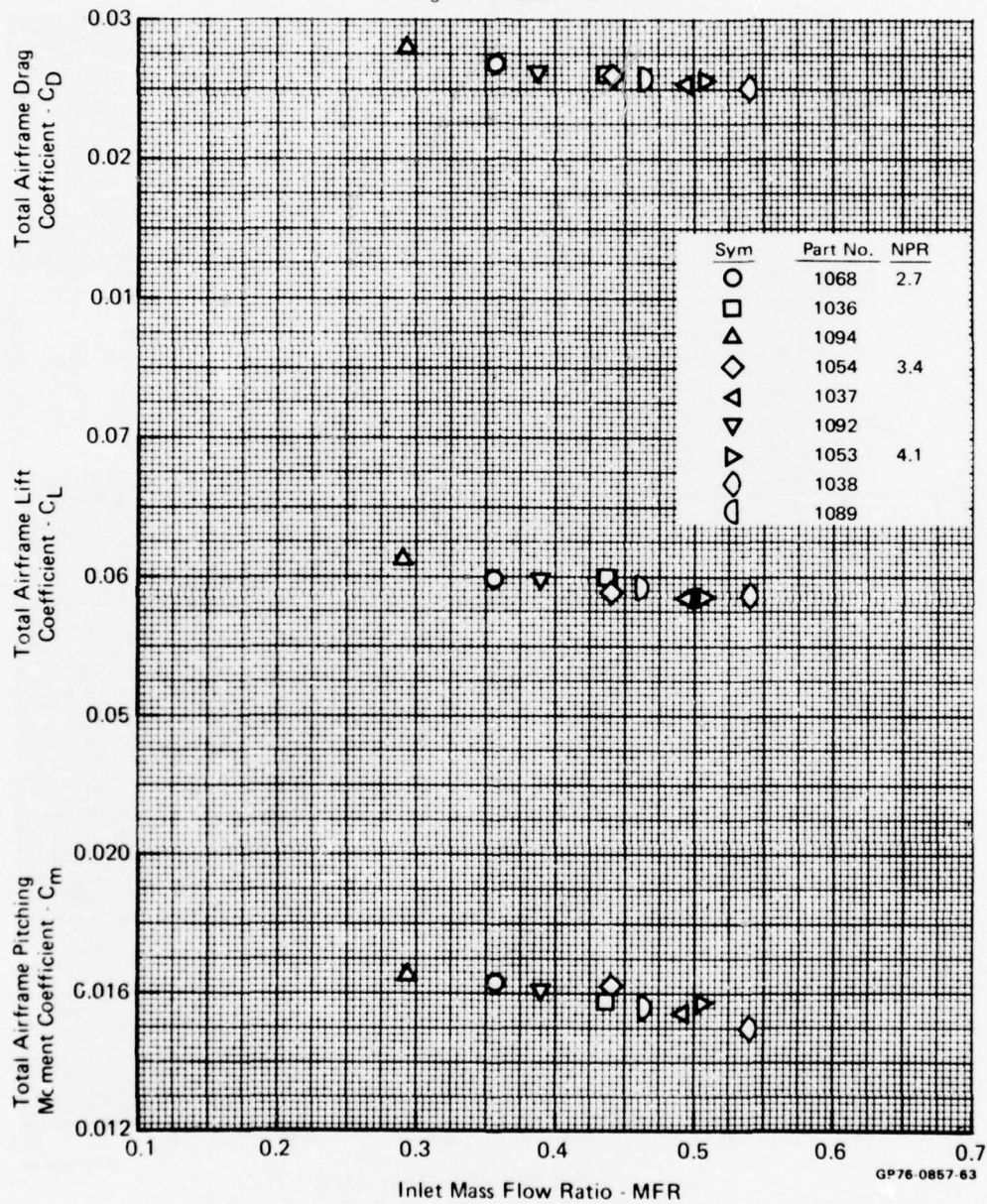


FIGURE D-80

TOTAL AIRFRAME PERFORMANCE VARIATION WITH INLET MASS FLOW RATIO

Test Mode - Simulator
 Nozzle - Dry
 Mach No. - 0.9
 Angle of Attack - 16°

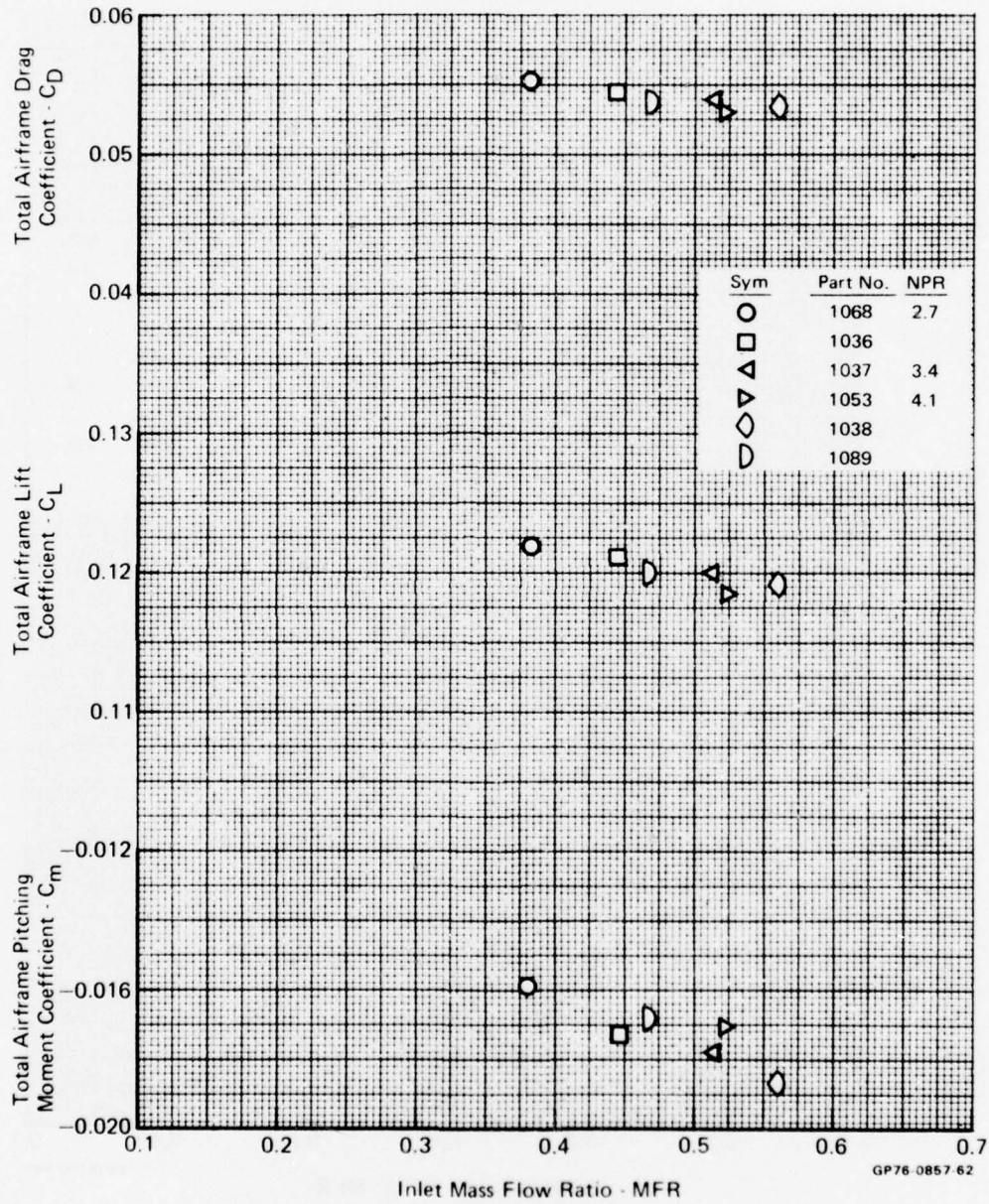


FIGURE D-81

TOTAL AIRFRAME PERFORMANCE VARIATION WITH INLET MASS FLOW RATIO

Test Mode - Simulator
 Nozzle - Dry
 Mach No. - 1.2
 Angle of Attack - 0°

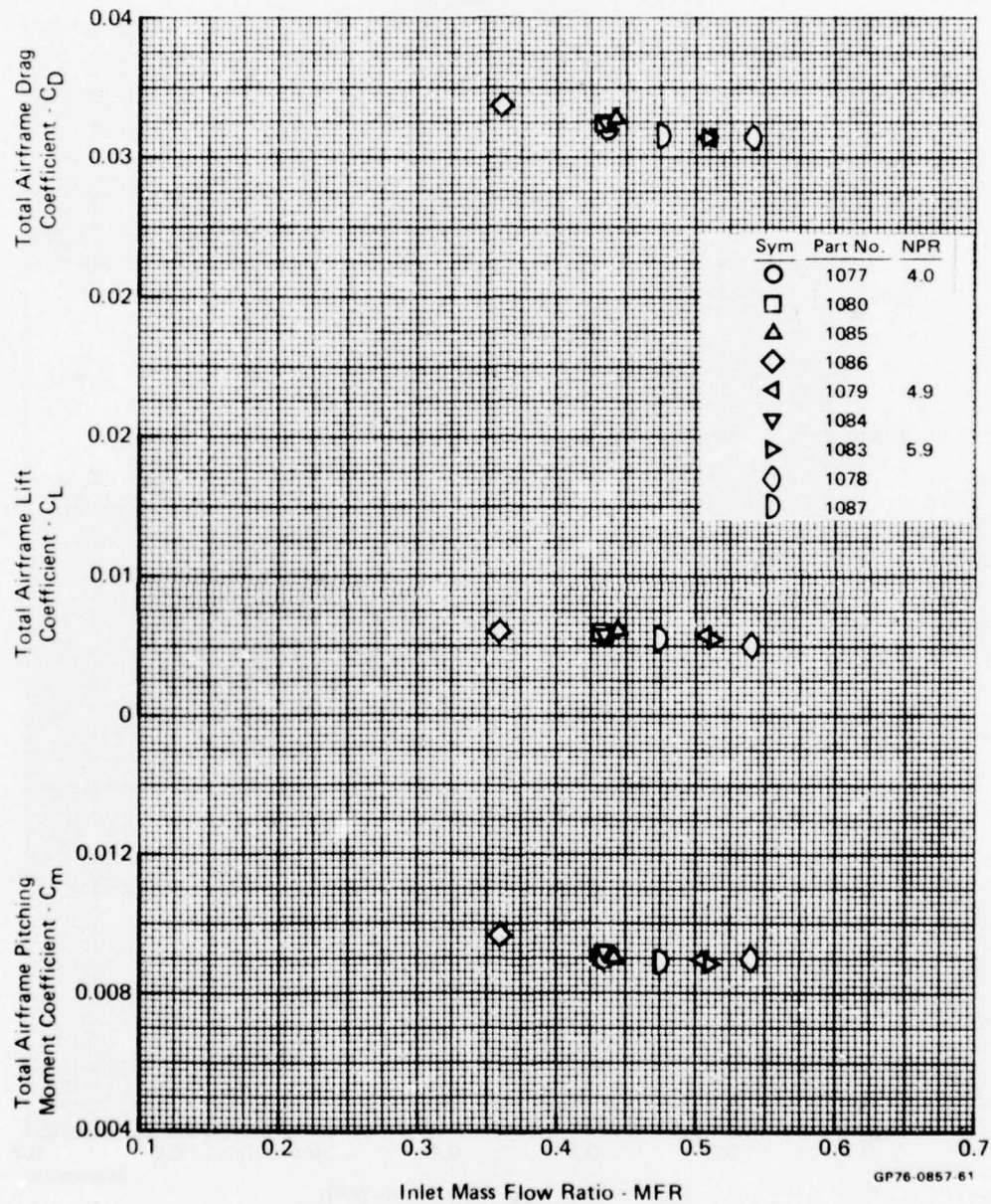


FIGURE D-82

TOTAL AIRFRAME PERFORMANCE VARIATION WITH INLET MASS FLOW RATIO

Test Mode - Simulator
 Nozzle - Dry
 Mach No. - 1.2
 Angle of Attack - 5°

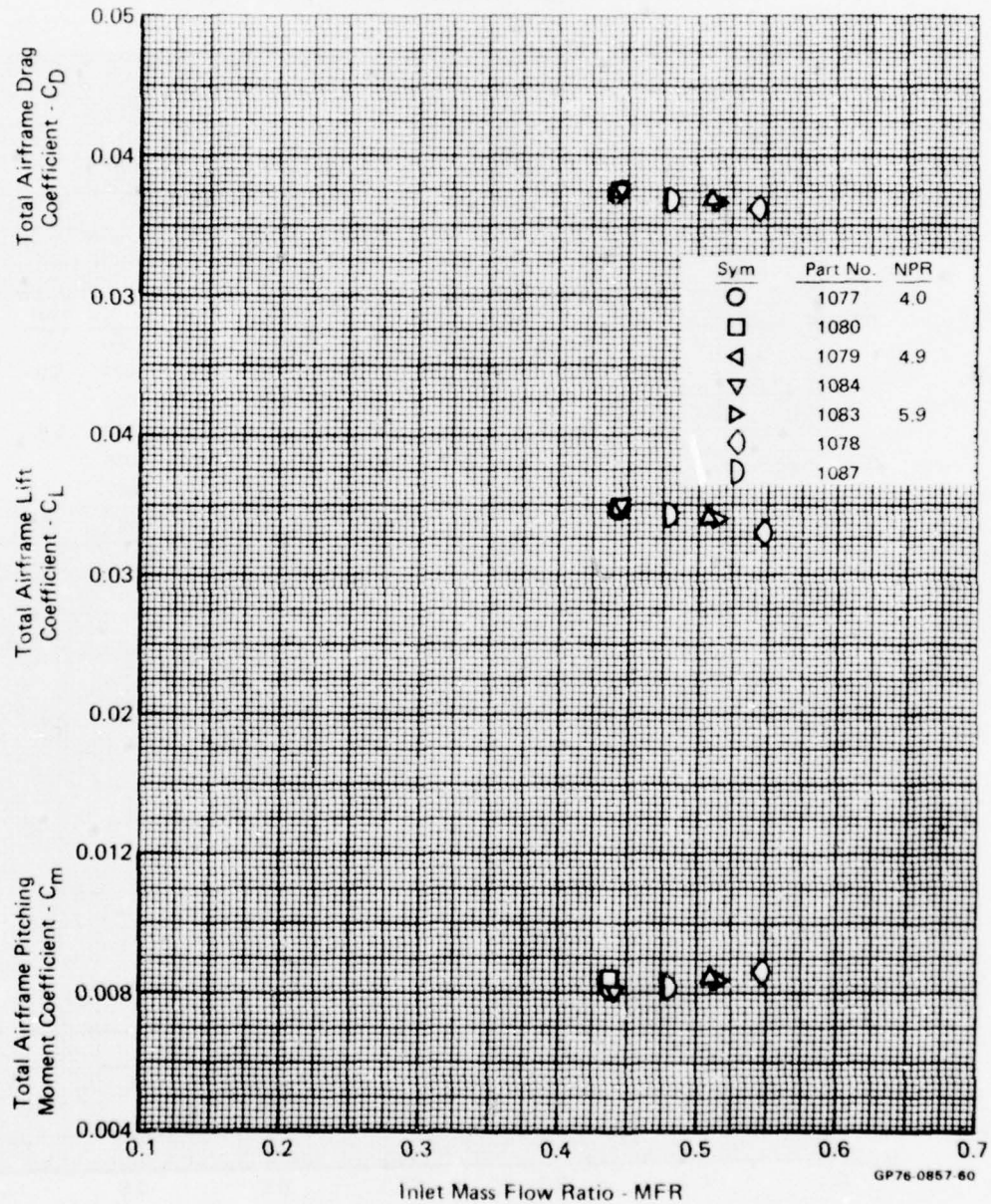


FIGURE D-83
 TOTAL AIRFRAME PERFORMANCE VARIATION WITH INLET MASS FLOW RATIO

Test Mode - Simulator
 Nozzle - Dry
 Mach No. - 1.2
 Angle of Attack - 10^0

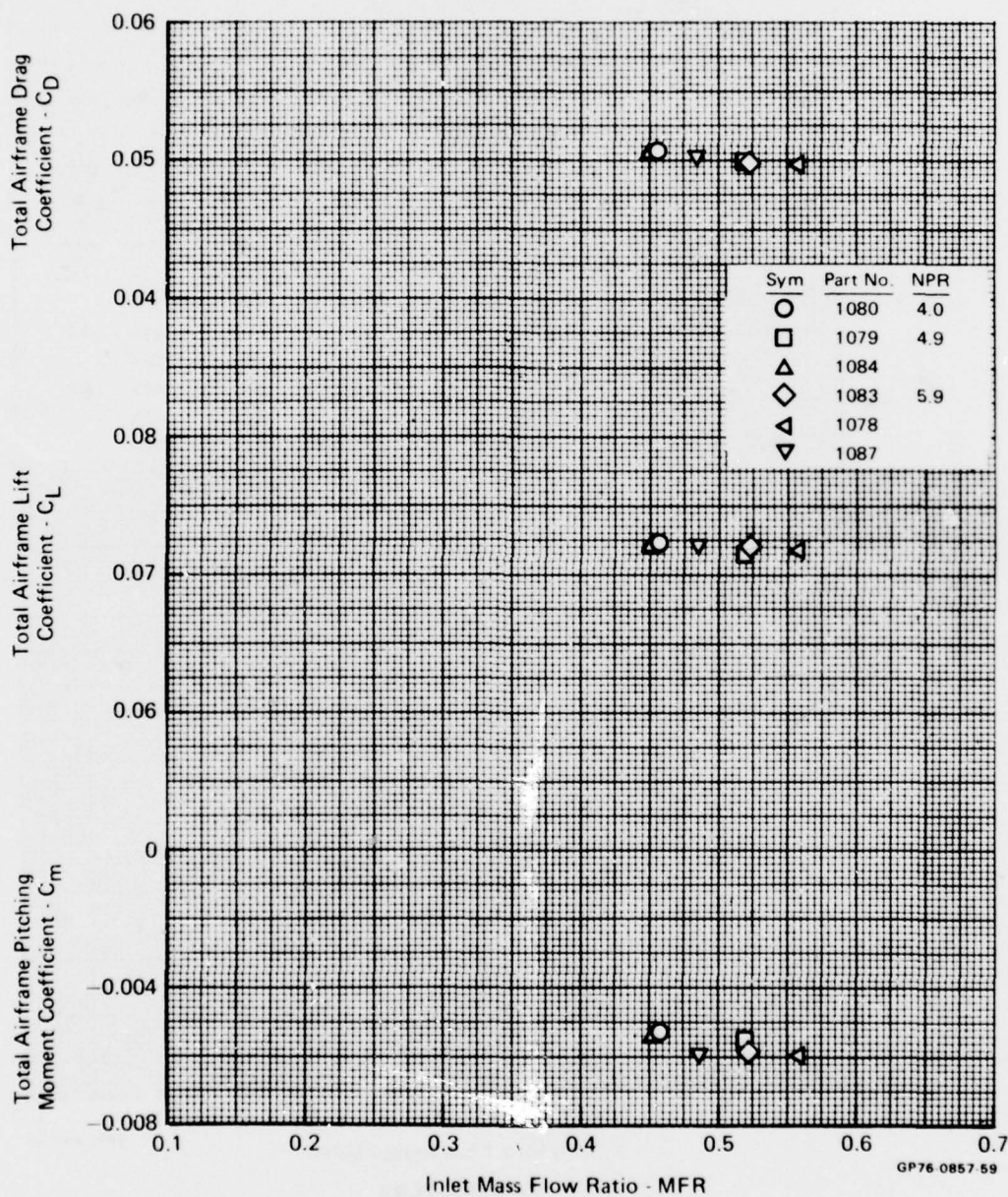


FIGURE D-84
 TOTAL AIRFRAME PERFORMANCE VARIATION WITH INLET MASS FLOW RATIO

Test Mode - Simulator
 Nozzle - Dry
 Mach No. - 0.6
 Angle of Attack - 0°

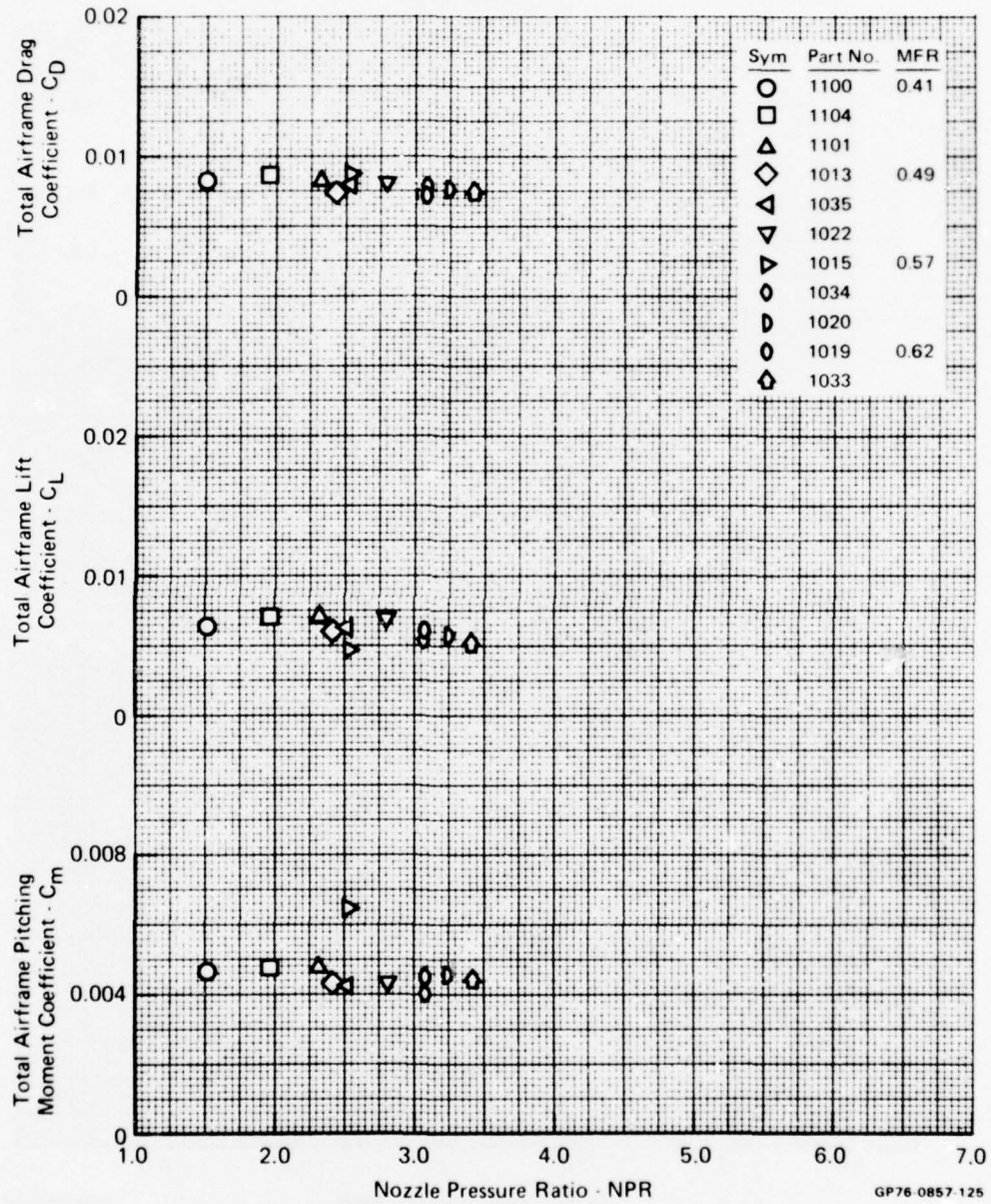


FIGURE D-85
 TOTAL AIRFRAME PERFORMANCE VARIATION WITH NOZZLE PRESSURE RATIO

Test Mode - Simulator
 Nozzle - Dry
 Mach No. - 0.6
 Angle of Attack - 5°

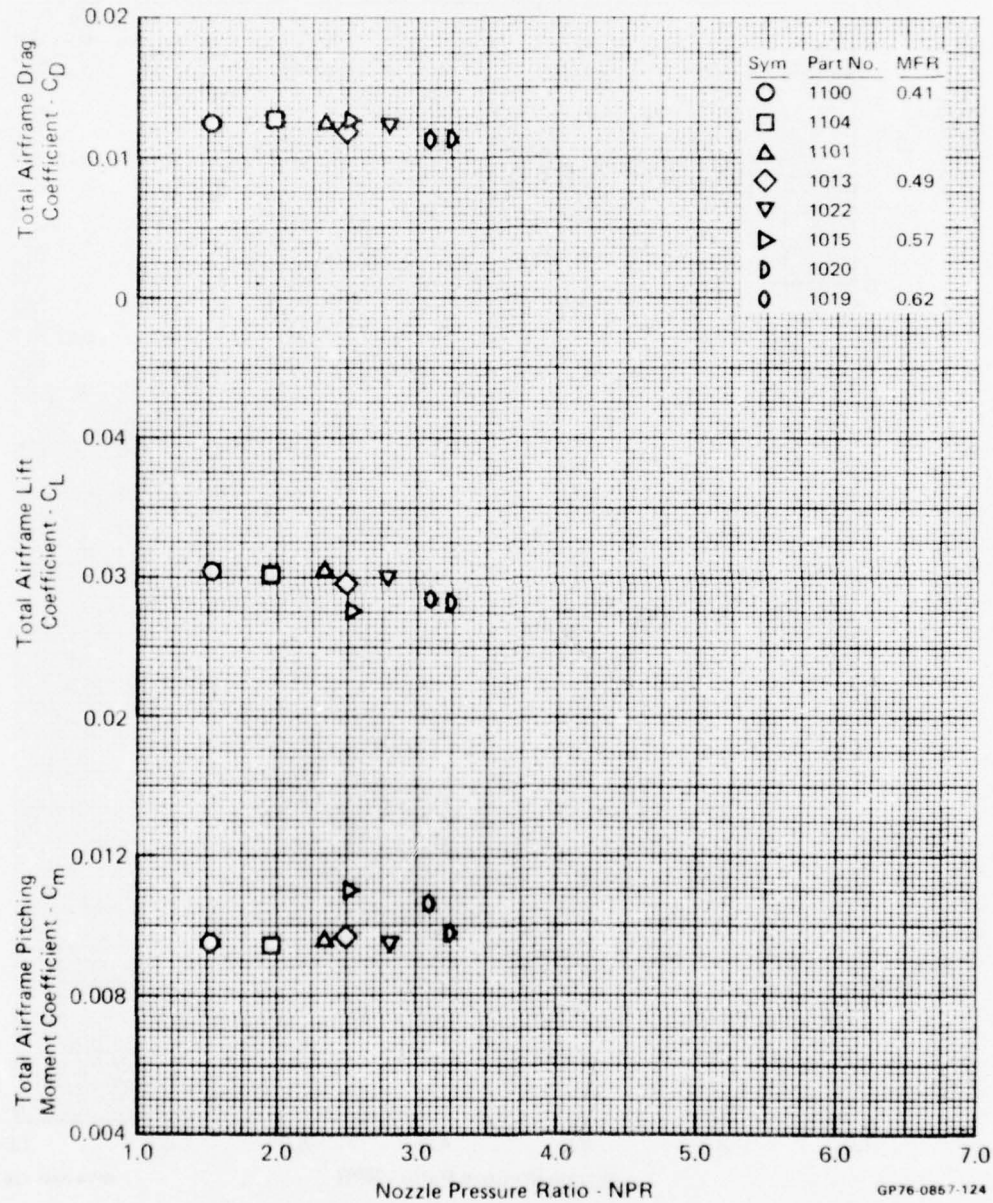


FIGURE D-86
TOTAL AIRFRAME PERFORMANCE VARIATION WITH NOZZLE PRESSURE RATIO

Test Mode - Simulator
 Nozzle - Dry
 Mach No. - 0.6
 Angle of Attack - 10°

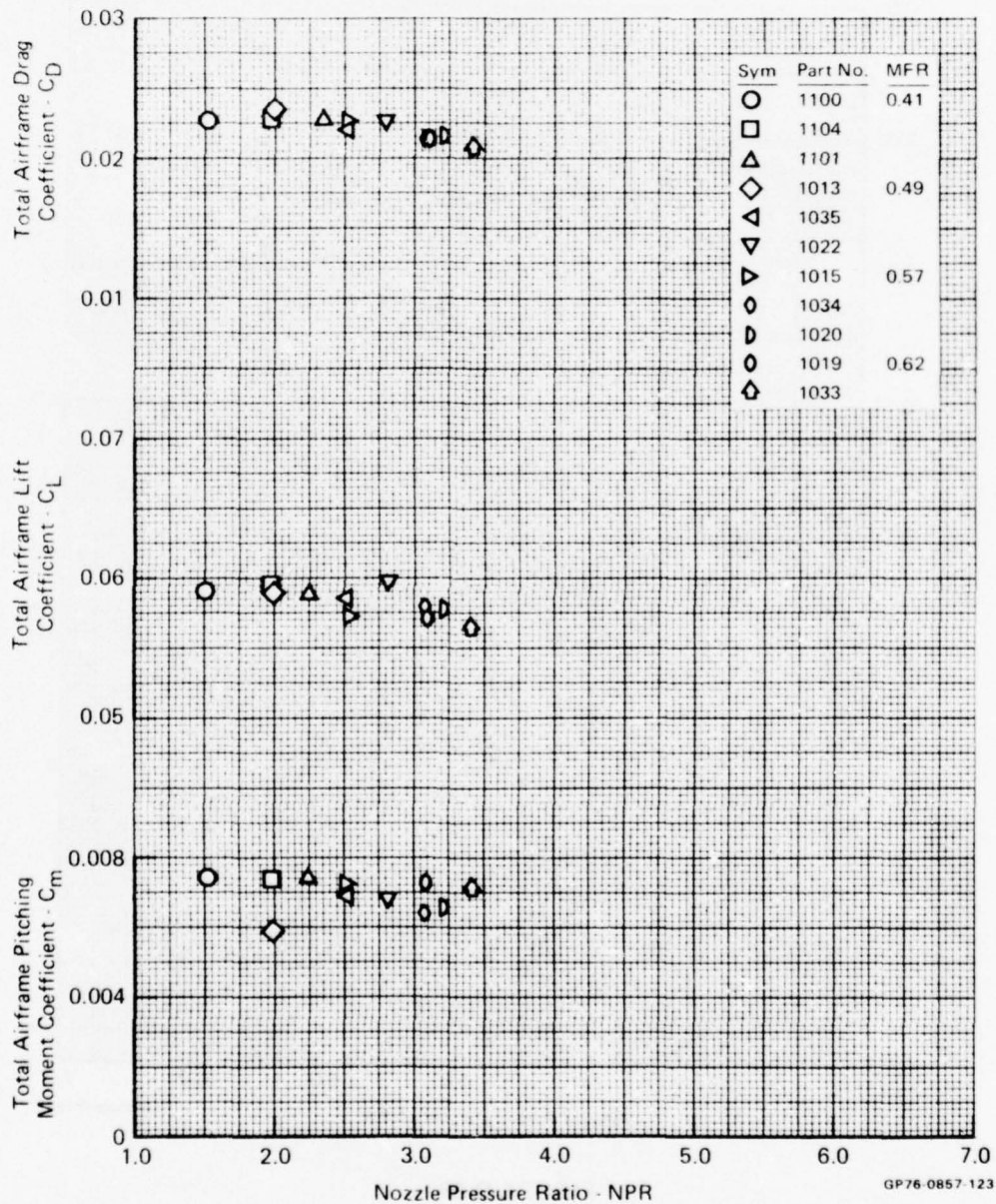


FIGURE D-87
 TOTAL AIRFRAME PERFORMANCE VARIATION WITH NOZZLE PRESSURE RATIO

Test Mode - Simulator
 Nozzle - Dry
 Mach No. - 0.6
 Angle of Attack - 16°

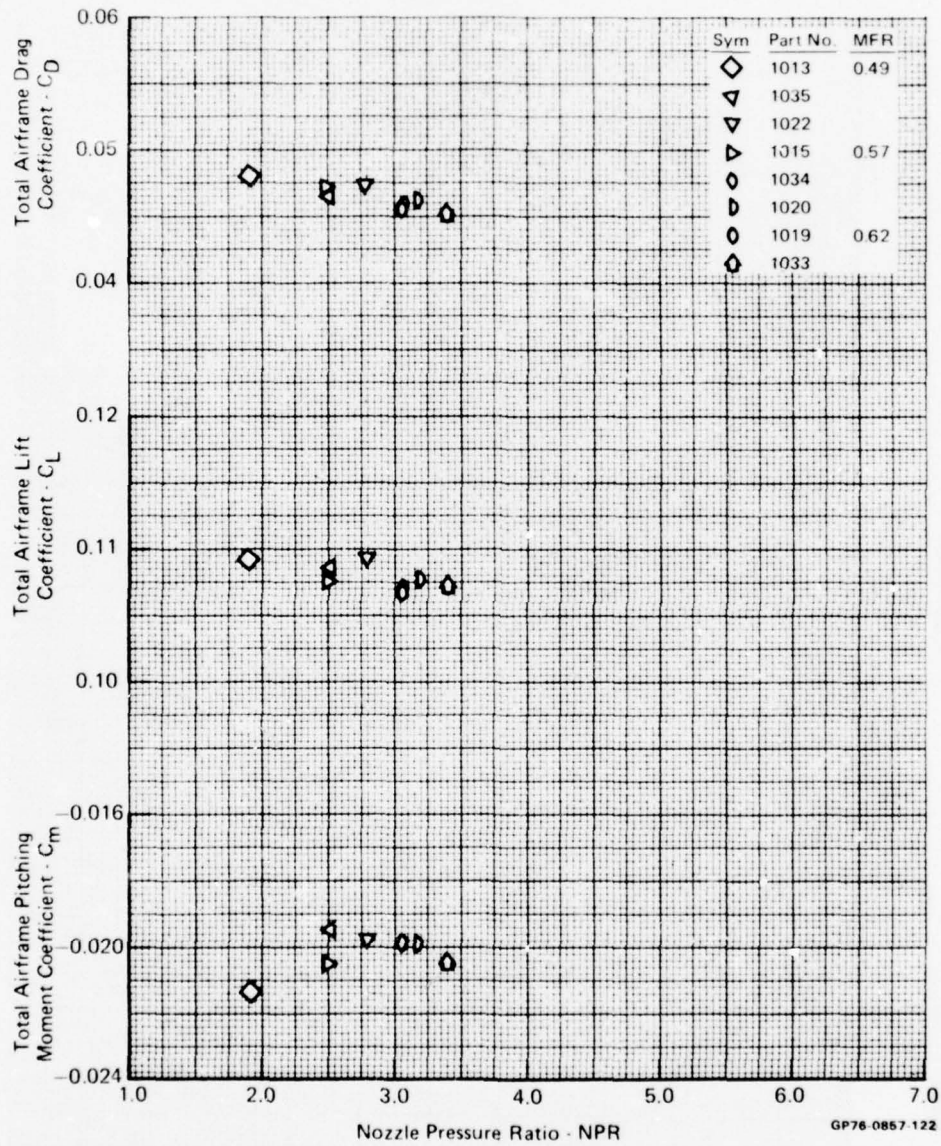


FIGURE D-88
 TOTAL AIRFRAME PERFORMANCE VARIATION WITH NOZZLE PRESSURE RATIO

Test Mode - Simulator
 Nozzle - Dry
 Mach No. - 0.9
 Angle of Attack - 0°

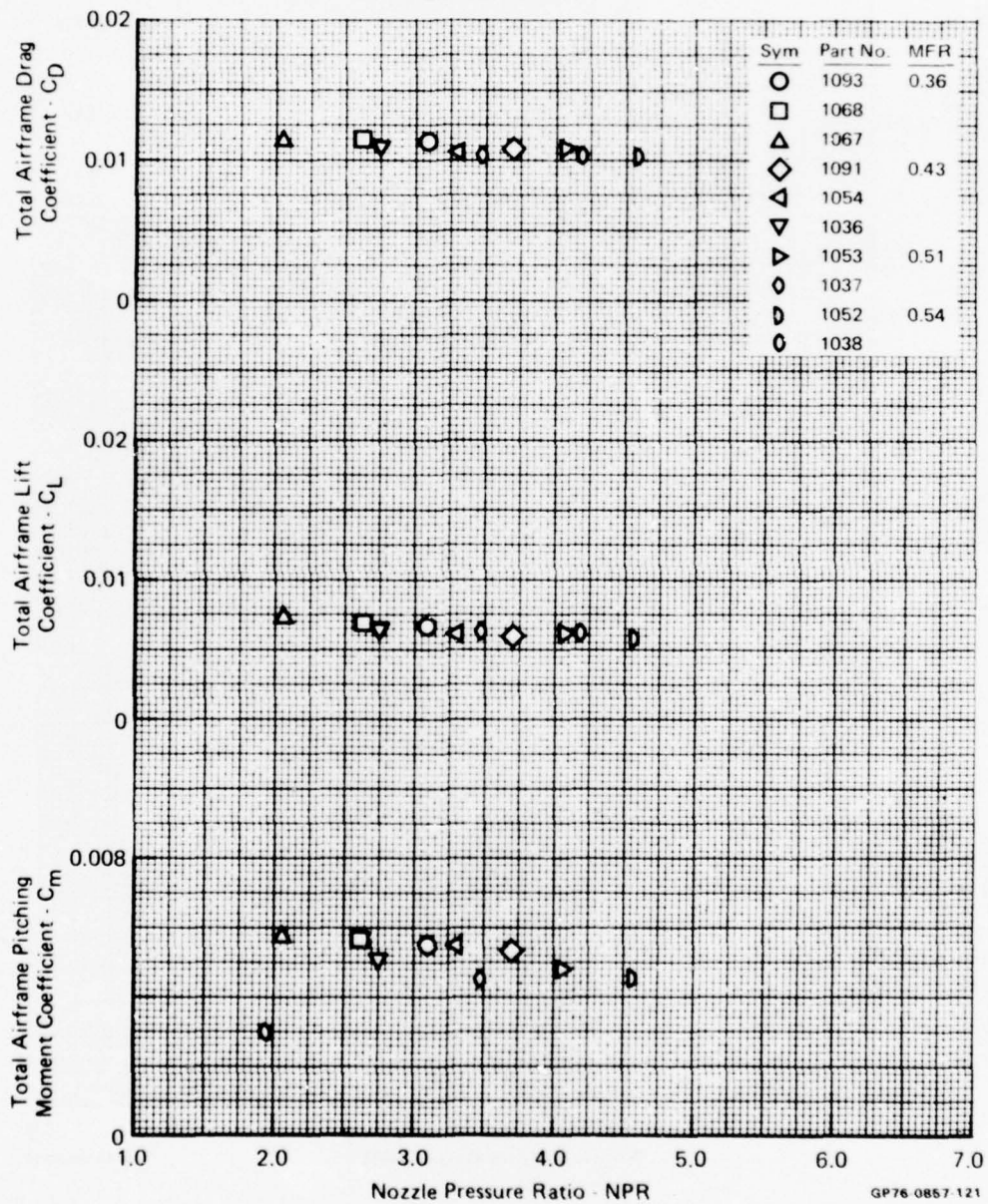


FIGURE D-89
 TOTAL AIRFRAME PERFORMANCE VARIATION WITH NOZZLE PRESSURE RATIO

Test Mode - Simulator

Nozzle - Dry

Mach No. - 0.9

Angle of Attack - 5°

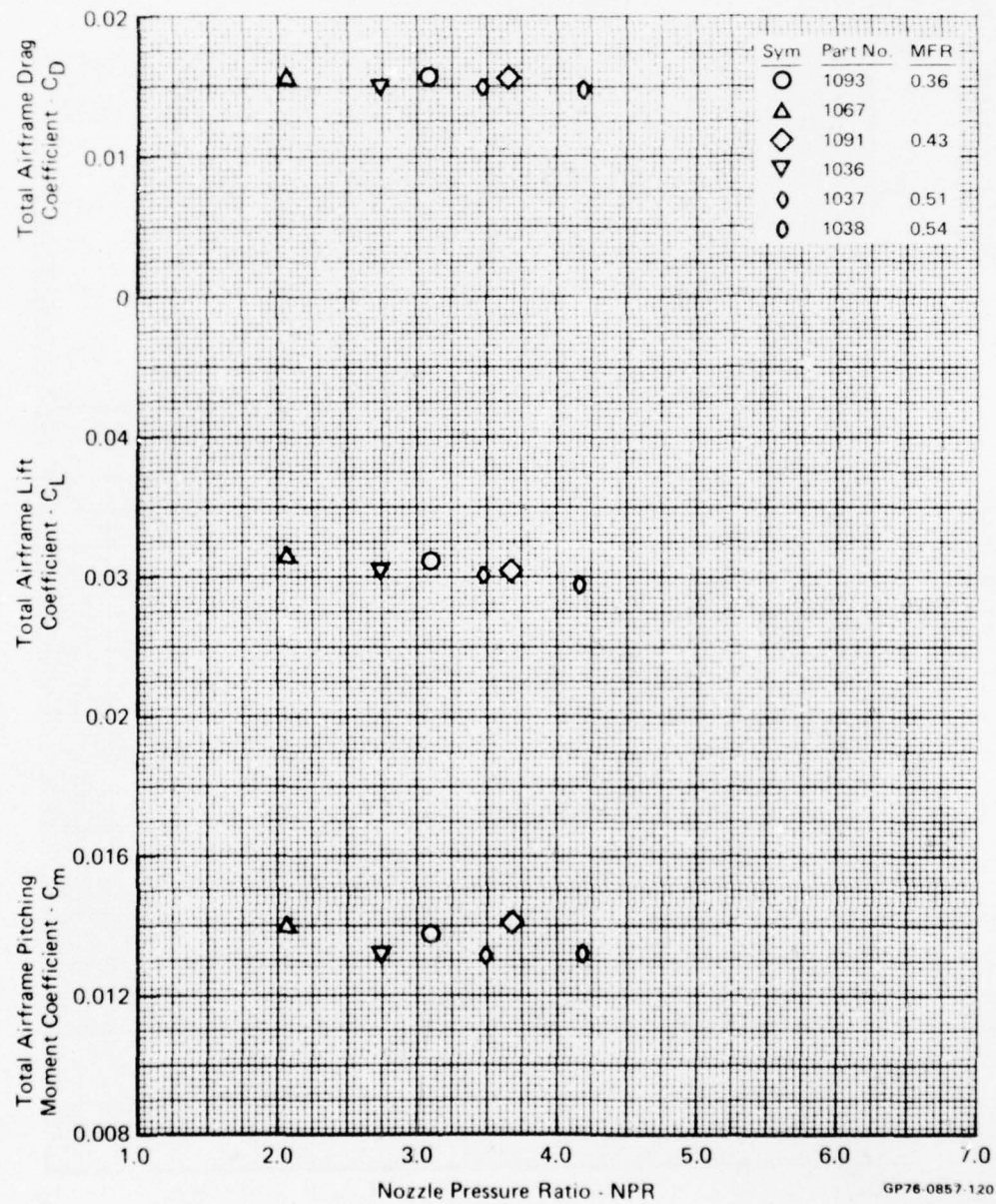


FIGURE D-90
TOTAL AIRFRAME PERFORMANCE VARIATION WITH NOZZLE PRESSURE RATIO

Test Mode - Simulator
 Nozzle - Dry
 Mach No. - 0.9
 Angle of Attack - 10°

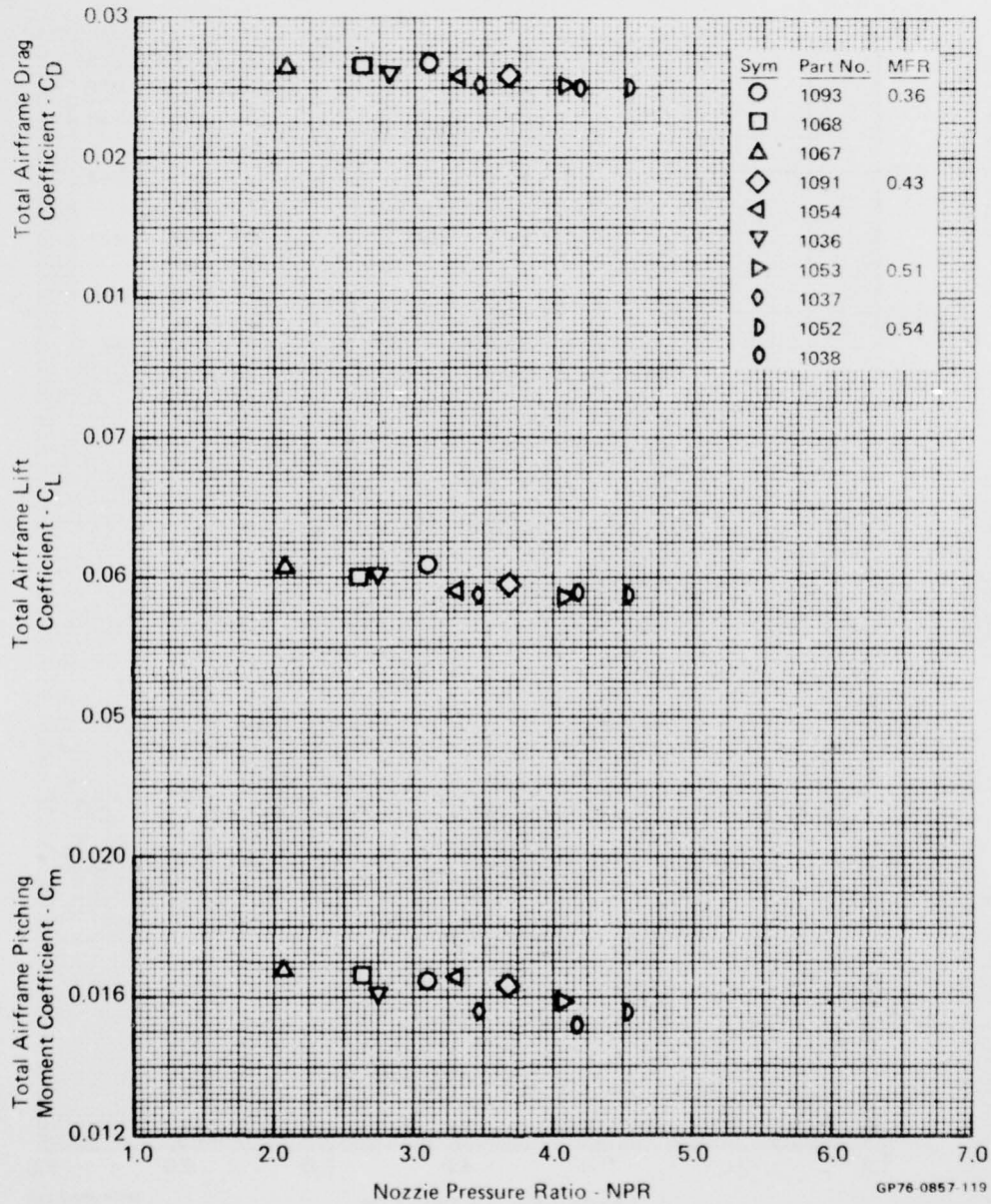


FIGURE D-91
 TOTAL AIRFRAME PERFORMANCE VARIATION WITH NOZZLE PRESSURE RATIO

Test Mode - Simulator
 Nozzle - Dry
 Mach No. - 0.9
 Angle of Attack - 16°

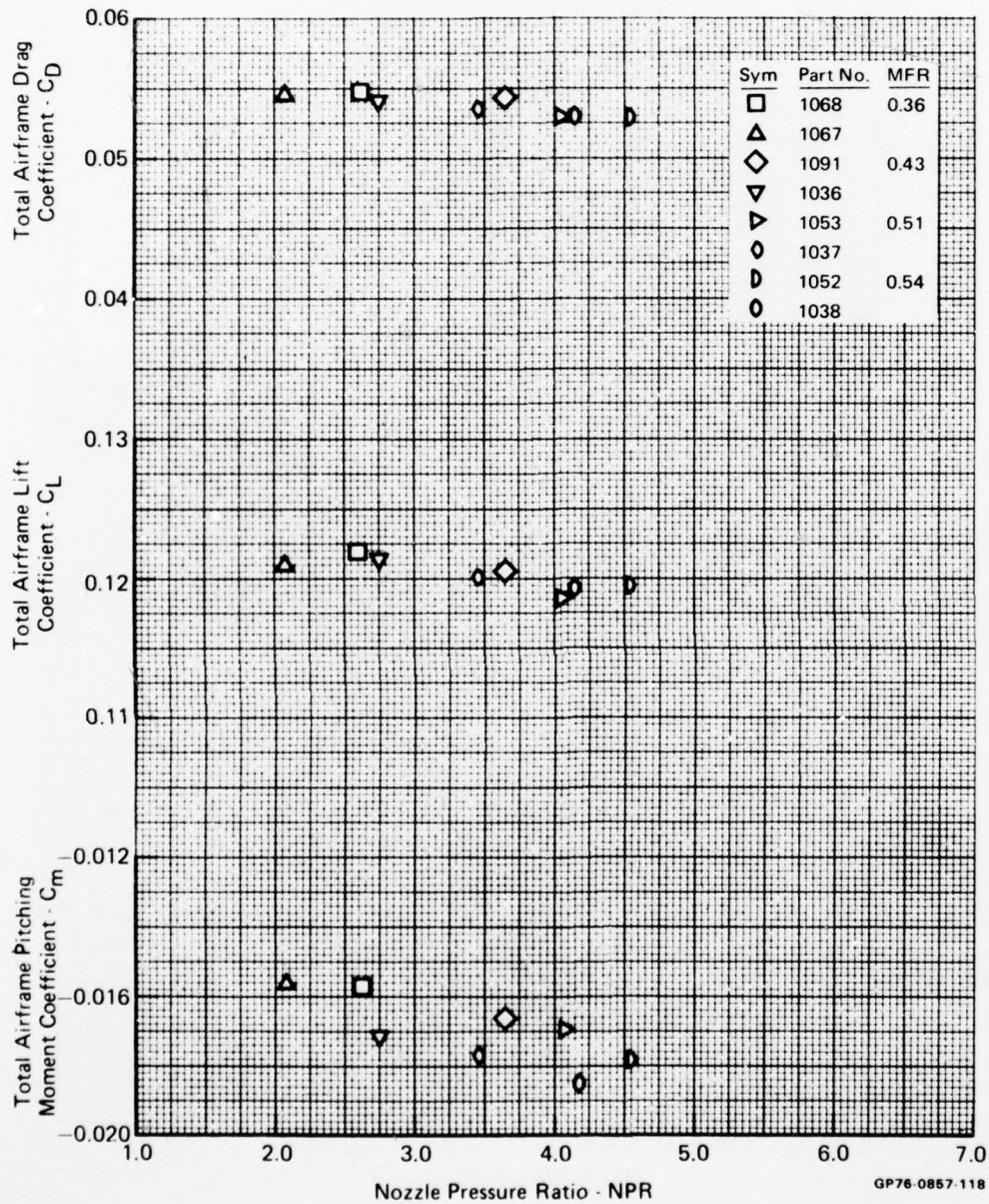


FIGURE D-92
 TOTAL AIRFRAME PERFORMANCE VARIATION WITH NOZZLE PRESSURE RATIO

Test Mode - Simulator
 Nozzle - Dry
 Mach No. - 1.2
 Angle of Attack - 0°

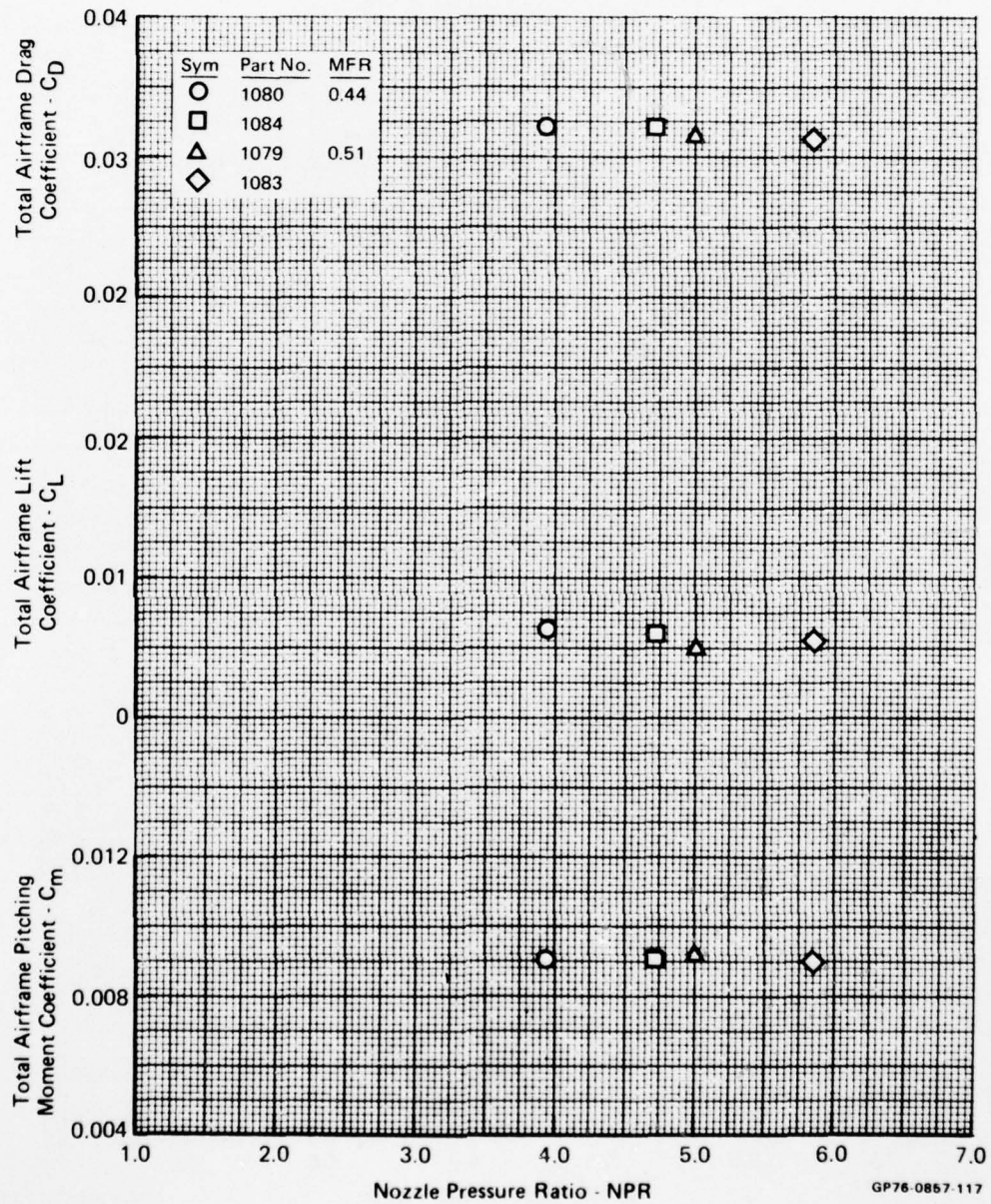


FIGURE D-93
 TOTAL AIRFRAME PERFORMANCE VARIATION WITH NOZZLE PRESSURE RATIO

Test Mode - Simulator
 Nozzle - Dry
 Mach No. - 1.2
 Angle of Attack - 5°

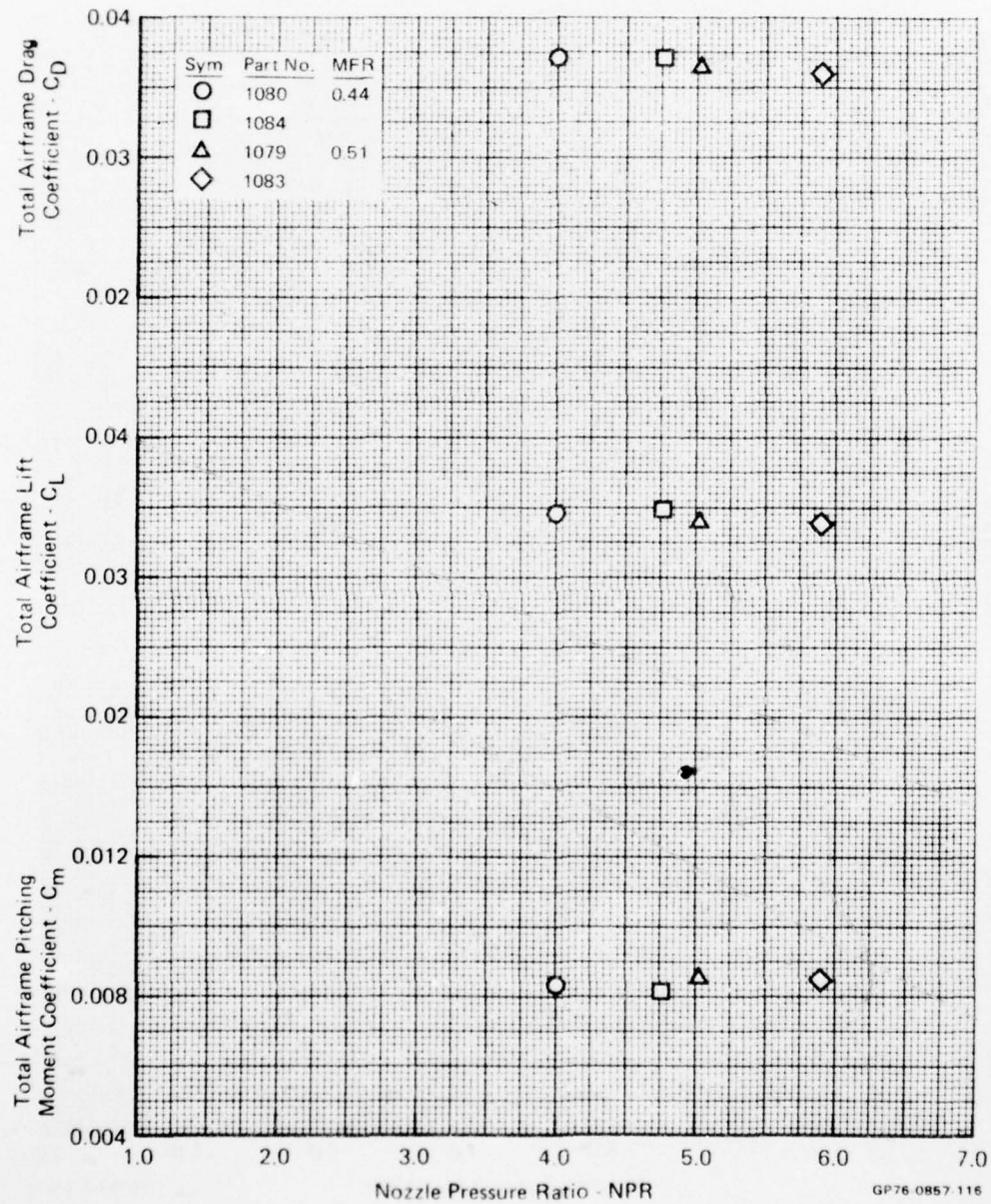


FIGURE D-94
 TOTAL AIRFRAME PERFORMANCE VARIATION WITH NOZZLE PRESSURE RATIO

Test Mode - Simulator

Nozzle - Dry

Mach No. - 1.2

Angle of Attack - 10°

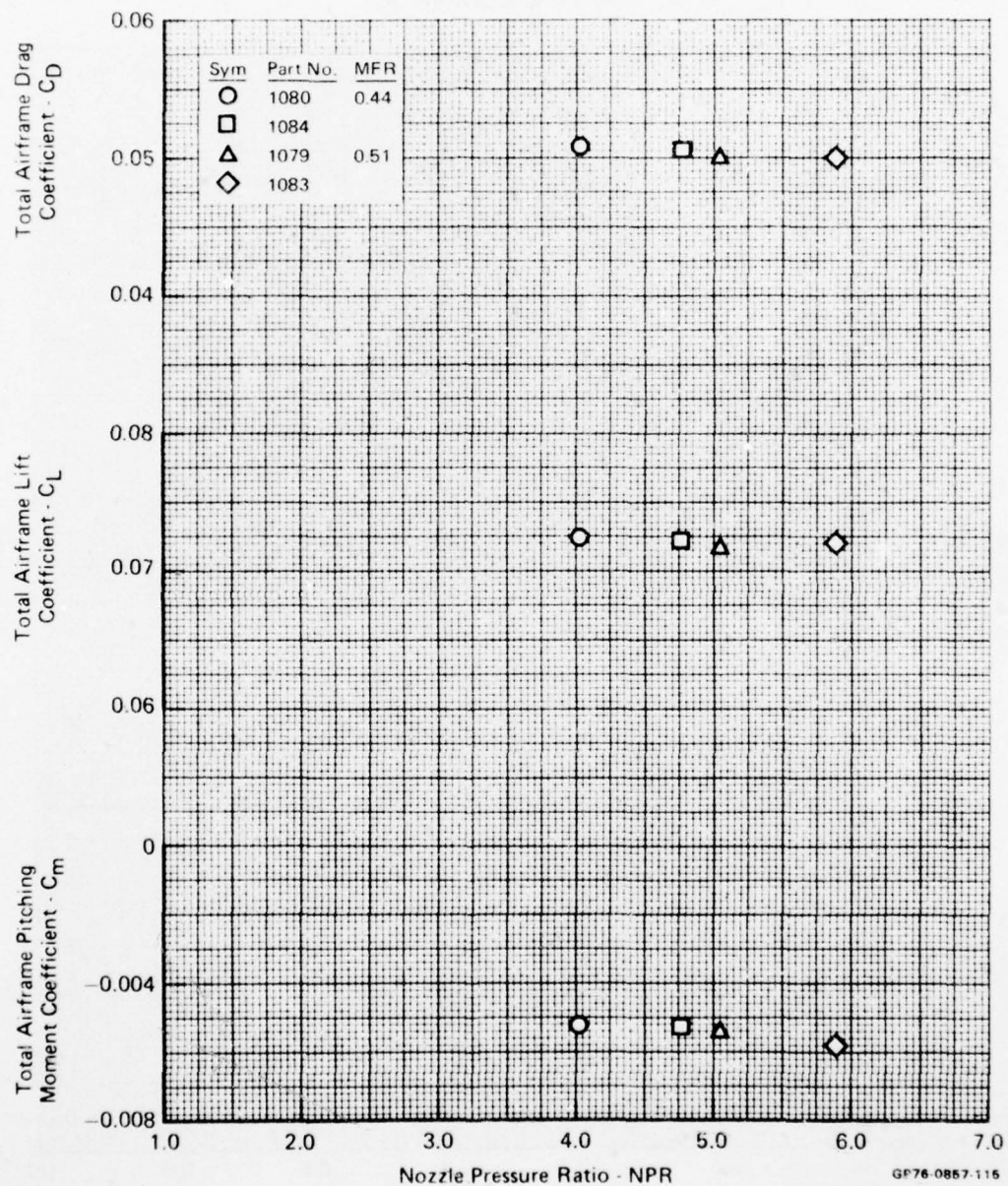


FIGURE D-95
TOTAL AIRFRAME PERFORMANCE VARIATION WITH NOZZLE PRESSURE RATIO

Test Mode - Simulator
 Nozzle - Dry
 Mach No. 0.6
 Angle of Attack - 0°

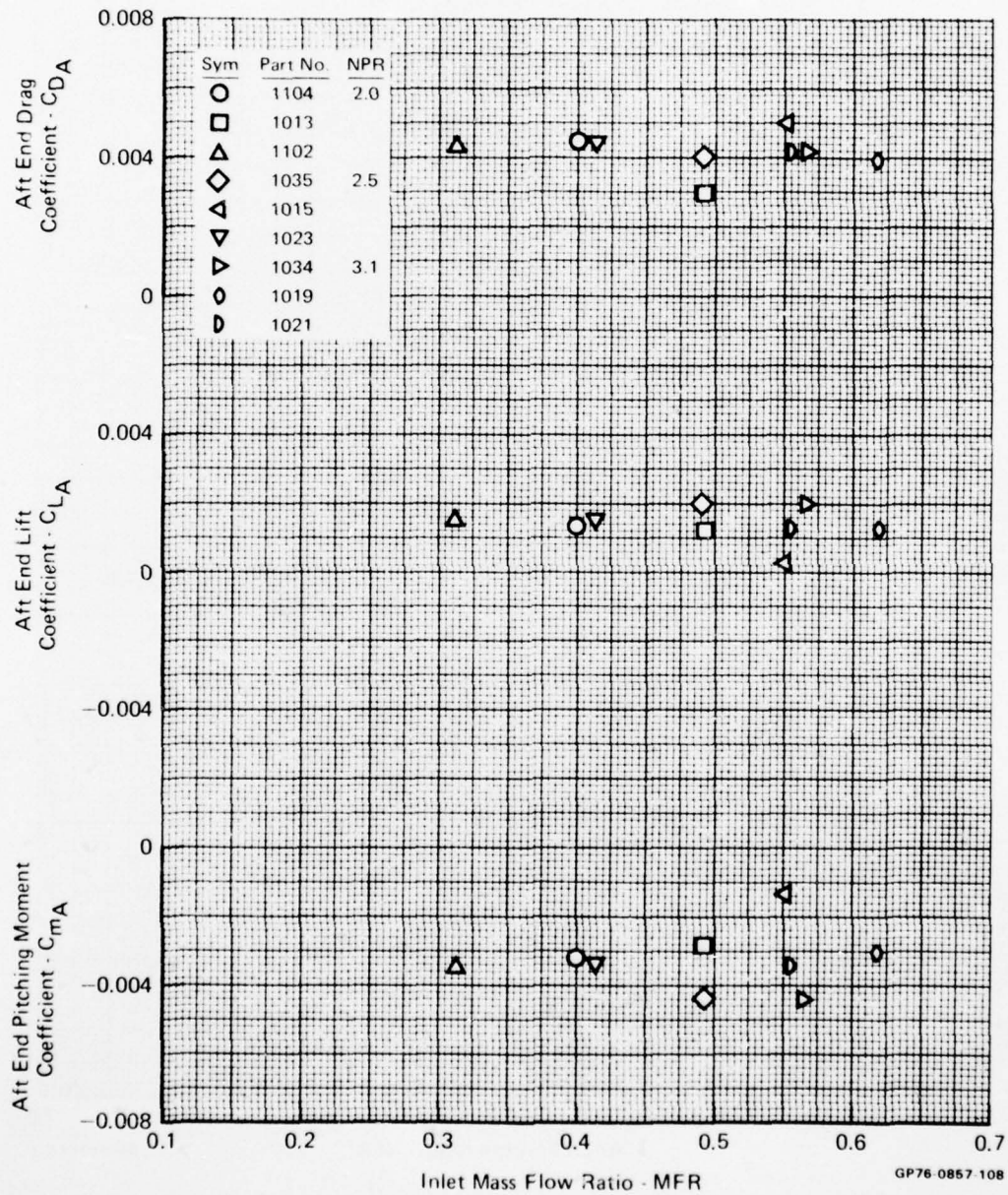


FIGURE D-96
 AFT END PERFORMANCE VARIATION WITH INLET MASS FLOW RATIO

Test Mode - Simulator
 Nozzle - Dry
 Mach No. - 0.6
 Angle of Attack - 5°

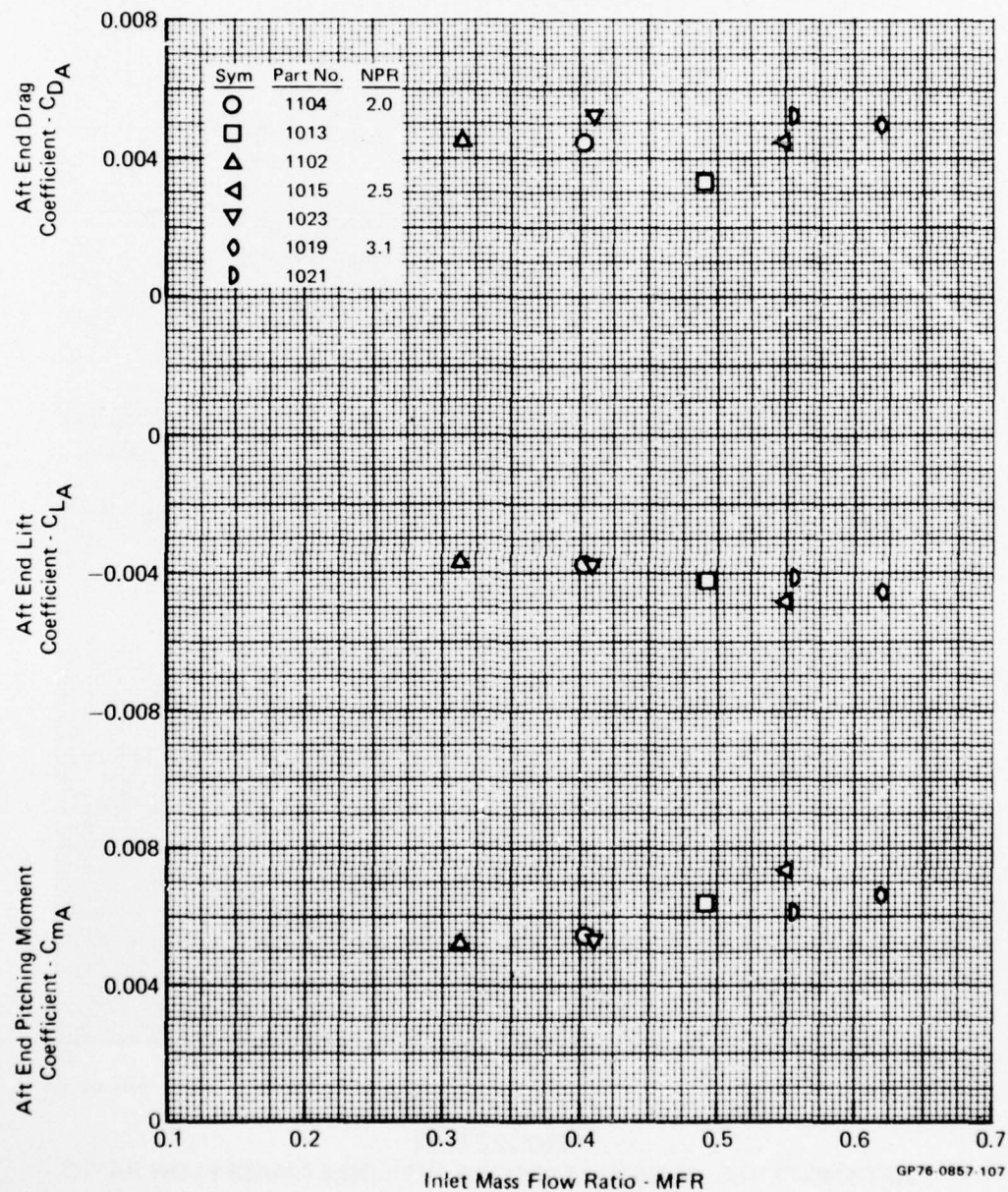


FIGURE D-97
 AFT END PERFORMANCE VARIATION WITH INLET MASS FLOW RATIO

Test Mode - Simulator
 Nozzle - Dry
 Mach No. - 0.6
 Angle of Attack - 10^0

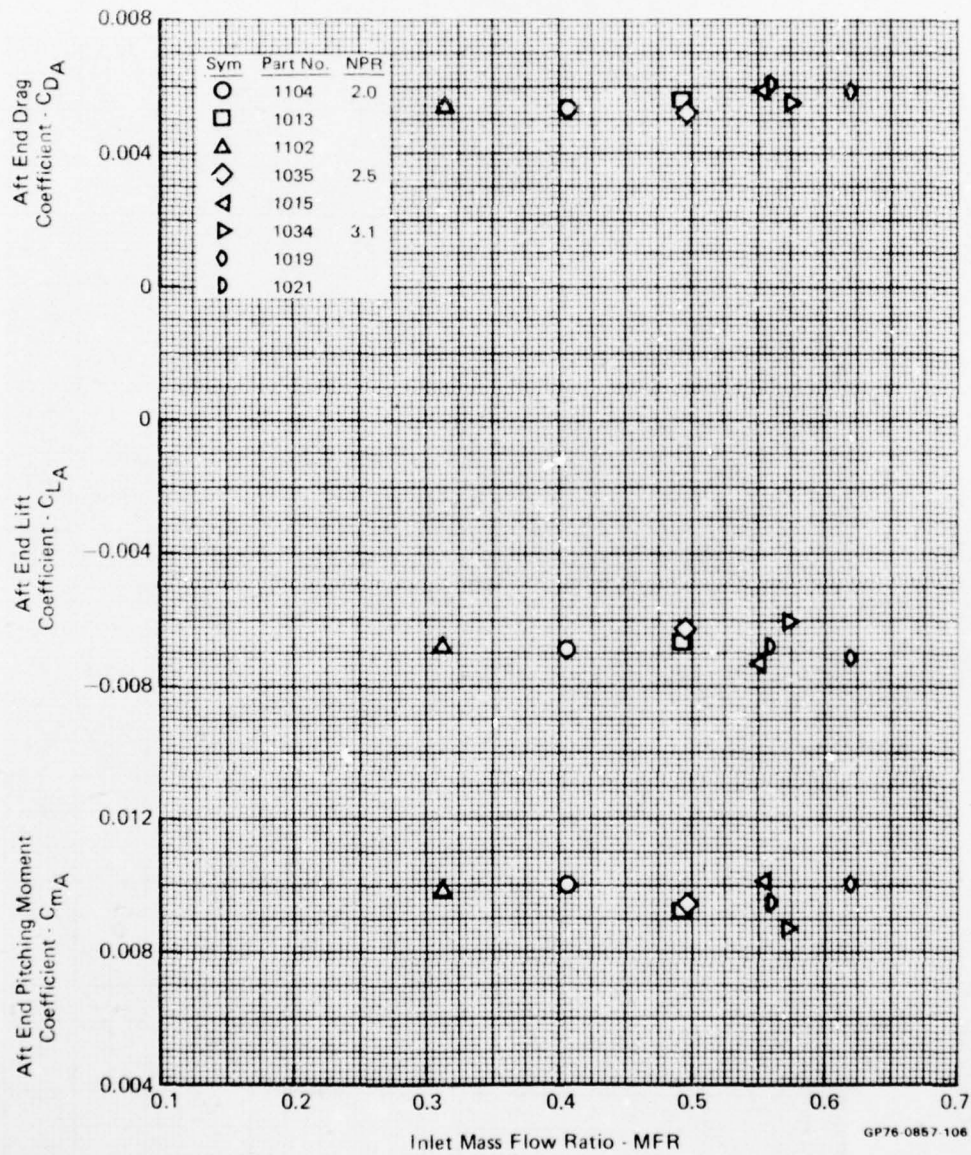


FIGURE D-98
AFT END PERFORMANCE VARIATION WITH INLET MASS FLOW RATIO

Test Mode - Simulator
 Nozzle - Dry
 Mach No. - 0.6
 Angle of Attack - 16°

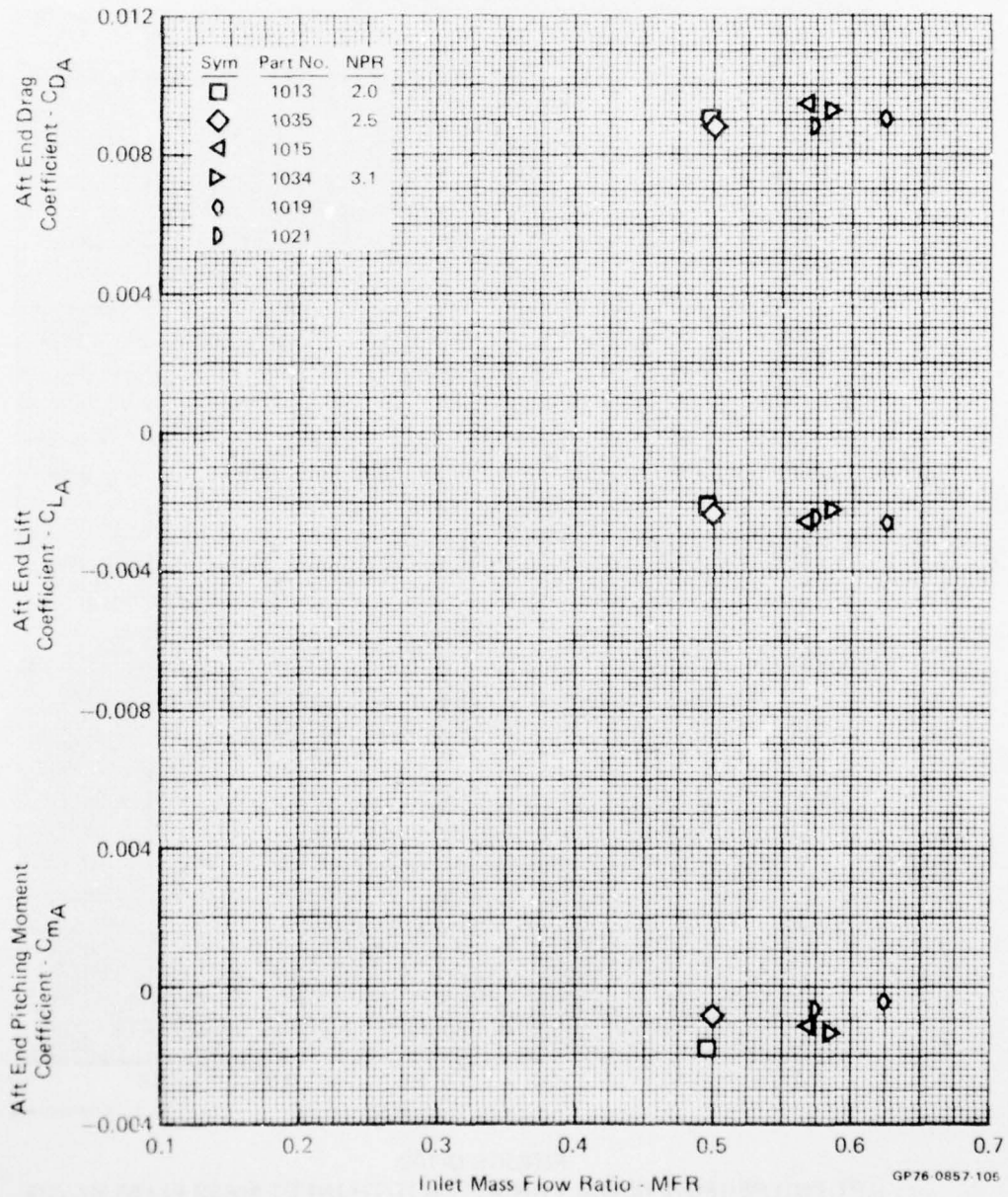


FIGURE D-99
 AFT END PERFORMANCE VARIATION WITH INLET MASS FLOW RATIO

Test Mode - Simulator
 Nozzle - Dry
 Mach No. - 0.9
 Angle of Attack - 0°

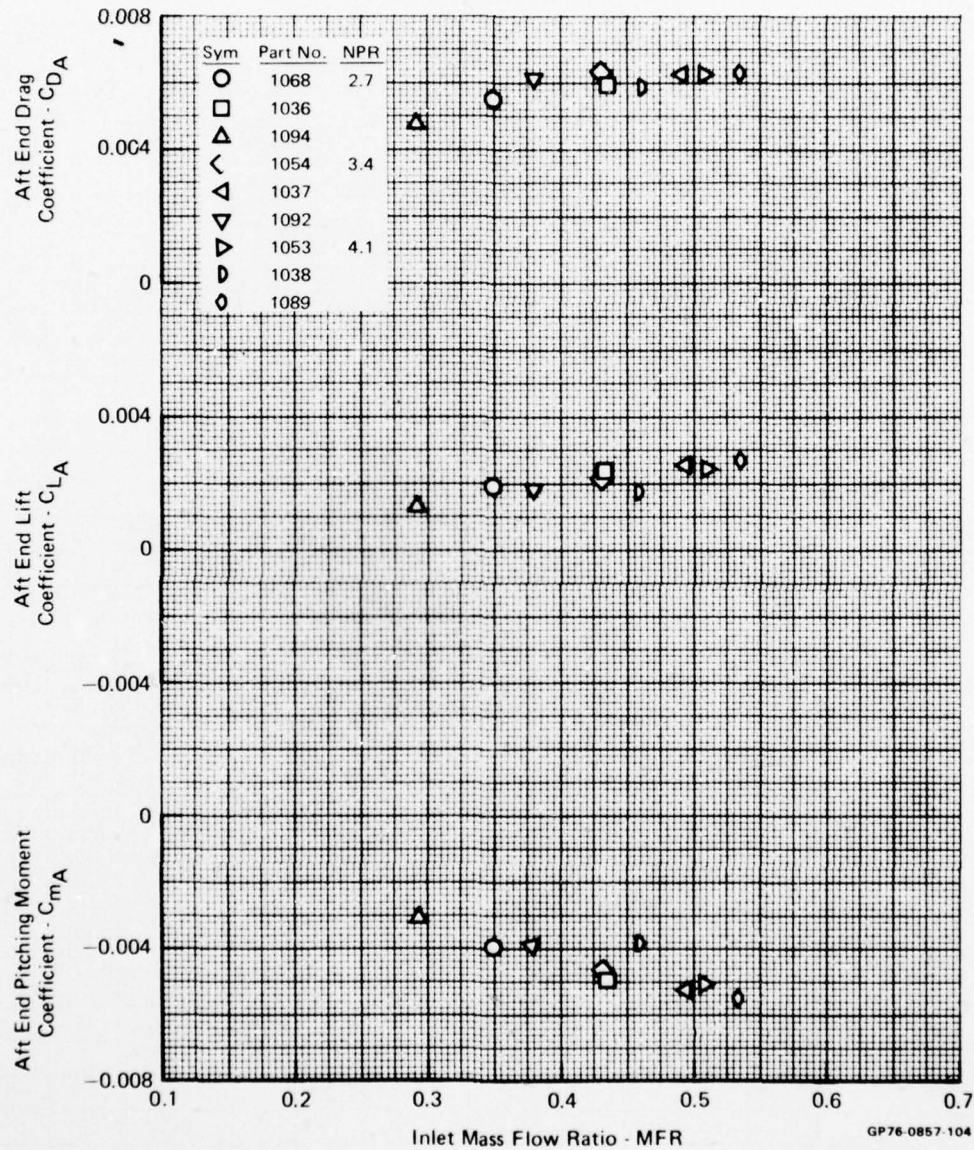


FIGURE D-100
 AFT END PERFORMANCE VARIATION WITH INLET MASS FLOW RATIO

Test Mode - Simulator

Nozzle - Dry

Mach No. - 0.9

Angle of Attack - 5°

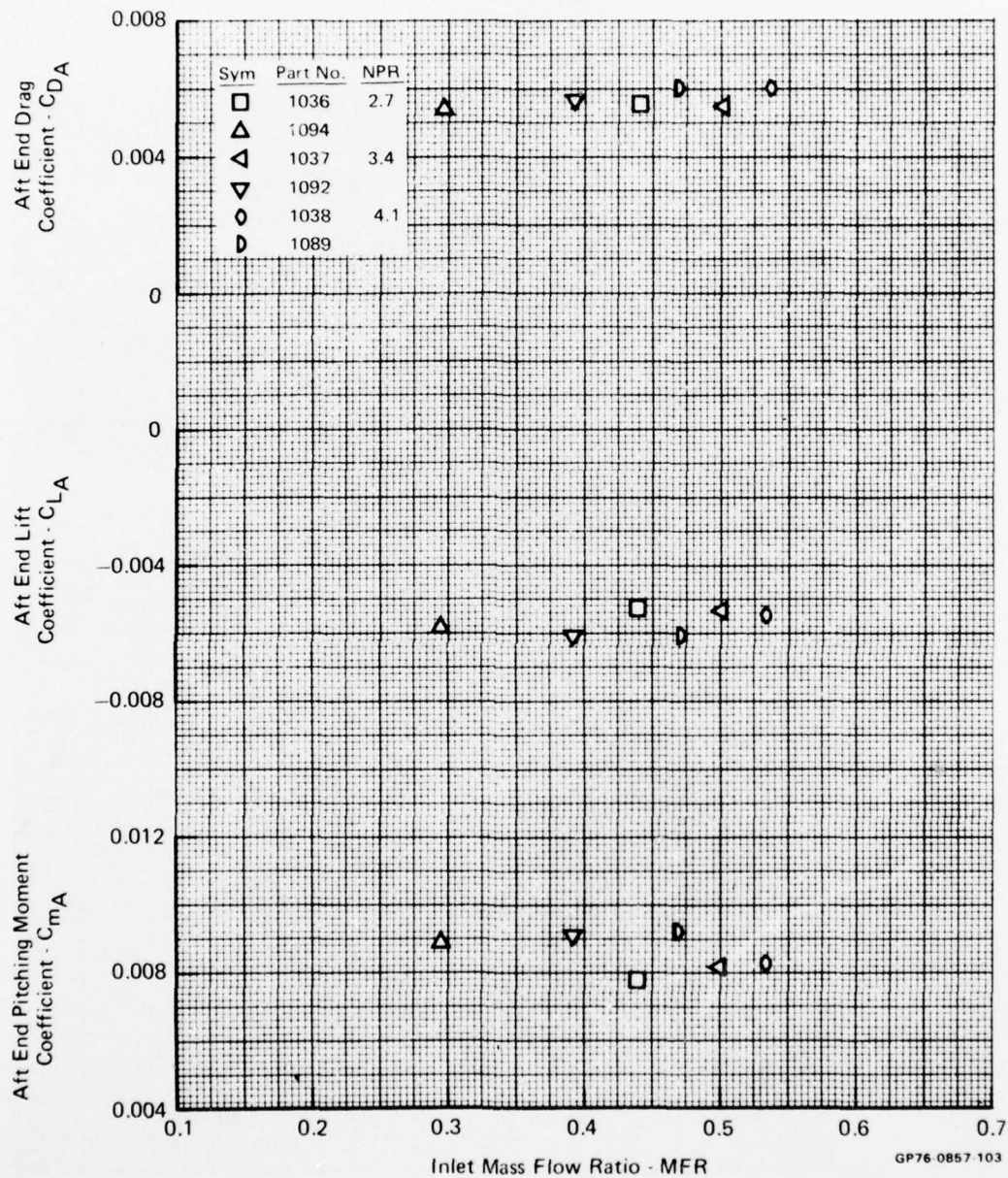


FIGURE D-101

AFT END PERFORMANCE VARIATION WITH INLET MASS FLOW RATIO

Test Mode - Simulator
 Nozzle - Dry
 Mach No. - 0.9
 Angle of Attack - 10°

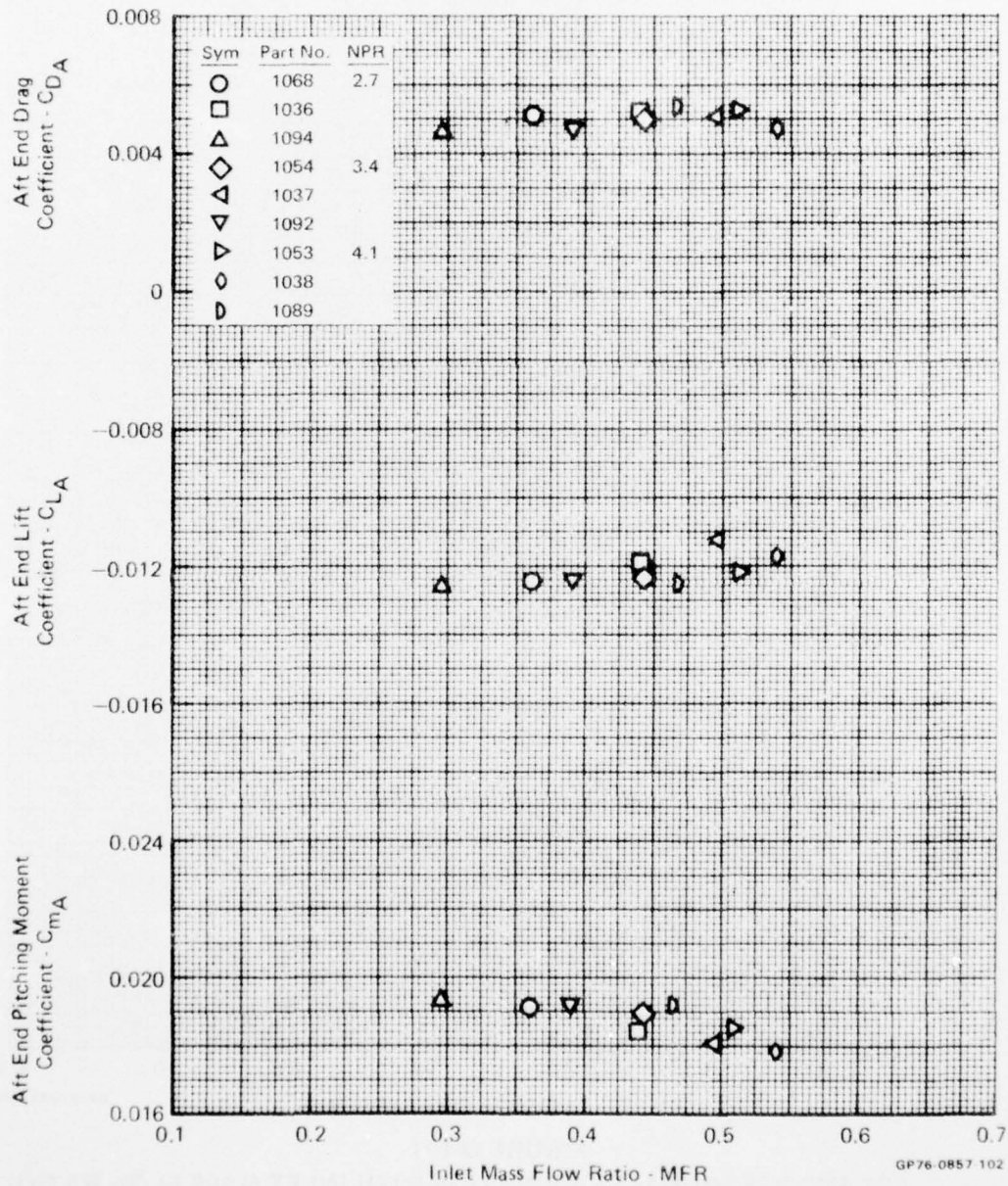


FIGURE D-102
 AFT END PERFORMANCE VARIATION WITH INLET MASS FLOW RATIO

Test Mode - Simulator
 Nozzle - Dry
 Mach No. - 0.9
 Angle of Attack - 16°

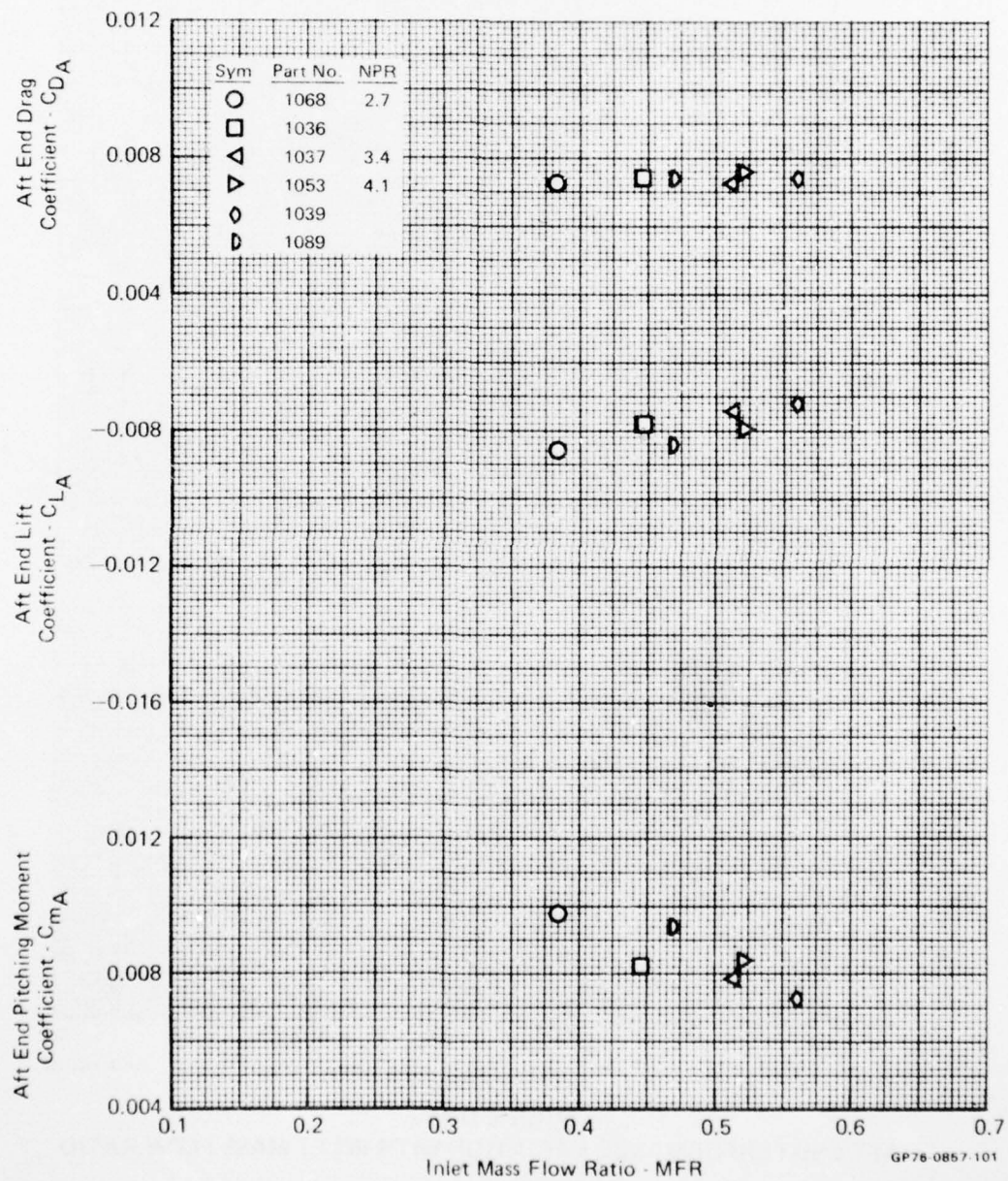


FIGURE D-103
AFT END PERFORMANCE VARIATION WITH INLET MASS FLOW RATIO

Test Mode - Simulator
 Nozzle - Dry
 Mach No. - 1.2
 Angle of Attack - 0°

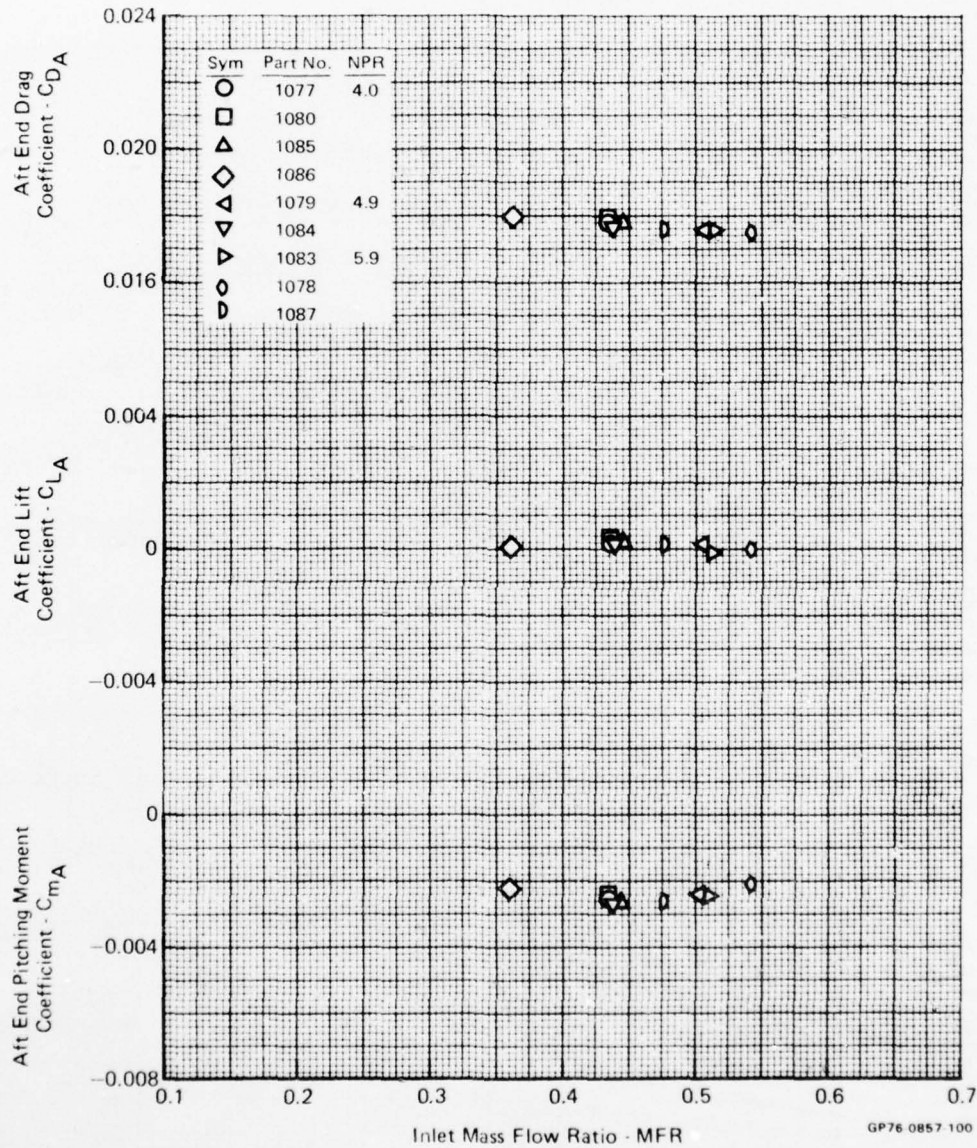


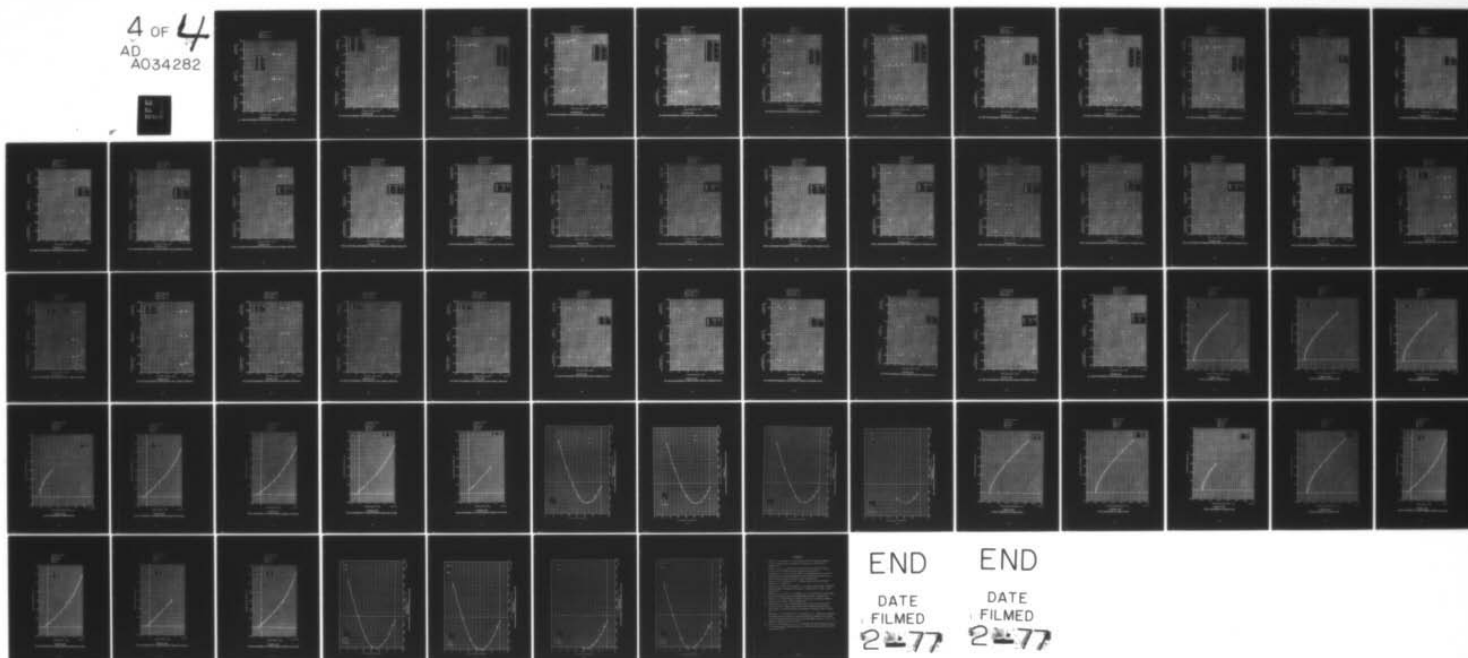
FIGURE D-104
 AFT END PERFORMANCE VARIATION WITH INLET MASS FLOW RATIO

AD-A034 282

MCDONNELL AIRCRAFT CO ST LOUIS MO
TURBINE ENGINE MULTI-MISSION PROPULSION SIMULATOR WIND TUNNEL D--ETC(U)
NOV 76 M F EIGENMANN, R L BEAR, T C CHANDLER F33615-73-C-2051
AFAPL-TR-76-73 NL

UNCLASSIFIED

4 OF 4
AD
A034282

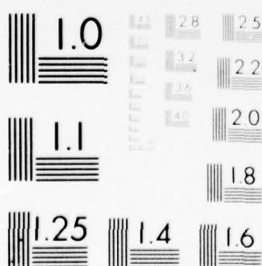


4 OF

4

AD

A034282



MICROCOPY RESOLUTION TEST CHART
NATIONAL BUREAU OF STANDARDS-1963-A

Test Mode - Simulator
 Nozzle - Dry
 Mach No. - 1.2
 Angle of Attack - 5°

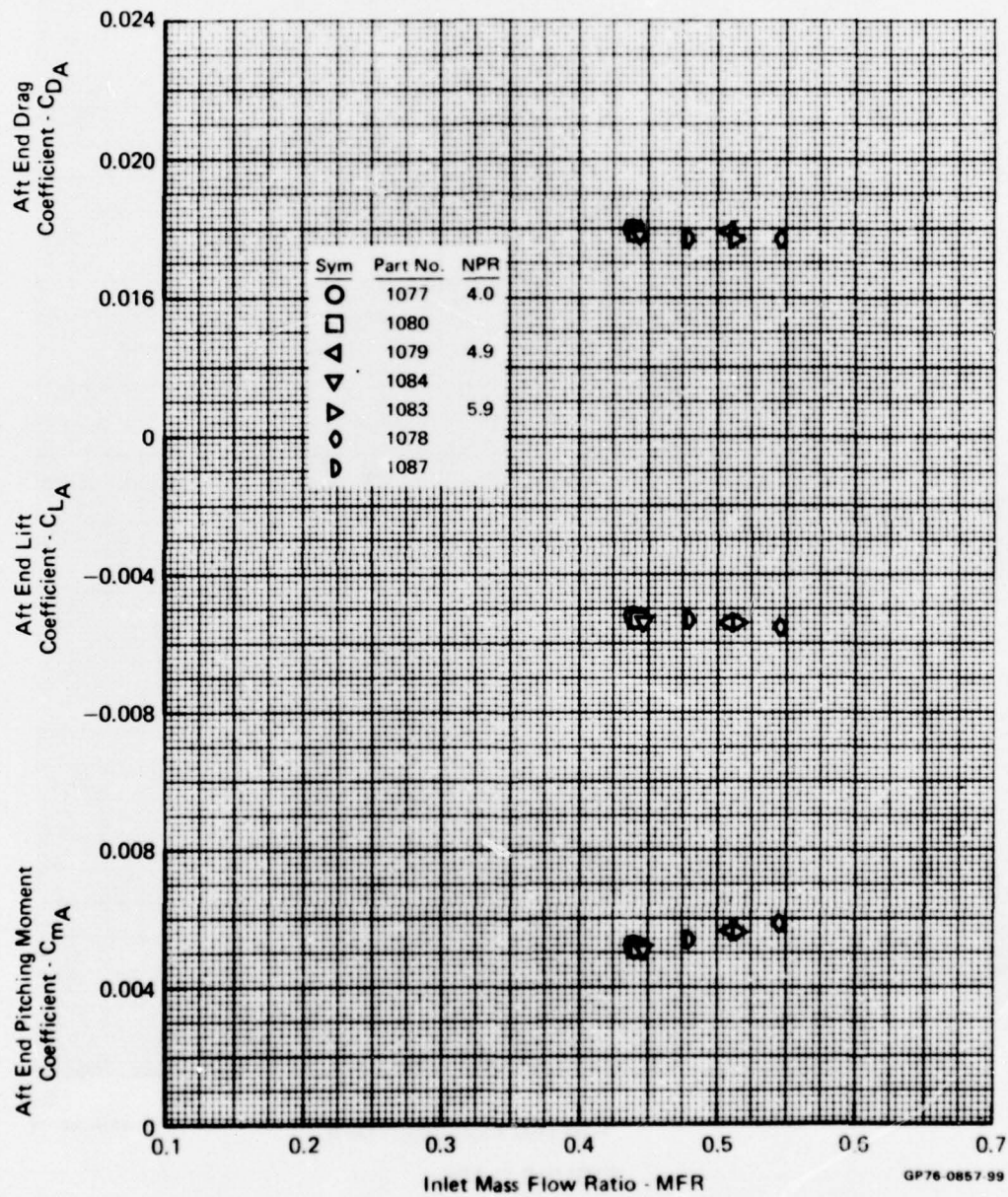


FIGURE D-105
 AFT END PERFORMANCE VARIATION WITH INLET MASS FLOW RATIO

Test Mode - Simulator

Nozzle - Dry

Mach No. 1.2

Angle of Attack - 10^0

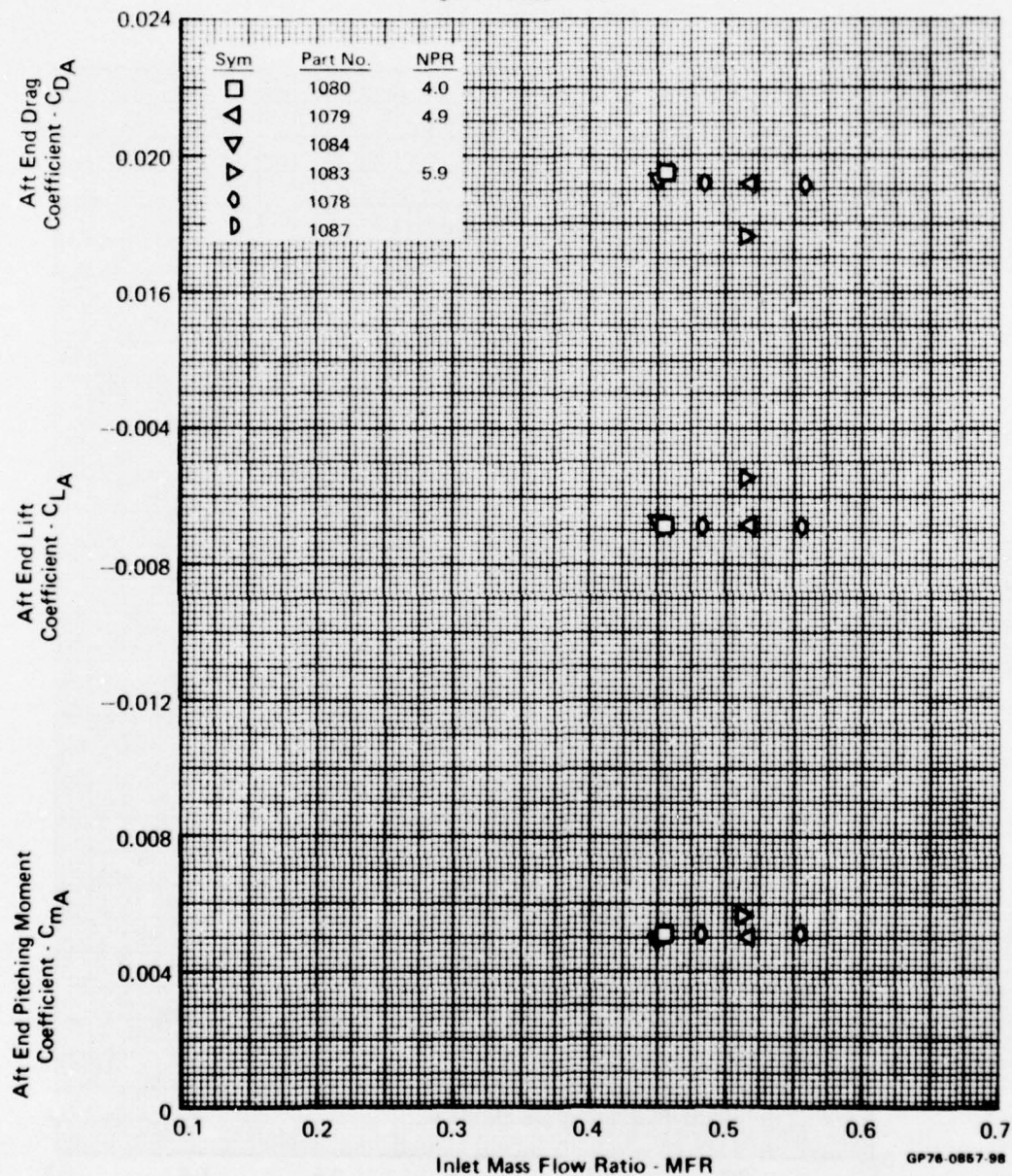


FIGURE D-106
AFT END PERFORMANCE VARIATION WITH INLET MASS FLOW RATIO

Test Mode - Simulator

Nozzle - Dry

Mach No. - 0.6

Angle of Attack - 0°

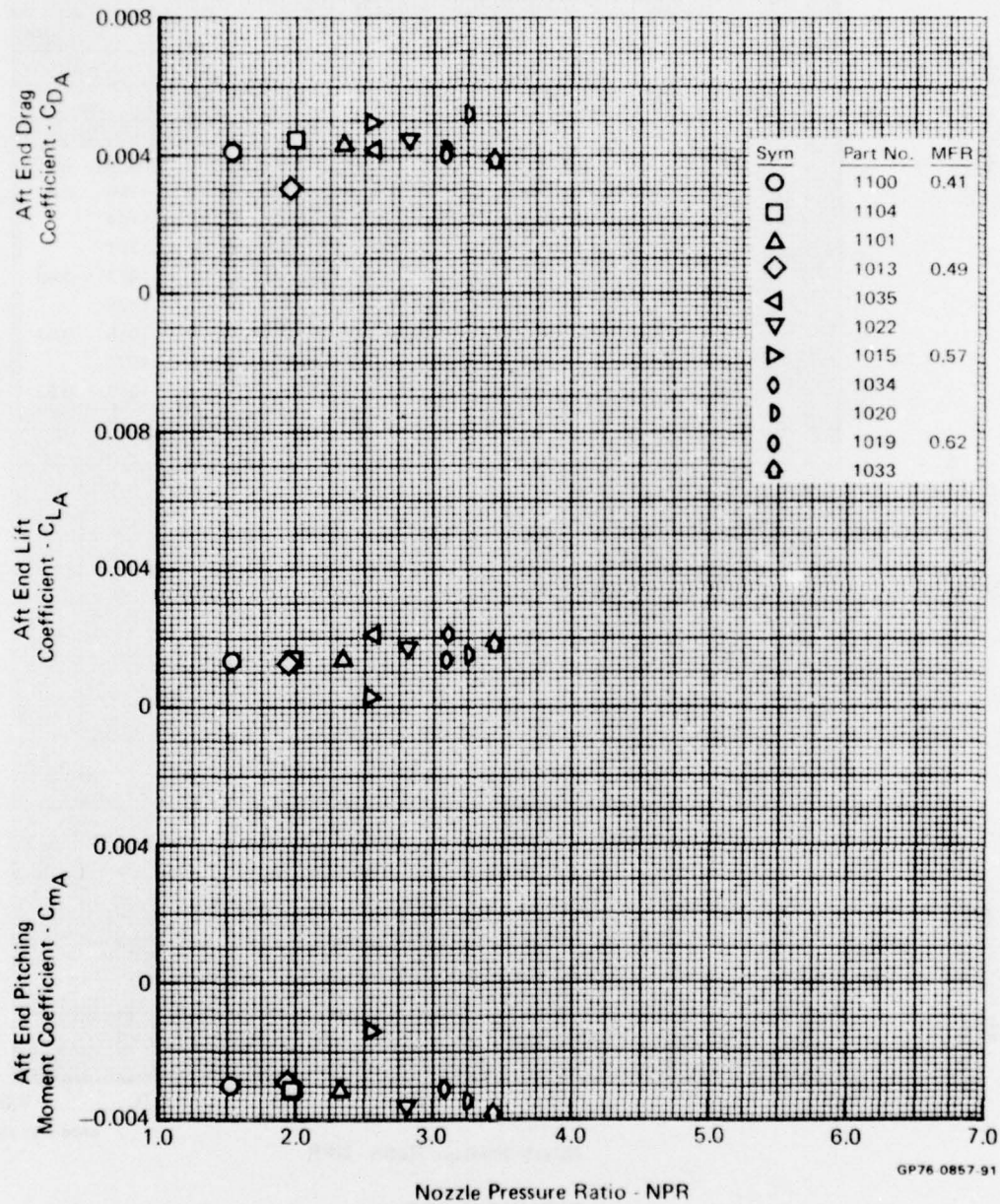


FIGURE D-107
AFT END PERFORMANCE VARIATION WITH NOZZLE PRESSURE RATIO

Test Mode - Simulator
 Nozzle - Dry
 Mach No. - 0.6
 Angle of Attack - 5°

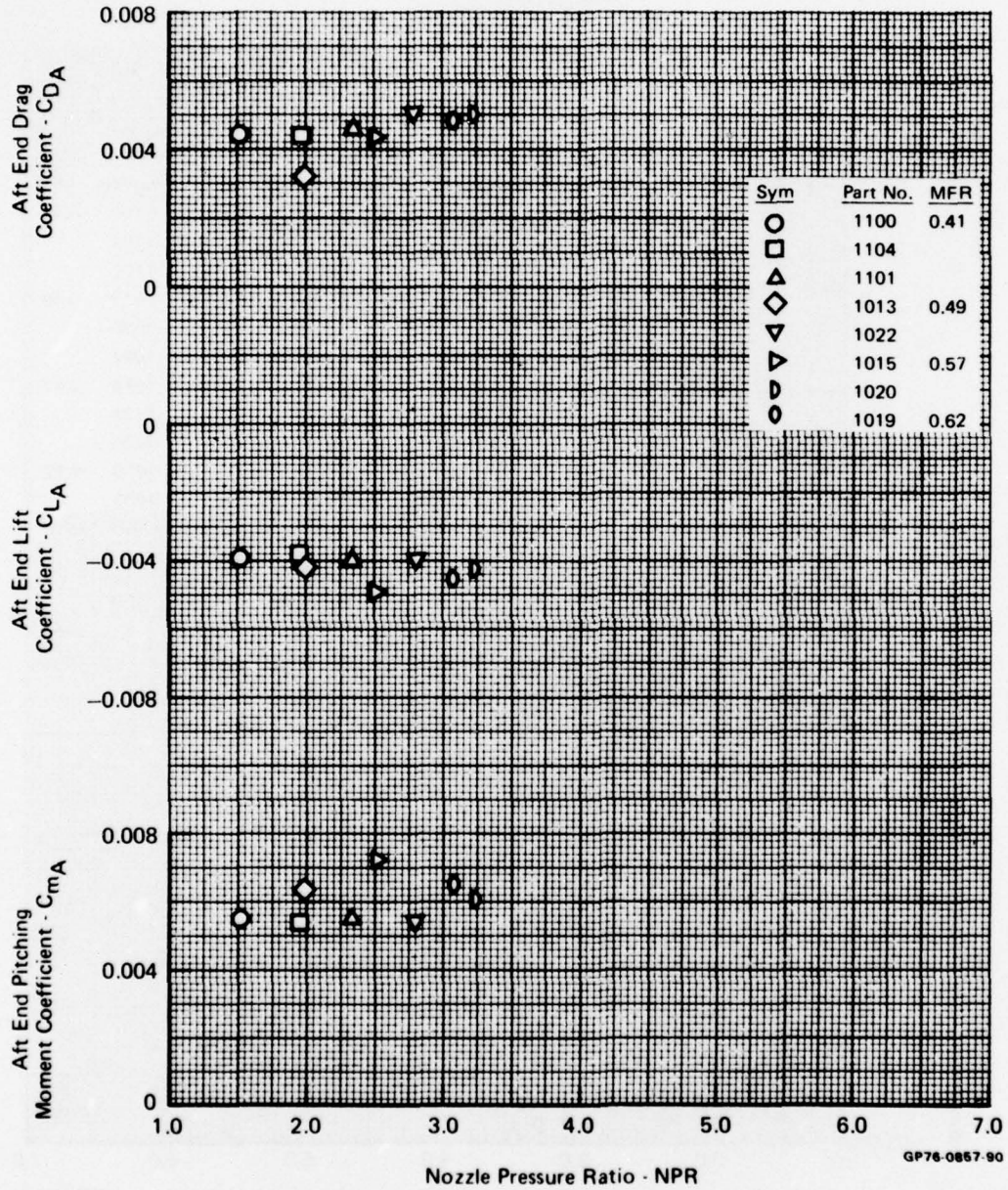


FIGURE D-108
AFT END PERFORMANCE VARIATION WITH NOZZLE PRESSURE RATIO

Test Mode - Simulator
 Nozzle - Dry
 Mach No. - 0.6
 Angle of Attack - 10°

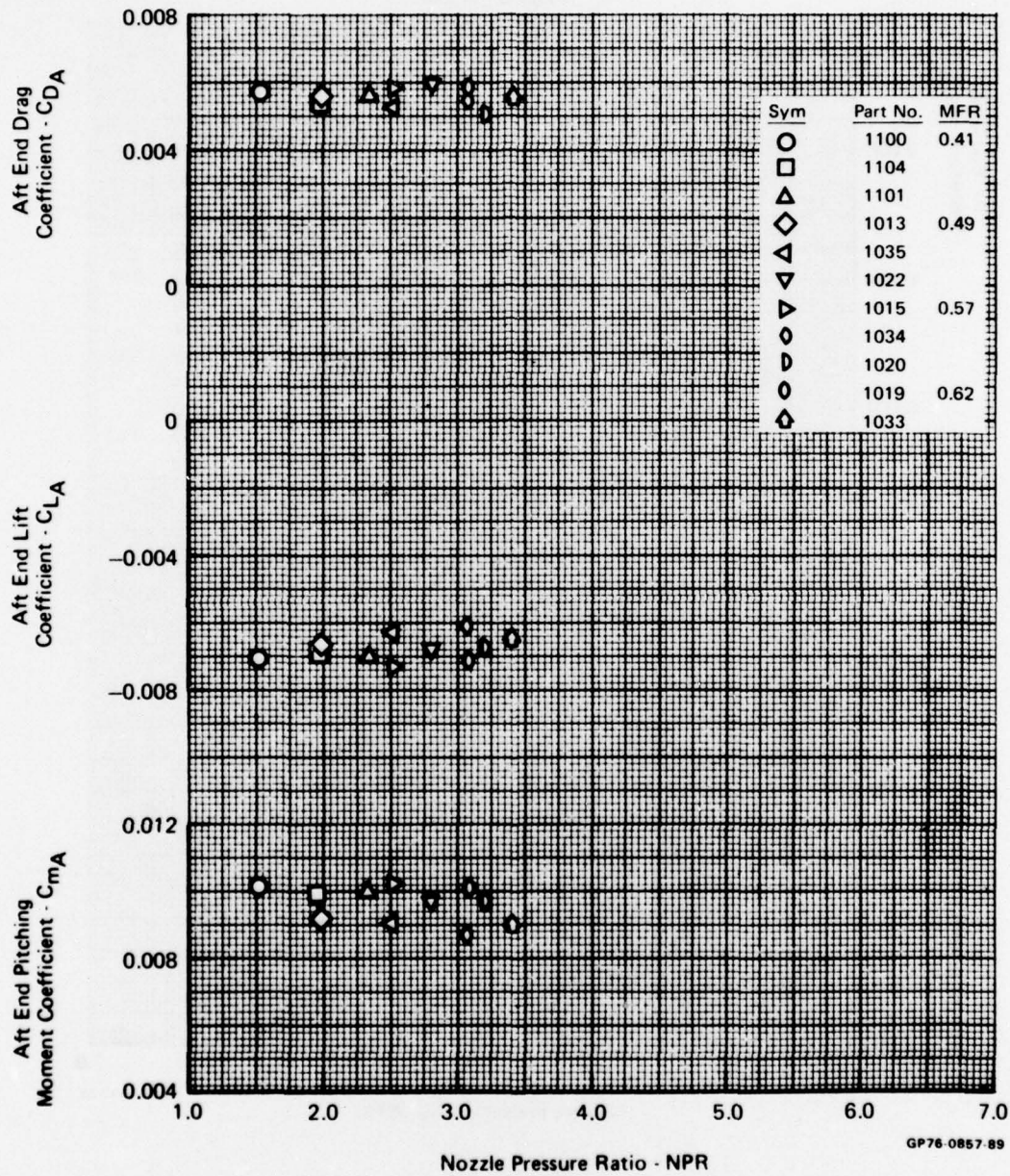


FIGURE D-109
 AFT END PERFORMANCE VARIATION WITH NOZZLE PRESSURE RATIO

Test Mode - Simulator
 Nozzle - Dry
 Mach No. - 0.6
 Angle of Attack - 16°

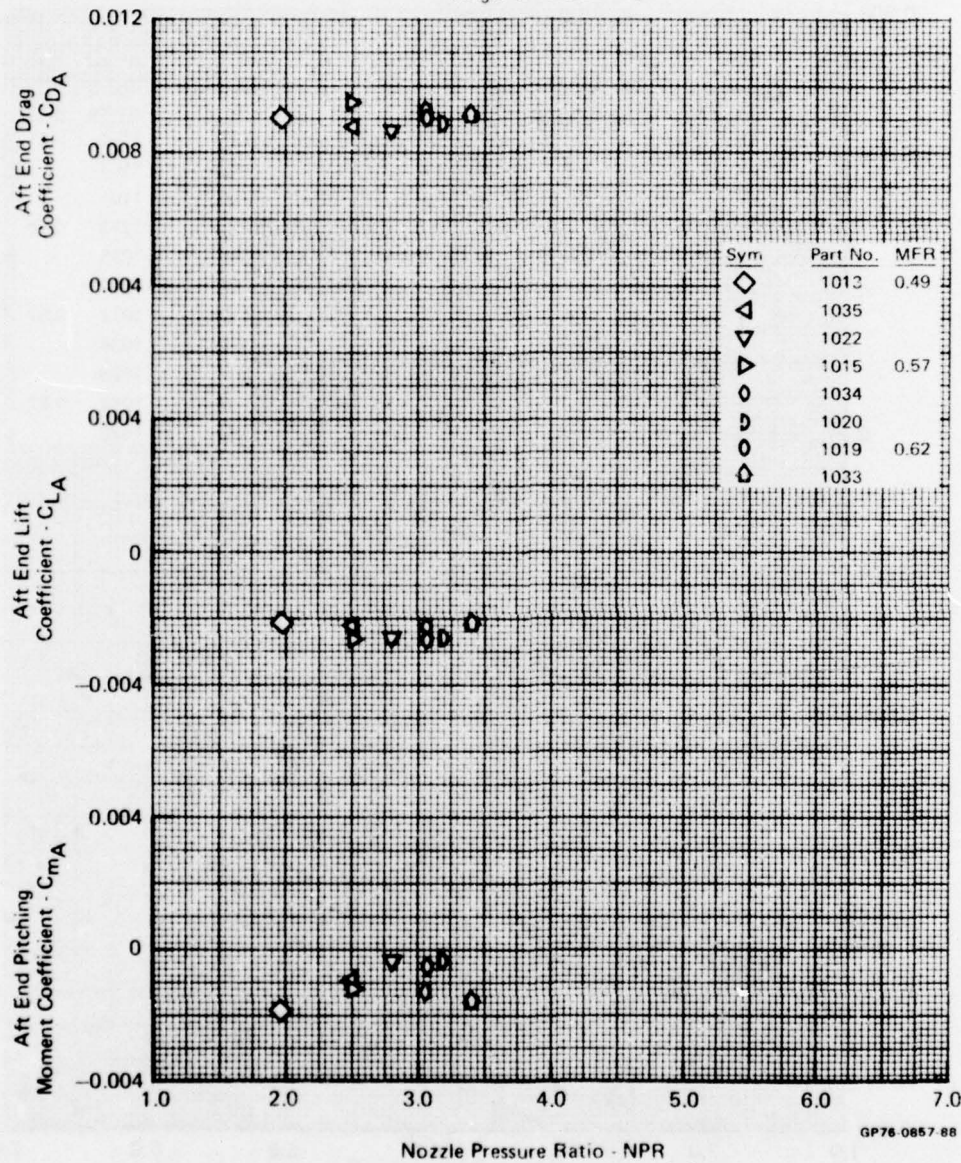


FIGURE D-110
 AFT END PERFORMANCE VARIATION WITH NOZZLE PRESSURE RATIO

Test Mode - Simulator
 Nozzle - Dry
 Mach No. - 0.9
 Angle of Attack - 0°

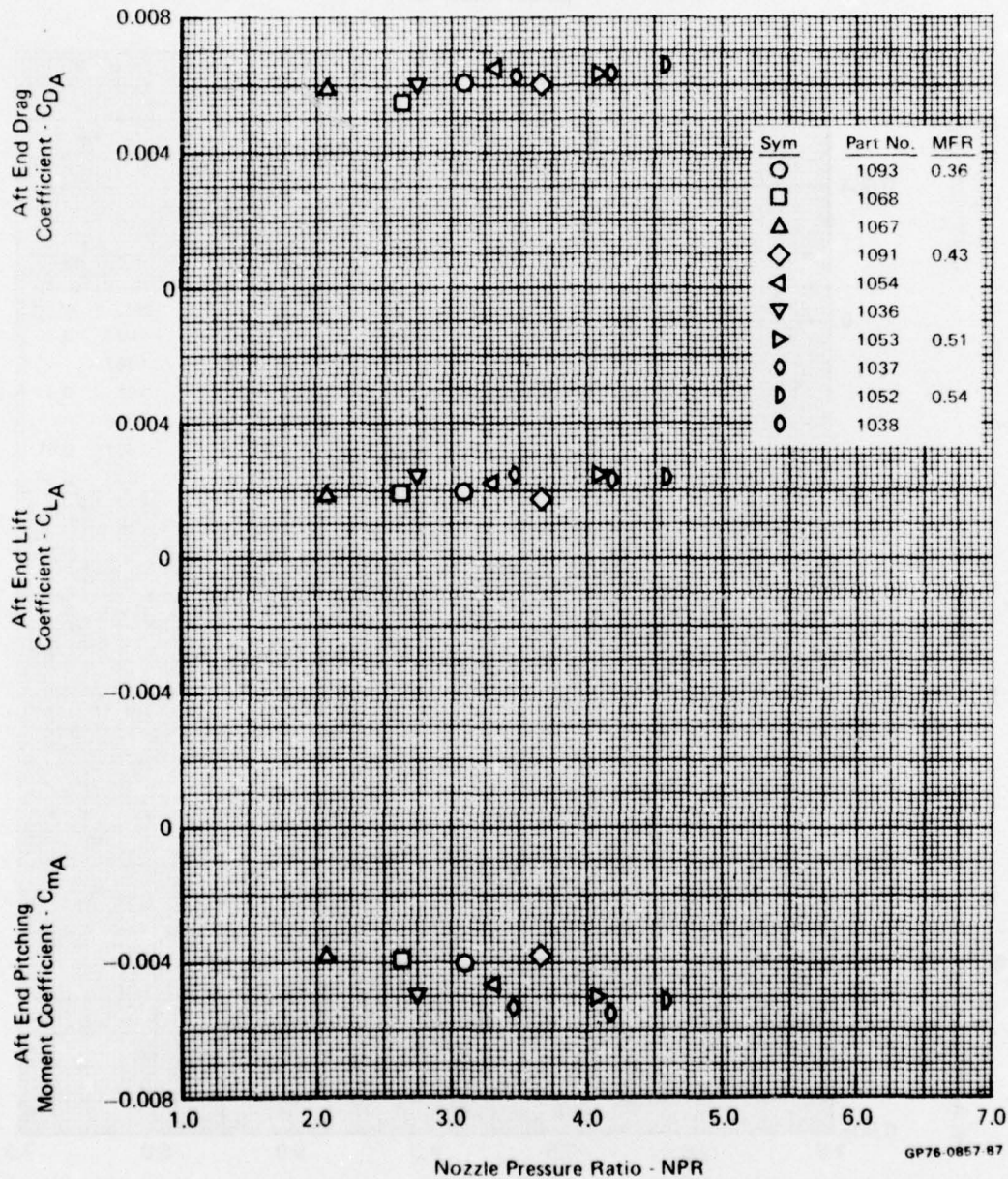


FIGURE D-111
 AFT END PERFORMANCE VARIATION WITH NOZZLE PRESSURE RATIO

Test Mode - Simulator
 Nozzle - Dry
 Mach No. - 0.9
 Angle of Attack - 5°

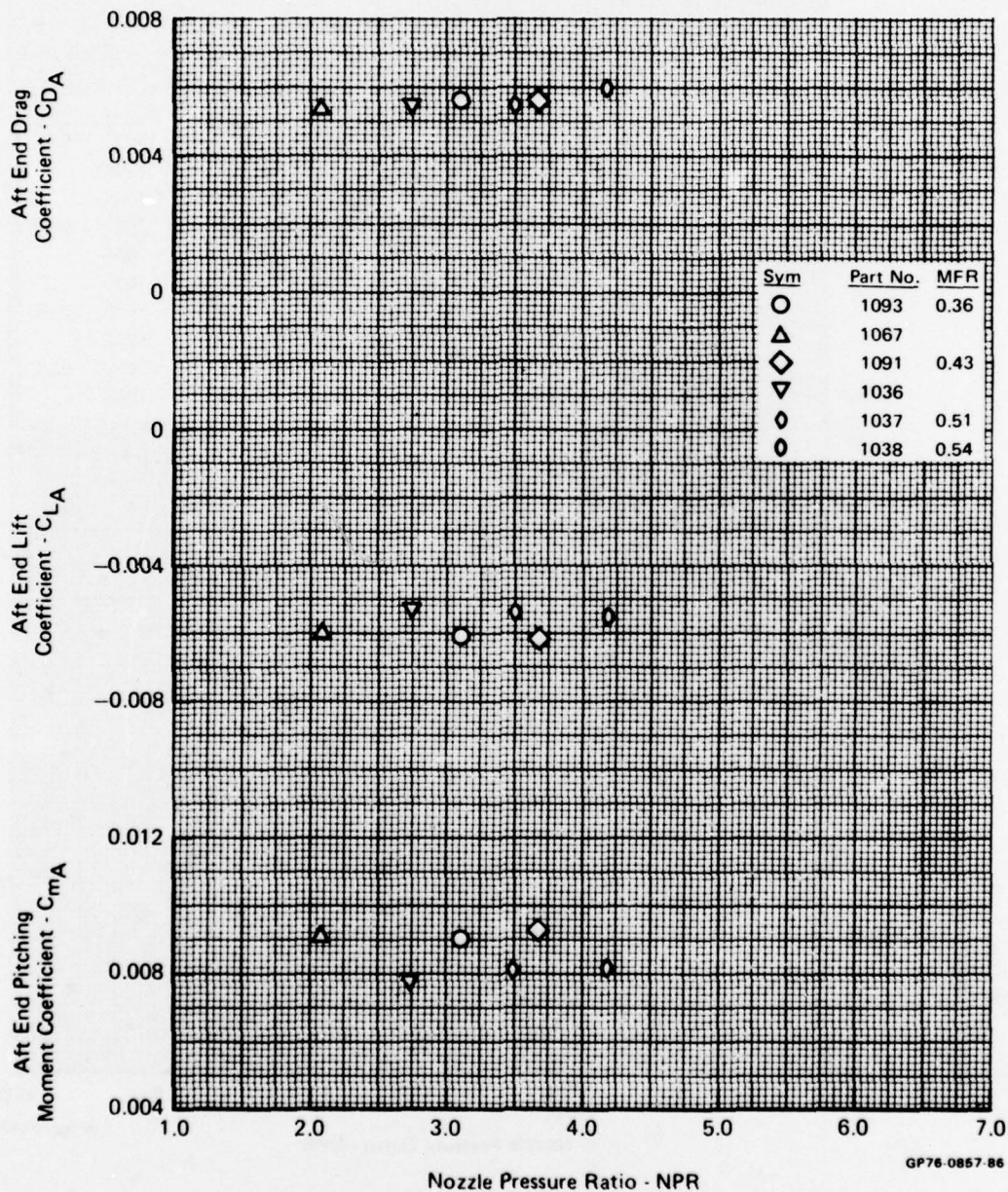


FIGURE D-112
AFT END PERFORMANCE VARIATION WITH NOZZLE PRESSURE RATIO

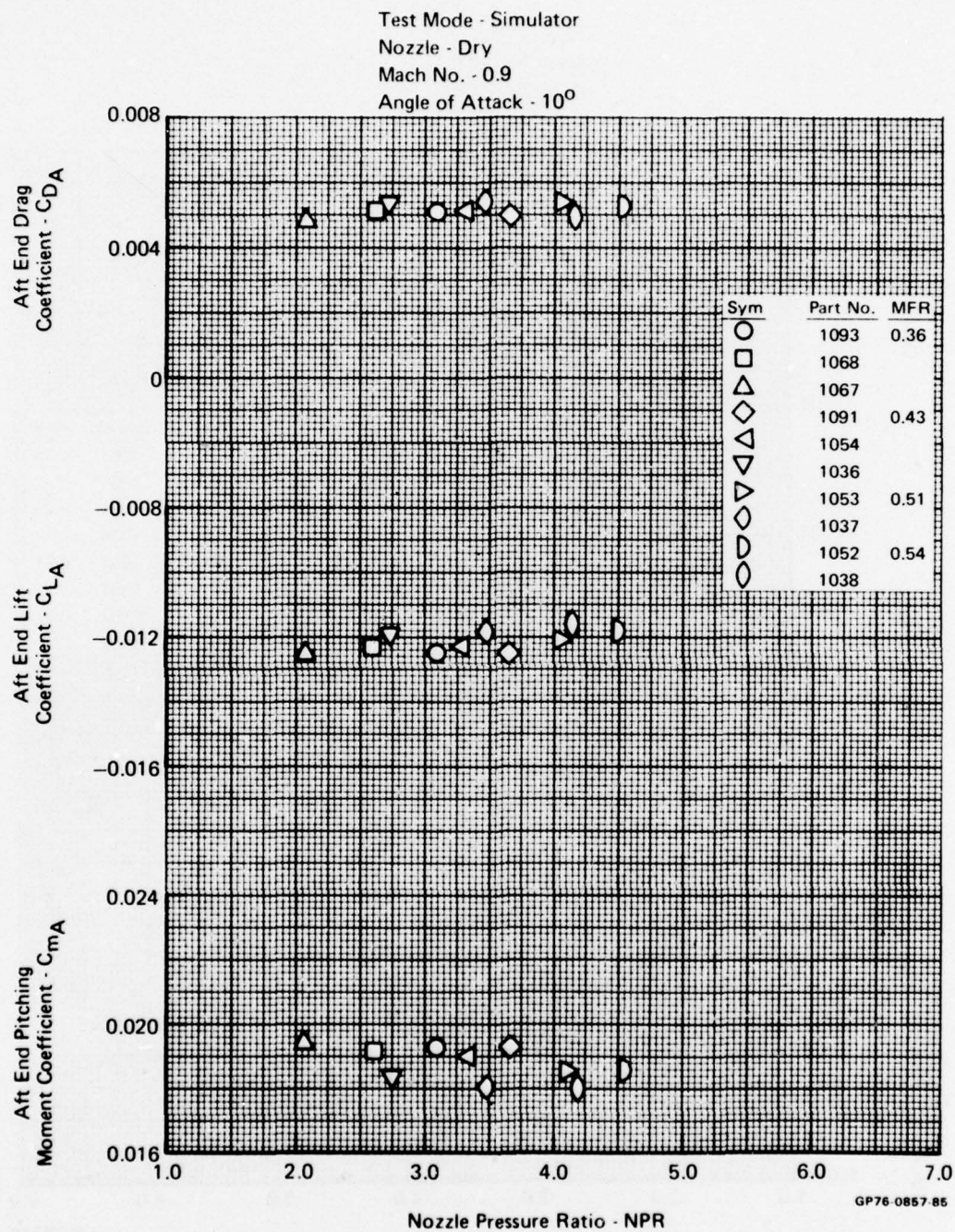


FIGURE D-113
 AFT END PERFORMANCE VARIATION WITH NOZZLE PRESSURE RATIO

Test Mode - Simulator
 Nozzle - Dry
 Mach No. - 0.9
 Angle of Attack - 16°

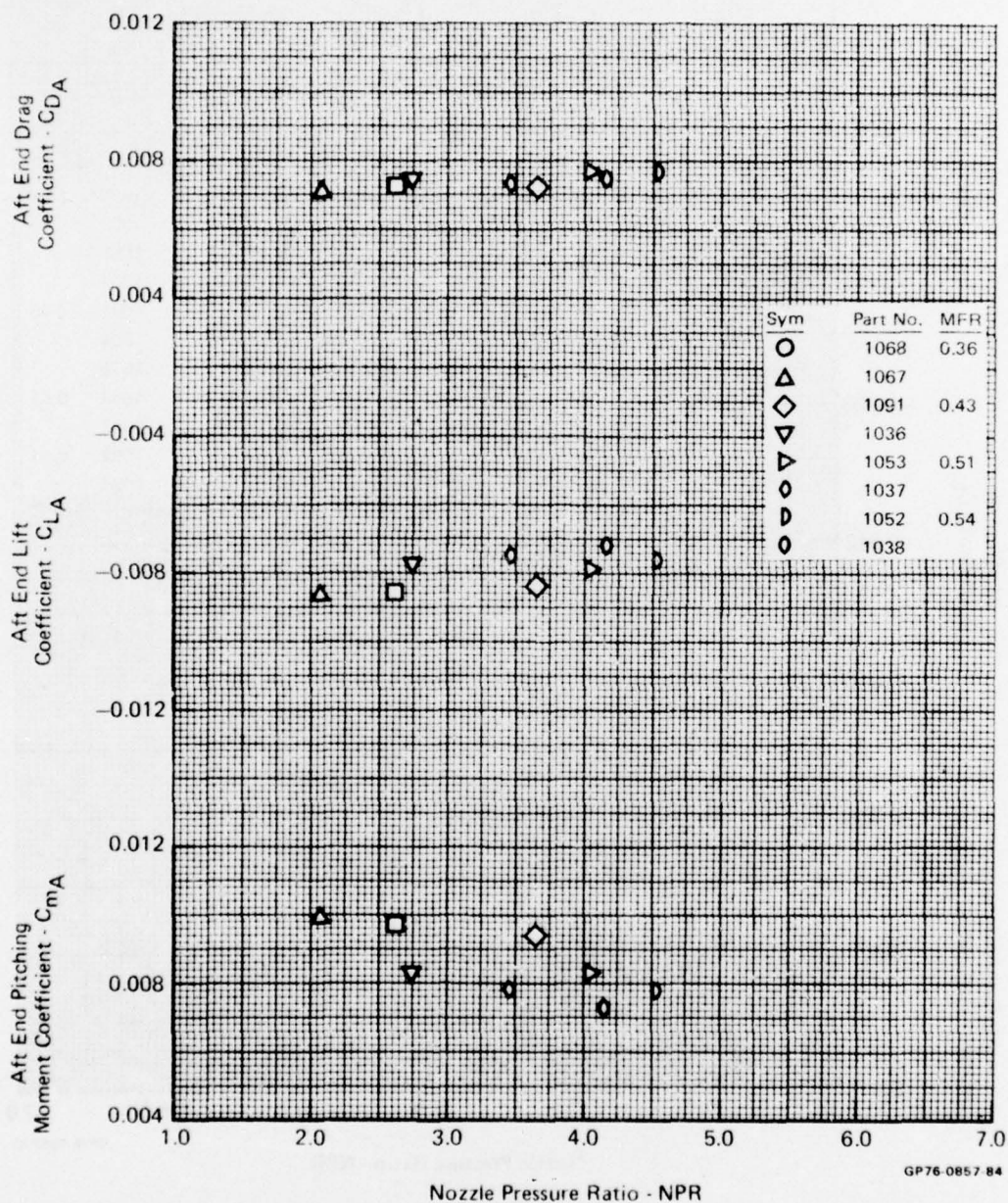


FIGURE D-114
AFT END PERFORMANCE VARIATION WITH NOZZLE PRESSURE RATIO

Test Mode - Simulator
 Nozzle - Dry
 Mach No. - 1.2
 Angle of Attack - 0°

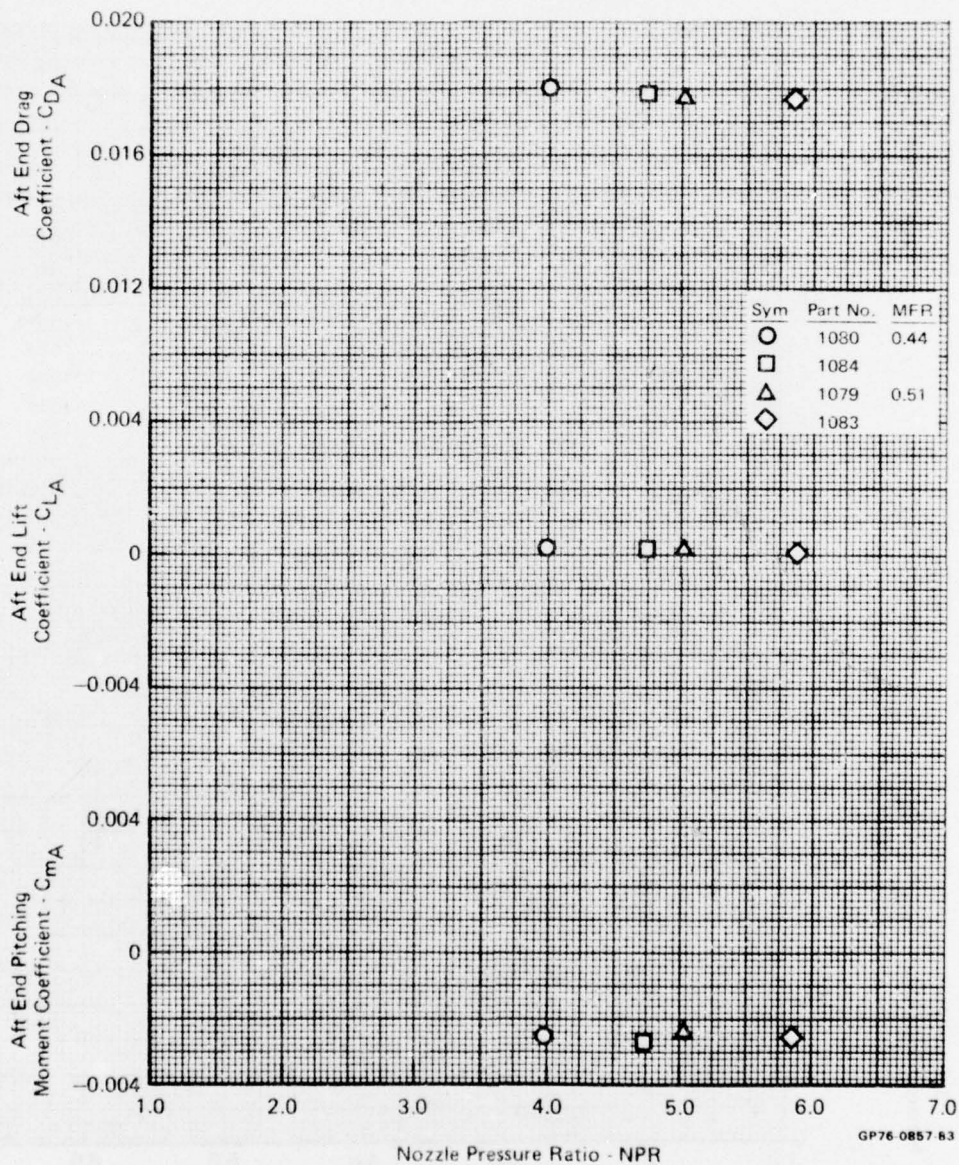


FIGURE D-115
 AFT END PERFORMANCE VARIATION WITH NOZZLE PRESSURE RATIO

Test Mode - Simulator

Nozzle - Dry

Mach No. - 1.2

Angle of Attack - 5°

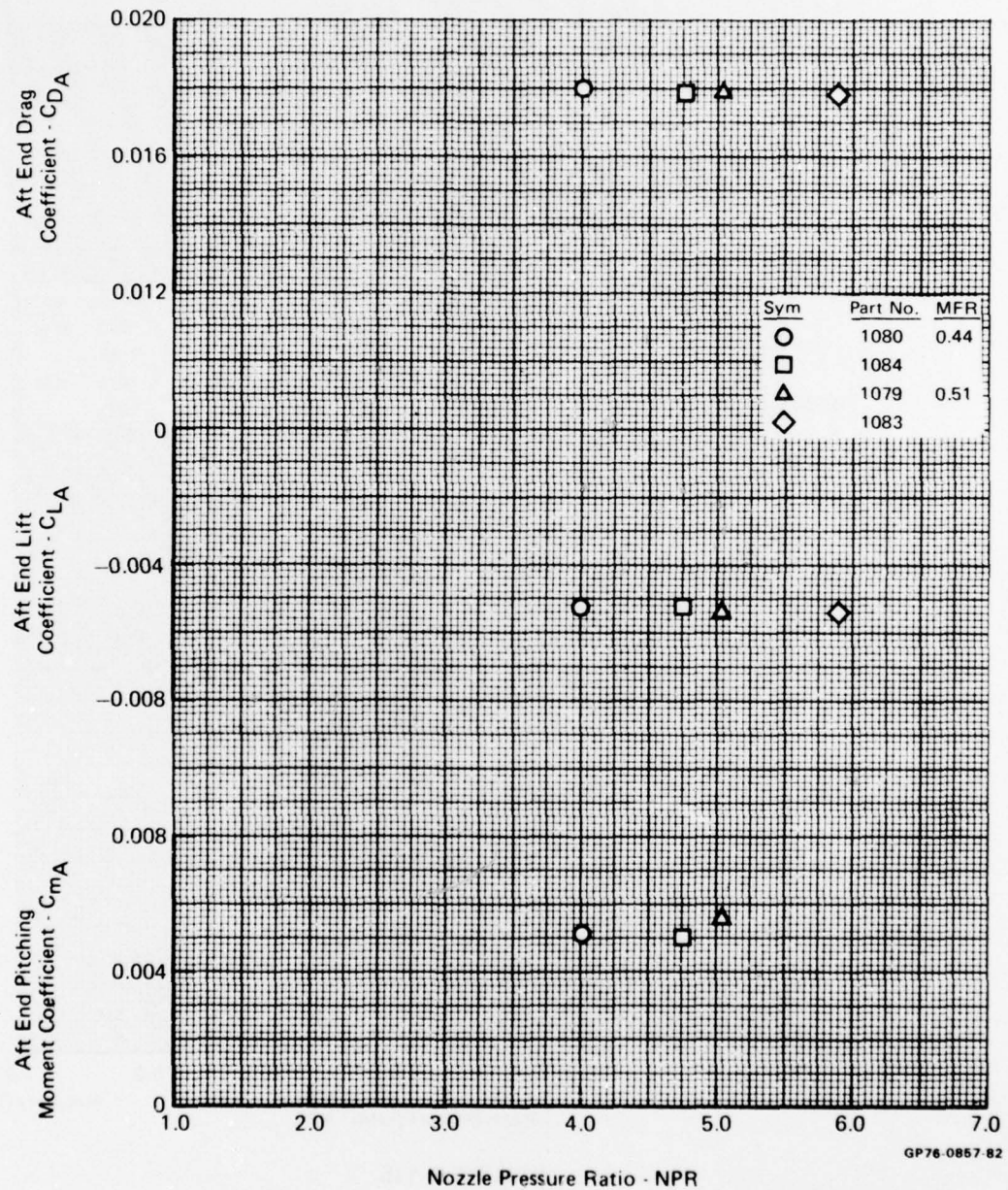


FIGURE D-116
AFT END PERFORMANCE VARIATION WITH NOZZLE PRESSURE RATIO

Test Mode - Simulator
 Nozzle - Dry
 Mach No. - 1.2
 Angle of Attack - 10°

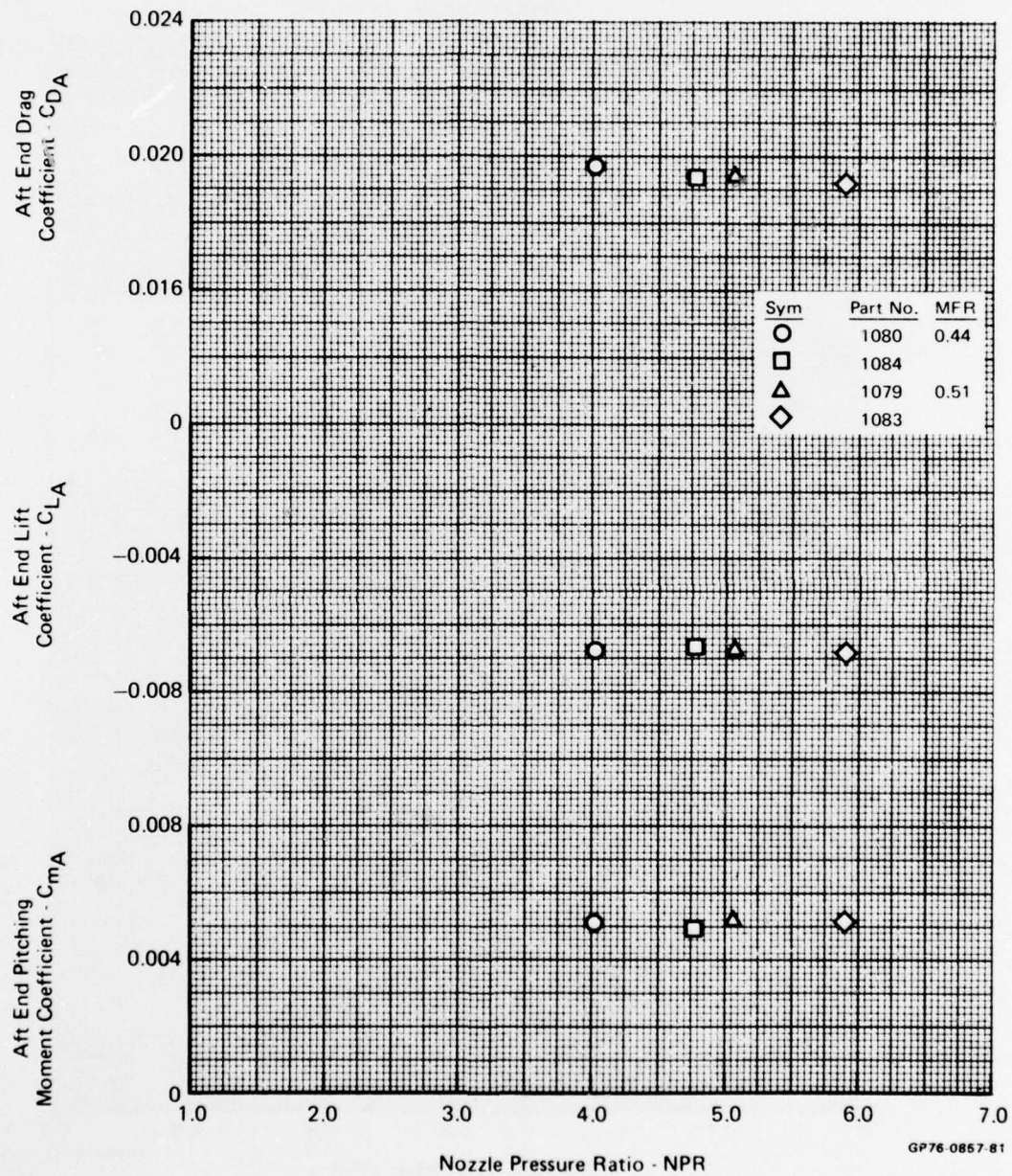


FIGURE D-117
AFT END PERFORMANCE VARIATION WITH NOZZLE PRESSURE RATIO

Test Mode - Simulator
 Nozzle - Afterburning
 Mach No. - 0.6
 Angle of Attack - 0°

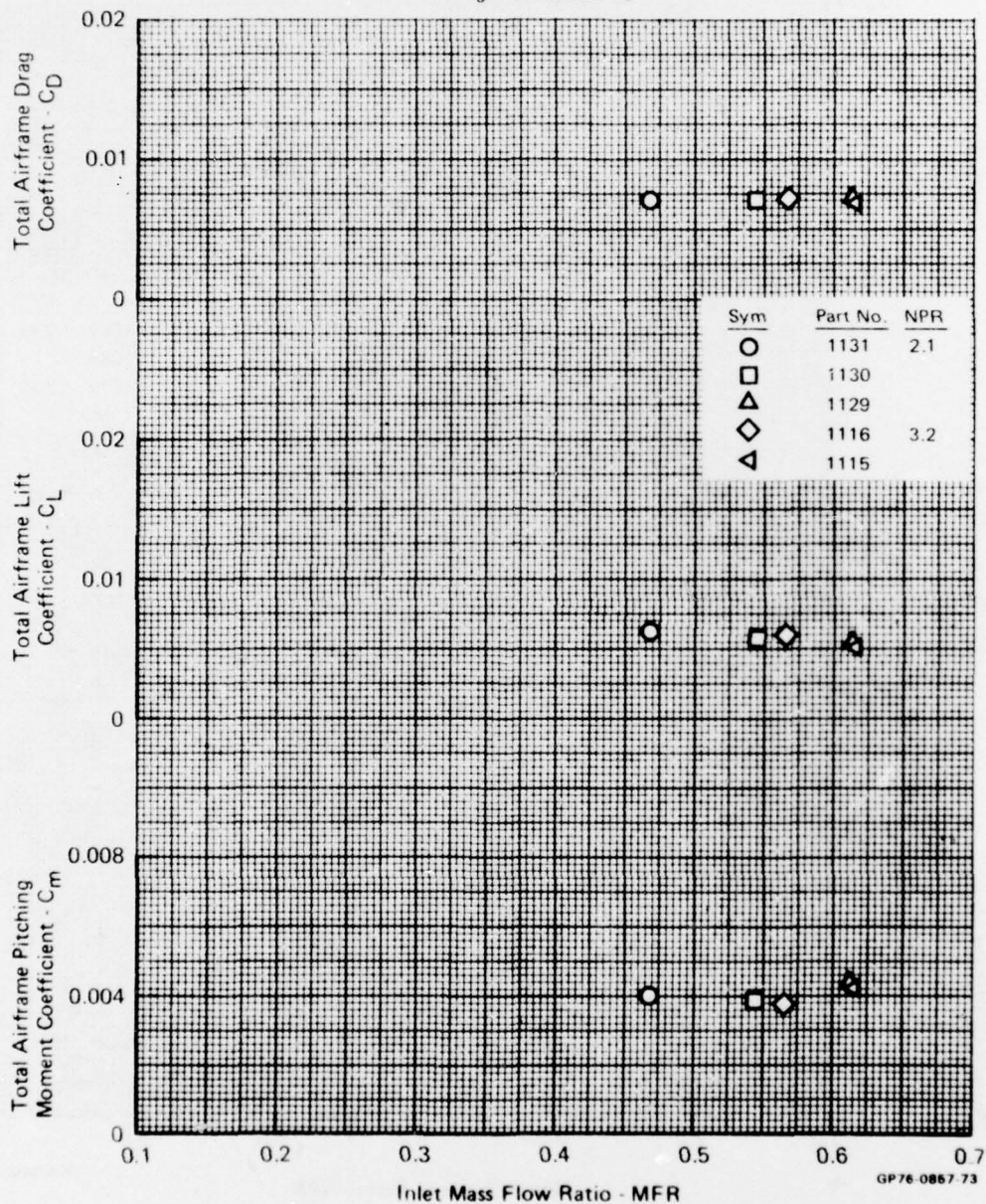


FIGURE D-118

TOTAL AIRFRAME PERFORMANCE VARIATION WITH INLET MASS FLOW RATIO

Test Mode - Simulator
 Nozzle - Afterburning
 Mach No. - 0.6
 Angle of Attack - 5°

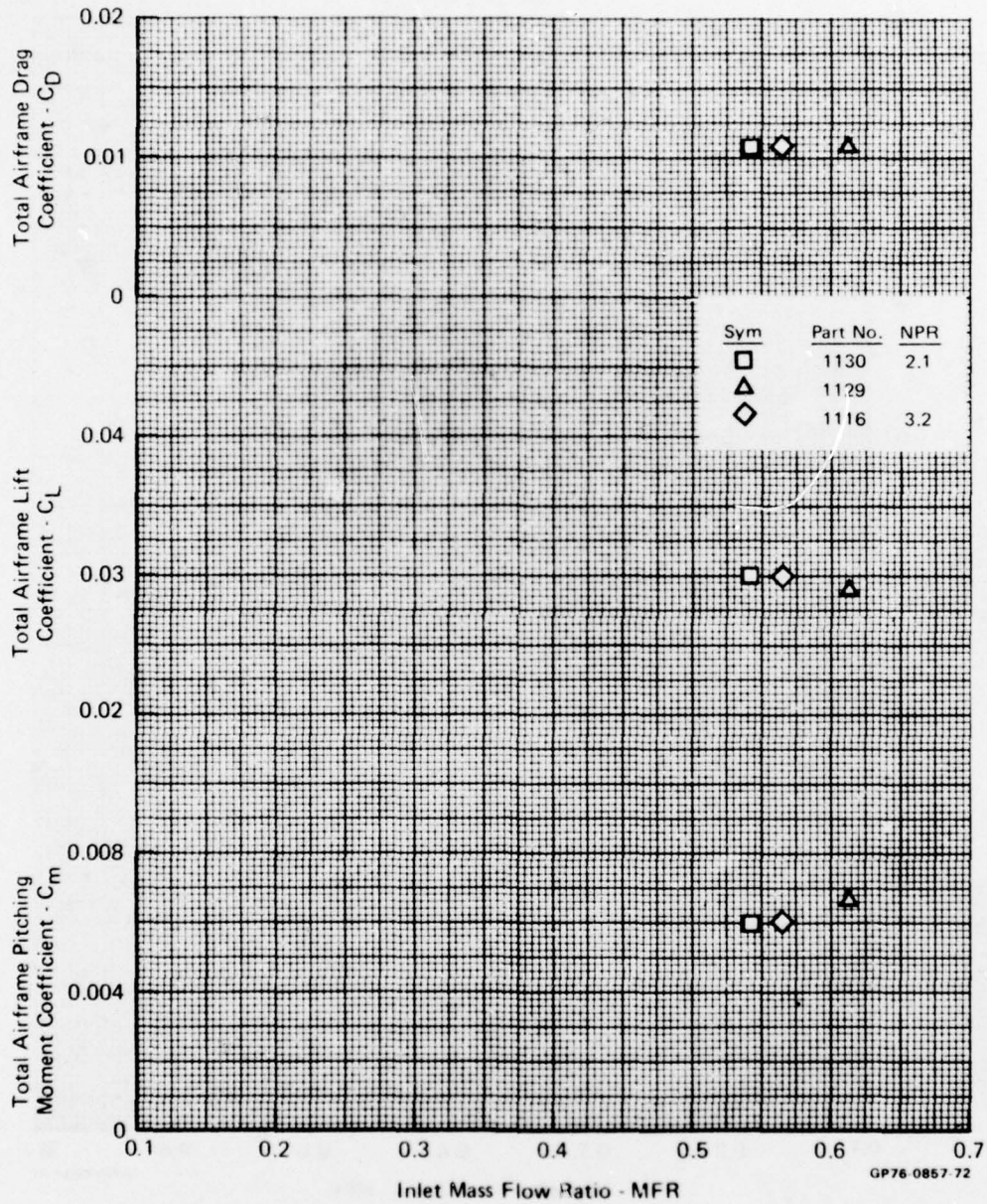


FIGURE D-119
TOTAL AIRFRAME PERFORMANCE VARIATION WITH INLET MASS FLOW RATIO

Test Mode - Simulator
 Nozzle - Afterburning
 Mach No. - 0.6
 Angle of Attack - 10°

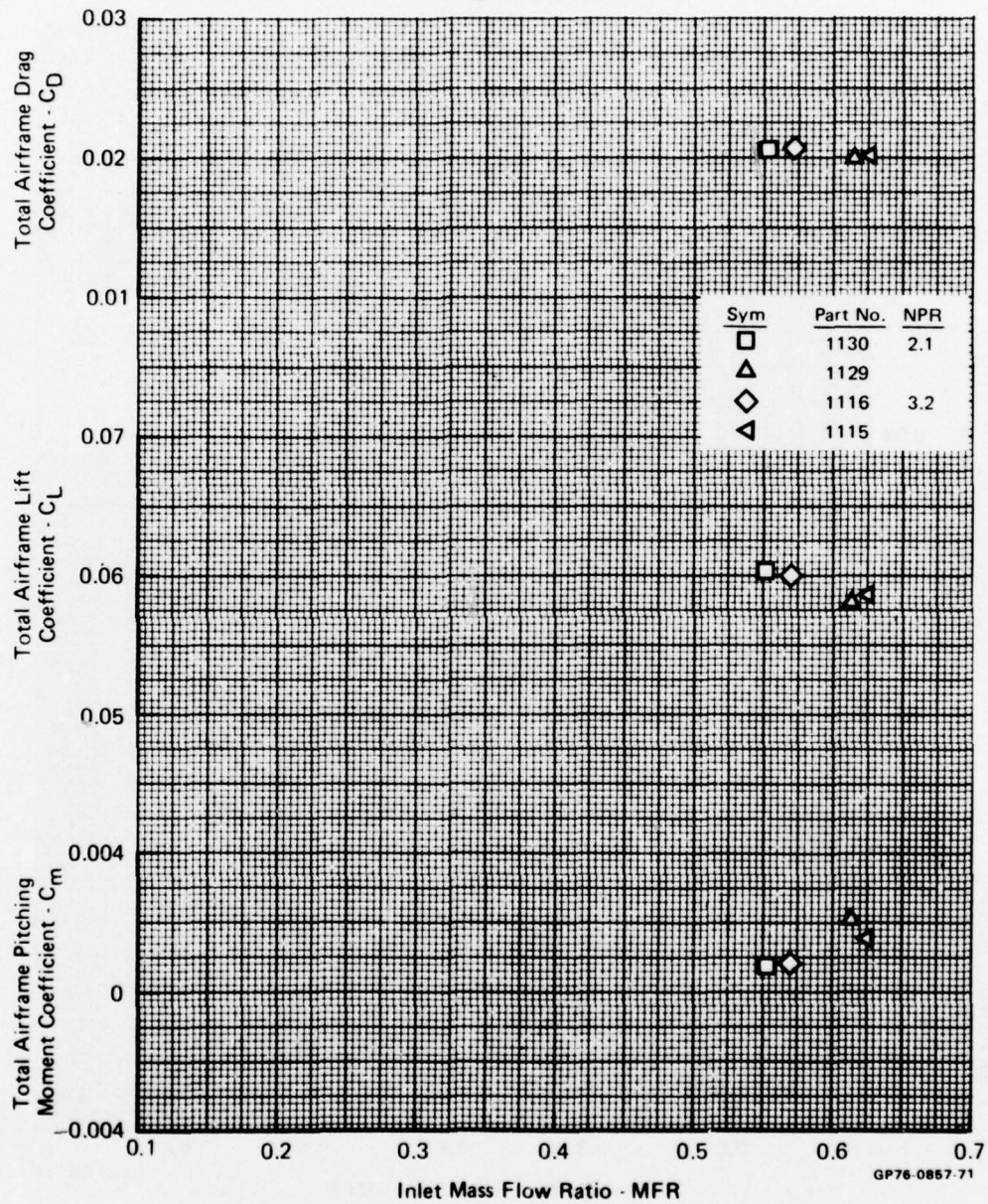


FIGURE D-120
TOTAL AIRFRAME PERFORMANCE VARIATION WITH INLET MASS FLOW RATIO

Test Mode - Simulator
 Nozzle - Afterburning
 Mach No. - 0.9
 Angle of Attack - 0°

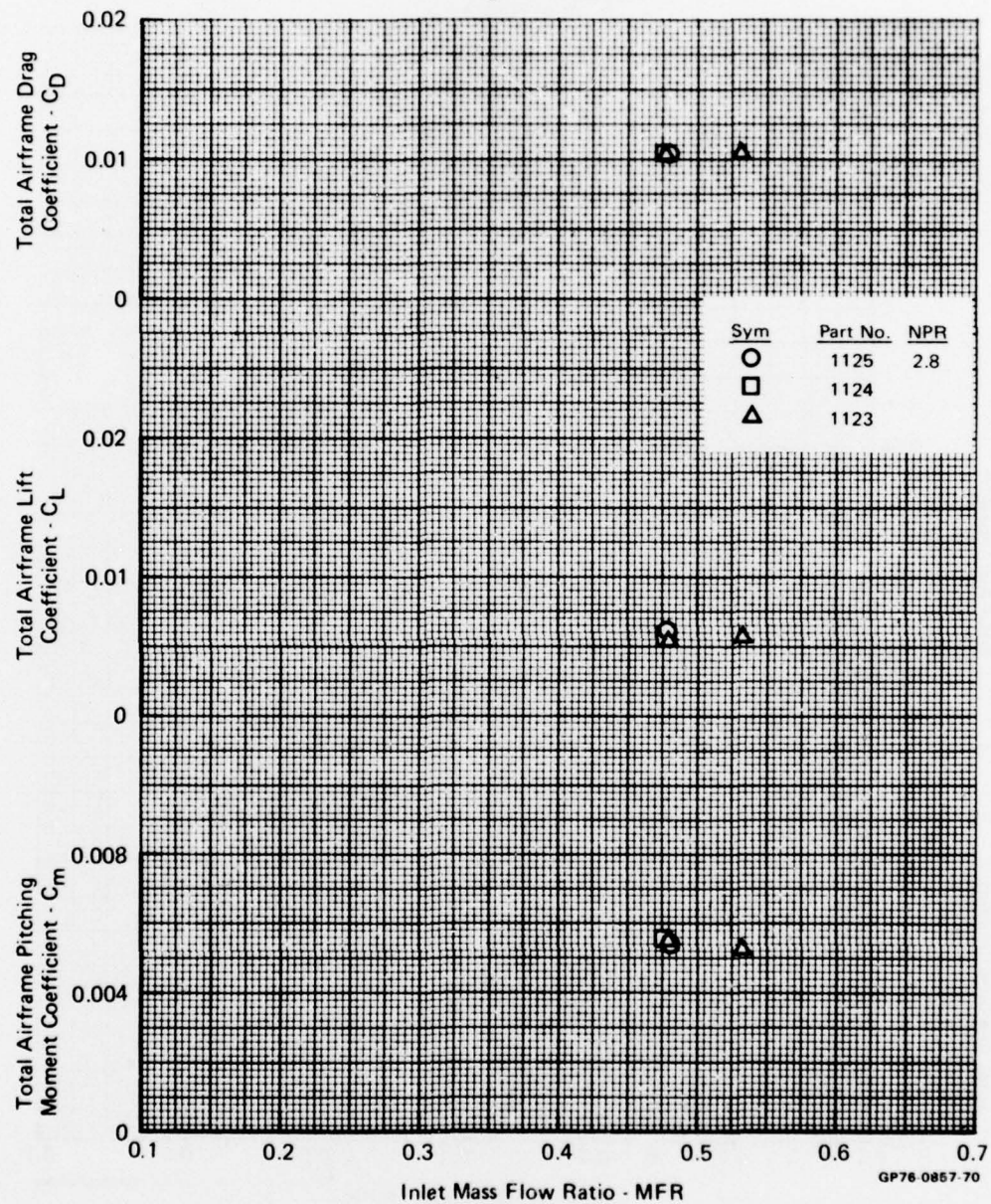


FIGURE D-121
 TOTAL AIRFRAME PERFORMANCE VARIATION WITH INLET MASS FLOW RATIO

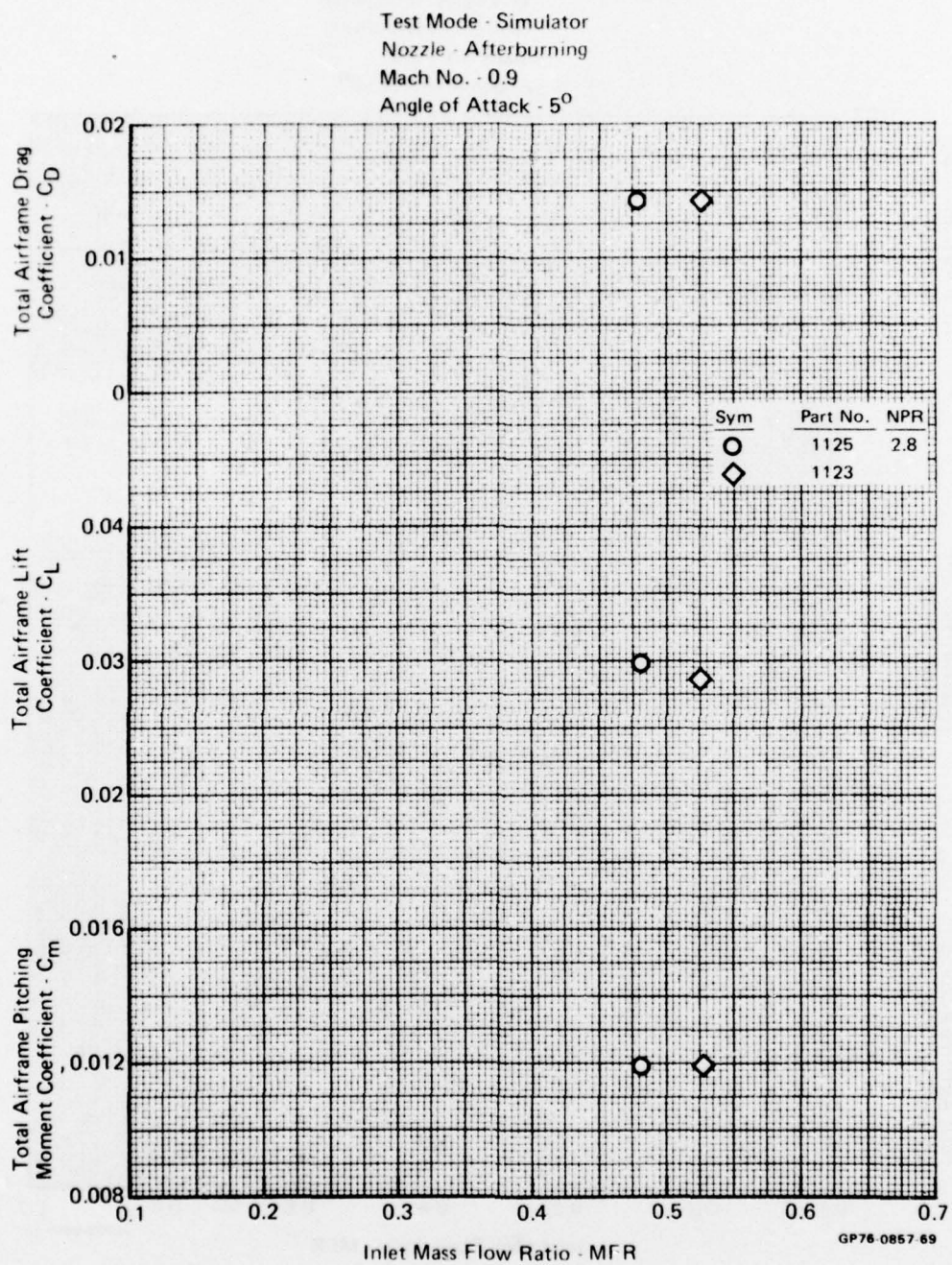


FIGURE D-122
TOTAL AIRFRAME PERFORMANCE VARIATION WITH INLET MASS FLOW RATIO

Test Mode - Simulator
 Nozzle - Afterburning
 Mach No. - 0.9
 Angle of Attack - 10°

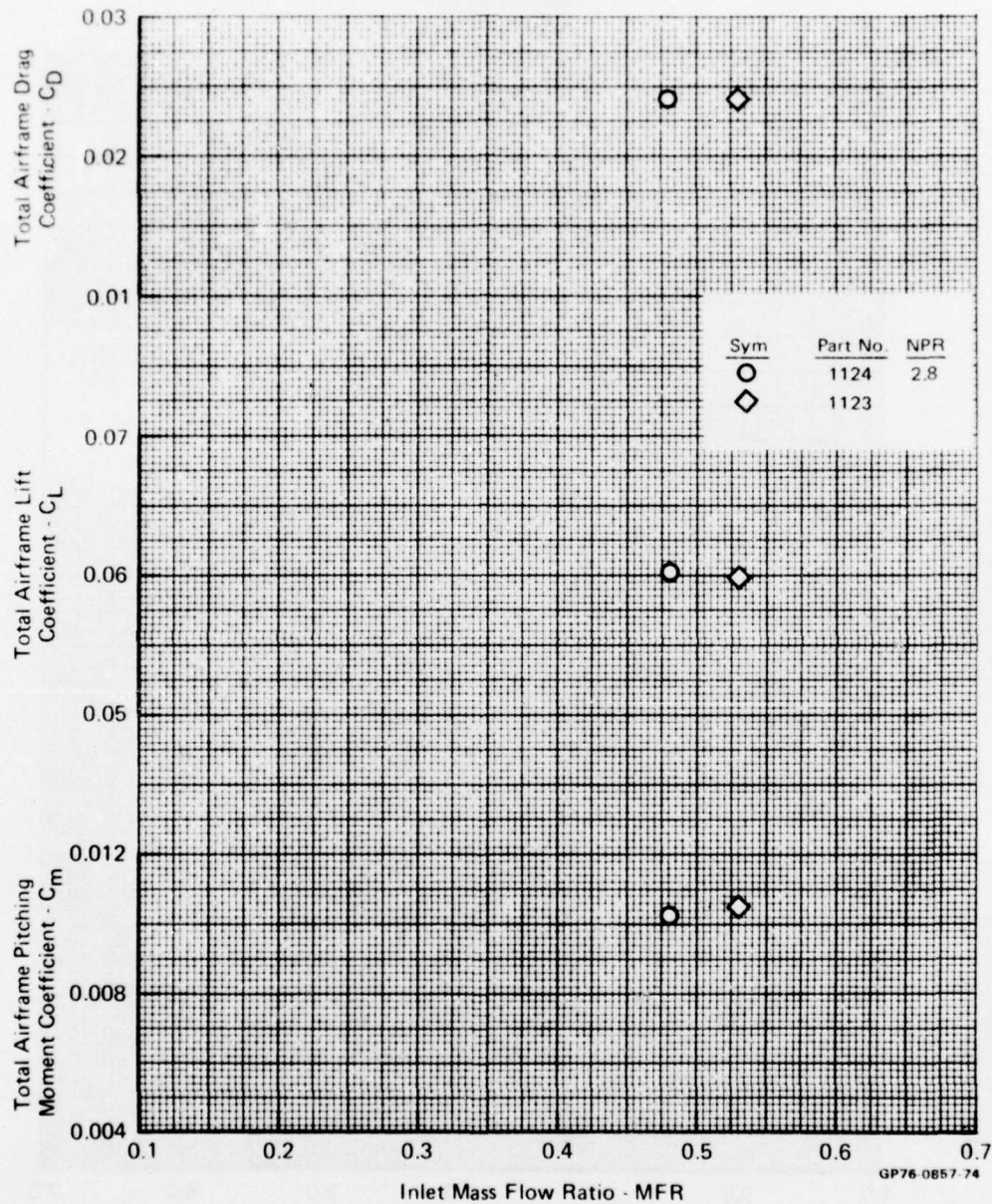


FIGURE D-123
TOTAL AIRFRAME PERFORMANCE VARIATION WITH INLET MASS FLOW RATIO

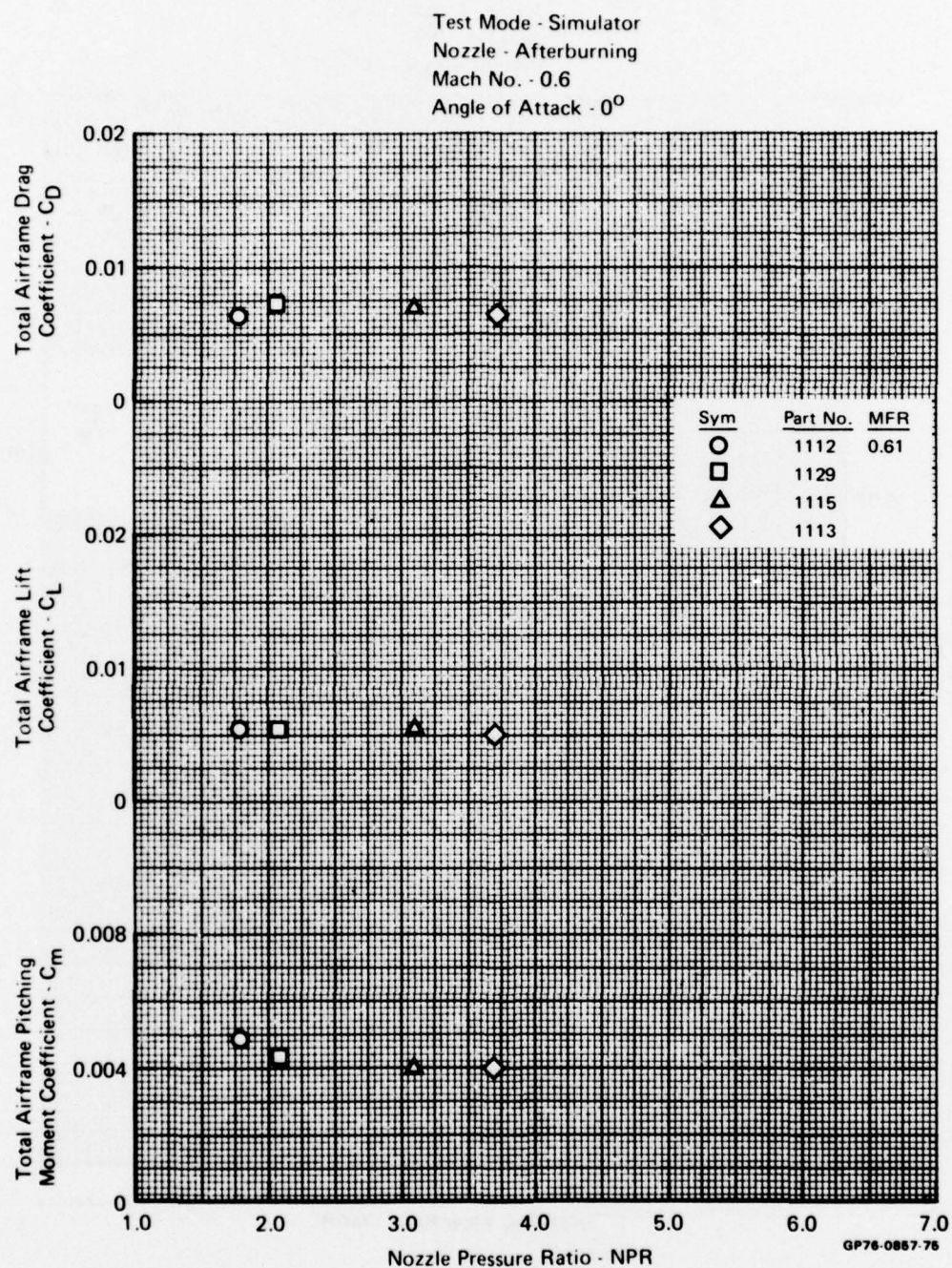


FIGURE D-124
TOTAL AIRFRAME PERFORMANCE VARIATION WITH NOZZLE PRESSURE RATIO

Test Mode - Simulator
 Nozzle - Afterburning
 Mach No. - 0.6
 Angle of Attack - 5°

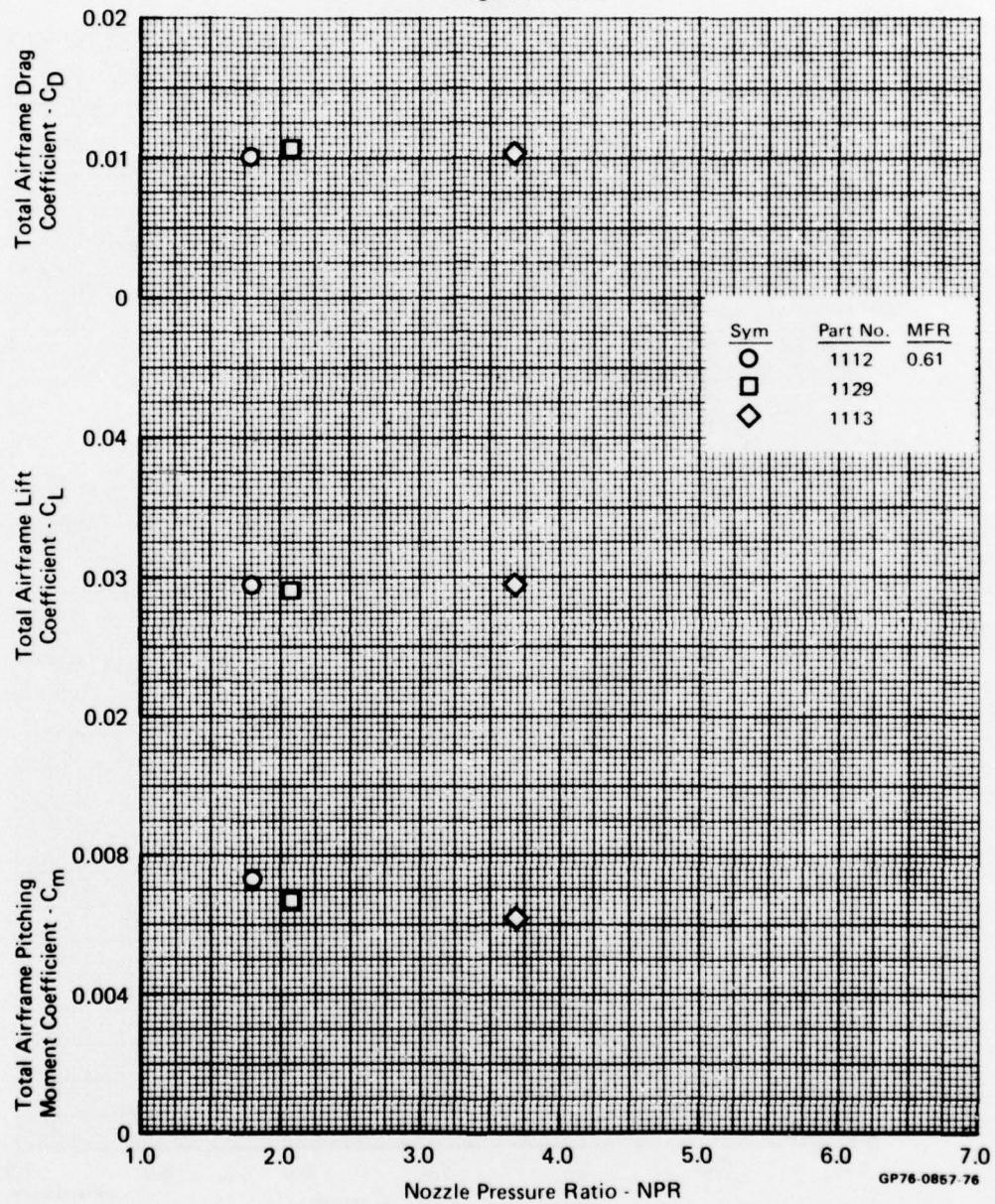


FIGURE D-125
TOTAL AIRFRAME PERFORMANCE VARIATION WITH NOZZLE PRESSURE RATIO

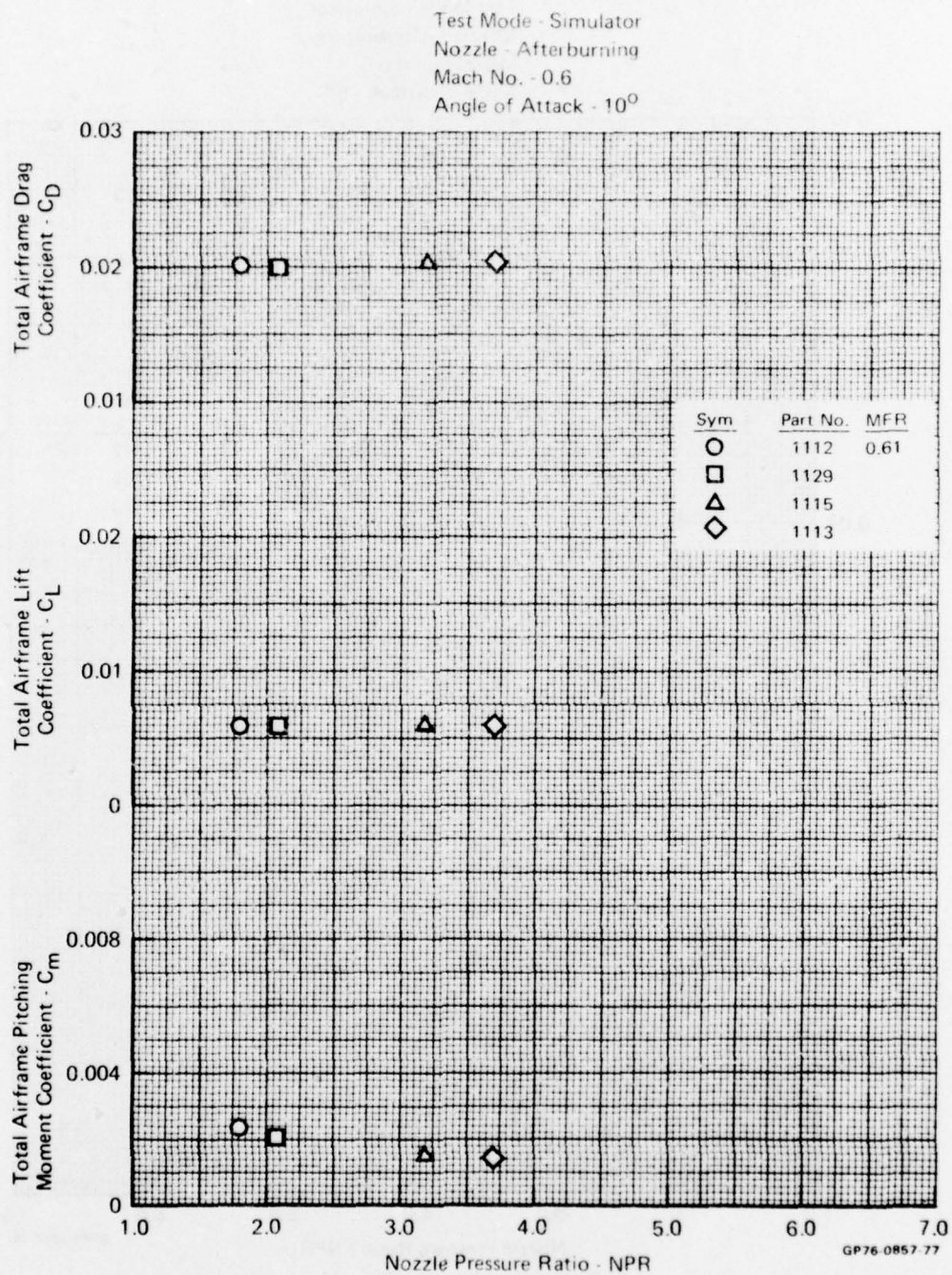


FIGURE D-126
TOTAL AIRFRAME PERFORMANCE VARIATION WITH NOZZLE PRESSURE RATIO

Test Mode - Simulator

Nozzle - Afterburning

Mach No. - 0.9

Angle of Attack - 0°

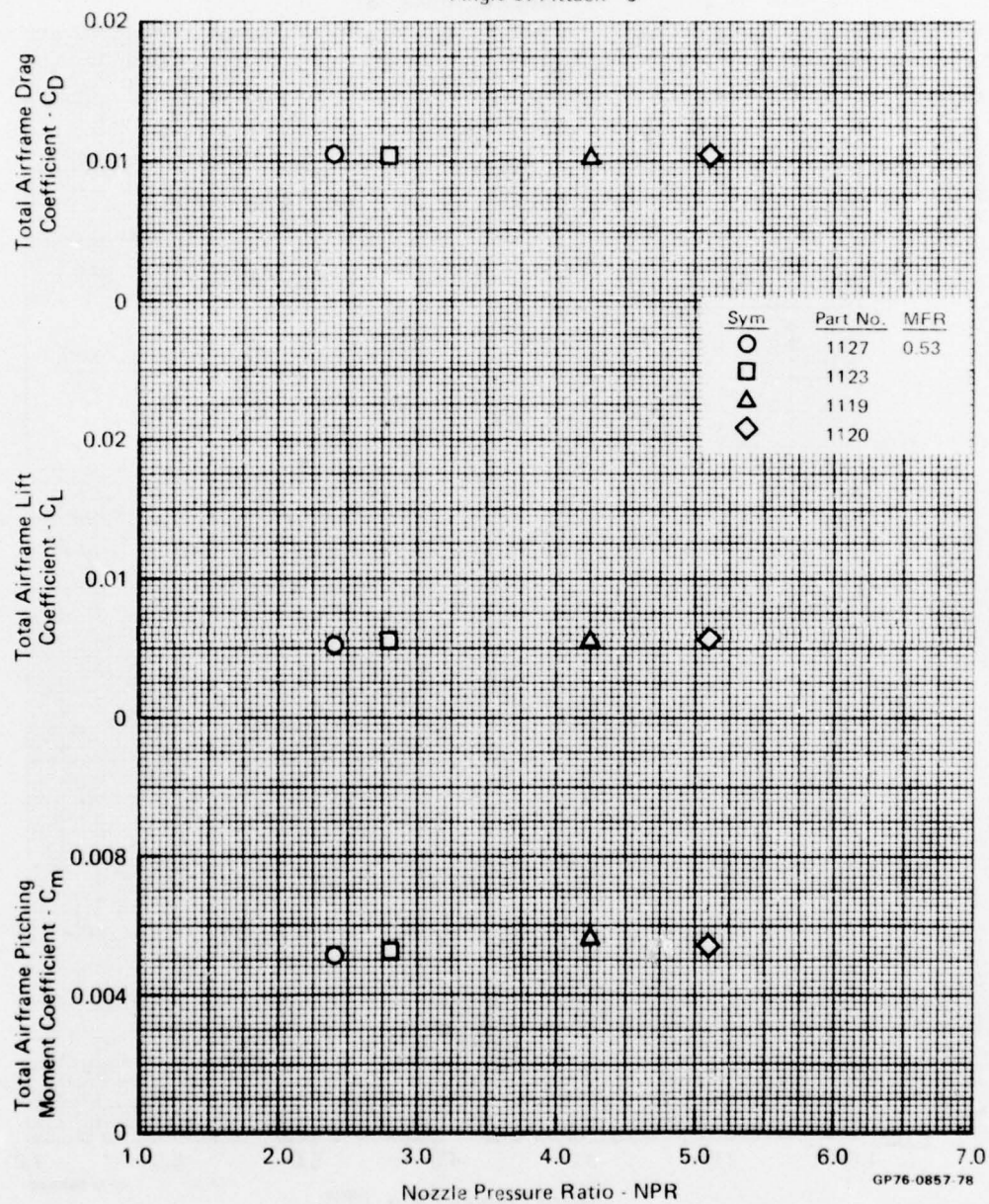


FIGURE D-127
TOTAL AIRFRAME PERFORMANCE VARIATION WITH NOZZLE PRESSURE RATIO

Test Mode - Simulator
 Nozzle - Afterburning
 Mach No. - 0.9
 Angle of Attack - 5°

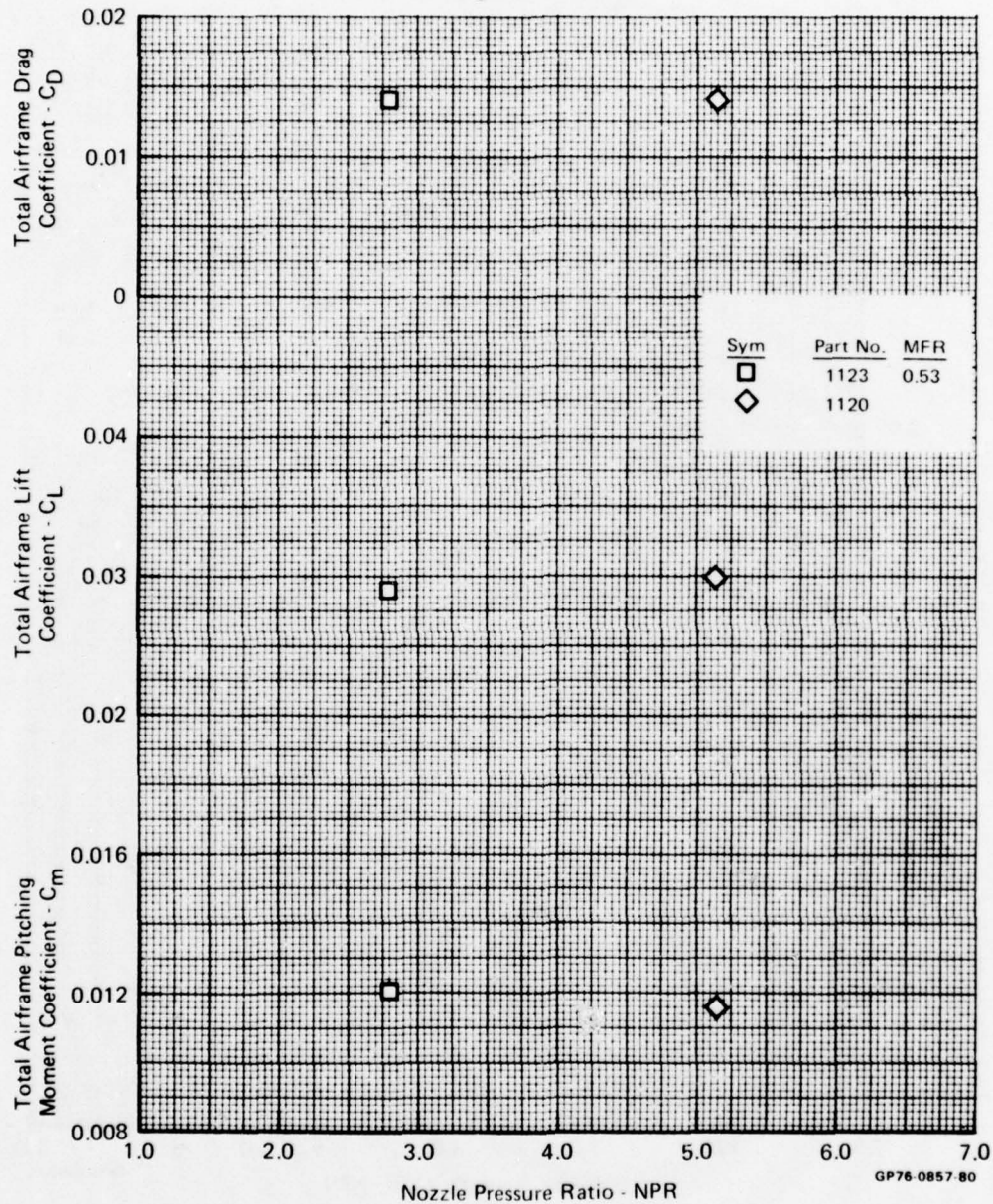


FIGURE D-128
TOTAL AIRFRAME PERFORMANCE VARIATION WITH NOZZLE PRESSURE RATIO

Test Mode - Simulator
 Nozzle - Afterburning
 Mach No. - 0.9
 Angle of Attack - 10^0

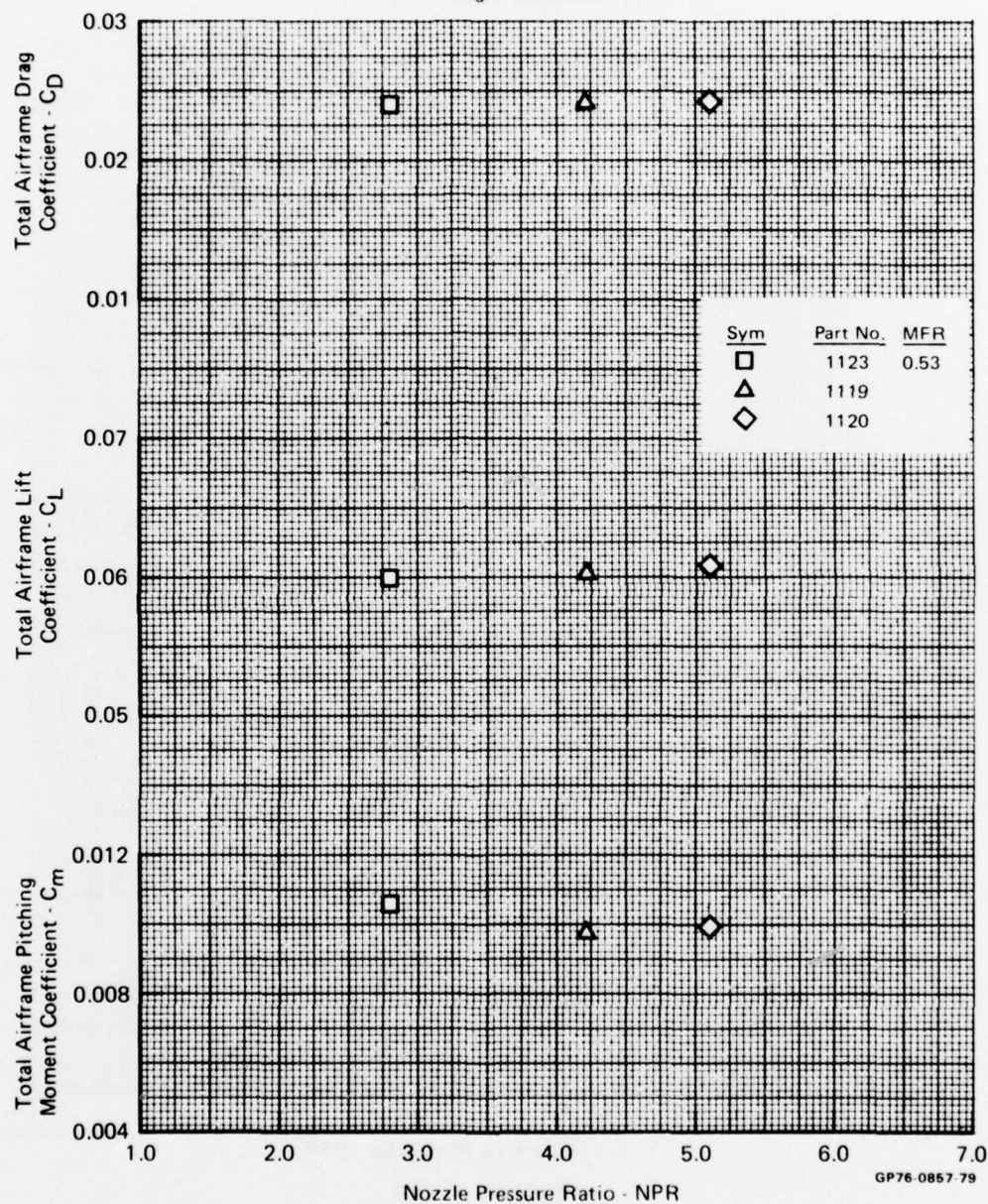


FIGURE D-129
TOTAL AIRFRAME PERFORMANCE VARIATION WITH NOZZLE PRESSURE RATIO

Test Mode - Simulator
 Nozzle - Afterburning
 Mach No. - 0.6
 Angle of Attack - 0°

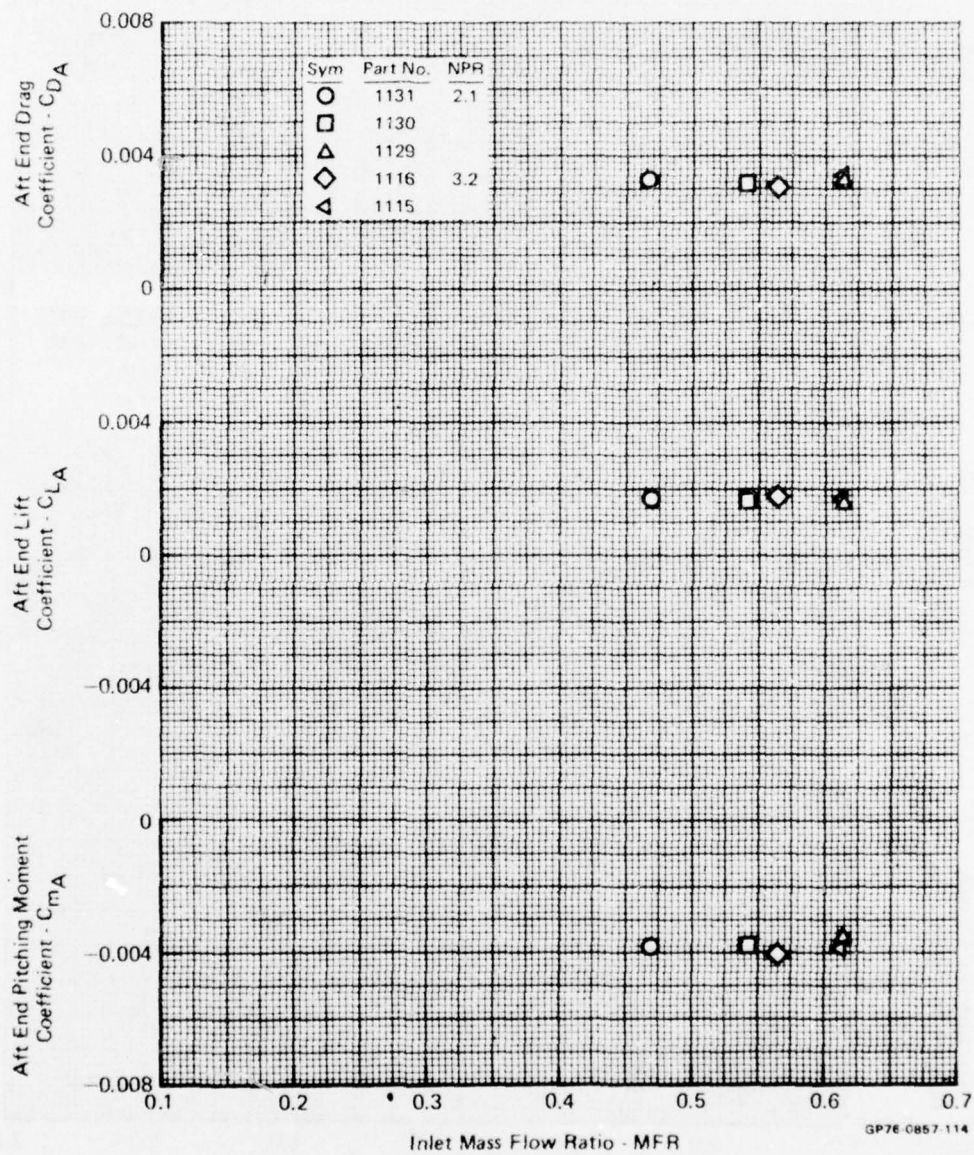


FIGURE D-130
 AFT END PERFORMANCE VARIATION WITH INLET MASS FLOW RATIO

Test Mode - Simulator
 Nozzle - Afterburning
 Mach No. - 0.6
 Angle of Attack - 5°

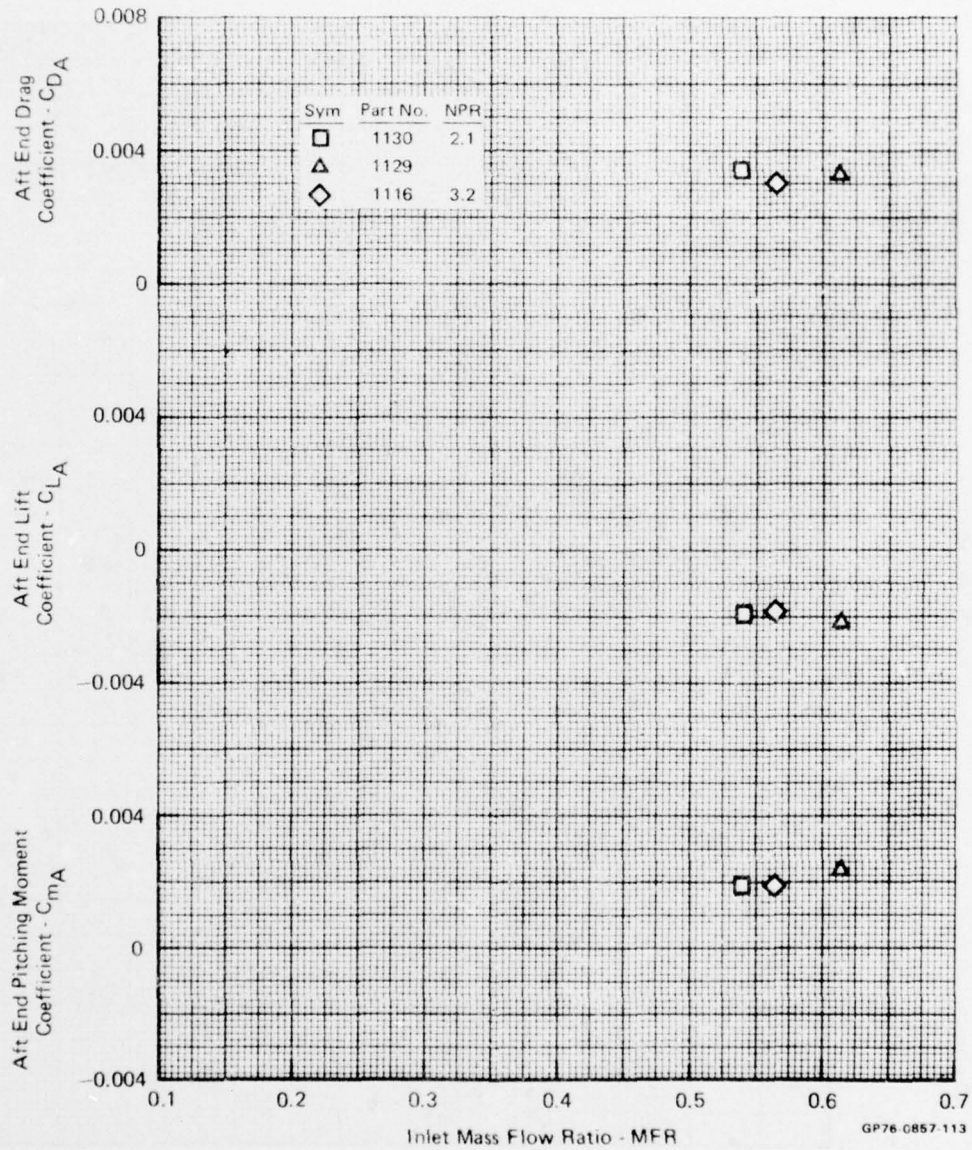


FIGURE D-131
 AFT END PERFORMANCE VARIATION WITH INLET MASS FLOW RATIO

Test Mode - Simulator
 Nozzle - Afterburning
 Mach No. - 0.6
 Angle of Attack - 10°

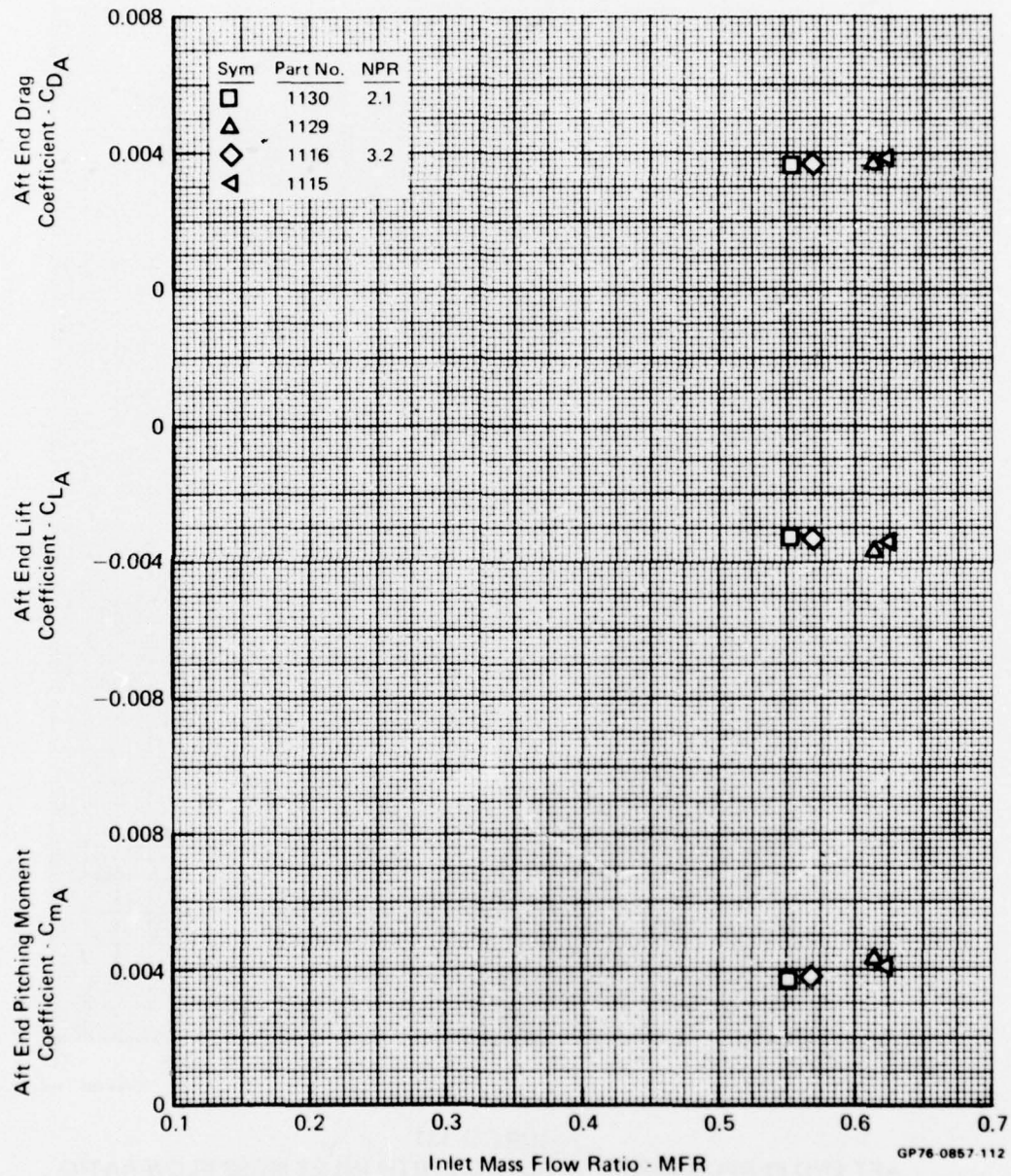


FIGURE D-132
 AFT END PERFORMANCE VARIATION WITH INLET MASS FLOW RATIO

Test Mode - Simulator
 Nozzle - Afterburning
 Mach No. - 0.9
 Angle of Attack - 0°

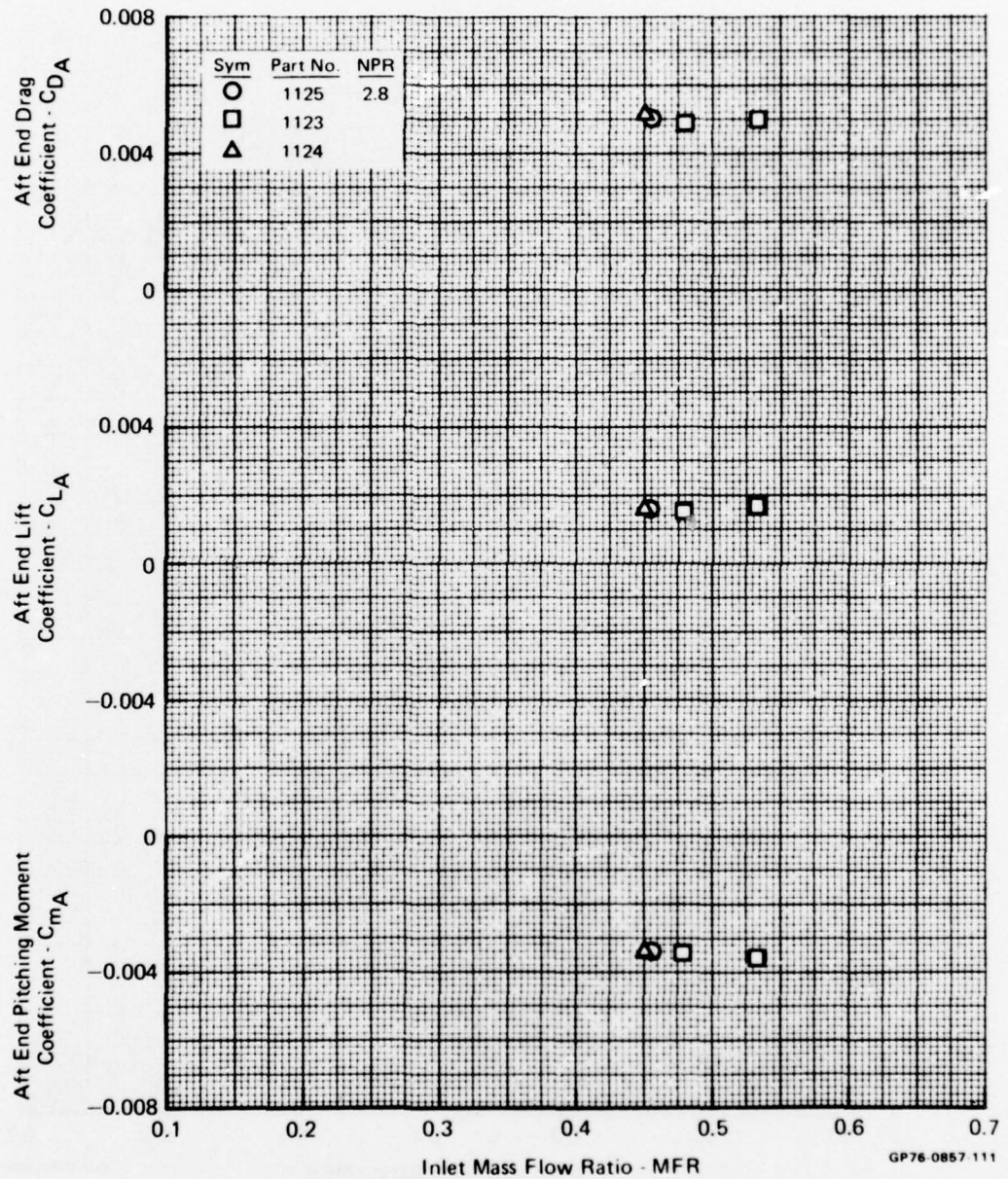


FIGURE D-133
 AFT END PERFORMANCE VARIATION WITH INLET MASS FLOW RATIO

Test Mode - Simulator
 Nozzle - Afterburning
 Mach No. - 0.9
 Angle of Attack - 5°

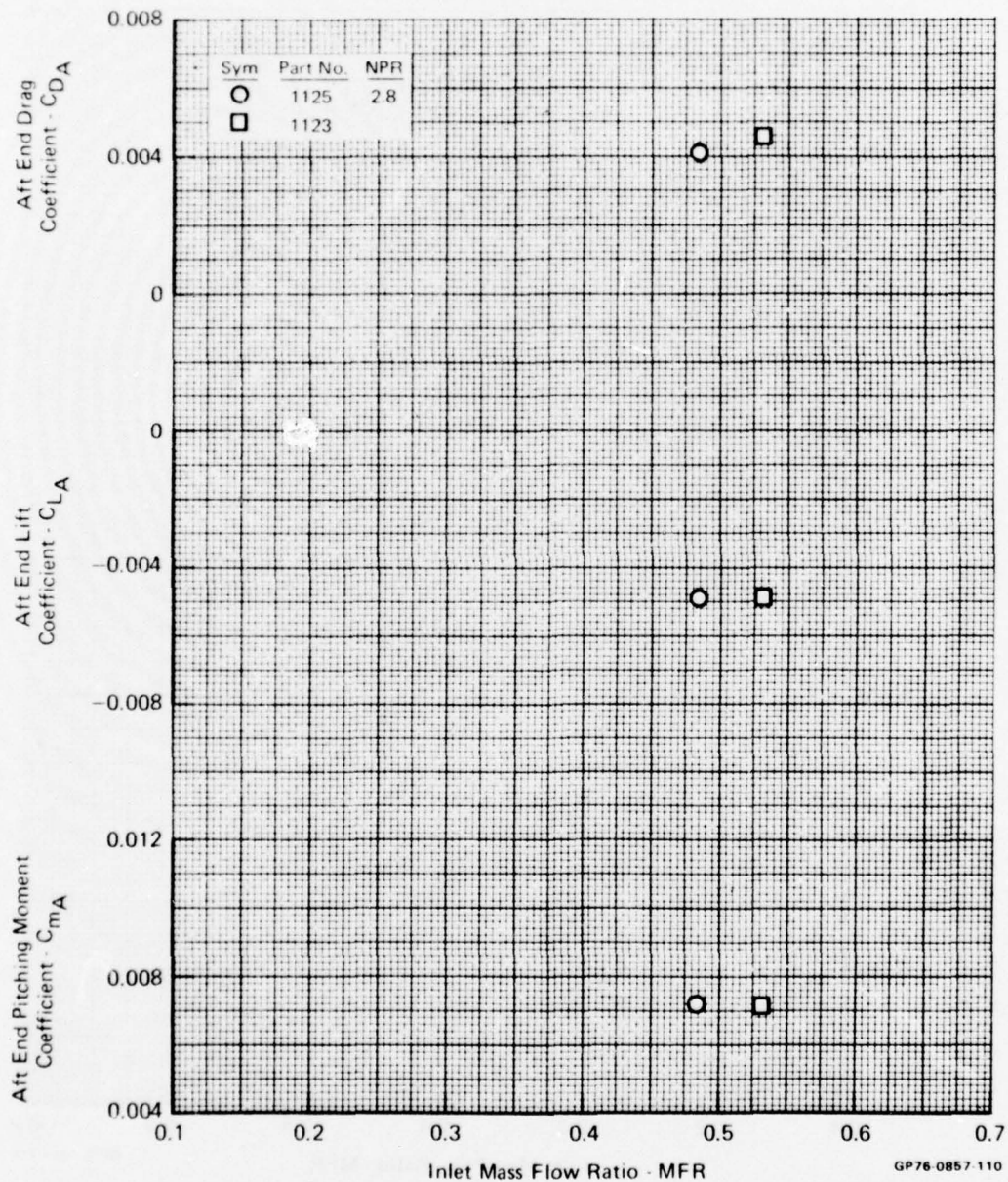


FIGURE D-134
AFT END PERFORMANCE VARIATION WITH INLET MASS FLOW RATIO

Test Mode - Simulator
 Nozzle - Afterburning
 Mach No. - 0.9
 Angle of Attack - 10^0

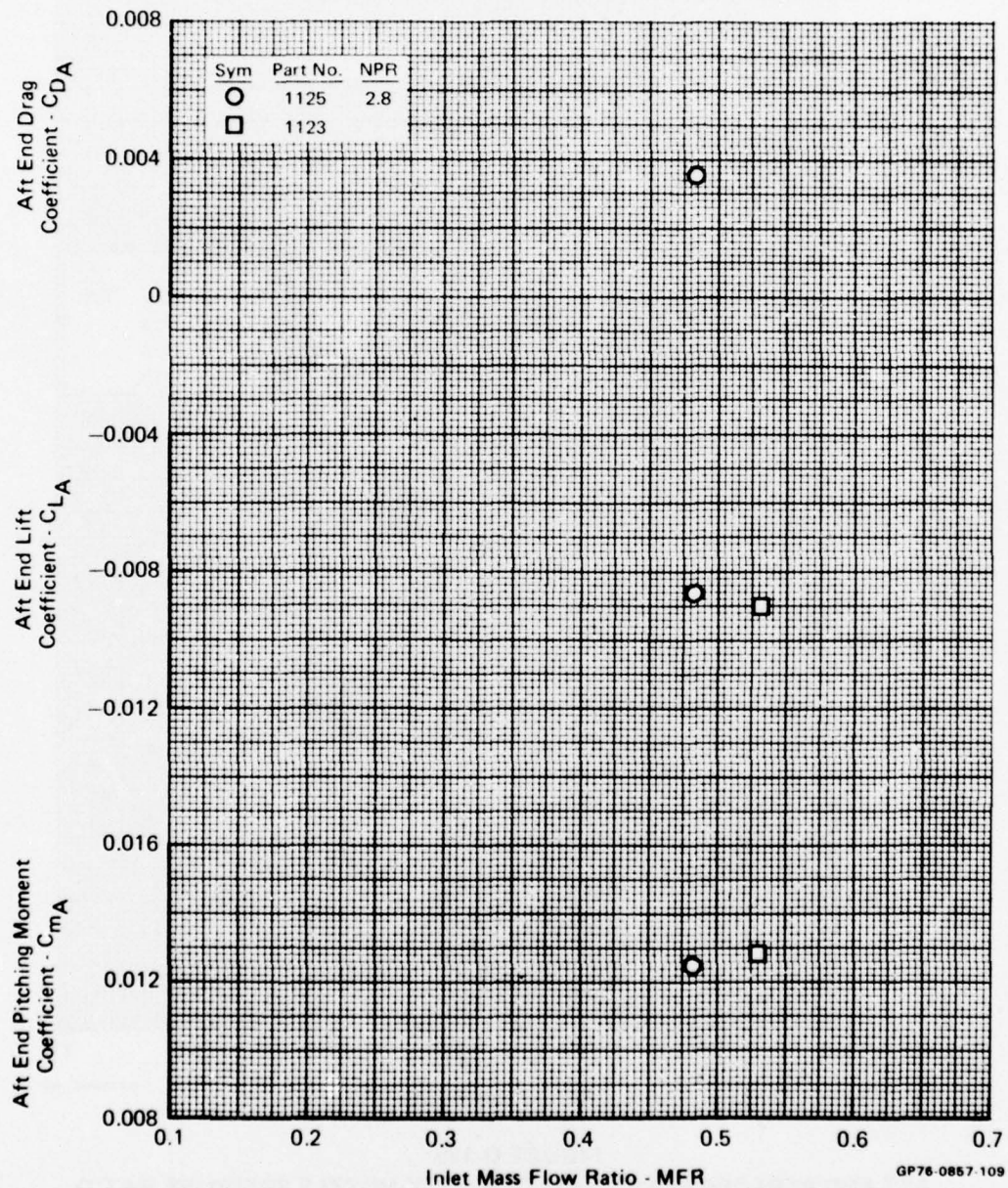


FIGURE D-135
 AFT END PERFORMANCE VARIATION WITH INLET MASS FLOW RATIO

Test Mode - Simulator
 Nozzle - Afterburning
 Mach No. - 0.6
 Angle of Attack - 0°

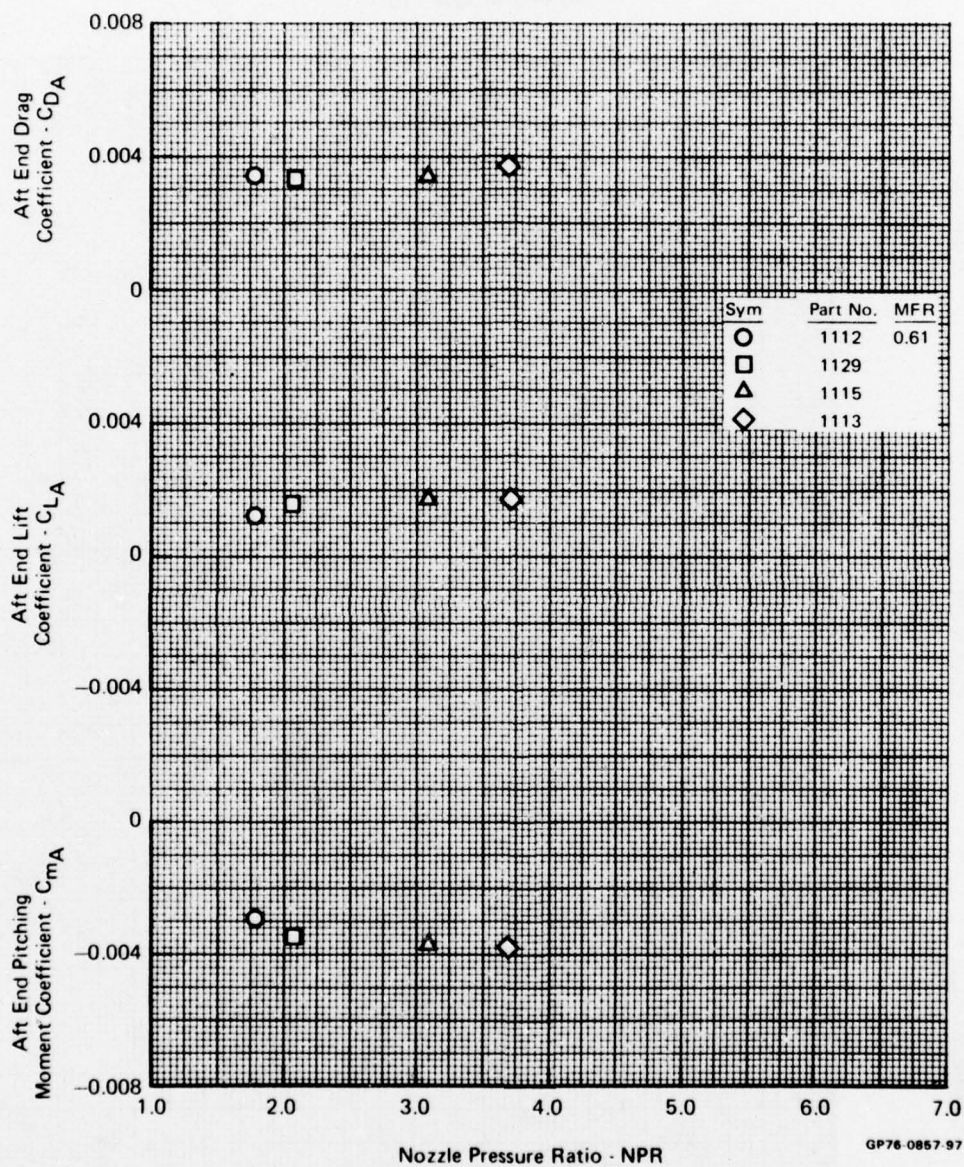


FIGURE D-136
 AFT END PERFORMANCE VARIATION WITH NOZZLE PRESSURE RATIO

Test Mode - Simulator
 Nozzle - Afterburning
 Mach No. - 0.6
 Angle of Attack - 5°

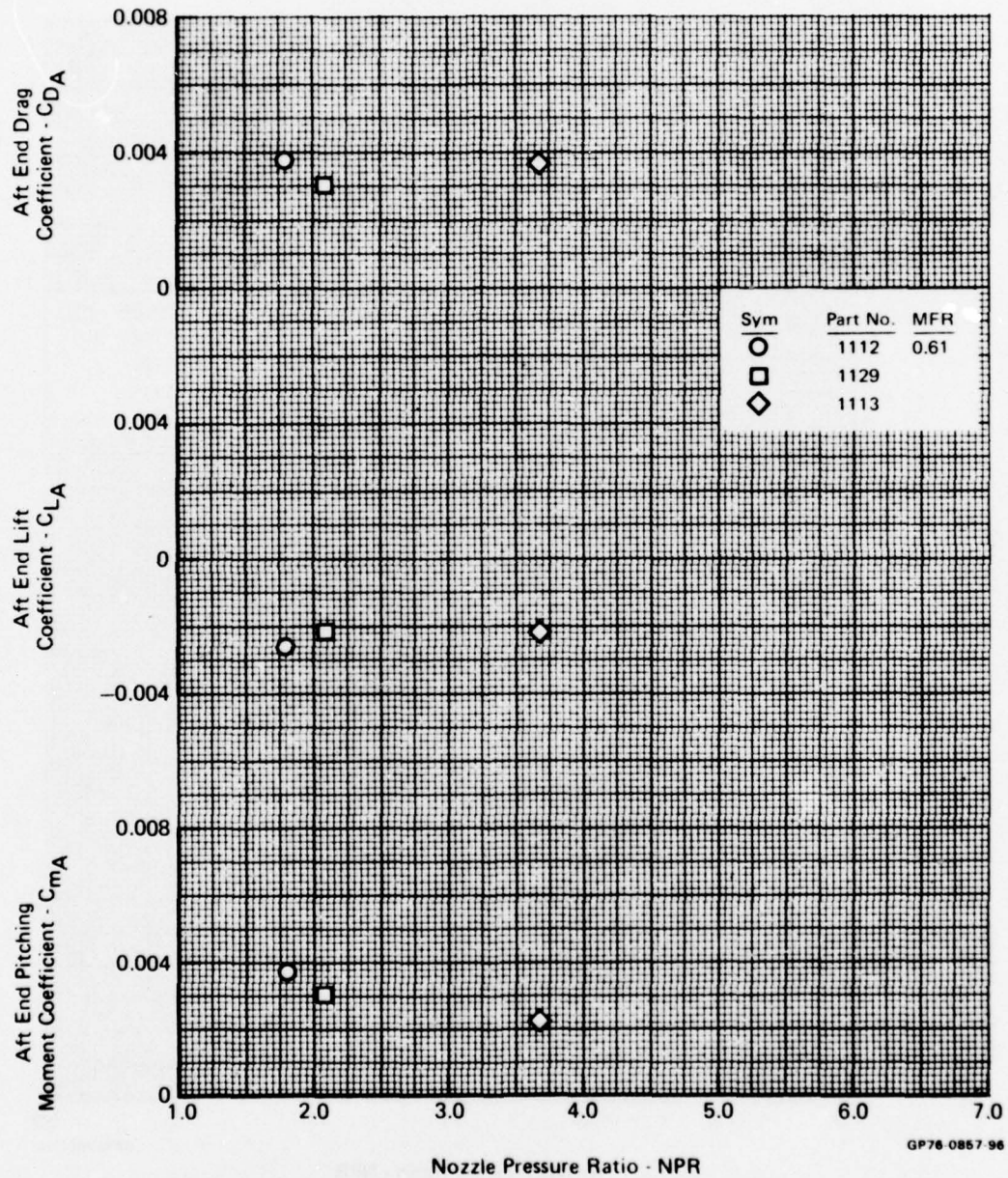


FIGURE D-137
 AFT END PERFORMANCE VARIATION WITH NOZZLE PRESSURE RATIO

Test Mode - Simulator
 Nozzle - Afterburning
 Mach No. - 0.6
 Angle of Attack - 10°

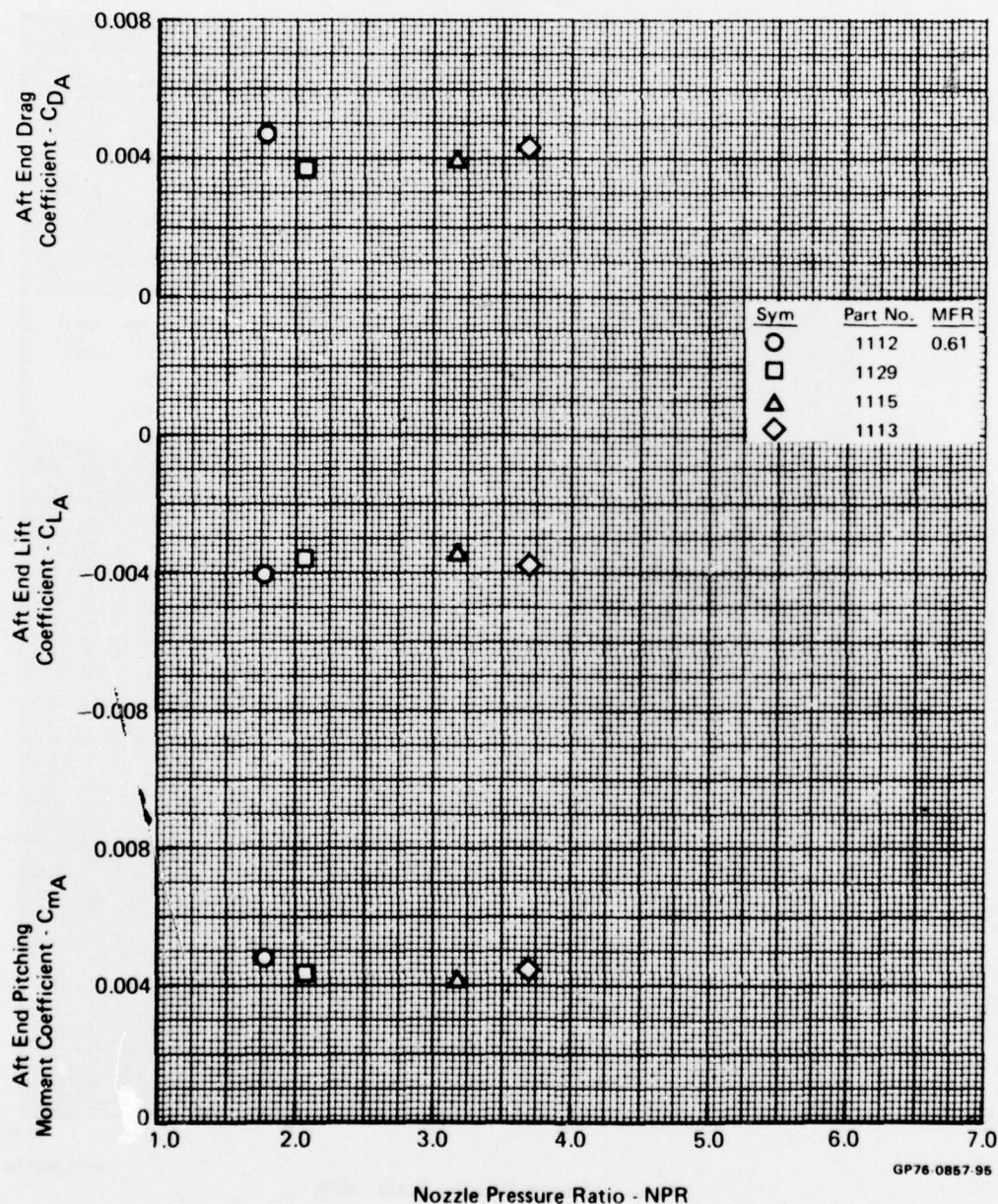


FIGURE D-138
 AFT END PERFORMANCE VARIATION WITH NOZZLE PRESSURE RATIO

Test Mode - Simulator
 Nozzle - Afterburning
 Mach No. - 0.9
 Angle of Attack - 0°

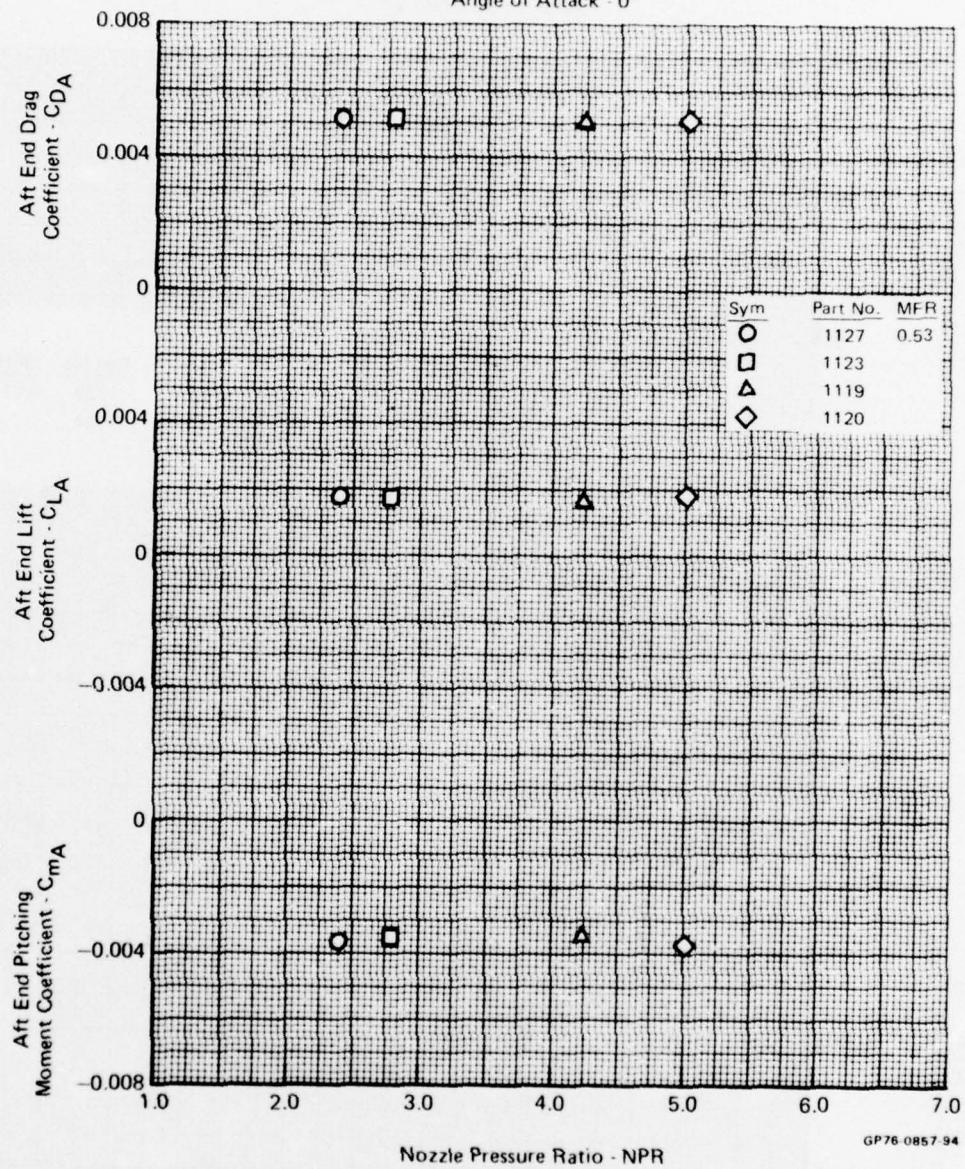


FIGURE D-139
 AFT END PERFORMANCE VARIATION WITH NOZZLE PRESSURE RATIO

Test Mode - Simulator
 Nozzle - Afterburning
 Mach No. - 0.9
 Angle of Attack - 5°

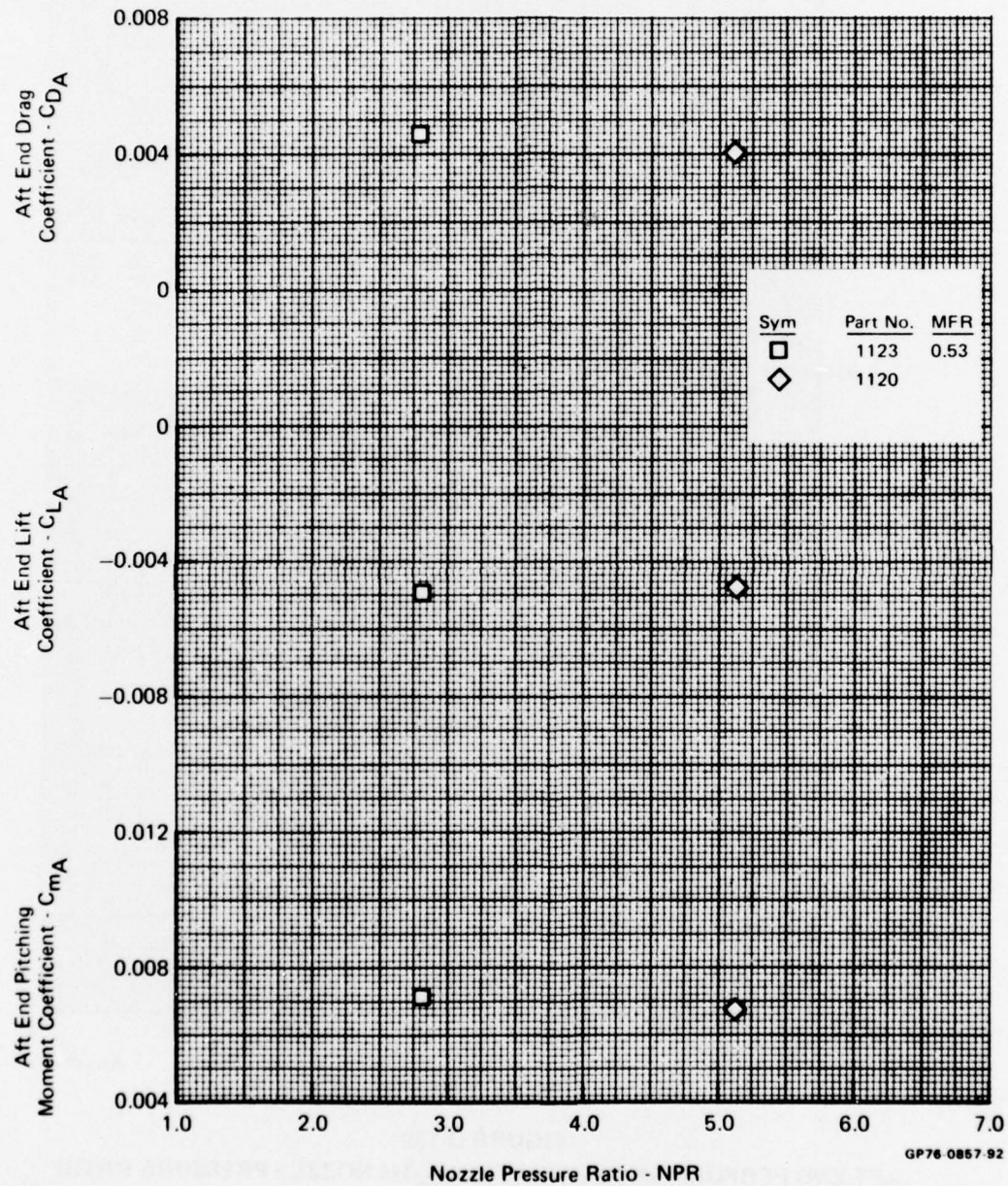


FIGURE D-140
 AFT END PERFORMANCE VARIATION WITH NOZZLE PRESSURE RATIO

Test Mode - Simulator
 Nozzle - Afterburning
 Mach No. - 0.9
 Angle of Attack - 10°

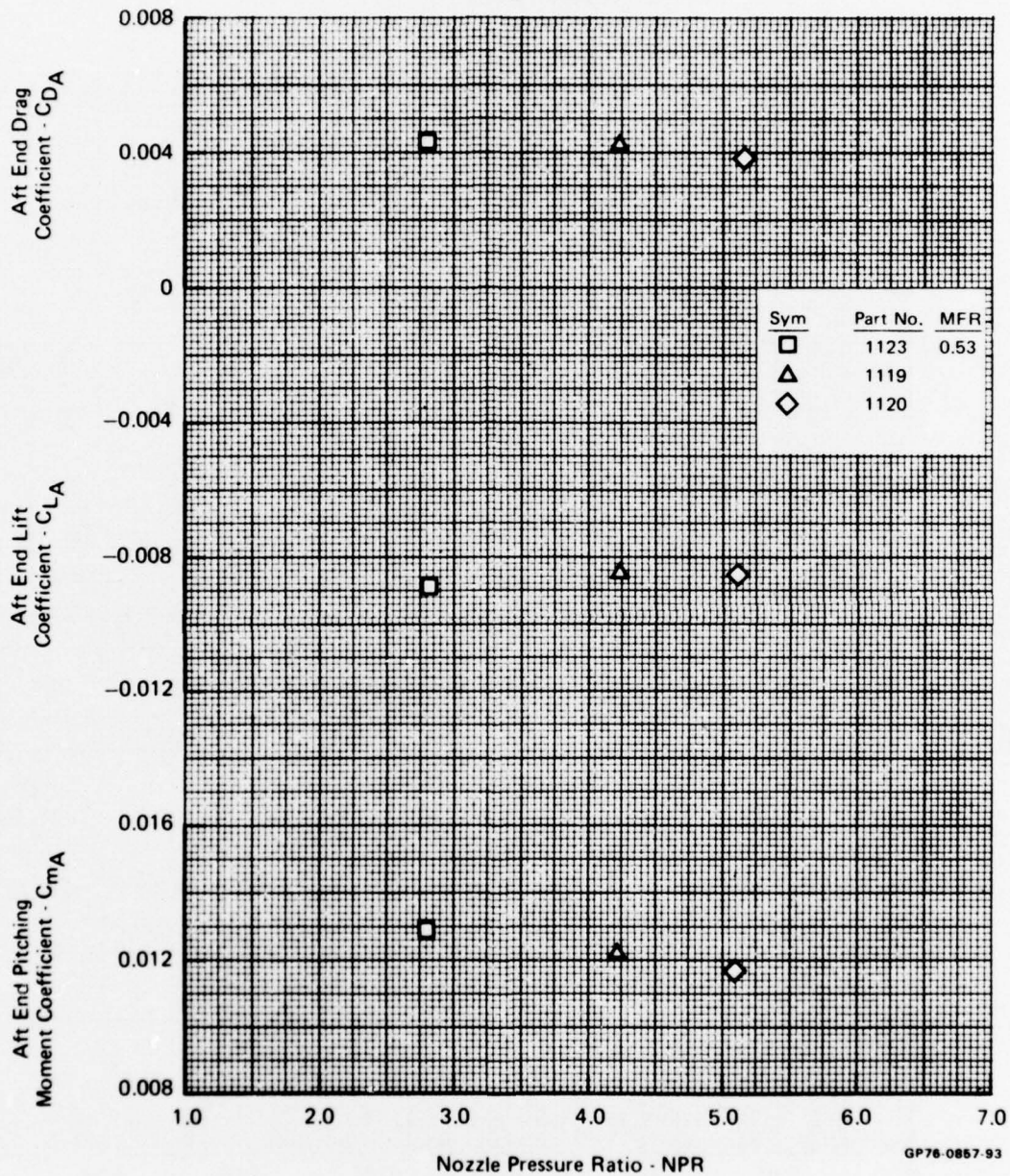


FIGURE D-141
AFT END PERFORMANCE VARIATION WITH NOZZLE PRESSURE RATIO

Test Mode - Simulator
Nozzle - Dry
Mach No. - 0.6
MFR - 0.62
NPR - 3.4

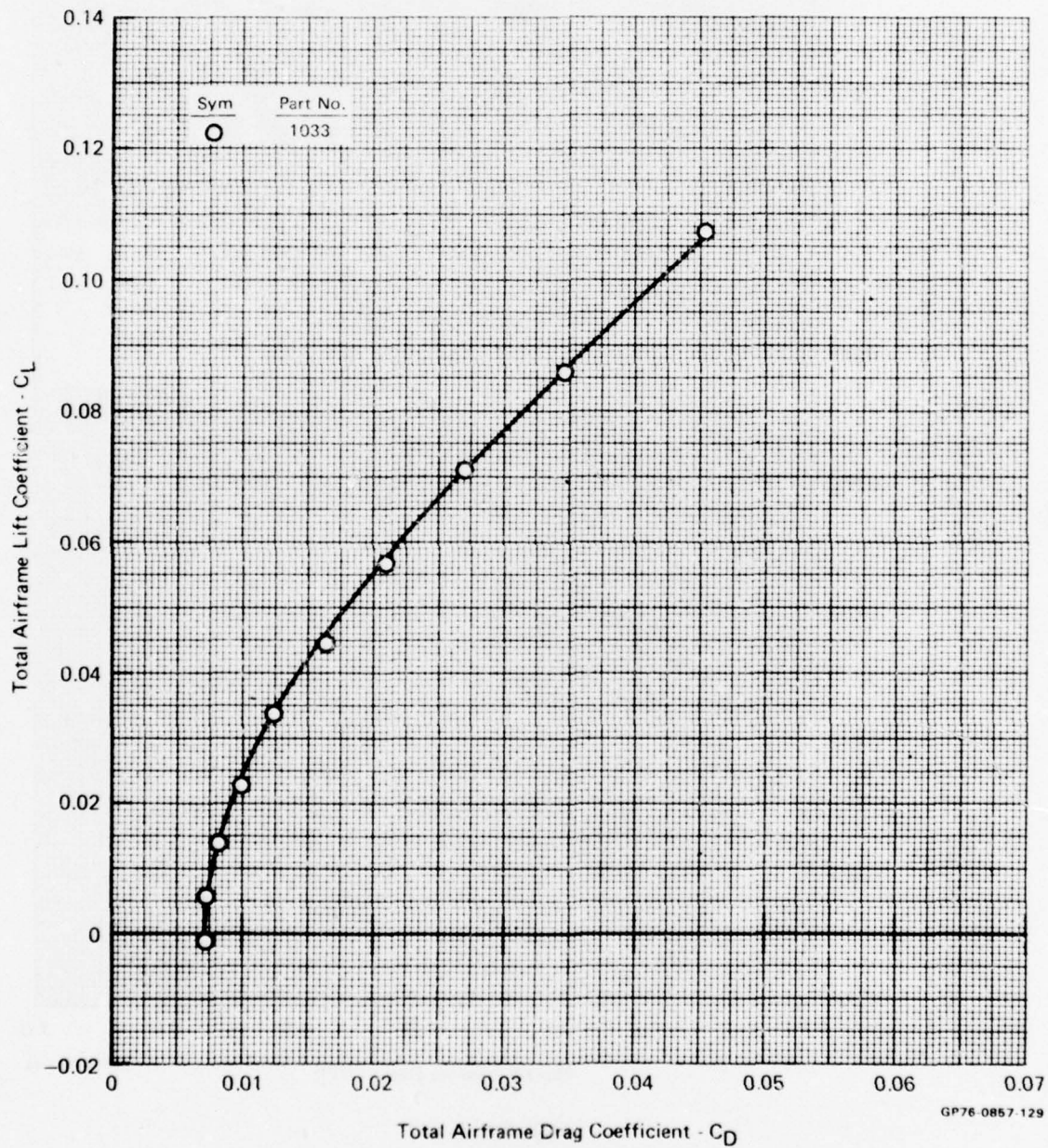


FIGURE D-142
TOTAL AIRFRAME LIFT/DRAG POLAR

Test Mode - Simulator
Nozzle - Dry
Mach No. - 0.6
MFR - 0.57
NPR - 3.1

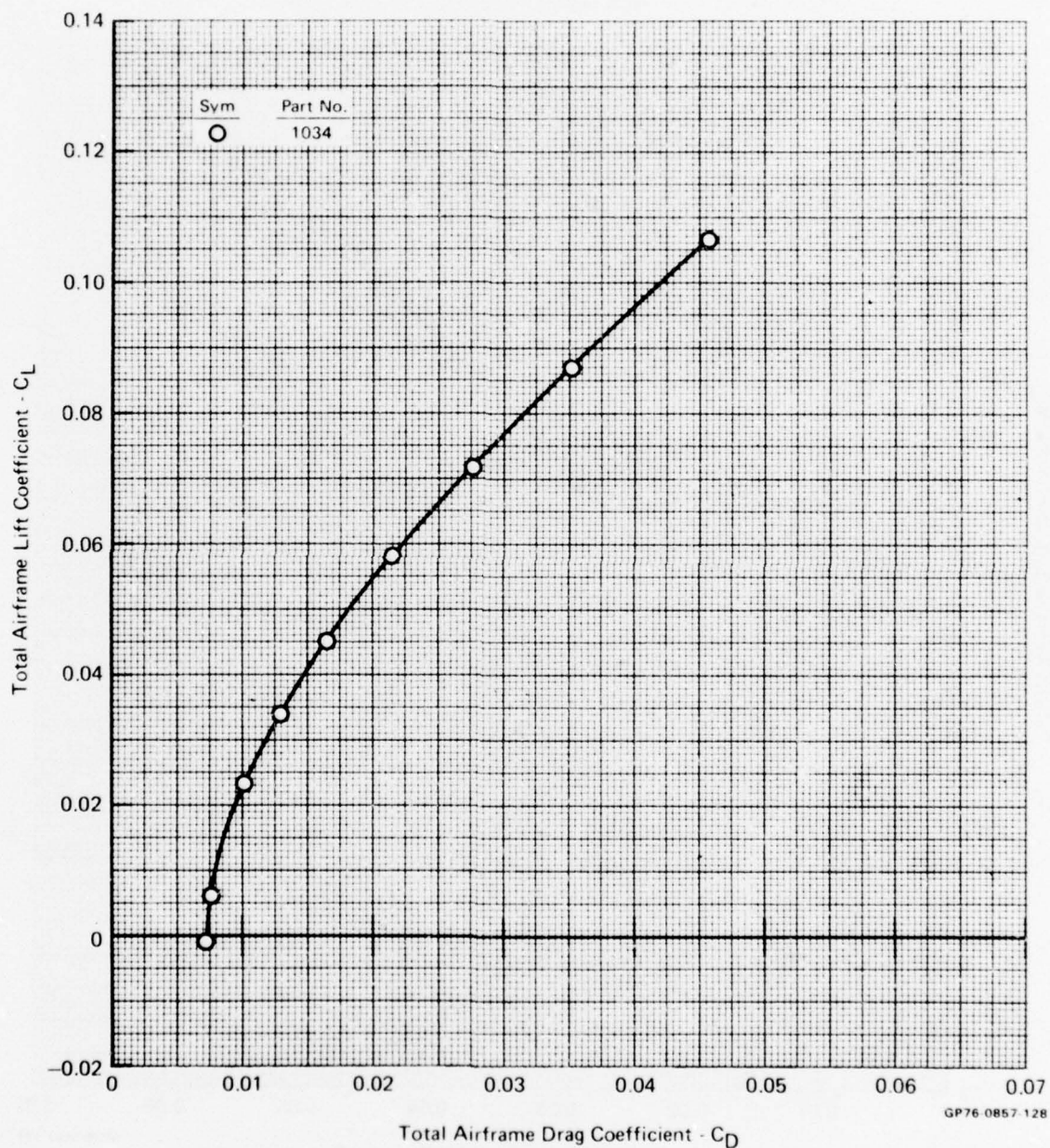


FIGURE D-143
TOTAL AIRFRAME LIFT/DRAG POLAR

Test Mode - Simulator
Nozzle Dry
Mach No. - 0.6
MFR - 0.49
NPR - 2.5

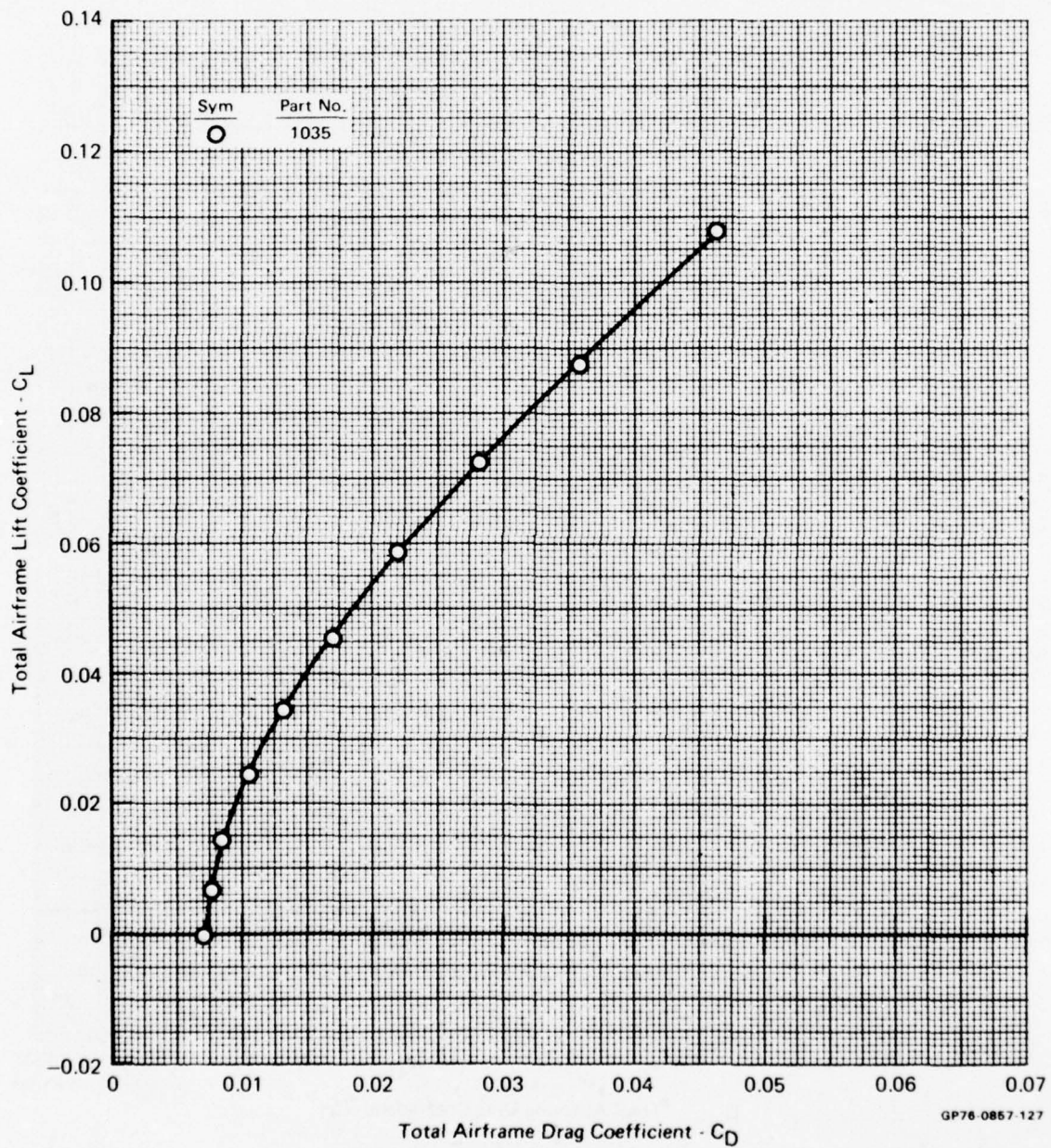


FIGURE D-144
TOTAL AIRFRAME LIFT/DRAG POLAR

Test Mode - Simulator
Nozzle - Dry
Mach No. - 0.6
MFR - 0.40
NPR - 2.0

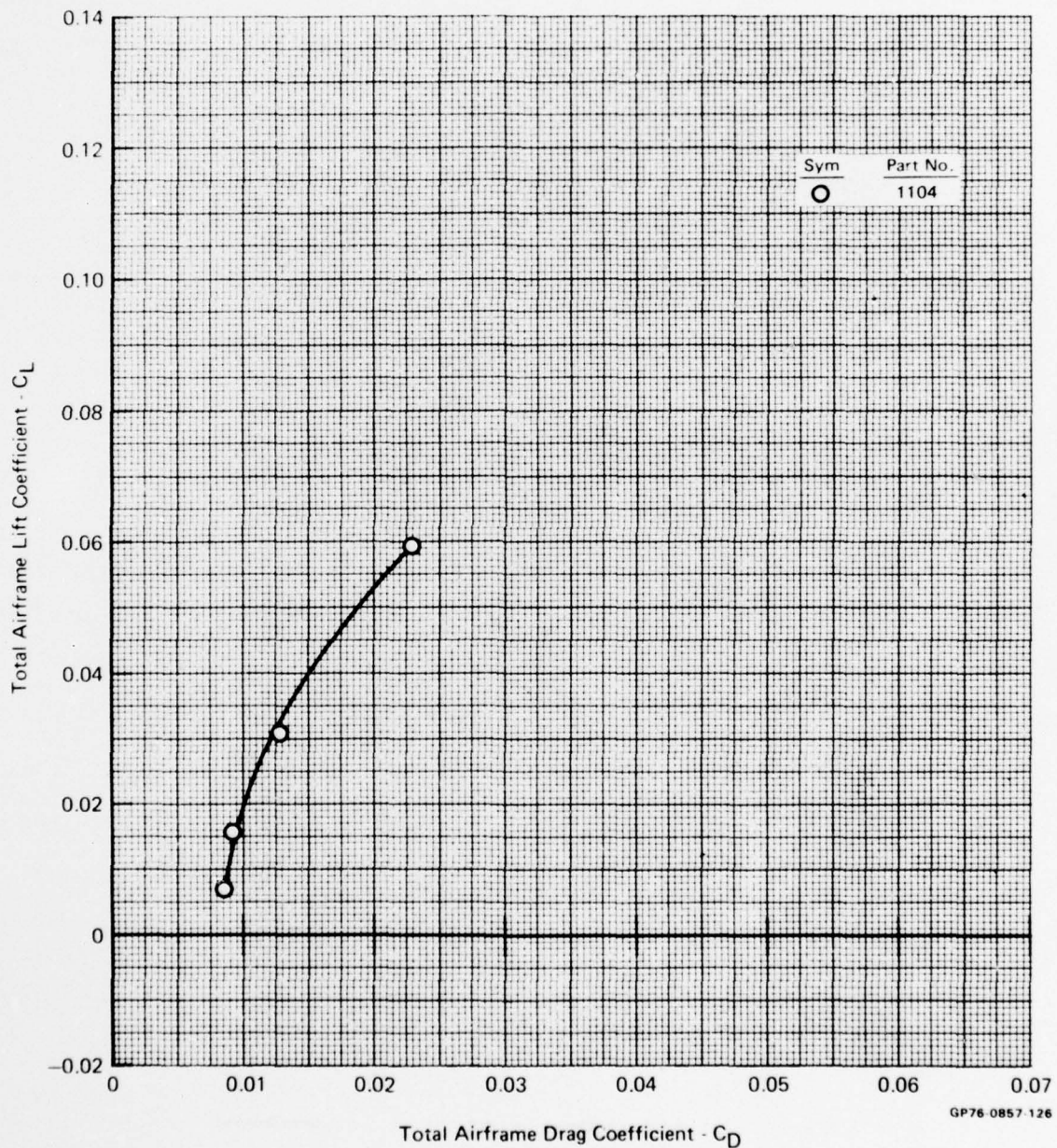


FIGURE D-145
TOTAL AIRFRAME LIFT/DRAG POLAR

Test Mode - Simulator
Nozzle - Dry
Mach No. - 0.6
MFR - 0.62
NPR - 3.4

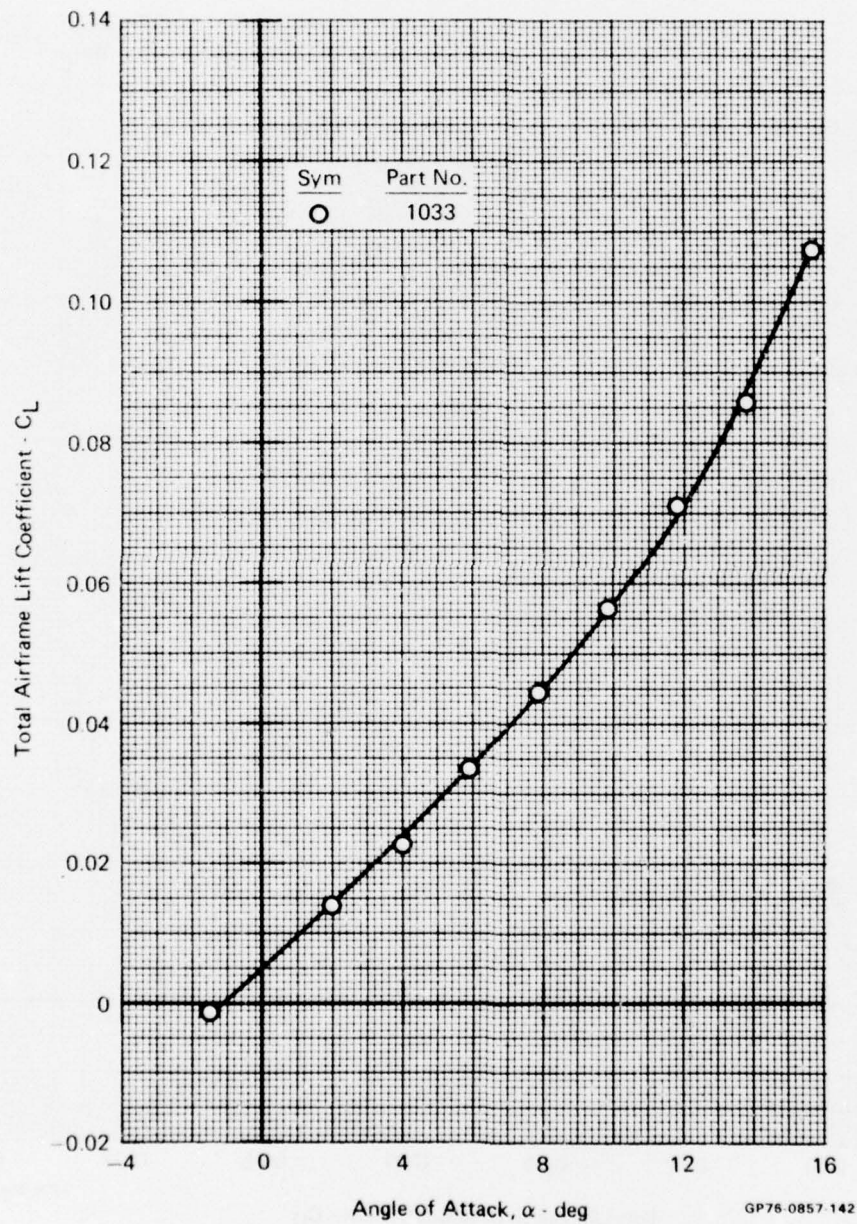


FIGURE D-146
TOTAL AIRFRAME LIFT VARIATION WITH ANGLE OF ATTACK

Test Mode - Simulator
Nozzle - Dry
Mach No. - 0.6
MFR - 0.57
NPR - 3.1

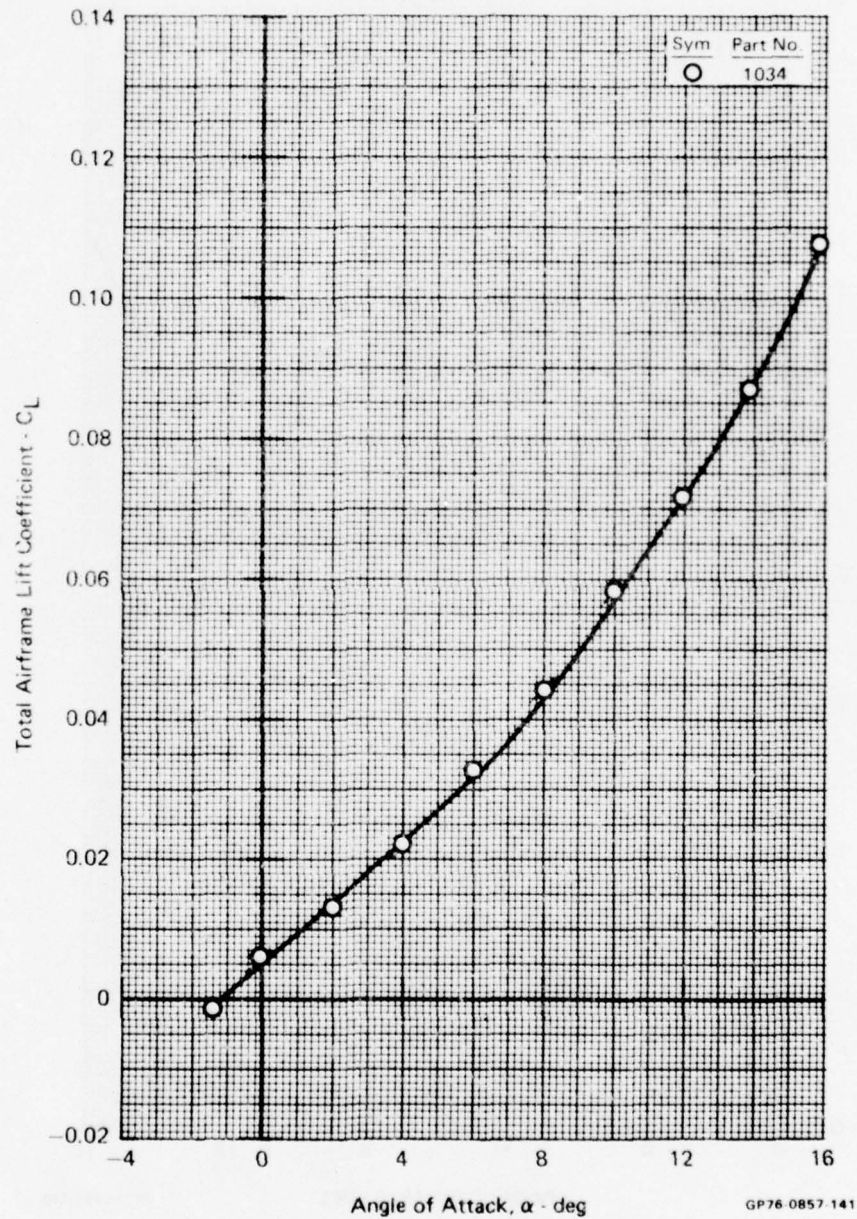


FIGURE D-147
TOTAL AIRFRAME LIFT VARIATION WITH ANGLE OF ATTACK

Test Mode - Simulator
Nozzle - Dry
Mach No. - 0.6
MFR - 0.49
NPR - 2.5

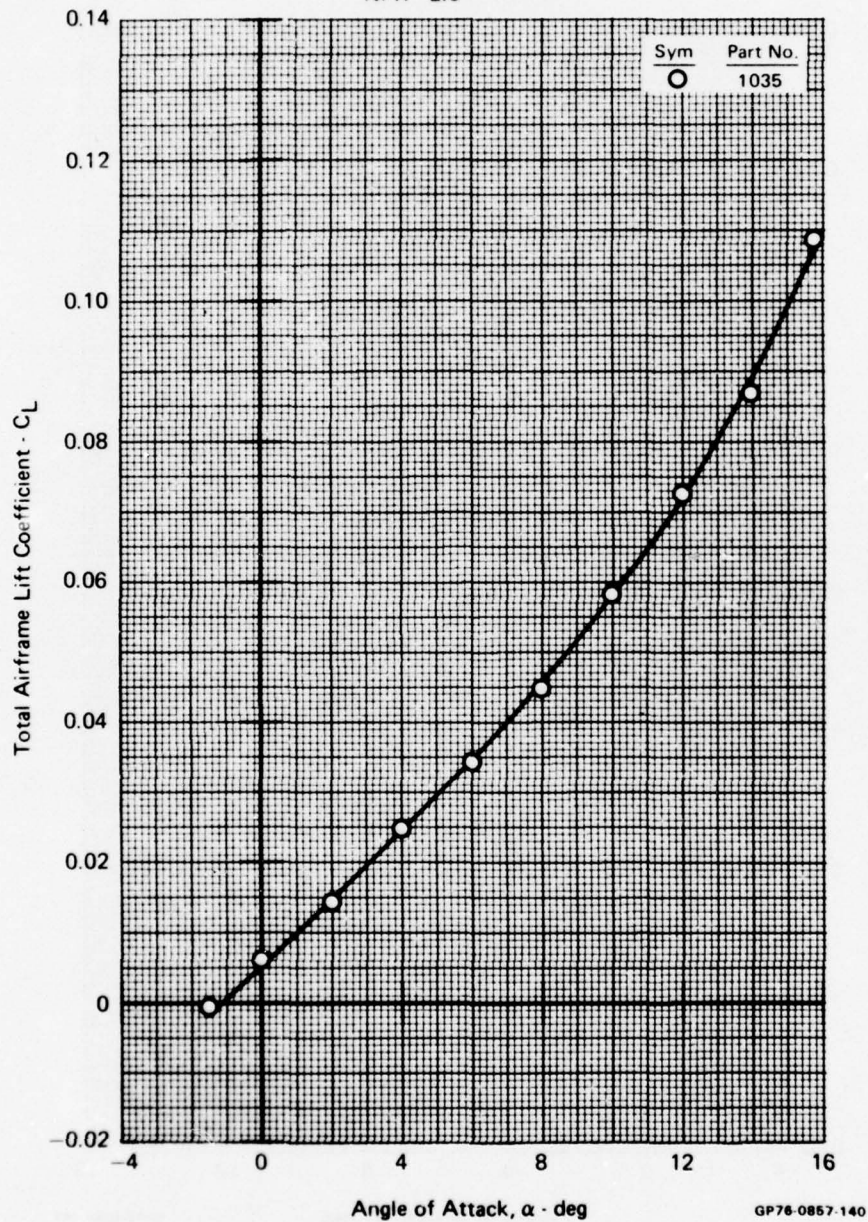


FIGURE D-148
TOTAL AIRFRAME LIFT VARIATION WITH ANGLE OF ATTACK

Test Mode - Simulator
Nozzle - Dry
Mach No. - 0.6
MFR - 0.40
NPR - 2.0

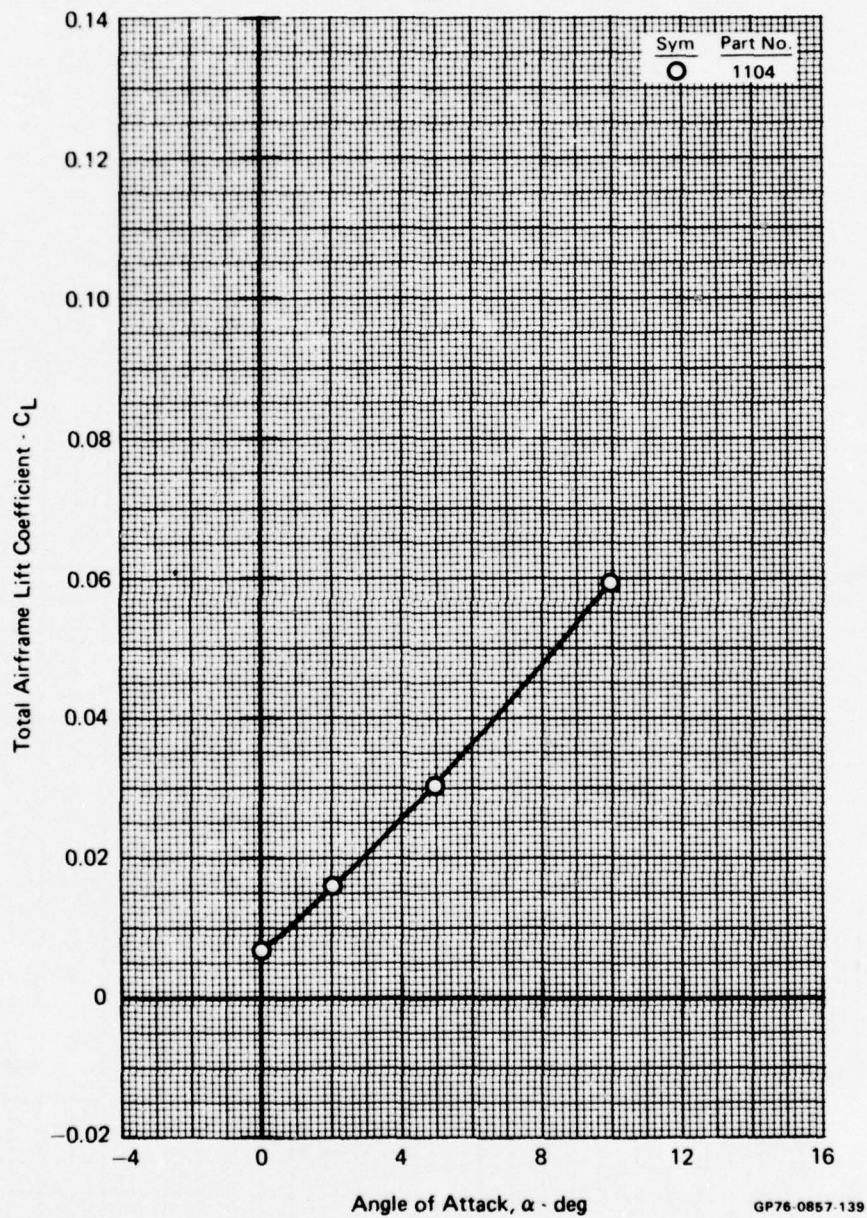


FIGURE D-149
TOTAL AIRFRAME LIFT VARIATION WITH ANGLE OF ATTACK

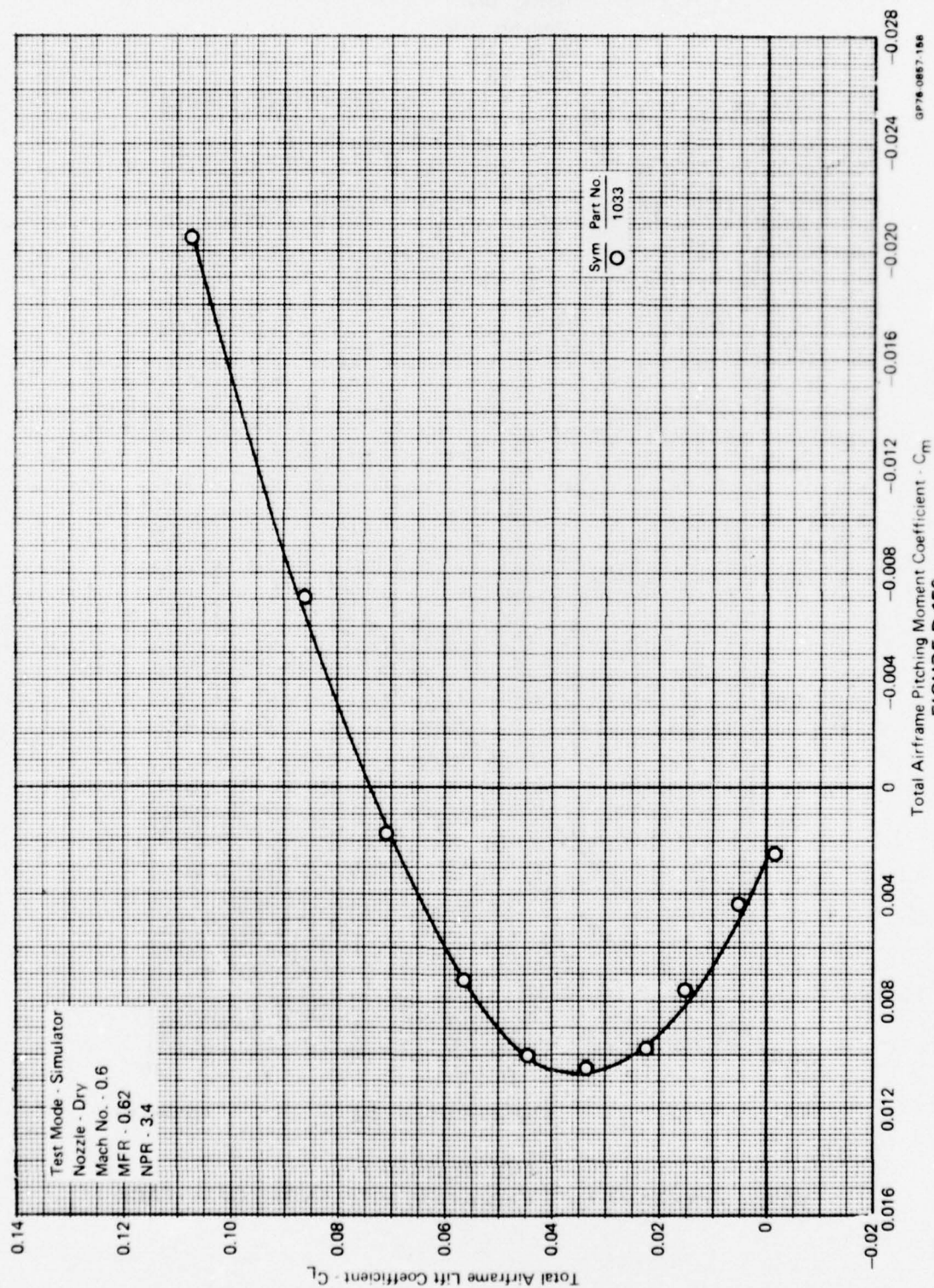


FIGURE D-150
TOTAL AIRFRAME LIFT/PITCHING MOMENT VARIATION

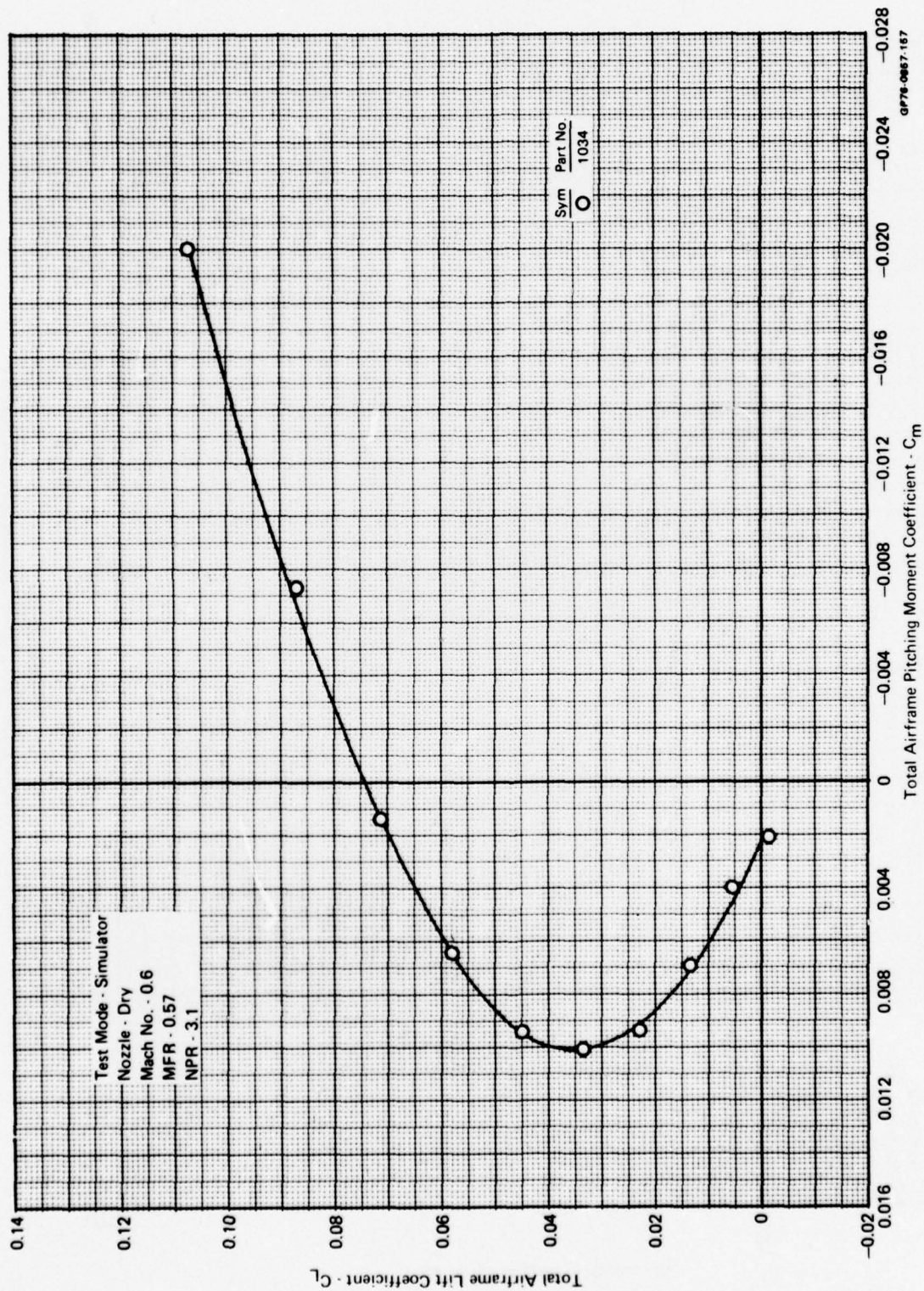


FIGURE D-151
 TOTAL AIRFRAME LIFT/PITCHING MOMENT VARIATION

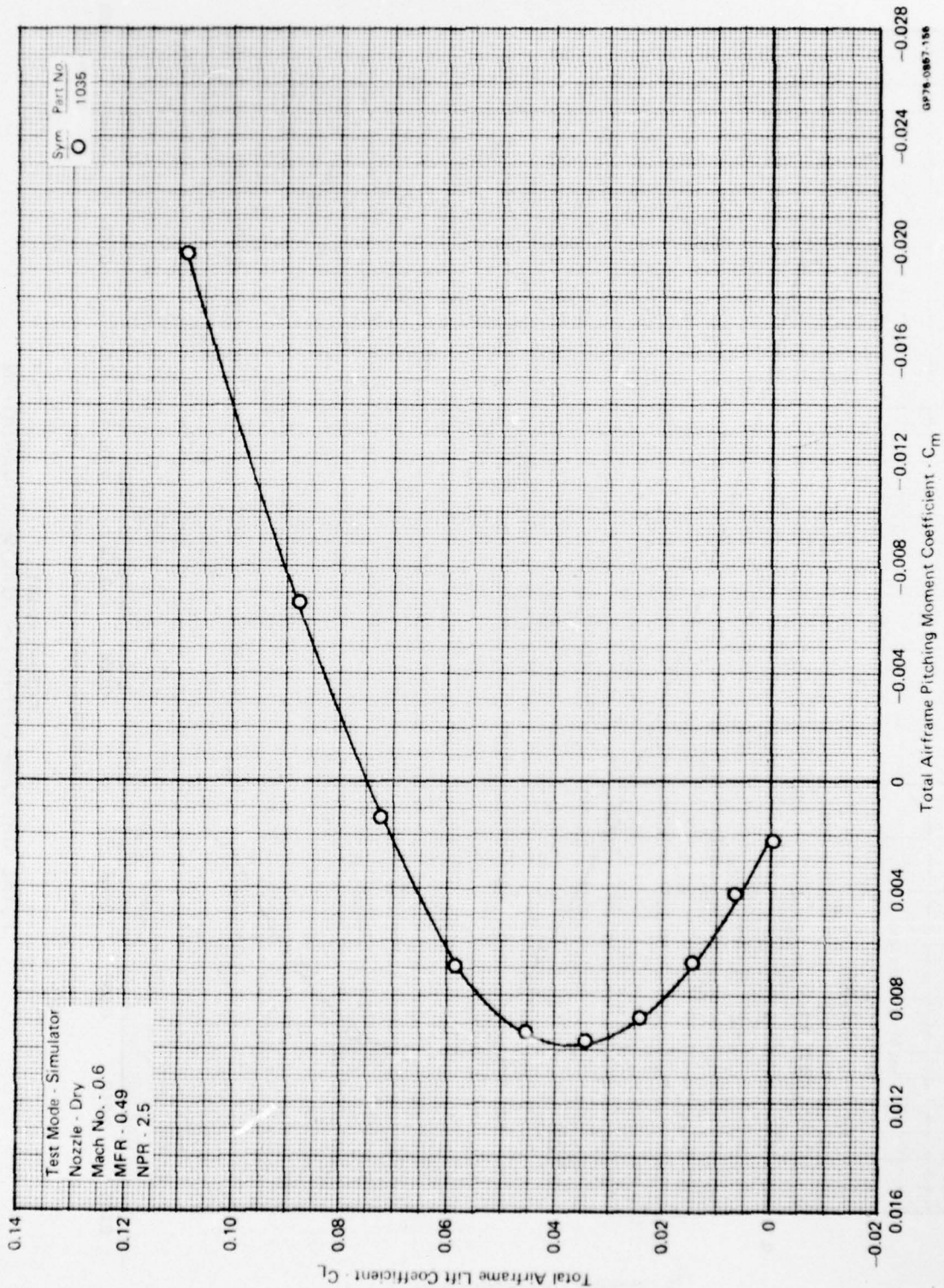


FIGURE D-152
 TOTAL AIRFRAME LIFT/PITCHING MOMENT VARIATION

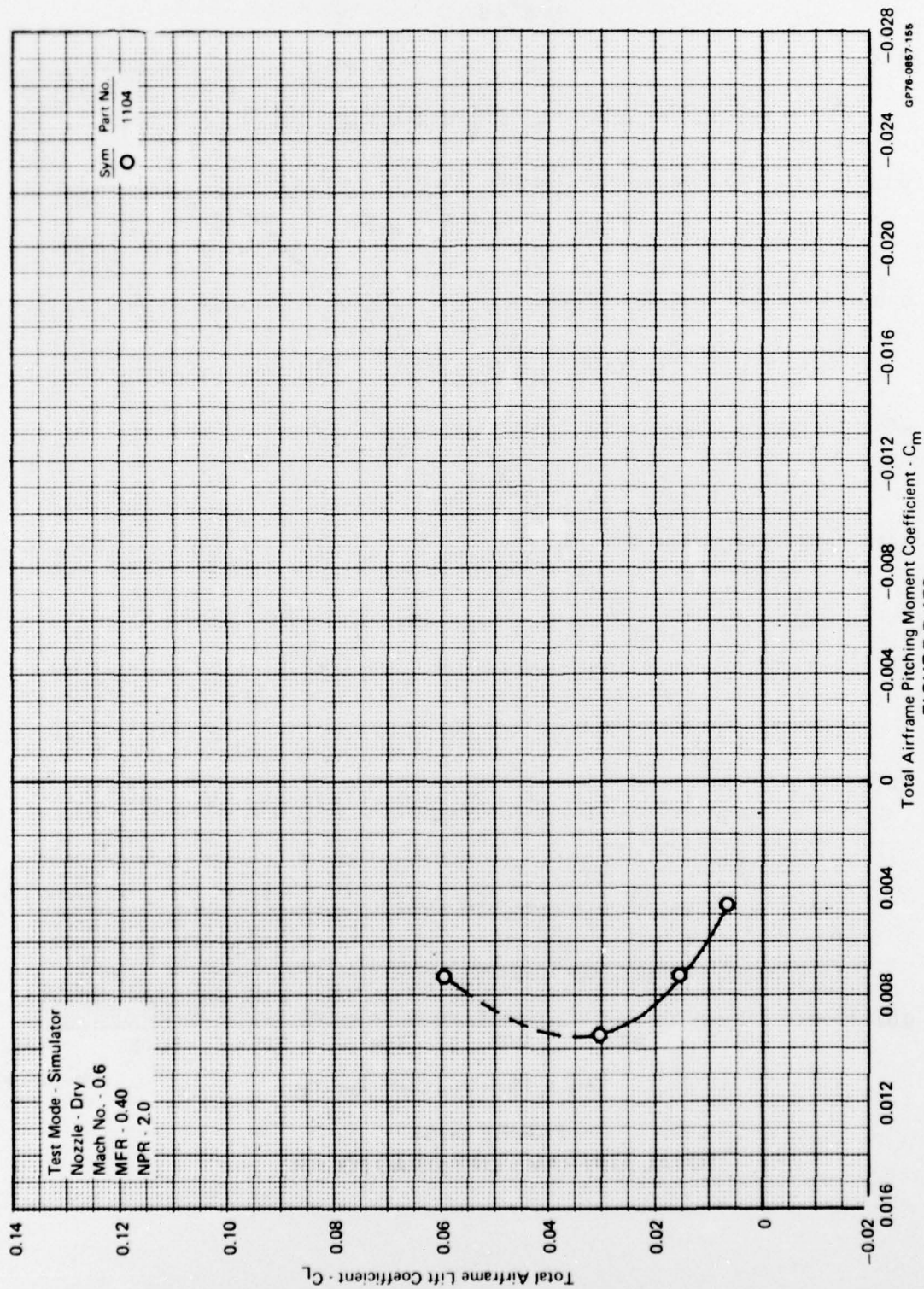


FIGURE D-153
 TOTAL AIRFRAME LIFT/PITCHING MOMENT VARIATION

Test Mode - Simulator
Nozzle - Dry
Mach No. - 0.9
MFR - 0.53
NPR - 4.6

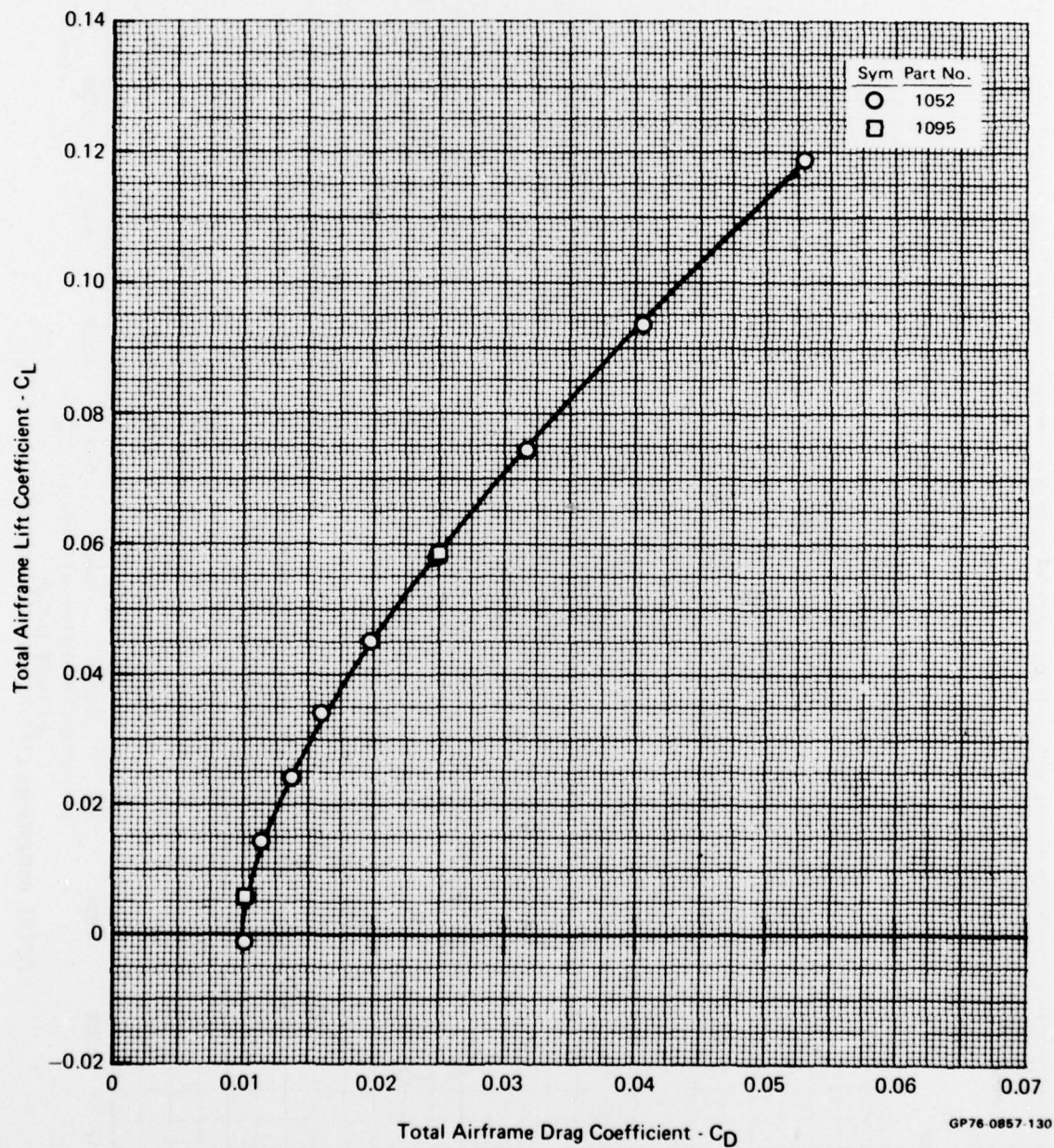


FIGURE D-154
TOTAL AIRFRAME LIFT/DRAG POLAR

Test Mode - Simulator

Nozzle - Dry

Mach No. - 0.9

MFR - 0.51

NPR - 4.1

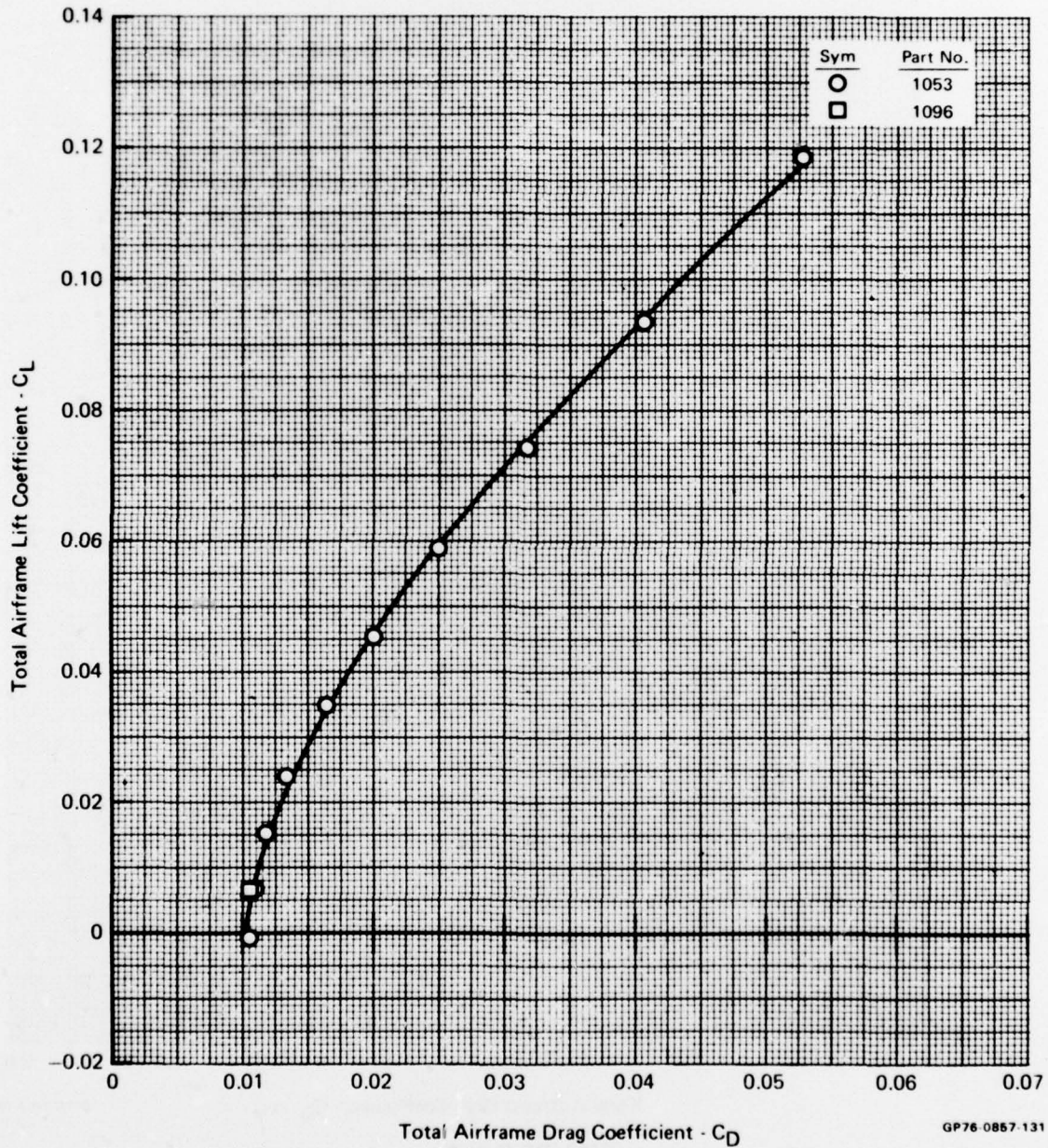


FIGURE D-155
TOTAL AIRFRAME LIFT/DRAG POLAR

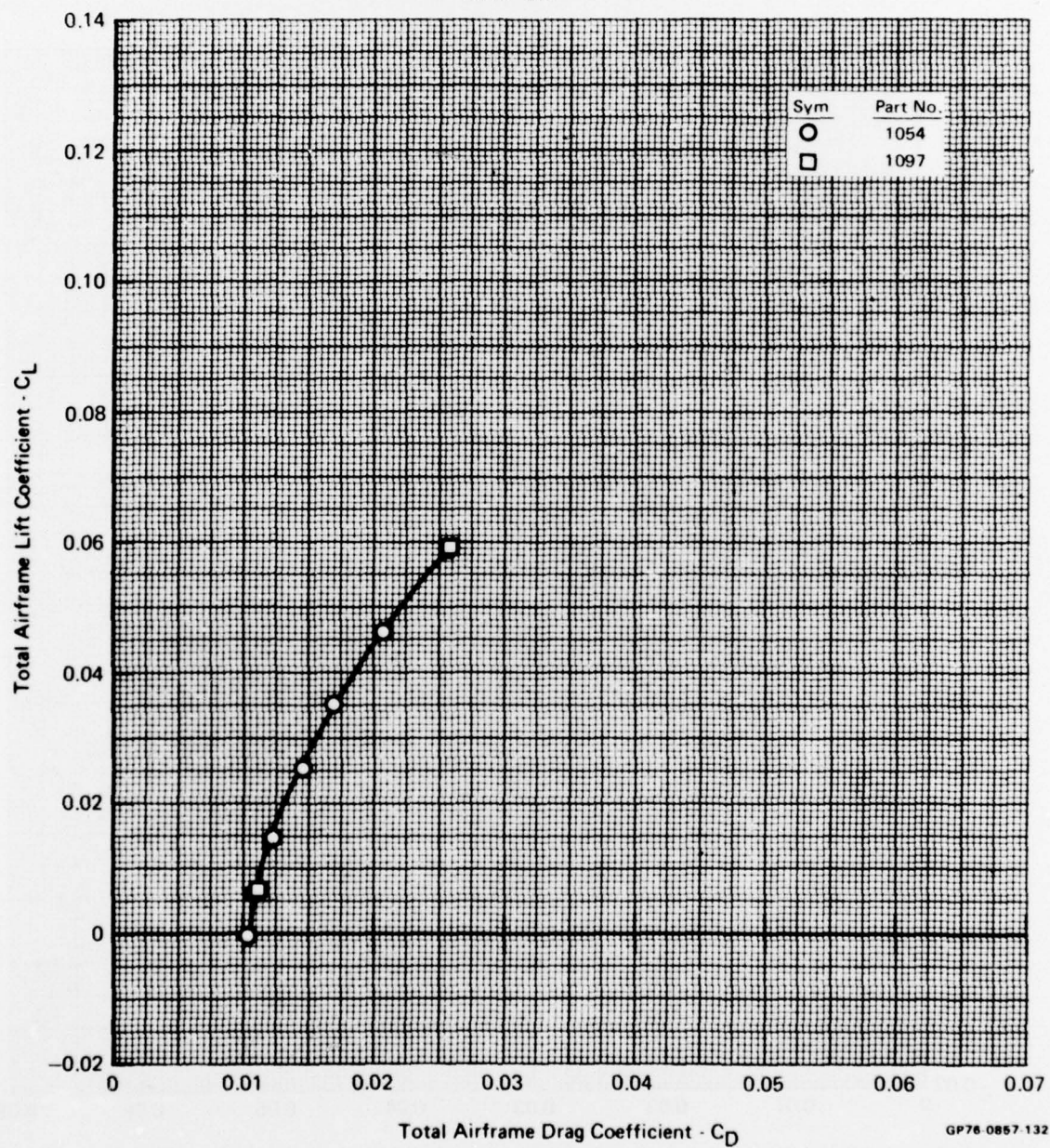
Test Mode - Simulator

Nozzle - Dry

Mach No. - 0.9

MFR - 0.43

NPR - 3.3



GP76 0857 132

FIGURE D-156
TOTAL AIRFRAME LIFT/DRAG POLAR

Test Mode - Simulator
Nozzle - Dry
Mach No. - 0.9
MFR - 0.37
NPR - 2.6

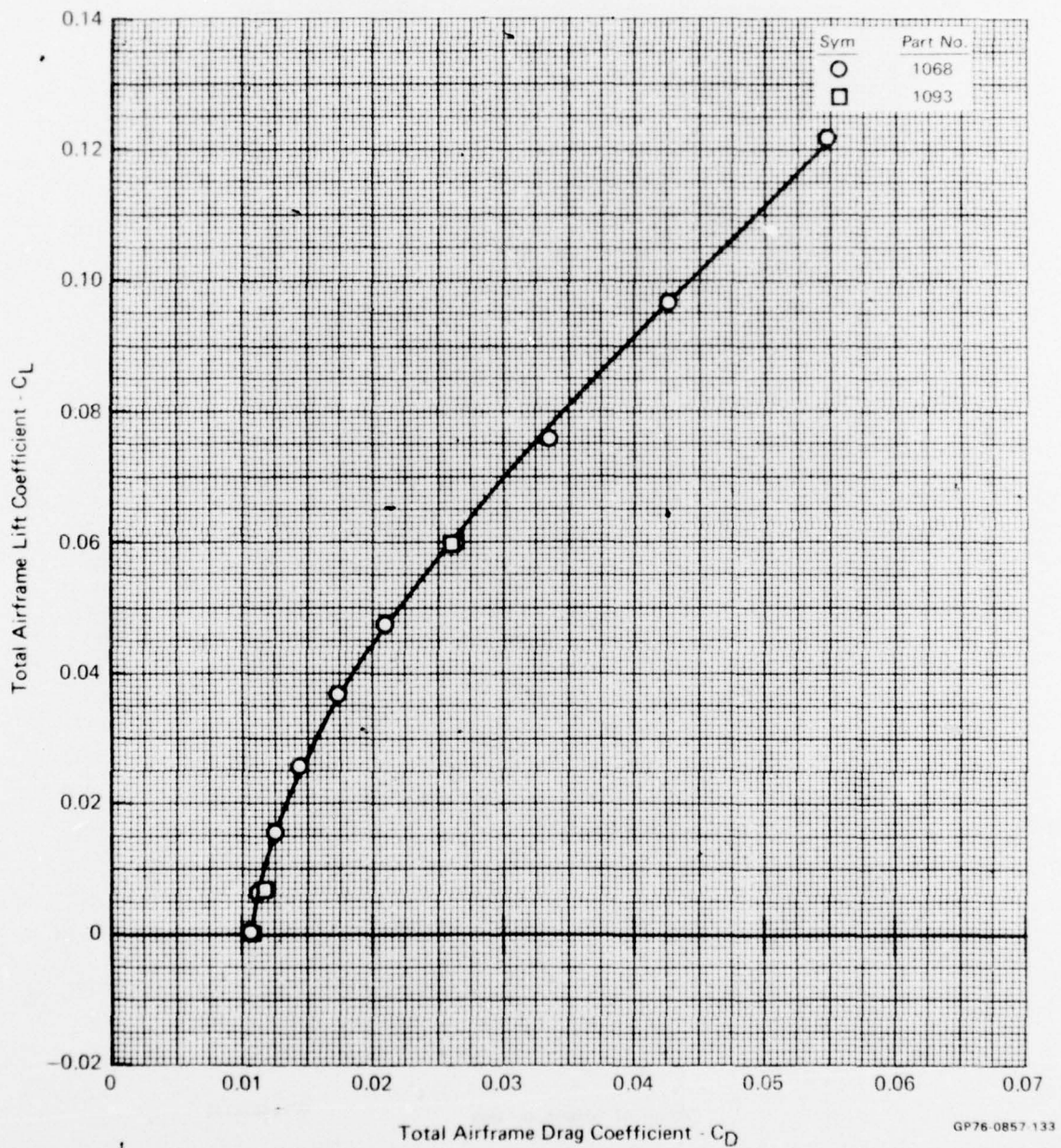


FIGURE D-157
TOTAL AIRFRAME LIFT/DRAG POLAR

Test Mode - Simulator
Nozzle - Dry
Mach No. - 0.9
MFR - 0.53
NPR - 4.6

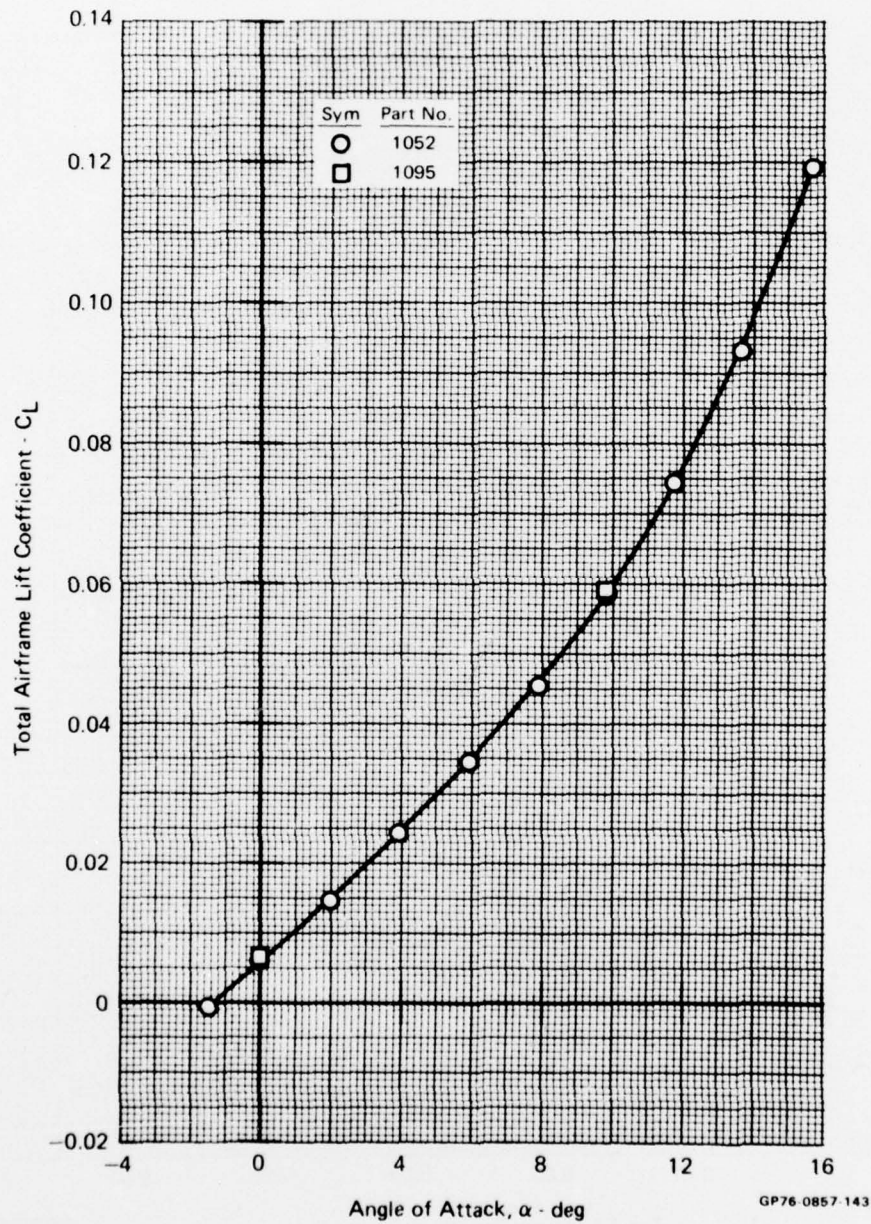


FIGURE D-158
TOTAL AIRFRAME LIFT VARIATION WITH ANGLE OF ATTACK

Test Mode - Simulator
Nozzle - Dry
Mach No. - 0.9
MFR - 0.51
NPR - 4.1

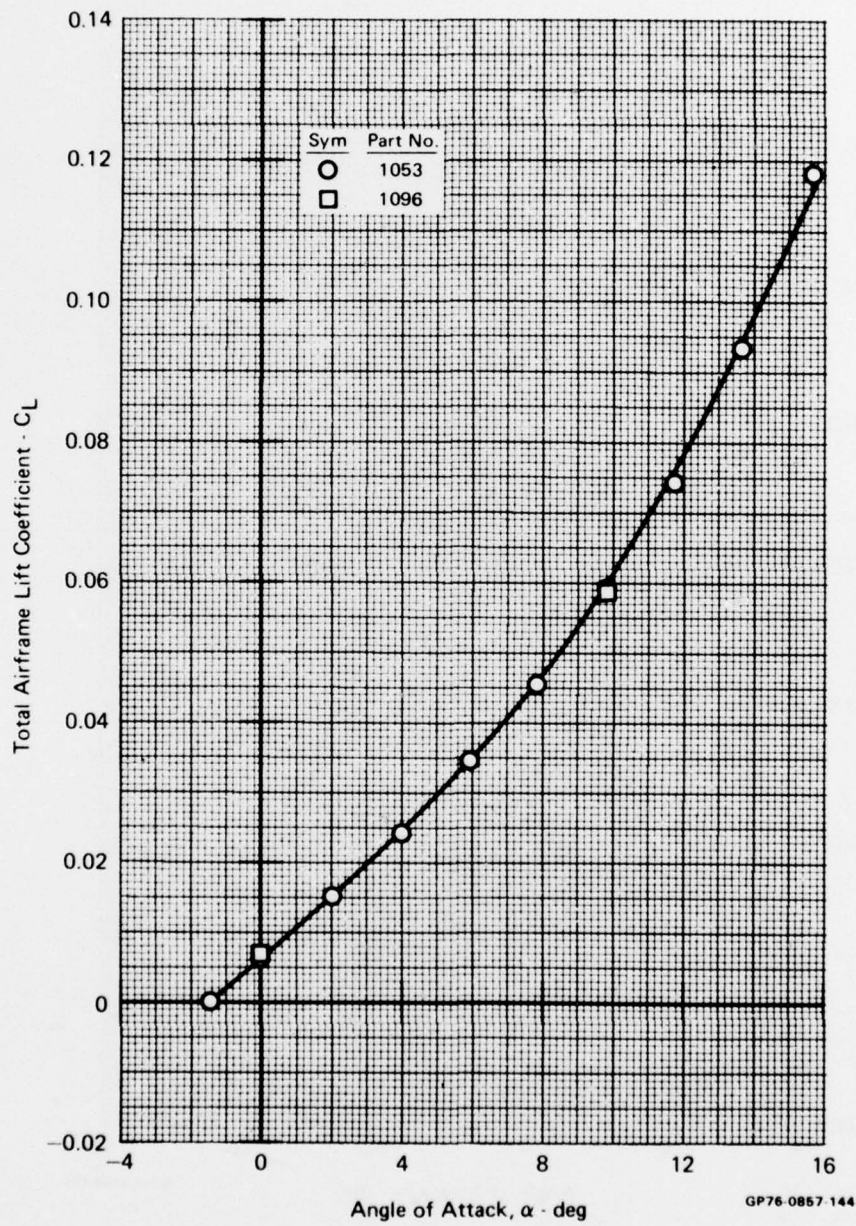


FIGURE D-159
TOTAL AIRFRAME LIFT VARIATION WITH ANGLE OF ATTACK

Test Mode - Simulator
Nozzle - Dry
Mach No. - 0.9
MFR - 0.43
NPR - 3.3

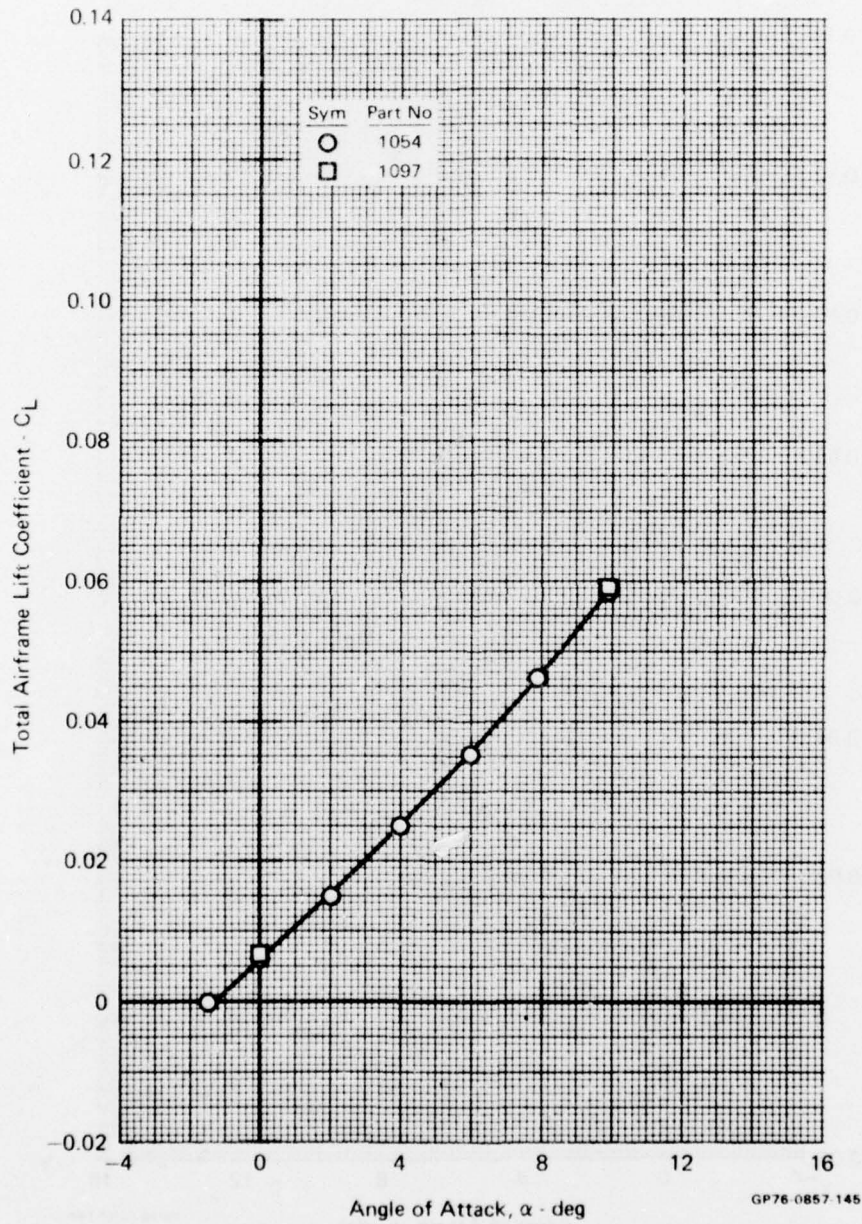


FIGURE D-160
TOTAL AIRFRAME LIFT VARIATION WITH ANGLE OF ATTACK

Test Mode - Simulator
Nozzle - Dry
Mach No. - 0.9
MFR - 0.37
NPR - 2.6

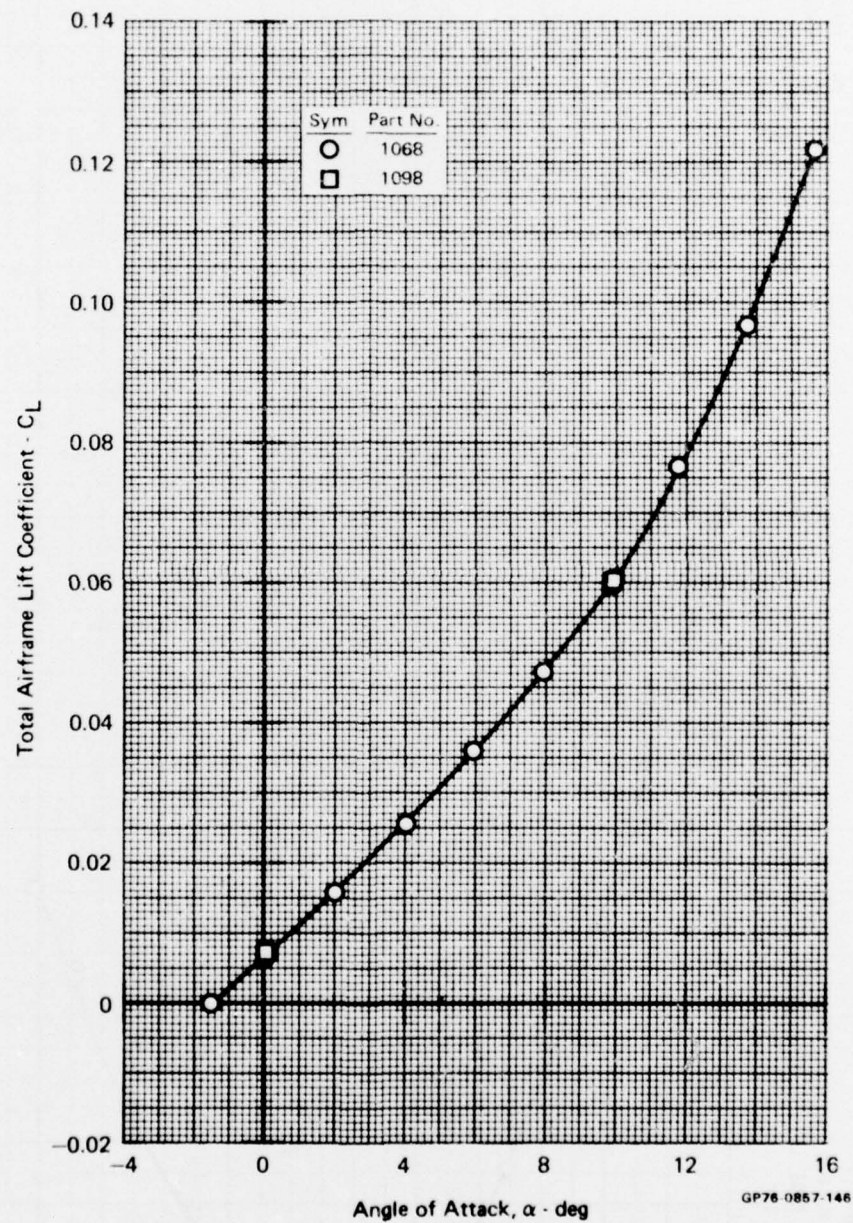
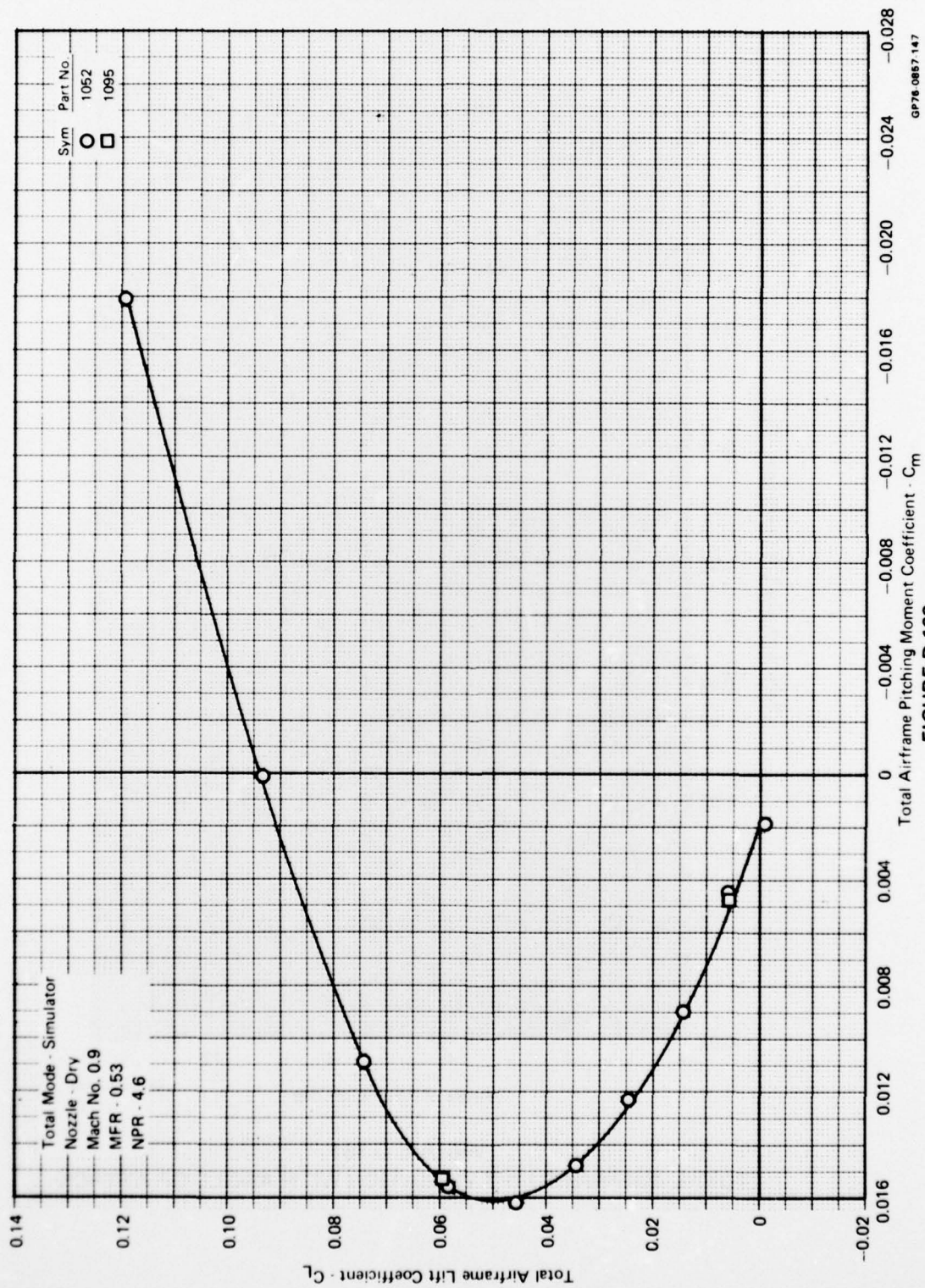


FIGURE D-161
TOTAL AIRFRAME LIFT VARIATION WITH ANGLE OF ATTACK



GP76 0867 147

FIGURE D-162
TOTAL AIRFRAME LIFT/PITCHING MOMENT VARIATION

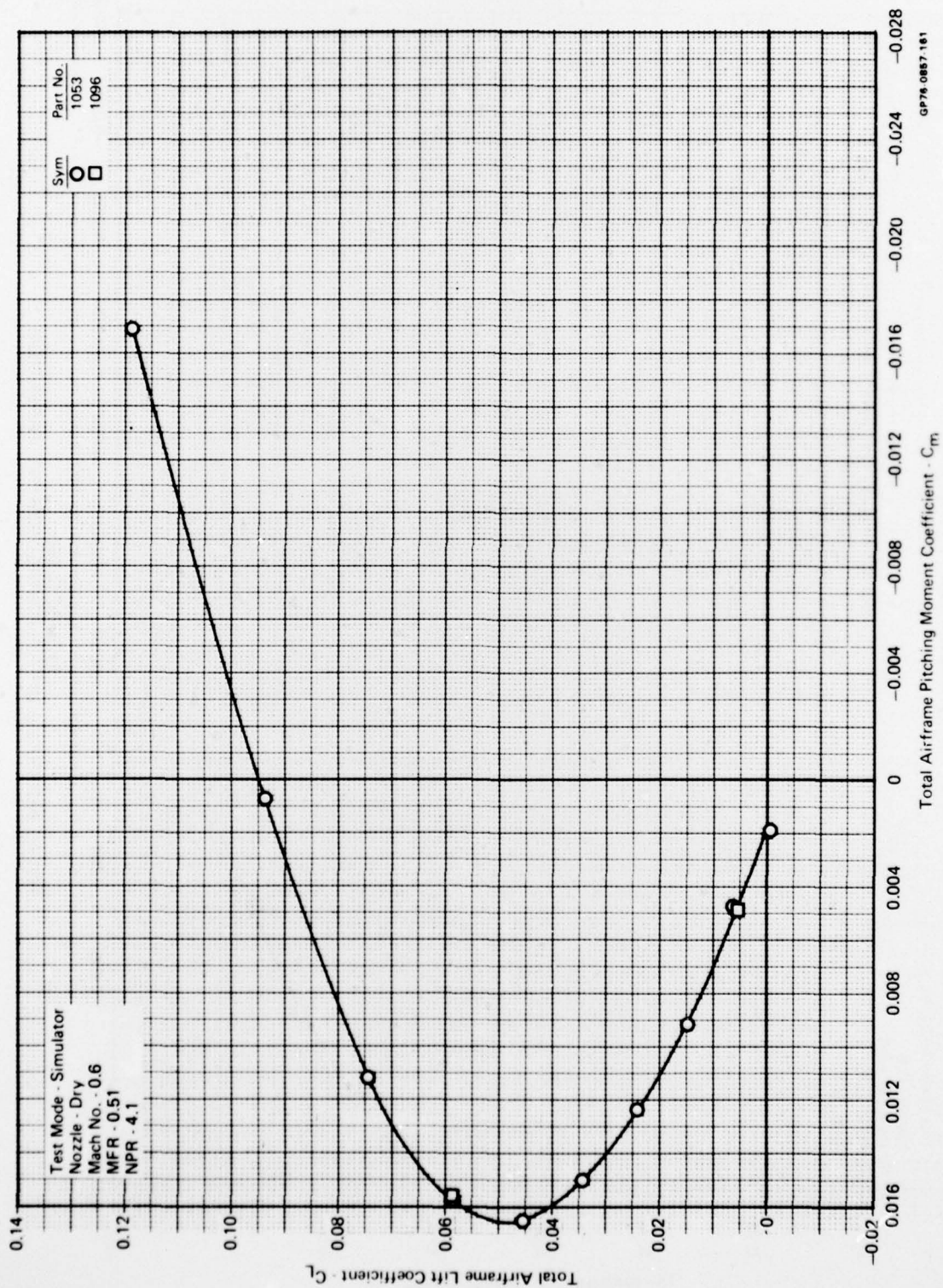
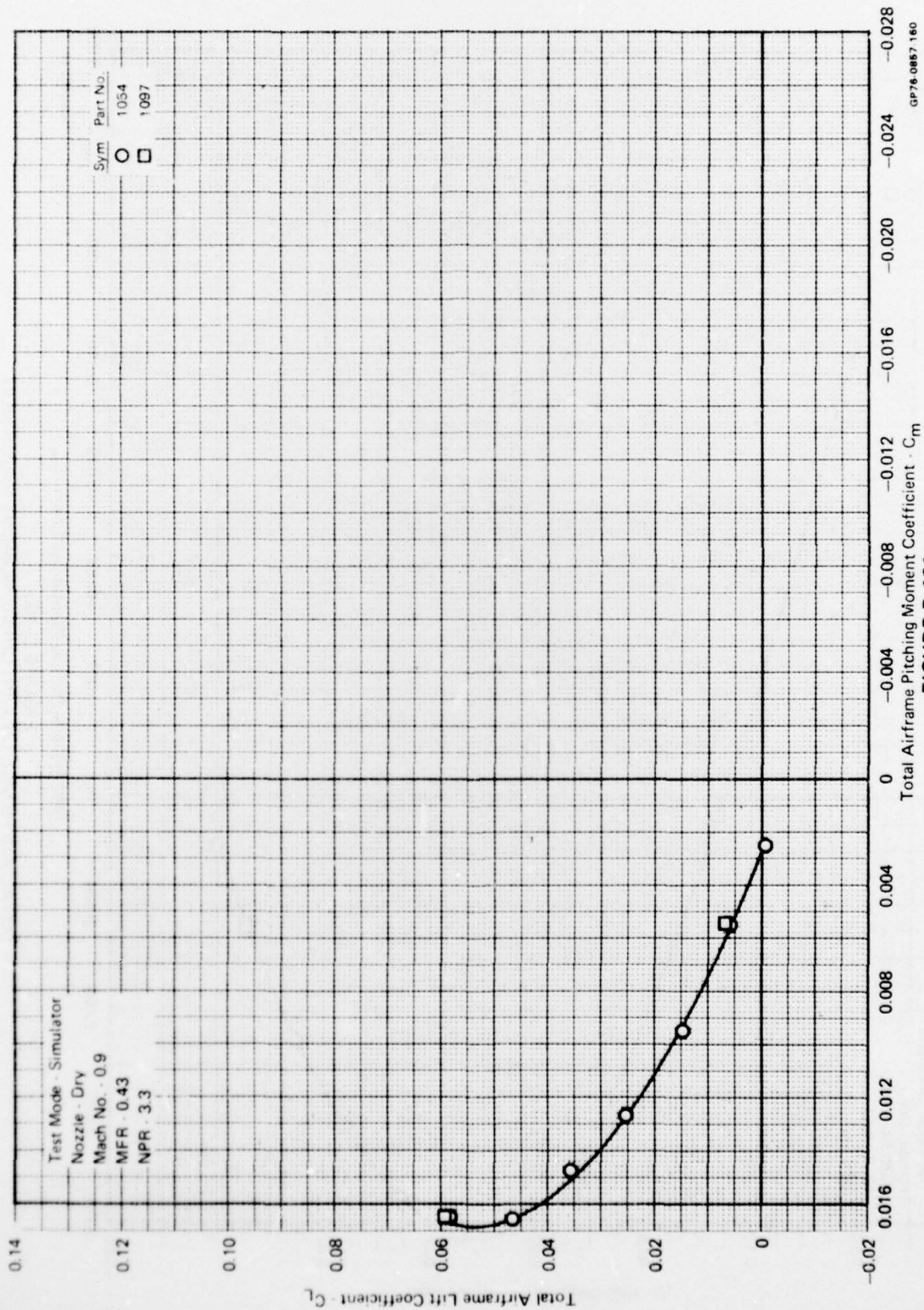


FIGURE D-163
TOTAL AIRFRAME LIFT/PITCHING MOMENT VARIATION



GP78-0887 160

FIGURE D-164
TOTAL AIRFRAME LIFT/PITCHING MOMENT VARIATION

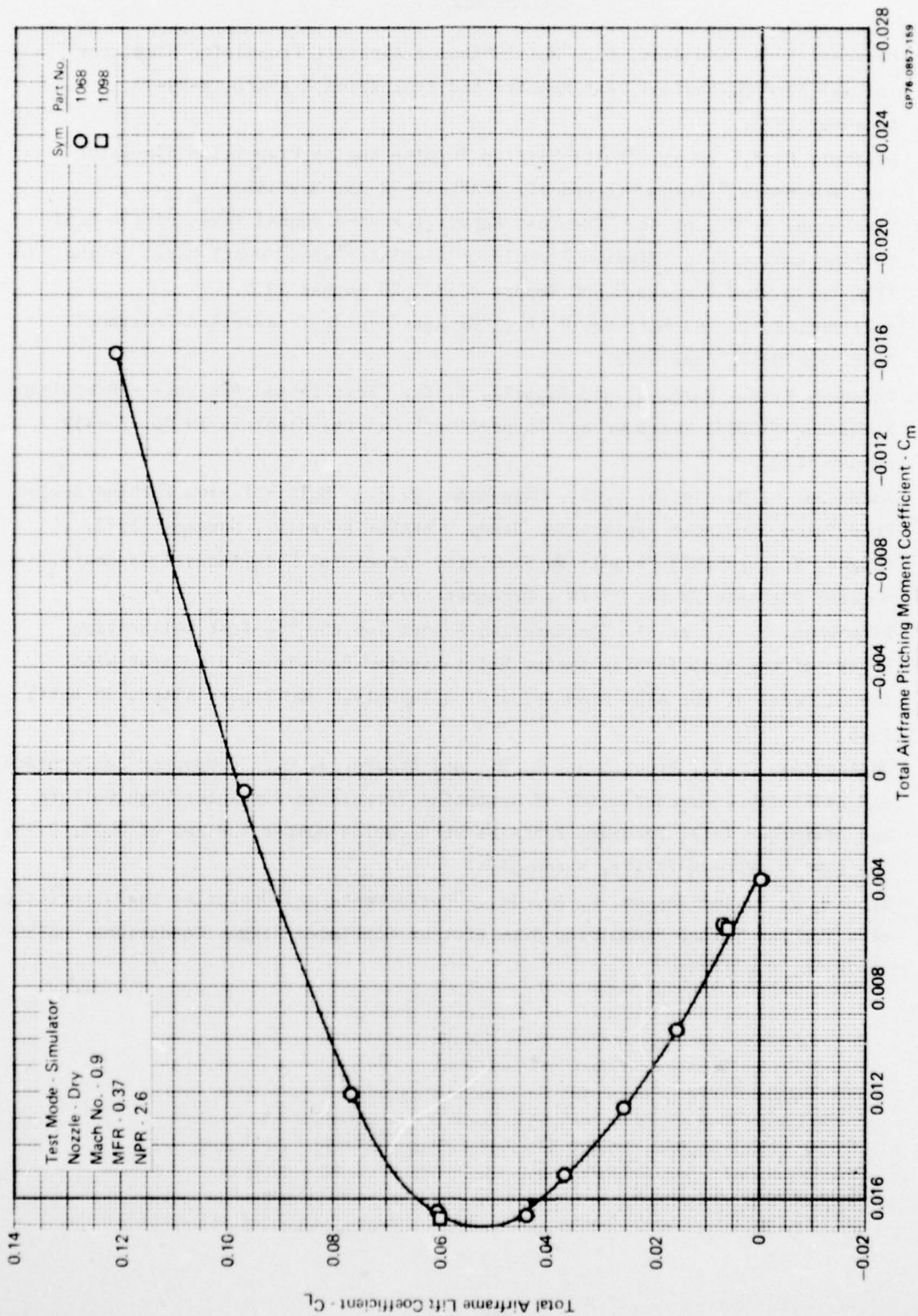


FIGURE D-165
TOTAL AIRFRAME LIFT/PITCHING MOMENT VARIATION

REFERENCES

1. Delaney, B. R. and West, H., "Multi-Mission Aircraft Propulsion Simulator Initial Aero/Mechanical Test Results and Evaluation," AFAPL-TR-73-77, December 1973.
2. Delaney, B. R., et al, "Multi-Mission Turbine Engine Propulsion Simulator User's Console," Volumes I and II, AFAPL-TR-73-25, May 1973.
3. Eigenmann, M. F., et al, "Pre-Test Report for Wind Tunnel Tests of the 8.5% Turbine Engine Multi-Mission Propulsion Simulator Wind Tunnel Model in the AEDC 16T/S Wind Tunnels," MDC Report A3582, 20 August 1975.
4. Anderson, R. D. and Martens, R. E., "Exhaust System Interaction Program," AFAPL-TR-73-57, June 1973.
5. Delaney, B. R., West, H. and Russell, T. E., "Results and Analysis - Propulsion Simulator SN002/2 Teardown and Inspection," General Electric TM No. 76-459, August 1976.
6. Anderson, R. M., Taich, M. S., Eigenmann, M. F., "Multi-Mission Turbine Engine Propulsion Simulator Application Study," AFAPL-TR-72-107, November 1972.
7. Knight, G. L., "XM2R Propulsion Simulator Structural Life Analysis Summary," General Electric TM No. 75-795, December 1975.
8. Eigenmann, M. F., et al, "Calibration Report for the Pre-Test Calibration Effort of the 8.5% Turbine Engine Multi-Mission Propulsion Simulator Wind Tunnel Model at the AEDC Propulsion Wind Tunnels," MDC Report A3466, 30 April 1975.
9. Darlington, C. R., Brookshank, R. M., and Brooks, J. O., "Component Performance and Stability Characteristics of an Engine Propulsion Simulator With Uniform and Distorted Inlet Pressure Profiles at Reynolds Number Indices of 0.39, 0.78, and 0.91," AEDC-TR-73-172, March 1974.
10. Brooks, J. O. and Wasson, R. A., Jr., "Performance and Operating Characteristics of a Turbine Engine Propulsion Simulator at Simulated Flight Conditions," AEDC-TR-76-76, May 1976.